# Università degli Studi di Ferrara

DOTTORATO DI RICERCA IN

SCIENZE DELL' INGEGNERIA

CICLO XXVIII

COORDINATORE Prof. STEFANO TRILLO

# A systematic approach for calibrating and validating the agro-hydrological SWAT model for policy support and decision making in large European River Basins

Settore Scientifico Disciplinare ICAR/02


**Dottorando**

Dott. Malago` Anna

_____

**Tutore**

Prof. Franchini Marco

_____

**Correlatore**

Bouraoui Faycal, PhD

_____


Anni 2013/2015

**Università degli Studi di Ferrara**
Engineering Department in Ferrara

**Dottorato di Ricerca in Scienze dell'Ingegneria, XXVIII ciclo**
Doctoral thesis in Engineering Science, XXVIII cycle

*Doctoral Program*: Engineering
*Curriculum:* Civil and Environmental Engineering
*Branch of study*: Environmental and Territorial Engineering
*Title*: A systematic approach for calibrating and validating the agro-hydrological SWAT model for policy support and decision making in large European River Basins

*Author*: Ing. Anna Malago'
*Supervisor*: Prof. Franchini Marco
*Co-advisor*: Faycal Bouraoui, PhD
Printed: March 2016

*PhD Coordinator:*
Prof. Stefano Trillo, Università degli Studi di Ferrara

*PhD Jury:*
Prof. Renato Sante OLIVITO, Università della Calabria (rs.olivito@unical.it)
Prof. Simone SECCHI, Università di Firenze (simone.secchi@unifi.it)
Prof. Giuseppe MANCINI, Università di Catania (gmancini@dica.unict.it)
Dr. Tommaso MORAMARCO, IRPI – CNR Perugia (t.moramarco@irpi.cnr.it)
Prof. Gabriele BITELLI, Università di Bologna, (gabriele.bitelli@unibo.it)

Supplementary members:
Prof. Antonino DI BELLA, Università di Padova (antonino.dibella@unipd.it)
Prof. Fabio CONTI, Università dell'Insubria (fabio.conti@uninsubria.it)
Prof. Marco FRANCHINI, Università di Ferrara (marco.franchini@unife.it)
Prof. Antonio TRALLI, Università di Ferrara (tra@unife.it)

# Contents

Contents ..... V

List of Figures ..... XI

List of Tables ..... XXIII

List of the abbreviations ..... XXVII

List of Scientific Publications (2013-2015) ..... XXIX

CHAPTER 1 ..... 31

1 Introduction ..... 31

CHAPTER 2 ..... 37

2 The SWAT Model, concepts data requirements and calibration ..... 37

2.1 Chapter Introduction ..... 37

2.2 SWAT model description: structure and processes ..... 38

2.2.1 SWAT structure ..... 38

2.2.2 The Hydrological component ..... 41

2.2.3 Crop management and the Best Management Practices (BMPs) ..... 43

2.2.4 The Qualitative component ..... 45

2.2.5 The Sediment component ..... 50

2.3 The SWAT model executable and its modifications ..... 52

2.3.1 The new outputs ..... 53

2.3.2 The new hillslope length algorithm ..... 53

2.3.3 Modification of the MUSLE equation ..... 54

2.3.4 The representation of karst process ..... 55

2.4 Calibration and Validation (C/V): an innovative approach ..... 57

2.4.1 The key aspects of the model setup and the simulation period ..... 59

2.4.2 Calibration of crop yields ..... 60

2.4.3 The calibration of streamflow and its components ..... 61

2.4.4 Calibration of sediments ..... 66

2.4.5 Calibration of nutrients ..... 67

2.4.6 Performance indicators ..... 67

CHAPTER 3 ..... 69

3 Hydrological SWAT applications, sensitivity analysis at different spatial scales and modifications ..... 69

3.1 Chapter description ..... 69

3.2 Iberian and Baltic peninsula: SWAT calibration and validation at different climate regimes ..... 70

3.2.1 Synopsis ..... 70

3.2.2 The study area ..... 70

3.2.3 The performance of the calibration datasets ..... 71

3.2.4 The performance after the regionalization approach ..... 74

3.2.5 Sensitivity analysis of step-wise calibration ..... 76

3.2.6 Spatial variability of parameters of the NOP ..... 77

3.2.7 Conclusions of section ..... 81

3.3 The Danube basin: validation of the water balance trough the Budyko approach 82

3.3.1 Synopsis ..... 82

3.3.2 The study area ..... 83

3.3.3 Summary of Danube SWAT Model setup and the C/V results of monthly streamflow in the Danube ..... 87

3.3.4 The aridity index in the Danube River Basins ..... 89

3.3.5 The diagnosis of evapotranspiration and baseflow ..... 92

3.3.6 The n and m coefficient in the water management regions ..... 95

3.3.7 The impact of anthropogenic activities ..... 99

3.3.8 The final water balance of Danube River Basins ..... 102

3.3.9 Conclusions of the section ..... 106

3.4 The Upper Danube: sensitivity analysis of the SWAT model with respect to the hillslope length parameter and DEM pixel size ..... 107

3.4.1 Synopsis ..... 107

3.4.2 The study area ..... 108

3.4.3 DEM derivatives of the six DEML configurations....110
3.4.4 Results of model calibration and validation....112
3.4.5 Analysis of behavioral parameter sets....116
3.4.6 Impact of hillslope length on streamflow components....120
3.4.7 Impact of hillslope length on water yield predictions at different spatial and temporal scales....122
3.4.8 Impact of hillslope length on water balance....124
3.4.9 The recommended DEML configurations....126
3.4.10 Conclusions of section....127
3.5 Crete Island: how to represent the karst phenomena using the SWAT model..129
3.5.1 Synopsis....129
3.5.2 The study area....130
3.5.3 The karst geology and hydrology of island of Crete....131
3.5.4 Streamflow and springs measurements....132
3.5.5 The application of KSWAT in Crete Island....133
3.5.6 Hydrological simulation....135
3.5.7 The estimated recharge areas of karst springs....141
3.5.8 Spatial and temporal variation of hydrological components in Crete....142
3.5.9 The estimated water balance of Crete....145
3.5.10 Conclusions of section....148
CHAPTER 4....149
4 Water quality and sediment modeling....149
4.1 Chapter Introduction....149
4.2 Nutrients representation: a case study applied to the Danube River Basin....149
4.2.1 Synopsis....149
4.2.2 The Danube River Basin SWAT model: the nutrients setup....151
4.2.3 Analysis of river concentrations and loads....157
4.2.4 The sensitivity analysis of nutrients parameters....162
4.2.5 The calibration of crop yields....167

4.2.6 The calibration of denitrification process ..... 169
4.2.7 Results of calibration and evaluation of nutrients ..... 175
4.2.8 The long-term annual nutrients balance of the Danube River Basin ..... 194
4.2.9 Conclusions of the section ..... 196
4.3 Sediment yields representation: a case study applied to the Upper Danube river 197
4.3.1 Synopsis ..... 197
4.3.2 Sensitivity analysis and parametrization ..... 198
4.3.3 Topography settings ..... 200
4.3.4 The calibration of Gross Erosion (GE) ..... 201
4.3.5 Calibration and validation of suspended sediment concentration (SSC) ..... 203
4.3.6 Evaluation of specific sediment yields (RSSY) ..... 204
4.3.7 Best configuration ..... 205
4.3.8 Sediment balance in the Upper Danube ..... 208
4.3.9 Conclusions of the section ..... 208
4.4 Balancing environmental advantages with investment costs: a multi-objective approach ..... 209
4.4.1 Synopsis ..... 209
4.4.2 The multi-objective optimization tool ..... 210
4.4.3 Conclusions of the section ..... 212
CHAPTER 5 ..... 215
5 Benchmarking ..... 215
5.1 Chapter Introduction ..... 215
5.2 Comparing SWAT performances with other models of different structure with reference to a real case: the Danube River Basin. ..... 216
5.2.1 Scope and approach of the inter-comparison ..... 216
5.2.2 Streamflow comparison ..... 219
5.2.3 Total Nitrogen comparison ..... 225
5.2.4 Total Phosphorous comparison ..... 230

5.2.5 Conclusions of the section ....236
CHAPTER 6 ....241
6 Conclusion ....241
Appendix....249
A1. Summary of the main input data used in the different SWAT applications ....249
A2. Summary of model discretization and hard data ....250
A3. Table of BMPs applied in the Danube SWAT model ....254
A4. Budyko framework ....255
A5. R-SWAT-DM model ....258
A6. Benchmarking modelling approach: some details ....262
Bibliography ....265
Acknowledgements....289

# List of Figures

FIGURE 1. CONCEPTUAL SWAT MODEL WATER BALANCE: P: PRECIPITATION; ET, EVAPOTRANSPIRATION; BF, BASEFLOW FROM SHALLOW AQUIFER; $BF_{DA}$, BASEFLOW FROM DEEP AQUIFER; INF, INFILTRATION IN THE SOIL; LF, LATERAL FLOW; SR, SURFACE RUNOFF; $DA_{RCHRG}$, THE DEEP AQUIFER RECHARGE; $GW_{RCHRG}$, THE SHALLOW AQUIFER RECHARGE; WYLD: WATER YIELD. ..... 41

FIGURE 2. CONCEPTUAL SWAT MODEL NUTRIENT BALANCE: DS: DIFFUSE SOURCES; PS: POINT SOURCES; $PLANT_{YR}$: NUTRIENTS REMOVED WITH PLANT YIELD; LEACH: NUTRIENTS LEACHING IN THE SHALLOW AQUIFER; DE: DIFFUSE EMISSIONS; $DE_{RF}$: DIFFUSE EMISSION AFTER THE RIPARIAN FILTERING REDUCTION; LOADS: NUTRIENTS LOADS IN THE OUTPUT OF THE BASIN. 46

FIGURE 3. CONCEPTUAL SWAT MODEL NITROGEN BALANCE: THE DIFFUSION SOURCES ARE REPRESENTED BY THE SUM OF NITROGEN APPLIED TO THE PLANT BIOMASS VIA FIXATION ($N_{FIX}$), NITROGEN TRANSPORTED TO THE SOIL WITH THE PRECIPITATION ($N_{RAIN}$) AND THE NITROGEN APPLIED AS FERTILIZER ($N_{APP}$); $N_{PS}$ IS THE NITROGEN LOADING TO THE REACH FROM POINT SOURCES; THE DIFFUSION EMISSIONS ARE THE NITRATES LOADING TO REACH IN TILE DRAINAGE SYSTEM (NTILE), IN LATERAL FLOW (LFN), IN SURFACE RUNOFF (SRN), IN BASEFLOW (BFN) AND THE ORGANIC NITROGEN TRANSPORTED WITH THE WATER YIELD (ORGN); $ORGN_{RF}$ AND $SR_{RF}$ ARE RESPECTIVELY THE ORGANIC NITROGEN AND NITRATES REDUCED BY RIPARIAN FILTERING; $N_{LEACH}$ IS THE NITROGEN LEACHED TO AQUIFER; $N_{PYR}$, $N_{SOILR}$, $N_{AQ}$, $N_{RF}$ AND $N_{RIVERR}$ ARE RESPECTIVELY THE REDUCTION OF NITROGEN APPLIED BY PLANT, SOIL, AQUIFER, RIPARIAN FILTER STRIP AND RIVER; $N_{LOAD}$ IS THE TOTAL NITROGEN LOADS AT THE OUTLET OF THE BASIN. ..... 49

FIGURE 4. CONCEPTUAL SWAT MODEL PHOSPHOROUS BALANCE: THE DIFFUSION SOURCES ARE REPRESENTED BY PHOSPHOROUS APPLIED AS FERTILIZER ($P_{APP}$); $P_{PS}$ IS THE PHOSPHOROUS LOADING TO THE REACH FROM POINT SOURCES; THE DIFFUSION EMISSIONS ARE THE SOLUBLE PHOSPHOROUS (PHOSPHATE) TRANSPORTED IN TILE DRAINAGE SYSTEM (PTILE) AND WATER YIELD (SOLP), THE ORGANIC PHOSPHOROUS LOADING TO THE REACH (ORGP) AND THE MINERAL PHOSPHOROUS ADSORBED TO SEDIMENT AND TRANSPORTED INTO THE REACH ($SEDP_{RF}$); $SOLP_{RF}$, $ORGN_{RF}$ AND $SEDP_{RF}$ ARE RESPECTIVELY THE SOLUBLE, ORGANIC AND MINERAL PHOSPHOROUS REDUCED BY RIPARIAN FILTERING; $P_{PYR}$, $P_{SOILR}$, $P_{RF}$ AND $P_{RIVERR}$ ARE RESPECTIVELY THE REDUCTION OF PHOSPHOROUS APPLIED BY PLANT, SOIL, RIPARIAN FILTER STRIP AND RIVER; $P_{LOAD}$ IS THE TOTAL NITROGEN LOADS AT THE OUTLET OF THE BASIN. ..... 49

FIGURE 5. CONCEPTUAL SWAT MODEL SEDIMENT BALANCE: THE SOURCES OF EROSION ARE REPRESENTED BY THE HILLSLOPE EROSION FROM DIFFERENT LAND COVER AND THE STREAM EROSION; THE SINKS OF SEDIMENTS DERIVED FROM DEPOSITION IN STREAM AND FLOODPLAIN, AS WELL AS FROM TRAPPING PROCESS IN RESERVOIRS. THE SY (SEDIMENT YIELD) IS ALSO FURTHER AFFECTED BY THE PRESENCE OF RIPARIAN FILTER STRIPS THAT REMOVE SEDIMENT THROUGH THE REDUCTION OF THE RUNOFF VELOCITY. $SY_{RF}$ IS THE SEDIMENT YIELDS AFFECTED BY RIPARIAN FILTER STRIPS. ..... 52

FIGURE 6. KARST SWAT MODEL CONFIGURATION (KSWAT MODEL) AS COMBINATION OF THE ADAPTED SWAT MODEL LINKED WITH THE KARST-FLOW MODEL, WHERE: ET, EVAPOTRANSPIRATION; INF, INFILTRATION; TLOSS, TRIBUTARY STREAM LOSSES; SR, SURFACE RUNOFF; TWLWET, LOSSES FROM THE BED OF WETLANDS; $DA_{RCHRG}$, AMOUNT OF DIRECT RECHARGE OF DEEP AQUIFER FROM SEVERAL SUBBASINS (INLET OF THE KARST-FLOW MODEL); A1, FRACTION OF $DA_{RCHRG}$ TO THE UPPER RESERVOIR; A2, FRACTION OF FLOW FROM UPPER TO LOWER RESERVOIR; Q1, OUTLET OF UPPER RESERVOIR; Q2, OUTLET OF LOWER RESERVOIR; $Q_K$, CALIBRATED SPRING'S DISCHARGE; $SR_N$, SURFACE RUNOFF EXCLUDING TLOSS AND TWLWET. ..... 56

FIGURE 7. STRATEGIC C/V APPROACH USING THE SWAT MODEL ..... 58

Figure 8. Example of comparison between simulated (Sim.yields) and observed (Obs.yields) yields for wheat in the Upper Danube Basin. The dot line represents the simulated biomass (Sim.biomass), while the bar plots represent the annual precipitation in mm. These help understanding the reliability of simulated yields. For instance, in year 2003 simulated yields and biomass decrease in accordance with the extreme climate condition (drought), and generally the annual variation of simulated values follows that of the observations. ..... 60
Figure 9. Step-wise calibration approach. NOP: near optimal parameter set; Q: streamflow ($m^3/s$); SR, surface runoff ($m^3/s$); LF: lateral ($m^3/s$). See Table 2 for parameters explanation. ..... 63
Figure 10. Map of the Iberian Peninsula (left) and Scandinavian Peninsula (right) along with the calibration subbasins: #81 in Iberian Peninsula and #61 in Scandinavia (# number of gauging stations) ..... 70
Figure 11. Cumulative frequency curves for NSE and $br^2$ before (DEF) and after the step-wise calibration (CAL). ..... 71
Figure 12. $br^2$ coefficient obtained for each subbasin comparing the simulated and monthly components of the streamflow (a: surface runoff; b: lateral flow; c: baseflow) in Scandinavia during the step-wise calibration. ..... 72
Figure 13. Box-and-whisker plots of $br^2$ obtained comparing the simulated and monthly components of the streamflow for each step of calibration and for each components of the streamflow. a) surface runoff performance in each step; b) lateral flow performance in each step; c) baseflow performance in each step. ..... 73
Figure 14. Cumulative frequency curves for NSE and $br^2$ before (DEF), after the step-wise calibration (CAL) and the results for the traditional calibration (TRAD). ..... 73
Figure 15. Cumulative frequency curves for NSE and br2 before (DEF) and after the validation (VAL) ..... 74
Figure 16. $br^2$ coefficient after regionalization in 215 and 346 monitoring points respectively for Iberian Peninsula (left) and Scandinavia (right). DEF is the run with default parameters; EXT is the run with transposed parameters (Validation) ..... 75
Figure 17. NSE coefficient after regionalization in 215 and 346 monitoring points respectively for Iberian Peninsula (left) and Scandinavia (right). DEF is the run with default parameters; EXT is the run with transposed parameters (Validation) ..... 75
Figure 18. Box-and-whisker plots of objective functions ($r^2$ and $br^2$) for each calibration step for Scandinavia (left) and Iberian Peninsula (right) ..... 77
Figure 19. Box-and-whisker plots of behavioral Near Optimal Parameter sets from calibrated subbasins. The "abs value/factor/coefficient" represents he absolute value for adimensional parameter, "rate value" represents the increment/decrement for which the absolute value is increased (positive rate) or decrease (negative rate). ..... 79
Figure 20. Map of the spatial variation of Near Optimal Parameters values for the Iberian and Scandinavian Peninsulas considering only the sensitive subbasin for each step of calibration. ..... 80
Figure 21. The Danube River Basin. Description of altitude and identification of the three main part of the Danube (Upper, Middle and Lower Danube). Sources: Tockner et al. (2009) ..... 84

FIGURE 22. MAP OF THE 18 WATER MANAGEMENT REGIONS IN THE DANUBE BASIN: 1 = DANUBE SOURCE; 2 = INN; 3 = AUSTRIAN DANUBE; 4 = MORAVA; 5 = VAH-HRON-IPEL; 6 = PANNONIAN DANUBE; 7 = DRAVA; 8 = SAVA; 9 = TISA; 10 = VELIKA MORAVA; 11 = MIDDLE DANUBE; 12 =JIU ; 13 =OLT; 14 =ARGES VEDEA; 15 =SILISTRA DANUBE; 16 =BUZAU-IALOMITA; 17 = SIRET-PRUT; 18= DELTA. ..... 86
FIGURE 23. COMPARISON BETWEEN MONTHLY OBSERVED AND SIMULATED HYDROGRAPHS AT THE OUTLETS OF THE WHOLE DANUBE (DELTA, REGION 18), THE MIDDLE DANUBE (REGION 11), THE PANNONIA DANUBE (REGION 6) AND AUSTRIAN DANUBE (REGION 3). ..... 89
FIGURE 24. MAP OF LONG-TERM MEAN ANNUAL PRECIPITATION (PERIOD 1995-2009) IN THE DANUBE RIVER BASIN. ..... 90
FIGURE 25. MAP OF LONG-TERM MEAN ANNUAL POTENTIAL EVAPOTRANSPIRATION (PERIOD 1995-2009) IN THE DANUBE RIVER BASIN. ..... 91
FIGURE 26. MAP OF THE ARIDITY INDEX (AI=PET/P, PET=POTENTIAL EVAPOTRANSPIRATION, P=PRECIPITATION) IN THE DANUBE RIVER BASIN. ..... 91
FIGURE 27. BUDYKO DRIAGRAMS AND CURVES (BC) OBTAINED USING OBSERVATIONS (A) AND SIMULATED VALUES (B) AT 418 GAUGING STATIONS. IN (C) THE BC CONSIDERING ALL SUBBASINS IN THE DANUBE RIVER BASIN. EI IS THE EVAPORATIVE INDEX, BFI IS THE BASEFLOW INDEX AND AI THE ARIDITY INDEX; N AND M ARE THE COEFFICIENT OF BYDYKO-TYPE CURVES RESPECTIVELY RELATED TO EI AND BFI. THE ABBREVIATION "OBS" AND "SIM" REFER TO OBSERVATION AND SIMULATION RESPECTIVELY. ..... 93
FIGURE 28. BUDYKO DIAGRAMS OF ALL SUBBASINS IN THE DANUBE RIVER BASIN AND THE BYDYKO CURVES OBTAINED USING THE OBSERVATION IN 418 GAUGING STATIONS (N=18 AND M=3.8) (SEE ALSO FIGURE 27 A). THE SUBBASINS ARE CLASSIFIED BY ELEVATION (A), SLOPE (B), PRECIPITATION (C), AND PERCENTAGE OF AREA COVERED BY CROP LAND IN EACH SUBBASIN. .. 95
FIGURE 29. THE RELATIONSHIP BETWEEN N AND M COEFFICIENTS OF BUDYKO-TYPE CURVES OBTAINED FOR EACH WATER MANAGEMENT REGIONS WITH RESPECT TO THE COEFFICIENT VALUE OF THE OBSERVED BUDYKO CURVE (N=1.8, M=3.8) (A); IN (B) AND (C) THE SPATIAL DISTRIBUTION OF COEFFICIENTS IN THE WATER MANAGEMENT REGIONS. IN (A) THE REGION 2 (INN RIVER BASIN) IS OMITTED SINCE THE M COEFFICIENT IS LARGER THAN 20. ..... 97
FIGURE 30. BUDYKO CURVE FROM OBSERVATION (N=1.8) WITH POINTS REPRESENTING THE 18 WATER MANAGEMENT REGIONS. LARGE AND LIGHT BLUE CIRCLES DENOTE THE LARGEST REGIONS AND SMALL BLUE CIRCLES DENOTE THE SMALLEST REGIONS. ..... 98
FIGURE 31. COMPLEMENTARY BUDYKO CURVE FROM OBSERVATION (M=3.8) WITH POINTS REPRESENTING THE 18 WATER MANAGEMENT REGIONS. LARGE AND LIGHT BLUE CIRCLES DENOTE THE LARGEST REGIONS AND SMALL BLUE CIRCLES DENOTE THE SMALLEST REGIONS. ..... 98
FIGURE 32. THE INTERPRETATION OF THE RELATIONSHIP BETWEEN N AND M COEFFICIENTS OF BUDYKO-TYPE CURVES OBTAINED FOR EACH WATER MANAGEMENT REGION WITH RESPECT TO THE COEFFICIENT VALUES OF THE OBSERVED BUDYKO CURVE (N=1.8, M=3.8). ..... 99
FIGURE 33. COMPLEMENTARY BUDYKO CURVE FROM OBSERVATION (M=1.8) WITH POINTS REPRESENTING THE 18 WATER MANAGEMENT REGIONS. LARGE AND LIGHT BLUE CIRCLES DENOTE THE LARGEST REGIONS AND SMALL BLUE CIRCLES DENOTE THE SMALLEST REGIONS. THE HALLOW CIRCLES REPRESENT THE WATER MANAGEMENT REGIONS WHEN THE ANTHROPOGENIC STORAGE WHERE CONSIDERED IN THE MODEL. ..... 100
FIGURE 34. THE INN SOURCES AND THE ANTHROPOGENIC IMPACTS. ..... 101

FIGURE 35. OBSERVED (A) AND SIMULATED (B) MONTHLY TIME SERIES AT THE INN SOURCES (A) AT TARASP, IN SCHOLKHOF TRIBUTARY OF INN BEFORE THE INN AT KAJETSNSBRUCK. IN EVIDENCE THE IMPACT OF MARTINA PLANT ON THE OBSERVED STREAMFLOW AT KAJETSNSBRUCK. ..... 102
FIGURE 36. THE LONG-TERM ANNUAL WATER BALANCE FOR THE DANUBE RIVER BASIN AS SIMULATED WITH SWAT FOR THE PERIOD 1995-2009. AS EXPLAINED IN FIGURE 1 : P: PRECIPITATION; ET, EVAPOTRANSPIRATION; BF, BASEFLOW FROM SHALLOW AQUIFER; INF, INFILTRATION IN THE SOIL; LF, LATERAL FLOW; SR, SURFACE RUNOFF; $DA_{RCHRG}$, THE DEEP AQUIFER RECHARGE; $GW_{RCHRG}$, THE SHALLOW AQUIFER RECHARGE; WYLD: WATER YIELD. ..... 103
FIGURE 37. OVERVIEW OF THE UPPER DANUBE BASIN WITH LOCATION OF GAUGING STATIONS USED FOR MODEL CALIBRATION (#98 FOR PERIOD 1995-2006) AND VALIDATION (#150 FOR PERIOD 1995-2009). THE MONITORING STATIONS FOR CALIBRATION WERE INCLUDED IN THE MONITORING STATIONS USED FOR VALIDATION EXTENDED THE PERIOD OF SIMULATION FROM YEAR 2006 TO 2009. THE BACKGROUND IN SCALE OF GREY COLORS INDICATES THE ELEVATION (METERS) FROM DEM100. DANUBE RIVER AND TWO OF ITS MAIN TRIBUTARIES (INN AND MORAVA) ARE HIGHLIGHTED. THE MAIN TOWNS ARE SHOWN AS WELL. THE SYMBOL # REPRESENTS THE NUMBER OF STATIONS. ..... 110
FIGURE 38. SUBBASIN MAIN DEM DERIVATIVES IN THE SWAT CONFIGURATIONS. (A) ELEVATION (M) IN THE 100 M DEM PIXEL SIZE (DEM100) IN RELATION TO 25 M DEM PIXEL SIZE (DEM25); (B) SLOPE (%) IN THE DEM100 IN RELATION TO DEM25; HILLSLOPE LENGTH (M) OF THE DEM CONFIGURATIONS OF TABLE 7 IN RELATION TO SLOPE (%) (C) AND ELEVATION (M) (D). ..... 111
FIGURE 39. BOX-AND-WHISKER PLOTS OF PERCENTAGE RESIDUALS BETWEEN SIMULATED AND OBSERVED STREAMFLOW OF THE SIX DEML CONFIGURATIONS ANALYZED IN THIS STUDY (SEE TABLE 7) FOR THE CALIBRATION (A) AND VALIDATION (B) DATASET. THE SYMBOL # REPRESENTS THE NUMBER OF STATIONS IN THE CALIBRATION AND VALIDATION DATASETS. THE CONTINUOUS GREY LINES INDICATE THE MAXIMUM 75% AND 25% ACROSS THE SIX DEML CONFIGURATIONS; THE DASHED GREY LINE REPRESENTS THE ABSENCE OF RESIDUALS. ..... 114
FIGURE 40. PERCENT BIAS (PBIAS) OF MONTHLY STREAMFLOW OF CONFIGURATION 25L2 AT THE 150 GAUGING STATIONS (1995-2009). THE LETTERS A–B INDICATE THE LOCATION OF TWO STATIONS FOR WHICH TIME-SERIES SIMULATIONS ARE PROVIDED IN FIGURE 41 AND FIGURE 42. ..... 115
FIGURE 41 COMPARISON OF SWAT OUTPUTS FOR 25L2 (GREY LINES) WITH OBSERVATIONS (BLACK LINES) AT TWO SELECTED MONITORING GAUGING STATIONS (LOCATIONS A SHOWN IN FIGURE 40). A: OUTLET OF UPPER DANUBE BASIN AT MEDVEDOV (SLOVAKIA) ON DANUBE RIVER. ..... 115
FIGURE 42. COMPARISON OF SWAT OUTPUTS FOR 25L2 (GREY LINES) WITH OBSERVATIONS (BLACK LINES) AT TWO SELECTED MONITORING GAUGING STATIONS (LOCATIONS B SHOWN IN FIGURE 40). B: INN RIVER AT PASSAU-INGLING (GERMANY). ..... 116
FIGURE 43. BOX-AND-WHISKER PLOTS OF BEHAVIORAL NEAR OPTIMAL PARAMETER SETS FROM "DONORS" SUBBASINS. THE NUMBERS IN THE SQUARE BRACKETS INDICATE THE STEP-WISE HYDROLOGICAL PROCESS OF CALIBRATION: [1] SNOW PROCESS, [2] SURFACE RUNOFF, [3] LATERAL FLOW, AND [4] BASEFLOW. THE "ABS VALUE/FACTOR" REPRESENTS THE ABSOLUTE VALUE FOR ADIMENSIONAL PARAMETER; "RATE VALUE" REPRESENTS THE INCREMENT/DECREMENT FOR WHICH THE ABSOLUTE VALUE IS INCREASED (POSITIVE RATE) OR DECREASED (NEGATIVE RATE). ..... 119
FIGURE 44. BOX-AND-WHISKER PLOTS OF SIMULATED AND OBSERVED STREAMFLOW SURFACE RUNOFF (SR), LATERAL FLOW (LF) AND BASEFLOW (BF) FOR CALIBRATED MONITORING POINTS (#98; PERIOD 1995-2006). THE CONTINUOUS GREY LINES INDICATE THE 75% AND 25% OF OBSERVATIONS. NOTE THE VARYING RANGES OF THE Y AXIS. ..... 120

FIGURE 45. BOX-AND-WHISKER PLOTS OF RESIDUALS BETWEEN SIMULATED AND OBSERVED LATERAL FLOW (LF) FOR CALIBRATED MONITORING POINTS (#98; PERIOD 1995-2006) WITH RESPECT TO THREE CLASSES OF ELEVATIONS: 0-500 M (#28 MONITORING POINTS), 500-1000 M (#48 MONITORING POINTS) AND >1000 M (#22 MONITORING POINTS)..... 122
FIGURE 46. LONG-TERM MEAN ANNUAL (A, C, E, G) AND MONTHLY (B, D, F, G) SURFACE RUNOFF (SR), LATERAL FLOW (LF), BASEFLOW (BF) AND WATER YIELD (WYLD, ALL IN MM) GENERATED IN ALL 822 HRUS IN THE SIX DEML CONFIGURATIONS (SEE TABLE 7) FOR THE PERIOD 1995-2009. THE GREY BAND REPRESENTS THE INTERQUARTILE OF OBSERVED GAUGING STATIONS FROM CALIBRATION DATASET EXTENDED THE PERIOD TO 2009. NOTE THE VARYING RANGES OF THE Y AXIS. .. 123
FIGURE 47. BAR PLOTS OF MEAN ANNUAL WATER BALANCE PARTITIONING. IN (A, C, E) WATER BALANCE COMPONENTS: EVAPOTRANSPIRATION (ET, %) AND WATER YIELD (WYLD, %) (PCP IS THE TOTAL PRECIPITATION AS SUM OF ET AND WYLD). IN (B, D, F) WATER YIELD COMPONENTS: SURFACE RUNOFF (SR, %), LATERAL FLOW (LF, %) AND BASEFLOW. 125
FIGURE 48. MAP OF PREFECTURES (A); THE MAIN CARBONATE ROCKS OF CRETE (KARST AREAS FROM GEOLOGICAL MAP) WITH SPRINGS AND STREAMFLOW GAUGING STATIONS (B) A, WHITE MOUNTAINOUS; B, IDI; C, DIKTI; D, SITIA; MAP OF THE MAIN RIVER BASINS (C)..... 132
FIGURE 49. RIVERS AND SUBBASINS (A); DEFINITION OF KARST GEOLOGICAL FEATURES: KARST AREAS FROM GEOLOGICAL MAP (B) AND THE SUBBASINS WITH KARST SOILS (KARST SUBBASINS) (C). ..... 134
FIGURE 50. SOME EXAMPLES, COMPARISON BETWEEN MONTHLY SIMULATED AND OBSERVED STREAMFLOW VALUES FROM 1983 TO 2009 AFTER THE ALLOCATION OF SPRINGS IN THE SWAT MODEL..... 137
FIGURE 51. SOME EXAMPLES, COMPARISON BETWEEN DAILY SIMULATED AND OBSERVED SPRING'S VALUES FROM 1983 TO 2009 (MONTHLY COMPARISON FOR SP54). ..... 138
FIGURE 52. EXAMPLES OF ESTIMATED KARST RECHARGE AREA OF SELECTED SPRINGS. ..... 141
FIGURE 53. MAPS OF MONTHLY VARIATIONS OF PRECIPITATION, EVAPOTRANSPIRATION AND THE DEEP AQUIFER RECHARGE ($MM^3$/MONTH). ..... 144
FIGURE 54. ANNUAL WATER BALANCE IN DIFFERENT HYDROLOGICAL CONDITIONS (IN PERCENTAGE), AVERAGE OF 27 YEARS (TOTAL VOLUME OF PRECIPITATION 6370 $MM^3$/Y), NORMAL YEAR (TOTAL VOLUME OF PRECIPITATION 6400 $MM^3$/Y), DRY YEAR (TOTAL VOLUME OF PRECIPITATION 3700 $MM^3$/Y) AND WET YEAR (TOTAL VOLUME OF PRECIPITATION 9600 $MM^3$/Y). ET, EVAPOTRANSPIRATION; $SR_N$, SURFACE RUNOFF EXCLUDING LOSSES FROM TRIBUTARIES AND WETLANDS; LF, LATERAL FLOW; BF BASEFLOW; $DA_{RCHRGN}$, AMOUNT OF WATER RECHARGE IN THE DEEP AQUIFER WITHOUT THE CONTRIBUTION FOR SPRINGS THAT DISCHARGE INSIDE (QKIN) AND OUTSIDE (QKOUT) CRETE WATERSHED; SA, SHALLOW AQUIFER STORAGE. ..... 145
FIGURE 55. ANNUAL WATER BALANCE SCHEMATIZATION IN DIFFERENT HYDROLOGICAL CONDITIONS, DRY (A), NORMAL (B) AND WET (C) YEAR. ET, EVAPOTRANSPIRATION; INF, INFILTRATION IN THE SOIL; $SR_N$, SURFACE RUNOFF EXCLUDING THE LOSSES FROM TRIBUTARIES AND WETLANDS; LF, LATERAL FLOW; BF, BASEFLOW; $DA_{RCHRGN}$, AMOUNT OF WATER RECHARGE IN THE DEEP AQUIFER WITHOUT THE CONTRIBUTION FOR SPRINGS THAT DISCHARGE INSIDE (QKIN) AND OUTSIDE (QKOUT) CRETE; $WYLD_K$, FRESHWATER CONTRIBUTION; SA, SHALLOW AQUIFER STORAGE..... 147
FIGURE 56. SPATIAL DISTRIBUTION OF LAND COVER IN SWAT IN THE DANUBE RIVER BASIN. ..... 152
FIGURE 57. SPATIAL DISTRIBUTION OF TOTAL NITROGEN APPLIED AS FERTILIZER IN THE DANUBE RIVER BASIN..... 154
FIGURE 58. SPATIAL DISTRIBUTION OF TOTAL PHOSPHOROUS APPLIED AS FERTILIZER IN THE DANUBE RIVER BASIN. ..... 154
FIGURE 59.SPATIAL DISTRIBUTION OF FIXED NITROGEN BY PLANTS IN THE DANUBE RIVER BASIN. ..... 155

FIGURE 60. SPATIAL DISTRIBUTION OF NITROGEN APPLIED TO SOIL FROM ATMOSPHERIC DEPOSITION IN THE DANUBE RIVER BASIN. .....155
FIGURE 61. SPATIAL DISTRIBUTION OF TOTAL NITROGEN DISCHARGED IN THE RIVER NETWORK FROM POINT SOURCES. .....156
FIGURE 62. SPATIAL DISTRIBUTION OF TOTAL PHOSPHOROUS DISCHARGED IN THE RIVER NETWORK FROM POINT SOURCES. .....156
FIGURE 63. LONG-TERM MEAN ANNUAL NITRATE-NITROGEN CONCENTRATION (N-NO3, MG/L) AT 314 GAUGING STATIONS IN THE DANUBE RIVER BASIN. .....158
FIGURE 64. LONG-TERM MEAN ANNUAL TOTAL NITROGEN CONCENTRATION (TN, MG/L) AT 85 GAUGING STATIONS IN THE DANUBE RIVER BASIN. .....159
FIGURE 65. LONG-TERM MEAN ANNUAL TOTAL PHOSPHOROUS CONCENTRATION (TP, MG/L) AT 290 GAUGING STATIONS IN THE DANUBE RIVER BASIN. .....159
FIGURE 66. LONG-TERM MEAN ANNUAL NITRATE-NITROGEN LOADS (N-NO3, KG/YEAR) AT 204 GAUGING STATIONS IN THE DANUBE RIVER BASIN. .....160
FIGURE 67.LONG-TERM MEAN ANNUAL TOTAL NITROGEN LOADS (TN, KG/YEAR) AT 130 GAUGING STATIONS IN THE DANUBE RIVER BASIN. .....161
FIGURE 68. LONG-TERM MEAN ANNUAL TOTAL PHOSPHOROUS LOADS (TP, KG/YEAR) AT 204 GAUGING STATIONS IN THE DANUBE RIVER BASIN. .....161
FIGURE 69. GLOBAL SENSITIVITY ANALYSIS FOR PARAMETERS RELATED TO NITROGEN AND ITS FORMS USING T-TEST AND P-VALUE. THE LETTER V INDICATES THAT THE DEFAULT PARAMETER VALUE WAS REPLACED BY A GIVEN VALUE IN THE AVAILABLE RANGE, WHILE R MEANS THAT THE DEFAULT VALUE IS MULTIPLIED BY (1+A GIVEN RATE VALUE). THE FIGURE WAS EXTRACTED FROM THE SWAT-CUP MODEL (ABBASPOUR ET AL., 2008) .....165
FIGURE 70. GLOBAL SENSITIVITY ANALYSIS FOR SOME PARAMETERS RELATED TO PHOSPHOROUS AND ITS FORMS USING DOT-PLOTS. THE LETTER V INDICATES THAT THE DEFAULT PARAMETER VALUE WAS REPLACED BY A GIVEN VALUE IN THE AVAILABLE RANGE. THE FIGURE WAS EXTRACTED FROM THE SWAT-CUP MODEL (ABBASPOUR ET AL., 2008). .....165
FIGURE 71. COMPARISON OF ANNUAL OBSERVED (OBS, CONTINUOUS BLACK LINE) AND SIMULATED (SIM, CONTINUOUS RED LINE) CROP YIELDS (TON/HA) FOR THE SWAT CROP AGRR. THE BLACK DOTTED LINES INDICATE THE MEAN OF ANNUAL OBSERVED VALUES IN THE ENTIRE DANUBE, WHILE THE CONTINUOUS BLUE LINES INDICATE THE BIOMASS (TON/HA). AT: AUSTRIA; BA: BOSNIA AND HERZEGOVINA; BG: BULGARIA; CS: SERBIA AND MONTENEGRO; CZ: CZECH REPUBLIC; DE: GERMANY; HR: CROATIA; HU: HUNGARY; RO: ROMANIA; SI: SLOVENIA; SK: SLOVAKIA; UA: UKRAINE. .....168
FIGURE 72. COMPARISON OF ANNUAL OBSERVED (OBS, CONTINUOUS BLACK LINE) AND SIMULATED (SIM, CONTINUOUS RED LINE) CROP YIELDS (TON/HA) FOR THE SWAT CROP SWHT. THE BLACK DOTTED LINES INDICATE THE MEAN OF ANNUAL OBSERVED VALUES IN THE ENTIRE DANUBE, WHILE THE CONTINUOUS BLUE LINES INDICATE THE BIOMASS (TON/HA). AT: AUSTRIA; BA: BOSNIA AND HERZEGOVINA; BG: BULGARIA; CS: SERBIA AND MONTENEGRO; CZ: CZECH REPUBLIC; DE: GERMANY; HR: CROATIA; HU: HUNGARY; RO: ROMANIA; SI: SLOVENIA; SK: SLOVAKIA; UA: UKRAINE; MD: MOLDOVA. .....169
FIGURE 73. LONG-TERM MEAN ANNUAL DENITRIFICATION VALUES (KG/HA, PERIOD 1995-2009) IN THE DANUBE RIVER BASIN WITH 9 COMBINATIONS OF CDN AND SDNCO. .....171
FIGURE 74. SPATIAL VARIATION OF LONG-TERM MEAN ANNUAL DENITRIFICATION (KG/HA) IN THE DANUBE RIVER BASIN (PERIOD 1995-2009) WITH 9 COMBINATIONS OF CDN AND SDNCO. COMBINATIONS: A1: CDN=0.6; SDNCO=1, A2:

CDN=0.6; SDNCO=0.9, A3: CDN=0.6; SDNCO=0.8, B1: CDN=1.4; SDNCO=1, B2: CDN=1.4; SDNCO=0.9, B3: CDN=1.4; SDNCO=0.8, C1: CDN=3; SDNCO=1, C2: CDN=3; SDNCO=0.9, C3: CDN=3; SDNCO=0.8. ..... 172
FIGURE 75. SPATIAL LONG-TERM MEAN ANNUAL DENITRIFICATION (KG/HA) IN THE DANUBE RIVER BASIN WITH CDN AND SDNCO RESPECTIVELY TO 2.5 AND 1. ..... 174
FIGURE 76. BOX AND WHISKER PLOTS OF LONG-TERM MEAN ANNUAL DENITRIFICATION (KG/HA) SIMULATED IN THE PERIOD 1995-2009 IN EACH WATER MANAGEMENT REGION (CDN=2.5; SDNCO = 1). THE GREY DOTTED LINE INDICATES THE LONG-TERM MEAN ANNUAL DENITRIFICATION SIMULATED IN THE WHOLE DANUBE; THE GREY CONTINUOUS LINES INDICATE THE 25TH AND 75TH OF DENITRIFICATION VALUES FROM SOFT DATA (OENEMA ET AL., 2009). ..... 174
FIGURE 77. LONG-TERM MEAN MONTHLY DENITRIFICATION (KG/HA, PERIOD 1995-2009) WITH CDN AND SDNCO RESPECTIVELY TO 2.5 AND 1. ..... 175
FIGURE 78. PERCENT BIAS (PBIAS %) CALCULATED BETWEEN MONTHLY SIMULATED AND OBSERVED NITRATE-NITROGEN CONCENTRATION (MG/L) IN THE CALIBRATION DATASET (PERIOD 1995-2009); POSITIVE PBIAS% INDICATES OVERESTIMATION, WHILE NEGATIVE PBIAS% INDICATES UNDERESTIMATION. IN THE REACHES THE LONG-TERM MEAN MONTHLY NITRATE-NITROGEN CONCENTRATIONS ARE SHOWED. ..... 179
FIGURE 79. PERCENT BIAS (PBIAS %) CALCULATED BETWEEN MONTHLY SIMULATED AND OBSERVED NITRATE-NITROGEN LOADS (TON/MONTH) IN THE EVALUATION DATASET (PERIOD 1995-2009); POSITIVE PBIAS% INDICATES OVERESTIMATION, WHILE NEGATIVE PBIAS% INDICATES UNDERESTIMATION. IN THE REACHES THE LONG-TERM MEAN MONTHLY LOADS ARE SHOWED. ..... 179
FIGURE 80. PERCENT BIAS (PBIAS %) CALCULATED BETWEEN MONTHLY SIMULATED AND OBSERVED TOTAL NITROGEN CONCENTRATIONS (MG/L) IN THE CALIBRATION DATASET (PERIOD 1995-2009); POSITIVE PBIAS% INDICATES OVERESTIMATION, WHILE NEGATIVE PBIAS% INDICATES UNDERESTIMATION. IN THE REACHES THE LONG-TERM MEAN MONTHLY TOTAL NITROGEN CONCENTRATIONS ARE SHOWED. ..... 180
FIGURE 81. PERCENT BIAS (PBIAS %) CALCULATED BETWEEN MONTHLY SIMULATED AND OBSERVED TOTAL NITROGEN LOADS (TON/MONTH) IN THE EVALUATION DATASET (PERIOD 1995-2009); POSITIVE PBIAS% INDICATES OVERESTIMATION, WHILE NEGATIVE PBIAS% INDICATES UNDERESTIMATION. IN THE REACHES THE LONG-TERM MEAN MONTHLY LOADS ARE SHOWED. ..... 180
FIGURE 82. PERCENT BIAS (PBIAS %) CALCULATED BETWEEN MONTHLY SIMULATED AND TOTAL PHOSPHOROUS CONCENTRATION (MG/L) IN THE CALIBRATION DATASET (PERIOD 1995-2009); POSITIVE PBIAS% INDICATES OVERESTIMATION, WHILE NEGATIVE PBIAS% INDICATES UNDERESTIMATION. IN THE REACHES THE LONG-TERM MEAN MONTHLY TOTAL PHOSPHOROUS CONCENTRATIONS ARE SHOWED. ..... 181
FIGURE 83. PERCENT BIAS (PBIAS %) CALCULATED BETWEEN MONTHLY SIMULATED AND OBSERVED TOTAL PHOSPHOROUS LOADS (TON/MONTH) IN THE EVALUATION DATASET (PERIOD 1995-2009); POSITIVE PBIAS% INDICATES OVERESTIMATION, WHILE NEGATIVE PBIAS% INDICATES UNDERESTIMATION. IN THE REACHES THE LONG-TERM MEAN MONTHLY LOADS ARE SHOWED. ..... 181
FIGURE 84. A) DISTRIBUTION OF MONTHLY CONCENTRATION OF N-NO3 (MG/L) OBSERVED IN THE WATER MANAGEMENT REGIONS OF THE DANUBE BASIN (1995-2009); B) SWAT SIMULATIONS RESIDUALS (SIMULATION –OBSERVATION) FOR THE SAME DATA ENTRIES AS REPORTED FOR EACH BOX AND WHISKER PLOT. THE GREY DOTTED LINE INDICATES THE MEDIAN VALUE OF THE WHOLE DATASET, WHILE THE CONTINUOUS GREY LINES INDICATE THE INTERQUARTILE RANGE..... 182

FIGURE 85. MONTHLY TIME SERIES OF N-NO3 CONCENTRATION (MG/L) AS OBSERVED AT THE OUTLET OF SOME WATER MANAGEMENT REGIONS (BLACK LINE) AND AS SIMULATED BY SWAT MODEL (RED LINE) FOR THE PERIOD 1995-2009. NOTE THE DIFFERENCES IN Y AXIS. ..... 183
FIGURE 86. A) DISTRIBUTION OF MONTHLY LOADS OF N-NO3 (TON/MONTH IN LOG10 SCALE) "OBSERVED" IN THE WATER MANAGEMENT REGIONS OF THE DANUBE BASIN (1995-2009); B) SWAT SIMULATIONS RESIDUALS (SIMULATION – OBSERVATION) FOR THE SAME DATA ENTRIES AS REPORTED FOR EACH BOX AND WHISKER PLOT. THE GREY DOTTED LINE INDICATES THE MEDIAN VALUE OF THE WHOLE DATASET, WHILE THE CONTINUOUS GREY LINES INDICATE THE INTERQUARTILE RANGE ..... 184
FIGURE 87. MONTHLY TIME SERIES OF N-NO3 LOADS (TON/MONTH INDICATE WITH TN IN THE PLOTS) AS "OBSERVED" AT THE OUTLET OF SOME WATER MANAGEMENT REGIONS (BLACK LINE) AND AS SIMULATED BY SWAT MODEL (RED LINE) FOR THE PERIOD 1995-2009. NOTE THE DIFFERENCES IN Y AXIS ..... 185
FIGURE 88. A) DISTRIBUTION OF MONTHLY CONCENTRATION OF TN (MG/L) OBSERVED IN THE WATER MANAGEMENT REGIONS OF THE DANUBE BASIN (1995-2009); B) SWAT SIMULATIONS RESIDUALS (SIMULATION –OBSERVATION) FOR THE SAME DATA ENTRIES AS REPORTED FOR EACH BOX AND WHISKER PLOT. THE GREY DOTTED LINE INDICATES THE MEDIAN VALUE OF THE WHOLE DATASET, WHILE THE CONTINUOUS GREY LINES INDICATE THE INTERQUARTILE RANGE ..... 186
FIGURE 89. MONTHLY TIME SERIES OF TN CONCENTRATION (MG/L) AS OBSERVED AT THE OUTLET OF SOME WATER MANAGEMENT REGIONS (BLACK LINE) AND AS SIMULATED BY SWAT MODEL (RED LINE) FOR THE PERIOD 1995-2009. NOTE THE DIFFERENCES IN Y AXIS. ..... 187
FIGURE 90. A) DISTRIBUTION OF MONTHLY LOADS OF TN (TON/MONTH IN LOG10 SCALE) "OBSERVED" IN THE WATER MANAGEMENT REGIONS OF THE DANUBE BASIN (1995-2009); B) SWAT SIMULATIONS RESIDUALS (SIMULATION – OBSERVATION) FOR THE SAME DATA ENTRIES AS REPORTED FOR EACH BOX AND WHISKER PLOT. THE GREY DOTTED LINE INDICATES THE MEDIAN VALUE OF THE WHOLE DATASET, WHILE THE CONTINUOUS GREY LINES INDICATE THE INTERQUARTILE RANGE ..... 188
FIGURE 91. MONTHLY TIME SERIES OF TN LOADS (MG/L) AS "OBSERVED" AT THE OUTLET OF SOME WATER MANAGEMENT REGIONS (BLACK LINE) AND AS SIMULATED BY SWAT MODEL (RED LINE) FOR THE PERIOD 1995-2009. NOTE THE DIFFERENCES IN Y AXIS. ..... 189
FIGURE 92. A) DISTRIBUTION OF MONTHLY CONCENTRATION OF TP (MG/L) OBSERVED IN THE WATER MANAGEMENT REGIONS OF THE DANUBE BASIN (1995-2009); B) SWAT SIMULATIONS RESIDUALS (SIMULATION –OBSERVATION) FOR THE SAME DATA ENTRIES AS REPORTED FOR EACH BOX AND WHISKER PLOT. THE GREY DOTTED LINE INDICATES THE MEDIAN VALUE OF THE WHOLE DATASET, WHILE THE CONTINUOUS GREY LINES INDICATE THE INTERQUARTILE RANGE ..... 190
FIGURE 93. MONTHLY TIME SERIES OF TP CONCENTRATION (MG/L) AS OBSERVED AT THE OUTLET OF SOME WATER MANAGEMENT REGIONS (BLACK LINE) AND AS SIMULATED BY SWAT MODEL (RED LINE) FOR THE PERIOD 1995-2009. NOTE THE DIFFERENCES IN Y AXIS. ..... 191
FIGURE 94. A) DISTRIBUTION OF MONTHLY LOADS OF TP (TON/MONTH IN LOG10 SCALE) "OBSERVED" IN THE WATER MANAGEMENT REGIONS OF THE DANUBE BASIN (1995-2009); B) SWAT SIMULATIONS RESIDUALS (SIMULATION – OBSERVATION) FOR THE SAME DATA ENTRIES AS REPORTED FOR EACH BOX AND WHISKER PLOT. THE GREY DOTTED LINE INDICATES THE MEDIAN VALUE OF THE WHOLE DATASET, WHILE THE CONTINUOUS GREY LINES INDICATE THE INTERQUARTILE RANGE ..... 192

FIGURE 95. MONTHLY TIME SERIES OF TP LOADS (TON/MONTH) AS OBSERVED AT THE OUTLET OF SOME WATER MANAGEMENT REGIONS (BLACK LINE) AND AS SIMULATED BY SWAT MODEL (RED LINE) FOR THE PERIOD 1995-2009. NOTE THE DIFFERENCES IN Y AXIS. ..... 193
FIGURE 96. NITROGEN FLUXES AND RETENTION (KG/HA) IN THE DANUBE RIVER BASIN ACCORDING TO SWAT MODEL RESULTS IN THE PERIOD 1995-2009. SEE FIGURE 3 FOR THE SYMBOLS/ABBREVIATIONS. ..... 195
FIGURE 97. PHOSPHOROUS FLUXES AND RETENTION (KG/HA) IN THE DANUBE RIVER BASIN ACCORDING TO SWAT MODEL RESULTS IN THE PERIOD 1995-2009. SEE FIGURE 4 FOR THE SYMBOLS/ABBREVIATIONS. ..... 195
FIGURE 98. SUBBASIN SLOPE LENGTH (LS) FACTORS AGAINST SLOPE GRADIENT FOR ALL THE POSSIBLE COMBINATIONS BETWEEN 4 L FACTORS AND 3 LS ALGORITHMS ..... 201
FIGURE 99. GROSS EROSION RATES (GE, T/HA/YEAR) FOR THREE MAJOR LAND USE TYPES AS MEASURED ON RUNOFF PLOTS IN OR NEAR THE UPPER DANUBE BASIN, AS DERIVED FROM PREVIOUSLY PUBLISHED EROSION MAPS, OR AS PREDICTED WITH USLE FOR THE PERIOD 1995–2009 IN THE UPPER DANUBE BASIN UNDER THE INDICATED L–LS CONFIGURATIONS. PLOT=SOIL LOSS DATA FROM THE REGION EXTRACTED FROM A PLOT DATABASE COMPILED BY MAETENS ET AL. (2012); EIONET=MEDIAN EROSION RATES FOR SWAT HRUS AS ESTIMATED IN EIONET NATIONAL ASSESSMENT (PANAGOS ET AL., 2014); CERDAN=MEDIAN EROSION RATES FOR SWAT HRUS AS ESTIMATED BY CERDAN ET AL. (2010). LS2 CONFIGURATIONS (TABLE 19) ARE NOT SHOWN, BUT WERE CLOSE TO LS3. # INDICATES THE NUMBER OF UNITS FOR EACH BOXPLOT. ..... 202
FIGURE 100. BOX-AND-WHISKER PLOT OF SUSPENDED SEDIMENT CONCENTRATIONS (SSC) RESIDUALS (=SIMULATION – OBSERVATION) OF THE MEAN ANNUAL VALUES FOR THE OBSERVATIONS OF THE 13 SWAT CONFIGURATIONS ANALYZED IN THIS STUDY (TABLE 19). # IS THE NUMBER OF STATION-YEAR ENTRIES IN THE CALIBRATION AND VALIDATION PERIODS. THE GREY HORIZONTAL LINES INDICATE AN ERROR OF + / – 15 MG/L. NOTE THAT Y AXIS IS CUT AT +/- 100 MG/L. ..... 203
FIGURE 101. BOX-AND-WHISKER PLOT OF REACH SPECIFIC SEDIMENT YIELDS (RSSY) RESIDUALS (= SIMULATION – OBSERVATION; T/KM$^2$/Y) OF THE 13 SWAT CONFIGURATIONS ANALYZED IN THIS STUDY (TABLE 19). RESIDUALS ARE FOR THE FULL SIMULATION PERIOD 1995-2009 (86 STATION-YEAR ENTRIES). THE GREY HORIZONTAL LINES INDICATE AN ERROR OF +/ – 10 T/KM$^2$/Y. NOTE THAT Y AXIS ARE LIMITED AT +/- 100 T/KM$^2$/Y. ..... 205
FIGURE 102. MEAN ANNUAL REACH SEDIMENT OUTPUTS IN THE UPPER DANUBE FOR THE SIMULATION PERIOD 1995-2009: A) SIMULATED SUSPENDED SEDIMENT CONCENTRATION (SSC, MG/L) IN RELATION TO RESERVOIRS/DAM/LOCKS; B) SPECIFIC SEDIMENT YIELDS (RSSY, T/KM$^2$/Y) WITH PERCENT BIAS (PBIAS, %) AT THE AVAILABLE GAUGING STATIONS. THE LETTERS A-B INDICATE THE LOCATION OF TWO STATIONS FOR WHICH TIME-SERIES SIMULATIONS ARE PROVIDED IN FIGURE 103. THE RESULTS REFER TO CONFIGURATION L2LS3. ..... 206
FIGURE 103.COMPARISON OF SWAT OUTPUTS (GREY LINES) WITH OBSERVATIONS (BLACK LINES) AT THREE SELECTED MONITORING GAUGING STATIONS (LOCATIONS SHOWN IN FIGURE 103B). A: KIRCHDORF STATION (GERMANY) ON THE INN RIVER: (A1: MEAN ANNUAL SUSPENDED SEDIMENT CONCENTRATION SSC, MG/L; A2: REACH SPECIFIC SEDIMENT YIELD RSSY, T/KM$^2$/Y). B) BRATISLAVA (SLOVAKIA), AT THE OUTLET OF THE UPPER DANUBE BASIN (B1: SSC; B2: RSSY). NOTE THE VARYING RANGES OF THE Y AXIS. THE RESULTS REFER TO CONFIGURATION L2LS3. ..... 207
FIGURE 104. THE MODELED SEDIMENT BUDGET OF THE UPPER DANUBE BASIN FOR THE SIMULATION PERIOD (1995–2009). 208
FIGURE 105. COMPARISON BETWEEN ECONOMIC AND ENVIRONMENTAL OBJECTIVE FOR ITERATIVE SIMULATIONS. THE BLS FERTILIZER ITERATION (BLACK POINT) REFERS TO THE VARIATION OF THE RATE OF FERTILIZATION EQUALLY IN ALL HRUS. STRATEGIES OF UPGRADING ALL WWTPS ARE SHOWN AS BLUE TRIANGLE FOR THE *BLS* AND RED SQUARE FOR THE

*SmartFert* strategy (both *BLS* and *SmartFert* points are the actual WWTP status; WWTP->1: all the plants are upgraded to CND level; WWTP->2: all plants are upgraded to CNDP level as described in Appendix A5). ..... 211
Figure 106. The Pareto front strategies for the multi-objective scenarios compared to strategies of Figure 105. ..... 211
Figure 107. Long-term mean monthly N-NO3 concentration (mg/L) in each reach in the Upper Danube applying three different management strategies. In (a): BLS; (b) SmartFert; (c) OptiG. The results refer to the period of simulation 1995-2009. ..... 213
Figure 108. Temporal scale of model simulations. The red lines define the period of interest for this study (2000-2009). ..... 217
Figure 109. Gauging stations used in performing the benchmarking approach ..... 217
Figure 110. Map of the mean annual streamflow (period 2000-2009) in the Danube Basin. The three model outputs are compared to available observations. ..... 219
Figure 111. Cumulative annual streamflow estimated along the Danube River with SWAT, GREEN and MONERIS models for the period 2000-2009. The black bars represent the observation at the outlets of the water management regions. The red arrows indicate the position of the two main reservoirs, the Gabcikovo and the Iron Gate, along the Danube River. ..... 220
Figure 112. Bar plot (a) and Taylor Diagram for streamflow of Region 1 (period 200-2009). In (a) the error bars in red indicate the 95% confidence intervals. ..... 221
Figure 113. Bar plot (a) and Taylor Diagram for streamflow in Region 6 (period 2000-2009). In (a) the error bars in red indicate the 95% confidence intervals. ..... 221
Figure 114. Taylor Diagrams of annual streamflow ($m^3/s$) in the period 2000-2009 for Region 7 and 8. ..... 222
Figure 115. Bar plot (a) and Taylor Diagram (b) for streamflow Region 11. In (a) the error bars in red indicate the 95% confidence intervals. ..... 223
Figure 116. Bar plot (a) and Taylor Diagram (b) for streamflow in Region 16. In (a) the grey bar represents the average of annual streamflow for the three model predictions as observations were not available (period 2000-2009). The error bars in red indicate the 95% confidence intervals. ..... 224
Figure 117.Bar plot (a) and Taylor Diagram (b) for streamflow in Region 18 (period 2000-2009). In (a) the error bars in red indicate the 95% confidence intervals. ..... 225
Figure 118. Map of long mean annual total nitrogen (TN, ton/y) for the decade 2000-2009 in the Danube River Basin. The three model outputs are compared to available observations. ..... 226
Figure 119. Cumulative annual total nitrogen loads estimated along the Danube River with SWAT, GREEN and MONERIS models for the period 2000-2009. The black bars represent the "observed" loads at the outlets of the water management regions. The red arrows indicate the position of the two main reservoirs, the Gabcikovo and the Iron Gate, along the Danube River. ..... 226
Figure 120. Bar plot (a) and Taylor Diagram (b) for total nitrogen (TN) in Region 4. In (a) the grey bar represents the average of annual loads for the three model predictions as observations were not available (period 2000-2009). The error bars in red indicate the 95% confidence intervals. ..... 227
Figure 121.Taylor Diagrams of annual total nitrogen for Region 7 (a) and 9 (b) (period 2000-2009). ..... 228

FIGURE 122. TAYLOR DIAGRAMS OF ANNUAL TOTAL NITROGEN FOR REGION 11 (A) AND 15 (B) (PERIOD 2000-2009). ..... 229
FIGURE 123. BAR PLOT (A) AND TAYLOR DIAGRAM (B) OF ANNUAL TOTAL NITROGEN FOR REGION 18 (PERIOD 2000-2009). IN (A) THE ERROR BARS IN RED INDICATE THE 95% CONFIDENCE INTERVALS. ..... 230
FIGURE 124. MAPS OF THE LONG MEAN ANNUAL TOTAL PHOSPHOROUS COMPARISONS (PERIOD 2000-2009) IN EACH REGION. THE THREE MODEL OUTPUTS ARE COMPARED TO AVAILABLE OBSERVATIONS. ..... 231
FIGURE 125. CUMULATIVE ANNUAL TOTAL PHOSPHOROUS LOADS ESTIMATED ALONG THE DANUBE RIVER WITH SWAT, GREEN AND MONERIS MODELS FOR THE PERIOD 2000-2009. THE BLACK BARS REPRESENT THE "OBSERVED" LOADS AT THE OUTLETS OF THE WATER MANAGEMENT REGIONS. THE RED ARROWS INDICATE THE POSITION OF THE TWO MAIN RESERVOIRS, THE GABCIKOVO AND THE IRON GATE, ALONG THE DANUBE RIVER..... 231
FIGURE 126. BAR PLOT (A) AND TAYLOR DIAGRAM (B) OF ANNUAL PHOSPHOROUS FOR REGION 2 (PERIOD 2000-2009). IN (A) THE ERROR BARS IN RED INDICATE THE 95% CONFIDENCE INTERVALS. ..... 232
FIGURE 127. BAR PLOT (A) AND TAYLOR DIAGRAM (B) OF ANNUAL TOTAL PHOSPHOROUS FOR REGION 4 (PERIOD 2000-2009). IN (A) THE ERROR BARS IN RED INDICATE THE 95% CONFIDENCE INTERVALS. ..... 233
FIGURE 128. BAR PLOT (A) AND TAYLOR DIAGRAM (B) OF ANNUAL TOTAL PHOSPHOROUS FOR REGION 6 (PERIOD 2000-2009). IN (A) THE ERROR BARS IN RED INDICATE THE 95% CONFIDENCE INTERVALS. ..... 234
FIGURE 129. BAR PLOT (A) AND TAYLOR DIAGRAM (B) OF ANNUAL TOTAL PHOSPHOROUS FOR REGION 8 (PERIOD 2000-2009). IN (A) THE GREY BAR REPRESENTS THE AVERAGE OF THE THREE MODEL PREDICTIONS AS OBSERVATIONS WERE NOT AVAILABLE. THE ERROR BARS IN RED INDICATE THE 95% CONFIDENCE INTERVALS..... 235
FIGURE 130. BAR PLOT (A) AND TAYLOR DIAGRAM (B) OF ANNUAL TOTAL PHOSPHOROUS FOR REGION 114 (PERIOD 2000-2009). IN (A) THE ERROR BARS IN RED INDICATE THE 95% CONFIDENCE INTERVALS. ..... 235
FIGURE 131. BAR PLOT (A) AND TAYLOR DIAGRAM (B) OF ANNUAL TOTAL PHOSPHOROUS FOR REGION 18 (PERIOD 2000-2009). IN (A) THE ERROR BARS IN RED INDICATE THE 95% CONFIDENCE INTERVALS. ..... 236

# List of Tables

TABLE 1. MAIN SIMULATED PROCESSES AND RELATED ALGORITHMS IMPLEMENTED IN SWAT ..... 40

TABLE 2. PARAMETERS AND INITIAL PARAMETER RANGES USED IN THE STEP-WISE CALIBRATION RANKED IN ALPHABETIC ORDER .. 65

TABLE 3. DEPENDENT AND INDEPENDENT (RESPECTIVELY STREAMFLOW AND SUBBASIN CHARACTERISTICS) VARIABLES FOR PLSR ANALYSIS ..... 66

TABLE 4. GENERAL PERFORMANCE RATINGS ACCORDING TO MORIASI ET AL. (2007B) ..... 68

TABLE 5. THE 18 REGIONS OF DANUBE RIVER BASIN AND THEIR GENERAL CHARACTERIZATION, AS WELL AS THE NUMBER OF STREAMFLOW GAUGING STATION IN EACH REGION, WITH REFERENCE TO THE AREA ($KM^2$). THE MEAN ANNUAL OBSERVED STREAMFLOW IN GREY WAS OBTAINED FROM LITERATURE INFORMATION. ..... 87

TABLE 6. MEAN ANNUAL WATER BALANCE OF THE WATER MANAGEMENT REGIONS OF THE DANUBE BASIN AS SIMULATED WITH SWAT FOR THE PERIOD 1995-2009. PCP: PRECIPITATION (MM); ET: EVAPOTRANSPIRATION (MM); SR: SURFACE RUNOFF (MM), BF: BASEFLOW; DA: DEEP AQUIFER RECHARGE; QTILE: TILE FLOW (MM); WYLD: WATER YIELDS (MM). ..... 105

TABLE 7. CHARACTERISTICS OF THE SIX SWAT CONFIGURATIONS COMPARED IN THIS STUDY (DEML CONFIGURATIONS) AS GENERATED BY THE COMBINATION OF TWO DIGITAL ELEVATION MODELS (DEM) WITH THREE HILLSLOPE LENGTH METHODS. L1 = SWAT DEFAULT METHOD BASED ON LOOK-UP SLOPE TABLE; L2 = FLOW ACCUMULATION METHOD, L3 = CONSTANT HILLSLOPE LENGTH ..... 108

TABLE 8. SUMMARY OF CALIBRATION AND VALIDATION OF MONTHLY STREAMFLOW SIMULATIONS IN THE UPPER DANUBE BASIN FOR EACH DEML CONFIGURATION. ..... 112

TABLE 9. SPEARMAN'S RANK CORRELATION COEFFICIENT P BETWEEN THE MONTHLY RESIDUALS OF LATERAL FLOW (LF, $M^3/S$) OF DEML CONFIGURATIONS FOR THE CALIBRATED DATASET (#98 GAUGED STATIONS, 1995-2006). ..... 121

TABLE 10. DESCRIPTION OF AVAILABLE STREAMFLOW AND SPRING DISCHARGES MEASUREMENTS IN THE CRETE ISLAND PROVIDED BY THE BUREAU OF WATER RESOURCES AT THE DECENTRALIZED ADMINISTRATION OF THE REGION OF CRETE. THE SYMBOL # REPRESENT THE NUMBER. ..... 133

TABLE 11. PARAMETERS AND PARAMETER RANGES USED IN THE CALIBRATION (IN ALPHABETIC ORDER), IN THE *ADAPTED SWAT MODEL* AND IN THE *KARST-FLOW MODEL*. IN COLUMN "PROCESS" THE INFORMATION ABOUT THE ORDER AND GROUP OF CALIBRATION PROCESSES: 1, SNOW PROCESS; 2, RUNOFF PROCESS; 3, LATERAL FLOW PROCESS; 4: GROUNDWATER PROCESS; 5: KARST PROCESS. ..... 135

TABLE 12. COMPARISON OF OBSERVED AND SIMULATED STREAMFLOW IN THE PERIOD 1983-2009 AFTER THE INTRODUCTION OF THE SPRINGS (COMPLETE VALIDATION): IN THE FIRST TWO COLUMNS THE CODE AND NAME OF THE STATIONS; IN THE THIRD COLUMN THE DRAIN AREA ($KM^2$); THE *% DATA* REPRESENTS THE % OF MONTHLY VALUES IN THE PERIOD 1983-2009 (324 TOTAL MONTHS); THE OBSERVED AND SIMULATED VOLUMES ARE RESPECTIVELY *$MM^3$/YEAR OBS* AND *SIM;* THE PERFORMANCE INDICATORS BETWEEN MONTHLY OBSERVED AND SIMULATED STEAMFLOW ARE THE NORMALIZED ROOT MEAN SQUARE ERROR (NRMSE %), THE PERCENT BIAS (PBIAS%), THE NASH SUTCLIFFE COEFFICIENT (NSE), THE COEFFICIENT OF DETERMINATION ($R^2$) AND THE COEFFICIENT OF DETERMINATION MULTIPLIED BY THE SLOPE OF THE REGRESSION LINE BETWEEN SIMULATED AND OBSERVED VALUES ($BR^2$). ..... 136

TABLE 13. COMPARISON OF OBSERVED AND SIMULATED SPRING DISCHARGES IN THE PERIOD 1983-2009: IN THE FIRST TWO COLUMNS THE CODE AND NAME OF THE STATIONS; IN THE THIRD THE KARST AREA THAT CONTRIBUTES OF EACH SPRING ($KM^2$) AND INVOLVES THE AREA INSIDE THE HYDROLOGICAL BASIN AND OUTSIDE; THE *% DATA* REPRESENTS THE PERCENTAGE

of monthly values in the period 1983-2009 (324 total months); the observed and simulated volumes are respectively *$Mm^3$/year OBS* and *SIM;* the performance indicators calculated between daily observed and simulated spring discharges are the normalized root mean square error (NRMSE %), the percent bias (PBIAS%), the Nash Sutcliffe Coefficient (NSE), the coefficient of determination ($r^2$) and the coefficient of determination multiplied by the slope of the regression line between simulated and observed values ($br^2$). ..... 139

Table 14. Overview of the land cover characteristics, amount of fertilizers and nutrient discharges from point sources (PS) in the water management regions of the Danube Basin. The percentage is calculated excluding upstream area. $N_{APP}$: total nitrogen (TN) fertilizer applied; $NO3_{APP}$: Nitrate fertilizer applied; $NH3_{APP}$: ammonia fertilizer applied; $ORGN_{APP}$: organic nitrogen applied; $P_{APP}$: total phosphorous (TP) fertilizer applied; $SOLP_{APP}$: mineral phosphorous applied; $ORGP_{APP}$: organic phosphorous applied; $N_{RAIN}$: nitrate added to soil profile by rain; $N_{FIX}$: nitrogen fixation. ..... 153

Table 15. List of SWAT parameters used in the sensitivity analysis for N-NO3 and TN. The parameters are in alphabetic order. For each parameter is reported the related input file (i.e. parameter AI1 is defined in the file wwq). ..... 163

Table 16. List of SWAT parameters used in the sensitivity analysis for TP. The parameters are in alphabetic. For each parameter is reported the related input file (i.e. parameter AI2 is defined in the file wwq). ..... 164

Table 17. Final ranges and values for nutrients parameters. The values in the bracket represent the average of calibrated values. In these table are excluded the parameters RCN, SHALLEST_N and the initial concentration in reservoirs since they were involved in the setup of the model. For each parameter is reported the related input file (i.e. parameter CDN is defined in the file bsn). ..... 167

Table 18. Overview of calibration and evaluation results in terms of performance rating as explained in Table 4. For each class of performance, the percentage (%) of gauging stations that reached each of them is reported. The symbol # represents the number of gaging stations. ..... 176

Table 19. Default and modified SWAT configurations evaluated in this study. For the number of equation see section 2. ..... 198

Table 20. Results of a global sensitivity analysis of the mean annual suspended sediment concentrations (SSC; mg/L) and annual reach specific sediment yields (RSSY, $t/km^2/y$) for the modified SWAT (configuration L2LS3) evaluated in this study. Sensitivity was conducted on 1500 runs changing all parameters in the specified range. t = t test value of the regression coefficient of each parameter against the objective function; in brackets the probability p value. Rank = from highest to lowest sensitivity. ..... 199

Table 21. Water management regions code, names, drain area ($km^2$), and gauging stations of reference used in the inter-comparison. The term "available" indicates that observed data for the variable were available for at least five years in the decade 2000-2009. ..... 218

Table 22. Mean annual water streamflow ($m^3/s$) in the period (2000-2009) ("average" column) and the statistics derived from Taylor diagram. The table includes where available the observations (and correlated statistics) in black, otherwise the average of the three model simulations (and correlated statistics) in grey. ..... 238

TABLE 23. MEAN ANNUAL TOTAL NITROGEN (TN, TON/Y) IN THE PERIOD (2000-2009) ("AVERAGE" COLUMN) AND THE STATISTICS DERIVED FROM TAYLOR DIAGRAM. THE TABLE INCLUDES WHERE AVAILABLE THE OBSERVATIONS (AND CORRELATED STATISTICS) IN BLACK, OTHERWISE THE AVERAGE OF THE THREE MODEL SIMULATIONS (AND CORRELATED STATISTICS) IN GREY. ..... 239
TABLE 24. MEAN ANNUAL TOTAL PHOSPHOROUS (TP, TON/Y) IN THE PERIOD (2000-2009) ("AVERAGE" COLUMN) AND THE STATISTICS DERIVED FROM TAYLOR DIAGRAM. THE TABLE INCLUDES WHERE AVAILABLE THE OBSERVATIONS (AND CORRELATED STATISTICS) IN BLACK, OTHERWISE THE AVERAGE OF THE THREE MODEL SIMULATIONS (AND CORRELATED STATISTICS) IN GREY. ..... 240

# List of the abbreviations[1]

AI: aridity index

Avg: average

BF: baseflow

BFI: baseflow index

BMP: Best Management Practice

C/V: Calibration/Validation

DE: diffuse emission

DEM: Digital Elevation Model

DS: diffuse sources

ET: evapotranspiration

GE: gross erosion

GREEN: Geospatial Regression Equation for European Nutrient losses

H/WQ: Hydrological and Water Quality models

HRU: Hydrological Response Unit

KSWAT: Karst flow model linked with SWAT

L: hillslope length

LF: lateral flow

MONERIS: Modeling Nutrient Emissions into River Systems

N-NO3: nitrate nitrogen

PS: point sources

Q: streamflow or water discharge

RSSY: specific sediment yields

SR: surface runoff

SSC: suspended sediment concentration

SWAT: Soil and Water Assessment Tool

[1] In the list only the main abbreviations are reported. For specific symbols and abbreviations, the reader can refer to figures and related description in each section.

TN: total nitrogen

TP: total phosphorous

WYLD: water yield

# List of Scientific Publications (2013-2015)

- Malagó, A., Pagliero, L., Bouraoui, F., Franchini, M., 2015a. Comparing calibrated parameter sets of the SWAT model for the Scandinavian and Iberian peninsulas. Hydrological Sciences Journal. Special issue: Evaluation of Water Resources with SWAT. doi: 10.1080/02626667.2014.978332.
- Malagó, A., Vigiak, O., Bouraoui, F., Franchini, M., 2015b.The hillslope Length impact on SWAT streamflow prediction in large Basins. Submitted to Journal of Environmental Informatics in May 2015.
- Malagó, A., Efstathiou, D., Bouraoui, F., Nikolaidis, N.P., Franchini, M., Bidoglio, G., Kritsotakis, M., 2015c. Regional scale hydrologic modeling of a karst-dominant geomorphology: the case study of the island of Crete. Submitted to Journal of Hydrology in April 2015.
- Malagó A., Venohr M., Gericke A., Vigiak O., Bouraoui F., Grizzetti B., Kovacs A., 2015d. Modelling nutrient pollution in the Danube River Basin: a comparative study of SWAT, MONERIS and GREEN models. JRC TECHNICAL REPORT. EUR 27676 EN . Scientific and Technical Research series – ISBN 978-92-79-54239-8.
- Vigiak O., Malagó A., Bouraoui F., Vanmaercke M., Poesen J., 2015a. Adapting SWAT hillslope erosion model to predict sediment concentrations and yields in large Basins. Science of the Total Environment. 538, 855–875.
- Vigiak, O., Malagó, A., Bouraoui, F., Pastori, M., Borrelli, P., Pistocchi, A. 2015b. Impact of current conservation practices on sediment load reduction in the Danube River Basin. In Cau et al. (eds) SWAT 2015 Conference, 24th-26th June 2015, Pula (Italy), Book of Abstracts, pp 66. http://swat.tamu.edu/media/114758/d3-2-vigiak.pdf.
- Udias, A., Malagó, A., Reynaud, A., Pastori, M., Vigiak, O., Bouraoui, F., 2015. A new R-SWAT Decision Making Framework for the Spatial Identification of BMP Related to Freshwater Management. In Cau et al. (eds) SWAT 2015 Conference, 24th-26th June 2015, Pula (Italy), Book of Abstracts, pp 35. http://swat.tamu.edu/media/114734/b3-3-vigiak.pdf.

# CHAPTER 1

# 1 Introduction

Since the nineties of the last century, the interest for water and related environmental problems (i.e. water pollution and resource depletion) changed from small scale to large scale due to the need to sustainably manage large river basins. Doll and Fiedler (2008) define “large-scale” studies those referring to areas with extension between a few thousand $km^2$ to the whole globe.

A clear difference between small and large-scale environmental problems concerns the processes and “actors” involved (i.e. agriculture and industrial sectors), as well as their interaction and heterogeneity, and their impacts on the system. This creates a complex situation, in which agreement on rules on how to manage the environment and their enforcement are very difficult (Sun et al., 2010). In this context, large-scale environmental problems require governance from international cooperation to local engagement (Dietz et al., 2003). For instance, a concrete example of cooperation is the Danube River Protection Convention signed on June 1994 by eleven countries which have agreed to co-operate in the Danube River Basin to ensure that surface waters and groundwater are managed and used sustainably and equitably.

Among the large-scale environmental problems, environmental pollution and natural resources depletion are strongly interconnected. In this regard, in December 2000, the Water Framework Directive (WFD) of the European Union (EU) was enforced (EC, 2000) to provide a new legislative basis for water management, in terms of water quantity and quality in Europe. The main goals of the WFD are to achieve and maintain good status for all surface waters and groundwater by year 2015, and to prevent deterioration and ensure the conservation of high water quality where it still exists.

For many EU Members States, the WFD poses a difficult challenge because the Directive requires an integrated management involving all stakeholders influencing the water resources at the river basin scale, including large basins (Lindenschmidt et al., 2007). The WFD primarily relies on the concept of Integrated Water Resources Management. However, new challenges have emerged in the context of the recent “Nexus thinking”. The term ‘nexus’ refers to linkages and connections between economic sectors related to water for an integrated management across them (Bazilian et al., 2011). It is most commonly used to examine interactions between water, energy and food (WEF). In their simplest form, WEF relationships can be set out as follows: water is needed to generate energy, energy is needed to supply water; energy is needed to produce food, food can be used to produce

energy, water is needed to grow food while food transports water, often using energy (Stringer et al., 2014). Changes to any one of water, energy or food can have knock-on implications for the remaining two across a range of scales (Hussey and Pittock 2012).

In this context, computer modeling systems furnish an important contribution to the process of integrated management and decision support, in particular for establishing action plans to implement, identify the appropriate management measures, to optimize the monitoring and sampling programs of the water bodies and to accompany the implementation and evaluation of the measures and their impacts (Lindenschmidt et al., 2007).

Large-scale hydrologic and water quality models (H/WQ) are increasingly used to determine the environmental impacts of climate variability, land management, conservation practices on soil and water resources (Doll et al., 2008). They are increasingly being applied to large diversity of agricultural landscapes to address contemporary water resource issues (Jayakrishnan et al., 2005), providing valuable information for making sound management, policy and regulatory decisions (Arnold et al., 2012b). H/WQ models are valuable because they represent processes operating at various spatial and temporal scales simultaneously in a complex and interrelated manner (Moriasi et al., 2015) and at large-scale they have the potential to encompass many river basins, cross-regional and international boundaries and represent a number of different physiographic and climatic zones (Alcamo et al., 2003; Raje et al., 2013; Widén-Nilsson et al., 2007). Furthermore, the application of multi-subbasin modelling at the large-scale is widely used to predict the hydrological and quality response at ungauged subbasins (Donnelly et al., 2015; Pagliero et al., 2014; Malagò et al., 2015a).

Without being exhaustive, the H/WQ models commonly used at large-scale are SWAT (Arnold et al.,1998), WARMF (Herr and Chen, 2012), HSPF (Duda et al, 2012) and MIKE-SHE (Jaber ans Shukla, 2012). They have the capacity to represent appropriately spatial-temporal heterogeneity through a distributed or semi-distributed spatial discretization (Baffaut et al, 2015).

The Soil and Water Assessment Tool (SWAT) (Arnold et al.,1998) has been extensively used and its popularity is explained by its many advantages including: modularity between quantity and quality components, computational efficiency, ability to predict long-term impacts as a continuous model, ability to use readily available global datasets, availability of a reliable user and developer support, possibility to change code by users, and, the GIS integration and tools for sensitivity and uncertainty analysis (see for more details Gassman et al., 2010; Abbaspour et al., 2008; Di Luzio et al., 2004).

An impressive number of SWAT model applications has been reported ranging from subbasin to continental scales addressing different environmental issues (see overviews in Gassman et al., 2007, 2014; Krysanova and Arnold, 2008; Douglas-Mankin et al., 2010;

Tuppad et al., 2011; Krysanova and Srinivasan 2015; Krysanova and White, 2015). Usually, SWAT is applied to assess hydrological regimes and water resources (water discharge, groundwater dynamics, soil water, snow dynamics, irrigation, impoundment and water management); water quality assessment (such as diffuse pollution, sediment losses, and best management practices in agriculture); land use and land management change, as well as climate change impact assessment.

The suitability of SWAT for very large-scale applications has been illustrated for the first time in the ‘‘Hydrologic Unit Model for the United States’’ project (HUMUS), where Arnold et al. (1999) used SWAT to predict streamflow at around 6000 gauging stations covering the entire U.S.A. Gosain et al. (2006) modeled twelve large river catchments in India with the purpose of quantifying the climate change impact on hydrology. Schuol et al. (2008) simulated hydrology of the Africa Continent with SWAT and evaluated the spatial distribution of water resources in term of blue and green water at different spatial and temporal scale. Faramarzi et al. (2013) used SWAT to study the impact of climate change in Africa, while Faramarzi et al. (2009) simulated the hydrology and crop yields in Iran (1,648,000 $km^2$). In Europe, Pagliero et al. (2014) and Rouholahnejad et al. (2014) applied SWAT in the Danube River Basin (802,000 $km^2$) and in the Black Sea Basin (2,300,000 $km^2$) focusing on the calibration and validation strategies (C/V) in view of delivering an accurate water resources assessment. Recently, SWAT was applied in the whole Europe (Abbaspour et al., 2015) where different components of water resources, crop yield and water quality were simulated, while in U.S.A., White et al. (2014) provided a comprehensive assessment of nutrients fluxes in the Gulf of Mexico via the Mississippi River Basins (3,220,000 $km^2$). Finally, it is noteworthy that SWAT has been just tested as an alternative to global models (i.e. WaterGAP and UNH/GRDC) by Scherer et al. (2015).

Usually these studies, as well as other many large-scale SWAT applications, report satisfactory to very good fit between modeling results and observed data, albeit they may not realistically simulate the processes in the hydrological and water quality balances, thus obtaining a good fit for “wrong” reasons (Moriasi et al., 2015).

Furthermore, the applications of SWAT at large-scale, as well as of other H/WQ models, are subject to several sources of uncertainty, which may be caused by imperfect process understanding, model parameterization or input data (Gudmundsson et al., 2012). For instance, large river basins are often strongly influenced by human activities (e.g. irrigation, reservoirs, river and groundwater use) for which information is rarely available (Döll et al., 2009) and thus usually neglected. In addition, the commonly used global data sets can be inconsistent, erroneous, and only available at a coarse resolution (Hunger and Döll, 2008) or for limited areas. Physical properties (e.g. topography, land uses and soil type) in large

areas generally show higher spatial variability and thus larger heterogeneity in system behavior which affects model parameters (Coron et al., 2012; Sawicz et al., 2011; Kumar et al., 2013). A further complication is the parameterization in the calibration procedure that could lead to equifinality (non-uniqueness) problem. In addition, large-scale modeling is more prone to technical problems and data inconsistencies which become apparent when running the model (and therefore should be resolved early in the model setup process; Pechlivanidis and Arheimer, 2015).

To date, few guidelines have been defined to help users to perform a reliable modeling, but they are not exhaustive focusing only on model performance results. Thus, the main objective of this thesis concerns the development of a systematic modeling approach for calibrating and validating the SWAT model for large-scale applications leading to realistic simulation of all critical processes (i.e. surface runoff, lateral flow, baseflow, erosion and sedimentation, plant growth, nutrients cycle/fate/transport, karst phenomena, etc.). The result will thus contribute significantly to the scientific knowledge of water quantity and quality remodeling in large River Basins in Europe and support sustainable water management effort across Europe.

The proposed approach for large-scale SWAT applications involves in cascade: the definition of a suitable setup, the process-based calibration and validation (C/V) strategy for quantity and quality assessment, as well as the comparisons with other modeling studies (Malagò et al., 2015a,b,c,d; Vigiak et al., 2015a). Furthermore, the approach is complemented by a tool for optimal selection of Best Management Practices, BMPs (such as conservation tillage, nutrient management, waste and water treatment plat upgrading, and riparian areas), that involves the linkage of SWAT model with economic components. For policy and management purposes, the proposed systematic approach helps addressing correctly the BMPs implementation, looking at both the investments costs and environmental benefits.

In particular, the main innovative aspects of the procedure concern the C/V strategy. The calibration of streamflow and its components based on a limited group of independent gauged subbasins (headwaters) is pursued adjusting step by step selected parameters underpinning each hydrological process. A regionalization technique is then performed to transfer the calibrated parameters to ungauged subbasins. This technique allows decreasing the computation time for calibration at large-scale and also gaining good knowledge and insights of each hydrological process. In addition, the calibration of sediment and nutrients (nitrate, total nitrogen and phosphorous) is performed using concentrations rather than loads (which is usually done in most studies) to remove the uncertainty in the

loads estimation, but above all to capture the true temporal variability of the concentration rather than that of the load which is controlled mostly by the fluctuations of the water flow.

In the research work special emphasis is also put on (i) validation of the simulated components of water balances using the Budyko framework (Budyko, 1974); (ii) sensitivity analysis of topographic attributes with focus on hillslope length parameter and its impact on SWAT hydrology; (iii) representativeness of karst processes through the use of a karst-flow model linked with SWAT (KSWAT model); (iv) nutrients and sediment assessment at large-scale, providing insightful improvement; (v) comparative evaluations of SWAT model outputs (streamflow and nutrients) with simulations from other widely used large-scale models (GREEN, Grizzetti et al., 2008; 2012; MONERIS; Behrendt et al., 2000 and Venohr et al., 2011); (vi) application of a multi-objective optimization tool for complex scenarios of BMPs implementation.

Several SWAT model case studies were used to illustrate these topics covering approximately 55% of Europe Union. The Iberian (556,000 $km^2$) and the Scandinavia (1,000,000 $km^2$) Peninsulas were used to assess the impact of climate regimes on C/V strategy. The Danube River Basin (800,000 $km^2$) characterized by a wide range of landscapes and heterogeneous topography, large climate variations, several land covers/uses and soil types, was used for arguing topics (i), (ii), (iv), (v) and (vi) mentioned above. Crete, (8,400 $km^2$) having a dominant karst morphology that approximately cover the 40% of the Island was selected for validating the new SWAT karst component.

All these case studies can be considered valid for any H/WQ model that shares a structure similar to that of the SWAT model, and for this reason the term “systematic approach” is used to describe the proposed procedure. Following this procedure, users could increase the quality, consistency and repeatability of model results, as well as the utility of model applications for policy support and decision making in large River Basins.

The layout of the present thesis is the following.

In Chapter 2, the basic characteristics of the SWAT model and its main hydrological and qualitative (sediment and nutrients) components are presented, as well as the C/V strategy. A special emphasis is put on the hydrological, sediment and nutrients balances and on the modifications of the SWAT code to extract more useful variables, new algorithms related to topography factors and sediment estimations, as well as the setting/integration of SWAT model for describing important missing processes, such as the karst phenomena.

Chapter 3 focuses on the water quantity aspects describing at first the application of the proposed C/V strategy in two very different macroregions in Europe (the Scandinavian and Iberian Peninsulas). Then a Budyko framework approach is described analyzing the impact

of climate on the water regime of the Danube River Basin for validating the water balance components. Furthermore, the Chapter describes the effects of SWAT modifications on streamflow and its components, on the reliability of the sediments prediction, as well as the application of the adapted/integrated SWAT model for the description of karst phenomena in the Island of Crete.

Chapter 4 describes the application of sediment and nutrients calibration strategy in the Danube River Basin, as well as the proposed water quality-economic scenarios based on a multiple-objective optimization.

Afterwards, in Chapter 5 a comparative model assessment of long-term annual streamflow and nutrient loads is presented. Three models (SWAT, GREEN and MONERIS) that differ for structure and complexity are compared in the Danube River Basin.

Finally, Chapter 6 provides the conclusions of the research work, while specific information of the SWAT model applications of this thesis are provided in the Appendix (i.e. input data and C/V dataset), as well as insights related to the methodology.

# CHAPTER 2

# 2 The SWAT Model, concepts data requirements and calibration

## 2.1 Chapter Introduction

The Soil and Water Assessment Tool (SWAT) model has emerged as one of the most widely used hydrological and water quality watershed models worldwide. Its international use is largely due to its flexible structure that allows it to address different water resource problems, as well as the available complete documentation, supporting software and its open source code that can be adapted by model users for specific applications (Gassman et al, 2007). Because of the large existing literature (Arnold et al., 2012b; Gasman et al., 2007, 2014: Arnold and Fohrer, 2005; Borah and Bera, 2003, 2004; Shepherd et al., 1999), only a short description of the model structure and its hydrological and qualitative (sediments and nutrients) components are given herewith. The description will focus on the water, nutrients and sediment balances and their key processes within a basin.

The definition of a balance offers a useful mean of improving our understanding of catchment response to different land use scenarios and management programs, as well as to long-term climate change studies (Walling and Collins, 2008). For these reasons the water quantity and quality balances are identified as practical frameworks for policy makers and basin managers in targeting mitigation strategies (e.g. Wilkinson et al., 2005).

In this context, to provide reliable balances some modifications of the SWAT model were necessary, supported by a robust strategy of calibration and validation for large-scale modelling. The modifications consisted in the development of new algorithms related to topographic factors and sediment estimations for overcoming some limitations of SWAT predictions at large scale, and the integration of important processes not accounted for, such as the karst phenomena.

This Chapter will detail the major water, sediment and nutrient processes included in SWAT, and then it will provide a detailed description of the new development included in the model and then it will explain the proposed calibration-validation strategy.

## 2.2 SWAT model description: structure and processes

### 2.2.1 SWAT structure

The Soil and Water Assessment Tool (SWAT; Arnold et al., 1998) operates on a daily time step and is designed to predict the impact of land use and management on water, sediment, and agricultural chemical yields in ungauged watersheds. The model is process based, computationally efficient, and capable of continuous simulation over long time periods. Major model components include weather, hydrology, soil temperature and properties, plant growth, nutrients, pesticides, bacteria and pathogens, and land management (Gassman et al., 2007; Arnold et al., 2012a).

In SWAT, a watershed is divided into multiple subbasins, which are then further subdivided into hydrologic response units (HRUs) that consist in a unique combination of soil, land use/cover and slope. The HRUs are represented as a percentage of the subbasin area and they are not spatially identified, nevertheless they are considered hydrologically isolated. Alternatively, a watershed can be subdivided into only subbasins that are characterized by dominant land use, soil type, and management. This is often applied in the large scale application (Pagliero et al., 2014; Malagó et al., 2015a).

The subbasin is a spatially defined region that comprises a main reach and its contributing area, which is composed by one or more HRUs. The HRUs are ideally connected with tributary channel, a lower order channel, that drain the fluxes in the main reach.

SWAT allows considering only one reservoir by subbasin, characterized by an inlet (the outlet of the corresponding subbasin) and an outlet (the inlet of the downstream reach).

The subbasins, main reaches and reservoirs are combined in a node-link system that defines the stream network from the headwaters to the outlet. The overall hydrologic balances, as well as sediment and nutrient balances, are simulated for each HRU, summarized at the subbasin level, and then routed through the stream network to the watershed outlet.

The SWAT model structure comprises two phases: a land phase solved at HRU level, and a stream phase solved at reach level (Neitsch et al., 2011).

In the land phase the hydrologic cycle controls the amount of water, sediments, nutrients and pesticide loadings to the main channel in each subbasin. Instead, in the routing phase the movement of water, sediments, and nutrients is simulated.

For each of them SWAT writes two different outputs (namely respectively *output.hru* and the *output.rch)* with a temporal step (daily, monthly or annual) depending of the configuration of the simulation.

Specific information about topography (i.e. elevation and slope), climate, soils, and land use are required to run the model. The main processes simulated and the related algorithms used by SWAT are summarized in Table 1. A more depth description is given by Neitsch et al. (2011).

Table 1. Main simulated processes and related algorithms implemented in SWAT

| Component | Process | Algorithms | Reference |
|---|---|---|---|
| **Hydrology** | Surface runoff | SCS Curve Number method; Green & Ampt Infiltration method | USDA Soil Conservation Service (1972); Green and Ampt (1911 ) |
| **Hydrology** | Peak runoff rate | Modified Rational Formula | Neitsch et al. (2011) |
| **Hydrology** | Lateral flow | Kinetic storage method | Sloan et al. (1983); Sloan and Moore (1984); Neitsch et al. (2011) |
| **Hydrology** | Baseflow | Baseflow recession constant; groundwater storage; re-evaporation | Neitsch et al. (2011) |
| **Hydrology** | Percolation | Storage routing method | Neitsch et al. (2011) |
| **Hydrology** | Potential Evapotranspiration | Penman-Monteith;Hargreaves;Priestley-Taylor | Hargreaves et al. (1985); Priestley and Taylor (1972); Monteith (1965) |
| **Hydrology** | Evapotranspiration (actual) | Specific algorithms to calculate canopy interception, crop transpiration and soil evaporation | Neitsch et al. (2011) |
| **Hydrology** | Channel routing | Variable storage routing method; Muskingum routing method | Williams (1969); Neitsch et al. (2011) |
| **Hydrology** | Reservoir water routing | Input measured outflow; water release rate; monthly target volumes | Neitsch et al. (2011) |
| **Hydrology** | Tile drainage flow | SWAT-M; Houghoudt and Kirkham drainage equations. | Du et al, 2005; Green et al 2006; Moriasi et al. (2007a, 2013a, 2013b); |
| **Plant Growth** | Biomass and crop yields | EPIC model equations | (Williams et al., 1984) |
| **Quality** | Nitrogen and Phosphorous cycle | i.e. loading function; equations from Epic model, PAPRAN mineralization model | Neitsch et al. (2011); McElroy (1976); Williams and Hann (1978);Seligman and van Keulen, 1981) |
| **Quality** | Nitrate movement and soluble phosphorous movement | i.e. exponential decay weighting function for transport in aquifer | Neitsch et al. (2011);Venetis (1969); Sangrey et al. (1984) |
| **Quality** | In stream nutrient-processes | QUAL2E model | Brown and Barnwell (1987) |
| **Quality** | Nutrient in water bodies | Nitrogen and phosphorous mass balance | Chapra (1997) |
| **Quality** | Riparian land | Empirical equations based on runoff reduction (%) | White and Arnold (2009); Neitsch et al. (2011) |
| **Quality** | Nutrient and phosphorous in tile drainage system | Equations function of tile flow ($m^3/d$), concentration in solution in the layer containing the tile drain and the percolation coefficient | Neitsch et al. (2011); (Moriasi et al.,2013b) |
| **Sediment** | Erosion | Modified Universal Soil Loss Equation (MUSLE) | Williams (1975) |
| **Sediment** | Sediment transport, bank and bed erosions in channel | Simplified Bagnold equation (default method); Kodatie model; Molinas and Wu model; Yang equation. | Neitsch et al. (2011) |

### 2.2.2 The Hydrological component

The hydrological land phase and in-stream phase include the computation of HRU daily water balance and the routing of water in each reach.

The HRU daily water balance solves the change in soil water storage (in mm $H_2O$) as a function of daily precipitation, surface runoff, evapotranspiration, infiltration in the vadose zone, and baseflow. The conceptualization of SWAT water balance is shown in Figure 1 and can be estimated as follow:

[eq. 1] $$P = ET + SR + LF + BF + BF_{DA} + DA_{RCHRG} + TLOSS$$

where P is the precipitation (mm), ET is the evapotranspiration (mm), SR is the surface runoff (mm), LF is the lateral flow contribution to stream flow (mm), BF and $BF_{DA}$ are respectively the baseflow contribution to streamflow from shallow and deep aquifer aquifer (mm), the $DA_{RCHRG}$ is the amount of water that from the shallow aquifer recharges the deep aquifer, and the TLOSS (not reported in Figure 1) is the bed transmission losses (mm) from the main reach or tributary channel.

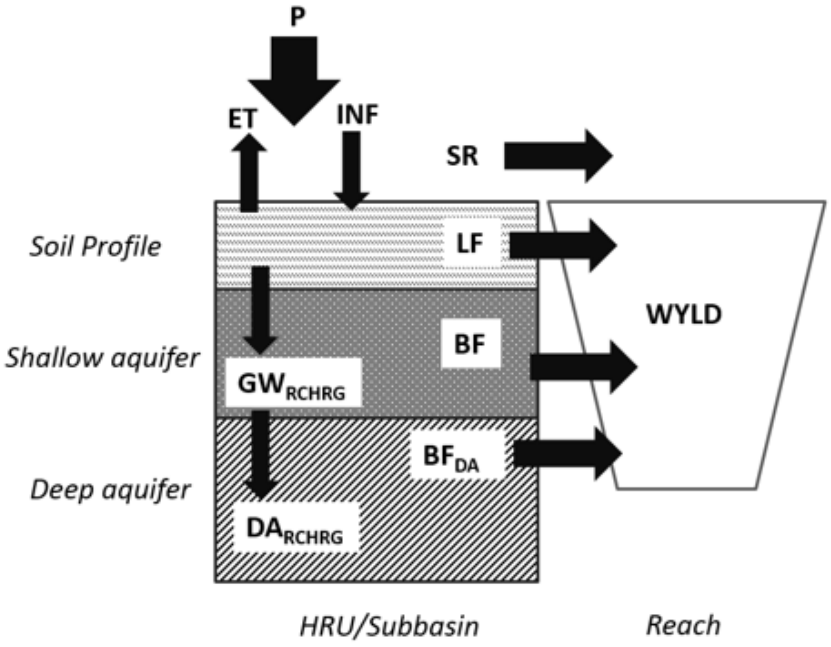


Figure 1. Conceptual SWAT model water balance: P: precipitation; ET, evapotranspiration; BF, baseflow from shallow aquifer; $BF_{DA}$, baseflow from deep aquifer; INF, infiltration in the soil; LF, Lateral flow; SR, Surface Runoff; $DA_{RCHRG}$, the deep aquifer recharge; $GW_{RCHRG}$, the shallow aquifer recharge; WYLD: water yield.

The climatic inputs used in SWAT include daily precipitation (P), maximum and minimum temperature, solar radiation data, relative humidity, and wind speed data. The potential evapotranspiration (PET) was estimated using the Penman-Monteith method (Monteith,

1965), and the actual evapotranspiration (ET) is calculated including the processes of canopy interception, crop transpiration and soil evaporation (Neitsch et al., 2011).

The average air temperature is also used to determine if precipitation should occur as snowfall, while the maximum and minimum temperature inputs are used in the calculation of daily soil and water temperatures.

To account for the increase in precipitation and decrease in temperature with elevation that is typically observed in mountainous regions, SWAT allows implementing the elevation bands (Neitsch et al., 2011)

The total amount of water leaving the HRU (sum of SR, LF and BF) and entering the main channel during the time step is the water yield (WYLD). The accurate estimation of these components is of primary importance when assessing the impact of pollutant transport and for a sustainable water resources use. In this thesis the flow generated from HRUs is referred to as WYLD, whereas the flow routed in the reach (streamflow) is referred to as Q.

SWAT uses two linear reservoirs to partition groundwater into two aquifer systems: a shallow aquifer which contributes baseflow to streams (BF) and a deep aquifer which can also contribute baseflow to streams ($BF_{DA}$). The remaining portion in the deep aquifer ($DA_{RCHRG}$ - $BF_{DA}$) can be considered lost from the system. It is noteworthy that in this thesis the contribution of baseflow from deep aquifer was considered negligible. The recharge for a specific day is calculated as a linear function of the daily seepage, the recharge of the previous day and the groundwater delay. Daily seepage includes seepage through the soil profile and through ponds or wetlands and loosing streams (tributaries and main channels). All seepage losses are added together and assumed to travel vertically to the aquifer with the same velocity.

The surface runoff (SR, mm) is estimated using the SCS curve number method (USDA Soil Conservation Service, 1972) as modified by Williams (1985) to account for the impact of slope on the curve number. SWAT calculates SR according to the equation:

[eq. 2] $$SR = \frac{(P_i - I_a)^2}{(P_i - I_a + S)}$$

where $P_i$ is the precipitation for the day (mm), $I_a$ is the initial abstraction which include surface storage, interception and infiltration prior to runoff (mm), and S is the retention parameter (mm) which is a function of the curve number (CN) for the day.

The peak runoff rate ($q_{peak}$, $m^3/s$) is calculated with the modified rational formula:

[eq. 3] $$q_{peak} = \frac{\alpha \cdot SR \cdot Area}{3.6 \cdot t_{conc}}$$

where Area is the HRU area ($km^2$), $t_{conc}$ is the time of concentration (h), and α is the fraction of daily runoff that occurs during the time of concentration. The time of concentration is calculated with a modified rational method (Chow et al., 1988) as:

[eq. 4] $$t_{conc} = t_{ov} + t_{ch}$$

where $t_{ov}$ is the overland flow time and $t_{ch}$ is the channel flow time. The latter is depending on channel length (km), Manning's roughness coefficient of the channel, and channel slope (% or m/m), while the overland flow time is the time that water takes to travel from the furthest point in the subbasin to a stream channel and it is computed as:

[eq. 5] $$t_{ov} = \frac{L1^{0.6} \cdot n^{0.6}}{18 \cdot slp^{0.3}}$$

where L1 is the average subbasin hillslope length (m), slp is the average subbasin slope (% or m/m), and n is Manning's roughness coefficient.

The lateral flow (LF, mm) occurs whenever the water content of the soil exceeds its water content at field capacity and it is calculated as:

[eq. 6] $$\mathrm{LF} = 0.024 \left(\frac{2 \cdot \mathrm{SW_{ly,excess}} \cdot \mathrm{K_{sat}} \cdot \mathrm{slp}}{\Theta_d \cdot \mathrm{L1}}\right)$$

where $SW_{ly,excess}$ is the drainable volume of water stored in saturated zone of the HRU per unit area (mm), $K_{sat}$ is the saturated hydraulic conductivity (mm/h), $\Theta_d$ is the drainable porosity of the soil (mm/mm), and L1 is the hillslope length (m).

Multiplying the $K_{sat}$ with slp gives the LF velocity at the HRU outlet ($v_{lat}$; Neitsch et al., 2011):

[eq. 7] $$\mathrm{v_{lat}} = \mathrm{K_{sat}} \cdot \sin(\alpha_{\mathrm{hill}}) = \mathrm{K_{sat}} \cdot \tan(\alpha_{\mathrm{hill}}) = \mathrm{K_{sat}} \cdot \mathrm{slp}$$

where $\alpha_{\mathrm{hill}}$ is the HRU gradient (degree). In SWAT it is assumed $\sin(\alpha_{\mathrm{hill}}) \sim \tan(\alpha_{\mathrm{hill}})$ to simplify the equation, thus slp is equivalent to $\tan(\alpha_{\mathrm{hill}})$.

The baseflow (BF) from the shallow aquifer is calculated based on the aquifer recharge (GW_RCHRG, mm $H_2O$), the deep aquifer recharge ($DA_{RCHRG}$, mm $H_2O$) and the baseflow recession constant (ALPHA_BF, 1/day). Similarly, the baseflow from the deep aquifer ($BF_{DA}$) depends on the deep aquifer recharge and on the deep-baseflow recession constant (ALPHA_BF_D, 1/day).

### 2.2.3 Crop management and the Best Management Practices (BMPs)

SWAT simulates the land management practices and can incorporate very detailed management information (Sood et al., 2010). Management practices are broadly divided into agriculture management, water management and urban areas management.

Some of the agricultural practices include plant growth cycle, timing and quantity of fertilizer, type of tillage, removal of plant biomass, as well as pesticide application.

SWAT uses a single plant growth model to simulate growth and yield of all types of crop. The crop growth is inspired from the Erosion Productivity Impact Calculator (EPIC) model (Williams et al., 1984) which bases the phenological development of the plant on accumulated heat units which are a function of the minimum and maximum air temperatures. In particular, plant growth is modeled by simulating leaf area development, light interception and conversion of intercepted light into biomass (Jiang et al., 2014). The model calculates the daily accumulated heat units (PHU) and when plant maturity is reached, the plant ceases to transpire and to take up water and nutrients. Then the simulated plant biomass remains stable until the plant is killed or harvested by using a harvest index to define the fraction of dry biomass that is removed as yield. Crop yield is simulated on a dry weight basis.

Water management includes irrigation, tile drainage systems, reservoirs/impounded/depressed areas, water uses, and loading from point sources. Simulation of irrigation can be performed using five alternative water sources: reach, reservoir, shallow aquifer, deep aquifer, or a water body source external to the watershed. The irrigation applications can be simulated on user selected specific dates or with an autoirrigation routine, which activates irrigation events according to a water stress threshold (plant or soil water deficit) (Gassman et al, 2007). Similarly, the fertilization could be applied manually or in automatic way (Arnold et al., 2012a).

For the urban areas, the model estimates the surface runoff with the SCS curve number method or the Green & Ampt equation, while sediment and nutrients are simulated using a linear regression equations developed by the USGS (Driver and Tasker, 1988) or a 'build up/wash off' approach, similar to SWMM-Storm Water Management Model (Huber and Dickinson,1988). In this thesis the SCS curve number method and the 'build up/wash off' approach were selected.

Best Management Practices (BMPs) are also simulated in SWAT and Table A3.1 in Appendix 3 provides the BMPs implemented in the case study of the Danube River Basin. The conservation practices include cover crops, conservation tillage, residue management, terraces, artificial drainage systems, riparian filtering, and wetlands. Recently the riparian filter strips and the artificial drainage systems algorithms have been updated by SWAT developers/users in order to improve their reliability and replicability at different spatial scale.

White and Arnold (2009) proposed a new routine to simulate the riparian filtering, overcoming some limitations of the previous algorithm, such as the use of the same filtering

efficiency for sediment and all nutrients forms. The new routine consists in empirical equations developed from a combination of measured data derived from literature and simulation results of the Vegetative Filter Strip MODel (VFSMOD) (Munoz-Carpena et al., 1999). These equations allow calculating the sediment and nutrients reductions based on an empirical runoff reduction (in %), that is only used for this purpose without affecting the water balance.

The subsurface tile drainage is simulated by SWAT using two methods. The first tile drainage algorithm calculates tile flow as a function of a water table depth (wtd), the distance between soil surface and a user defined impervious layer (DEP_IMP), tile depth (DDRAIN) and the time required to drain the soil to field capacity (TDRAIN), as well as the drain tile lag time (GDRAIN) (Du et al, 2005; Green et al., 2006). This method assumes that the tile systems have equidistant tile spacing and size. The second tile drainage algorithm computes tile flow using Hooghoudts (1940) steady state and Kirkham (1957) tile drain equations that are a function of water table depth, tile drain depth, size, and spacing (Moriasi et al., 2007a, 2013a, 2013b). For both methods, SWAT allows calculating wtd using the SWAT-M approach (Du et al, 2005) or the modified DRAINMOD approach (Moriasi et al., 2012).

Currently, there is a lack of documentation of the Hooghoudt and Kirkham method and the modified DRAINMOD approach in Neitsch et al., 2011), however details of the theory and practical case studies can be found in Moriasi et al. (2007a, 2013a and 2013b). Albeit this limitation, these latter methods are used in this thesis, and were tested in the Danube River Basin (section 4).

Scenarios analyses of BMPs application are often performed with SWAT model, albeit only focusing on qualitative benefits (i.e. Cerro et al., 2014; Aouissi et al., 2014). However, for policy and management purpose, the investment-cost assessments are an essential task that should be integrated with the environmental analysis. Thus in this thesis, the SWAT model is complemented by a tool for optimal selection of Best Management Practices, BMPs (i.e fertilizer reduction and upgrading of waste water treatment plant), that involves the linkage of SWAT model with economic components (herewith called as R-SWAT model). In Appendix A5, the R-SWAT model is described, while in section 4.4 the application of the case study of the Upper Danube is provided.

### 2.2.4 The Qualitative component

The SWAT model distinguishes the nutrient pollution (N, nitrogen and P, phosphorous) from diffuse sources (DS) and from point sources (PS). Diffuse source pollution can be caused by a variety of activities that have no specific point of discharge. For instance, agriculture is

a key source of diffuse pollution, but urban land and atmospheric deposition can also be important sources. Conversely, point source pollution comes from one source like an industry or a waste water treatment plant. These sources can lead to several water quality problems, such as the eutrophication phenomena in rivers and reservoirs/lakes. The impact of diffuse sources is reduced in part by the natural retention of soil system and by the effects of the riparian filtering that decrease the amount of diffuse emission (DE) toward the river, as well as the river retention reduces the nutrient load in the rivers coming from both point and nonpoint sources.

Figure 2 shows the general conceptualization of nutrients balance by the SWAT model, that however differ for nitrogen and phosphorous as shown in Figure 3 and Figure 4.

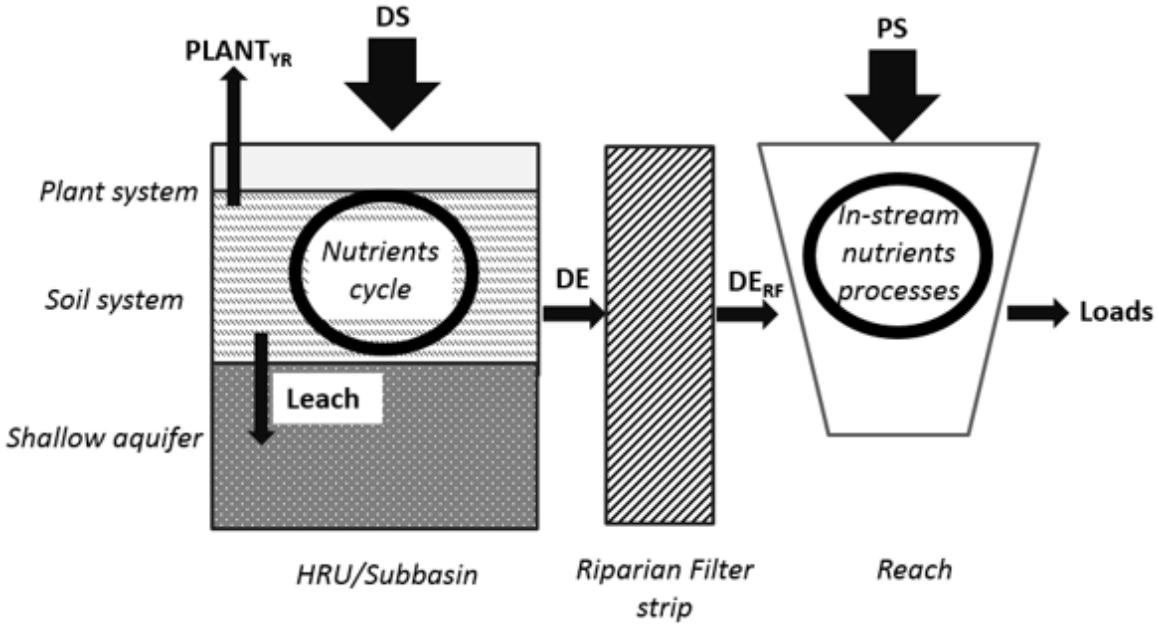


Figure 2. Conceptual SWAT model nutrient balance: DS: diffuse sources; PS: Point sources; PLANT$_{YR}$: nutrients removed with plant yield; Leach: nutrients leaching in the shallow aquifer; DE: diffuse emissions; DE$_{RF}$: diffuse emission after the riparian filtering reduction; Loads: nutrients loads in the output of the Basin.

The transformation and movement of nitrogen and phosphorus from diffuse sources (DS) within an HRU/Subbasins are simulated in SWAT as a function of nutrient cycles consisting of several inorganic and organic pools (Figure 2). Within the reach, instead, SWAT adopted a modified version of the QUAL2E model (Brown and Barnwell, 1987) to simulate in−stream nutrient transformations. The sub−components of QUAL2E include models of the biochemical dynamics of algae as chlorophyll−a, dissolved oxygen, carbonaceous oxygen demand and the various chemical forms of nitrogen and phosphorous. Between the HRU/Subbasin and reach, the SWAT riparian filter strips can reduce the diffuse nutrient emission as a function of an empirical reduction of surface runoff, as described in the previous section 2.2.3. In addition, SWAT simulates the nutrient removed by crop harvest

($PLANT_{YR}$ in Figure 2, $N_{YR\ and}$ $P_{YR}$ respectively for nitrogen and phosphorous in Figure 3 and Figure 4) using a supply−and−demand approach, as well as the nitrate leached (Leach) to the shallow aquifer (Figure 3). Instead, the soluble P leaches only from the top 10 mm of the soil into the first soil layer due to its low mobility as shown in Figure 4 (Neitsch et al., 2011).

Figure 3 shows in details the conceptual SWAT model nitrogen (N) balance. The diffuse sources include the nitrogen fixation by plants ($N_{FIX}$), the nitrogen deposited on the soil with the precipitation ($N_{RAIN}$) and the nitrogen applied as fertilizer ($N_{APP}$). Nitrogen processes simulated in the soil include mineralization, residue decomposition, immobilization, nitrification, ammonia volatilization and denitrification. While in the reach, among the aforementioned processes simulated by QUAL2-E model, the denitrification is not represented and the nitrogen retention is the result of sedimentation and uptake by algae.

SWAT also includes a simple empirical model to predict the trophic status of water bodies, allow the users to define the nutrients settling rates.

In particular, SWAT determines the amount of nitrate lost by denitrification in the soil as following:

[eq. 8] $N_{DENIT,ly} = NO3_{ly}\left(1 - e^{\left[-CDN \cdot \gamma_{tmp,ly} \cdot SOL\_CBN_{ly}\right]}\right)$ if $\gamma_{sw,ly} \geq SDNCO$

[eq. 9] $N_{DENIT,ly} = 0.0$ if $\gamma_{sw,ly} < SDNCO$

where $ND_{ENIT,ly}$ is the amount of nitrogen lost through denitrification (kg N/ha), $NO3_{ly}$ is the amount of nitrate in layer *ly* (kg N/ha), CDN is the rate coefficient for denitrification, $\gamma\ t_{mp,ly}$ is the nutrient cycling temperature factor for layer *ly*, $\gamma_{\ sw,ly}$ is the nutrient cycling water factor for layer *ly*, $SOL\_CBN_{ly}$ is the amount of organic carbon in the layer *ly* (%) and SDNCO is the threshold value of nutrient cycling water factor for denitrification to occur. The default value of CDN is 1.4 and ranged between 0 and 3, while SDNCO is set by default to 1.1.

Nitrate, which is very susceptible to leach, can be lost through surface runoff (SRN), lateral flow (LFN) and percolate out of the soil profile and enter in the shallow aquifer ($N_{LEACH}$). The amount of nitrate in surface runoff (SRN) is only considered in the top soil layer (10 mm thickness). Amounts of N-NO3 contained in lateral subsurface flow and percolation are estimated as products of the water volume and the average concentration of nitrate in each layer. The organic nitrogen (ORGN) transport with sediment is calculated using a loading function (McElroy et al., 1976; Williams and Hann, 1978) based on the concentration of organic N in the top soil layer, the sediment yield, and the enrichment ratio. The enrichment ratio (ERORGN) is the ratio of the mass of organic nitrogen in the sediment to that in the soil. Nitrate is transported also via tile drainage system (NTILE) and it is obtained multiplying

tile flow ($m^{3/}d$) by N-NO3 concentration in solution in the layer containing the tile drain and the NPERCO parameter (nitrate percolation coefficient) (Moriasi et al.,2013b). Nitrate in the shallow aquifer may be lost by biological and chemical denitrification that SWAT simulates using the nitrate half-life parameter. The remaining part can transport to the river with the baseflow (BFN).

Figure 4 shows the SWAT conceptualization of the phosphorous (P) balance. SWAT considers as unique form of diffuse source for P the fertilizer application ($P_{APP}$). The amount of soluble phosphorus removed in runoff (SOLP) is predicted using the labile P concentration in the top 10 mm of the soil, the runoff volume, and a partitioning factor (Neitsch et al., 2011). Sediment transport of P (SEDP) is simulated by a loading function, as described for ORGN, based on an enrichment ratio (ERORGP). As for NTILE, the phosphorous transported via tile drainage system (PTILE) is simulated by SWAT multiplying tile flow ($m^3/d$) by the phosphorous concentration in the layer with the tile drain and the PHOSKD parameter (phosphorous percolation coefficient) (Moriasi et al., 2013b).

Finally, it is noteworthy, that the reduction of pollution due to the riparian filter strips has not impact on NTILE and PTILE, as well as on LFN and BFN (Figure 3 and Figure 4). In practice, to evaluate the impact of riparian filtering on nutrients diffuse emissions, the model outputs have to be compared with outputs from SWAT simulation in absence of riparian filter.

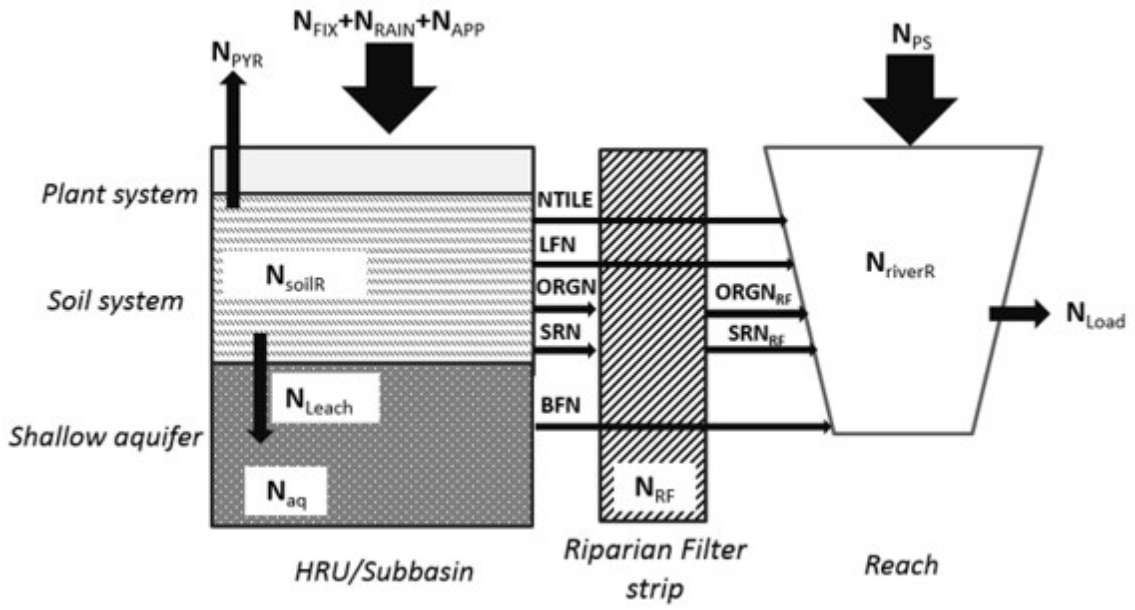


Figure 3. Conceptual SWAT model nitrogen balance: the diffusion sources are represented by the sum of nitrogen applied to the plant biomass via fixation ($N_{FIX}$), nitrogen transported to the soil with the precipitation ($N_{RAIN}$) and the nitrogen applied as fertilizer ($N_{APP}$); $N_{PS}$ is the nitrogen loading to the reach from point sources; the diffusion emissions are the nitrates loading to reach in tile drainage system (NTILE), in lateral flow (LFN), in surface runoff (SRN), in baseflow (BFN) and the organic nitrogen transported with the water yield (ORGN); $ORGN_{RF}$ and $SR_{RF}$ are respectively the organic nitrogen and nitrates reduced by riparian filtering; $N_{LEACH}$ is the nitrogen leached to aquifer; $N_{PYR}$, $N_{soilR}$, $N_{aq}$, $N_{RF}$ and $N_{riverR}$ are respectively the reduction of nitrogen applied by plant, soil, aquifer, riparian filter strip and river; $N_{Load}$ is the total nitrogen loads at the outlet of the Basin.

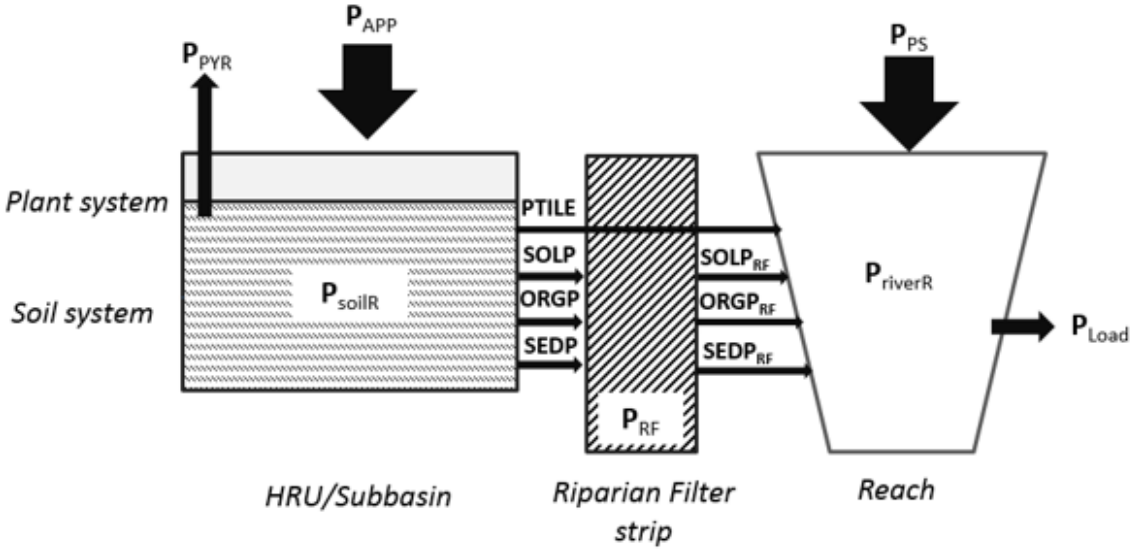


Figure 4. Conceptual SWAT model phosphorous balance: the diffusion sources are represented by phosphorous applied as fertilizer ($P_{APP}$); $P_{PS}$ is the phosphorous loading to the reach from point sources; the diffusion emissions are the soluble phosphorous (phosphate) transported in tile drainage system (PTILE) and water yield (SOLP), the organic phosphorous loading to the reach (ORGP) and the mineral phosphorous adsorbed to sediment and transported into the reach ($SEDP_{RF}$); $SOLP_{RF}$, $ORGN_{RF}$ and $SEDP_{RF}$ are respectively the soluble, organic and mineral phosphorous reduced by riparian filtering; $P_{PYR}$, $P_{soilR}$, $P_{RF}$ and $P_{riverR}$ are respectively the reduction of phosphorous applied by plant, soil, riparian filter strip and river; $P_{Load}$ is the total nitrogen loads at the outlet of the Basin.

### 2.2.5 The Sediment component

The SWAT model estimates soil erosion and sediment yields from the landscape (HRU/subbasin) and in−stream (reach) simulating depositional and degrading processes. The sediment yield from non–urban HRU/subbasin is calculated by the Modified Universal Soil Loss Equation (MUSLE) (Williams, 1975). Instead, sediment deposition and degradation in the reach are both calculated during the sediment routing.

The MUSLE equation estimates the sediment yields as following:

[eq. 10 ] $$SY = 11.8 \cdot \left(SR \cdot q_{peak} . A\right)^{0.56} (C \cdot P \cdot K \cdot L \cdot LS1 \cdot F_{CRFG})$$

where SY is the HRU sediment yield (t/day); SR is the surface runoff (mm); $q_{peak}$ is the runoff peak rate ($m^3/s$) (see [eq. 3]); A is the HRU area (ha); C, P, K, and LS1 are dimensionless factors accounting for HRU crop cover, soil protection, soil erodibility, and topography as defined in the original Universal Soil Loss Equation (USLE; Wishmeier and Smith, 1978), while $F_{CRFG}$ is a dimensionless factor to account for coarse fragment cover. In particular, LS1 factor is calculated in SWAT using the original Universal Soil Loss Equation (USLE, Wishmeier and Smith, 1978):

[eq. 11] $$LS1 = \left(\frac{L1}{22.13}\right)^{m} \cdot (65.41 \cdot (\sin\theta)^2 + 4.56 \cdot \sin\theta + 0.065)$$

Where L1 is the SWAT hillslope length (m), θ is the hillslope slope gradient (in radians) and the exponent m depends on θ.

The maximum amount of sediment that can be transported during channel sediment routing in a reach is determined by the modified Bagn*old's equation (*Bagnold, 1977):

[eq. 12] $$C_{max=} c_{sp} \cdot \left(\frac{prf \cdot q_{ch}}{A_{ch}}\right)^{e_{sp}}$$

where $C_{max}$ is the maximum daily concentration of sediments ($ton/m^3$) that can be transported in the reach; the elements between the brackets define the peak chanel velocity (m/s) as a function of $q_{ch}$ (reach peak flow rate, $m^3/s$), $A_{ch}$ (channel cross sectional area, $m^2$) and prf (sediment peak rate adjustment factor in the main channel). The coefficients $cs_p$ *(or SPCON)* and $e_{sp}$ (or *SPEXP)* regulate the linear and exponential relationship between the stream power and the peak velocity. They may be defined by the user during the model calibration. SPCON should be between 0.0001 and 0.01 and SPEXP normally ranges from 1.0 to 2.0. The larger are these two parameters, more sediments are transported and less deposition occurs.

If the incoming sediment concentration exceeds $C_{max}$, the excess sediments are deposited in the reach (aggradation). Conversely, if sediment inputs are below the stream transport capacity, deposited sediments followed by channel and bank erosion (degradation) may

occur. Several options are available to define the channel erosion rate, and in this thesis a physics-based approach that uses a channel flow shear stress resistance threshold was used (see for more details Neitsch et al., 2011). In this approach, the erosion rate of channel banks and bed depends on the effective streamflow shear stress ($\tau_e$, Pa), on the channel erodibility ($\kappa_b$, $cm^3/N$), and on a critical flow shear stress threshold ($\tau_c$, Pa) below which no erosion occurs. The critical flow shear stress threshold $\tau_c$ and channel erodibility $\kappa_b$ can be defined by the user based on measurements, or derived from bank and bed vegetation cover and sediment characteristics (Knapen et al., 2007; Neitsch et al., 2011; Vigiak et al., 2015a).

The daily sediment balance (Figure 5) in a large basin includes the source (erosion) and sinks of sediments (deposition and trapping). The sources of sediment are identified with the hillslope erosion that can be further partitioned between land cover types, and the stream erosion. Instead, the sinks of sediments are represented by the deposition in the reaches and in the floodplain, as well as the sediment trapping in reservoirs. Another important reduction is also applied by the riparian filter strips.

As described above, in this thesis the hillslope erosion is calculated for non-urban and urban HRU/subbasin using respectively the MUSLE equation and the 'build up/wash off' approach, while the stream erosion, as well as the stream deposition, is evaluated using the maximum daily concentration approach.

In particular, the floodplain deposition occurs during large storm events when the streamflow level can rise above the channel depth and expand over the floodplain, drastically increasing its cross-sectional area and thus reducing velocity and allowing fine sediments deposition (silt and clay particles) (Neitsch et al.,2011).

Concerning reservoirs, it is well documented that all reservoirs or natural lakes are subject to some degree of sediment inflow and deposition. When stream flow enters a reservoir, transport capacity of the water is reduced; hence sediments are accumulated within a reservoir based on grain size, physical shape of the reservoir, and operational practices (Duru 2015; Neitsch et al., 2011).

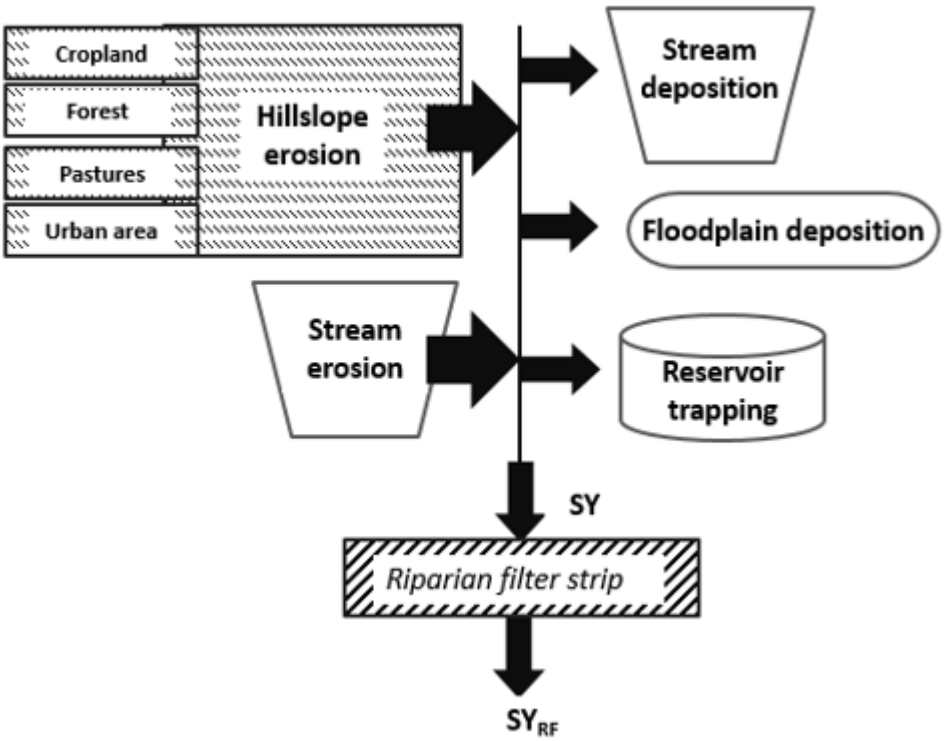


Figure 5. Conceptual SWAT model sediment balance: the sources of erosion are represented by the hillslope erosion from different land cover and the stream erosion; the sinks of sediments derived from deposition in stream and floodplain, as well as from trapping process in reservoirs. The SY (Sediment Yield) is also further affected by the presence of riparian filter strips that remove sediment through the reduction of the runoff velocity. $SY_{RF}$ is the sediment yields affected by riparian filter strips.

Riparian filtering has a significant impact on sediments estimation by removing sediment due to reduced runoff velocity caused by the increased resistance of the vegetation and infiltration (Barfield et la., 1998). As a consequence, to evaluate the impact of riparian filtering on final sediment yields, the model outputs has to compared to outputs that would occur in the absence of riparian filter strips (simulation of SWAT model without riparian filter strips).

## 2.3 The SWAT model executable and its modifications

In this study two versions of the SWAT model are used: SWAT model 2009 Version 511 and the recent SWAT model 2012 Version 622. The two versions work on different ArcGIS support (respectively ArcGIS 9.3.1 and ArcGIS 10.1), and they have some differences in algorithms at the process level. For this reason, during the period of the thesis it was necessary to move up to the recent version, where several bugs present in version 2009 were fixed. For more details, the revision history of SWAT model versions at the SWAT website (http://swat.tamu.edu/software/swat-executables/revisions/) provides a complete description.

The SWAT open source code written in Fortran (Clive G. Page, 1988) allows changing some of its parts improving the interpretation of outputs and the solidity of SWAT algorithms, such as the simulation of lateral flow and sediment flux (Malago' et al., 2015c; Vigiak et al., 2015a).

The main changes involved the creation of new outputs (subflow.rch, sedflow.rch, qualflow.rch) containing daily, monthly and annual results (depending on the configuration of simulation), the change of slope length algorithm, the modification of MUSLE equation [eq. 10], the substitution of the SWAT topography factor (LS) equation with a new formulation, as well as the addition of missing processes such as the karst phenomena.

### 2.3.1 The new outputs

The *subflow.rch* contains the streamflow and its components (surface runoff, lateral flow, baseflow), as well as the logarithm of streamflow (in $m^3/s$). The *sedflow.rch* improves the existing *output.sed* (in SWAT 2012) writing 26 variables that were originally subdivided in the *output.sed* and *output.rch* (one of the most important file of SWAT that writes the simulated streamflow output and related qualitative characteristics in each reach). Thus *sedflow.rch* includes streamflow ($m^3/s$), sediment concentration (mg/l), sediment loads (ton) and specific loads ($ton/km^2$), as well as the amounts of channel deposition (ton) and erosion (ton).

Instead, the *qualflow.rch* is a new output file that writes the concentration (mg/l) of total nitrogen and phosphorous, as well as its chemical forms (Nitrate-N, N-NH3, Nitrite-N, N-NH2, Organic nitrogen ORGN, Ammonium-N, N-NH4, Phosphate-P, P-PO4 and Organic phosphorus, ORGP).

These files were written so that they are compatible with SWAT-CUP software (Abbaspour et al, 2008), that was used in the calibration strategy as explained in section 2.4.

### 2.3.2 The new hillslope length algorithm

According to Wishmeier and Smith (1978), the hillslope length is defined as the horizontal distance from the point of origin of surface runoff to the point where runoff enters a river. The best estimates for hillslope length are obtained from field measurements (Yao et al., 2010), but these are not always available or practical, especially at watershed scale (Zhang et al., 2013). In a basin the hilllsope length is very difficult to calculate and it is not solely dependent on slope gradient (Bieger et al., 2015). In the SWAT model the hillslope length (L1) is calculated based on slope gradient using Wishmeier and Smith (1978) lookup table. The slope gradient is derived from pre-analyses of the Digital Elevation Model (DEM) at subbasin level using the ArcSWAT interface (Winchell et al., 2013). L1 takes the maximum

value of 122 m when the slope gradient is less than 2%, and decreases to 9 m when the slope gradient is more than 25%. However, the original look-up table was proposed for setting hillslope length in the case of contour support practices and may not be appropriate in the absence of these.

A compressive analysis of L1 potential effect on SWAT outputs is currently lacking, albeit this parameter has a primary role in the definition of streamflow components (see equations [eq. 5] and [eq. 6]) and sediments yields via peak runoff rate and LS factor (see equation [eq. 10] and [eq. 11]).

As a consequence, two alternative algorithms, called L2 and L3, are proposed (Malago' et al., 2015c):

- L2 estimates hillslope length from a DEM flow accumulation analysis. The freeware LS-TOOL developed by Zhang et al. (2013) is used here. LS-TOOL calculates hillslope length through a step-process that requires setting an accumulated area threshold ($A_s$, $m^2$) above which water flow is channelized. $A_s$ is a very sensitive parameter; Zhang et al. (2013) demonstrated that when increasing $A_s$, the hillslope length increases until a maximum value that depends on DEM pixel size, after which it remains quite constant. In this thesis, $A_s$ is defined as the area for which the maximum possible hillslope length was 122 m (i.e. the DEM pixel size times 122 m).
- L3 is that suggested by Neitsch et al. (2011) in the presence of coarse or inaccurate DEM, i.e. setting hillslope length to 50 m everywhere.

In section 3.4 the three L methods are combined with two DEM pixel sixe (25 m and 100 m) resulting in 6 different SWAT model configurations. These combinations are analyzed to assess the impact on streamflow and its components.

### 2.3.3 Modification of the MUSLE equation

The Modified Universal Soil Loss Equation [eq. 10] was originally developed for small catchments with and area of around 40 $km^2$ and successfully tested on catchments ranging between 0.01 and 234 $km^2$ (Williams and Hann,1978). However, Chen and Mackay (2004) showed that the HRU specific sediment yields (HSSY, t/ha) are non-linearly related to the HRU area. This nonlinearity is undesirable because it makes predictions for HRUs with similar environmental characteristics but different sizes unrealistic (Vigiak et al., 2015a). In addition, LS factor has been criticized for producing excessively large LS factors in steep slopes, increasing the concerns about using the SWAT MUSLE equation.

As a consequence, to improve the solidity of SWAT sediment flux assessments in large basins, the sediment yield (t/day) in equation [eq. 10] is modified as follow:

[eq. 13] $$SY = \left[11.8 \cdot \left(SR \cdot q_{peakL} \cdot A_{min}\right)^{0.56} (C \cdot P \cdot K \cdot L \cdot LS_M \cdot F_{CRFG})\right] \left(\frac{A}{A_{min}}\right)$$

where $q_{peakL}$ is the runoff peak rate linearized by area A ($m^3/s/ha$) using this expression:

[eq. 14] $$q_{peakL} = q_{peak} \cdot \left(\frac{A_{min}}{At}\right)$$

where $A_{min}$ is the minimum area between the HRU area and $A_t$ is a threshold area defined by the user (Vigiak et al., 2015a).

$LS_M$ is a modified version of topographic factor. Two alternative methods respect to SWAT equation [eq. 11] were proposed:

- LS2 (McCool et al., 1989):

[eq. 15] $$LS2 = \left(\frac{L}{22.13}\right)^{m_2} \cdot S; \text{ where } S = \begin{matrix} 10.8 \sin\theta + 0.03 \; for \; \theta \leq 9\% \\ 16.8 \sin\theta - 0.5 \; for \; \theta > 9\% \end{matrix}$$

where L is the hillslope length (m); θ is the hillslope slope gradient (in radians); and the exponent $m_2$ depends on θ.

- LS3 (Moore and Wilson, 1992):

[eq. 16] $$LS3 = \left(\frac{A_S}{22.13}\right)^{m} \left(\frac{\sin\theta}{0.0896}\right)^{n}$$

where the hillslope length is replaced by the accumulation area per contour length $A_s$ ($m^2/m$). The exponent *m* may vary in the range 0.4-0.6, while the exponent *n* may vary in 1.2-1.3 (Vigiak et al, 2015a).

In section 4.3, the three LS calculation methods in [eq. 11], [eq. 15] and [eq. 16] are combined with hillslope lengths L1, L2 and L3 to assess the impact of topography on the SWAT sediment yields and concentrations. Including the SWAT default configuration and accounting for the different combinations of DEM resolution (25 m DEM pixel size and 100 m DEM pixel size), hillslope lengths and LS factor calculation methods, 13 different SWAT model configurations are defined and analyzed (see Chapter 4, section 4.3).

### 2.3.4 The representation of karst process

In Europe, soluble carbonate rocks are widespread in Western, Southern and Eastern part covering 35% of whole Europe (Daly, 2002), so that the karst processes are significant components of the physical geography of the Mediterranean basins. In particular, limestones reach great thickness in Spain, southern France, Italy, the Balkan Peninsula, Turkey and in many islands in the Mediterranean (Crete, Majorca and Sicily). As a

consequence, karst aquifers and springs are an important source of water supply for Mediterranean countries and special strategies are required to manage the quantity and quality of their waters. However, despite some exceptions (i.e. Hartamann et al., 2015), the karst processes are not considered in many European applications of SWAT model and in other large scale hydrological and water quality models.

In order to simulate the specific characteristics of karst aquifers and to calculate the contribution of the karst areas to streamflow as spring flow, the SWAT model structure in Figure 1 is modified as shown in Figure 6.

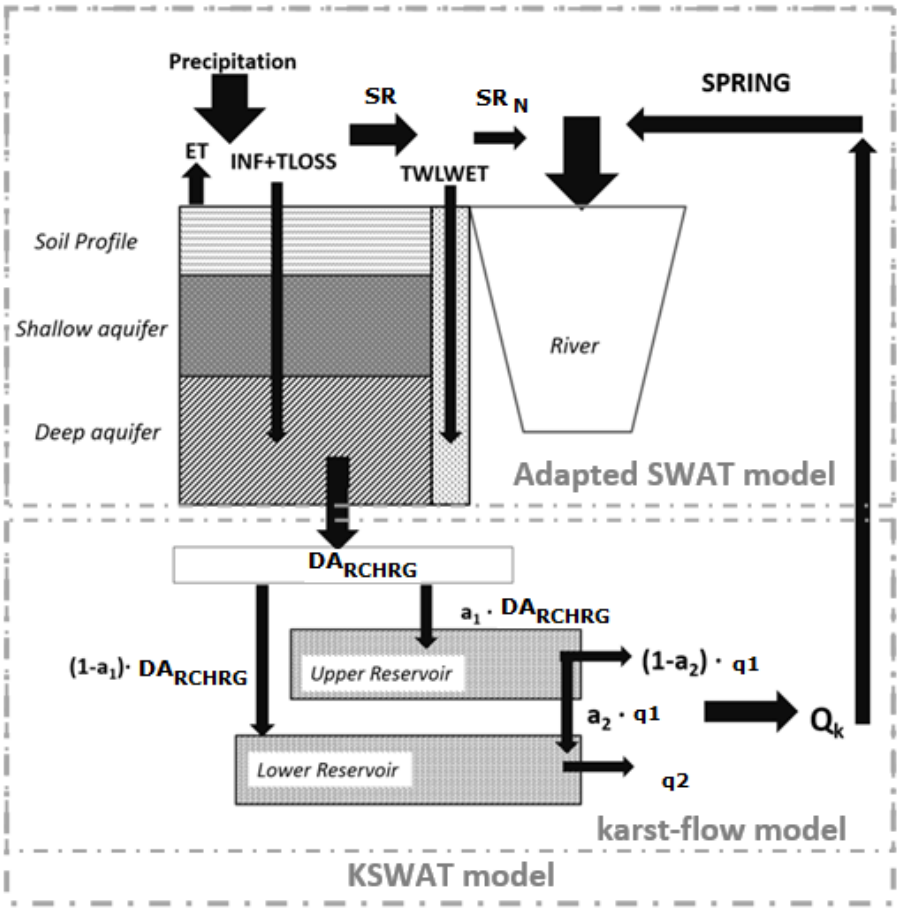


Figure 6. Karst SWAT model configuration (KSWAT model) as combination of the adapted SWAT model linked with the karst-flow model, where: ET, evapotranspiration; INF, infiltration; TLOSS, tributary stream losses; SR, Surface Runoff; TWLWET, losses from the bed of wetlands; $DA_{RCHRG}$, amount of direct recharge of deep aquifer from several subbasins (inlet of the karst-flow model); a1, fraction of $DA_{RCHRG}$ to the Upper Reservoir; a2, fraction of flow from Upper to Lower Reservoir; q1, outlet of Upper Reservoir; q2, outlet of Lower Reservoir; Qk, calibrated spring's discharge; $SR_N$, Surface Runoff excluding TLOSS and TWLWET.

This new SWAT model structure is the result of the combination of two main studies: Baffaut and Benson (2009) and Nikolaidis et al. (2013) and represents the concept of the karst model and its hydrological pathways. Hereafter, this model configuration is called KSWAT and combines an adapted SWAT model and a karst-flow model.

The adapted SWAT model consists in representing sinkholes by wetlands with small drainage area and a large hydraulic conductivity at the bottom of the wetlands and loosing streams were represented by tributary channels with high hydraulic conductivity in the stream bed.

All the percolation in the soil profile, stream losses and seepage from the bottom of wetlands directly recharge the deep aquifer ($DA_{RCHRG}$, mm H2O). This is achieved by setting the deep aquifer percolation fraction (RCHRG_DP) to 1, imposing minimum groundwater delay (GW_DELAY equal to 1) and setting the groundwater coefficient of capillarity rise ("revap") 0.1 in order to avoid that the water moves from shallow into the overlying unsaturated zone and baseflow from shallow and deep aquifer was set to the smallest possible value.

The quantification of spring's discharges is simulated with a karst-flow model developed in the "Excel" environment by Nikolaidis et al. (2013). The input is the daily deep aquifer recharge ($DA_{RCHRG}$, mm) calculated by the SWAT model.

The karst-flow model is composed by an upper reservoir with faster response that represents wide conduits in a karst system and a lower reservoir with a slower response that simulates narrow fractures (Kourgialas et al., 2010). The karst flow model uses the deep aquifer recharge of the nearest subbasins including/excluding through manual trial and error attempts their contribution changing the five parameters and controlling the karst flow output.

These parameters include: Qko, the initial karst flow ($m^3$/day), $a_1$ the fraction of deep groundwater discharge entering the upper reservoir, $a_2$ the fraction of flow from the upper reservoir discharge entering the lower reservoir and $k_u$ and $k_l$ are recession constants (1/d) for the upper and lower reservoirs. Further details about the karst-flow model equations can be found in Nikolaidis et al. (2013).

Finally, the outputs of the karst-flow model are aggregated at monthly time step and then introduced in SWAT as point sources.

The KSWAT model was applied in the case study of Crete Island as described in section 3.5.

## 2.4 Calibration and Validation (C/V): an innovative approach

Comprehensive calibration and validation (C/V) of models is essential to obtain the "right outcomes" for the "right reasons" (Holling, 1978; Kirchner, 2006). However, large-scale models are difficult to calibrate and validate due to the heterogeneity of involved processes that require a spatial landscape calibration, as well as a balance between the sources and sinks.

Having in mind that the main goal of the SWAT application in large River Basins in Europe is to use model results for water management plan and actions, as well as supporting regulatory requirements, a C/V approach is proposed. It includes an appropriate model setup and a robust and reproducible C/V strategy using both hard and soft data. Hard *data are* defined as long-term measured time series at a point in a watershed (i.e. streamflow and concentration measures), while *soft data* are defined as information on individual processes within a balance that may not been directly measured (i.e. ancillary data simulation from other models, GIS-map inspection, regional statistics and literature information). The use of *soft data* represents a new dimensional approach in a C/V strategy that enables the dialog between local experts, experimentalists and modelers, increases the reliability of the model results in ungauged areas and helps to better constrain model parameters (Seibert and McDonnel, 2002).

The proposed C/V strategy flowchart is shown in Figure 7 and involves in sequence: the setup of the model, the calibration of crop yields, the calibration/validation of streamflow and its components, followed by sediments and then nutrients calibration.

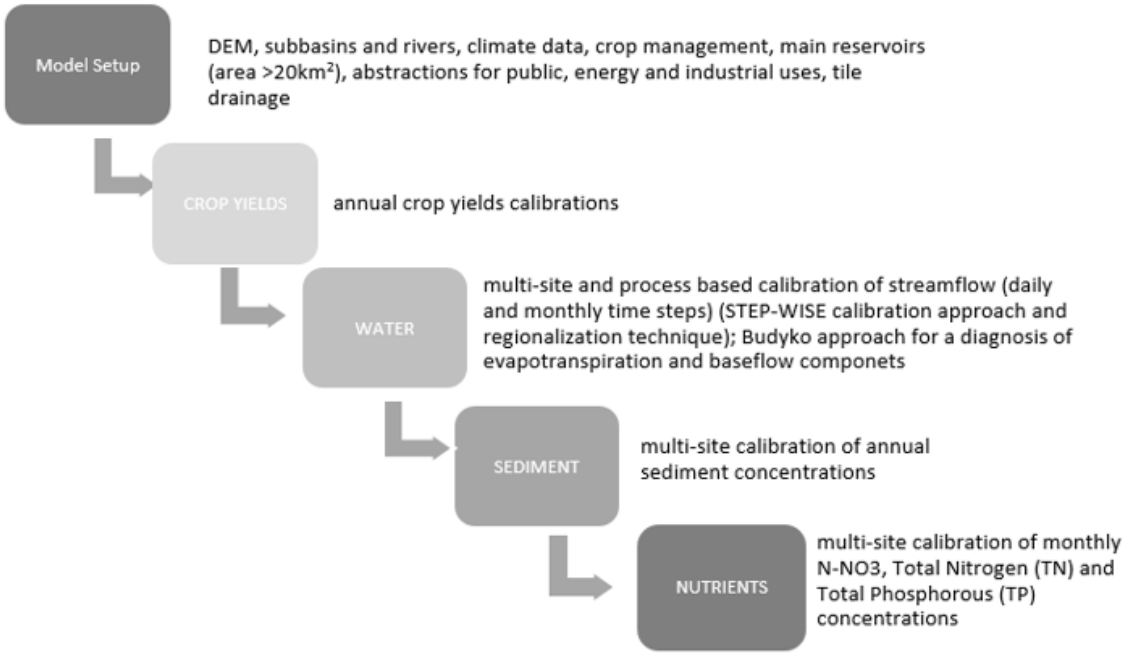


Figure 7. Strategic C/V approach using the SWAT model.

The sequential approach is essential due to the fact that each step is influenced by the previous one. For instance, the calibration of crop yields is necessary to obtain realistic evapotranspiration, as well as a correct nutrient plant uptake. The calibration of streamflow components is crucial for predicting reliable pollutant losses through the various pathways, and nutrients calibration follows sediment calibration since contaminants transported with

sediment is an important component of the nutrient balance as aforementioned in section 2.2.4.

### 2.4.1 The key aspects of the model setup and the simulation period

The setup of SWAT model at large scale requires a large amount of spatial information starting from the Digital Elevation Model (DEM), the landuse and soil map, climate data, up to water, crop and soil management. Detailed description of SWAT model input data with reference to the case studies reported in this thesis are summarized in Appendix A1.

In the thesis, the DEM, subbasin/reach delineation, landuse and soil map are the same in each model application, except for the case study of the Crete Island. At large scale the definition of dominant land use for subbasins or a reduced number of HRUs may misrepresent the correct crop distribution impacting both water and nutrients balance. For this reason, in all applications a particular attention is given to the assignation of crops area on subbasins with dominant arable land in order to match with the crops area reported by the statistical census (i.e. from EUROSTAT or statistics from local authority). For these purpose a crop optimization tool using the software ILOG CPLEX Optimization STUDIO (http://www-03.ibm.com/software/products/it/ibmilogcpleoptistud) has been developed and applied at NUTS2 level (Nomenclature of Territorial Units for Statistics of level 2).

Generally, the simulation period covers 20-years subdivided in three phase: the warm-up, the calibration and the validation periods. The “warm up” period generally covers the first five years to allow the model parameters to adjust to the watershed characteristics. The “calibration” covers a period long enough to contain a range of conditions to be expected in the watershed, such as wet and dry weather extremes over multiple years (Moriasi et al., 2015). Here the model calibration is performed by selected the parameters values within their respective uncertainty ranges by comparing model predictions with the observed data. Instead, in the the “validation” period the model is ran using parameters that were determined during the calibration process, and comparing the predictions to observed data not used in the calibration. Furthermore, calibration and validation are also typically performed by splitting spatially the available observed data. Thus, all the available data of a group of gauging stations are assigned to the calibration phase, while the remaining are assigned to the validation phase. It is noteworthy however, that the gauging stations involved in the calibration dataset should be well distributed in the watershed in order to capture the heterogeneous characteristics of large basins and thus to perform a more reliable parameterization.

Table A2.2 in Appendix A2 summarizes the number of gauging stations and the period involved in the calibration and validation dataset for each model developed in this thesis.

### 2.4.2 Calibration of crop yields

The plant component is highly interactive with components that are generally calibrated in more detail (i.e. streamflow and nutrients). The crop growth influences evapotranspiration, the largest component of the water balance in most climatic regions, and the plant uptake is the largest sink of nitrogen and phosphorus in both agricultural and forest ecosystems. In addition, crop residues are the primary carbon sources for soil organic matter (Arnold et al., 2015). For these reasons, the C/V strategy includes the calibration of crop yields.

In the proposed approach, the simulated mean annual crop yield is compared with that reported by EUROSTAT (EUROSTAT, 2013) for country. Generally, the period of simulation covers 10 years, except the 5 years of warm-up as mentioned in the previous section. However, to perform the comparison the SWAT crop yield data have to report as freshweight by using a conversion table available from the EPIC model. The calibration was preformed manually changing the crop harvest index (HVSTI), the optimal and minimum plant growth (T_OPT, T_BASE), as well as the heat units at HRU/Subbasin level when necessary. The visual appraisal of calibrated and simulated annual crop yields was used as criterion to define the near optimal parameter values. Figure 8 shows an example of comparison.

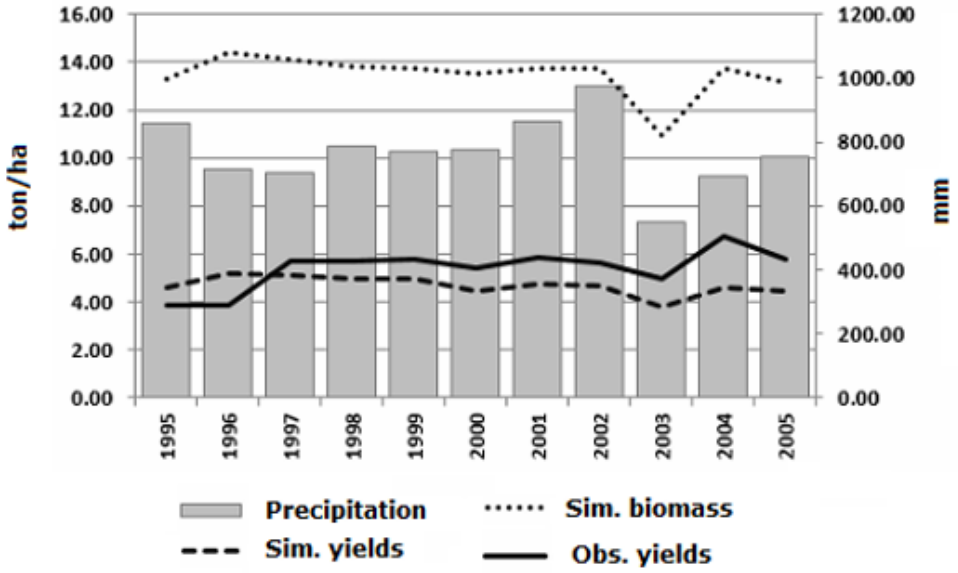


Figure 8. Example of comparison between simulated (Sim.yields) and observed (Obs.yields) yields for wheat in the Upper Danube Basin. The dot line represents the simulated biomass (Sim.biomass), while the bar plots represent the annual precipitation in mm. These help understanding the reliability of simulated yields. For instance, in year 2003 simulated yields and biomass decrease in accordance with the extreme climate condition (drought), and generally the annual variation of simulated values follows that of the observations.

### 2.4.3 The calibration of streamflow and its components

The calibration of streamflow and its components is performed using a step-wise approach (herewith called *step-wise calibration*) that involves sensitivity analysis, multi-variables calibration of headwater subbasins, and regionalization of the calibrated parameters (Pagliero et al., 2014; Malago` et al., 2015b). Figure 9 shows the flowchart of the method and detailed information of procedure is described as following.

The main innovative aspects of this procedure concern the calibration of streamflow and its components using a limited group of independent gauged subbasins (headwaters). This is pursued adjusting step by step selected parameters underpinning each hydrological process. Furthermore, to complete the calibration in ungauged subbasins, a regionalization technique is performed.

The available dataset of streamflow gauging stations is subdivided in calibration dataset and a validation dataset with different spatial and temporal distribution. The latter is used after the regionalization of calibrated parameters for the validation covering the whole period of simulation and all available gauging stations. The calibration dataset instead is involved in the calibration and consists of only gauged stations in headwater subbasins, because headwater subbasins are more likely to represent natural hydrological behaviour (Gudmundsson et al., 2012; Malagò et al., 2015a) and the streamflow components are more representative than in larger basins where streamflow is often influenced by human activities (Döll et al., 2008).

The daily streamflow of headwaters subbasins is divided into its main components (surface runoff SR, lateral flow LF and baseflow BF) using the SWAT filter (Lyne and Hollink, 1979). The implemented baseflow separation procedure is based on recursive digital filter commonly used in signal analysis and processing (Lyne and Hollink 1979). The filter is expressed as below:

[eq. 17] $$q_t = \beta \cdot q_{t-1} + \frac{(1+\beta)}{2} * (Q_t - Q_{t-1})$$

where $q_t$ is the filtered quick flow at the t time step, $Q_t$ is the daily measured streamflow, and $\beta$ is the filter parameter. Baseflow $b_t$ is calculated as:

[eq. 18] $$b_t = Q_t - q_t$$

The filter has to be reapplied to the daily quick flow in order to extract the lateral flow.

The streamflow components of the headwater subbasins are calibrated separately using the software SWAT-CUP and SUFI-2 algorithm (Abbaspour, 2008) method in four sequential steps that focused on different hydrological processes: snow processes, surface runoff, lateral flow, and baseflow. However, a fifth final step is performed by calibrating all

hydrological parameters in a reduced range to account for any covariance of parameters belonging to different hydrological groups. The new output *subflow.rch* is used to perform the step-wise approach in the SWAT-CUP program.

In order to perform a more transparent calibration, 19 parameters are grouped into categories corresponding to the different processes underpinning each calibration objective (Subgroup Process in Table 2). This classification is performed considering the SWAT model structure (Nietsch et al., 2011) and using the characteristic time scale of each process. Each subgroup represents a phase of the step-wise calibration. The parameters and their initial ranges (Table 2) are selected based on preliminary model runs, literature reviews (Van Griensven at al., 2006) and sensitivity test. Once the group of parameter and their initial ranges are assigned for each step, the SUFI-2 algorithm (Abbaspour et al., 2008) is used to perform 1000 interactions running 1000 samples of parameter values in their initial ranges based on a Latin Hypercube sampling. In particular, percentage-based variations of some parameters (i.e. the curve number, CN) are used to maintain their spatial variability.

The “Near Optimal Parameter set” in each step is selected optimizing the objective functions. The choice of the objective function in each step is the result of several tests since the differences between objective functions on parameter sets could be quite striking (Abbaspour et al., 2015). In the step-wise calibration the coefficient of determination ($r^2$; Taylor,1990) and the coefficient of determination multiplied by the slope of the regression line ($br^2$; Krause et al., 2005) were selected respectively for step 1 and for step 2, 3 and 4.

The deteils of different steps performed in this procedure are described below:

step1: calibration of the timing of the runoff signal by adjusting the snow parameters. The near optimal parameter step (NOP) is obtained among 1000 combinations of set of parameters maximizing the coefficient of determination $r^2$ between simulated and observed monthly discharge.

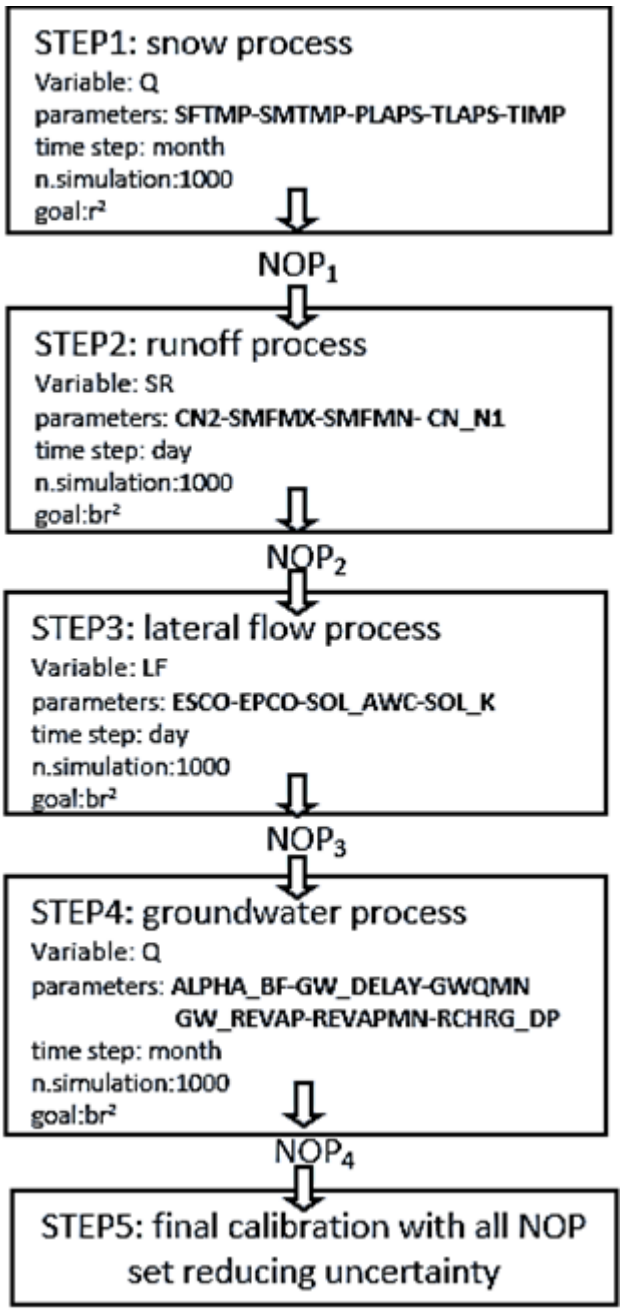


Figure 9. Step-wise calibration approach. NOP: near optimal parameter set; Q: streamflow ($m^3/s$); SR, surface runoff ($m^3/s$); LF: lateral ($m^3/s$). See Table 2 for parameters explanation.

step2: calibration of the surface runoff parameters. The daily streamflow is calibrated maximizing the criterion $br^2$ calculated calculated between the simulated and observed daily surface runoff using 1000 simulations.

step3: calibration of parameters for lateral flow. The calibrated parameter set of step 3 is obtained maximizing the $br^2$ between the simulated and observed daily lateral flow among 1000 different simulations.

step4: calibration of the parameters that control the baseflow; the predicted monthly streamflow is calibrated maximizing the $br^2$ between simulated and observed monthly streamflow

step5: calibration of the all previous calibrated parameters reducing their ranges between the 25$^{th}$ and 75$^{th}$ percentile of all available calibrated values. Finally, the predicted monthly streamflow is calibrated maximizing the $br^2$ between simulated and observed monthly streamflow.

After the step-wise calibration of headwaters the final NOP is transferred to ungauged subbasins using a *regionalization technique*. However, only the subbasins that reached "acceptable performance" of monthly streamflow simulation were selected as donors for use in the parameter regionalization. "Acceptable performance" for donors is defined if the percent bias (PBIAS; Gupta et al., 1999) is in the range +/-25%[2], as described in section 2.4.6.

Once the donors are selected, a regionalization technique coupled with a classification procedure based on a similarity approach is applied. The similarity approach is based on the assumption that similar catchments behave hydrologically similarly. The regionalization consistes in transferring the calibrated parameter sets (Near Optimal Parameter set, NOP; Malagò et al., 2015a) from donors to their hydrologically similar receptor subbasins.

The definition of the similarity measure is subjective and conditions the success of the regionalization (Heuvelmans et al., 2006). The regionalization is performed using the Partial Least Squares Regression method (PLSR; Wold, 1966; Geladi and Kowalski, 1986) that allows identification of similar subbasins based on the correlation between the watershed characteristics and the streamflow characteristics. In total, 19 independent variables representing the subbasin characteristics ("c" matrix of PLRS regressors) and 14 dependent streamflow variables ("q" matrix of PLRS responses) are used, as show in Table 3.

The PLSR analysis defined latent variables to identify "hydrological regions" using the Ward's minimum variance linkage method (Ward, 1963) together with the Euclidean distance similarity. To find the best number of "hydrological regions" two index are used: the corrected Rand index (Hubert and Arabie, 1985) and the Meilă index (Meilă, 2007).

Finally, in each hydrological region a *classification procedure* based on a supervising clustering approach (k-NN method; Dettling and Maechler, 2012) is performed. Each subbasin in a region, that is classified hydrologically similar to a given donor pertaining to

[2] In the case study of the Upper Danube the "acceptable performance" for donors was defined based on satisfactory PBIAS% coupled with positive values of Nash-Sutcliffe efficiency (NSE; Nash and Sutcliffe, 1970) in order to keep a more robust and well distributed group of donors in a basin with abundance of calibrated headwaters.

the same hydrological region, receives the donor NOP set. However, in some cases, where donors are not well spatial distributed for covering each hydrological region, the classification procedure is performed in the whole watershed (i.e. case study of Scandinavian and Iberian Peninsula), thus the latent variables are used directly in the classification of ungauged subbasins without the creation of hydrological regions.

The regionalization and classification analysis are performed using the statistical software R (R Development Core Team, 2008), using the packages (collection of mathematical functions) “pls” (Mevic and Wehrens 2007), “fpc” (Henning, 2010), and “supclust” (Dettling and Maechler 2012).

The C/V strategy is applied in each case study of this thesis.

Table 2. Parameters and initial parameter ranges used in the step-wise calibration ranked in alphabetic order

| **Parameter** | **Description** | **Subgroup Process** | **min** | **max** |
|---|---|---|---|---|
| ALPHA_BF | Baseflow alpha factor [d] | Groundwater | 0 | 1 |
| CN2 | SCS runoff curve number for moisture condition II | Surface Runoff | -15% | +15% |
| CH_N1 | Manning’s value for tributary channel | Surface Runoff | 0.025 | 0.30 |
| EPCO | Plant evaporation compensation factor | Lateral Flow | 0.01 | 1 |
| ESCO | Soil evaporation compensation factor | Lateral Flow | 0.01 | 1 |
| GW_DELAY | Groundwater delay [d] | Groundwater | 0 | 500 |
| GWQMN | Threshold depth of water in the shallow aquifer required for return flow to occur [mm] | Groundwater | 0 | 1000 |
| GW_REVAP | Groundwater ‘revap’ coefficient | Groundwater | 0.02 | 2 |
| PLAPS | Precipitation laps rate (mm/km) | Snow melt | 0 | 100 |
| RCHRG_DP | Groundwater recharge to deep aquifer [fr] | Groundwater | 0 | 1 |
| REVAPMN | Threshold depth of water in the shallow aquifer for revap to occur [mm] | Groundwater | 0 | 500 |
| SFTMP | Snowfall temperature [ºC] | Snow melt | -5 | 5 |
| SMFMN | Minimum melt rate for snow on Dec 21 [mm ºC$^{-1}$ d$^{-1}$] | Surface Runoff[1] | 0 | 10 |
| SMFMX | Minimum melt rate for snow on Jun 21 [mm ºC$^{-1}$ d$^{-1}$] | Surface Runoff[1] | 0 | 10 |
| SMTMP | Snowmelt base temperature | Snow melt | -5 | 5 |
| SOL_AWC | Available water capacity of the soil layer [fr] | Lateral Flow | -25% | +25% |
| SOL_K | Saturated hydraulic conductivity [mm h$^{-1}$] | Lateral Flow | -25% | +25% |
| TIMP | Snow pack temperature lag factor | Snow melt | 0.01 | 1 |
| TLAPS | Temperature laps rate (°C/km) | Snow melt | -10 | 0 |

1. SMFMN and SMFMX were calibrated using a daily time step and thus included in the surface runoff process, albeit they affected the snow melt process.

Table 3. Dependent and independent (respectively streamflow and subbasin characteristics) variables for PLSR analysis

| Subbasin characteristics | Streamflow characteristics |
|---|---|
| 1. River length [km] | 1. Mean annual discharge [mm yr-1] |
| 2. Maximum elevation [m] | 2. Coefficient of variation of annual discharge [-] |
| 3. Minimum elevation [m] | 3. Coefficient of variation of daily discharge [-] |
| 4. Average elevation [m] | 4. Coefficient of variation of annual minima [-] |
| 5. Median slope [%] | 5. Coefficient of variation of annual maxima [-] |
| 6. Clay content [%] | 6. Daily discharge with pbbexc[1] 90 [mm] |
| 7. Sand content [%] | 7. Daily discharge with pbbexc[1] 70 [mm] |
| 8. Shrub area [%] | 8. Daily discharge with pbbexc[1] 50 [mm] |
| 9. Bare soil area [%] | 9. Mean annual baseflow [mm yr-1] |
| 10. Forest area [%] | 10. Mean annual quickflow [mm yr-1] |
| 11. Water area [%] | 11. Baseflow/Discharge summer [-] |
| 12. Urban area [%] | 12. Baseflow/Discharge winter [-] |
| 13. Cropland area [%] | 13. Baseflow/Rainfall [-] |
| 14. Grassland area [%] | 14. Quickflow/Rainfall [-] |
| 15. Annual precipitation [mm yr-1] | |
| 16. Average maximum temperature [ºC] | |
| 17. Average minimum temperature [ºC] | |
| 18. Annual potential evapotranspiration [mm yr-1] | |
| 19. Average number of days with precipitation | |

1. pbbexc: probability of exceedance

### 2.4.4 Calibration of sediments

After streamflow calibration and validation, a step-wise procedure for sediment calibration and evaluation is applied (Vigiak et al., 2015a). The main innovations of this procedure, as well as for nutrients, is the direct calibration of concentrations that allows avoiding uncertainty issues related to loads estimation and the assessment of intra-watershed behavior.

This procedure consists in three steps:

1) broad calibration of crop USLE C and P parameters (see [eq. 13]) comparing SWAT USLE mean gross erosion, GE, (from output.hru file) with observations available from different sources (Maetens et al., 2012, Panagos et al., 2014, Cerdan et al., 2010):
2) calibration of the threshold area $A_t$ of the modified MUSLE [eq.13]). Different methods could be used to define this parameter. Generally, it is broadly defined as the ratio of sediment yield to gross erosion (Vigiak et al., 2015a), or considering the area at which specific sediment yields (ton/km$^2$/y) start to decrease with catchment size (de Vente and Poesen, 2005);
3) calibration of in-stream parameters comparing simulated and observed annual concentration of sediments at multiple gauging stations. A calibration and validation dataset is defined subdividing spatially and temporally the dataset in two parts. This step required a global sensitivity analysis performed using the SUFI-2 algorithm, and then only the most sensitive parameters can be calibrated. The new output sedlflow.rch is necessary at this stage.

This procedure is tested in the case study of the Upper Danube as described in section 4.3.

### 2.4.5 Calibration of nutrients

Afterwards the best sediments estimation, the nutrients calibration is performed using a step-wise procedure that involves both the use of soft data, i.e. literature information or spatial data, and hard data as daily concentrations (aggregated monthly) for nitrates, total nitrogen and total phosphorous in multiple gauging stations. However, the procedure required their sequential calibration, thus nitrates are calibrated at first followed by the total nitrogen and total phosphorous. Due to the limited numbers of gauging stations generally available in this thesis the whole dataset of concentration was enrolled in the calibration, while loads were used in the evaluation of the model.

The main steps of the procedure are described as following:

1) Setting of nitrates deposited with precipitation using the average nitrogen concentration based on EMEP data (EMEP, 2001);
2) literature information (soft data) of denitrification (kg/ha) by Country (i.e. Oenema et al., 2009) and the monthly concentration of nitrates (mg N/l) at multiple gauging stations (hard data) are used to constrain the denitrification coefficients in [eq.8] and [eq.9] (SDNCO and CDN);
3) calibration of in-stream parameters related to nitrogen (TN) and phosphorous (TP) transformation is performed comparing simulated and observed monthly concentration of TN and TP at multiple gauging stations. As mentioned above for sediments, this step requires a global sensitivity analysis executed using the SUFI-2 algorithm, and then only the most sensitive parameters were calibrated. The new output qualflow.rch was used in this step.

However, simulated nutrients load (from output.rch) are compared with “observed” loads. Nutrient loads used as “observations” are estimated from nutrient concentration and daily streamflow, and are calculated based on different methods: flow weighted concentrations method proposed by Moatar and Meybeck (2005) as well as the ICPDR method described in the ICPDR yearbooks (ICPDR, 2000-2009a) and literature estimations (Van Gils, 2004). An additional validation was also performed by comparing the SWAT model outputs with the outputs of other models as explained in Chapter 5.

This procedure is applied to the entire Danube River Basin as described in section 4.2.

### 2.4.6 Performance indicators

The accuracy of model performance after calibration and regionalization-classification is evaluated by comparing the calibrated monthly streamflow with observed data using

statistic performance criteria according to the criteria of Moriasi et al. (2007b) (Table 4). Percent bias (PBIAS %) and Nash and Sutcliffe coefficient (NSE) are calculated using the R package “hydroGOF” (Zambrano and Bigiarini, 2013).

However, since these criteria measures only specific aspects of a model’s performance, box and whisker plots, visual appraisal of time-series, and residuals analysis (simulation – observation) are also used (Harmel et al., 2014; Bieger et al., 2012), as well as other performance indicators including the Normalized Root Mean Square Error (NRMSE), the coefficient of determination $r^2$ (Taylor, 1990) and the coefficient of determination $r^2$ multiplied by the slope of the regression line between simulated and observed values ($br^2$; Krause et al., 2005).

Table 4. General performance ratings according to Moriasi et al. (2007b)

| **Performance rating** | **Nusch-Sutcliffe efficiency coefficient (NSE)** | **Percent bias (PBIAS %)** | | |
|---|---|---|---|---|
| | | **Streamflow** | **Sediment** | **Nutrients (N, P)** |
| Very good | 0.75<NSE≤1.00 | PBIAS<±10 | PBIAS<±15 | PBIAS<±25 |
| Good | 0.65<NSE≤0.75 | ±10≤PBIAS<±15 | ±15≤PBIAS<±30 | ±25≤PBIAS<±40 |
| Satisfactory | 0.50<NSE≤0.65 | ±15≤PBIAS<±25 | ±30≤PBIAS<±55 | ±40≤PBIAS<±70 |
| Unsatisfactory | NSE≤0.50 | PBIAS≥±25 | PBIAS≥±55 | PBIAS≥±70 |

# CHAPTER 3

# 3 Hydrological SWAT applications, sensitivity analysis at different spatial scales and modifications

## 3.1 Chapter description

This Chapter focuses on the water quantity assessment applying the proposed C/V strategy in different large basins to predict the streamflow at different spatial and temporal scale and to evaluate the water balance and the reliability of its components.

Two contrasting macroregions in Europe, the Scandinavian and Iberian Peninsulas, are selected to investigate the strength and weakness of the procedure in capturing the main hydrological processes. The model results are compared in terms of performance indicators and a sensitivity analysis of each step of calibration is performed. A further explanation of the spatial variability of the calibrated parameters is provided. Three specific studies to investigate SWAT sensitivity and its ability to describe realistically all the flow components are described.

1. Albeit the calibration procedure constrains the parameters to reproduce the water yield components reasonably, to guarantee that the main components of the water balance are well simulated, the Budyko framework approach is applied in the Danube River Basin and compared to the SWAT model results. In particular, the evapotranspiration and the baseflow are investigated in detail for each water management regions, given generally behavior rules of processes as function of Budyko coefficients. The water balance of the Danube River is then described, comparing the main contribution among the water management regions and providing a valuable assessment of water resources in the regions.
2. The reliability of water yield components is not only influenced by the C/V strategy, but also by the setup parametrization and the resolution of DEM. Here, a study about hillslope length algorithm related to DEM resolution is described providing recommendations for obtaining more realistic and physically meaningful predictions of the streamflow and its components.
3. Finally, karst processes are included in SWAT model using the KSWAT model in the interesting case study of the Island of Crete.

## 3.2 Iberian and Baltic peninsula: SWAT calibration and validation at different climate regimes

### 3.2.1 Synopsis

The proposed innovative modelling protocol that involves sensitivity analysis, multi-variables calibration and regionalization of the calibrated parameters is here described. The main objective of this research is to study the spatial variation of calibrated parameter sets obtained for selected subbasins and the identification of the most relevant hydrological processes in regions with very different climate conditions. In particular, two large regions have been considered: the Scandinavian and the Iberian Peninsulas.

### 3.2.2 The study area

The Scandinavian Peninsula covers Norway, Sweden and Finland, for a total area of approximately $10^6$ km$^2$. In SWAT it was divided into 5447 subbasins, with 61 gauged head subbasins and others 346 gauged subbasins. The Iberian Peninsula covers Spain and Portugal for a total area of $556 \cdot 10^3$ km$^2$. It was divided in 3019 subbasins, with 81 gauged head basins and others 215 gauged subbasins (Figure 10). The headwaters were used in the step-wise calibration, while the remaining were used in the validation. In this case study the calibration dataset was not involved in the validation.

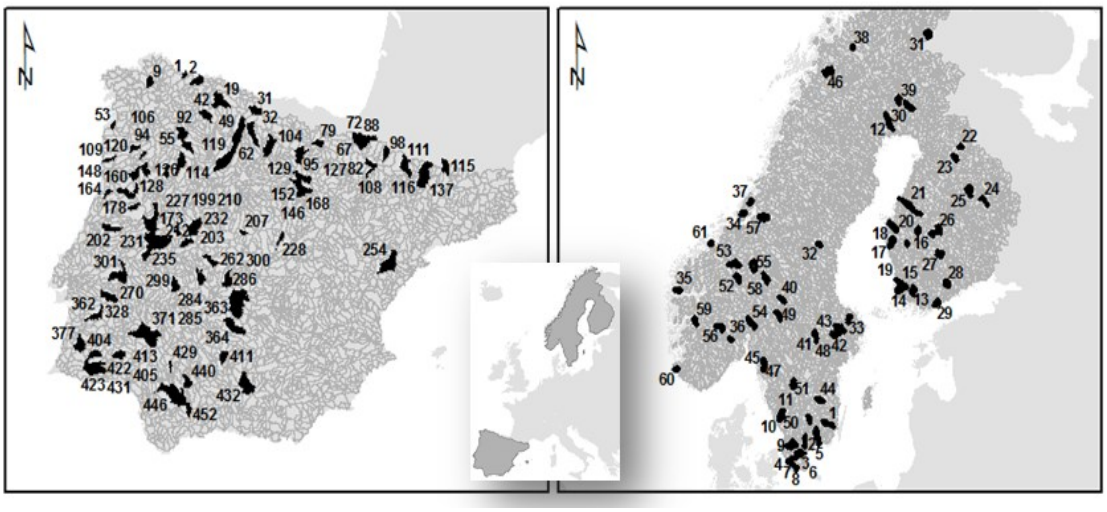

Figure 10. Map of the Iberian Peninsula (left) and Scandinavian Peninsula (right) along with the calibration subbasins: #81 in Iberian Peninsula and #61 in Scandinavia (# number of gauging stations)

These regions have very different climatic conditions. Mediterranean climate is dominant in the Iberian Peninsula. The Mediterranean climate is characterized by dry and warm summers and cool and wet winters. In Scandinavia more classes of climate are present including Continental Subarctic or Boreal (taiga) in Finland and in the mid-north Sweden and Norway, Polar climates in Norway, in mountainous areas and in the northern coastal

areas of Finland, and Oceanic in southern part of Sweden and Norway. Scandinavia is mostly covered by forest and pasture with arable land concentrated in the south. In the Iberian Peninsula the dominant land use is arable land and pasture.

A detailed information of the input data of the Scandinavia and Iberian Peninsula is provided in Appendix A1.

### 3.2.3 The performance of the calibration datasets

Nash-Sutcliffe efficiencies (NSE) and the $br^2$ values for the calibrated head subbasins in Scandinavia and Iberian Peninsulas are displayed as cumulative frequency in Figure 11. It can be seen that there is an improvement of Nash-Sutcliffe efficiencies and $br^2$ for head subbasins with respect to the default simulations in each studied region.

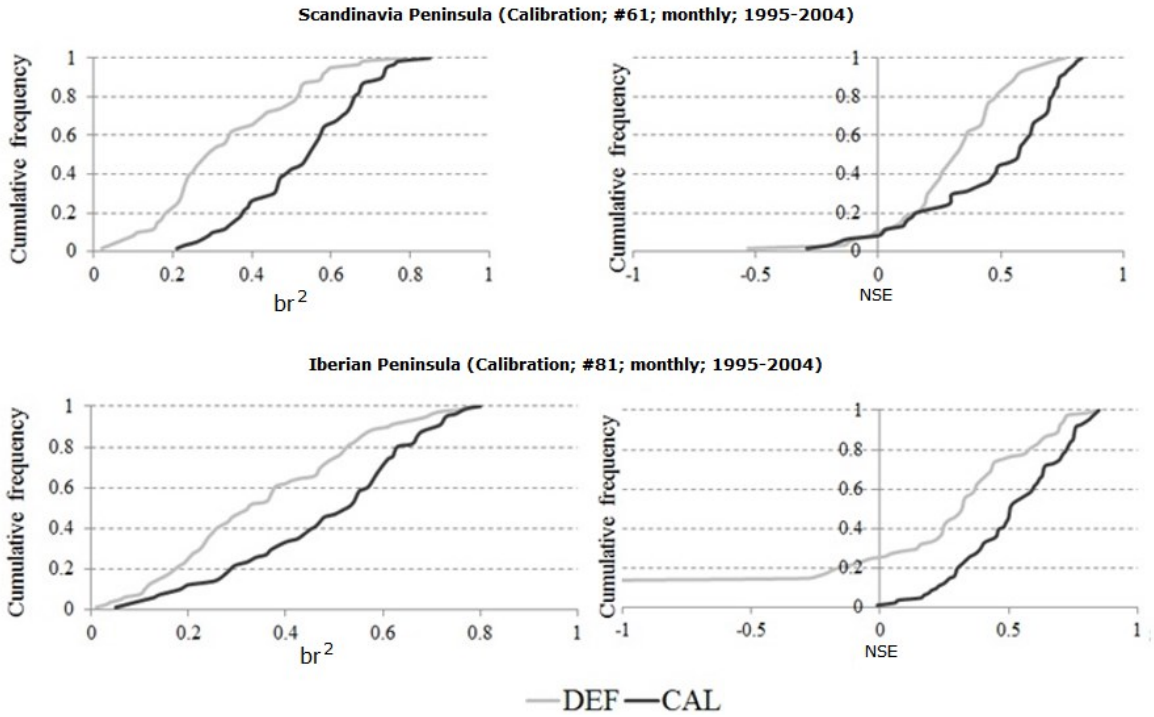


Figure 11. Cumulative frequency curves for NSE and $br^2$ before (DEF) and after the step-wise calibration (CAL).

The performance in each single step is not significantly influenced by the performances in subsequent steps as shown in Figure 12 and Figure 13.

Figure 12 (a), (b) and (c) show the best $br^2$ coefficient obtained for each subbasin in each step of calibration for monthly surface runoff (a), lateral flow (b) and baseflow (c), respectively. The black and red lines represent the results before and after the calibration of specific component of the flow. For instance, it can be seen in Figure 12 (a) that after the calibration of the surface runoff there are no variations of $br^2$ values in step3 and step4.

Consequently, the calibrations of the specific parameter set in step2 and step3 don't alter the performance of the model in the calibration of the surface runoff obtained in step1.

The same results are shown in Figure 12 (b) where the $br^2$ in each subbasin after the calibration of lateral flow is very similar to step 4. Concerning the baseflow calibration, Figure 12 (c) shows that the $br^2$ remains stable in each subbasin and in each step (step1, step2, step3) until the calibration of baseflow in step4.

Thus, there is not a significant influence between the parameter sets in the different steps. For instance, in Figure 13 (a) the variation of $br^2$ for the surface runoff changes significantly in step 2 (specific step of calibration of surface runoff) and then remains stable in the subsequent steps (step3 and step4) in spite of the progressive calibration of different parameter set involved.

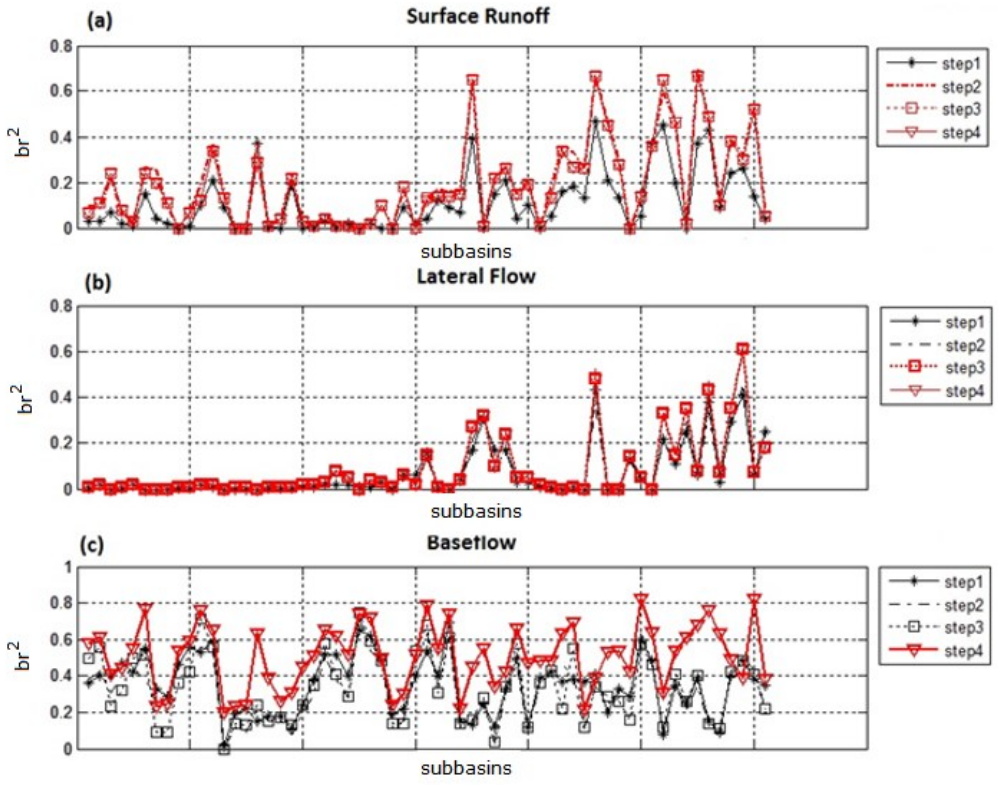


Figure 12. $br^2$ coefficient obtained for each subbasin comparing the simulated and monthly components of the streamflow (a: surface runoff; b: lateral flow; c: baseflow) in Scandinavia during the step-wise calibration.

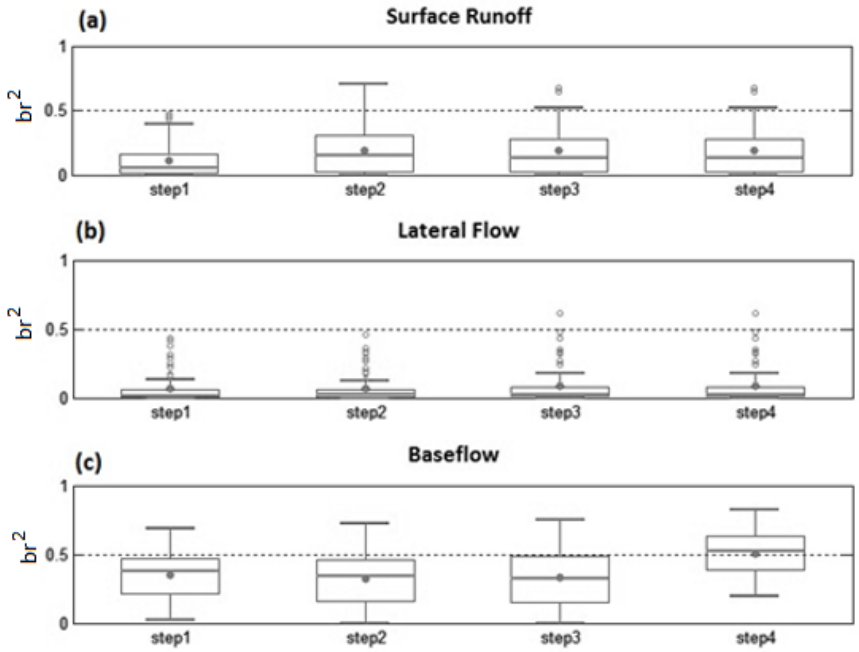


Figure 13. Box-and-whisker plots of $br^2$ obtained comparing the simulated and monthly components of the streamflow for each step of calibration and for each components of the streamflow. a) surface runoff performance in each step; b) lateral flow performance in each step; c) baseflow performance in each step.

In addition, the step-wise calibration allows obtaining a better modelling performance compared to the traditional calibration that involves all sensitive parameters together and the total monthly or daily total flow using one objective function. Figure 14 shows the Nash Sutcliffe efficiencies and $br^2$ values for calibrated head subbasins in Scandinavia for the default simulations (DEF), the traditional calibration (TRAD) and the step-wise calibration (CAL). The traditional calibration was performed using all parameters together and maximising the br2 for monthly flow. Unlike the step-wise calibration, the traditional calibration results in more than 35% of calibrated subbasins having NSE equal to zero and with a small improvement of $br^2$ values.

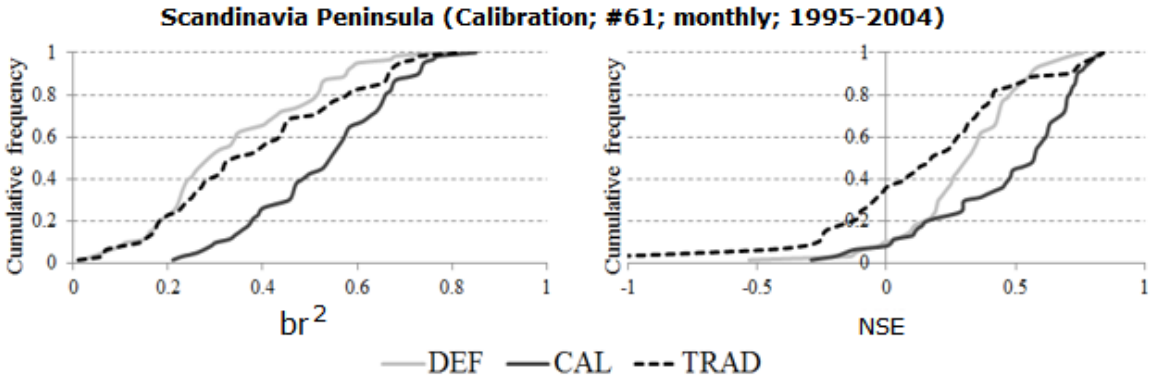


Figure 14. Cumulative frequency curves for NSE and $br^2$ before (DEF), after the step-wise calibration (CAL) and the results for the traditional calibration (TRAD).

### 3.2.4 The performance after the regionalization approach

Four components were selected as latent variables in both studied regions after the analysis of the root mean square error of predictions (RMSEP) for all dependent variables. 61 calibrated subbasins in Scandinavia and 65 calibrated subbasins in Iberian Peninsula were selected as 'donor subbasins' characterized by NOP (Near Optimal Parameter) obtained during the step-wise calibration. The K-Nearest-Neighbor classification rule was used to associate the 5386 subbasins in Scandinavia to similar donor subbasins (61) and the 2954 subbasins in Iberian Peninsula to similar donor subbasins (65). The Near Optimal Parameter set of the donor subbasins were transposed to the corresponding similar subbasins.

The efficiency of the transferability of the NOP in the hydrological similar subbasins was verified comparing the simulated and observed monthly discharge in 346 gauged subbasins in Scandinavia and 215 gauged subbasins in the Iberian Peninsula.

Figure 15 shows the Nash Sutcliffe efficiencies and $br^2$ cumulative frequency curves of all gauged subbasins in Scandinavian and Iberian Peninsulas before and after extrapolation of calibrated parameters set in each classified subbasins. For each region the $br^2$ and NSE increase with the transposition of calibrated parameter sets in 'similar subbasins' with respect to the corresponding values obtained by using the default parameters.

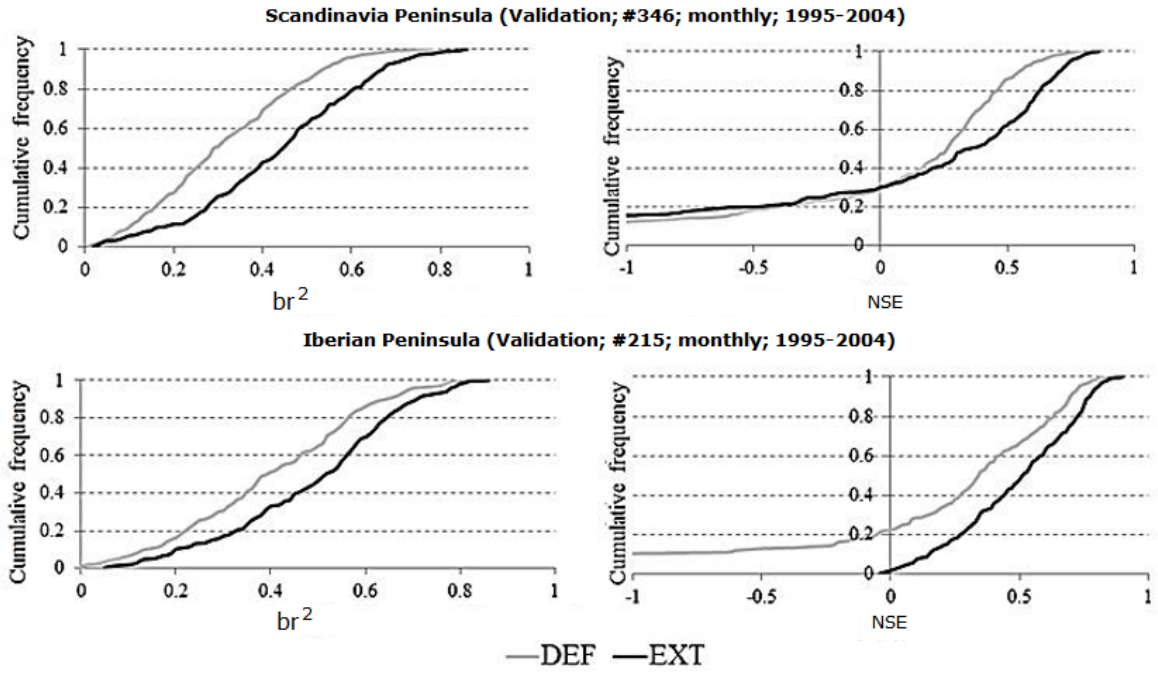


Figure 15. Cumulative frequency curves for NSE and br2 before (DEF) and after the validation (VAL).

However, Figure 16 and Figure 17 show that in the central part of the Spain and in Finland the 'classification' of calibrated parameters did not increase the performance of the model.

In particular, in the Finnish Lakeland (Figure 17), the largest lake region of Europe with about thousands of lakes, the Nash Sutcliffe efficiencies are less than -1. These poor performances could be correlated to the assumptions introduced in our model, in particular to the selection of only lakes with area greater than 20 km$^2$, thus not reproducing accurately the interconnectivity of these water bodies.

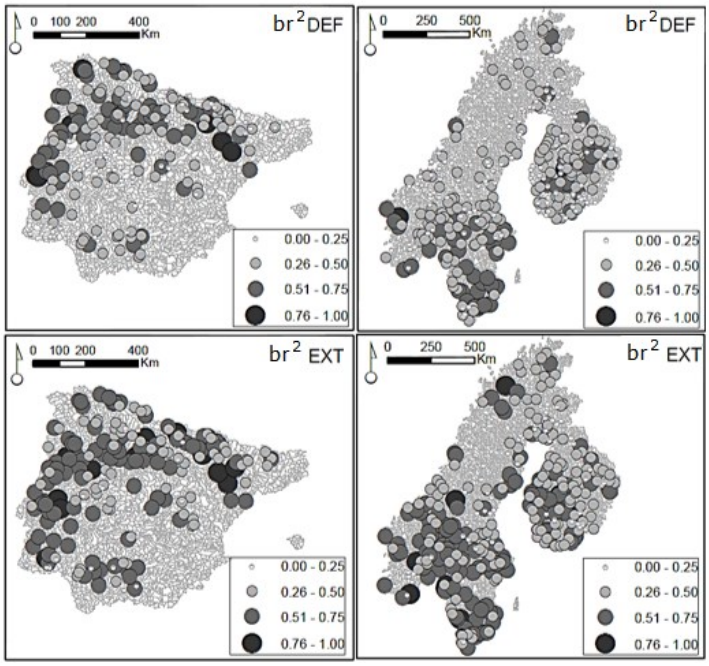


Figure 16. br$^2$ coefficient after regionalization in 215 and 346 monitoring points respectively for Iberian Peninsula (left) and Scandinavia (right). DEF is the run with default parameters; EXT is the run with transposed parameters (Validation)

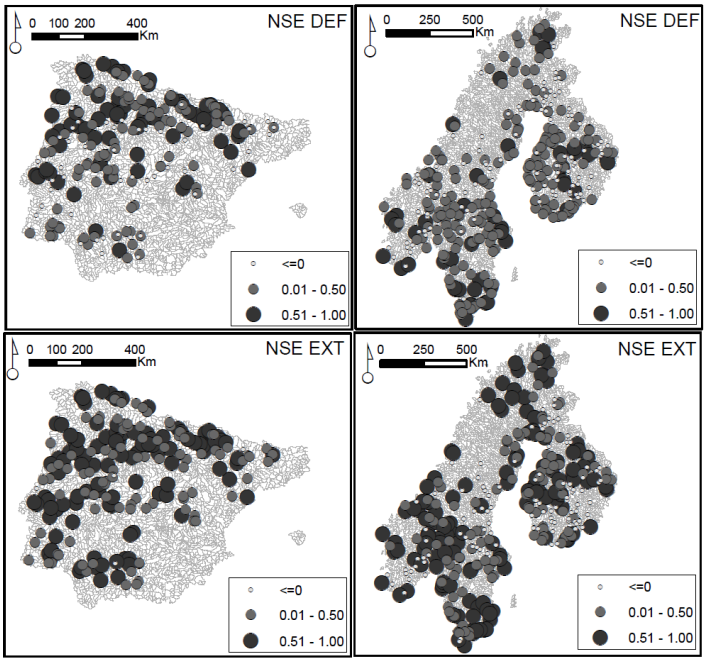


Figure 17. NSE coefficient after regionalization in 215 and 346 monitoring points respectively for Iberian Peninsula (left) and Scandinavia (right). DEF is the run with default parameters; EXT is the run with transposed parameters (Validation).

### 3.2.5 Sensitivity analysis of step-wise calibration

The sensitivity analysis of the step-wise calibration was performed using the different 1000 iterations of each step. The following criterion based on standard deviation of the optimization criteria of 1000 runs was used to define which calibrated subbasins were considered sensitive in each step of calibration:

[eq. 19] $\text{If } 2.7\sigma_{i,j} \geq 0.1 \text{ the subbasins are sensitive}$

where i represents the subbasin and j the step of calibration, and σ is the standard deviation of the optimization criteria.

Figure 18 shows that 100% of subbasins in the Scandinavian Peninsula are sensitive in step 4 (a, b) and 97% in step 1 (snow process). About 11% of the subbasins are sensitive in step 2 and only 3% in step 3. For the Iberian Peninsula: 98% of subbasins are sensitive in step 4 (a, b), 12% in step 2 and 2% in step 3. Only, the 4% of subbasins are sensitive in step1.

These results confirm that the performance of SWAT in predicting water flow in Scandinavia is controlled by the snow parameters. In addition, the results suggest that in each studied region, the calibration is mostly controlled by snowmelt and baseflow processes while the calibration of surface runoff and lateral flow parameters have little impact on the global performance. This can be explained by the fact that precipitation being very low in large portions of the Iberian and Scandinavian Peninsulas, the surface runoff and lateral flow are less dominant than groundwater flow. In addition, the pedo-transfer functions, used to parameterize the soil component of SWAT, were developed at the point scale, and they might have the tendency to underestimate soil hydraulic properties, because they do not consider the effect of heterogeneities like preferential flow paths that affect the soil hydraulic behaviour at larger scales (Heuvelmans et al., 2004).

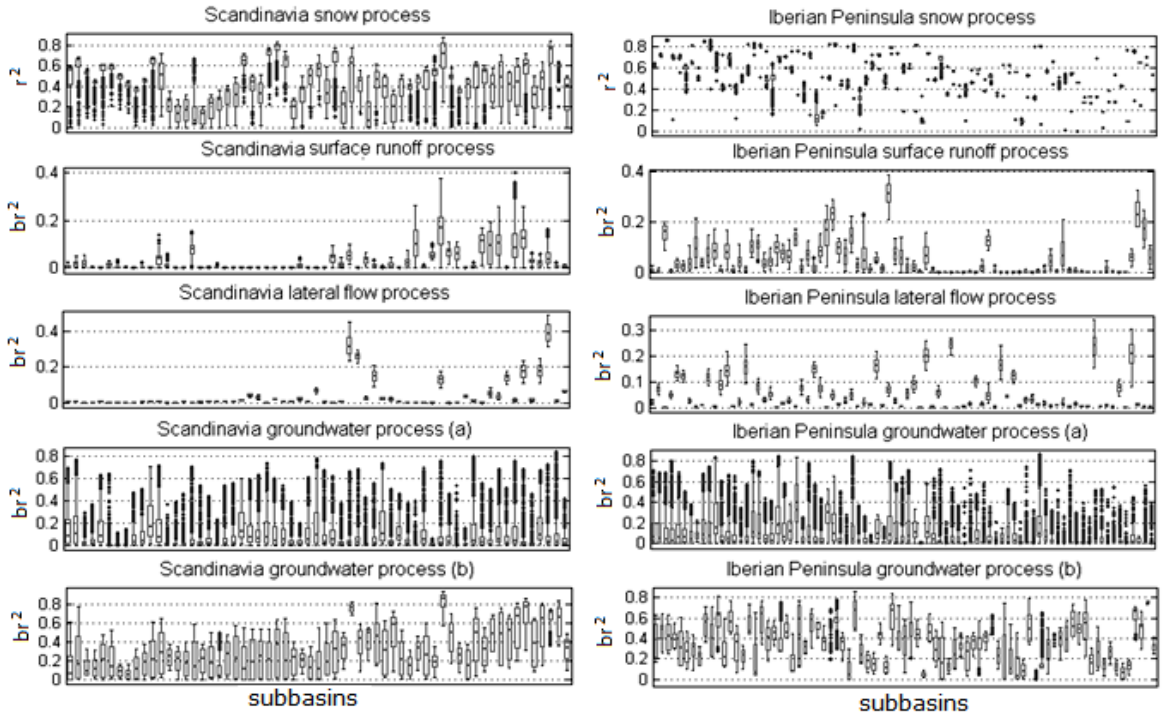


Figure 18. Box-and-whisker plots of objective functions ($r^2$ and $br^2$) for each calibration step for Scandinavia (left) and Iberian Peninsula (right).

### 3.2.6 Spatial variability of parameters of the NOP

The box plot of each parameter of NOP in a specific step is shown in Figure 19 and the spatial variation of each parameter is illustrated in Figure 20.

The results show that ranges of calibrated snow parameters are very different between the two studied regions. In the Iberian Peninsula the snowfall temperature (SFTMP) ranges from -0.7 to 1, while the snowmelt base temperature (SMTMP) values are all above zero. In the Iberian Peninsula the median of the snow pack temperature lag factor (TIMP) approaches 1.0, thus the snow pack temperature is influenced by the main air temperature on the current day. In Scandinavia the median TIMP approaches 0.5. Thus the snow pack temperature lag factor is influenced by the temperature of the previous day showing some more inertia in the snowmelt process.

In the Scandinavian Peninsula there is a more significant decrease in temperature with decreasing elevation (TLAPS) than in the Iberian Peninsula. Same results are found for the precipitation laps rate (PLAPS): Scandinavia is more marked by a higher precipitation with increasing elevation than the Iberian Peninsula. One explanation is the underestimation of the precipitation in Scandinavia at higher elevations due to the lack of observation gauges at those altitudes. In general, the stream flow simulation is often challenging in mountainous watersheds because of irregular topography and complex hydrological processes. Incorrectly represented rates of change in precipitation and temperature with respect to

elevation often limit the ability to reproduce stream runoff by hydrological models (Rahman et al., 2013).

Ranges of SOL_AWC and SOL_K parameters are very different between the studied regions, with however a similar proportion of sensitive subbasins for step 3 (2% and 3% for the Iberian Peninsula and Scandinavia, respectively). The Iberian Peninsula is characterized by high variations in soil hydraulic features (SOL_AWC and SOL_K). This increment of the soil hydraulic conductivity and available soil water content during the calibration process is highly connected with the presence of macropores and rock fragments that are widespread in the Mediterranean.

The Scandinavian Peninsula is characterized by a decrease of the soil hydraulic parameter values (available water content and hydraulic conductivity) during the calibration. This fact can be explained by the negative relationship between organic matter OM and saturated hydraulic conductivity (Nemes et al., 2005). Consequently, in the northern part of Europe where the organic carbon component is high (from 4 to 6%) (Rusco et al., 2001) a decrease of hydraulic conductivity and available water content is expected.

This spatial pattern between these two macro-regions may reflect a difference in runoff generating mechanism. In the Iberian Peninsula runoff occurs mostly in periods of intensive storms while snow melt over frozen soils in Scandinavia Peninsula is one major source of surface runoff during the spring.

Figure 19 shows how the soil evaporation compensation factor (ESCO) value decreases from 1 (default value) to lower values for each studied regions. ESCO adjusts the depth distribution for evaporation from the soil to account for the effect of capillary action, crusting, and cracking. Decreasing ESCO allows lower soil layers to compensate for a water deficit in upper layers and causes higher soil evapotranspiration.

The plant evaporation compensation EPCO factor in the SWAT model explains how available soil water could be used to meet plant water uptake, either from upper layers or from deeper profiles. When EPCO is near 1, soil water from deeper soil profiles could be used, while when EPCO is near 0, soil water from the top layers is most likely used. In the Iberian Peninsula, the median of EPCO is near 0.2 and is about 0.4 in Scandinavia. Thus, in the Iberian Peninsula most water used by vegetation comes from the upper soil profile unlike the Scandinavian Peninsula and the difference in land use, where in Scandinavia deep rooted trees are dominants, helps to explain this aspect.

Figure 19 shows also the shallow aquifer transit time parameter, GW_DELAY (days). The delay decreased from default value (31 days) in most subbasins in each region. However, larger delays are found in south-east part of Sweden with values ranging between 50 to 100

days. In the Iberian Peninsula, in south-west and in the center GW_DELAY parameter is between 1-5 days. In addition, Figure 19 shows how the optimal deep aquifer percolation fraction is very low in each region.

Concerning the spatial variation of GW-REVAP, which is an indicator of capillary rise, some subbasins in the middle of Scandinavia and north east of Finland have large GW_REVAP and relatively small REVAPMN (Figure 20). These values are probably connected to land use, in particular forested areas where it is more likely that more water from shallow aquifer is lost through evapotranspiration (Heuvelmans et al., 2004).

Figure 20 shows also the spatial variation of the ALPHA factor, which is a direct index of groundwater flow response to change in recharge (Smedema and Rycroft 1983). In the centre and north-west of the Iberian Peninsula, and in some sensitive subbasins in the south of Scandinavia (south of Sweden) ALPHA values vary between 0.01-0.4 days; the response to recharge is thus slow. Subbasins in southern Norway and in the coast west of Finland have rapid response to recharge (ALPHA_BF is larger than 0.8 days) indicating the presence of very shallow soils or the presence of very shallow groundwater.

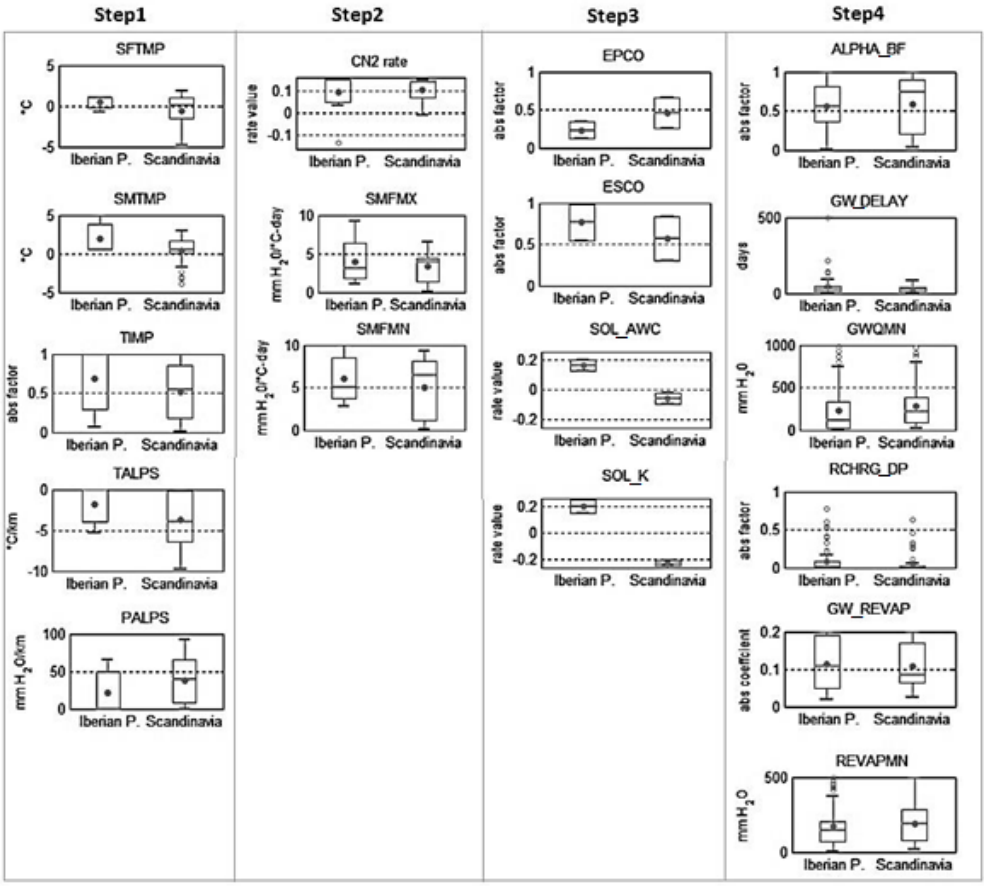


Figure 19. Box-and-whisker plots of behavioral Near Optimal Parameter sets from calibrated subbasins. The “abs value/factor/coefficient” represents he absolute value for adimensional parameter, “rate value” represents the increment/decrement for which the absolute value is increased (positive rate) or decrease (negative rate).

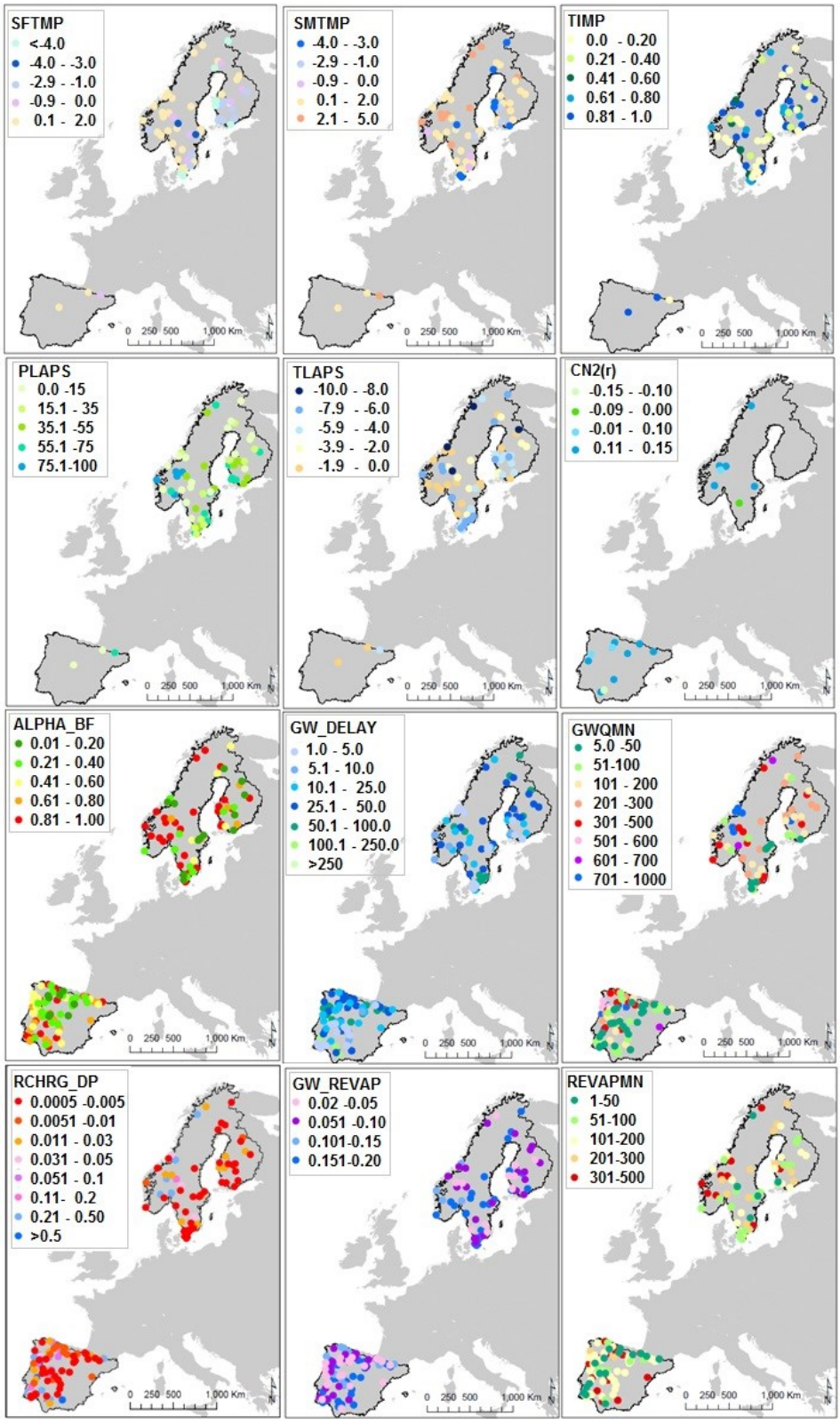


Figure 20. Map of the spatial variation of Near Optimal Parameters values for the Iberian and Scandinavian Peninsulas considering only the sensitive subbasin for each step of calibration.

### 3.2.7 Conclusions of section

This research analyses the strengths and weaknesses of a step-wise calibration applied at pan European scale using the SWAT model. It was demonstrated that the main advantages of this procedure illustrated by the good performance of the model obtained in gauged and ungauged subbasins. The step-wise calibration allows gaining a good knowledge of each hydrological process through the analysis of temporal and spatial variations of calibrated flow in the different regions.

The sensitivity analysis of the step-wise calibration has shown that snow processes are the most significant in Scandinavia, while groundwater processes are dominant both in Iberian Peninsula and Scandinavia. As a consequence, in Scandinavia the surface runoff is usually generated by snow melt over frozen soils, and by intensive storm in Iberian Peninsula. The calibrated soil hydraulic parameters have different ranges of values in each region, also showing this difference in runoff generating mechanisms. These results are very useful to understand how the amount and timing of rainfall, snowfall and soil properties influence loss of dissolved nutrients in surface runoff.

This modelling procedure has shown that the use homogenous continental input data to setup the model yields robust results despite some necessary simplifications needed to achieve a reasonable compromise between run time, and output accuracy. However, some of these simplifications, including the lack of specific reservoir rule management, and considering only lakes with areas larger than 20 $km^2$ can lower the performance of the model such as in lake and reservoir dominated areas of Finland.

Additional limitations might come from the lack of consideration of karst areas which are widely spread in Mediterranean countries. For instance, in the northern part of the Guadiana catchment (Spain) in Ciguela River, where the karst is dominant, the performances of the model are not high as in other regions in Spain. Different strategies have been proposed in the literature to model karst area (Baffaut et al., 2009), but all of these are strongly connected with the knowledge of the local system. In particular, many studies have addressed the karst issue in SWAT (Afinowicz et al., 2005; Spruill et al., 2000; Coffey et al., 2004; Benham et al., 2006), (see Gassman et al., 2007 for an extensive review) highlighting the difficulty of using the SWAT model to represent the baseflow of karst-streams.

These aspects can be overcome by collaborating with local authorities to increase knowledge of the management of man-made reservoirs, the springs and the soil parameters in karst areas as described in section 3.5.

## 3.3 The Danube basin: validation of the water balance trough the Budyko approach

### 3.3.1 Synopsis

The evapotranspiration (ET), that includes evaporation from the plant canopy, transpiration, sublimation, and evaporation from the soil, is the primary mechanism by which water is removed from a watershed (Dingman, 1994). It is thus an important component of the hydrologic cycle in the watershed, and its quantification is crucial to evaluate correctly the water balance (Wang et al., 2006). However, despite remote sensing data are used more frequently for its estimation (see for instance Kalma et al., 2008; Verstraeten et al., 2008; Overgaard et al., 2006), the measurement of ET remains difficult, time consuming, and costly because related to a number of factors (i.e. changes in leaf area, plant height, crop characteristics, soil and climate conditions, and management practices) (Doorenbos and Pruitt, 1977). For this reason, in order to control the ET component in the water balance of SWAT model, a simple diagnostic method based on Budyko approach (Budyko, 1974) was proposed.

Budyko (1958) demonstrated that the partitioning of precipitation into ET and streamflow is a function of available water in terms of precipitation and energy measured by potential evapotranspiration (PET), or rather depends on the aridity index. The aridity index (AI) is defined as the ratio of long term mean annual potential evapotranspiration (PET) to long term mean annual precipitation (P). It was demonstrated that when AI is high, most precipitation leaves the subbasins as evapotranspiration (ET); whereas, when the aridity index is low most precipitation leaves the subbasin as streamflow. Thus, AI has directly a key role in the control of ET and many studies have been performed on finding the relation between AI and the evaporative index, defined as the ratio of long term mean annual evapotranspiration to long term mean annual precipitation. Classical studies were done by Schreiber (1904), Ol'dekop (1911), Budyko (1974), Turc (1954), and Pike (1964), and generally they were called Budyko-type curves from the name of the most famous and widely used formulation. In this study a monoparametric Budyko-type equation was used (Turc-Pike equation; Turc, 1954 and Pike, 1964).

Similar to evaporative index, base flow index, which is defined as the ratio of mean annual base flow (BF) to precipitation, is also mainly controlled by climate aridity index (Wang and Wu, 2013). A complementary mono-parametric Budyko-type equation was derived from the Turc-Pike formulation by Wang and Wu (2012), and it was used in this study to control the baseflow component.

These Budyko-type equations were enrolled to explore the water balance partitioning simulated by the SWAT model and controlling the evapotranspitration and baseflow indeces at subbasins and main basin level.

In the Appendix A4 the Budyko approach was explained in detail, as well as the two monoparametric equations used in this study.

### 3.3.2 The study area

The Danube River basins was selected a case study to test the Budyko framework due to its large size, its diverse relief and large climate heterogeneity that have strong effects on the streamflow regime of the whole Basin and its main tributaries.

The Danube River Basin is the second largest river basin in Europe, covering approximately 803,000 $km^2$ of Central and South-Eastern Europe. In year 2015, 19 countries are sharing the catchment, 14 of which are called 'Danube countries' (with catchment areas >2000 $km^2$). The biggest shares of the catchment belong to Romania (30%) followed by Hungary, Serbia, and Austria (around 10%) (Habersack et al., 2013;Figure 21).

Due to its vast area and its topography ranging from lowlands to mountains above 3,000 m a.s.l., the Danube River Basin exhibits a pronounced climatic variability. The western region is influenced by the Atlantic climate, whereas the eastern region is characterised by a continental climate leading to lower precipitation and typically colder winters. The mean annual precipitation for the whole Danube basin for the period 1980 to 2009 was 597 mm/y, ranging from 220 mm/y near the outlet of the river to 1510 mm/y in the Alps (Pagliero et al., 2014). The mean annual temperature for the period was 9.7°C, ranging from 0.8 to 13°C. The mean annual streamflow at the outlet was estimated of about 6387 $m^3$ /s (Pagliero et al., 2014).

The Danube River Basin mainly consists of forest (35%), arable land (34%), and grassland (17%). The irrigated area is around 9000 $km^2$ (only ~1% of arable land), but the volume of irrigation is approximately $3000 \cdot 10^6$ $m^3$ (Portmann, et al., 2008).

The main pressure types in the Danube River Basin causing hydrological alterations are impoundments, water abstractions, and hydropeaking (ICPDR, 2009b). The water abstractions for industry and public use is around $10000 \cdot 10^6$ $m^3$ and the consumptive use for energy is $15000 \cdot 10^6$ $m^3$ (Vandecasteele et al, 2013).


Figure 21. The Danube River Basin. Description of altitude and identification of the three main part of the Danube (Upper, Middle and Lower Danube). Sources: Tockner et al. (2009)

The Danube River can be divided into three general sections and the Delta: the Upper, Middle, Lower Danube, and Danube Delta (Habersack et al., 2013). Within these sections, 18 water management regions were identified (DPR,1999; Vogel and Pall, 23002; ICPDR, 2009b). Table 5 provides information for each region.

The Upper Danube Basin (130,000 km$^2$) reaches from the sources in the Black Forest Mountains to the Gate of Devın, near Bratislava (so called “Porta Hungarica”). The amount of precipitation in the Upper Danube Basin shows a distinct gradient with the altitude. It rises from 650-900 mm/y in the lowland areas to more than 3,000 mm/y in the high mountain ranges exposed to the west and north (Rank et al., 2005). Major landuses within the watershed are forest (38 %) and pastures (18 %) mainly extended in Alpine regions, and cropland (34 %) in flat areas. This section comprises four water management regions: the Danube Source (Region 1), the Inn (Region 2), the Austrian Danube (Region 3) and the Morava (Region 3). The Upper Danube region (Region 1) goes from the source of the Danube to the Inn confluence, and is confined between the Swabian Alb mountain range in the north and the Bavarian alpine foothills in the south. The Inn River (Region 2) has a catchment of around 26000 km$^2$, is 515 km long, and drains part of the Austria, Switzerland and Germany. Its main tributary is the Salzach River. The Austrian Danube (Region 3) goes

from the confluence of the Inn to the alluvial forests downstream of Vienna and its important tributaries include the Traun and the Enns. The 354 km long Morava River is identified as Region 4 and is a Central European Lowland river that originates at 1275 m asl in the north western corner of Moravia, near the border between the Czech Republic and Poland (Tockner et al., 2009).

The Middle Danube basin extends from Bratislava to the Iron Gates dams (border between Romania and Serbia). With an area of 453,000 km$^2$ the Middle Danube Basin is about 4 times as large as the Upper Region and thus the largest one of the three regions. In this region, the Danube follows the eastern margin of the Alps southwards, turns at the southern border of the Pannonian Basin eastwards, and finally reaches the Iron Gate. At Visegrad Gate, it formes an immense alluvial fan that gradually filled the depression of the Great Hungarian Plain. This area embraces seven water management regions: the Vah-Hron-Ipel (Region 5), a part of the “Pannonian Basin System” (Region 6), the tributaries Drava (Region 7), Sava (Region 8), Tysa (Region 9), Velika Morava (Region 10) and the South of Great Hungarian Lowland (Region 11). In particular, the Pannonian Danube (Region 6) reaches the confluence of the Sava River at Belgrade. In this region, the Danube River section widens significantly, while bed slope decreases. River banks become sandier and bordered by alluvial forest. In the Middle Danube region, from the Sava confluence to the Iron Gate, the river is highly influenced by the large lock system that decreases flow velocity to almost stagnant water.

The Lower Danube basin (185,000 km$^2$) is a typical lowland river fringed by (formerly) wide floodplains (Tockner et al., 2009) and represents an ecologically highly valuable section, with numerous islands, natural banks and floodplain (Schneider, 2002). It covers the Romanian–Bulgarian Danube subbasins downstream of Cazane Gorge and the subbasins of the Siret and Prut River. It is confined by the Carpathians in the north, by the Bessarabian Upland Plateau in the east, and by the Dobrogea and Balkan Mountains in the south. The Olt, Siret and Prut are the main tributaries entering from north, while only smaller tributaries, such as the Iskar, enter from the south. In the Lower Danube, six water management regions were identified (from Region 12 to Region 17).

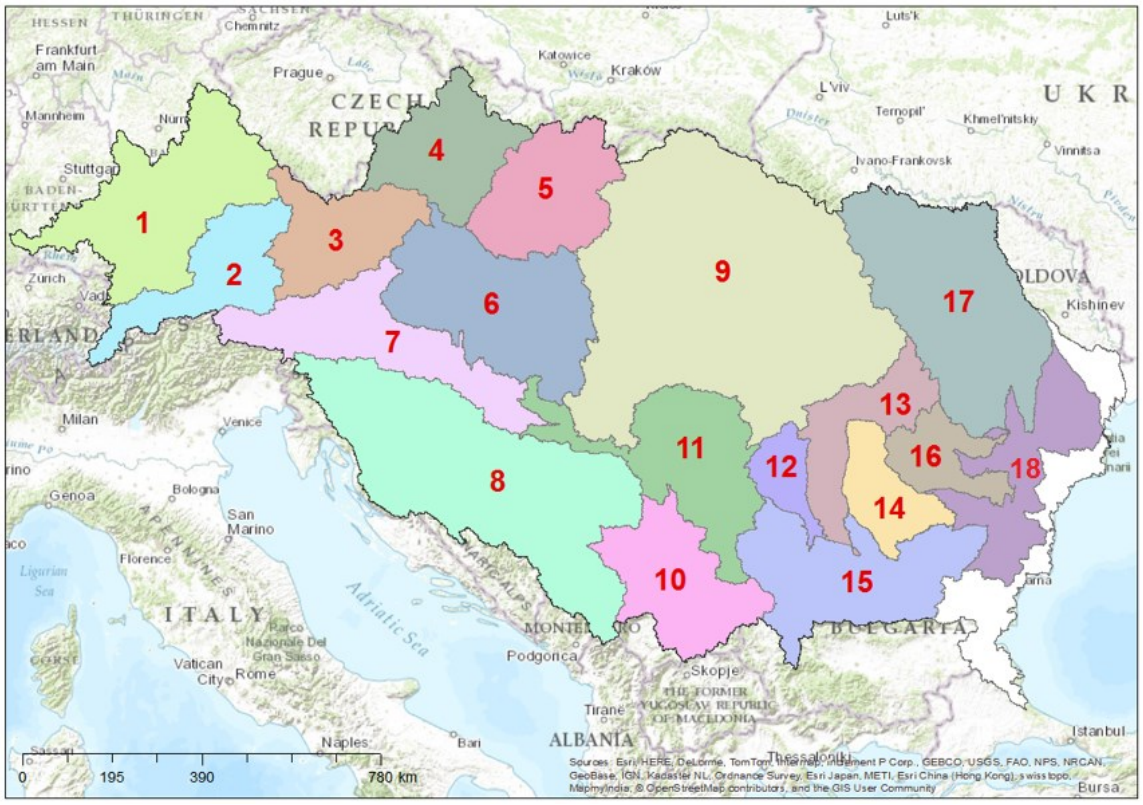


Figure 22. Map of the 18 water management regions in the Danube Basin: 1 = Danube Source; 2 = Inn; 3 = Austrian Danube; 4 = Morava; 5 = Vah-Hron-Ipel; 6 = Pannonian Danube; 7 = Drava; 8 = Sava; 9 = Tisa; 10 = Velika Morava; 11 = Middle Danube; 12 =Jiu ; 13 =Olt; 14 =Arges Vedea; 15 =Silistra Danube; 16 =Buzau-Ialomita; 17 = Siret-Prut; 18= Delta.

Finally, in the Delta region (the water management region 18) the 6$^{th}$ largest Delta of Europe extends from the confluence of the Prut River (Ukraine) to the mouth into the Black Sea (Ukraine). Here the Danube splits into three major arms and interconnected wetlands covering an area of 5,640 km$^2$ (about 20% in the Ukraine, 80% in Romania), including adjacent lakes and lagoons, covers some 5640 km$^2$.

The mean average discharges of the Danube reach approximately 2,000 m³/s at the gauge Bratislava, approximately 5,500 m³/s at the gauge Iron Gate, and approximately 6,500 m³/s at the Danube Delta at the Black Sea. The main tributaries with the highest mean annual runoff are the rivers Inn within the Upper Danube, and Sava and Tisza within the Middle Danube, leading to a significant increase of the mean annual runoff of the Danube at their confluences.

In correspondence of the closure of the 18 sections the International Commission regularly monitors the streamflow, physic-chemical and biological parameters (see table A2.2 in Appendix A2). Details information related to elevation, precipitation and streamflow regime were summarized in Table 5.

Table 5. The 18 Regions of Danube River Basin and their general characterization, as well as the number of streamflow gauging station in each region, with reference to the Area (km$^2$). The mean annual observed streamflow in grey was obtained from literature information.

| ID-Regions | Name | Area (km$^2$) | Drain Area (km$^2$) | Average of elevation (m) 1 | Long mean annual precipitation (mm) 2 | Mean annual observed streamflow (m$^3$/s) 3 | # of streamflow gauging stations |
|---|---|---|---|---|---|---|---|
| 1 | Danube Source | 49,769 | 49,769 | 620 | 950 | 700 | 117 |
| 2 | Inn | 25,999 | 25,999 | 1260 | 1200 | 760 | 75 |
| 3 | Austrian Danube | 26,036 | 101,803 | 800 | 1000 | 2,000 | 62 |
| 4 | Morava | 26,628 | 26,628 | 380 | 540 | 110 | 34 |
| 5 | Vah-Hron-Ipel | 30,587 | 30,587 | 470 | 720 | - | - |
| 6 | Pannonian Danube | 52,085 | 211,103 | 560 | 790 | 2,350 | 91 |
| 7 | Drava | 39,679 | 39,679 | 770 | 860 | 500 | 72 |
| 8 | Sava | 100,102 | 100,102 | 550 | 915 | 1572 | 87 |
| 9 | Tisa | 149,567 | 149,567 | 360 | 590 | 792 | 75 |
| 10 | Velika Morava | 37,702 | 37,702 | 630 | 600 | 277 | - |
| 11 | Middle Danube | 44,261 | 582,414 | 500 | 790 | 5,460 | 5 |
| 12 | Jiu | 10,333 | 10,333 | 440 | 570 | 97 | 1 |
| 13 | Olt | 23,841 | 23,841 | 630 | 570 | 140 | 2 |
| 14 | Arges Vedea | 18,118 | 18,118 | 380 | 560 | - | - |
| 15 | Silistra Danube | 50,615 | 685,320 | 490 | 710 | 4,570 | 6 |
| 16 | Buzau Ialomita | 16,358 | 16,358 | 310 | 530 | - | 1 |
| 17 | Siret-Prut | 66,250 | 66,250 | 270 | 560 | 300 | 36 |
| 18 | Delta | 34,104 | 802,032 | 490 | 710 | 6,700 | 5 |

1) The mean elevation was calculated from the Digital Elevation Model (DEM) considering the whole drained area of each region.
2) The long mean annual precipitation was obtained from the ESAF-meteo database (Ntegeva et al., 2013) considering the whole drained area of each region.
3)The mean annual observed streamflow at the outlet of each region was obtained from the correspondent gauged station where available, while for region 1, 8, 9,10 and 17 (in grey color) literature information were adopted. In particular, for Region 1 the mean annual streamflow was calculated as difference between the station Achleiten on Danube and Passau-Ingling on Danube; for region 8 (Sava) and 9 (Tisa) the estimations reported in Sommerwerk et al. (2009) were used; ICPDR (2004), Table 3.2, reported the mean annual streamflow for region 10 (Velika Morava), while the stations Serdreni and Giurgiulesti were used as reference for region 17 (Siret –Prut), albeit the negligible contribution of the small Buzau basin is included.

### 3.3.3 Summary of Danube SWAT Model setup and the C/V results of monthly streamflow in the Danube

The SWAT model of the Danube River Basin was built in SWAT2012 using the ArcGIS SWAT interface (Olivera et al., 2006). The total modeled domain is 833,908 km$^2$ subdivided in 4663 subbasins and 5181 Hydrological Response Units (HRUs) with respectively an average size of 179 km$^2$ and 160 km$^2$, ranging from 0.01 to 1232 km$^2$. However, 145 subbasins covering about 33,000 km$^2$ were not considered in the model evaluation since they drain directly into the Black Sea.

Spatial data used to set up the SWAT model are described in table A.1.1 in Appendix A1 and comprised a pan-European climatic dataset including daily precipitation, temperature, solar radiation, wind speed and relative humidity for 1990-2009 with a spatial resolution of 25 $km^2$ (EFAS-Meteo; Ntegeka et al., 2013), the 1 km resolution Harmonized World Soil Database (HWSD; FAO, 2008) and the land use/land cover information based on a 1 km pixel size land use map for year 2000 assembled from several databases (CAPRI, Britz, 2004; SAGE, Monfreda et al., 2008; HYDE 3, Klein Goldewijk and Van Drecht, 2006; GLC, Bartholome and Belward, 2005). Topography was based on the DEM 100 m pixel size (CCM2 DEM, Vogt et al., 2007) and hillslope length values were estimated using LS-Tool (Zhang et al., 2013) imposing a maximum theoretical *As* of 122 $m^2/m$. Point sources (UWWTD database; ICM, 2011) were insert in each subbasin.

SWAT hydrological setup and C/V procedure described in Pagliero (2014) were revised and improved including several changes to better accounting the requirement of the Water Framework Directive (WFD, 2000). Therefore, farming system management practices, riparian land, structure along the stream network, as well as artificial drainage systems and abstraction for water uses were implemented. Table A3.1 in Appendix 3 provides informationabout the BMPs implemented.

An extensive database of daily streamflow gauging stations was involved in the calibration (264 monitored stations for the period 1995-2006) and validation (708 monitored stations for the period 1995-2009, including the calibration dataset extended the period up to 2009). See Table A2.1 in Appendix A2 for more details.

Following the C/V strategy for streamflow calibration (see Chapter 2) the daily streamflow was subdivided in its components (surface runoff, lateral flow and baseflow) and each of them was calibrated. 70% (184) gauging stations in the calibrations dataset reached satisfactory PBIAS (+/-25%) comparing the observed and simulated monthly streamflow and were used as donors to transfer the NOP (Near Optimal Parameter) set to the ungauged subbasins in four hydrological regions. From the validated dataset, 60% (425) of gauging stations reached satisfactory performance and Figure 23 shows some example of monthly streamflow comparison between observed and simulated values.

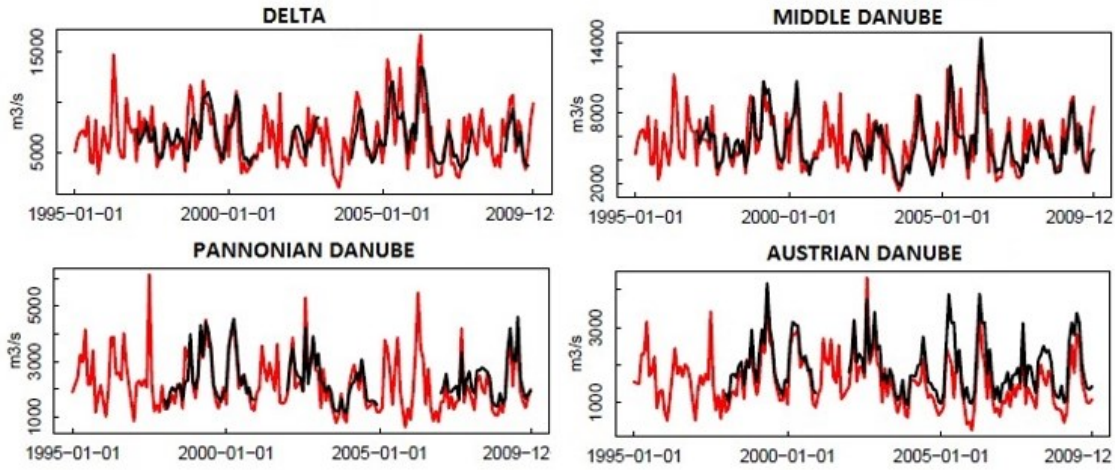


Figure 23. Comparison between monthly observed and simulated hydrographs at the outlets of the whole Danube (DELTA, region 18), the Middle Danube (Region 11), the Pannonia Danube (Region 6) and Austrian Danube (Region 3).

### 3.3.4 The aridity index in the Danube River Basins

Available energy (often expressed in terms of potential evaporation) and precipitation largely determine annual evapotranspiration and streamflow rates in a region. The ratio of annual potential evaporation to precipitation, referred to as the aridity index by Budyko, has been shown to describe the evaporation ratio (the ratio of annual evapotranspiration to precipitation) of catchments from a range of climatic regimes in a number of studies. It has been shown that aridity index alone can be used to obtain an estimate of ratio of long-term annual evapotranspiration (the evaporation index) using monoparametric or more complex equations, namely the Bydyko-type curve (i.e. Turc, 1954; Pike, 1964; Fu, 1981; Zhang et al., 2001; Yang et al., 2008). In Appendix A4 a complete description of the equations used in this study is provided.

Figure 24 and Figure 25 show respectively the spatial distribution of long-term annual precipitation (P) and the potential evapotranspiration calculated by SWAT using the Penman–Monteith formula in the Danube River Basin. Figure 26 shows the aridity index (calculated as the ratio of PET on P).

The mean annual precipitation for the whole Danube basin for the period 1995 to 2009 was 730 mm/y, ranging from 300 mm/y near the outlet of the river to over 1500 mm/y in the Alps. The Inn River Basin (region 2) and Austrian Danube (region 3) the highest values of long-term mean annual precipitation of about 1200 and 1000 mm/y respectively, while in Morava River Basin (region 4) and Sire-Prut region (17) the precipitation as lower and around 600 mm/y.

The average annual potential evapotranspiration is 830 mm, ranging from 60 in the Alps to over 1500 mm/y in crop land areas in the Middle and Lower Danube. In particular, in the Inn River Basin and Austrian Danube the PET was around 500 and 620 mm/y respectively, while in Morava River Basin reached highest value of 830 mm/y, as well as in the Buzau–Ialomita (region 16) with around 920 mm/y.

It is noteworthy that the PET is generally higher in land-crop areas where precipitation is lower.

The aridity index (potential evapotranspiration on precipitation) is very low in alpine areas (AI<0.5) and increase in the Hungarian Plain and in the south of Romania, Moldova and Delta. It was estimated that in the Inn River Basin the AI was was 0.4 and 0.6 respectively, while in Morava River Basin and in the Buzau–Ialomita was greater of 1.3 reflecting the aforementioned spatial distribution of PET in the region.

Based on the Budyko framework theory (see theory in Appendix A4), Figure 26 provides information of likely evapotranspiration and also baseflow. It is expected that in regions characterized by low values of aridity index (AI<1, i.e. alpine areas) the evapotranspiration is lower than in regions with aridity index greater than 1. Conversely, the baseflow is expected higher in regions characterized by AI<1 ("humid areas"), and lower in regions with AI>1 ("arid areas").

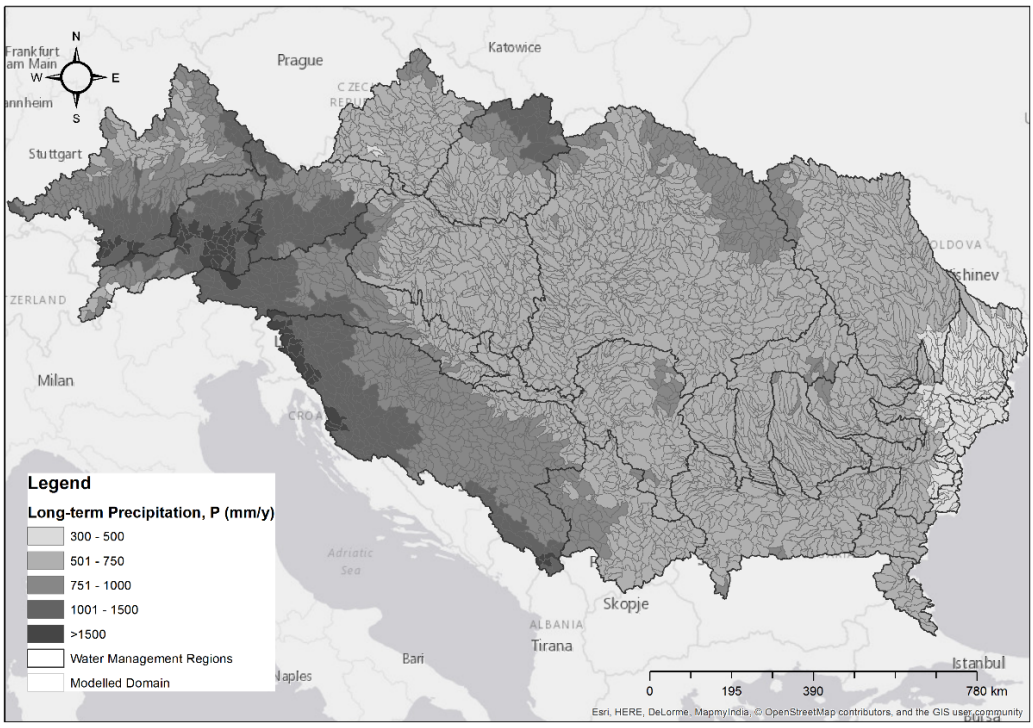


Figure 24. Map of long-term mean annual precipitation (period 1995-2009) in the Danube River Basin.

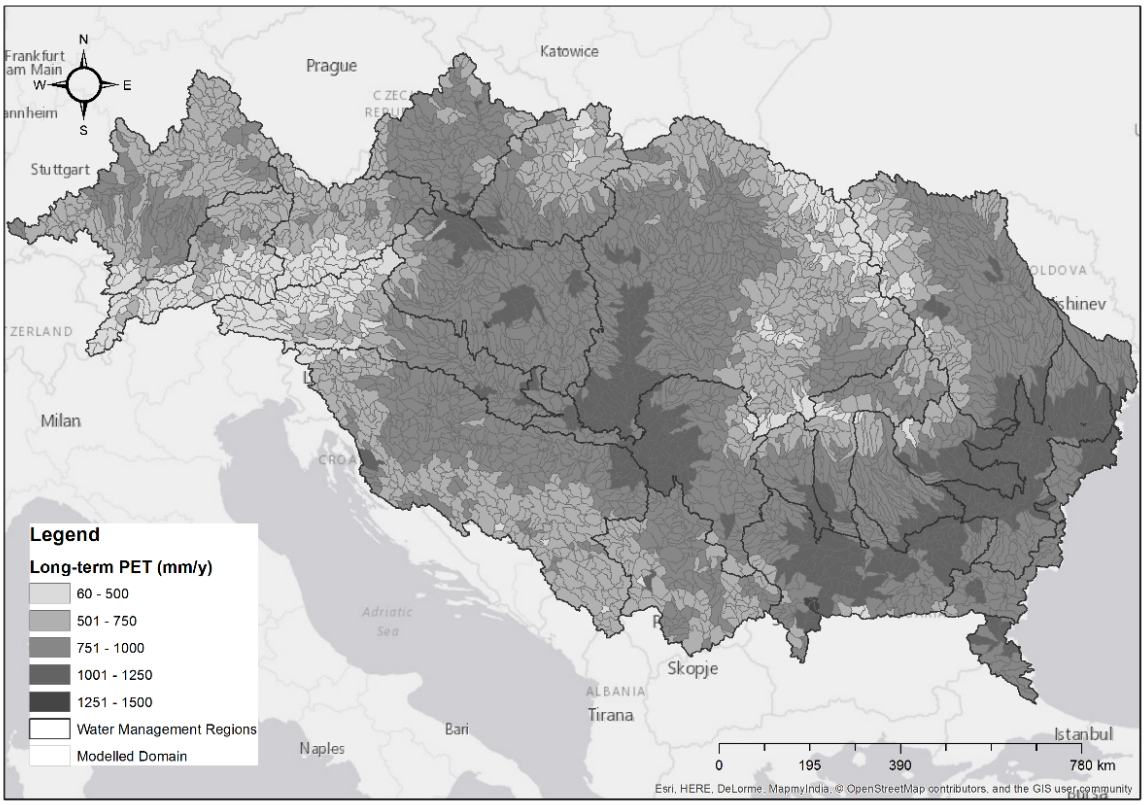


Figure 25. Map of long-term mean annual potential evapotranspiration (period 1995-2009) in the Danube River Basin.

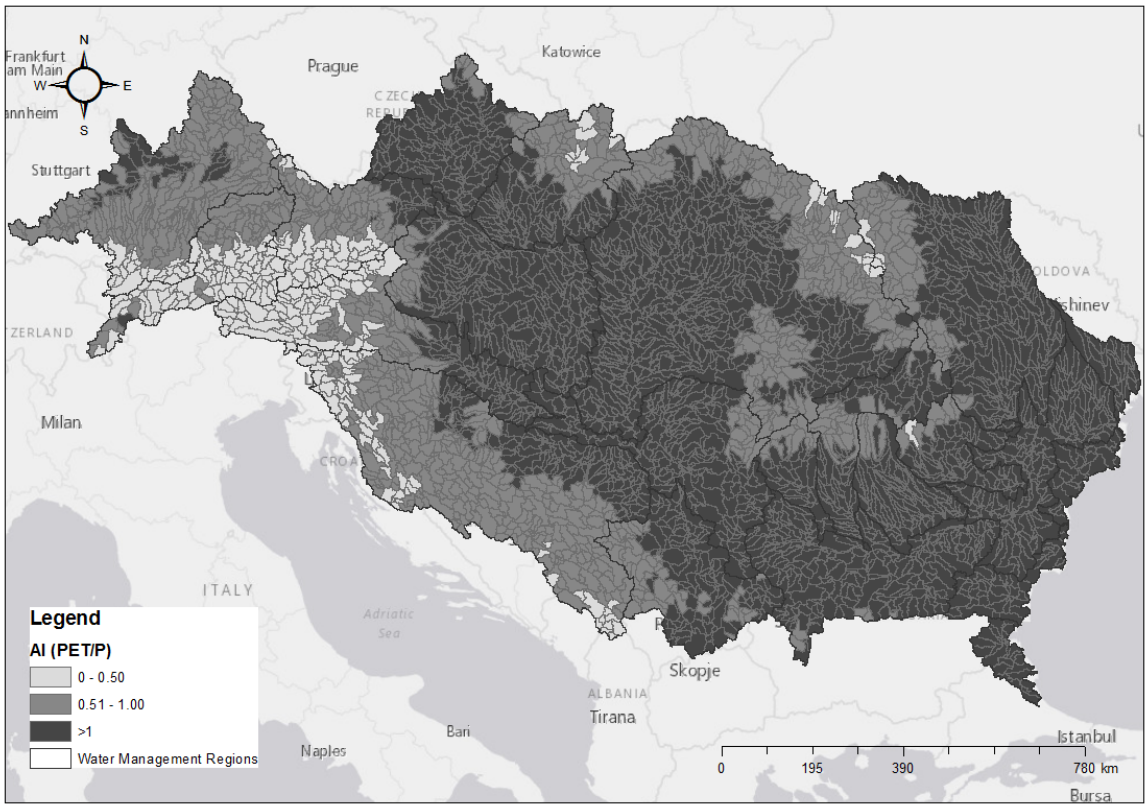


Figure 26. Map of the aridity index (AI=PET/P, PET=Potential Evapotranspiration, P=precipitation) in the Danube River Basin.

### 3.3.5 The diagnosis of evapotranspiration and baseflow

The Budyko formulation requires the definition of AI (aridity index), EI (evaporative index) and BFI (baseflow index) in each subbasin (headwaters or subbasins with Strahler order number equal to 1) or basin (characterized by Strahler order number >1) of the SWAT model. In particular, long-term annual mean of precipitation (P, mm), potential evapotranspiration (PET, mm) and evapotranspiration (ET, mm) were defined in those basins using a weighted average on the area of internal subbasins. The same method was applied for each water management regions (Figure 22).

P, PET and ET where extracted from the SWAT model. AI was calculated in each subbasin, basin or region, as the ratio between the long-term PET and the long-term precipitation (P), as well as EI (ET/P) and BFI (BF/P). In particular, in the precipitation term the contribution of irrigation is considered, due to its effect on evapotranspiration.

EI was defined from observation ($EI_{obs}$) as the difference between precipitation (P) and the observed mean annual streamflow (Q) divided by the precipitation. Q was calculated from daily observed streamflow ($m^3/s$) in the period 1995-2009 for 418 gauged stations well distributed in the Danube River Basin. Similarly, BFI was defined from observation ($BF_{obs}$). The BF was extracted from daily streamflow time series at 418 gauged stations, and then aggregated at annual time step to calculate the baseflow index. A digital filter (Lyne and Hollink 1979) was used to perform the separation of the components of streamflow.

The relationship between AI and EI, as well as between AI and $EI_{obs}$, was defined using a Budyko-type curve, namely Turc-Pike equation ([eq. A4.2] in Appendix A4). Similarly, the Budyko-type curve proposed by Wang and Wu (2013) ([eq. A4.3] in Appendix A4) was used to study the relationship between AI and BFI, as well as between AI and $BFI_{obs}$. Hereafter, for simplicity the “Budyko curve” term was used for both equations.

These curves are empirical relationship in which the coefficients *n* and *m*, respectively in Turc-Pike and Wang and Wu (2013) equations, are related to climate seasonality or spatial scales (e.g. Milly, 1994; Choudhury, 1999; Zhang et al., 2004; Potter et al., 2005). Although correlations between characteristics and *n* (or *m*) have been found, it remains a calibration parameter, and thus estimated for the specific case study. The coefficient n and m were calibrated using a simple nonlinear least squares curve fitting function.

The Figure 27 a and b shows respectively the observed and simulated long-term annual relationship for 413 subbasins in the Danube Regions, while Figure 27 c shows the Budyko curves from simulated values for the entire Danube.

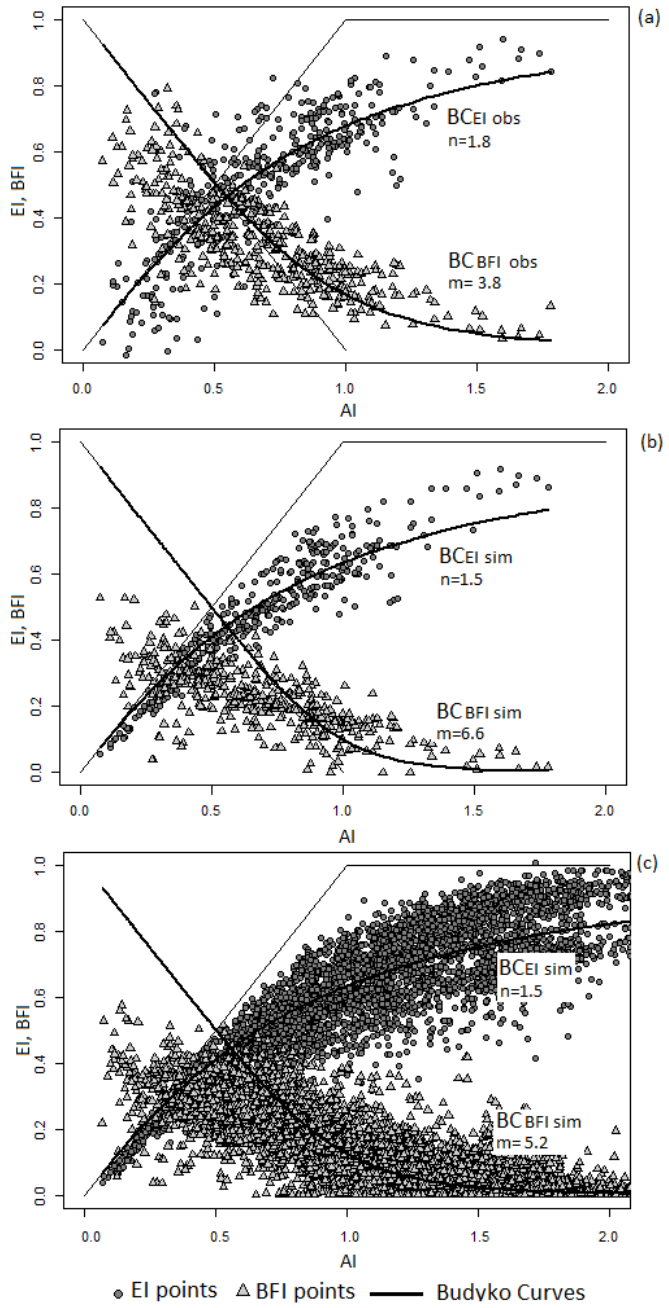


Figure 27. Budyko driagrams and curves (BC) obtained using observations (a) and simulated values (b) at 418 gauging stations. In (c) the BC considering all subbasins in the Danube River Basin. EI is the evaporative index, BFI is the baseflow index and AI the aridity index; n and m are the coefficient of Bydyko-type curves respectively related to EI and BFI. The abbreviation “obs” and “sim” refer to observation and simulation respectively.

Concerning the relationship AI versus EI for observations in the 418 gauging stations, Figure 27a shows that some subbasins are located outside the energy limit highlighting that for subbasins characterized by AI<0.5 the groundwater components (lateral flow, baseflow and deep aquifer recharge) are significant. This is confirmed by the complementary relationship between AI and BFI for which the subbasins with AI<0.5 had the highest BFI.

The coefficient n and m were estimated equal to 1.8 and 3.8 respectively, and hereafter were used as reference values.

Looking at Figure 27b, it is noteworthy that the SWAT model is able to predict correctly the evapotranspiration in the selected 418 gauging stations since all the points are well distributed around the Budyko curve. Furthermore, the subbasins with AI<0.5 are allocated below the energy limit, highlighting that the model had properly apportioned precipitation among ET, surface runoff and infiltration. The coefficient n was estimated equal 1.5. The simulated BFI instead was underestimated in subbains characterized by AI<0.5 since all the BFI points are allocated below the Budyko curve. Thus, the coefficient m was estimated equal to 6.6, about twice the m obtained using the observed values.

These findings were also found considering all subbasins in the Danube (Figure 27c). The coefficient m increased from 3.8 to 5.2 respectively for the Budyko curve obtained from observations and that using the simulated values in the whole Danube. The coefficient n however is confirmed equal to 1.5, very near to that obtained for the Budyko curve of observations (Figure 27c).

Figure 28 depicts the relationship between AI-EI, and the complementary relationship BFI-AI, considering all subbasins in the Danube, as shown before in Figure 27c, with respect to their elevation (Figure 28a), slope (Figure 28b), precipitation (Figure 28c) and percentage of area covered by crop land (Figure 28d).

The Budyko curves refer of those obtained from observation with n=1.8 and m=3.8.

As expected from the analysis of the map aridity index in Figure 26, the simulated EI was lower in the subbasins characterized by lower AI, such as in subbasins with high elevation, steep slope and abundant precipitation, as well as temperature are generally too low for higher EI. Conversely, EI is higher in flat crop land subbasins with low precipitation.

Concerning the BFI, it is noticeable that the index resulted underestimated in wet or humid subbasins (AI<0.5) characterized by high elevation, steep slope, rich precipitation, and they are mainly covered by forest and pastures as showed in Figure 28c by the brown points (subbasins with higher percentage of forest and pasture than crop land)

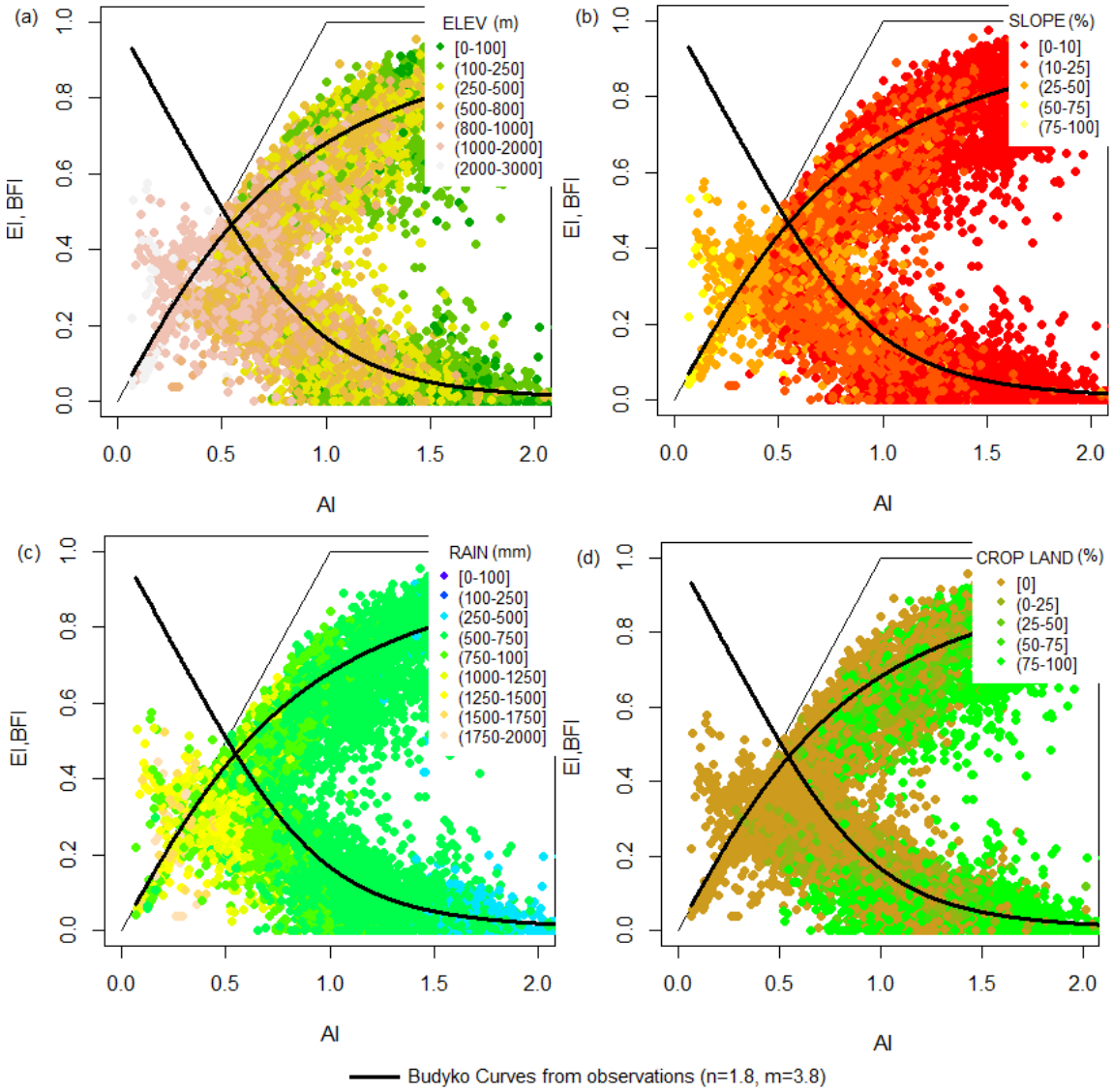


Figure 28. Budyko diagrams of all subbasins in the Danube River Basin and the Bydyko curves obtained using the observation in 418 gauging stations (n=18 and m=3.8) (see also Figure 27 a). The subbasins are classified by elevation (a), slope (b), precipitation (c), and percentage of area covered by crop land in each subbasin.

### 3.3.6 The n and m coefficient in the water management regions

The Budyko-type curves were also calculated in each water management regions, obtaining for each of them the coefficients n and m.

Figure 29a shows the relationship between the Budyko coefficients in the 18 water management regions with respect to the coefficients n=1.8 and m=3.8 obtained using the observations. Figure 29 b-c instead show the spatial distribution of the coefficients.

It can be observed that generally in the all water management regions the n coefficient was in the range of 1.4-1.6, excepted for region 2 (Inn), 12 (Jiu) and 14 (Olt) for which n is lower

(1.3, 1.4 and 1.31 respectively) and for region 16 (Buzau-ialomita) and 17 (Prut-Siret) where n is higher than 1.6.

The coefficient m is around 4 in 8 water movement regions (i.e. Morava, Tysa and Velika Morava), around 6 in other 6 (i.e. Pannonian Danube, Lower and Silistra Danube, as well as the Delta) and more than 8 in the Upper Danube, Inn, Drava e Sava River Basins. In particular, the highest value of m was found in the Inn River Basin.

Comparing n and m among the regions (Figure 29a), it can be observed that the Inn Basin (region 2) differed from the comprehensive Danube behavior, with the lowest n (equal to 1.3) and the highest m (more than 20, thus not visible in Figure 29a), the Drava Basin (basin 7) had instead the highest n (equal to 2) and an important m coefficients (equal to 18), while the Sava (region 8) had n equal to 1.54 and a significant m equal to 16.5.

To understand the meaning of the resulted coefficients for each region, Figure 30 and Figure 31 show the relationship between AI and EI (or BFI) for the 18 water management regions with respect to the Budyko curves obtained from observation with n=1.8 and m=3.8. Concerning the AI-EI relationship (Figure 30), all the regions are well distributed near the Buyko curve and, as expected, the Inn Basin (region 2) and Austrian Danube (region 3) had the lowest EI values since they are humid subbasins characterized by AI<1. Conversely, for instance, the Morava River Basin (region 4) and the Buzau-Ialomita (Region 16) had highest values of EI since they are classified as arid basins with AI>1.

The AI-BFI relationship (Figure 31) instead shows that the Inn basin (region 2), the Austrian Danube (region 3), as well as Drava, Sava and Danube Source (regions 7, 8 and 1 respectively) were allocated below the Budyko curve, thus indicating a likely underestimation of BFI.

Considering these results, Figure 32 provides a general understanding of the relationship n-m with respect to the EI and BFI values. Decreasing the n coefficient and increasing the m coefficient the baseflow index becomes significant and the evaporative index negligible. This is the case of the Inn basin (region 2). Conversely, increasing the n and decreasing the m coefficient, the baseflow is negligible and the evaporative index becomes an import factor in the water balance. This is the case of Siret-Prut (basin 17) and Ialomita basin (basin 16). Increasing both n and m, both the evaporative and baseflow index are important (i.e. in the Drava basin, basin 7), while decreasing both n and m, EI and BFI decrease.

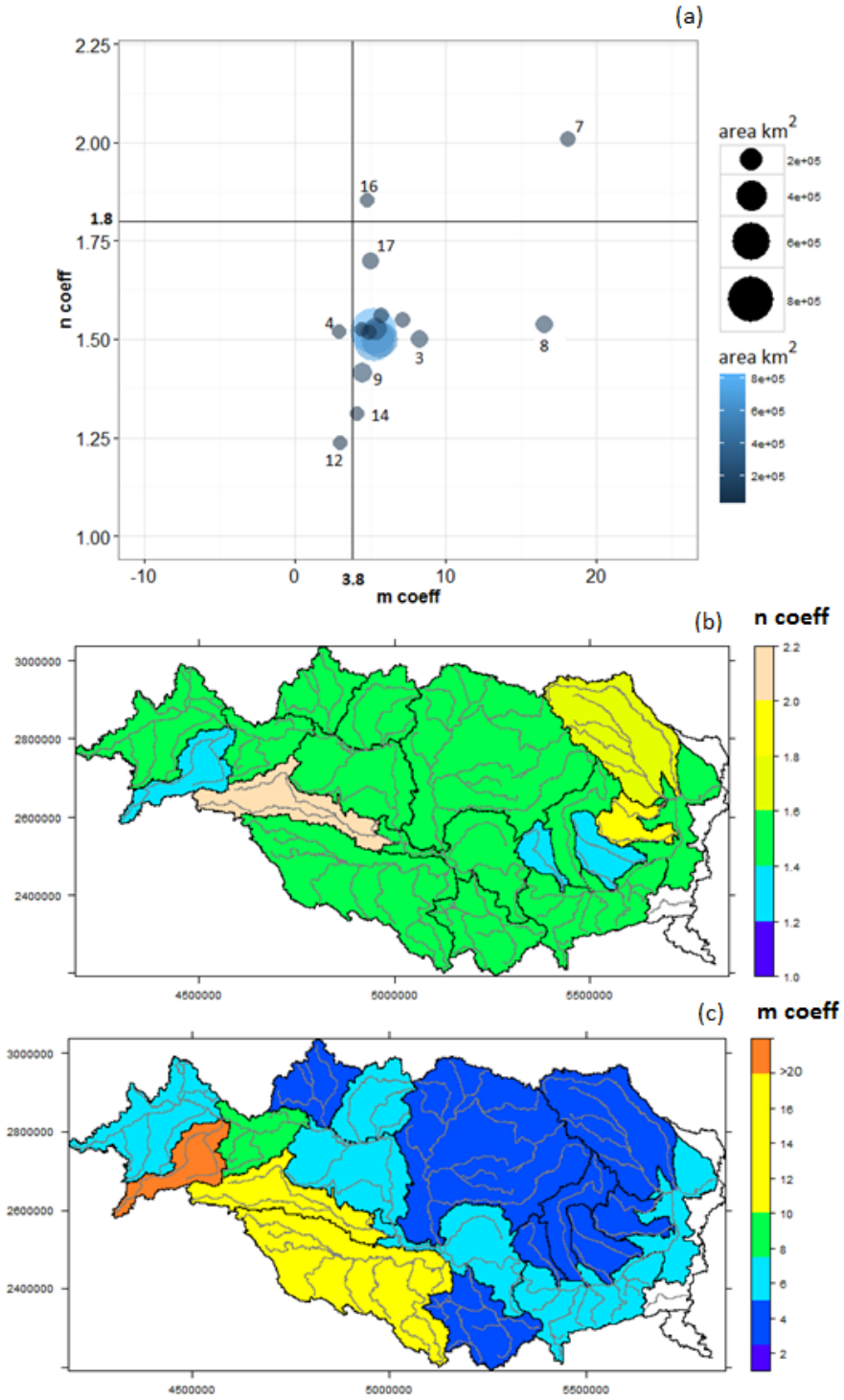


Figure 29. The relationship between n and m coefficients of Budyko-type curves obtained for each water management regions with respect to the coefficient value of the observed Budyko curve (n=1.8, m=3.8) (a); in (b) and (c) the spatial distribution of coefficients in the water management regions. In (a) the region 2 (Inn River Basin) is omitted since the m coefficient is larger than 20.

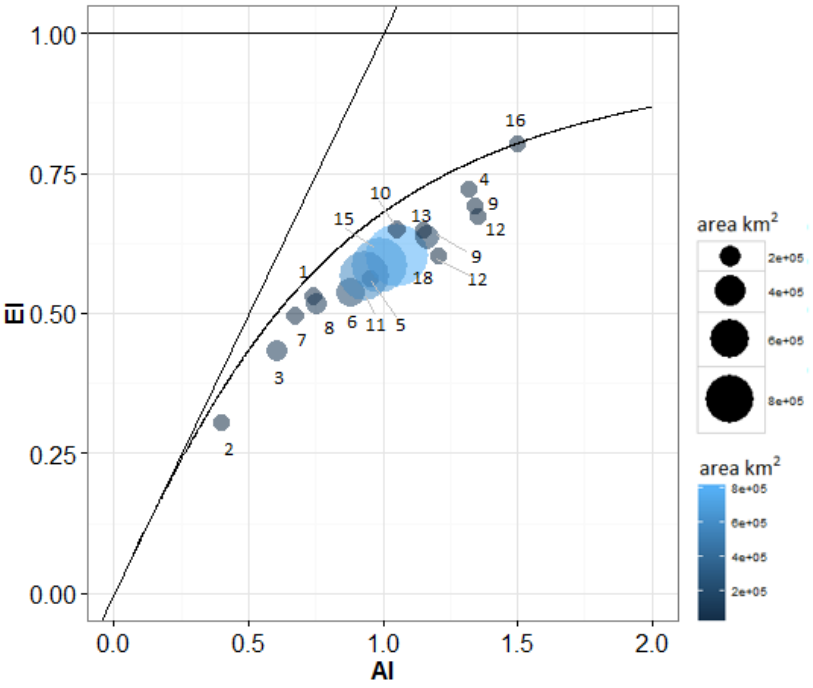


Figure 30. Budyko curve from observation (n=1.8) with points representing the 18 water management regions. Large and light blue circles denote the largest regions and small blue circles denote the smallest regions.

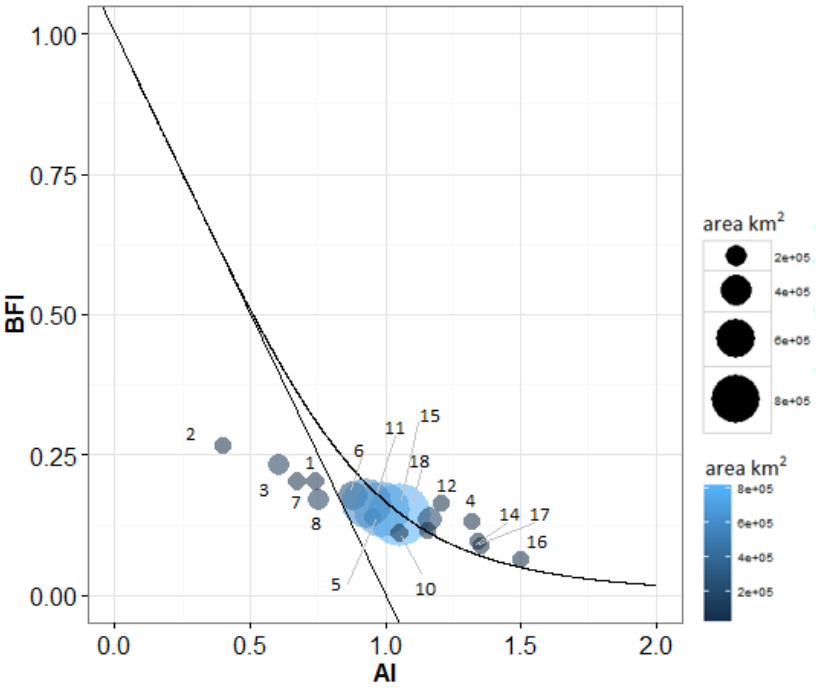


Figure 31. Complementary Budyko curve from observation (m=3.8) with points representing the 18 water management regions. Large and light blue circles denote the largest regions and small blue circles denote the smallest regions.

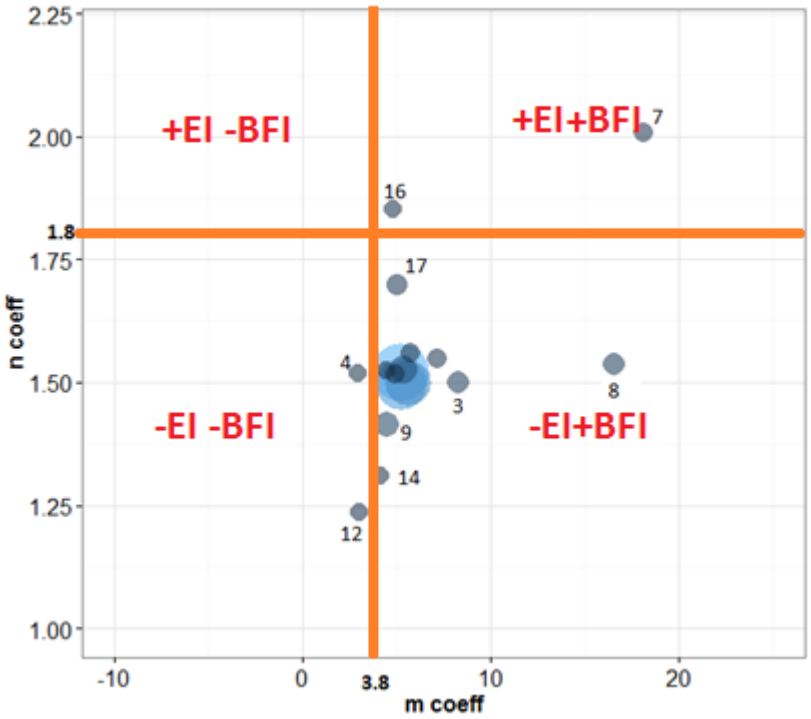


Figure 32. The interpretation of the relationship between n and m coefficients of Budyko-type curves obtained for each water management region with respect to the coefficient values of the observed Budyko curve (n=1.8, m=3.8).

### 3.3.7 The impact of anthropogenic activities

The previous results highlighted that the model suffers for an underestimation of BFI in the Upper Danube, in particular in the Inn River Basins. This underestimation has influenced also the predicted streamflow that was characterized by a negative bias of 26% respect to the monthly observation in the period 1995-2009.

The simulated water balance of the Inn River Basins showed that 31% of the precipitation is lost by evapotranspiration, 55% contributes to water yields (21% surface runoff, 7% lateral flow and 27% baseflow) and 15% of precipitation is lost by deep aquifer recharge. This means that there is a considerable amount of water lost by the systems that could contribute to baseflow. These findings immediately suggested that the calibrated headwaters used as donors in the regionalization were strongly influenced by derivations, storage of water outside the subbasins, as well as water released in other subbasins. It is noteworthy that the Inn River and its alpine headwaters are strongly influenced anthropogenic activities. Water resources are intensively used by agriculture, tourism, industry and energy providers (GLOWA, 2011). Furthermore, the Inn River Basin is ideally suited for hydroelectric power generation due to its high precipitation and runoff rates. The biggest runoff-river power plants are installed along the main river, and the most important reservoir power plants with

a range of 50 to 1000 GWh are situated in the southern part in the Central Alps (Koch, 2011).

Figure 33 shows the relationship between EI and BFI before and after the introduction of water lost by deep aquifer recharge as contribution to BF. It is noticeable that the water lost from the system as deep aquifer recharge improved the BFI estimation, moving the points closer to the Budyko curve.

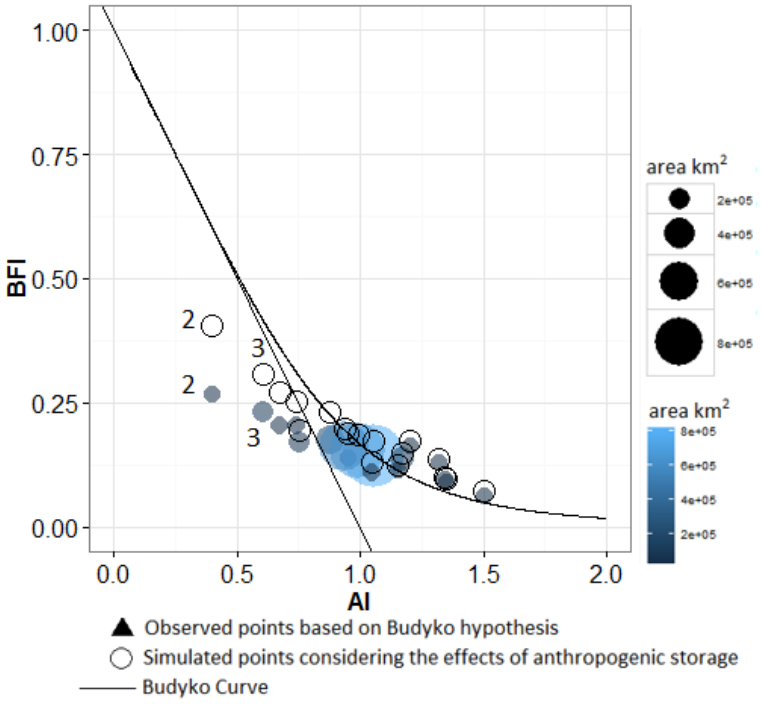


Figure 33. Complementary Budyko curve from observation (m=1.8) with points representing the 18 water management regions. Large and light blue circles denote the largest regions and small blue circles denote the smallest regions. The hallow circles represent the water management regions when the anthropogenic storage where considered in the model.

As a consequence, the calibrated parameter sets transposed in the hydrological similar subbasins has led to misrepresent the natural behavior of the Inn Basin as shows in Figure 34. The gauged station in the subbasin 2583 and 2451 are independent calibrated subbasins selected as donors in the regionalization technique since human impacts were initially assumed negligible.

Rossi (2014) reported that from Inn at S-Chanf, Vallember, Varush and Tantermozza (see subbasin 2662 in Figure 34), the water is stored and diverted to the Ova Spin hydroelectric plant through a pressure pipe (Figure 34). The Ova Spin collects also the important contribution from the compensating basin of Spol (33 $m^3/s$) and continues in a pressure pipe parallel to Inn collecting other water storages until the Pradella hydroelectric power plant, situated on the Inn, with 66 $m^3/s$ (see subbasin 2466 in Figure 34 before the

Kajetansburk gauged stations in the subbasin 2318). From this point another water diversion in a pressure pipe runs for 14 km until the Martina hydroelectric plant on the Inn River with 88 $m^3/s$. After that the Inn River receives a negligible contribution from subbasin 2451 and at the gauged station Kajetansburk (subbasin 2318) the streamflow resulted strongly influenced by the Martina plant.

In particular, Figure 35a shows the monthly observed streamflow on Inn at Tarasp (subbasin 2583), after the diversion and before the Pradella hydroelectric plant, and at Kajetsnsbruck (subbasin 2318) after the Martina plant. The figure shows also the negligible contribution of basin 2451 highlighting the strong impact of Martina plant on Kajetsnsbruck gauged station (subbasin 2318).

In SWAT the calibrated parameters of subbasin 2583 were transposed to the hydrological similar uncalibrated subbasin 2318, and Figure 34 shows the distribution of parameter RCHRG_DP (deep aquifer recharge parameter) in these and nearby subbasins. The simulated streamflow in subbasin 2318 (Figure 35a, Kajetsnsbruck station) resulted underestimated since the anthropogenic contribution from Martina plant and the diversion upstream were not considered in the modelling.


Figure 34. The Inn sources and the anthropogenic impacts.

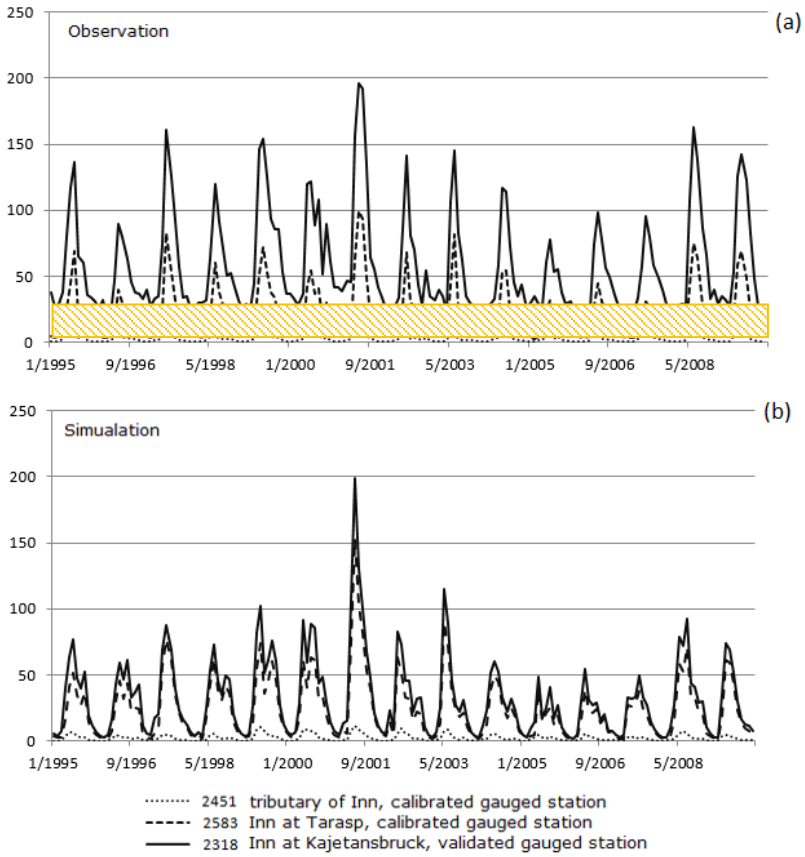


Figure 35. Observed (a) and simulated (b) monthly time series at the Inn sources (a) at Tarasp, in Scholkhof tributary of Inn before the Inn at Kajetsnsbruck. In evidence the impact of Martina plant on the observed streamflow at Kajetsnsbruck.

### 3.3.8 The final water balance of Danube River Basins

The Budyko-type curves analysis has helped to identify the subbasins with potential errors in evapotranspiration and baseflow estimation. Based on the previous insightful findings, the calibration in the Inn River Basin was manually adjusted, improving the reliability of baseflow estimation. In particular, the baseflow index increased from 27% to 34% while decreasing the deep aquifer recharge from 14% to 7% of precipitation.

Table 6 summarized the final water balance for each water management region, as well as some hydrological indices. Figure 36 shows the long-term annual water balance for the Danube River Basin as simulated with SWAT for the period 1995-2009, given a key of interpretation of the results in Table 6.

These results can be compared with numerous studies that applied hydrological and water quality models in the Danube River Basins. Fehér and Muerth (2015) provided an exhaustive water models inventory for the Danube Region giving details of models structure, spatial and temporal scale, as well as their project studies, main references and the aims of the application.

Among these studies, the SWAT model results in Table 6 are compared with the mean values reported by Petrovic et al. (2006) and EnviroGRIDS (2015). Petrovic et al. (2006) used WatBal model (Yates, 1996) in the Danube regions for the period 1961-1990, while EnviroGRIDS (2015) used SWAT to simulate streamflow and nutrients in the whole Black Sea Basin (Rouholahnejad et al., 2014). Its results are available online in GIS format at http://129.194.231.164/layers/ for the period 1973-2006. Generally, the estimates of evapotranspiration and water yields of these studies were very close to that reported Table 6.

For the Danube River Basin it was estimated that 60% of the precipitation is lost through evapotranspiration (ET) and 3% for percolation in the deep aquifer, 20% is infiltration and 37% is water yield (Figure 36). These water balance components were similar also in the Silistra Danube (Region 15) and in the Middle Danube (Region 11). Both of the aforementioned studies obtained very close percentages of evapotranspiration and water yield to the one estimated in this study.

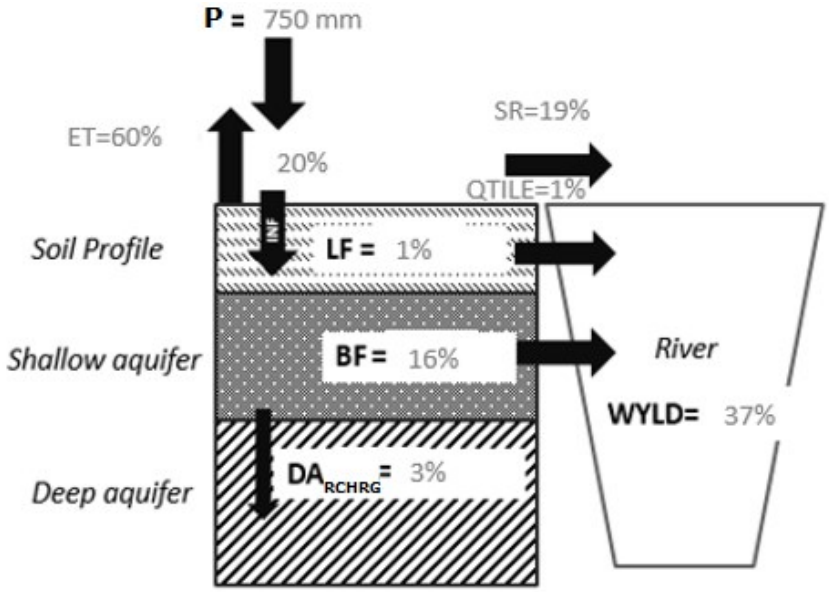


Figure 36. The long-term annual water balance for the Danube River Basin as simulated with SWAT for the period 1995-2009. As explained in Figure 1 : P: precipitation; ET, evapotranspiration; BF, baseflow from shallow aquifer; INF, infiltration in the soil; LF, Lateral flow; SR, Surface Runoff; $DA_{RCHRG}$, the deep aquifer recharge; $GW_{RCHRG}$, the shallow aquifer recharge; WYLD: water yield.

In the Danube Source (region 1), 53% of precipitation is lost through evapotranspiration and 40% is water yields. The main component of water yield is the baseflow with about 20% of the precipitation. Similar findings were obtained in the Austrian Danube, albeit the evapotranspiration decreased to 43% and the water yields increased to 49% due the larger baseflow and lateral flow contribution.

In the Inn river instead the evapotranspiration is very low (30%), while the water yields resulted 62% of precipitation with half of the contribution from the baseflow. Similarly, EnviroGRIDS (2015) and Petrovic et al. (2006) obtained 32% of evapotranspiration and 68% of water yields, thus a negligible difference of 5% is detected between the three models.

In the Morava River Baisin, as well as in the Buzau-Ialomita and Siret-Prut, the evapotransparion is the main component of the water balance reaching more than 70% of the precipitation. In the Vah-Hron-Ipel instead the evapotranspitation was estimated as 58% of precipitation and the water yield as 34%.

For the others management regions, the components were very similar in percentage to that obtained for the whole Danube.

Generally, it is observed that the surface runoff is around 18% in the whole Danube, ranged from 12% in the Morava River Basin to 25% in the Sava. Instead, the baseflow ranges from 7% of precipitation in the Buzau-Ialomita to the highest value in the Inn River Basin (34%).

Table 6. Mean annual water balance of the water management regions of the Danube basin as simulated with SWAT for the period 1995-2009. PCP: precipitation (mm); ET: evapotranspiration (mm); SR: surface runoff (mm), BF: baseflow; DA: deep aquifer recharge; QTILE: tile flow (mm); WYLD: water yields (mm).

| Region | Name | PCP (mm) | ET (mm) | SR (mm) | LF (mm) | BF (mm) | DA (mm) | QTILE (mm) | WYLD, Streamflow (mm) | SR/PCP | $Q_{TILE}$/PCP | LF/PCP | DA/PCP | BF/PCP | ET/PCP | PET/PCP |
|---|---|---|---|---|---|---|---|---|---|---|---|---|---|---|---|---|
| 1 | DANUBE SUORCE | 939.85 | 498.92 | 167.00 | 6.63 | 190.73 | 46.84 | 10.06 | 374.44 | 18% | 1% | 1% | 5% | 20% | 53% | 74% |
| 2 | INN | 1205.83 | 369.16 | 247.42 | 84.20 | 409.26 | 81.98 | 9.40 | 750.30 | 21% | 1% | 7% | 7% | 34% | 31% | 40% |
| 3 | AUSTRIAN DANUBE | 1027.37 | 445.60 | 206.93 | 29.46 | 259.51 | 56.25 | 10.82 | 506.72 | 20% | 1% | 3% | 5% | 25% | 43% | 60% |
| 4 | MORAVA | 622.83 | 453.07 | 71.79 | 2.61 | 81.94 | 3.56 | 12.44 | 168.78 | 12% | 2% | 0% | 1% | 13% | 73% | 133% |
| 5 | VAH-HRON-IPEL | 775.13 | 452.19 | 144.15 | 5.30 | 104.65 | 33.25 | 12.08 | 266.19 | 19% | 2% | 1% | 4% | 14% | 58% | 97% |
| 6 | PANNONIAN D. | 839.40 | 451.84 | 150.63 | 15.77 | 159.94 | 35.50 | 12.81 | 339.17 | 18% | 2% | 2% | 4% | 19% | 54% | 88% |
| 7 | DRAVA | 934.37 | 462.25 | 171.89 | 32.00 | 189.38 | 65.16 | 2.45 | 395.73 | 18% | 0% | 3% | 7% | 20% | 49% | 68% |
| 8 | SAVA | 998.55 | 514.35 | 246.66 | 12.53 | 170.67 | 25.01 | 2.89 | 432.76 | 25% | 0% | 1% | 3% | 17% | 52% | 75% |
| 9 | TISA | 653.66 | 416.55 | 108.22 | 3.19 | 88.61 | 8.52 | 22.37 | 222.40 | 17% | 3% | 0% | 1% | 14% | 64% | 117% |
| 10 | VELIKA-MORAVA | 713.34 | 463.53 | 129.06 | 11.74 | 78.87 | 14.22 | 0.65 | 220.35 | 18% | 0% | 2% | 2% | 11% | 65% | 105% |
| 11 | MIDDLE DANUBE | 804.97 | 456.35 | 152.73 | 11.97 | 132.93 | 25.27 | 12.27 | 309.91 | 19% | 2% | 1% | 3% | 17% | 57% | 94% |
| 12 | JIU | 675.23 | 410.00 | 131.21 | 3.78 | 110.93 | 6.73 | 0.00 | 245.92 | 19% | 0% | 1% | 1% | 16% | 61% | 121% |
| 13 | OLT | 671.61 | 437.37 | 141.76 | 3.65 | 77.98 | 6.32 | 0.09 | 223.49 | 21% | 0% | 1% | 1% | 12% | 65% | 116% |
| 14 | ARGES-VEDEA | 640.89 | 435.28 | 138.64 | 1.66 | 52.03 | 3.09 | 5.37 | 197.71 | 22% | 1% | 0% | 0% | 8% | 68% | 141% |
| 14 | BUZAU-IALOMITA | 608.57 | 489.32 | 81.34 | 2.23 | 39.60 | 6.41 | 0.00 | 123.20 | 13% | 0% | 0% | 1% | 7% | 80% | 152% |
| 15 | SILISTRA DANUBE | 780.00 | 456.12 | 146.92 | 10.56 | 121.47 | 22.17 | 10.77 | 289.74 | 19% | 1% | 1% | 3% | 16% | 58% | 100% |
| 16 | SIRET-PRUT | 605.71 | 443.72 | 99.99 | 3.09 | 57.85 | 3.18 | 0.00 | 160.93 | 17% | 0% | 1% | 1% | 10% | 73% | 132% |
| 18 | DELTA | 749.92 | 453.86 | 138.32 | 9.34 | 109.85 | 19.35 | 9.27 | 266.79 | 18% | 1% | 1% | 3% | 15% | 61% | 106% |

### 3.3.9 Conclusions of the section

The Budyko approach proposed in this study helped assessing the reliability of predicted streamflow controlling the evaporative index and baseflow index.

The Budyko-type curve that relates AI vs $EI_{obs}$ highlighted the importance to consider the infiltration components in subbasins where the aridity index was below 0.5, while the Budyko-type curve that relates AI vs BFI provides evidence of underestimation of baseflow index in Alpin areas, and in particular in the Inn basin.

Furthermore, the analysis of EI and BFI in each water management regions highlighted a negative correlation between the EI and BFI in the Danube Basin, suggesting that where the baseflow index is significant the evaporative index becomes negligible in terms of control factor of streamflow generation, albeit some exception occurred (i.e. for the Drava River Basin). The analysis of n and m coefficient of Bydyko curves has also provided a general understanding of the relationship n vs m with respect to EI vs BFI.

After this Budyko analysis, the SWAT model was improved by constraining the groundwater parameters in the Inn River Basin affected by anthropogenic activities. Finally, the mean annual water balance of all water management regions of the Danube was provided increasing the water resources knowledge in the regions.

## 3.4 The Upper Danube: sensitivity analysis of the SWAT model with respect to the hillslope length parameter and DEM pixel size

### 3.4.1 Synopsis

A main challenge for distributed hydrological modelling at large scale concerns the identification of the best input datasets in order to predict hydrological processes and water quality accurately. Digital elevation models (DEMs) represent the topography that drives surface runoff, and are arguably one of the most important data input to several hydrological models (Wechsler, 2007). With regard to the eco-hydrological model Soil and Water Assessment Tool (SWAT; Arnold et al., 1998), a considerable amount of research has addressed the impact of DEM pixel size on model outputs (Cotter et al., 2003; Chaubey et al., 2005; Chaplot et al., 2005; Di Luzio et al., 2005; Dixon and Earls, 2009; Lin et al., 2013; Chaplot, 2014; Zhang et al., 2014). Generally, research demonstrated that streamflow was unaffected by DEM pixel size, nutrients were slightly affected, but sediment yield was greatly influenced by DEM pixel size (see for instance Chaplot 2005; Chaplot 2014; and Zang et al., 2014). Conversely, the impact of DEM derivatives (topographic attributes) has been explored less frequently (i.e. Wu et al., 2008; Yao et al., 2010; Bieger et al., 2015), even though a profound understanding of DEM derivatives is essential for assessing the relationships between watershed topography and hydrologic processes (Wu et al., 2008).

Among DEM derivatives, the hillslope length plays an important role in predicting streamflow and sediment yield through the peak runoff. Currently, the default method to set hillslope length in SWAT is based on a look-up table that relates hillslope length to the subbasin slope gradient, albeit generally the hillslope length is not only dependent on slope gradient (Hickey, 2000). Often the hillslope length is arbitrarily set to reflect field conditions or calibrated to achieve the desired spatial variation of streamflow components within a watershed (Bieger et al., 2015), sometimes overcoming the recommended range (values below 90 m) by Arnold et al. (2012a).

For this reason, the aim of this study was to assess the impact of hillslope length estimation on streamflow and its components (surface runoff, lateral flow and baseflow). Here the assessment comprised three methods (L1, L2 and L3) to estimate hillslope length based on two DEMs of different resolution (25 and 100 m pixel size) for a total of six model configurations (Table 7). They differed for complexity of implementation (L3 is the simplest, followed by L1 and then L2) and have different magnitude of dependence by DEM pixel size (L2 is directly dependent, L1 is indirectly dependent and L3 is not dependent). As a consequence, it can be asserted that they may give a complete overview of possible

impacts of hillslope length estimations on SWAT simulated hydrological processes. The Upper Danube Basin (132000 km$^2$) was chosen as a study area because of its diversity in land cover and use, topography, and availability of gauging stations.

Table 7. Characteristics of the six SWAT configurations compared in this study (DEML configurations) as generated by the combination of two Digital Elevation Models (DEM) with three hillslope length methods. L1 = SWAT default method based on look-up slope table; L2 = flow accumulation method, L3 = constant hillslope length.

| DEML configurations | DEM pixel size (m) | Hillslope length method | Hillslope length range (m) | Description |
|---|---|---|---|---|
| 25L1 | 25 | L1 | 9-122 | SWAT default method based on slope calculated from DEM 25 m pixel size |
| 25L2 | 25 | L2 | 20-45 | Application of LS-TOOL (Zhang et al., 2013) using a DEM 25 m pixel size |
| 25L3 | 25 | L3 | 50 | Hillslope length fixed to 50 m |
| 100L1 | 100 | L1 | 9-122 | SWAT default method based on slope calculated from DEM 25 m pixel size |
| 100L2 | 100 | L2 | 50-64 | Application of LS-TOOL (Zhang et al., 2013) using a DEM 100 m pixel size |
| 100L3 | 100 | L3 | 50 | Hillslope length fixed to 50 m |

### 3.4.2 The study area

The study area is the Upper Danube Basin, which covers about 132000 km$^2$ across Austria, Germany, Czech Republic and Slovakia, extending from the Danube source down to the Gabcikovo Reservoir near Bratislava (Figure 37). The southern part of the Upper Danube Basin includes major parts of the Alps up to the watershed in the crystalline Central Alps and then the adjoining Swabian-Bavarian-Austrian foothills belt. The northern part of the basin is significantly smaller; it is confined by the heights of the Swabian and Franconian Alb, the Upper Falconian Forest, then parts of the Bavarian–Bohemian forests down to the Austrian Mühl and Waldviertel and the Bohemian-Moravian Upland (Schiller et al., 2010). The amount of precipitation in the Upper Danube Basin shows a distinct gradient with the altitude. It rises from 650-900 mm/y in the lowland areas to more than 3,000 mm/y in the high mountain ranges exposed to the west and north (Rank et al., 2005). Major landuses within the watershed are forest (38 %) and pastures (18 %) mainly extended in Alpine regions, and cropland (34 %) in flat areas.

The study area can be divided in three main sectors: the sector upstream of Passau (about 50000 $km^2$), the Inn River Basin (about 25900 $km^2$) and the sector between Passau and the outlet near Bratislava (56100 $km^2$).

The mean annual flow rate at Passau is around 670 $m^3/s$ (35 % of the flow rate at Vienna), with a maximum in March (880 $m^3/s$) and a minimum in October (520 $m^3/s$) (Rank et al., 2005). The mean altitude of this sector is relatively low (~ 800 m) compared to the Alpine regions (~ 1300 m). Groundwater discharge is the main mechanism forming baseflow in this part of the river. The period of high water is mainly controlled by precipitation and snow melting during late winter and early spring.

The Inn, which enters the Danube at Passau, has a hydrological regime typical of Alpine rivers and exhibits a nivo–glacial regime (Sommewerk et al., 2009). The average discharge at its mouth is 732 $m^3/s$ doubling the flow rate when it merges in the Danube. Maximum flow rates are observed in June/July (1200 $m^3/s$) and a minimum in January (400 $m^3/s$). In the Inn sector elevation ranges from 310 to 3,800 m; and mean annual precipitation ranges from 600 to more than 2000 mm/y (Parajka et al., 2007; Nester et al., 2011).

The sector between Passau and Gabcikovo reservoir is characterized by the influence of other Alpine rivers, with a mean annual flow rate of about 505 $m^3/s$ (27 % of the flow rate at Vienna) and by the Morava river with a mean annual discharge of 110 $m^3/s$ (Sommewerk et al., 2009). The Alpine rivers are characterized by a hydrological regime similar to that of the Inn, with maximum flow rates in May/June (800 $m^3/s$) and a minimum in January (270 $m^3/s$) (Rank et al., 2005), while the Morava is characterized by flow peaks in early summer (March/April) (Sommewerk et al., 2009). Long-term mean annual runoff volume of the Danube at Bratislava is estimated around 64533 mil.$m^3$ in the period 1876–2006 and the mean annual discharge is 2048 $m^3/s$ (Pekárová et al., 2008).

This study area was subdivided in 753 subbasins, with an average area of 180 $km^2$, and 822 HRUs were created. The main input data are summarized in Table A1.1 in the Appendix A1.

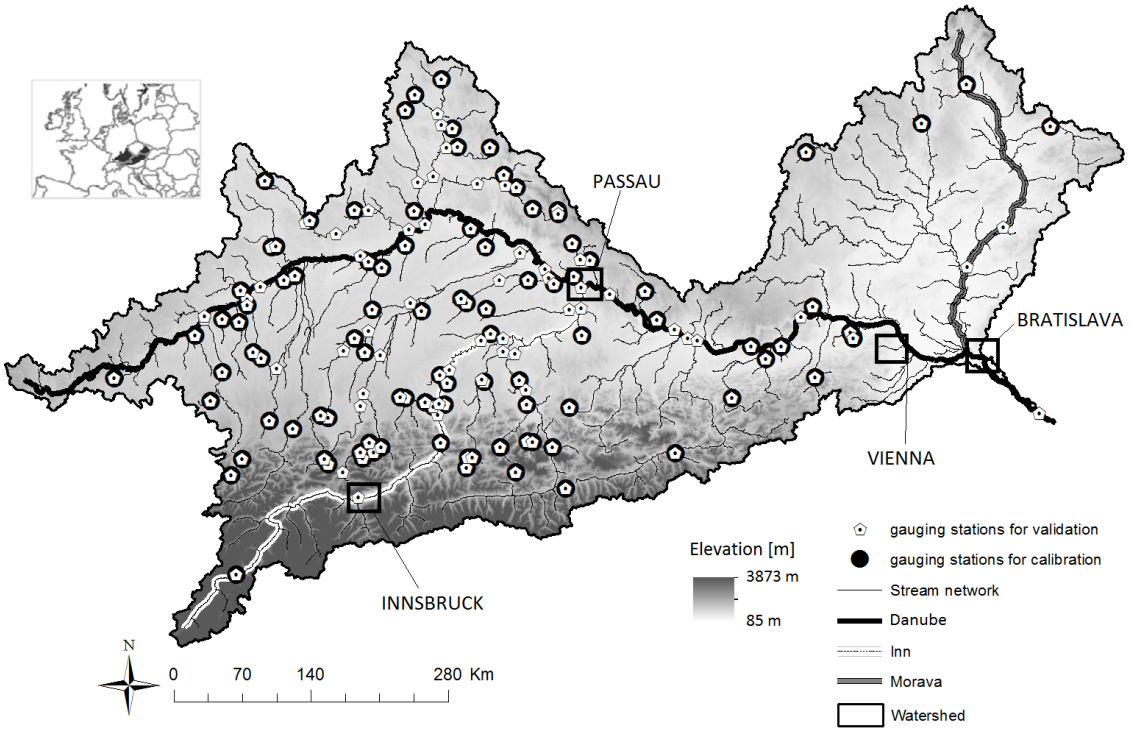


Figure 37. Overview of the Upper Danube Basin with location of gauging stations used for model calibration (#98 for period 1995-2006) and validation (#150 for period 1995-2009). The monitoring stations for calibration were included in the monitoring stations used for validation extended the period of simulation from year 2006 to 2009. The background in scale of grey colors indicates the elevation (meters) from DEM100. Danube River and two of its main tributaries (Inn and Morava) are highlighted. The main towns are shown as well. The symbol # represents the number of stations.

### 3.4.3 DEM derivatives of the six DEML configurations

Differences in mean elevation, slope gradient, and hillslope length of the six DEML configurations are presented in Figure 38. The two DEMs did not produce significant differences in the mean altitude of subbasins (Figure 38 a), but produced small differences in slope (Figure 38 b). The DEM100 resulted in lower slopes than the DEM25 confirming the results of other studies (e.g. Chaplot et al., 2005; Lin et al., 2013). The hillslope length L1 (25L1 and 100L1, Figure 38c) increased step-wise until 122 m with decreasing slope. L2 markedly changed from the finest to the coarsest DEM. In the 25L2 configuration, hillslope length was around 30 m whereas in 100L2 it was around 60 m, with no clear relationship with slope gradient. Hence, the coarser DEM resulted in lower slopes and longer hillslope lengths (Lin et al., 2013). It is noteworthy that the constant hillslope length of 50 m (L3) was in between of 25L2 and 100L2 hillslope lengths. Furthermore, the distribution of hillslope length (Figure 38 d) showed that L1 was also strongly correlated elevation. In the southern part of Upper Danube, in the Alps, at elevation higher than 2000 m, slopes were steep (50-70%), consequently L1 were shorter (9-20 m) than in other parts of the Basin. Conversely, in L2 and L3 configurations hillslope length was not correlated with elevation or slope.

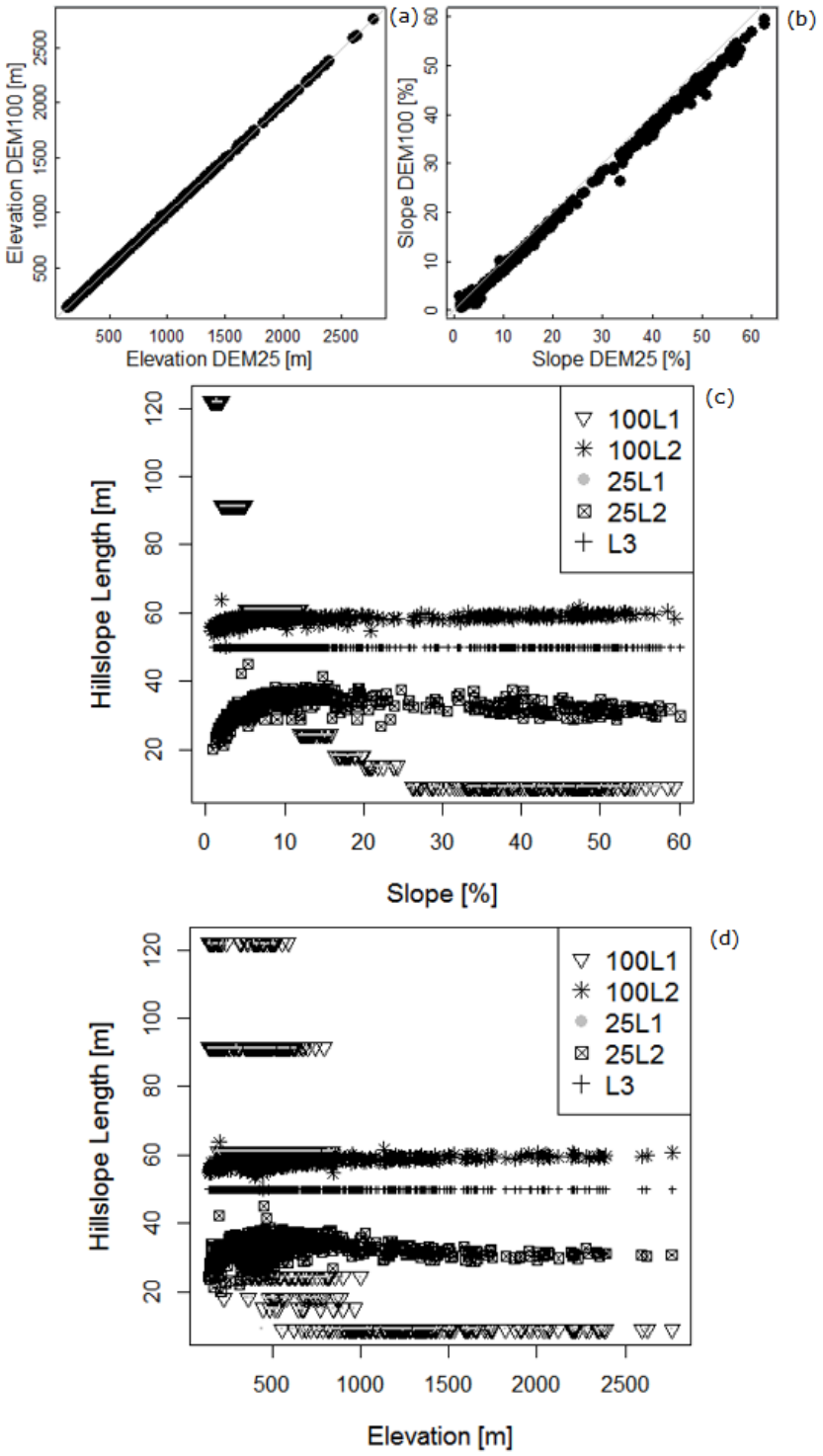


Figure 38. Subbasin main DEM derivatives in the SWAT configurations. (a) Elevation (m) in the 100 m DEM pixel size (DEM100) in relation to 25 m DEM pixel size (DEM25); (b) slope (%) in the DEM100 in relation to DEM25; hillslope length (m) of the DEM configurations of Table 7 in relation to slope (%) (c) and elevation (m) (d).

### 3.4.4 Results of model calibration and validation

The calibration of monthly streamflow yielded satisfactory PBIAS (PBIAS in the range of +/- 25) in more than 50% of calibration headwaters in all DEML configurations (Table 8). The configurations 25L2 and 25L3 reached 61% and 62% respectively of calibrated gauged stations with satisfactory PBIAS, followed by 100L2 and 100L3 with 59%, while 25L1 and 100L1 reached the lowest percentage (56% and 57% respectively).

Table 8. Summary of calibration and validation of monthly streamflow simulations in the Upper Danube Basin for each DEML configuration.

| C/V | Description | 25L1 | 25L2 | 25L3 | 100L1 | 100L2 | 100L3 |
|---|---|---|---|---|---|---|---|
| Calibration (1995-2006; #98 gauged stations) | Percentage of gauged stations with satisfactory PBIAS[1] (%) | 56 | 61 | 62 | 57 | 59 | 59 |
| | Median PBIAS (%) for satisfactory stations | 0 | -2.05 | -3.6 | -3.9 | -2.35 | -3.4 |
| | Percentage of gauged stations with satisfactory NSE[2] (%) | 31 | 32 | 32 | 31 | 32 | 31 |
| | Median of NSE of satisfactory stations | 0.68 | 0.67 | 0.67 | 0.66 | 0.66 | 0.69 |
| Validation (1995-2009; #150 gauged stations) | Percentage of gauged stations with satisfactory PBIAS[1] (%) | 70 | 73 | 72 | 72 | 72 | 71 |
| | Median PBIAS (%) for satisfactory stations | -0.1 | -1.7 | -3.75 | -2.6 | -2.1 | -3.3 |
| | Percentage of gauged stations with satisfactory NSE[2] (%) | 42 | 45 | 45 | 37 | 44 | 44 |
| | Median of NSE of satisfactory stations | 0.64 | 0.67 | 0.68 | 0.67 | 0.67 | 0.69 |

[1] model simulation can be judged as satisfactory if PBIAS +- 25% for monthly streamflow (Moriasi et al., 2007)

[2] model simulation can be judged as satisfactory if NSE >0.5 for monthly streamflow (Moriasi et al., 2007)

The median of PBIAS for the satisfactory gauged stations was in the range of -4%; -2% for all configurations, indicating a negligible underestimation of streamflow, except for 25L1 for which no bias was observed. NSE was satisfactory (NSE >0.5) in 30% of cases, however the median of NSE of these 30% calibrated station was close to 0.7.

The performances of monthly streamflow for the 150 validation gauged stations were better than for the calibration dataset. More than 70% of validation gauged stations reached satisfactory PBIAS in each configuration, and around 40% of the stations had NSE > 0.5

(Table 8). The highest number of subbasins with satisfactory streamflow predictions were obtained for 25L2 (73% of gauged subbasins with median PBIAS of -1.7% and 45% of gauged subbasins with median NSE close to 0.7) followed by 25L3 and 100L2, while 25L1 had the lowest numbers, but with the median PBIAS close to 0.

The analysis of monthly percentage residuals ([simulation-observation]/observation) confirmed that all configurations provide good simulations of streamflow with median residual values close to 8% in the calibration (Figure 39 a) dataset and absence of residuals for 50th percentile of gauging stations in the validation dataset (Figure 39 b). The interquartile range of monthly residuals for all configurations was within the interval -30% ~ 60% in the calibration dataset, indicating a slight tendency to overestimation of streamflow. The interquartile ranges were smaller, in the interval -30% ~ 40% in the validation dataset, for which the distribution of residuals was broadly symmetric around zero.

Spearman's rank correlation coefficients of the monthly streamflow residuals among the six configurations were all larger than 0.9, indicating that streamflow of DEML configurations were highly correlated. The lowest correlation was found between the configurations 100L1 and 25L3 (~0.93) and 100L1 and 100L3 (~0.93) in the calibration dataset, and between the configurations 25L1 and 100L3 (~0.91) and 25L1 and 25L3 (~0.93) in the validation one. These findings reflect the differences in the distributions of hillslope length L1 and L3. However, generally DEM pixel size and the hillslope length had a negligible impact on streamflow predictions and the spatial distribution of streamflow PBIAS showed no evident spatial pattern (e.g. Figure 40 for configuration 25L2).

Generally, low performances were associated with reaches where the hydrology was strongly influenced by human activities, in particular by diversion and regulation of streamflow, which were not accounted in SWAT, and are wide spread present in the study area. Mostly, barrages are built as cascades along river courses and more than 33 barrages are located along the Danube until Vienna, on the tributary rivers Iller, Lech, Isar, Inn, Salzach, and Enns. Additionally, there are a lot of deviations, diversions and intakes (Shiller et al., 2010).

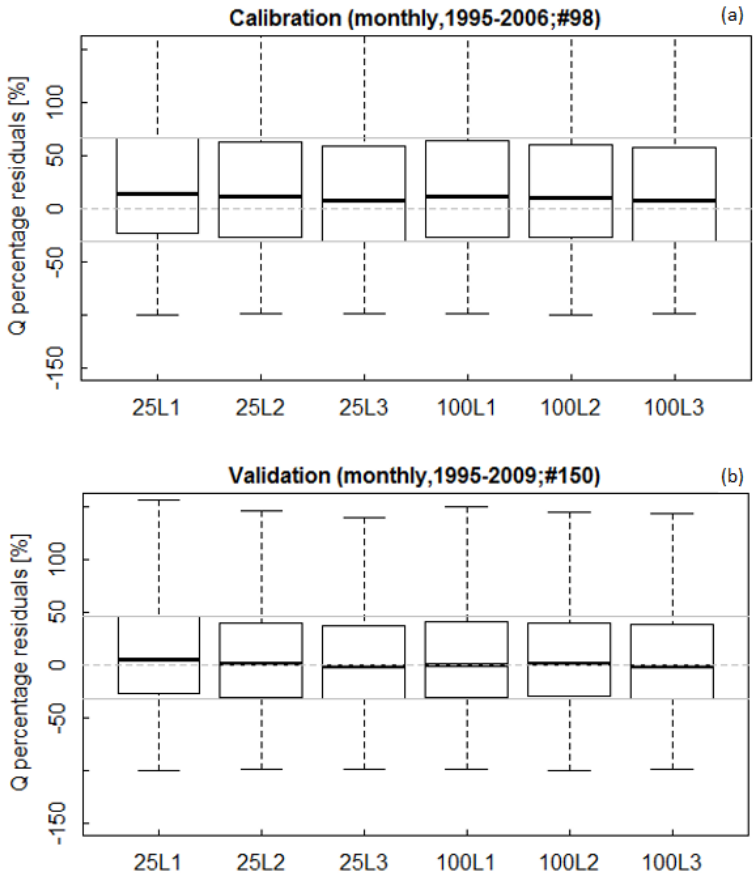


Figure 39. Box-and-whisker plots of percentage residuals between simulated and observed streamflow of the six DEML configurations analyzed in this study (see Table 7) for the calibration (a) and validation (b) dataset. The symbol # represents the number of stations in the calibration and validation datasets. The continuous grey lines indicate the maximum 75% and 25% across the six DEML configurations; the dashed grey line represents the absence of residuals.

Figure 41 and Figure 42 show the monthly time-series of SWAT simulations versus observations for two validation dataset stations, at the outlet of the Inn River and at the outlet of the entire Upper Danube basin, after the Gabcikovo reservoirs (locations are indicated in Figure 40). Although some discrepancies could be detected, visual appraisal of the time-series indicates good correlation between streamflow simulations and observations.

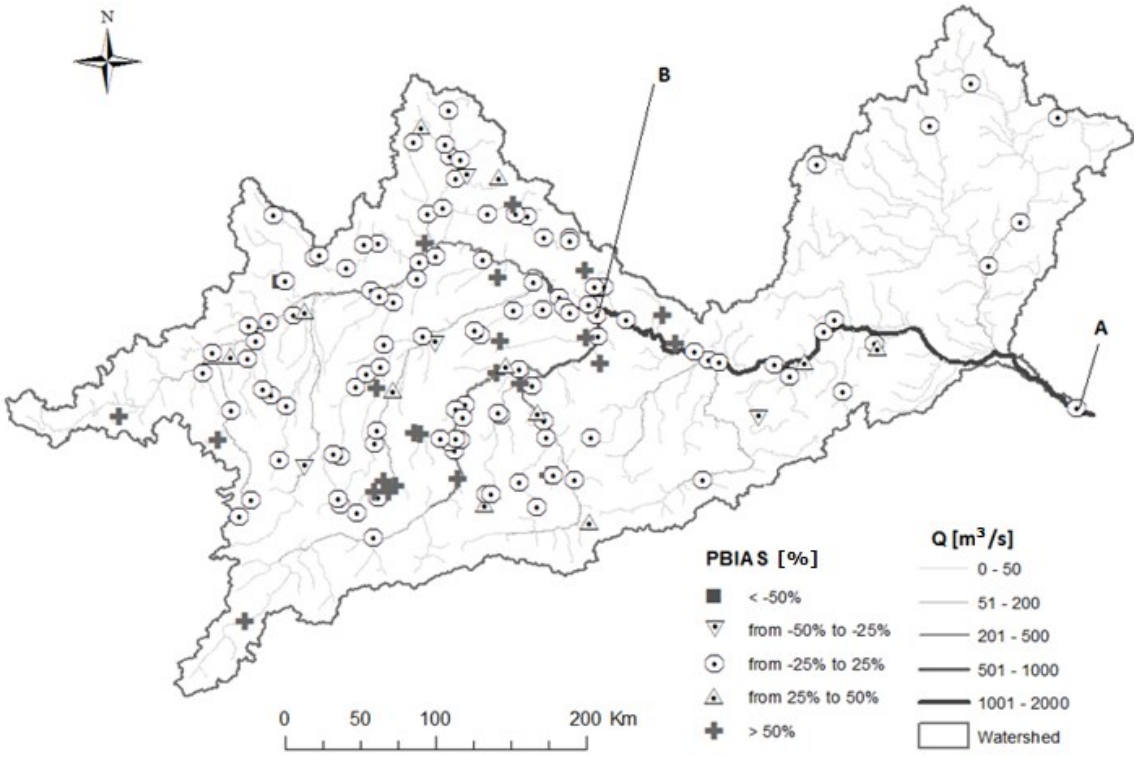


Figure 40. Percent bias (PBIAS) of monthly streamflow of configuration 25L2 at the 150 gauging stations (1995-2009). The letters A–B indicate the location of two stations for which time-series simulations are provided in Figure 41 and Figure 42.

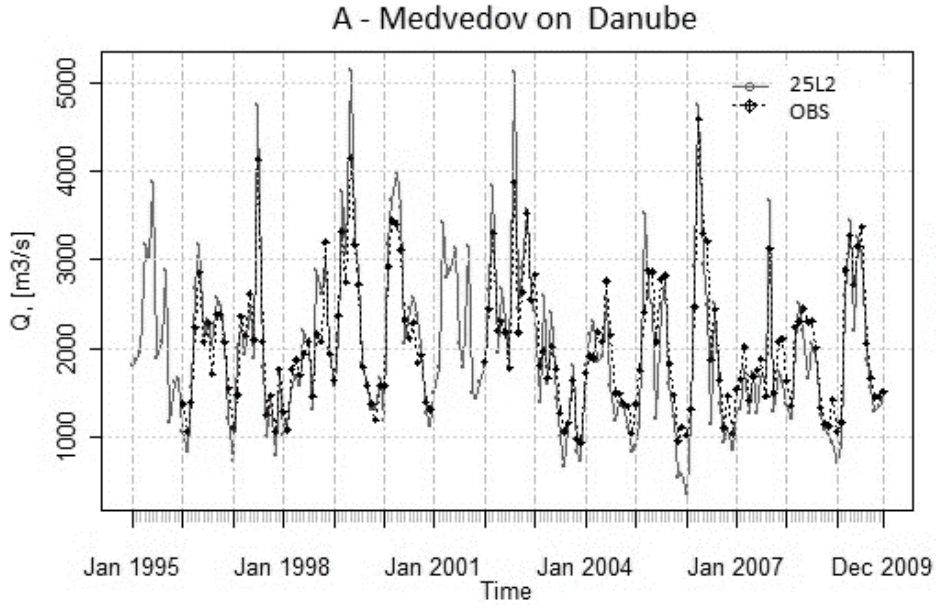


Figure 41 Comparison of SWAT outputs for 25L2 (grey lines) with observations (black lines) at two selected monitoring gauging stations (locations A shown in Figure 40). A: outlet of Upper Danube Basin at Medvedov (Slovakia) on Danube river.

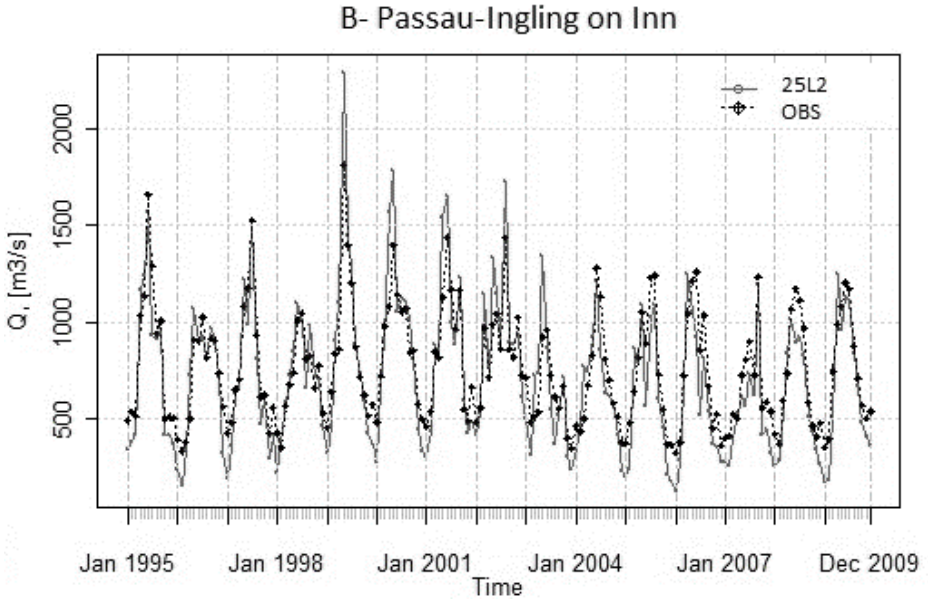


Figure 42. Comparison of SWAT outputs for 25L2 (grey lines) with observations (black lines) at two selected monitoring gauging stations (locations B shown in Figure 40). B: Inn river at Passau-Ingling (Germany).

### 3.4.5 Analysis of behavioral parameter sets

Figure 43 shows the distributions of NOP sets of donors for each configuration and indicates the hydrological processes upon which they were calibrated in the step-wise calibration (snow processes, step [1]; surface runoff, step [2]; lateral flow, step [3]; and baseflow, step [4]).

For the snow process parameters (parameters identified with [1] in Figure 43), all DEML configurations were quite similar, except for the snowfall (SMTMP, °C), the snowmelt temperatures (SFTMP, °C) and the precipitation lapse rate (PLAPS). SFTMP and SMTMP were generally lower and had a larger range in 25L2 (with a median around -0.3° C for SFTMP and 1.3 ° C for SMTMP). The highest median value for SFTMP and SMTMP were obtained for 25L3 with 0.63 °C and 2 °C respectively. The snow pack temperature lag factor (TIMP, adimensional) was slightly different across the six configurations, with minimum median values of 0.24 (100L1) and maximum of 0.43 (25L2). The temperature lapse rate (TLAPS, °C) was used to adjust temperature for elevations band in each subbasin; in all DEML configurations the median TLAPS was around -5°C indicating a decrease of temperature around 5°C with a 1 km increment of elevation. The increment of precipitation per km of elevation (PLAPS, mm/km) was higher for configuration 25L2 and 100L1 (around 65 mm/km of median value) than the others (around 50 mm/km of median value). The median initial snow content (SNOEB) in each elevation band ranged between 112 mm for configurations 100L1 and 160 mm for 100L2.

The surface runoff parameters (parameters identified with [2] in Figure 43) did not greatly differ among the DEML configurations. However, CN2 adjustment (rate value) had a larger range in 100L1 with a median relative increase of 12%, whereas in the other configurations CN2 increase was around 14%. The median of CH N1 slightly increased from L1 to L3 both for DEM25 (from 0.11 to 0.13), while for DEM100 is about 0.12. The melt factor for snow on December (SMFMN) was more sensitive than the melt factor on June (SMFMX) and configuration 100L1 and 25L2 had the highest and lowest median of 4.7 and 2.9 respectively. It is noteworthy that these parameters regulate the melt factor at daily time step, so should belong to snow processes group. However, their effect is to change the position in time of runoff hydrograph, so they were included in the "surface runoff step of step-wise calibration" (see Malagò et al., 2015) because that is the phase where runoff hydrograph is calibrated at daily time step.

In the calibration of lateral flow (see the parameters identified with [3] in Figure 43), the soil plant compensation factor (EPCO) and soil evaporation compensation factor (ESCO) had different ranges between the model configurations, implying differences in the water balance yield component estimations. The EPCO regulates water uptake by plants and it is a function of water required by plant transpiration and the amount of available water. If the upper layers in the soil profile do not contain enough water to meet the potential water uptake, an increase in the EPCO parameter allows water uptake to occur from the lower soil layers. EPCO values were higher in 25L2 with median values around 0.5, while for the others the median values were below 0.5, allowing less water uptake from the lower soil layers. The ESCO parameter represents the influence of capillarity on soil evaporation in each soil layer; it ranges between 0.01 and 1. When ESCO is low, the model extracts more water from lower soil layers to meet the evaporative demand. The configurations 25L2, 100L1 and 100L3 had median values around 0.4 and maximum interquartile between 0.26 and 0.5. Instead, 100L2 and 25L3 had respectively the smallest (0.2) and highest median value (0.6). The available water capacity (SOL AWC) adjustment (rate value) was lower for 25L1 and 100L1 (median value around 0.1) than other configurations (median values from 0.15 to 0.2), indicating the necessity for other configurations to increase of about 15-20% the water capacity in soil layers. The saturated hydraulic conductivity (SOL K) required the same adjustment of about 25% in all configurations, excepted for 100L1 that required 20% of increment.

Among the groundwater parameters (see the parameters identified with [4] in Figure 43), the recharge of deep aquifer (RCHRG DP) had the highest median value of around 0.18 for configurations 100L1, 100L2, 100L3 and 25L3, while 25L1 and 25L2 had the smallest median values (around 0.10) and interquartile. In addition, the median of the threshold depth of water in the shallow aquifer (GWQMN, mm H2O) increased from L1 to L3 (both DEM

pixel size) from approximately 500 mm to 600 mm, as well as the groundwater revap coefficient (GW REVAP) from 0.07 to 1 for DEM25. In addition, the median of the threshold depth of water in the shallow aquifer for revap was the highest for 100L1 (343 mm).

The baseflow alpha factor (ALPHA BF) values were very similar in each configuration, with median values around 0.75 indicating a rapid hydrological response of the subbasins. About the groundwater delay parameter (GW DELAY, days), 100L1 reached the lowest median value of about 27 days followed by 25L2, 100L2 and 100L3, while 25L1 and 25L3 reached the highest median values of 43 and 48 days respectively.

It may thus be concluded that the calibrated parameters were able to reflect the behaviour of the subbasins changing the DEML configurations. In particular, quite different parameter values were obtained between the configurations during the adjustment of lateral flow (i.e. SOL AWC and ESCO) and baseflow processes (i.e. RCHRG DP, GWQMN and GW REVAP) indicating that the DEML configurations may have a markedly impact on the prediction of the related streamflow components.

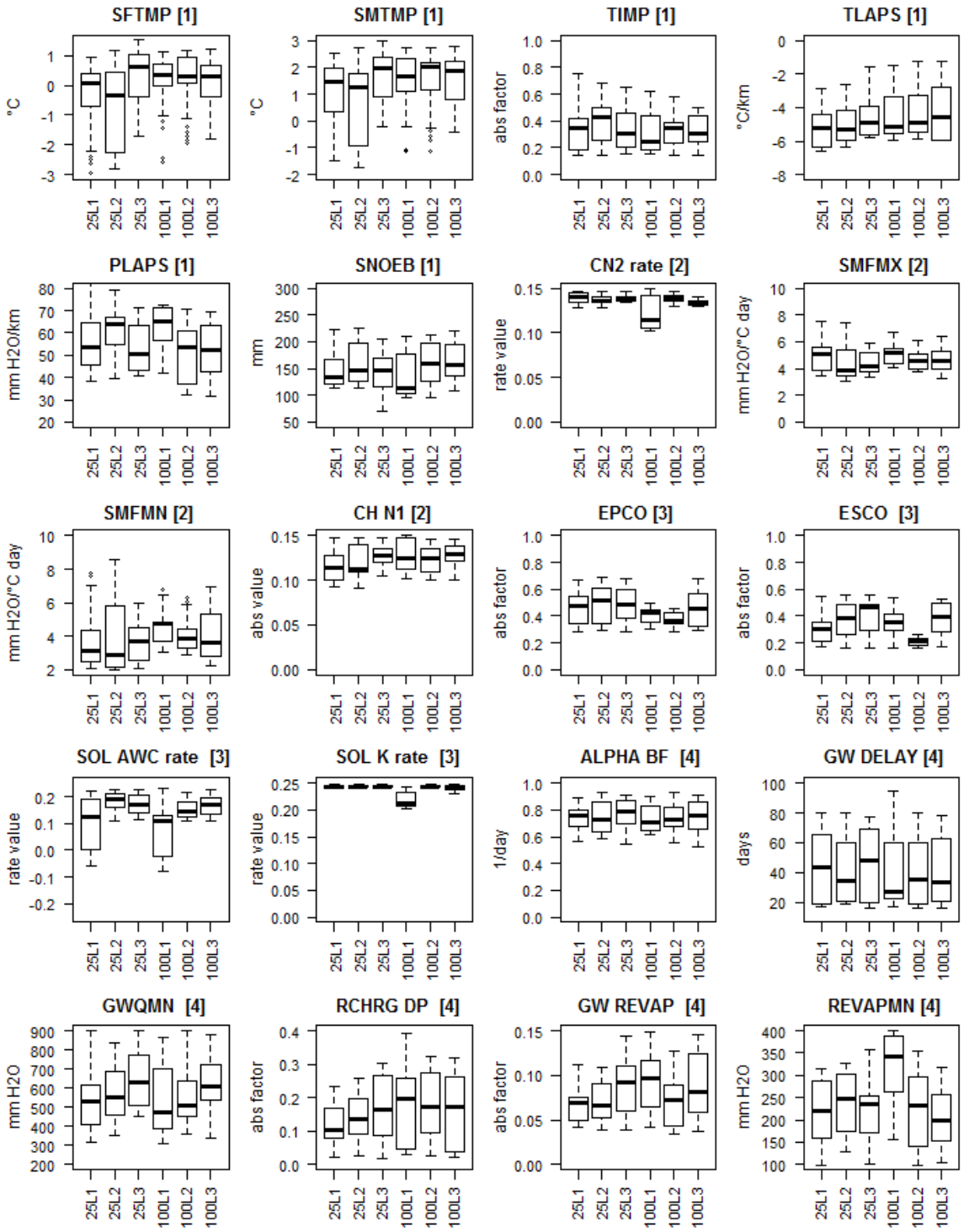


Figure 43. Box-and-whisker plots of behavioral Near Optimal Parameter sets from “donors” subbasins. The numbers in the square brackets indicate the step-wise hydrological process of calibration: [1] snow process, [2] surface runoff, [3] lateral flow, and [4] baseflow. The “abs value/factor” represents the absolute value for adimensional parameter; “rate value” represents the increment/decrement for which the absolute value is increased (positive rate) or decreased (negative rate).

### 3.4.6 Impact of hillslope length on streamflow components

While the impact of hillslope length on the total streamflow predictions appeares negligible, the analysis of streamflow components reveales some differences between DEML configurations as illustrated in Figure 44. The Figure 44 shows the comparisons between monthly simulated and observed surface runoff, SR, (Figure 44a), lateral flow, LF, (Figure 44b) and baseflow, BF, (Figure 44c) for the 98 calibrated gauging stations in the period 1995-2006 (see Table 8), that were considered more representative of the natural hydrological behavior.

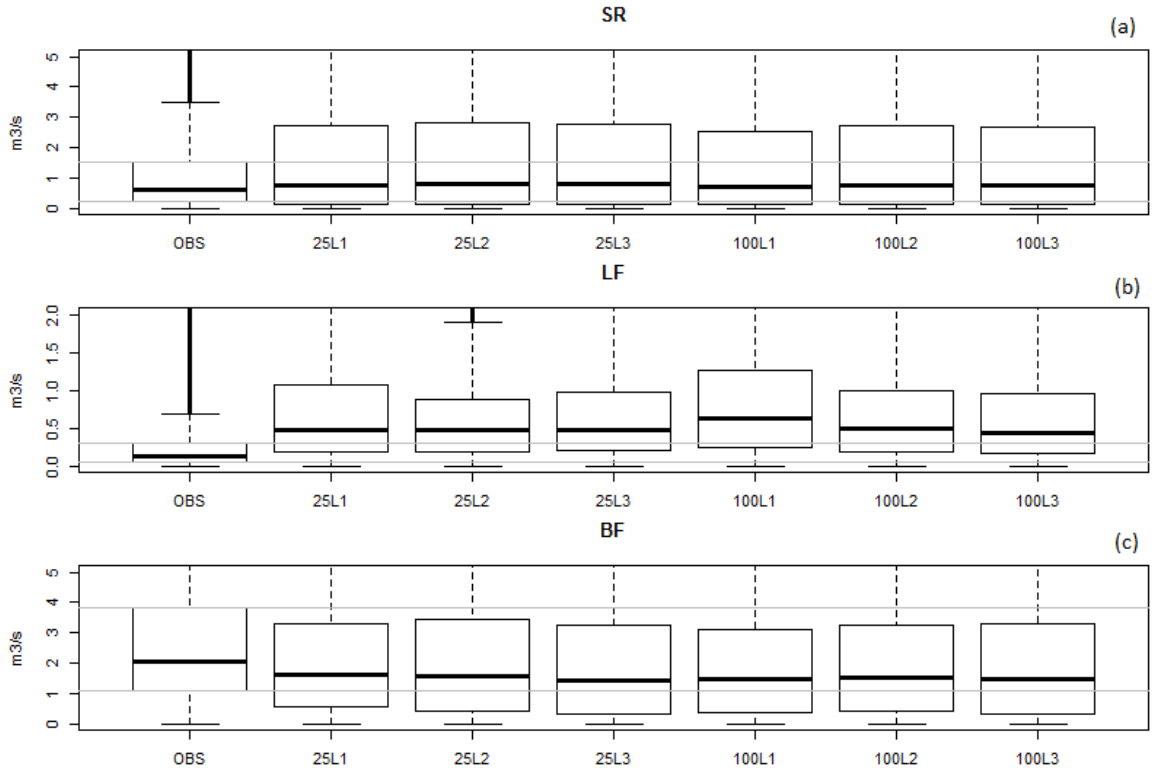


Figure 44. Box-and-whisker plots of simulated and observed streamflow surface runoff (SR), lateral flow (LF) and baseflow (BF) for calibrated monitoring points (#98; period 1995-2006). The continuous grey lines indicate the 75% and 25% of observations. Note the varying ranges of the y axis.

The interquartile of monthly SR ranged from 0.12 to 2.8 $m^3/s$ for all configurations (Figure 44a), with median values around 0.75 $m^3/s$ that fell on the observed interquartile (0.24-1.54 $m^3/s$). Spearman's rank correlation coefficients of the SR monthly residuals (simulation–observation) were all very high ($\rho>0.97$). These findings indicate that all DEML configurations simulated monthly SR well and in very similar way, thus the impact of DEM pixel size and hillslope length was negligible.

The interquartile range of lateral flow was overestimated in all configurations (maximum interquartile range from 0.17 to 1.3 $m^3/s$) compared to the observations (between 0.05-0.3 $m^3/s$) (Figure 44b). In particular, the median LF ranged from 0.44 $m^3/s$ (100L3) to 0.62 $m^3/s$

(100L1), while the median of observation was around 0.13 $m^3/s$. The Spearman's rank correlation coefficients ρ between LF monthly residuals of lateral flow of the calibration dataset (Table 9) reveal that configurations 100L2 and 25L3 are highly correlated (ρ=0.96), as well as 25L2-25L3 and 100L2-100L3 reflecting that L3 resulted in lateral flow values similar to L2 method. Conversely, configurations 100L1-100L2 and 100L1-25L3 had the lowest ρ coefficients, around 0.40, followed by 100L1-25L2 (ρ=0.54) and 100L1-100L3 (ρ=0.60), reflecting the differences in hillslope length distributions. Furthermore, the configurations 25L3, 25L1 and 25L2 were strongly correlated to 100L3, 100L1 and 100L2 respectively, indicating that the DEM pixel size didn't affect the lateral flow estimations.

Table 9. Spearman's rank correlation coefficient ρ between the monthly residuals of lateral flow (LF, $m^3/s$) of DEML configurations for the calibrated dataset (#98 gauged stations, 1995-2006).

| | 25L1 | 25L2 | 25L3 | 100L1 | 100L2 | 100L3 |
|---|---|---|---|---|---|---|
| 25L1 | 1 | | | | | |
| 25L2 | 0.79 | 1 | | | | |
| 25L3 | 0.66 | 0.93 | 1 | | | |
| 100L1 | 0.86 | 0.54 | 0.42 | 1 | | |
| 100L2 | 0.64 | 0.91 | 0.96 | 0.41 | 1 | |
| 100L3 | 0.68 | 0.86 | 0.90 | 0.60 | 0.90 | 1 |

The maximum interquartile range of baseflow was between 0.3 and 3.5 $m^3/s$ with a median around 1.5 $m^3/s$, slightly lower the median of observation (around 2 $m^3/s$).

Spearman's rank correlation coefficients ρ of BF residuals were all very high (ρ>0.9), indicating, as for surface runoff, DEM pixel size and hillslope length had negligible impact of baseflow estimation.

While the method used to subdivide the streamflow into its components introduced a certain degree of uncertainty (Huyck et al., 2005), an explanation of LF overestimation and its sensitivity to hillslope length can be found in SWAT equations ([eq. 6] and [eq. 7]). The assumption that $\sin(\alpha_{hill})\sim\tan(\alpha_{hill})$ is not valid in steep slopes for which the difference between tangent and sine is not negligible (Bieger et al., 2015). As a consequence, at steep slopes lateral flow resulted overestimated. The overestimation of LF means an underestimation of the amount of soil water that is available for percolation to the groundwater (Bieger et al., 2015), thus leads to the underestimation of baseflow. Figure 44c shows that configuration 100L1 produced the highest overestimation of lateral flow (median of value around 0.62 $m^3/s$) that corresponded to a larger underestimation of baseflow compared to other configurations (median around 1.4 $m^3/s$, Figure 44b), confirming this mechanism.

In addition, it was observed that the lateral flow monthly residuals increased with the elevation as showed in Figure 45. This figure shows the monthly residuals for three classes of elevation: from 0 to 500 m, from 500 to 1000 m and over 1000 m. In the class of the highest elevation, 25L1 and 100L1 reached the highest residuals (median values of around 0.7 $m^3/s$), indicating that the SWAT default configuration (both with finer and courser DEM) was not able to reproduce correctly the lateral flow in mountainous and steep subbasins.

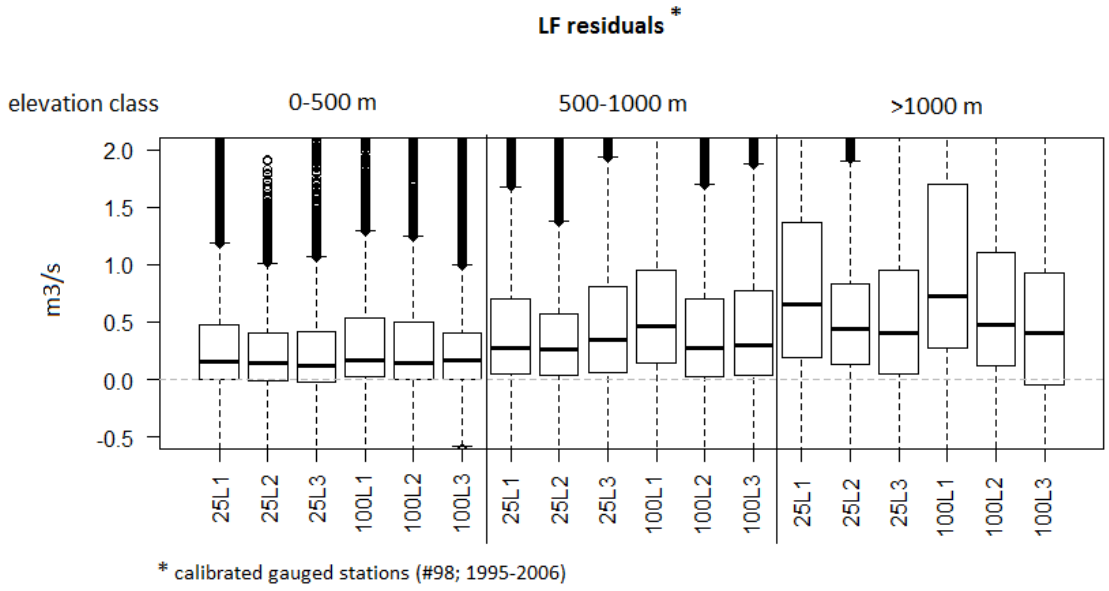


Figure 45. Box-and-whisker plots of residuals between simulated and observed lateral flow (LF) for calibrated monitoring points (#98; period 1995-2006) with respect to three classes of elevations: 0-500 m (#28 monitoring points), 500-1000 m (#48 monitoring points) and >1000 m (#22 monitoring points).

### 3.4.7 Impact of hillslope length on water yield predictions at different spatial and temporal scales

Figure 46 shows the impact of DEML configurations on the HRU water yield and its components (in mm) at annual and monthly time scale as mean during the simulation period (1995-2009) compared to the related interquartile of 98 calibrated stations for the same period.

Mean annual and monthly HRU surface runoff (SR) was very similar across all configurations (Figure 46 a and b), confirming that DEM pixel size and hillslope length did not impact the generation of surface runoff, nor the time of concentration (hr) or peak runoff rate ($m^3/s$). The median of time concentration was around 10 hours and the median of peak runoff rate was approximately 20 $m^3/s$ in all configurations. These results concur to Jarihani et al. (2015) findings on the impact of DEM-pixel size on hydrodynamic model, which demonstrated that the peak runoff rate did not change at DEM pixel size ranging from 30 m to 250 m and that the time of concentration did not change until a pixel size of 120 m.

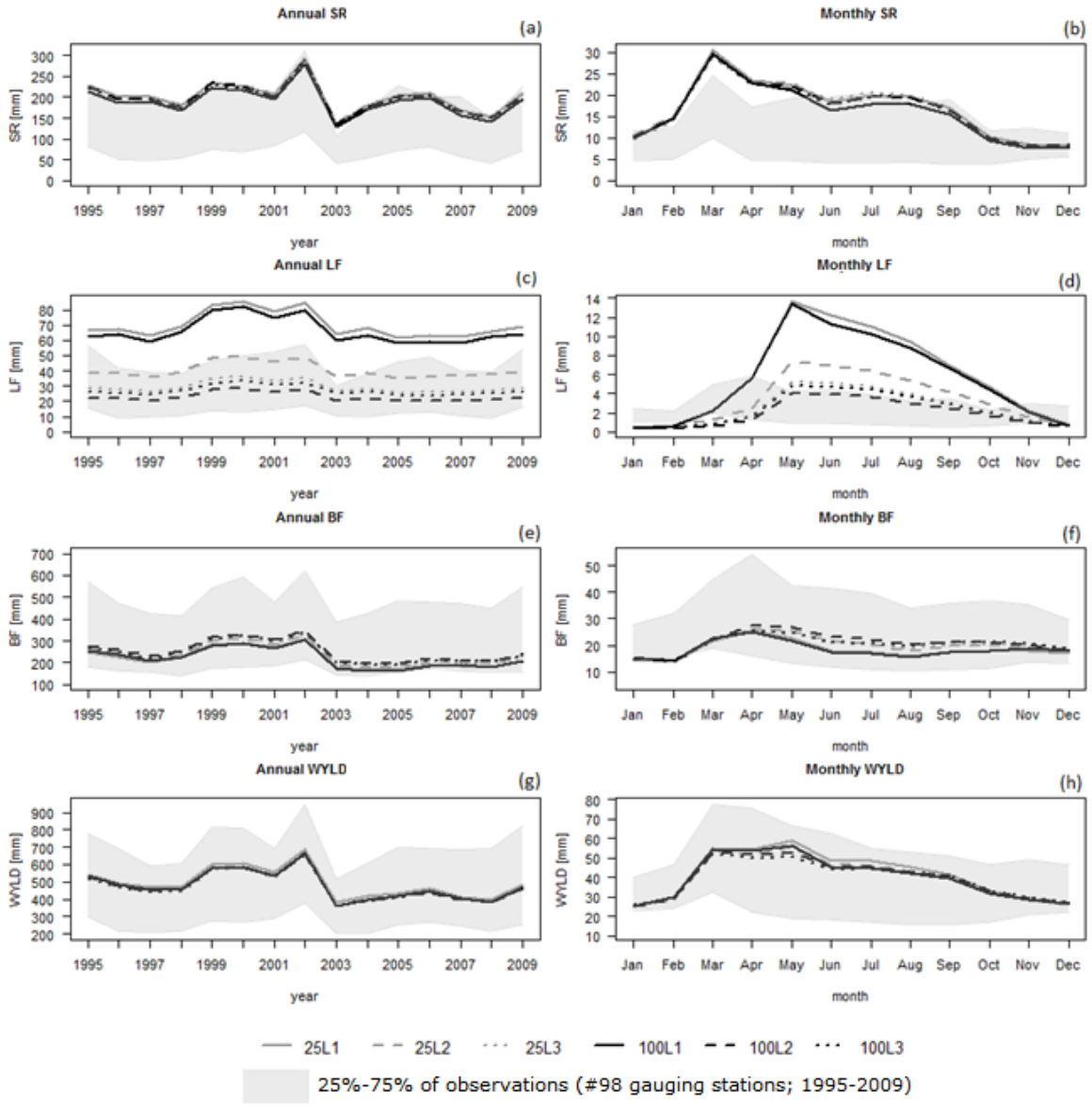


Figure 46. Long-term mean annual (a, c, e, g) and monthly (b, d, f, g) surface runoff (SR), lateral flow (LF), baseflow (BF) and water yield (WYLD, all in mm) generated in all 822 HRUs in the six DEML configurations (see Table 7) for the period 1995-2009. The grey band represents the interquartile of observed gauging stations from calibration dataset extended the period to 2009. Note the varying ranges of the y axis.

However, the long-term annual and monthly mean of SR were close to the 75th percentile of observations, highlighting a slightly long-term overestimation of observations.

Differences in HRU lateral flow (LF) and baseflow (BF) (Figure 46c, d, e, f) confirmed the sensitivity of LF to hillslope length due to [eq. 6] and [eq. 7], as well as its linked impact on BF already observed with the streamflow analysis. The configurations 25L1 and 100L1 produced the highest values of lateral flow, in the range of 60 ~ 85 mm/y dropping out to the interquartile of observations (from 9 mm in 2008 to 57 mm in 2002), while 100L2, 100L3 and 25L3 were within the observed range (Figure 46c).

The peak of mean monthly LF was observed in May; configurations 25L1 and 100L1 reached the maximum value of 13 mm/month followed by 25L2 with about 7 mm/month and then the other configurations with values in the range of 4-5 mm/month (Figure 46d).

For BF the impact of DEML configurations was the opposite than for LF, with configuration 100L2 generating the highest baseflow, from 194 mm/y (year 2004) to 344 mm/y (year 2002), while 100L1 generated the lowest, from 160 mm/y (year 2004) and 306 mm/y (year 2002; Figure 46e). The largest differences in monthly baseflow were from April to November, and the maximum difference between 100L1 and 100L2, about 5 mm/month, was observed in May (Figure 46f).

Mean annual and monthly water yields (WYLD, Figure 46g, h) didn't show remarkable differences between DEML configurations, except for 25L1, which resulted in the highest monthly water yield, particularly for the period March-September (Figure 46h). Figure 46 shows also that BF and WYLD were within the observed interquartile in all configurations both for annual and monthly time step.

### 3.4.8 Impact of hillslope length on water balance

Figure 47a, c and e show the influence of DEML configurations on the proportions of evapotranspiration (ET) and water yield (WYLD), while the proportions of water yield components (surface runoff, lateral flow and baseflow) are shown in Figure 47b, d and f.

The analysis was limited to the whole Upper Danube and two selected main tributaries with comparable drain area, the Morava and Inn River Basins that however differ in elevation, slopes, climate, and land cover. The Inn River Basin (25920 $km^2$) is characterized by a mean elevation of 1300 m, mean of precipitation of 1200 mm, median slope of 27% and the forest covers more than 50% of total area. Instead, the Morava (26628 $km^2$) River Basin is characterized by a mean elevation of 380 m, precipitation around 600 mm, negligible slope (mean value of 5%), and the cropland is dominant covering more than 60% of total area.

The impact of DEML configurations on ET and WYLD was negligible. This is not surprising considering that the same HRUs were kept in all DEML configurations, therefore interception, infiltration and surface runoff generation were not affected by the configuration. ET in the Upper Danube the ET was 50% of total precipitation (Figure 47a), while in the Morava it was about 80% of total precipitation (Figure 47c), and in the Inn river only about 30% (Figure 47e).

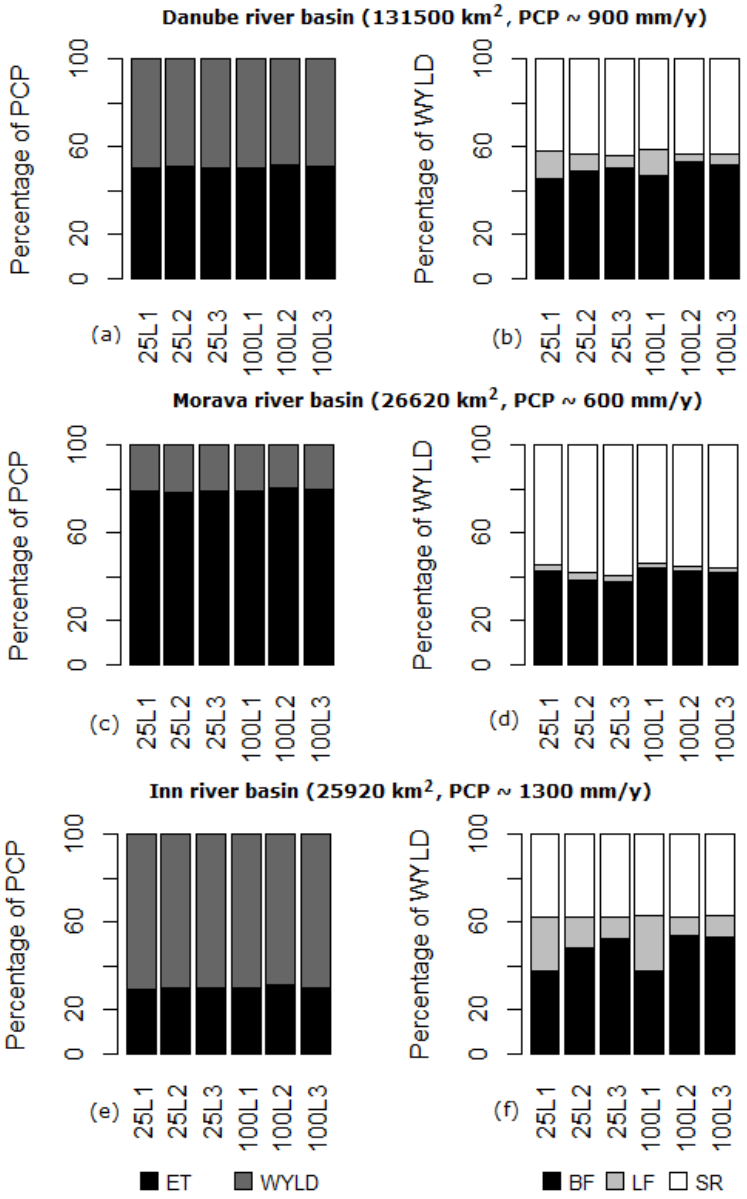


Figure 47. Bar plots of mean annual water balance partitioning. In (a, c, e) water balance components: evapotranspiration (ET, %) and water yield (WYLD, %) (PCP is the total precipitation as sum of ET and WYLD). In (b, d, f) water yield components: surface runoff (SR, %), lateral flow (LF, %) and baseflow.

Instead, some differences between the DEML configurations could be observed in the components of the water yields (Figure 47b, d, f), namely in the partitioning between lateral flow and baseflow, whereas surface runoff was very similar across configurations in all instances. For the whole Upper Danube (Figure 47b), the surface runoff was approximately 42% of total WYLD, while the lateral flow varied from 4% for 100L2 to 12% for 100L1. Baseflow volumes were higher where lateral flow volumes were lower, and varied from 46% (100L1) to 53% (100L2) of total WYLD. Differences in lateral flow and baseflow were even more noticeable in the Inn (~29920 km$^2$, Figure 47 d). In the Inn, the surface runoff was around 37% of total WYLD, and the lateral flow changed from 8% of 100L2 to 25% 100L1

and 25L1. Again, the baseflow were higher where the lateral flow was lower approximately 38% for configurations 25L1 and 100L1, while it was 54% for 100L2.

It is noteworthy that the highest lateral flow of 25L1 and 100L1 corresponds to very low values of hillslope length (median value approximately 15 m) in mountainous and steeper subbasins. Instead, at increasing values of hillslope length, lateral flow tended to decrease. Even in the Morava River Basin, where lateral flow was small due to the high evapotranspiration and the small water yield, differences in LF and the impact of hillslope length could still be detected. The median hillslope length was 60 m for configuration 25L1, 100L1 and 100L2, and the lateral flow was respectively 2.7%, 3.3% and 1.7% of total water yield. In 25L2, the median hillslope length was around 30 m, and lateral flow was higher, about 3.5%. However, these differences were negligible.

### 3.4.9 The recommended DEML configurations

The analysis indicated that the streamflow was well predicted in all DEML configurations, thus both DEMs and the three hillslope length methods could be valid (Figure 39). This confirms findings reported in other studies (i.e. Chaplot, 2005; Lin et al., 2010; Zhang et al, 2014) that focused mainly on DEM pixel size. However, the analysis of streamflow and water yield components revealed differences between the configurations affecting SWAT simulation of the hydrological processes.

Surface runoff was well simulated in all DEML configurations (Figure 44a), albeit there was a tendency of overestimation for all DEML configurations (Figure 46a, b). The generated surface runoff was unaffected by changes in DEM, hillslope length, or the simulation of lateral flow. An increase of lateral flow should lead to a larger amount of surface runoff due to higher soil water content in the footslopes, but SWAT cannot account for this. The adjustment of the Curve Number (CN) in steep slopes as pointed out for instance by Huang et al. (2006) and Bieger et al. (2015) could partly account for this, and would be recommended. As a consequence, in the surface runoff estimations the DEML configuration had a secondary role compared to the uncertainty of the model structure such as the model inaccuracy due to over-simplification of the processes considered in the model (Wagener and Gupta, 2005; Liu and Gupta, 2007; Clark et al., 2008).

Instead, DEML configurations impacted lateral flow simulation, which uses hillslope length and slope ([eq. 6]). When the hillslope length increases, the lateral flow decreases. Thus in steep areas, where hillslope length is the lowest when using SWAT default method, configurations 25L1 and 100L1 produced the highest lateral flow, followed by 25L2. Conversely, in flat areas, the differences between the configurations were negligible. This could be observed at HRU scale: for instance, the highest lateral flow was observed in forest

and pastures HRUs of the Alpine areas, while in the flatter cropland lateral flows was low. The same could be observed at basin level: in the Inn River Basin, characterized by high elevation, steep slopes, high precipitation, the lateral flow ranged 8% for 100L2 to around the 25% for 25L1 and 100L1 (Figure 47).

The high lateral flow estimations in mountainous areas in the 100L1 and 25L1 appear to be excessive (Figure 45). Indeed, all DEML configurations overestimated lateral flow in the calibrated headwaters (Figure 44b), due to approximation of the sine of the slope with its tangent in [eq. 7], which affected lateral flow estimation in steep slopes. Lateral flow in configurations 100L2, 100L3 and 25L3 appear more reasonable. Instead 25L2 slightly overestimated lateral flow albeit less than 25L1 and 100L1.

The overestimation of later lateral flow lead to an underestimation of baseflow (Figure 44c and Figure 47). The configurations 100L2, 25L3 and 100L3 appeared to predict reasonable baseflow, partly overcoming the lateral flow issue (Figure 46 and Figure 44).

In conclusion, configuration 100L2 best suited for a spatially distributed hydrological model. Configuration 25L3 and 100L3 were comparable to 100L2, and could be considerate as simple alternatives, that however should be evaluated in each specific case study.

### 3.4.10 Conclusions of section

Hillslope length plays an important role in controlling the hydrological response of a basin, since it exerts a primary control on the fluxes transported towards the river network through the soils and hillslopes. In this study the impact of hillslope length on SWAT streamflow predictions was investigated using three hillslope length methods (L1, L2, L3) and two DEMs of 25 m and 100 m pixel size given a complete overview of possible impacts of hillslope length estimations on SWAT simulated hydrological processes. These methods lead to different hillslope length distributions, but only L2 method (the three-dimensional DEM flow accumulation method) was sensitive to DEM resolution, resulting in longer hillslope length with the 100 m DEM pixel size (~ 60 m) than with the 25 m DEM (~ 30 m). Conversely, the SWAT default method (L1) was not affected by DEM pixel size.

While all configurations reached satisfactory simulation of monthly streamflow, the analysis of streamflow components (surface runoff, lateral flow, baseflow) highlighted differences in configuration outputs. The DEM resolution did not impact SWAT streamflow simulations; both DEMs were sufficient for streamflow modelling at this scale, confirming literature findings that a finer resolution DEM may not necessarily improve model simulations. Rather, the optimal DEM pixel size depends on the environmental characteristics, the desired level of prediction, and the model output of interest (Chaplot, 2014; Zhang et al., 2014).

The hillslope length method had no impact on total streamflow and surface runoff, but had an important impact on the partition between lateral flow and baseflow. This bears important consequences in the simulation of pollutant movements, like nitrates, in the landscape. The current default method L1 was shown to produce larger errors in the simulation of streamflow components in steep areas. In particular, the lateral flow always yields higher residuals where slopes are higher and the associated hillslope lengths smaller. This reflects the reported inverse power relationship between hillslope length and lateral flow estimation ([eq.6]). However, it seems that this inverse power relationship does not hold for larger catchments, where estimated values of hillslopes length lower than 10 meters might not be realistic (Figure 38).

The hillslope length method based on DEM analysis of flow accumulation (L2) resulted in the most adequate estimations of lateral flow and baseflow in steep regions. The L2 method is conceptually more consistent for application in spatially distributed models than the current method, since it provides a more reliable description of the landscape morphologies throughout a 3D analysis. Furthermore, the L2 method is sensitive to DEM resolution, since the use of different DEM pixel size produces different hillslope lengths, while the default ArcSWAT method returns the same values of hillslope lengths. For future SWAT development, the LS-TOOL (Zhang et al., 2013) should be integrated in ArcSWAT (interface GIS of SWAT) in order to replace the current hillslope length calculation. However, further efforts should be done for improving the representativeness of surface runoff according to the lateral flow estimations.

The combination of DEM100 m and L2 was the optimal configuration to predict streamflow in the Upper Danube and is recommended in general in large basins given that the use of DEM100 reduces the computational burden for SWAT application at large scale (i.e. time of calculation of topographic characteristics in the phase of “Automatic Watershed Delineation”).

Choosing a constant hillslope length of 50 m (L3) however was a good second alternative to be considered when DEM resolution is of 25 m or coarser, especially if the DEM accuracy is low. Furthermore, given the importance of hillslope length on sediment outputs reported in literature (Chaplot, 2014; Zhang et al., 2014) the impact of hillslope length on sediment predictions was explored in Vigiak et al. (2015), in a study that confirmed the suitability of L2 method for prediction of sediment yields.

These results can be considered as representative for a wide range of landscapes since the Upper Danube is characterized by heterogeneous topography, large climate variations, several land covers/uses and soil types. They can also be considered valid for any catchment hydrological model that shares a structure for runoff and lateral flow partitioning

similar to the SWAT ([eq. 1], [eq. 2] and [eq. 6]). In such models, a proper representation of DEM derivatives (such as hillslope length) commensurate to DEM pixel size is thus fundamental for a correct representation of hydrological processes.

## 3.5 Crete Island: how to represent the karst phenomena using the SWAT model

### 3.5.1 Synopsis

“Karst” identifies a specific geological landscape and morphology formed by the dissolving action of water on soluble carbonate rocks such as primarily limestone, but also marble, dolomite, and gypsum. These rocks are mechanically strong but chemically soluble with high degree of secondary porosity. As a consequence, the hydrological cycle provides the primary source of energy for karst formation because water is the solvent that dissolves carbonate rocks and then carries the ions away in solution (Williams P.W., 2004).

The process of dissolution (‘karstification’) leads to the development of caves, sinkholes, springs and sinking streams that are typical features of a karst system. With progressing karstification, groundwater flow in the karst aquifer develops from a flow in an interconnected fissure network to a flow concentrated in several large pipes, interconnected cavities and cave systems (EC, 2003; EC, 2004). The downstream end of a karst system usually is a spring where the underground conduit reaches the surface as an output point from an extensive network of groundwater conduits (Smart and Worthington, 2004).

In Europe, soluble carbonate rocks are widespread in Western, Southern and Eastern part covering 35% of whole Europe (Daly, 2002), so that the karst processes are significant components of the physical geography of Mediterranean basins. In particular, limestones reach great thickness in Spain, southern France, Italy, the Balkan Peninsula, Turkey and in many islands in the Mediterranean (Crete, Majorca and Sicily). As a consequence, karst aquifers and springs are an important source of water supply for Mediterranean countries and special strategies are required to manage the quantity and quality of their waters.

Bakalowicz (2015) pointed out the importance to study the karst aquifer functioning and the local geological evolution in order to manage in realistic and sustainable way the water resources. The monitoring and management of these resources are recognized in Europe as an essential issue and the European Union prompted the creation of COST Actions 620 and 621 to develop a comprehensive methodology for risk assessment and for the sustainable management of karst systems (EC, 2003; EC, 2004). Unfortunately, most

countries are lacking behind in monitoring the discharge of springs or wells and the exploitation of karst aquifers in generally is inappropriate (Bakalowicz, 2015).

In this context, large scale hydrologic models are essential tools for watershed management at regional scale. Regional scale models with an appropriate discretization of watershed can adequately account for the spatial heterogeneity improving water predictions (Wooldridge and Kalma, 2001).

In this thesis the SWAT model was integrated with a *karst-flow model* (Nikolaidis et al., 2013; Tzoraki and Nikolaidis et al., 2007). Karst-subbasins were defined in order to reproduce more accurately the water balance at regional scale.

This integrated model, KSWAT model, was applied to the island of Crete, one of the most intensively managed Mediterranean islands, where the major water use is irrigation (84.5% of the total consumption) and the main water source is karst aquifers.

### 3.5.2 The study area

The island of Crete occupies the southern part of Greece and is the largest island of Greece and the fifth in the Mediterranean. The island covers an area of 8336 $km^2$ and is divided into prefectures, including from east to west: Lasithi (1810 $km^2$), Heraklion (2626 $km^2$), Rethymno (1487 $km^2$) and Chania (2342 $km^2$) (Figure 48a). The maximum length of the island is 269 km and the maximum width 60 km. Four main mountains run west to east: the White Mountains in the west (2453 m), Idis mountain (2456 m) in the center, Asterousian (1280 m) in south Heraklion and Dikti (2148 m) in the east (Baltas and Tzoraki, 2013).

The island of Crete is characterized by a dry semi-humid Mediterranean climate with dry and warm summers and humid and relatively cold winters where mean annual rainfall decreases from west to east and from north to south, but increases with altitude (MEDIWAT, 2013). Annual precipitations are highly variable ranging between 300 mm in coastal areas and 2000 mm in headwaters in White Mountains. The mean annual temperature ranges from 18.5° in the west to 20° in the south of island and decreases with altitude.

The mountainous areas, in particular in the western part, have mountainous climate. As a consequence, Crete contains sub-regions with very different hydrological characteristics.

Crete has about 2550 $km^2$ of agriculture land, about 30% of whole Crete, with more than 1100 $km^2$ in Heraklion, and 3800 $km^2$ of pasture (45% of total areas of Crete). The main crops are olives, grapes, and the main vegetables crops are tomatoes, cucumbers, onions, potatoes, watermelons and melons. The demand for irrigation water is high (about 360 $Mm^3/y$), while only 47% (1200 $km^2$) of agricultural land is irrigated. In Heraklion the irrigated

area is around 600 km$^2$, followed by Lasithi and Chania with around 300 km$^2$, while a very small area in Rethymno is irrigated (Agriculture statistics of Greece, 2005).

### 3.5.3 The karst geology and hydrology of island of Crete

The geology of Crete is composed of carbonate rocks (limestone, marble and dolomite) which allow water to penetrate, creating major karst formation (Baltas and Tzoraki, 2013). More than 30% of carbonate rocks cover the total area of the Island and the major carbonate rocks of Crete are located in the White mountains (Lefka Ori), Idi, Dikti and Sitia (Figure 48b). The total karst area covers about 2730 km$^2$ and the water contribution to the karst aquifer is estimated around 2000 Mm$^3$/y which discharges out in many springs (Chartzoulakis et al., 2001).

There are 47 gauged springs in Crete with relative large flow, which are subdivided in three main classes: freshwater springs, brackish water springs and undersea springs. Most of springs are karst springs and refer to the same karst hydrogeological system (Lefka Ori, Idi, Dikti and Sitia) discharging around 500 Mm$^3$/y freshwater into rivers. The most important springs are Stylos, Platanos and Kourtaliotis that discharge 85 Mm$^3$/y in the Kalami/Koiliaris basin, 67 Mm$^3$/y in Plantanias Basin and 38 Mm$^3$/y in Kourtaliotis basin, respectively (Figure 48c).

Big brackish springs, located on coastal areas, include Almiros-Heraklion that discharges around 235 Mm$^3$/y, Almiros-Agios-Nikolaos (83 Mm$^3$/y) and brackish springs of lower discharge include Almiros-Mallia (3.2 Mm$^3$/y), Georgioupolis, Grammatikaki and Malavra. Brackish springs discharge directly about 285 Mm$^3$/y in the sea. Submarine discharges can be found in the southern part of Lefka Ori, Souda bay, Bali bay, Mallia bay, Elounta, Skinia, and the eastern part of the limestones of Zakros (MEDIWAT, 2013).

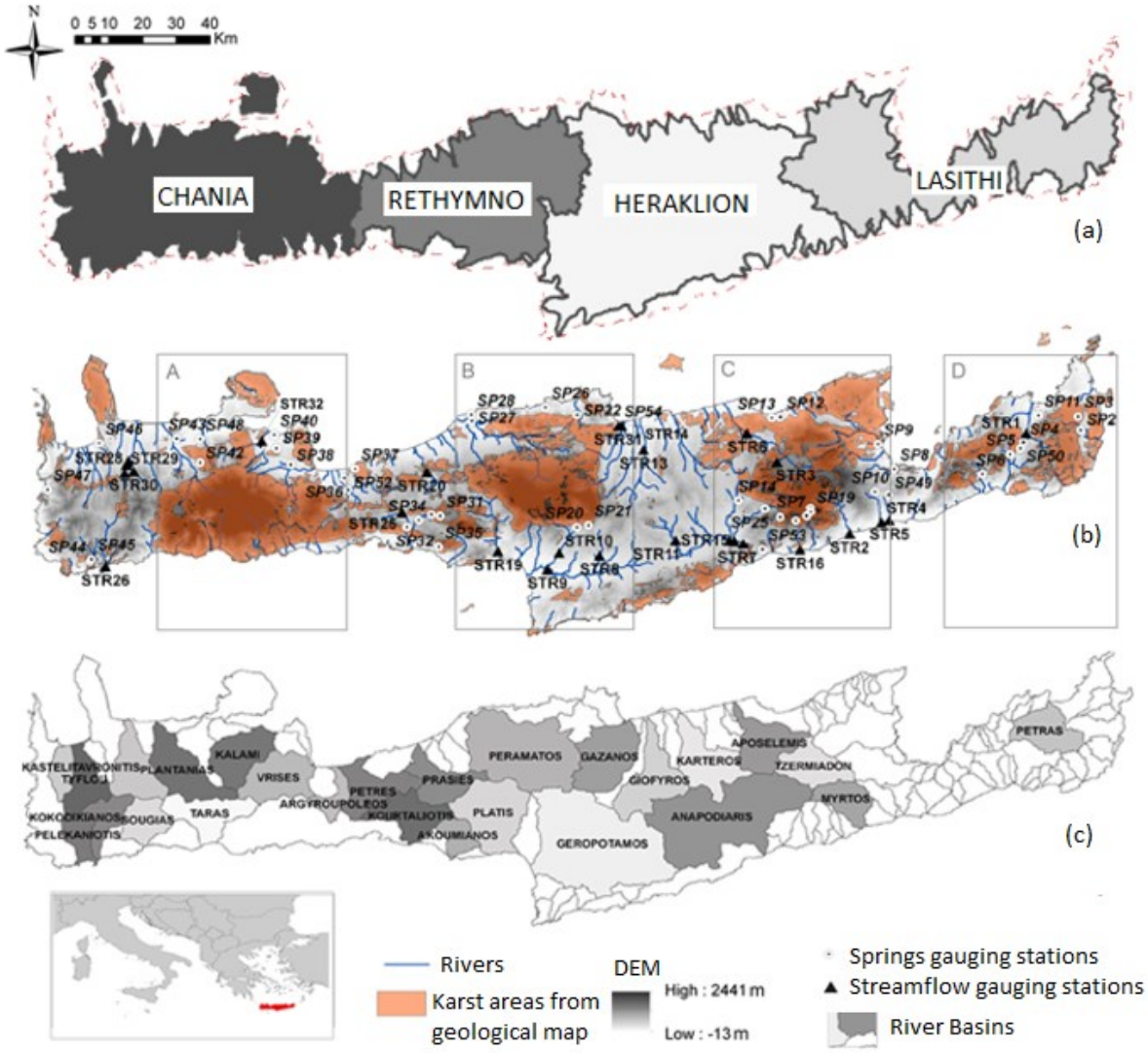


Figure 48. Map of prefectures (a); the main carbonate rocks of Crete (karst areas from geological map) with springs and streamflow gauging stations (b) A, White Mountainous; B, Idi; C, Dikti; D, Sitia; map of the main river basins (c).

### 3.5.4 Streamflow and springs measurements

Stream and spring discharge measurements were provided by the bureau of Water Resources at the Decentralized Administration of the Region of Crete that deals with data elaboration and the assessment of their accuracy. The stream measurements at 25 permanent locations were conducted using a continuous graphic record of the water depth. For a comprehensive description of continuous measurements of water depth, the reader can refer to Rantz et al. (1982).

These measurements were then converted to streamflow rate with an established rating curve (streamflow, $m^3/s$ vs water depth, m) calculated every year for each monitoring station following the procedure described in Buchanan and Somers (1976). The streamflow-water

depth relationship was adopted to calculate the streamflow at daily time step, and then aggregated at monthly time step. The available dataset for this study included 22 gauging stations because the streamflow stations STR30 and STR29 were excluded due to their uncertain localization and drain areas. STR5 was also excluded because observed data were lacking during the study period 1980-2009.

The spring's discharges measurements were directly calculated by measuring velocity once a month on surveyed cross-sectional channel geometry at 47 permanent locations. The only exception was the Almiros spring for which only the calculated monthly discharge was available. Table 10 summarizes the streamflow and springs data utilized in this study.

Table 10. Description of available streamflow and spring discharges measurements in the Crete Island provided by the bureau of Water Resources at the Decentralized Administration of the Region of Crete. The symbol # represent the number.

| Type of measure | # gauging stations | Type of location | Type of measures | Frequency | Period extension | # Calibrated gauging stations | # Validated gauging stations |
|---|---|---|---|---|---|---|---|
| Streamflow | 22 | Permanent gauging station | water depth | continuous measurements on a graphic record (Rantz et al., 1982) | 1980-2009 (30 years) | 15 | 7 |
| Spring Discharge | 47 | Permanent gauging station | water velocity | once a month | 1983-2009 (27 years) | 47 | - |

### 3.5.5 The application of KSWAT in Crete Island

The SWAT model consists in 352 subbasins with an average area of 19 $km^2$ covering 6700 $km^2$, and 502 HRUs with an average area of 19 $km^2$ (Figure 49a). The main input data are summarized in table A1.1 in Appendix A1.

Among the 352 subbasins, 134 subbasins were identified as karst-subbans using both the geological maps (soft data) and three dominant soils that, according to the European Soil Database, are Leptosols (European Soil Portal, 2014), poorly developed and shallow soils over hard rock and comprise of very gravelly or highly calcareous material. In particular, the geological map was used to define the extension of "wetlands" inside each karst-subbasin, generally covering the entire subbasins where the karst-soils are dominant, or only a percentage of subbasin area as in the case of the Kourtaliotis Basin. The resulted area covered by the karst-subbasins was estimated around 2600 $km^2$.

In these subbasins the KSWAT was applied (see Adapted SWAT model in Figure 6). In the other subbasins the classic structure of SWAT is kept (Figure 1).

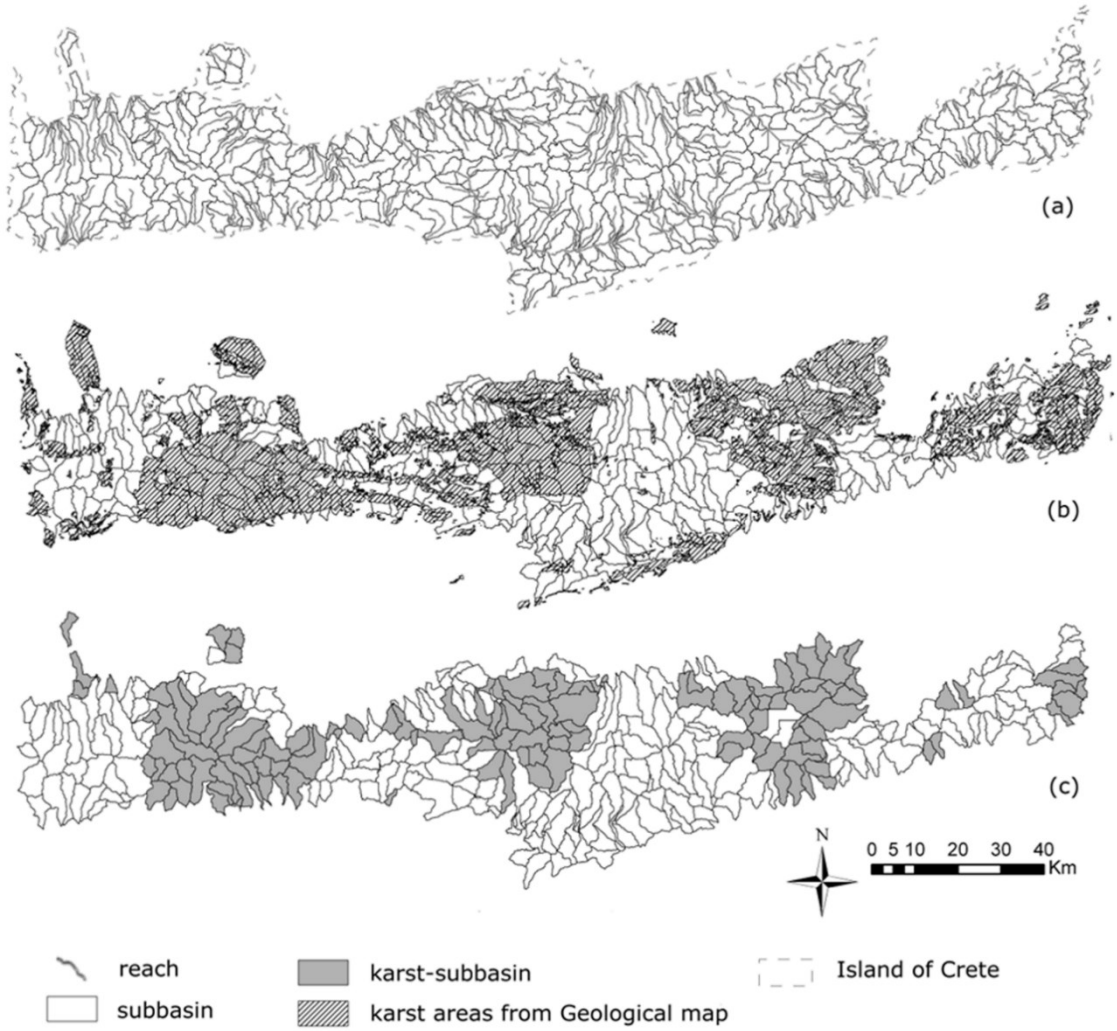


Figure 49. Rivers and subbasins (a); definition of karst geological features: karst areas from geological map (b) and the subbasins with karst soils (karst subbasins) (c).

Initially the model was calibrated in terms of monthly streamflow using the C/V strategy proposed in this thesis (step-wise calibration, Figure 9). Successively, using the predicted deep aquifer recharge the karst-flow model (Figure 6) was used to calibrate the spring's discharge outside the SWAT model. Finally, the calibrated springs discharges were introduced in SWAT as point sources, and after running the model the simulated streamflow was validated against observation.

The modified model parametrization respect to that presented in Table 2, is described hereafter in Table 11.

Table 11. Parameters and parameter ranges used in the calibration (in alphabetic order), in the *adapted SWAT model* and in the *karst-flow model*. In column "Process" the information about the order and group of calibration processes: 1, snow process; 2, runoff process; 3, lateral flow process; 4: groundwater process; 5: karst process.

| MODEL | Parameter | Description | Process | Range of calibration values | Range of values in karst-subbasins |
|---|---|---|---|---|---|
| karst-flow model | $a_1$ | Fraction of Inflow to Upper Reservoir | 5 | 0 - 1 | |
| karst-flow model | $a_2$ | Fraction of Upper Reservoir to Lower | 5 | 0 - 1 | |
| SWAT/Adapted SWAT model | ALPHA_BF | Baseflow recession constant [1/d] | 4/5 | 0 - 1 | 0.1 |
| SWAT | ALPHA_BF_D | Baseflow recession constant for deep aquifer [1/d] | 4 | 0 | 0 |
| Adapted SWAT model | CH_K (1) | Effective hydraulic conductivity in tributary channel alluvium [mm $h^{-1}$] | 5 | -- | 300 |
| Adapted SWAT model | CH_K (2) | Effective hydraulic conductivity in the main channel [mm $h^{-1}$] | 5 | -- | 5-500 * |
| SWAT | CN2 | SCS runoff curve number for moisture condition II | 2 | -15% - +15% | -- |
| SWAT | EPCO | Plant evaporation compensation factor | 3 | 0.01 - 1 | -- |
| SWAT | ESCO | Soil evaporation compensation factor | 3 | 0.01 - 1 | -- |
| SWAT/ Adapted SWAT model | GW_DELAY | Groundwater delay [d] | 4/5 | 0 - 500 | 1 |
| SWAT/ Adapted SWAT model | GW_REVAP | Groundwater 'revap' coefficient | 4/5 | 0.02-2 | 0.1 |
| SWAT | GWQMN | Threshold depth of water in the shallow aquifer required for return flow to occur [mm] | 4 | 0 - 1000 | -- |
| karst-flow model | $k_l$ | Upper reservoir recession constant [1/d] | 5 | 0 - 5 | -- |
| karst-flow model | $k_u$ | Lower reservoir recession constant [1/d] | 5 | 0 - 5 | -- |
| SWAT | PLAPS | Precipitation laps rate [mm/km] | 1 | 0 - 100 | -- |
| karst-flow model | $Q_{k0}$ | Initial karstic flow [$m^3$/day] | 5 | $0 – 3x10^5$ | -- |
| SWAT/ Adapted SWAT model | RCHRG_DP | Groundwater recharge to deep aquifer [fr] | 4/5 | 0 - 1 | 1 |
| SWAT | REVAPMN | Threshold depth of water in the shallow aquifer for revap to occur [mm] | 4 | 0 - 500 | -- |
| SWAT | SFTMP | Snowfall temperature [°C] | 1 | -5 - +5 | -- |
| SWAT | SMFMN | Minimum melt rate for snow on Dec 21 [mm °C$^{-1}$ $d^{-1}$] | 1 | 0 - 10 | -- |
| SWAT | SMFMX | Minimum melt rate for snow on Jun 21 [mm °C$^{-1}$ $d^{-1}$] | 1 | 0 - 10 | -- |
| SWAT | SMTMP | Snow melt base temperature | 1 | -5 - +5 | -- |
| SWAT | SNOEB | Initial snow water content [mm] | 1 | 0 | -- |
| SWAT | SOL_AWC | Available water capacity of the soil layer [fr] | 3 | -25% - +25% | -- |
| SWAT | SOL_K | Saturated hydraulic conductivity [mm $h^{-1}$] | 3 | -25% - +25% | -- |
| SWAT | TIMP | Snow pack temperature lag factor | 1 | 0.01 - 1 | -- |
| SWAT | TLAPS | Temperature laps rate [°C/km] | 1 | -10 - 0 | -- |
| Adapted SWAT model | WET_FR | Fraction of sub-basin area that drain into wetlands | 5 | -- | 0.1 – 1 ** |
| Adapted SWAT model | WET_K | Hydraulic conductivity through bottom of wetland [mm $h^{-1}$] | 5 | -- | 300 ** |

### 3.5.6 Hydrological simulation

The performance indicators obtained comparing the monthly observed and simulated streamflow for the 22 stream gauging stations after calibration, regionalization and the introduction of the calibrated springs are summarized in Table 12**.** It is noteworthy that about 64% of the calibrated gauging streamflow stations reached satisfactory PBIAS% (values in the range ±25%), while only 40% had NSE greater than 0.5 (see Table 4). Furthermore,

50% and 36% of calibrated streamflow gauging stations reached respectively $r^2$ and $br^2$ larger than 0.5.

Table 12. Comparison of observed and simulated streamflow in the period 1983-2009 after the introduction of the springs (complete validation): in the first two columns the code and name of the stations; in the third column the drain area ($km^2$); the *% data* represents the % of monthly values in the period 1983-2009 (324 total months); the observed and simulated volumes are respectively *$Mm^3$/year OBS* and *SIM;* the performance indicators between monthly observed and simulated steamflow are the normalized root mean square error (NRMSE %), the percent bias (PBIAS%), the Nash Sutcliffe Coefficient (NSE), the coefficient of determination ($r^2$) and the coefficient of determination multiplied by the slope of the regression line between simulated and observed values ($br^2$).

| Station | Name | Drain Area ($km^2$) | % data | $Mm^3$/year OBS | $Mm^3$/year SIM | NRMSE % | PBIAS % | NSE | $r^2$ | $br^2$ |
|---|---|---|---|---|---|---|---|---|---|---|
| STR32 | Koiliaris | 132.6 | 21% | 180.97 | 182.74 | 16.5 | 3.3 | 0.68 | 0.69 | 0.62 |
| STR19 [R] | Platis | 209.6 | 69% | 50.15 | 46.30 | 11.1 | 2.4 | 0.63 | 0.63 | 0.47 |
| STR7 [R] | AnapodiarisH | 522.7 | 54% | 30.13 | 31.55 | 6.9 | 16.5 | 0.78 | 0.8 | 0.73 |
| STR13 | Giofiros | 186.3 | 69% | 22.24 | 22.94 | 12.5 | 25.4 | 0.53 | 0.66 | 0.65 |
| STR20 | Prasanos | 101.9 | 54% | 17.83 | 22.17 | 13.2 | 2.8 | 0.23 | 0.36 | 0.27 |
| STR9 [R] | Geropotamos | 394.5 | 69% | 17.21 | 33.04 | 32.2 | 183.4 | -3.94 | 0.46 | 0.24 |
| STR3 | Katavothres | 21.35 | 54% | 16.63 | 11.56 | 11 | -32.7 | 0.53 | 0.62 | 0.3 |
| STR26 | Kakodikianos | 78.11 | 77% | 15.89 | 19.02 | 11.6 | 31.6 | -0.87 | 0.25 | 0.23 |
| STR27 | Sebreniotis | 28.48 | 80% | 15.83 | 12.45 | 8.5 | -17.9 | 0.58 | 0.6 | 0.38 |
| STR11 | Anapodiaris Pla | 89.51 | 47% | 11.89 | 12.91 | 13.4 | -2 | 0.64 | 0.65 | 0.53 |
| STR10 | Koutsoulidis | 132.2 | 54% | 11.53 | 13.07 | 5.7 | 17.2 | 0.83 | 0.84 | 0.82 |
| STR2 [R] | Mirtos | 96.34 | 84% | 10.87 | 11.31 | 15.3 | 39.9 | -0.35 | 0.29 | 0.26 |
| STR6 [R] | Aposelemis | 204.8 | 69% | 10.69 | 26.46 | 14.4 | 158.7 | -0.05 | 0.63 | 0.5 |
| STR28 | Rumatianos | 22.06 | 76% | 6.75 | 7.18 | 16.3 | 36.9 | -0.06 | 0.26 | 0.18 |
| STR8 | Litheos | 41.98 | 77% | 6.39 | 6.13 | 20.6 | 8.2 | -0.31 | 0.26 | 0.2 |
| STR14 [R] | Gazanos | 186.8 | 54% | 6.32 | 11.86 | 36.9 | 111.8 | -3.05 | 0.23 | 0.17 |
| STR1 | Patelis | 84.57 | 56% | 5.91 | 6.12 | 12.1 | 13.7 | 0.48 | 0.57 | 0.51 |
| STR4 | Kalamafkianos | 36.14 | 10% | 5.41 | 3.57 | 40.7 | 10.4 | -1.33 | 0.32 | 0.3 |
| STR15 | Baritis | 105.5 | 44% | 4.08 | 3.06 | 13.2 | 61.7 | -0.04 | 0.19 | 0.12 |
| STR25 | Agios Vasiliou | 35.64 | 74% | 2.37 | 4.62 | 28 | 103.4 | -2.38 | 0.26 | 0.2 |
| STR16 | Arvis | 26.53 | 80% | 1.66 | 1.14 | 11.1 | 11.2 | 0 | 0.32 | 0.23 |
| STR12 [R] | Iniotis | 105.9 | 44% | 1.56 | 2.21 | 23.7 | 57.3 | -0.81 | 0.16 | 0.12 |

[R] gauging stations used in the validation of regionalization technique

Figure 50 shows some examples of comparison of hydrographs. Even though some of the statistical indicators did not score very high, the hydrographs comparison illustrates that the model was able to reproduce accurately the monthly variations over a long period of simulation even in subbasins influenced by excessive water pumping, such as STR16. This gauging station was fed by precipitation and discharge of spring SP16. After the year 1990,

the spring's discharge was diverted to supply domestic uses reducing drastically the streamflow in particular during the summer and autumn.

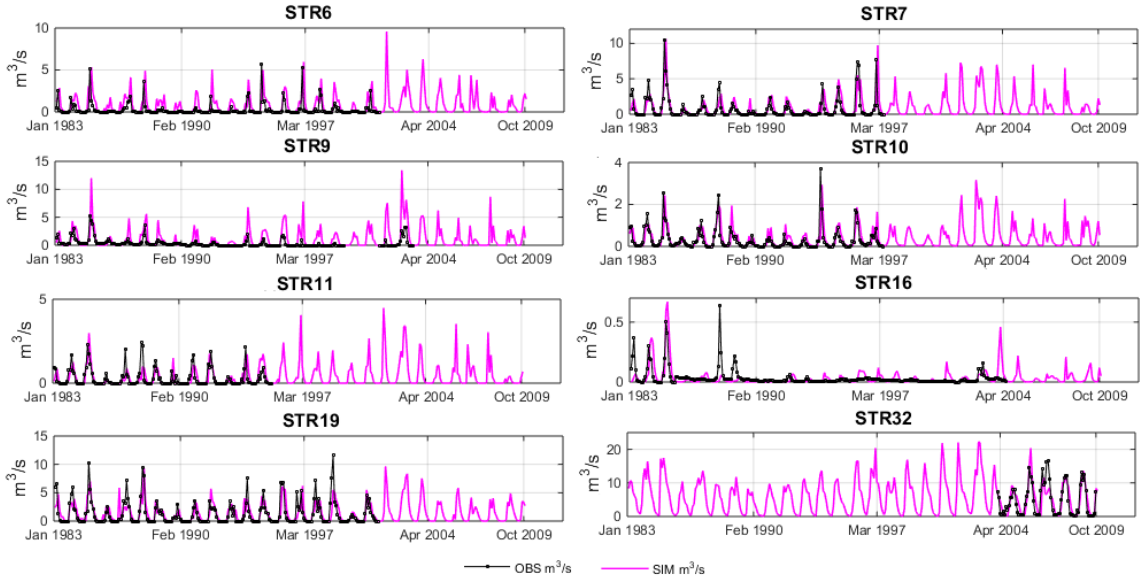


Figure 50. Some examples, comparison between monthly simulated and observed streamflow values from 1983 to 2009 after the allocation of springs in the SWAT model.

It was estimated that the percentage of streamflow gauging stations that reached satisfactory PBIAS (PBIAS<+/-25%, Moriasi et al., 2007) increased from 59% to 64% adding spring's discharges in the SWAT model highlighting the significant influence of springs in the water balance of Crete.

In particular, streamflow discharge of gauging stations STR32 (Koiliaris), STR16 (Avli), and STR10 (Koutsoulidis) were strongly influenced by the discharge of springs SP41 (Stylos), SP14-SP25 (Migilisi and Emparos) and SP20 (Zaros), respectively. For STR32 the PBIAS decreased to 3% and the NSE increased to 0.68, for STR16 the PBIAS % reached 11%, and finally for STR10 the PBIAS% and NSE were also satisfactory reaching 17% and 0.83 respectively (Table 12).

These results demonstrated that the *karst-flow model* correctly simulated the discharge of springs increasing the SWAT model performance.

Figure 51 shows some examples of comparison between daily observed and simulated spring flows (only for SP54 monthly comparison), and Table 13 summarizes the comparison between monthly and observed long-term annual discharge on the period 1983-2009 and the performance indicators for all springs. It is noteworthy that for more than 70% of the calibrated springs the PBIAS% is within the range of ±25%, indicating that the performance of the *karst-flow model* was satisfactory (Moriasi et al, 2007). NSE was positive for 80% of

calibrated springs, while $r^2$ and $br^2$ had a wide range of values with around 50% of the values larger than 0.4.

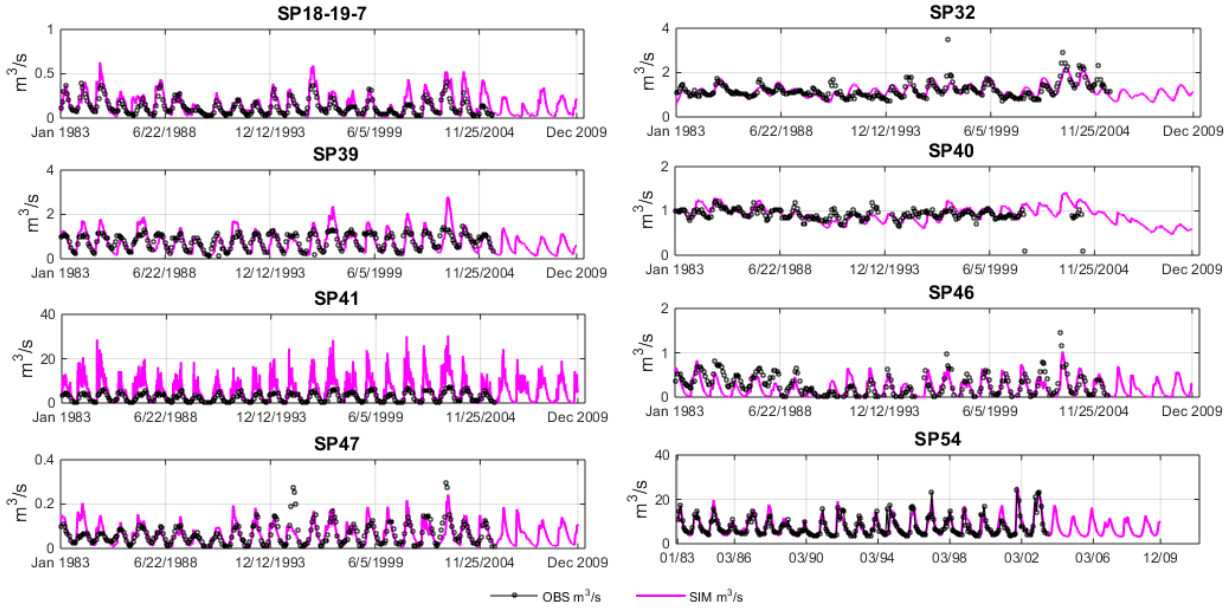


Figure 51. Some examples, comparison between daily simulated and observed spring's values from 1983 to 2009 (monthly comparison for SP54).

However, the *karst-flow model* markedly overestimated the discharge for springs SP4-50 (Agios Georgios Sitia- Sikia Sitia), SP14 (Avli Migilisi), SP16 (Mega Vrisi), SP41 (Stylos) and SP51 (Loutraki) maybe due to the quality of the observed data.

Concerning SP41, the most studied spring in Crete (Nikolaidis et al, 2013; Moraetis et al., 2011; Kourgialias et al., 2010), was intentionally calibrated to overestimate the flow in order to take into account the contribution of ungauged springs. Nikolaidis et al. (2013) reported that Stylos spring has two permanent springs at elevation +17 m AMSL (with 85 $Mm^3$/year of volume), but there was also an ungauged intermittent spring (Anavreti at elevation +24 m AMSL). Both contributed to Koiliaris discharge. The authors argued that these springs have a total average discharge around 154 $Mm^3$/y (2007-2010), and this volume was in agreement with the total overestimated volume of Stylos in this work (150 $Mm^3$/y, for the same period 2007-2010, 170 $Mm^3$/y considering 1983-2009). Finally, it is noteworthy that the spring SP46 (Figure 51**)** had two different hydrological behaviors: observed data were higher prior to year 1988, then the values decreased sharply highlighting changes in the regime of discharge. This may be explained by a change in the method of measurement or more probably by an excessive pumping of water as occurred for the STR16 spring.

Table 13. Comparison of observed and simulated spring discharges in the period 1983-2009: in the first two columns the code and name of the stations; in the third the karst area that contributes of each spring ($km^2$) and involves the area inside the hydrological basin and outside; the *% data* represents the percentage of monthly values in the period 1983-2009 (324 total months); the observed and simulated volumes are respectively *$Mm^3$/year OBS* and *SIM;* the performance indicators calculated between daily observed and simulated spring discharges are the normalized root mean square error (NRMSE %), the percent bias (PBIAS%), the Nash Sutcliffe Coefficient (NSE), the coefficient of determination ($r^2$) and the coefficient of determination multiplied by the slope of the regression line between simulated and observed values ($br^2$).

| Station | Name | Estimated karst recharge area ($km^2$) | % data | $Mm^3$/year OBS | $Mm^3$/year SIM | NRMSE % | PBIAS % | NSE | $r^2$ | $br^2$ |
|---|---|---|---|---|---|---|---|---|---|---|
| SP54* | Almiros-Heraklion | 323.48 | 77% | 235.72 | 236.59 | 9.8 | 0.7 | 0.77 | 0.8 | 0.8 |
| SP41 | Stylos | 185.01 | 79% | 85.81 | 168.85 | 66 | 102.7 | -4.8 | 0.64 | 0.31 |
| SP9 | Almiros-Agios-Nikolaos | 155.42 | 80% | 83.22 | 83.73 | 15.9 | 3.9 | 0.22 | 0.54 | 0.56 |
| SP43 | Platanos/kalamionas-Agia | 110.18 | 10% | 67.11 | 67.43 | 23.8 | 6.1 | 0.18 | 0.55 | 0.59 |
| SP32 | Kourtaliotis | 103.37 | 84% | 37.99 | 37.08 | 9.9 | -0.8 | 0.44 | 0.43 | 0.45 |
| SP42 | Meskla | 114.2 | 84% | 30.7 | 30.94 | 17.4 | 11.2 | 0.31 | 0.32 | 0.38 |
| SP40 | Kourbos | 53.32 | 68% | 29.85 | 28.68 | 14.6 | 2.1 | -0.61 | 0.12 | 0.12 |
| SP38 | Vrisses | 20.21 | 77% | 26.95 | 26.53 | 13.4 | -3 | 0.48 | 0.41 | 0.51 |
| SP39 | Armenoi | 78.48 | 84% | 24.79 | 24.09 | 26.1 | 1.2 | -0.08 | 0.5 | 0.5 |
| SP37 | Petres | 26.2 | 70% | 13.77 | 13.76 | 15.2 | 2 | 0.34 | 0.26 | 0.39 |
| SP44_45 | Elliniki-Konto Kinigi | 40.32 | 84% | 13.5 | 13.52 | 9.5 | 5.3 | 0.44 | 0.32 | 0.45 |
| SP34 | Spilianos | 34.07 | 84% | 12.65 | 11.24 | 10.7 | -6.3 | 0.36 | 0.21 | 0.36 |
| SP36 | Mousela Xalikouti | 47.95 | 77% | 11.95 | 11.26 | 9.4 | 18.9 | 0.24 | 0.36 | 0.41 |
| SP46 | Drapania | 40.9 | 75% | 9.87 | 6.35 | 14.9 | -21.9 | 0.16 | 0.21 | 0.32 |
| SP48 | Therisos | 12.6 | 42% | 9.68 | 9.35 | 16.6 | -3 | 0.32 | 0.18 | 0.32 |
| SP28 | Geropotamos | 25.58 | 64% | 7.75 | 7.81 | 14.2 | -2.5 | 0.13 | 0.13 | 0.22 |
| SP2 | Zakros | 28.45 | 80% | 5.4 | 5.77 | 9.5 | -1.8 | 0.62 | 0.59 | 0.63 |
| SP3 | Chochlakies | 34.75 | 49% | 5.33 | 5.47 | 17.3 | 2.3 | 0.34 | 0.38 | 0.46 |
| SP27 | Panormos Almiro Nero | 16.74 | 69% | 4.68 | 4.65 | 13.1 | 4 | 0.07 | 0.49 | 0.5 |
| SP18_19_7 | Kria Vrisi-Simis-Kefalovrisi Viannou | 35.14 | 84% | 4.65 | 4.74 | 20.6 | 26.7 | 0.17 | 0.55 | 0.67 |
| SP22 | Fodele | 22.45 | 84% | 3.78 | 3.99 | 8.7 | -3.2 | 0.21 | 0.13 | 0.22 |
| SP52 | Argiroupoli | 24.23 | 44% | 3.67 | 3.54 | 18.7 | 18.7 | 0.09 | 0.51 | 0.6 |

| | | | | | | | | | | |
|---|---|---|---|---|---|---|---|---|---|---|
| SP49 | Kefalovris/Kalamoukas-Ierapetra | 17.91 | 84% | 3.54 | 3.59 | 10 | -4.8 | 0.41 | 0.33 | 0.46 |
| SP12_13 | Almiros Mallia-Grammatikaki | 22.89 | 80% | 3.51 | 3.43 | 12.7 | 10.4 | 0.49 | 0.48 | 0.56 |
| SP6 | Archon Stavrochoriou -Sitia | 28.91 | 83% | 3.26 | 3.23 | 12.5 | -1.7 | 0.38 | 0.49 | 0.51 |
| SP20 | Zaros - Votomos | 26.38 | 10% | 3.15 | 3.03 | 32.4 | -0.1 | -0.06 | 0.04 | 0.04 |
| SP30 | Spili | 14.21 | 21% | 3.07 | 3.1 | 30.4 | -2 | -0.85 | 0.1 | 0.11 |
| SP8 | Kalo Chorio | 14.61 | 76% | 3.05 | 3.1 | 14.3 | 1.2 | 0.29 | 0.26 | 0.3 |
| SP11 | Zou | 29.54 | 48% | 2.14 | 2.14 | 13.2 | -14.7 | 0.51 | 0.35 | 0.52 |
| SP47 | Sfinari | 32.57 | 84% | 1.96 | 1.99 | 12.8 | -0.2 | 0.42 | 0.43 | 0.49 |
| SP31 | Agia Fotia-Spili | 14.21 | 35% | 1.94 | 1.97 | 21.4 | -9.7 | 0.29 | 0.26 | 0.36 |
| SP25 | Emparos | 16.14 | 36% | 1.53 | 1.52 | 13 | 11.5 | -0.11 | 0.01 | 0.02 |
| SP26 | Seises | 2.5 | 80% | 1.53 | 1.23 | 16.7 | -20.9 | 0.05 | 0.3 | 0.4 |
| SP4_50 | Agios Georgios Sitia-Sikia Sitia | 18.27 | 42% | 1.52 | 1.49 | 23.8 | 103.4 | -1.06 | 0.26 | 0.35 |
| SP21 | Gergeri | 41.8 | 17% | 1.49 | 1.86 | 14.8 | -8.3 | 0.57 | 0.57 | 0.63 |
| SP35 | Ligres | 8.35 | 17% | 1.46 | 1.41 | 14.7 | 14 | 0.41 | 0.46 | 0.47 |
| SP5 | Lithines-Sitia | 18.73 | 81% | 1.38 | 1.31 | 11.9 | -3.6 | 0.54 | 0.42 | 0.56 |
| SP14 | Avli Migilisi | 18.85 | 4% | 1.15 | 1.02 | 50.7 | 43.8 | -1.04 | 0.41 | 0.62 |
| SP51 | Loutraki | 33.22 | 58% | 1.09 | 1.19 | 19.1 | 27.2 | -0.1 | 0.42 | 0.49 |
| SP10 | Petikou | 3.22 | 80% | 1.01 | 1.02 | 8.1 | 11.5 | 0.62 | 0.56 | 0.63 |
| SP16 | Mega Vrisi | 28.97 | 34% | 0.65 | 0.64 | 20.3 | 32.7 | 0.04 | 0.1 | 0.16 |
| SP53 | Agios Georgios-Viannou | 3.69 | 33% | 0.11 | 0.2 | 19.1 | 7 | 0.22 | 0.37 | 0.39 |

* For SP54 the performance indicators were calculated using monthly values

### 3.5.7 The estimated recharge areas of karst springs

The karst recharge areas of springs cover karst-subbasins and karst areas for a total of 1928 km$^2$, about the 70% of total karst areas in Crete (Table 13). The main karst recharge area drains more than 300 km$^2$ into Almiros Heraklion Spring (SP54), followed by the karst recharge area of Almiros-Agios-Nikolaos Spring (SP9) that cover about 155 km$^2$, and 130 km$^2$ of karst recharge area of springs in Koiliaris Basin. Figure 52 shows some schematic examples of recharge areas of springs obtained considering the subbasins that contribute with their deep aquifer recharge to the calibration of springs.

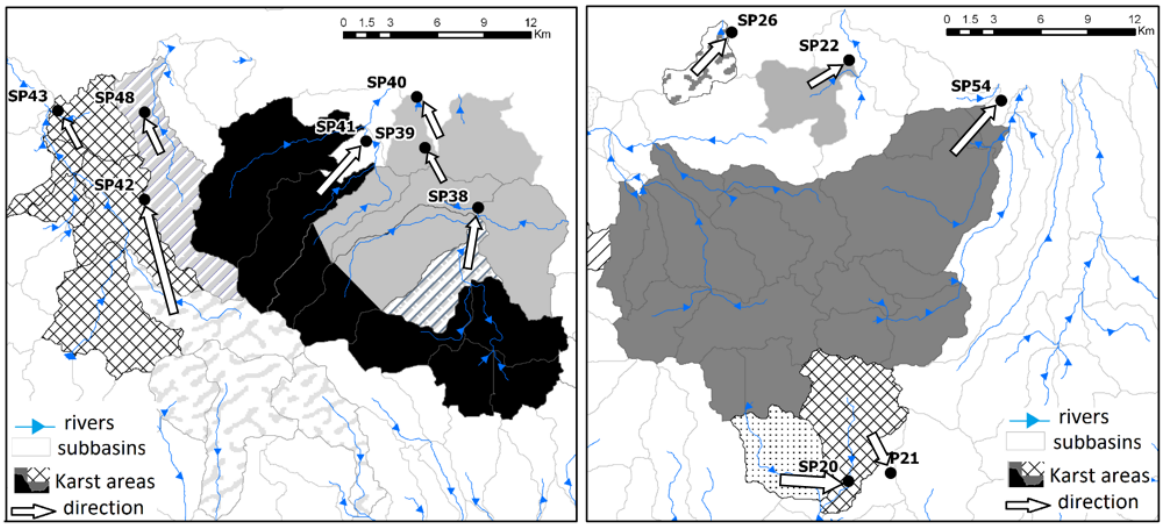


Figure 52. Examples of estimated karst recharge area of selected springs.

To the best of our knowledge this work was the first estimation of karst recharge areas of all gauged springs in the Island of Crete, providing valuable information for water resources management. The only exception was the karst area drained by Almiros Spring and the knowledge of extended areas (outside the hydrological boundary of basin) of springs in Koiliaris Basin.

Bonacci and Fistanic (2006) pointed out the difficulties to define the karst area drained by Almiros Spring due to complex geology and hydrogeology. There were different assumptions of its boundaries and size which varies from 300 km$^2$ (Arfib et al., 2000) to 500 km$^2$ (Lambrakis et al., 2000). However, Bonacci et al. (1995) and Bonacci and Ljubenkov (2005) estimated the karst recharge area of Almiros of about 300 km$^2$, similar to our finding.

The area outside the Koiliaris Basin that contributed to the karst recharge area of Stylos Spring and other ungauged springs in Koiliaris Basin was estimated around 80 km$^2$ (7 subbasins that contribute with 70% of their total area). As a consequence, more than 60% of karst recharge area of Koiliaris springs was outside the boundary of the hydrological basin. This result was confirmed by Nikolaidis et al. (2013) that estimated an extended karst

area of springs in Koiliaris Basin of 79 km$^2$ based on hydrologic modelling and geologic cross-sections.

Albeit this approach may be criticized by the fact that karst recharge areas should be only delineated based on hydrogeological considerations derived i.e. by tracer tests, it has to be taken into account that there are limits in the use of tracer studies in karst areas such as in Koiliaris basin. In a geological karst area which discharges a large volume of water there is a risk of high degree of dilution of tracers (Knithakis, 1995) which in turn limits the usefulness of the methods in delineating the extend area. In addition, breakthrough curves are highly dependent on the flow conditions, often necessitating the repetition of the tracing experiment under low flow and high flow conditions as observed by Goldscheider (2005) and Ravbar et al. (2011).

### 3.5.8 Spatial and temporal variation of hydrological components in Crete

The mean annual precipitation ranges from 550 mm (driest year) to 1400 mm (wettest year) during the period 1983-2009, with a decreasing gradient from west to east. The precipitation was higher at high elevation, reaching more than 2500 mm in the wet years (1996, 1997, 2001 and 2003) and around 1000 mm in the central north areas, while in the plain areas and along the south cost the average annual rainfall was below 1000 mm.

The mean calculated actual evapotranspiration of Crete varied from 340 mm/y (driest year) to 390 mm/y (wettest year) reaching the maximum values long the north coast and, in particular in Karteros, Aposelemis, Tzermiadon, Myrtos and Anapodiaris basins (east-central part of Crete).

Large values of surface runoff were simulated in the western part of Crete and in particular in Tavronitis Basin with maximum value in wet years, such as in 1997 and 2003 (more than 1100 mm). Minor contributors to the water balance include lateral flow and baseflow. The baseflow reached high values in Kourtaliotis, Akoumianos and Platis basins (south-central Crete). The annual and spatial variations of deep aquifer recharge were strongly correlated to the precipitation, as a consequence in zones with high precipitation the deep aquifer recharge reached the largest values since the main mountainous systems were associated with the most important karst systems, allowing water to penetrate directly to the deep aquifer as showed in Figure 53. In particular, Figure 53 illustrates how precipitation, evapotranspiration and recharge of the deep aquifer change during the year. Precipitation and deep aquifer recharge changed during the year decreasing from January (~1120 and 463 Mm$^3$/month respectively) to August (~18 and 62 Mm$^3$/month respectively) and increasing from September (~163 and 63 Mm$^3$/month respectively) to December (~1250 and 416 Mm$^3$/month respectively). During the wettest months, the west part of Crete

reached the highest values of precipitation and also the highest value of deep aquifer recharge. The evapotranspiration increased from January (~ 240 $Mm^3$/month) to April (~ 320 $Mm^3$/month), in particular in subbasins long the cost, and then decreased until August (~ 54 $Mm^3$/month) and increased from September (~ 71 $Mm^3$/month) to December (~ 240 $Mm^3$/month). These long-term spatially and monthly variations could be very useful for planning and implementing conservations measures and programs and evaluating their performance.

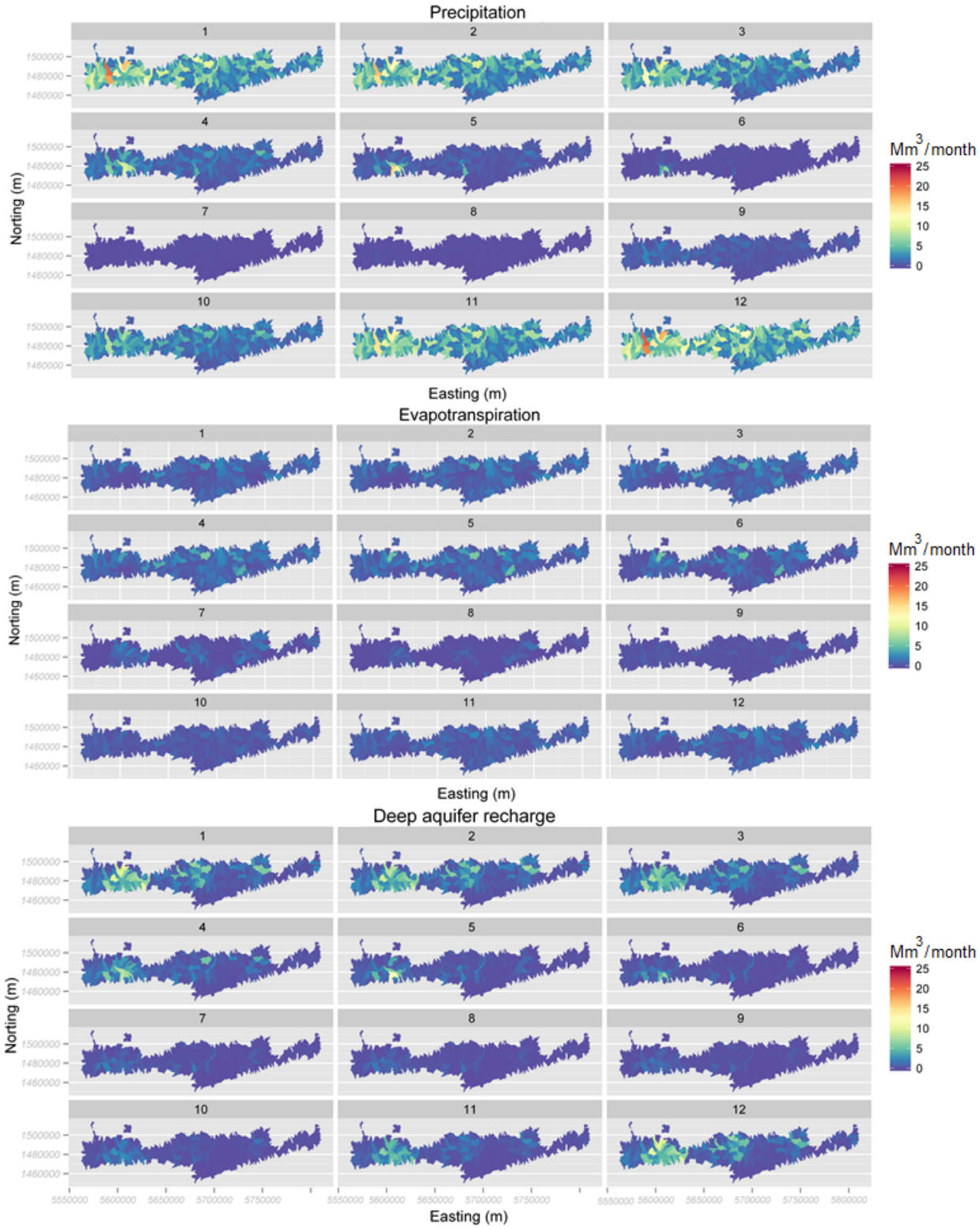


Figure 53. Maps of monthly variations of Precipitation, Evapotranspiration and the Deep aquifer recharge ($Mm^3$/month).

### 3.5.9 The estimated water balance of Crete

Chartzoulakis et al. (2001) and many other studies (RCG, 2002; Vardavas et al., 2004; MEDIWAT, 2013; Koutroulis et al., 2013; Baltas and Tzoraki, 2013) pointed out the importance of the evapotranspiration on the water balance of the whole Crete giving infiltration a secondary role. Conversely to these findings, the Crete SWAT model has allowed the estimation of the water balance of Crete resulting in significantly different estimates. Figure 54 summarizes the percentage of flow contribution of the water balance main components with respect to the long-term average volumes and different hydrological conditions during the period 1983-2009.

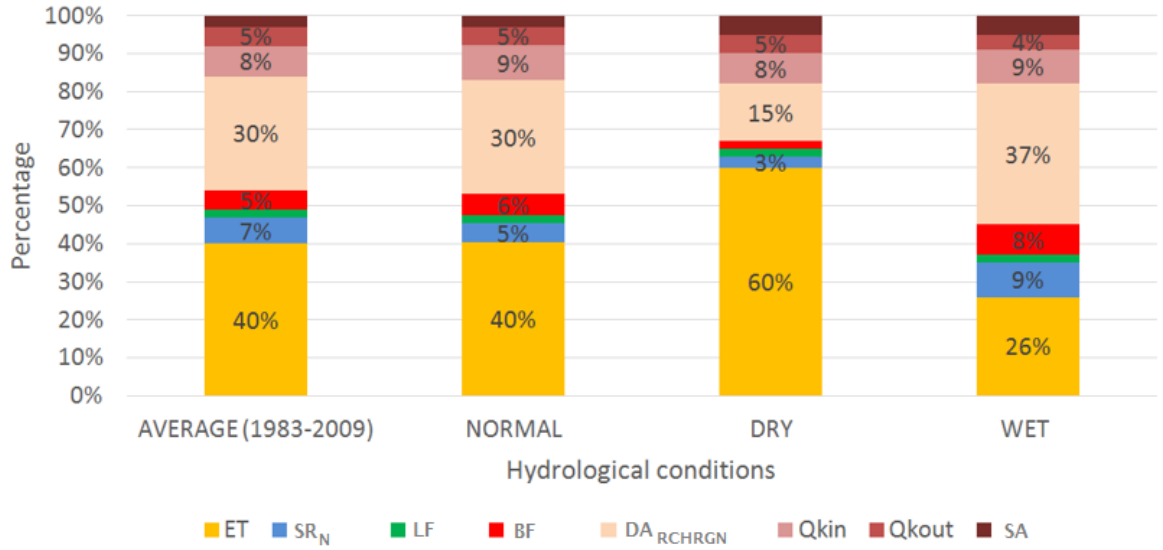


Figure 54. Annual water balance in different hydrological conditions (in percentage), average of 27 years (total volume of precipitation 6370 $Mm^3/y$), normal year (total volume of precipitation 6400 $Mm^3/y$), dry year (total volume of precipitation 3700 $Mm^3/y$) and wet year (total volume of precipitation 9600 $Mm^3/y$). ET, evapotranspiration; $SR_N$, surface runoff excluding losses from tributaries and wetlands; LF, lateral flow; BF baseflow; $DA_{RCHRGN}$, amount of water recharge in the deep aquifer without the contribution for springs that discharge inside (Qkin) and outside (Qkout) Crete Watershed; SA, shallow aquifer storage.

In addition, Figure 55 represents the previous results following the KSWAT model approach providing a more readable and systematic information of the fluxes.

The evapotranspiration volume ranged from around 2250 $Mm^3/y$ in the driest year to 2500 $Mm^3/y$ in the wettest year exhibiting a small variation in terms of absolute values but with a significant variation with respect to the total volume of precipitation (Figure 54). In the wettest year the main component of hydrological processes was the deep aquifer recharge, while in the driest year the evapotranspiration had the main role. From dry to wet year the

surface runoff increased from 95 $Mm^3/y$ to more than 800 $Mm^3/y$ and the total net water available in the deep aquifer increased from 550 $Mm^3/y$ to around 3500 $Mm^3/y$ in dry and wet year, respectively.

As a consequence, during the wet conditions there was high infiltration, but also the surface runoff was larger than that during driest and normal hydrological condition. On the other hand, in dry years there was also significant percolation to the deep aquifer (1000 $Mm^3/y$). This result was also highlighted by Hartmann et al. (2014, 2015) pointing out that karst regions might be more resilient to climate change in terms of both flooding and droughts. Furthermore, the authors demonstrated the existence a nonlinear relationship between precipitation and recharge rate indicating that the recharge of deep aquifer is more sensitive to a decrease than to an increase of precipitation (Hartmann et al., 2014). This was confirmed also in this study where the total deep aquifer recharge was estimated 28% of precipitation in driest year, while was 50% in wettest year departing of 16% and 6% from normal conditions, respectively.

Concerning the percentage of water balance components (Figure 55), it was estimated that from the total precipitation of 6400 $Mm^3/y$ about 40% was lost through evapotranspiration, 55% infiltrates and only 5% was surface runoff. The surface runoff including lateral flow (LF), baseflow (BF) and spring's discharge (Qkin) contribution to streamflow represents 22% of total precipitation. The total amount of deep aquifer recharge was around 44% of which 14% contributed as springs discharge to streamflow (Qkin=9%) or sea (Qkout=5%) (Figure 55b). These percentages were valid for all years in normal hydrological conditions (for instance year 1987), but they changed in extreme hydrological conditions.

Considering the driest year (year 1990, Figure 55c), it was estimated that from the total precipitations of 3700 $Mm^3/y$ about 60% was lost through evapotranspiration, 37% infiltrated and only 3% was surface runoff.

The amount of deep aquifer recharge decreased with respect to the normal hydrological condition to 28% of which 13% contributed as springs discharge to streamflow (Qkin=9%) or sea (Qkout=4%). The total contribution to freshwater decreased to 14% with respect to the normal condition.

In the wettest year (year 2003, Figure 55c), considering a total volume of precipitation around 9600 $Mm^3/y$, evapotranspiration was estimated around 26%, 65% was infiltration and 9% was surface runoff. The deep aquifer recharge reached the highest percentage of 50% and the water yield increased to 28%. Our work has shown that the evapotranspiration ranged between 2250 $Mm^3/y$ in a driest year and of 2500 $Mm^3/y$ in wettest year, corresponding to 60% and 26% of total precipitation, respectively. These results suggested the importance of karst water supply during dry periods.

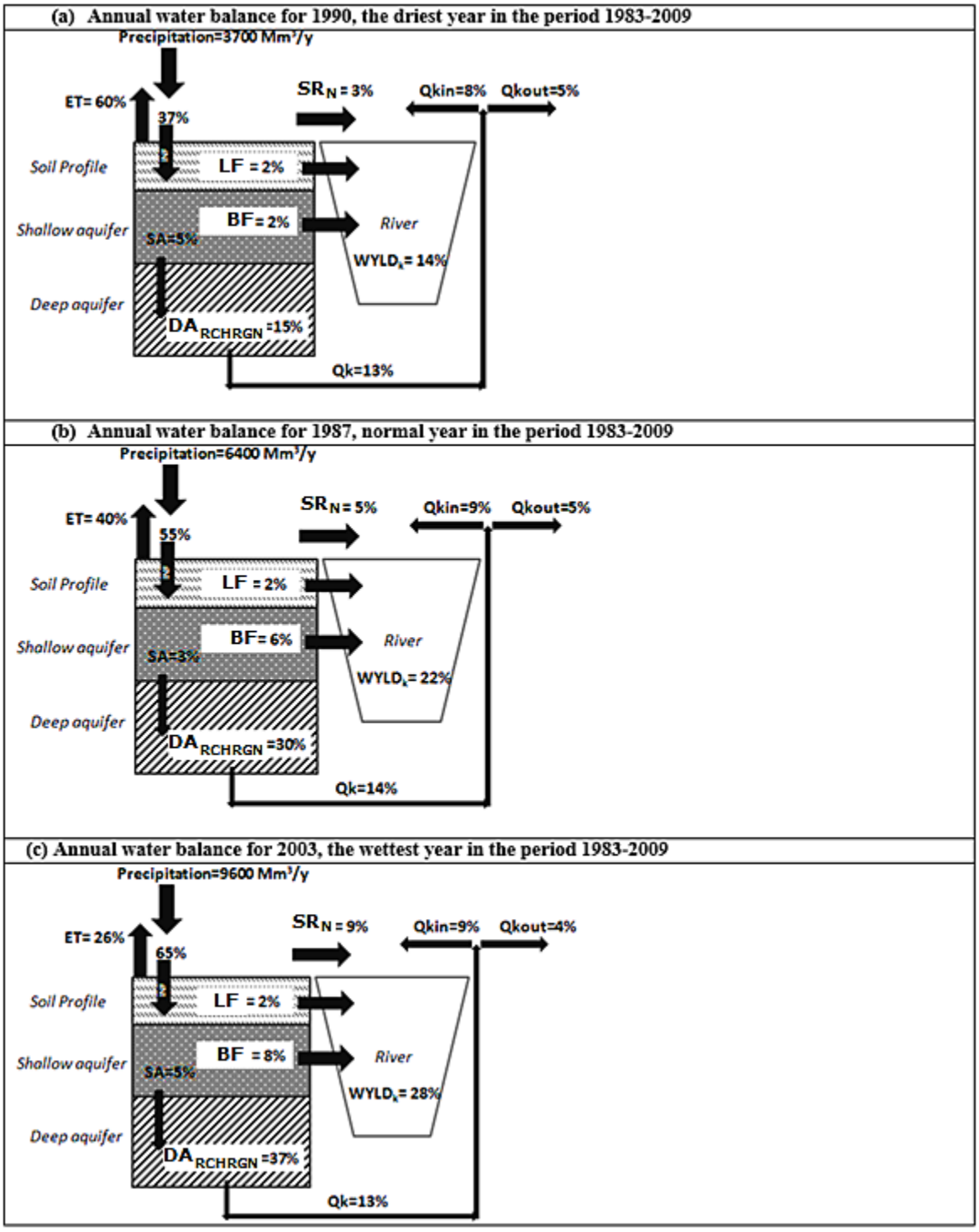


Figure 55. Annual water balance schematization in different hydrological conditions, dry (a), normal (b) and wet (c) year. ET, evapotranspiration; INF, infiltration in the soil; $SR_N$, surface runoff excluding the losses from tributaries and wetlands; LF, lateral flow; BF, baseflow; $DA_{RCHRGN}$, amount of water recharge in the deep aquifer without the contribution for springs that discharge inside (Qkin) and outside (Qkout) Crete; $WYLD_k$, freshwater contribution; SA, shallow aquifer storage.

### 3.5.10 Conclusions of section

The Crete SWAT model was able to capture the spatial and temporal variability of streamflow and karst flow in Crete, in spite of the inherent uncertainty in the observed data. In particular, the monthly time step of streamflow has limited the application of step-wise calibration not allowing a reliable estimation of each component of the streamflow.

However, a scaling-up methodology was developed based on the regionalization of parameters obtained in monitored subbasins and extended to ungauged subbasins. In particular, the KSWAT model allowed calibrating the daily spring' discharges in 47 gauging stations, estimating their karst recharge areas and their introduction in the SWAT model increased the performance of streamflow prediction in karst-subbasins. These springs contributed significantly to total discharge with 300 $Mm^3/y$ and 850 $Mm^3/y$ respectively in dry and wet hydrological conditions. In addition, the seasonal variation of volume of springs suggests that these valuable sources should be conserved and preserved in particular from April to September when available volumes are the lowest and agriculture and tourism demand increases.

The analysis of the water balance also showed that water resources are not homogeneously distributed in Crete and change significantly in different hydrological conditions. In particular, the western part of Crete has a surplus of water resources with respect to the eastern part where there is low water availability and high demand. Messara Valley (Geropotamos Basin) is an example of intensively managed basin in south-eastern Crete where an overexploitation of groundwater is occurring in a large number of wells since 1984 that continue to decrease groundwater levels at alarming proportions (Kritsotakis and Tsanis, 2009).

In this context, the present study provides a methodology and a tool for the integrated water management of Crete and other similar areas, by providing detailed spatially distributed hydrologic balances and accurate estimation of water availability using both hard and soft data.

# CHAPTER 4

# 4 Water quality and sediment modeling

## 4.1 Chapter Introduction

This Chapter describes the application of nutrients and sediments calibration strategy described in Chapter 2. In addition, it details the proposed water quality-economic scenarios based on a multiple-objective optimization. The procedure is applied in the Danube River Basin.

## 4.2 Nutrients representation: a case study applied to the Danube River Basin

### 4.2.1 Synopsis

Water quality models are usually evaluated through the comparison of modelled and estimated nutrients loads using established performance criteria (i.e. Moraisi et al., 2007b), and the processes and responses within watershed that govern these global fluxes are often neglected (Yen et al., 2014).

In SWAT due to the large number of parameters available for calibration, excellent model performances may be achieve using inaccurate magnitudes of these “intra-watershed” responses. Furthermore, the unrealistic prediction of nutrients fluxes, may lead to inaccurate conclusions when assessing the effects of BMPs. As a consequence, the soft data that describe internal watershed behavior (i.e. crop yields and denitrification) are crucial and should be included in the model calibration in addition to the appropriate field data.

However, for the parameter estimation purpose the objective remains minimizing the errors between observation and model predictions at stream locations where observed time series are available. In this context, the use of nutrients loads increases the model uncertainty since the choice of the load estimation technique has been shown to have a large impact on the final estimate, as well as the combined uncertainty of streamflow and concentration measurements and their frequency (Lloyd et al., 2015; Ullrich and Volk, 2010).

In this study, data related to internal watershed behavior are used to maintain realistic intra-watershed responses while also matching available in-stream nutrient concentrations in at multiple gauging stations decreasing the uncertainty on predicted nutrients fluxes and increasing the reliability of the SWAT model for BMPs implementation. In particular, the crop yields are simulated and validated on annual basis for a more accurate estimation of

the nutrients crop uptake. In addition, the annual denitrification (kg/ha) in the soil obtained from literature sources was used to better constrain the parameters related to denitrification process. The loads were not used directly for calibration, but were employed in the evaluation of the model results in terms of monthly and annual loads. In particular, the annual loads were involved in a model-inter-comparison study as described later in Chapter 5.

The methodology is applied in the Danube River Basin where water quality has become a key issue for over the last 50 years (Schmidt, 2001). A detailed description of the Danube River Basin is given in section 3.3.2.

The first attempt to map the water quality in the basin is reported by Liepolt (1967). Between the 1950s and 1970s, water quality was particularly degraded downstream of cities and industrial areas in the Upper Danube and the self-purification capacity of the river suffered from toxic industrial wastewater inputs. In the early 1980s, construction of wastewater treatment plants (WWTP) led to a major reduction of biodegradable organic matter and improved the water quality in the Upper Danube (Wachs, 1997). Instead, water quality in the Middle and Lower Danube remained relatively good between 1950 and the 1970s (Russev, 1979), but deteriorated afterwards due to rapid industrial development, poor pollution control, and inputs from heavily polluted tributaries (Tockner et al., 2009).

Since the EU Water Framework Directive entered into forced and the International Commission for the Protection of Danube River (ICPDR) was established, a legal background for water quality management in the whole Danube Basin was developed. In particular, nutrients including nitrogen and phosphorus are key elements impacting the quality of Danube and Black Sea.

The ICPDR has historically relied on the Modeling Nutrient Emissions into River Systems model (MONERIS; Behrendt et al., 2000; Venohr et al., 2011) to provide an annual assessment of nutrient diffuse emissions and loads. The application of the model has a quite long story in the Danube countries and at the basin scale as well in the field of river basin management and establishment of nutrient balances.

This study aimed at developing a SWAT nutrients model of the Danube River Basin to provide an accurate representation of nutrient transformations and losses and identify potential knowledge gaps. Unlike other studies, this study will focus on the prediction of the seasonal nutrient concentration including also the use of soft data to capture the intra-behavior dynamics of the Basin. The hydrological simulations and water balance were previously described in section 3.3 and are not further discussed here. Here instead, after presenting a comprehensive review of the data collected, the model calibration and evaluation results are analyzed across the water management regions (see Figure 22 in

section 3.3.2). Furthermore, the long-term mean annual nutrients balances are presented for the entire Danube Basin.

### 4.2.2 The Danube River Basin SWAT model: the nutrients setup

As described in section 3.3.2, the Danube SWAT model consists in a modelled area of about 830000 $km^2$ subdivided in 4663 subbasins and 5181 HRUs. 145 of these subbasins, namely *other basins*, contribute directly to the Black Sea.

The spatial data used to setup the Danube model are summarized in Table A1.1 (Appendix A1) and include the main nutrients inputs such as the amount of mineral and manure fertilizers retrieved from the CAPRI model (Britz, 2004), the atmospheric depositions of nutrients taken from the Cooperative Programme for the Monitoring and Evaluation of the Long-Range Transmission of Air Pollutants in Europe (EMEP, 2001) and the nutrient discharges in the river network from point sources (UWWTD database; ICM, 2011). The biological nitrogen fixation simulated by SWAT is another nutrient input that depends on the crop-specific fixation rate in each HRUs according to the climate, plant type and growth.

Furthermore, to proceed with the calibration and assessments of nutrient fluxes, the SWAT model was activated to perform water quality transformation in the reach (ISUBQ=1), and initial values of nitrates concentration in the shallow aquifer, as well as nitrogen and phosphorous concentration in reservoirs were introduced allowing to initialize the nutrients pool with 5 years of warm up.

The initial concentration of nitrates in the shallow aquifer (identified as SHALLST_N parameter) was calculated using measured values in wells. Instead, the long-term mean of nutrients concentrations at streamflow gauging stations immediately located downstream to a reservoir were used to initialize its concentration. Table 14 summarizes the land cover characteristics (see also Figure 56) for each water management region, as well as the amount of applied fertilizers, the nutrients discharged in the river network from point sources and the fixed nitrogen by plants.

The total nitrogen fertilization rate applied in the Danube river basin was around 34 kg/ha, subdivided in 57% of nitrate (19.5 kg/ha), 8% of ammonia (2.7 kg/ha) and 35% of organic nitrogen (12 kg/ha). The largest amount of nitrogen fertilizers was applied in the Danube Source (108 kg/ha), in Morava River Basin (78 kg/ha) and in Pannonia Danube (68 kg/ha). The total phosphorus applied ranged from 1.8 kg/ha in the Jiu River Basin (region 12) to 15 kg/ha in the Danube Source, with an average of 5.6 kg/ha in the entire Danube. In particular, the inorganic phosphorus contributed for 80% to total phosphorous applied as fertilizer. Figure 58 and Figure 59 show the spatial distribution of total nitrogen and phosphorous in

the Danube River Basin. The nitrogen fixed by plants was around 31.4 kg/ha in the entire Danube, with highest values in the Lower Danube.

The nitrogen applied to the soil from the atmospheric deposition is computed by SWAT per day in each subbasin according to the precipitation and the average nitrogen concentration in precipitation. This average concentration (identified with parameter RCN) was fixed equal to 1.8 accordingly to the EMEP data for the period 1995-2005 (EMEP, 2001). The resulted input of nitrogen from atmospheric deposition applied by SWAT was around 12.6 kg/ha in the entire Danube, reaching 22 kg/ha in the Inn River Basin, as shown in Figure 60.

In the Danube nutrient pollution from point sources is mainly caused by emission from insufficiently or untreated wastewater treatment plant into streamflow. These data retrieved from the UWWTD database (ICM, 2011) were aggregated at subbasin level and introduced in SWAT as point sources.

Figure 61 and Figure 62 show the spatial distribution of the total nitrogen (TN) and total phosphorous (TP) discharges from point sources in the streamflow. About 220 kton/y of TN and 21 kton/y of TP contributed to pollute the Danube River Basin. In particular, the Sava river basin was affected by about 43 kton/y of TN and 4 kton/y of TP.

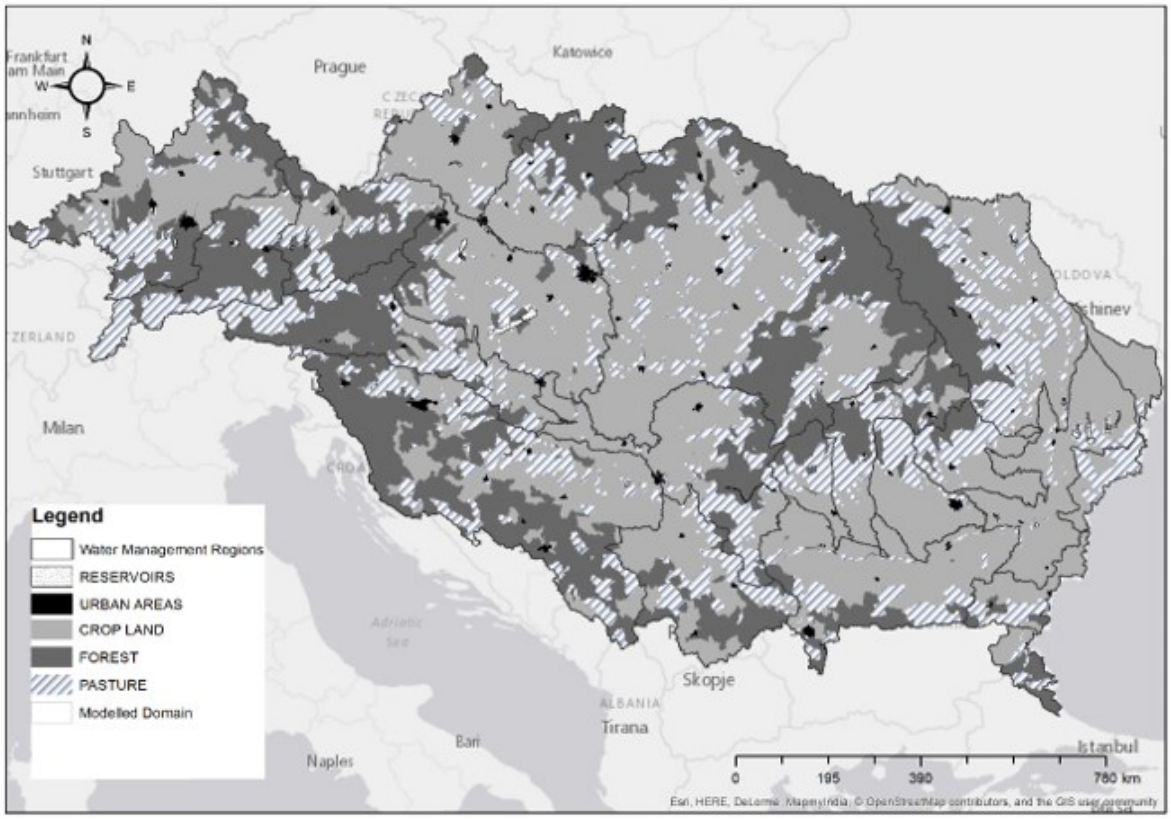


Figure 56. Spatial distribution of land cover in SWAT in the Danube River Basin.

Table 14. Overview of the land cover characteristics, amount of fertilizers and nutrient discharges from point sources (PS) in the water management regions of the Danube Basin. The percentage is calculated excluding upstream area. $N_{APP}$: total nitrogen (TN) fertilizer applied; $NO3_{APP}$: Nitrate fertilizer applied; $NH3_{APP}$: ammonia fertilizer applied; $ORGN_{APP}$: organic nitrogen applied; $P_{APP}$: total phosphorous (TP) fertilizer applied; $SOLP_{APP}$: mineral phosphorous applied; $ORGP_{APP}$: organic phosphorous applied; $N_{RAIN}$: nitrate added to soil profile by rain; $N_{FIX}$: nitrogen fixation.

| ID | Name | Area ($km^2$) | Drain Area ($km^2$) | CROP LAND | IRRIGATED Area[1] | ARTIFICIAL DRAIN AREA | FOREST | PASTURE | $N_{APP}$ | $NO3_{APP}$ | $NH3_{APP}$ | $ORGN_{APP}$ | $P_{APP}$ | $SOLP_{APP}$ | $ORGP_{APP}$ | $N_{RAIN}$ | $N_{FIX}$ | TN from PS | TP from PS |
|---|---|---|---|---|---|---|---|---|---|---|---|---|---|---|---|---|---|---|---|
| | | | | (%) | (%) | (%) | (%) | (%) | kg/ha | kg/ha | kg/ha | kg/ha | kg/ha | kg/ha | kg/ha | kg/ha | kg/ha | kton/y | kton/y |
| 1 | Danube Source | 49,769 | 49,769 | 44% | 0% | 6% | 36% | 19% | 107.87 | 57.72 | 9.16 | 41.00 | 14.68 | 10.73 | 3.97 | 16.41 | 18.59 | 14.35 | 0.98 |
| 2 | Inn | 25,999 | 25,999 | 8% | 0% | 2% | 51% | 41% | 20.57 | 9.81 | 1.98 | 8.86 | 3.53 | 2.71 | 0.86 | 22.05 | 35.35 | 6.19 | 0.38 |
| 3 | Austrian Danube | 26,036 | 101,803 | 18% | 0% | 4% | 54% | 27% | 25.37 | 13.61 | 2.15 | 9.62 | 5.81 | 4.96 | 0.93 | 17.86 | 36.38 | 6.52 | 0.34 |
| 4 | Morava | 26,628 | 26,628 | 73% | 1% | 6% | 13% | 13% | 78.00 | 51.51 | 4.87 | 21.88 | 10.49 | 8.57 | 2.11 | 11.07 | 18.10 | 5.45 | 0.23 |
| 5 | Vah-Hron-Ipel | 30,587 | 30,587 | 39% | 3% | 15% | 40% | 21% | 33.30 | 20.43 | 2.39 | 10.71 | 5.32 | 4.40 | 1.03 | 13.21 | 27.21 | 6.55 | 0.77 |
| 6 | Pannonian Danube | 52,085 | 211,103 | 71% | 1% | 17% | 14% | 13% | 68.35 | 47.31 | 3.87 | 17.31 | 9.82 | 8.37 | 1.67 | 10.87 | 22.06 | 20.19 | 1.29 |
| 7 | Drava | 39,679 | 39,679 | 21% | 0% | 3% | 47% | 32% | 29.12 | 17.22 | 2.19 | 9.82 | 5.33 | 4.44 | 0.95 | 16.00 | 46.52 | 10.45 | 0.92 |
| 8 | Sava | 100,102 | 100,102 | 32% | 0% | 5% | 48% | 20% | 30.52 | 15.11 | 2.86 | 12.81 | 5.16 | 4.12 | 1.24 | 17.60 | 36.57 | 42.89 | 3.94 |
| 9 | Tisa | 149,567 | 149,567 | 50% | 1% | 17% | 33% | 16% | 36.60 | 22.29 | 2.67 | 11.95 | 5.31 | 4.30 | 1.16 | 11.63 | 24.88 | 25.76 | 2.68 |
| 10 | Velika Morava | 37,702 | 37,702 | 48% | 0% | 1% | 30% | 22% | 33.57 | 18.75 | 2.72 | 12.19 | 4.61 | 3.59 | 1.18 | 12.67 | 38.28 | 10.06 | 0.86 |
| 11 | Middle Danube | 44,261 | 582,414 | 54% | 0% | 22% | 22% | 23% | 40.19 | 23.04 | 3.21 | 14.36 | 6.25 | 5.23 | 1.39 | 12.04 | 36.20 | 13.16 | 1.32 |
| 12 | Jiu | 10,333 | 10,333 | 32% | 2% | 0% | 30% | 38% | 8.44 | 5.56 | 0.56 | 2.50 | 1.85 | 1.67 | 0.24 | 12.13 | 63.34 | 2.08 | 0.27 |
| 13 | Olt | 23,841 | 23,841 | 31% | 2% | 0% | 40% | 28% | 15.86 | 7.94 | 1.49 | 6.67 | 2.98 | 2.43 | 0.65 | 12.05 | 42.60 | 5.11 | 0.70 |
| 14 | Arges Vedea | 18,118 | 18,118 | 68% | 3% | 3% | 4% | 27% | 22.99 | 14.03 | 1.73 | 7.73 | 4.78 | 4.23 | 0.75 | 11.22 | 32.68 | 13.48 | 1.87 |
| 15 | Silistra Danube | 50,615 | 685,320 | 68% | 2% | 3% | 14% | 17% | 29.25 | 18.54 | 2.00 | 8.93 | 4.17 | 3.48 | 0.86 | 10.91 | 20.69 | 9.15 | 1.25 |
| 16 | Buzau-Ialomita | 16,358 | 16,358 | 51% | 9% | 0% | 16% | 33% | 14.43 | 9.36 | 0.95 | 4.27 | 3.04 | 2.76 | 0.41 | 10.63 | 51.00 | 3.03 | 0.32 |
| 17 | Siret-Prut | 66,250 | 66,250 | 39% | 1% | 0% | 27% | 34% | 15.99 | 7.14 | 1.66 | 7.45 | 3.30 | 2.67 | 0.72 | 10.77 | 36.94 | 12.17 | 1.54 |
| 18 | Delta | 34,104 | 802,032 | 91% | 2% | 3% | 0% | 9% | 25.51 | 13.12 | 2.32 | 10.39 | 5.15 | 4.36 | 1.00 | 8.64 | 14.42 | 6.99 | 0.90 |
| NA | Other basins | 31,877 | 31,877 | 59% | 0% | 1% | 14% | 27% | 26.31 | 14.19 | 2.25 | 10.07 | 4.41 | 3.59 | 0.97 | 9.07 | 19.32 | 6.37 | 0.83 |

1 Irrigated area was calculated for water management regions excluding upstream are

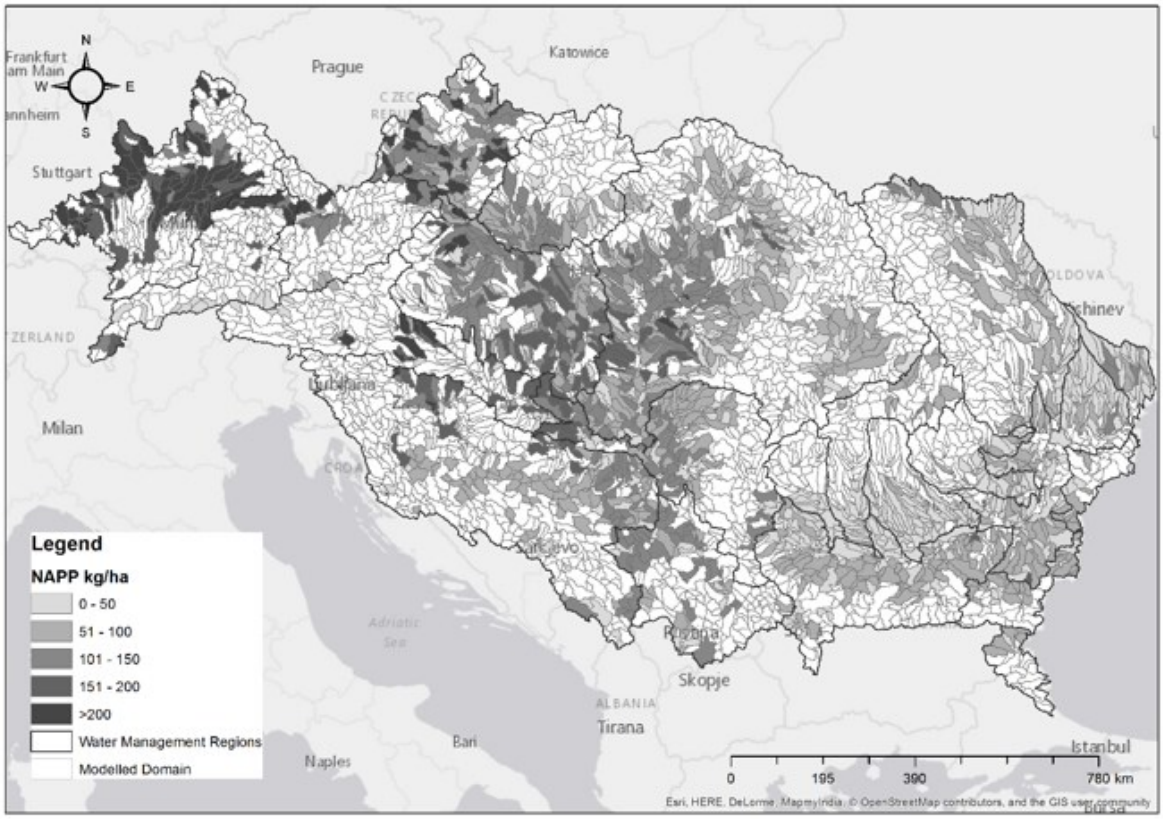


Figure 57. Spatial distribution of total nitrogen applied as fertilizer in the Danube River Basin.

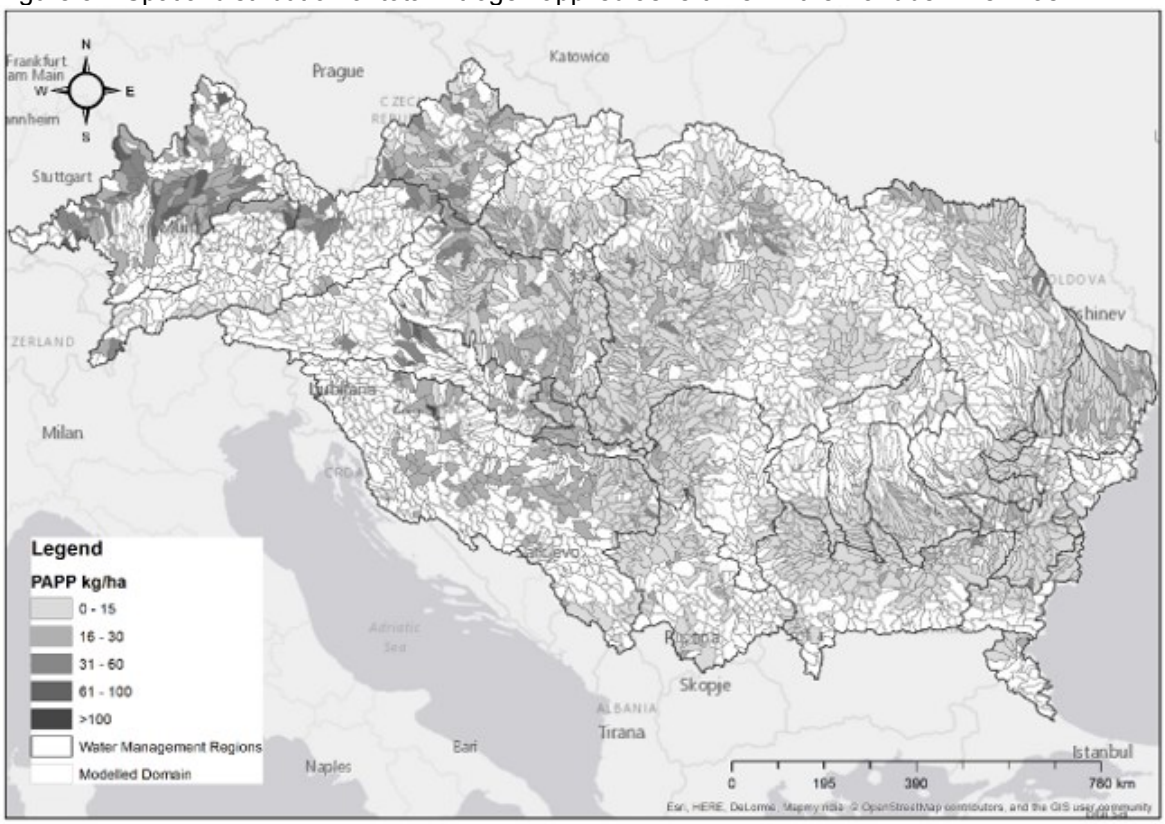


Figure 58. Spatial distribution of total phosphorous applied as fertilizer in the Danube River Basin.

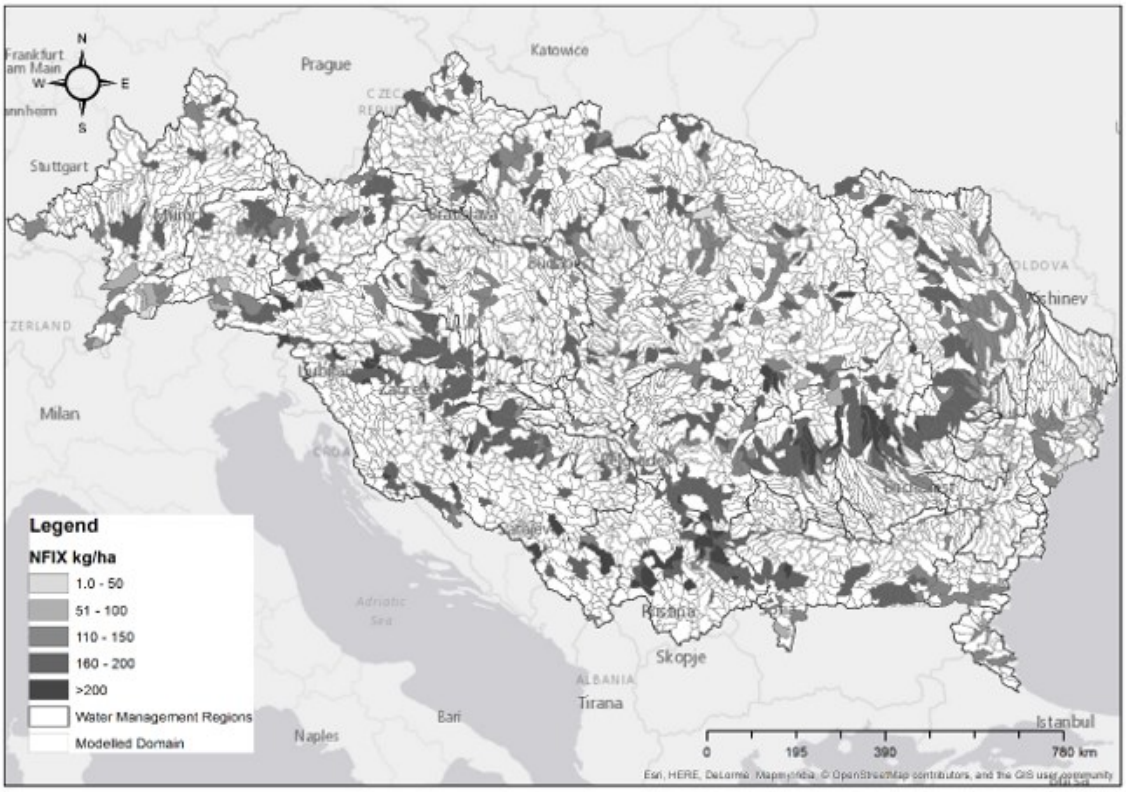


Figure 59.Spatial distribution of fixed nitrogen by plants in the Danube River Basin.

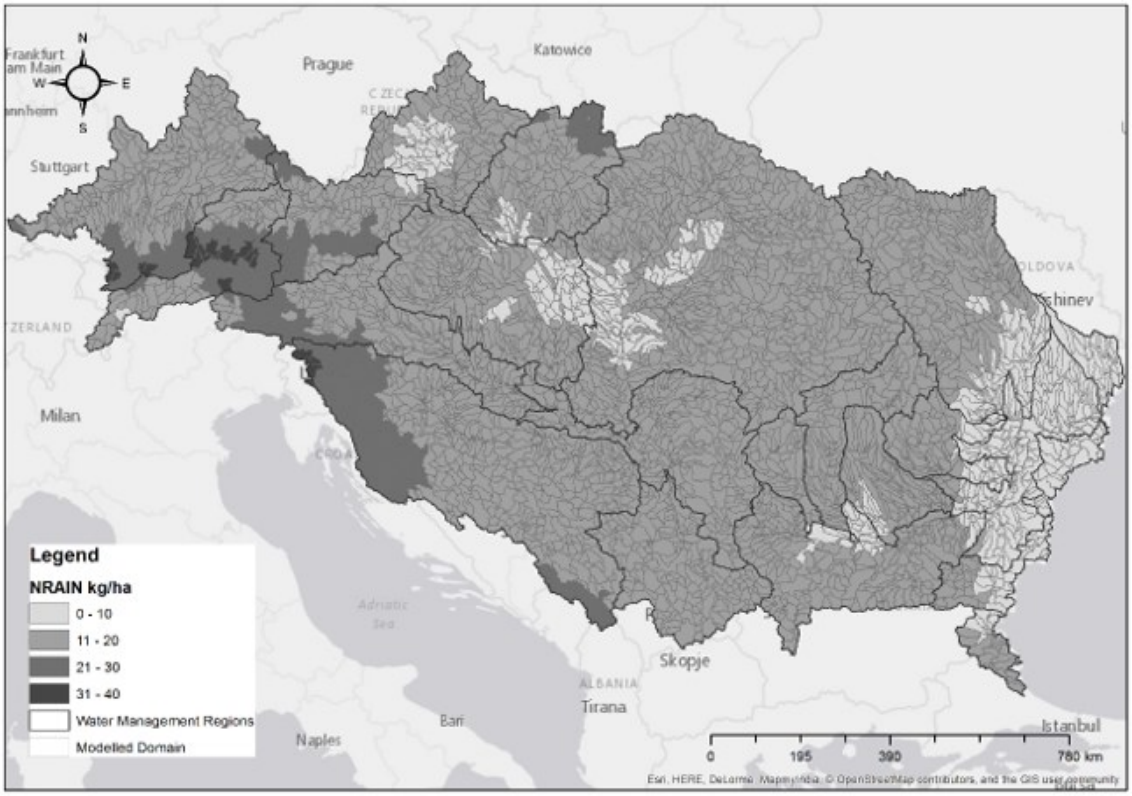


Figure 60. Spatial distribution of nitrogen applied to soil from atmospheric deposition in the Danube River Basin.

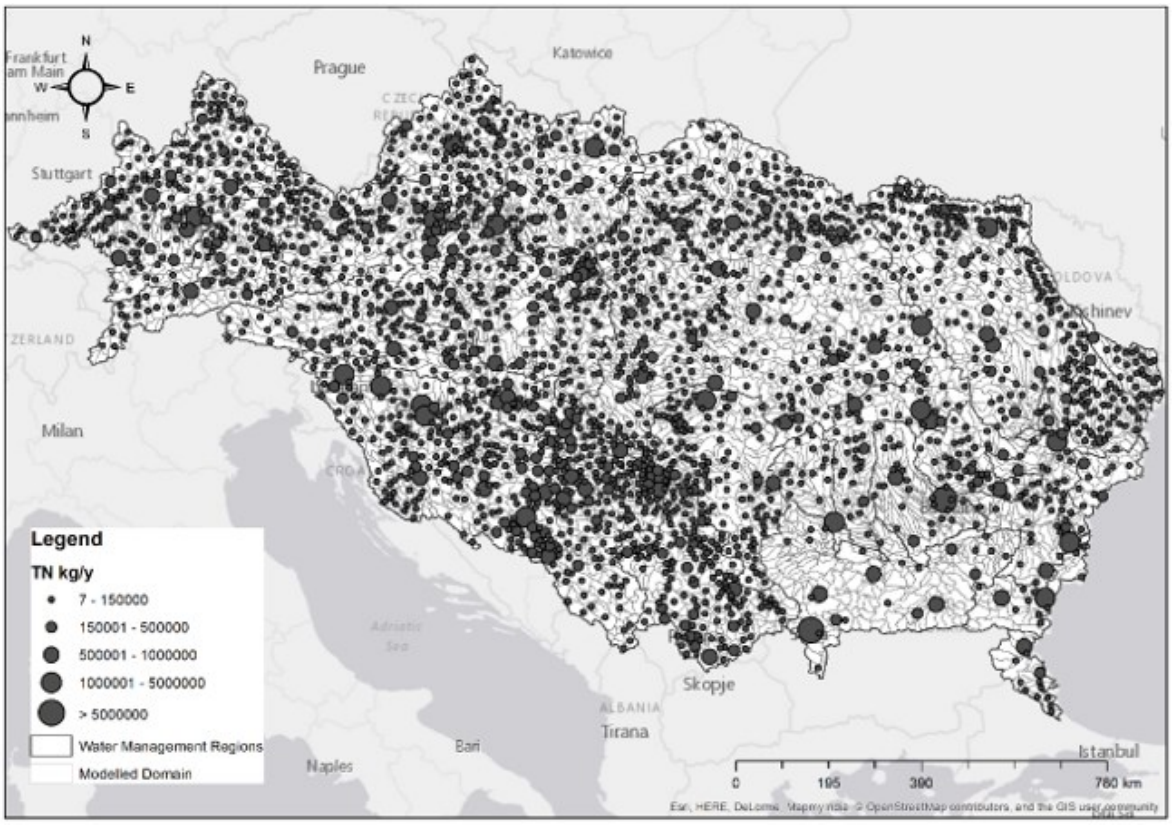


Figure 61. Spatial distribution of total nitrogen discharged in the river network from point sources.

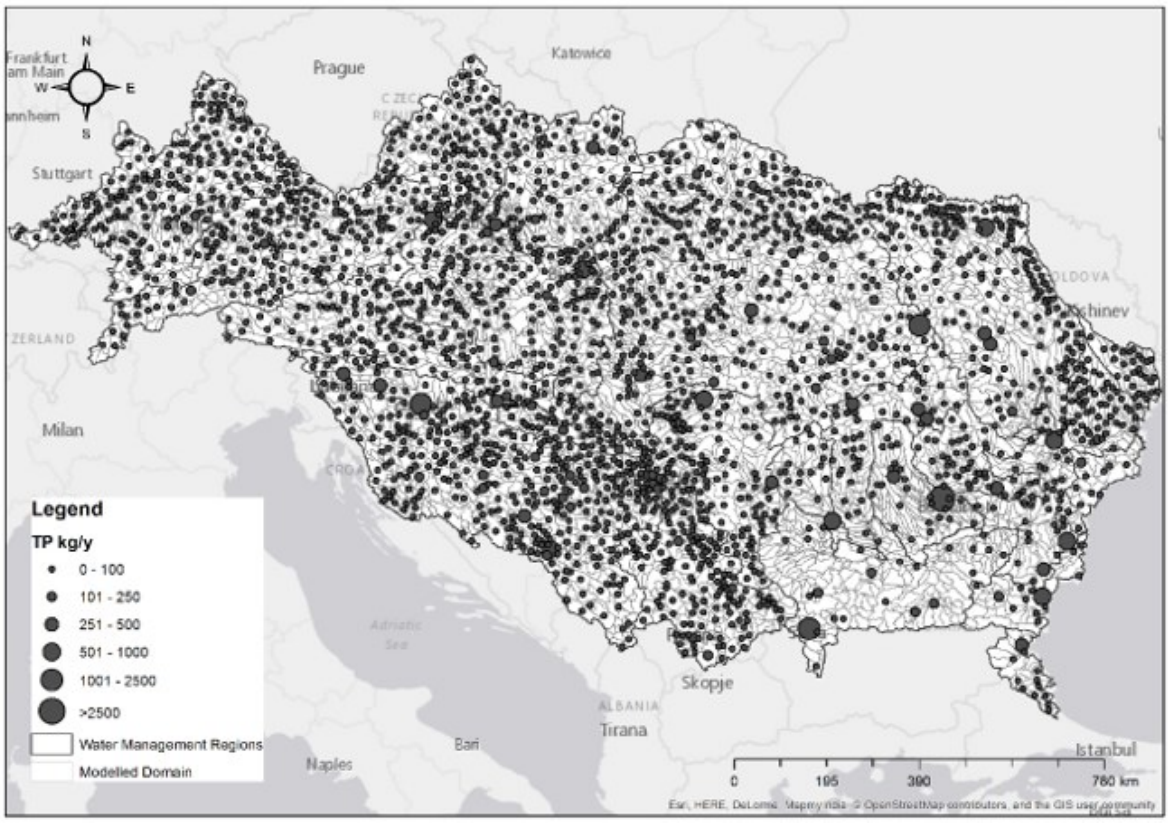


Figure 62. Spatial distribution of total phosphorous discharged in the river network from point sources.

### 4.2.3 Analysis of river concentrations and loads

An extensive database of nutrient concentration (mg/l) in the Danube River Basin was assembled from several sources (Table A2.2 in Appendix A2) covering the period 1995-2009 (15 years). Despite the fact that the data collection concerns both mineral and organic forms of total nitrogen (N-NH4, N-NO2, N-NO3, ORGN) and phosphorous (P-PO4), in this study only nitrates (N-NO3 mg/l or NO3 mgN/l), total nitrogen (TN, mg/l) and total phosphorous (TP, mg/l) were considered.

It is noteworthy however that an extensive correction of the reported measured values was necessary due to the encountered unrealistic values. Generally, these unrealistic values were due to typing errors, wrong units, or sometimes when the concentration referred to molecules instead of each element (i.e. nitrate, NO3 mg/l, instead of nitrate-nitrogen, N-NO3 mg /l). The corrections were applied identifying the concentrations that exceeded the median of the long-term seasonal values, as well as based on visual appraisal of the entire times series. Furthermore, the total nitrogen and phosphorus were verified by adding the different forms of element (TN or TP) for each data entry.

The frequency of sampling is generally once a month, but sometimes the measurements referred to three or more sampling locations (i.e. on the left, in the middle or on the right bank of the river) not always well documented. For stations with multiple sampling, the average concentrations were calculated each month.

Figure 63, Figure 64 and Figure 65 show the spatial and temporal long-term average concentration of N-NO3, TN and TP respectively. The long term-average concentration was calculated from the available data in three step: first, the average of available concentrations was performed each month; second, for each year the mean of concentration was calculated considering at least 9 monthly values albeit not restrictions were imposed on the distribution over the year; third, the long-term average of concentration for each station was calculated if almost 5 years with values was available. It is noteworthy that the concentration at the outlet of the Delta water management region was calculated as average of concentration in three gauging stations.

Although the spatial distribution of gauging stations is not homogeneous across the entire basin, a preliminary assessment of data available were performed across the whole Danube.

The long-term nitrate-nitrogen concentrations N-NO3 (Figure 63) reached the highest values in the Morava River Basin (mean value around 3 mg/l), followed by the Pannonian Danube region (mean value ~2.8 mg/l) and the Middle Danube (median value ~2 mg/l) . It was observed comparing N-NO3 and TN that nitrate-nitrogen is the main components of

TN (about 70% of TN) and that both concentrations decrease with increasing river size. The long-term average value is around 1.7 mg/l at the Delta.

The long-term nitrogen TN (Figure 64) is not available at all quality gauging stations since the organic nitrogen is not sampled frequently in the Danube River Basin (van Gils, 2004). The log-term TN concentration is the highest value in the Drava river basin and in the Pannonia Danube region with mean values of 6.7 and 4.5 mg/l respectively. At the Delta the long-term average N-NO3 concentration is around 2.3 mg/l.

The long-term total phosphorous (Figure 65) reached the highest values in Tisa River Basin and in the Pannonia Danube region with a mean value of around 0.37 mg/l, and decreased from the gauging station Hercegszanto (situated upstream of the confluences of the Drava-Tisa-Sava) up to 0.11 mg/l at the Delta.

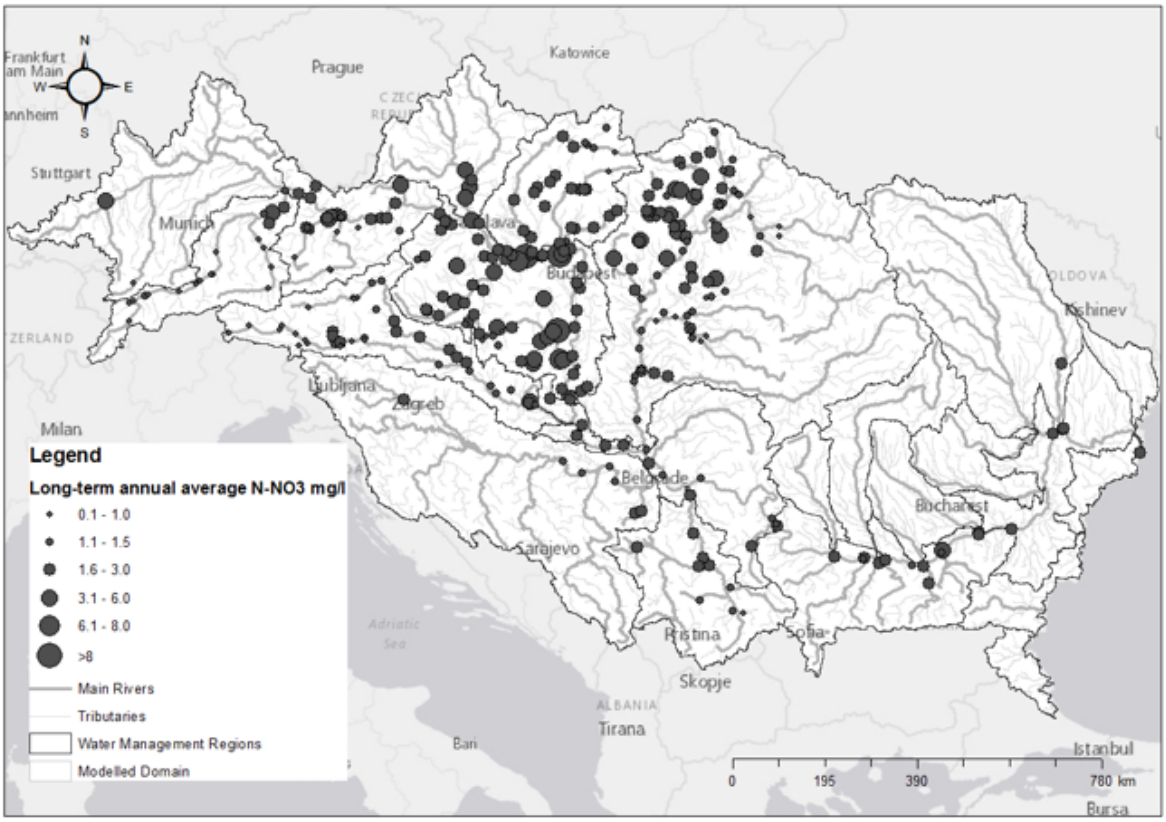


Figure 63. Long-term mean annual nitrate-nitrogen concentration (N-NO3, mg/l) at 314 gauging stations in the Danube River Basin.

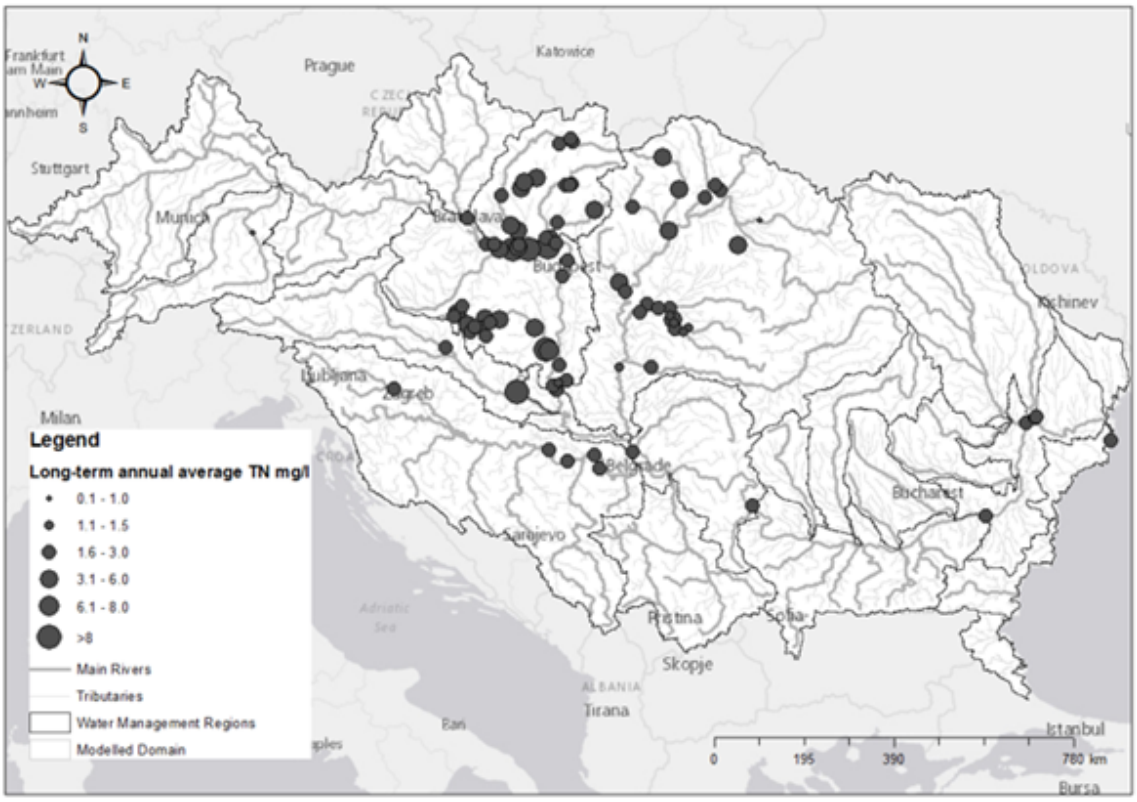


Figure 64. Long-term mean annual total nitrogen concentration (TN, mg/l) at 85 gauging stations in the Danube River Basin.

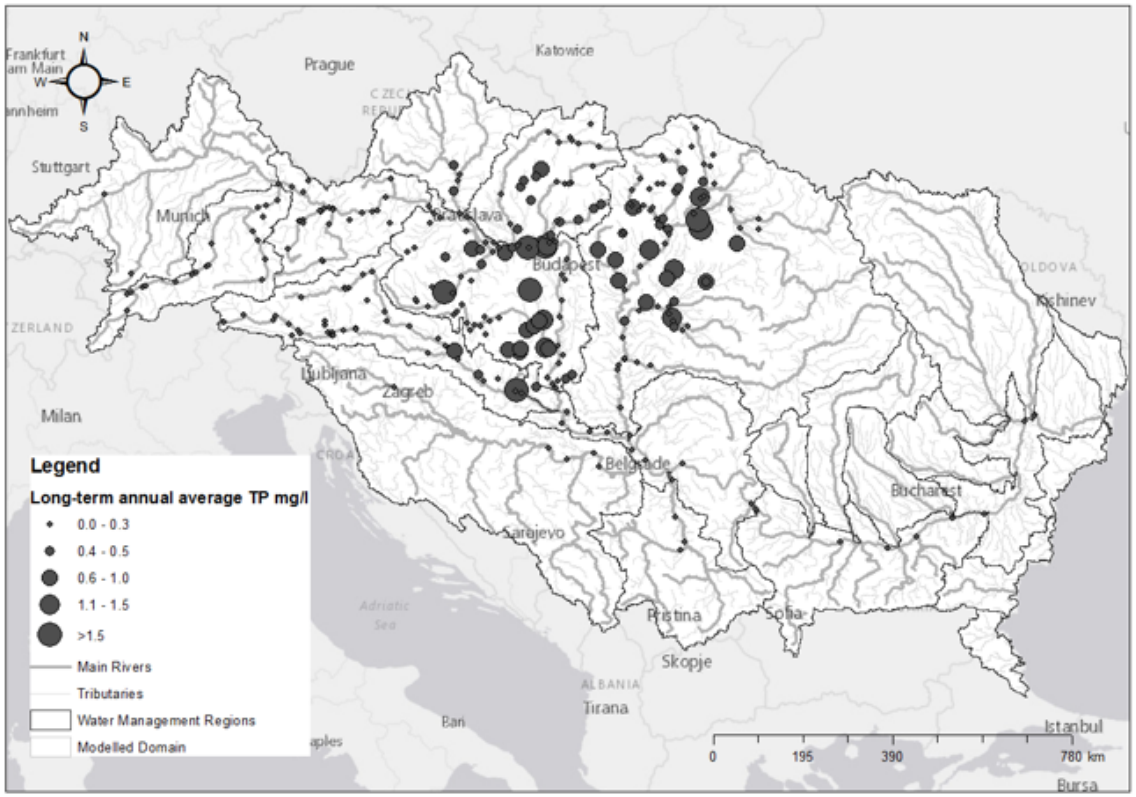


Figure 65. Long-term mean annual total phosphorous concentration (TP, mg/l) at 290 gauging stations in the Danube River Basin.

The monthly and annual loads were calculated as described in Chapter 2, using both nutrient concentration and daily flow using the flow weighted concentrations method proposed by Moatar and Meybeck (2005). For streamflow information, the reader can refer to section 3.3 and Table A2.1 and A2.2 in Appendix A2.

Here, for a comprehensive analysis of data available the long-term annual loads were described, albeit the monthly loads were used in this Chapter for model evaluation.

Figure 66, Figure 67 and Figure 68 show the long-term annual loads at several gauging stations in the Danube River Basin. They were calculated when at least 5 years of values were available. It is noteworthy that the figures show a spatial gradient very similar to the streamflow, albeit a larger year to year variation especially in Lower Danube was observed (see also van Gils, 2004).

The long-term loads of N-NO3 and TN at the Delta was 340000 and 450000 ton/y respectively. The TP instead was calculated as around 23000 ton/y, a lower value respect the upstream Middle Danube region that was around 25300 ton/y.

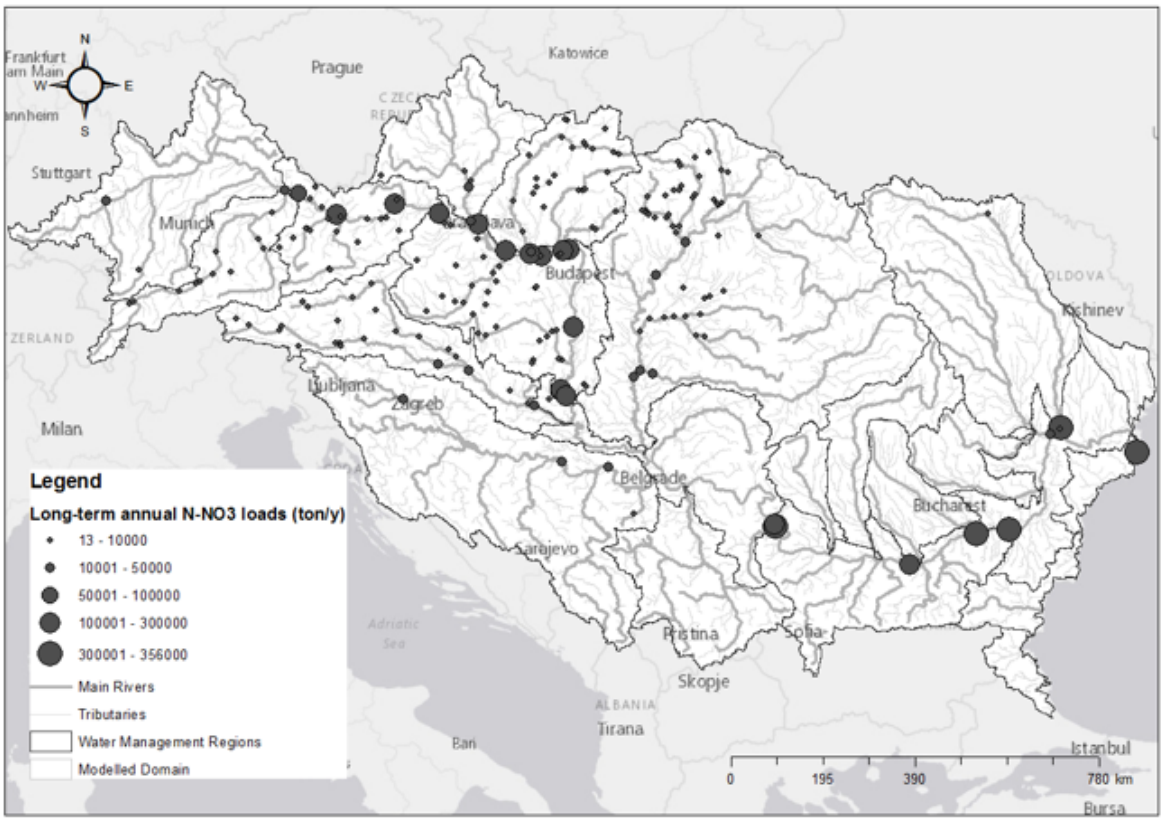


Figure 66. Long-term mean annual nitrate-nitrogen loads (N-NO3, kg/year) at 204 gauging stations in the Danube River Basin.

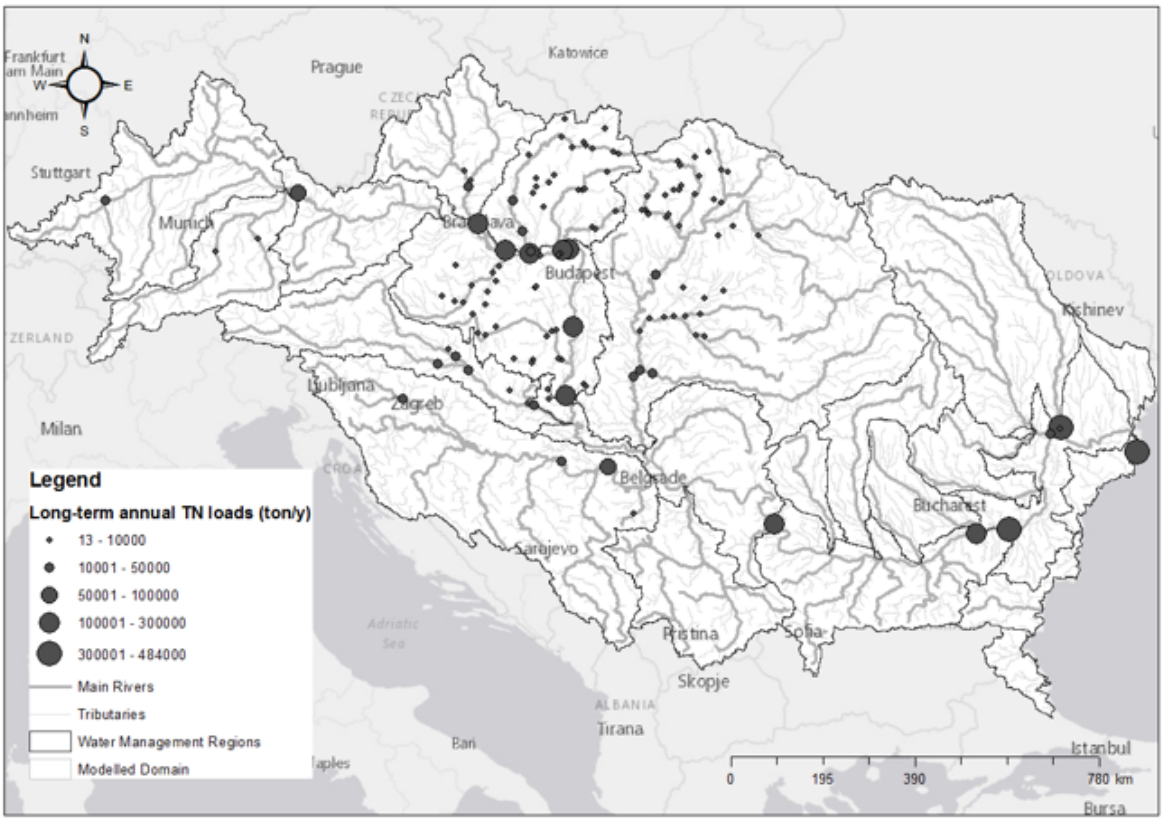


Figure 67.Long-term mean annual total nitrogen loads (TN, kg/year) at 130 gauging stations in the Danube River Basin.

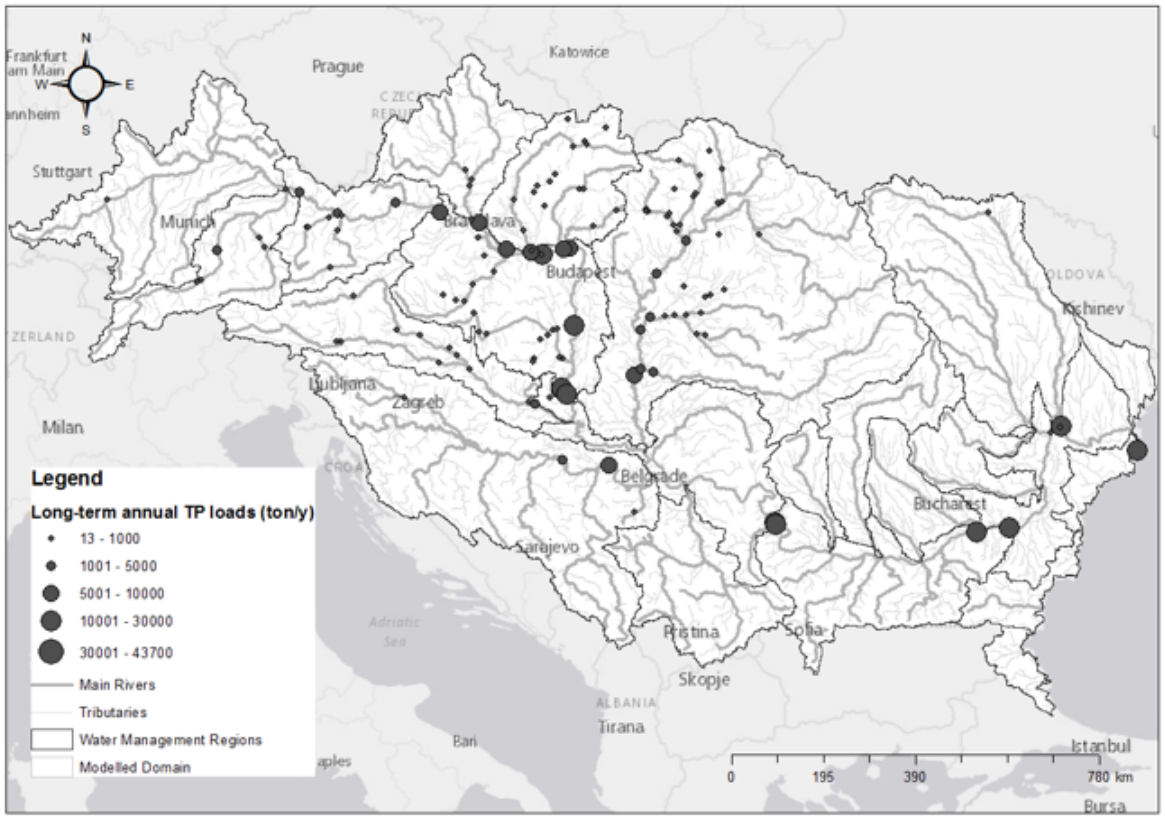


Figure 68. Long-term mean annual total phosphorous loads (TP, kg/year) at 204 gauging stations in the Danube River Basin.

Given the characteristics of the available nutrients data, the in-stream calibration was performed at monthly time step. In particular, the available gauging stations were all split into two groups, namely *calibration* and *evaluation* datasets. Unfortunately, the validation was not performed due to the limited spatial distribution of available gauging stations that if reduced may misrepresent the nutrients processes in large basins where the most sensitive parameters refer to the whole watershed (see section 4.2.4).

The calibration dataset comprised 340, 191 and 333 gauging stations of monthly concentration of N-NO3, TN and TP respectively. Instead, the evaluation dataset involved the monthly loads (ton/month) using respectively 202, 121 and 202 gauging stations for N-NO3, TN and TP.

### 4.2.4 The sensitivity analysis of nutrients parameters

The parameters selected from the SWAT model for sensitivity analysis were based on existing literature (i.e. Me et al., 2015; Haas et al., 2015; Yen et al., 2014; Cerro et al., 2012; Omani et al., 2012; Chu et al., 2003), personal judgments, and suggestions in SWAT's user manual. The selected parameters are summarized in Table 15 and Table 16. The SUFI-2 algorithm (Abbaspour, 2008) was used to explore parameter sensitivity of these parameters. Parameters were sampled in a Latin hypercube sampling scheme of 1000 model runs. The objective function was the root mean square error of the simulations divided by the standard deviation of the observations (RSR; Moriasi et al., 2007). The global sensitivity was measured by the value of the t-test (and associated probability level p-value) of the regression coefficient of each parameter against the objective function, as well as using a visual appraisal of dot-plots (parameter values vs RSR).

Concerning the use of t-test and related p-value, the larger in absolute term is the t-test value (and the lower is the probability p-value), the more sensitive is the parameter (Abbaspour, 2008). Instead using the dot-plots, the sensitivity is highlighted by a prevalent gradient of dot distribution.

The analysis was carried out for the main tributaries of the Danube River Basin, and since similar findings were obtained for each of them, hereafter the global sensitivity is described for the Morava River Basin where agriculture is the largest source of nutrients and contributes more than 65% of the total nitrogen and 30% of total nutrient load in the river (Tockner et al., 2009).

In the Morava River Basin, the t-test (p-value) was used for the global sensitivity analysis of parameters related to nitrogen and nitrate-nitrogen (Figure 69), while dot-plots were enrolled for parameters that influence the prediction of total phosphorous (Figure 70), thus exploring both the aforementioned techniques.

Table 15. List of SWAT parameters used in the sensitivity analysis for N-NO3 and TN. The parameters are in alphabetic order. For each parameter is reported the related input file (i.e. parameter AI1 is defined in the file wwq).

| Parameter | Process | Definition | Unit | Ranges | Default value |
|---|---|---|---|---|---|
| AI1.wwq | In-stream | Fraction of algal biomass that is nitrogen | mg N $mg^{-1}$ algae | 0.07-0.09 | 0.08 |
| BC1.swq | In-stream | Rate constant for biological oxidation of ammonium–nitrogen to nitrite–nitrogen in the reach at 20°C | $day^{-1}$ | 0.1-1 | 0.55 |
| BC2.swq | In-stream | Rate constant for biological oxidation of nitrite–nitrogen to nitrate–nitrogen in the reach at 20°C | $day^{-1}$ | 0.2-2 | 1.1 |
| BC3.swq | In-stream | Rate constant for hydrolysis of organic nitrogen to ammonium–nitrogen in the reach at 20°C | $day^{-1}$ | 0.2-0.4 | 0.21 |
| CDN.bsn | Denitrification in the soil | Denitrification exponential rate coefficient | NA | 0-3 | 1.4 |
| CMN.bsn | Mineralization in the soil | Rate factor for humus mineralization of active organic nitrogen | NA | 0.0001-0.0003 | 0.0003 |
| ERORGN.hru | Organic N losses via sediment | Organic nitrogen enrichment ratio | NA | 0-5 | 0 |
| HLIFE_NGW.gw | N in shallow aquifer and baseflow | Half-life of nitrate–nitrogen in the shallow aquifer | $day^{-1}$ | 0-200 | 0 |
| NPERCO.bsn | N in surface runoff | Nitrogen percolation coefficient | NA | 0-1 | 0.2 |
| NSETLR1.lwq | In-reservoir | Nitrogen settling rate | m/year | 1-15 | 5.5 |
| RCN.bsn | Nitrogen in precipitation | Concentration of nitrogen in rainfall | mgN/l | 0-15 | 0 |
| RS3.swq | In-stream | Benthic (sediment) source rate for ammonium–nitrogen in the reach at 20°C | mg $m^{-2}$ $day^{-1}$ | 0-1 | 0.5 |
| RS4.swq | In-stream | Rate coefficient for organic nitrogen settling in the reach at 20°C | $day^{-1}$ | 0.001-0.1 | 0.05 |
| RSDCO.bsn | Crop residue | Residue decomposition coefficient | NA | 0.02-1 | 0.05 |
| SDNCO.bsn | Denitrification in the soil | Denitrification threshold water content | NA | 0-1 | 1.1 |
| SHALLEST_N.gw | N in shallow aquifer | Nitrate–nitrogen concentration in the shallow aquifer | mg/l | 0-1000 | 0 |

Table 16. List of SWAT parameters used in the sensitivity analysis for TP. The parameters are in alphabetic. For each parameter is reported the related input file (i.e. parameter AI2 is defined in the file wwq).

| Parameter | Process | Definition | Unit | Ranges | Default value |
|---|---|---|---|---|---|
| AI2.wwq | In-stream | Fraction of algal biomass that is nitrogen | mg N $mg^{-1}$ algae | 0.07-0.09 | 0.08 |
| BC4.swq | In-stream | Rate constant for decay of organic phosphorous to dissolved - phosphorous in the reach at 20°C | $day^{-1}$ | 0.1-1 | 0.35 |
| ERORGP.hru | Organic P losses via sediment | Organic phosphorous enrichment ratio | NA | 0-5 | 0 |
| GWSOLP.gw | P-PO4 in baseflow | Soluble phosphorous in baseflow | mg/l | 0-1000 | 0 |
| PHOSKD.bsn | P in soil | Phosphorus soil partitioning coefficient | NA | 100-200 | 175 |
| PPERCO.bsn | P in surface runoff | Phosphorus percolation coefficient | NA | 10-17.5 | 10 |
| PSETLR1.lwq | In -reservoir | Phosphorus settling rate | m/year | 2-20 | 10 |
| RS2.swq | In-stream | Benthic (sediment) source rate for dissolved phosphorus in the reach at 20°C | mg $m^{-2}$ $day^{-1}$ | 0.001-0.1 | 0.05 |
| RS5.swq | In-stream | Organic phosphorus settling rate in the reach at 20°C | $day^{-1}$ | 0.001-0.1 | 0.05 |

Figure 69 shows the resulted t-test and p-value for each parameters of Table 15. The nitrate percolation coefficient NPERCO, which regulates the transport of nitrate via surface runoff, had the highest sensitivity, followed by ERORGN, that controls organic N losses via sediment yields, and the parameters that regulate the denitrification in the soil (CDN and SDCNO). The rate coefficient for organic nitrogen settling in the reach, RS4, resulted quite sensitive, while the other parameters had a negligible impact on calibrating NO3-N and TN concentration.

The most sensitive parameters related to phosphorus were ERORGP (Figure 70a), that controls organic P losses via sediment yields, followed by the in-stream parameter that regulates the transformation of organic P to dissolved P (BC4, Figure 70b). Figure 70c shows also that the soluble P concentration in the baseflow had a lower sensitivity respect to ERORGP and BC4. However, it increases when the concentration was larger than 0.1. All the other parameters had a negligible sensitivity, such as the phosphorus percolation coefficient PPERCO as showed in Figure 70d.

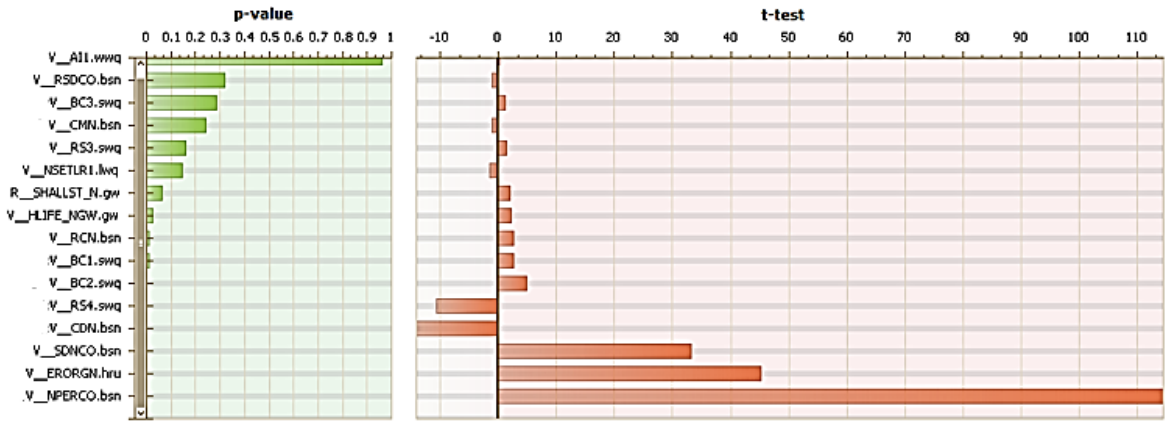


Figure 69. Global sensitivity analysis for parameters related to nitrogen and its forms using t-test and p-value. The letter V indicates that the default parameter value was replaced by a given value in the available range, while R means that the default value is multiplied by (1+a given rate value). The figure was extracted from the SWAT-CUP model (Abbaspour et al., 2008).

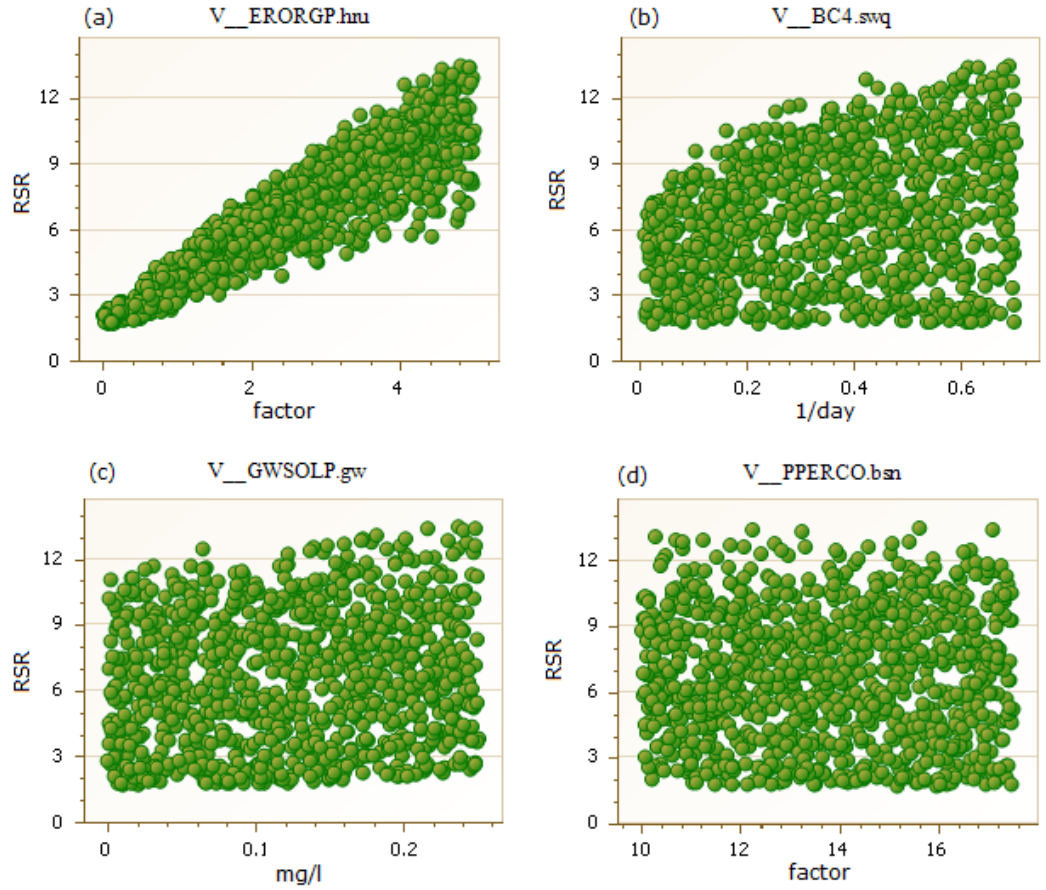


Figure 70. Global sensitivity analysis for some parameters related to phosphorous and its forms using dot-plots. The letter V indicates that the default parameter value was replaced by a given value in the available range. The figure was extracted from the SWAT-CUP model (Abbaspour et al., 2008).

The results of global sensitive analysis have allowed restricting the number of parameters involved in the calibration. However, despite the fact that some parameters resulted not sensitive they were parametrized using soft data and were considered as setup values. This is the case of nitrogen concentration in precipitation (RCN) and in shallow aquifer (SHALLEST_N) as described in the previous section. If necessary, these values were adjusted relatively (using rate values) during the calibration.

All in-stream parameters were excluded since they had a minor effect on model prediction, and since the limited available knowledge of in-stream processes didn't allow a reliable parametrization. Also GWSOLP was not included in the calibration since no relation between baseflow and phosphorus was found.

In conclusion, for calibrating the monthly concentration of nitrate-nitrogen and total nitrogen, 9 parameters were manually adjusted to give a best match with the monthly measured concentration at 340 and 191 gauging stations respectively, while only two parameters were calibrated for total phosphorous using 333 gauging stations.

The final ranges and values of these calibrated parameters are included Table 17 of which 7 of 11 are watershed parameters.

In particular, the denitrification exponential rate coefficient (CDN) and the denitrification threshold water content (SDNCO) were respectively adjusted to 2.5 and 1. Section 4.2.6 describes in detail the reliability of this parameterization.

The rate factor for humus mineralization of active organic nitrogen (CMN) was set to 0.000145 decreasing the default nitrogen mineralized from the humus active organic nitrogen pool, as well as the rate coefficient for mineralization of the residue fresh organic nutrients (SDNCO) that was set to 0.2. The most sensitive parameter NPERCO was set to 0.5 meaning that the concentration of nitrates in the surface runoff is the half of the concentration in percolate.

Hass et al. (2015) demonstrated that N_UPDIS had a high sensitivity in springs season during medium nitrate concentration in the river and low streamflow condition. As a consequence, N_UPDIS was slightly increased from the default value (20) to 28 albeit it was not involved in the sensitivity analysis.

The half-life parameter of nitrate in the shallow aquifer (HLIFE_NGW) was calibrated in each subbasin in the range 0-200 1/day, resulting in about 116 1/day (mean value) for the entire Danube.

Finally, the nitrogen and phosphorous settling rates in reservoirs were kept constant during the year and their range was set larger than the default values accordingly to Paniska and Robertson (1999). In particular, the highest values of settling rate, both for nitrogen and

phosphorous, were set in the Sava River Basin to better simulate the noticeable retention of largest wetlands not implemented in SWAT (i.e. two Ramsar sites, three important bird areas and the alluvial wetlands in the Spacva –Bosut depression; Scheneider-Jacoby, 2005).

The RCN parameter was kept to the setup value (1.8 mg/l), while SHALLEST_N was increased of about 10% in all subbasins.

Table 17. Final ranges and values for nutrients parameters. The values in the bracket represent the average of calibrated values. In these table are excluded the parameters RCN, SHALLEST_N and the initial concentration in reservoirs since they were involved in the setup of the model. For each parameter is reported the related input file (i.e. parameter CDN is defined in the file bsn).

| Nutrient | Parameter | Definition | Unit | Range | Calibrated value |
|---|---|---|---|---|---|
| Nitrogen | CDN.bsn | Denitrification exponential rate coefficient | NA | 0-3 | 2.5 |
| | CMN.bsn | Rate factor for humus mineralization of active organic nitrogen | NA | 0.0001-0.0003 | 0.000145 |
| | ERORGN.hru | Organic nitrogen enrichment ratio | NA | 0-5 | 0.05-4.5 (0.7) |
| | HLIFE_NGW.gw | Half-life of nitrate–nitrogen in the shallow aquifer | $day^{-1}$ | 0-200 | 0-200 (116) |
| | NPERCO.bsn | Nitrogen percolation coefficient | NA | 0-1 | 0.5 |
| | NSETLR1.lwq= NSETLR2.lwq[1] | Nitrogen settling rate | m/year | 1-150[2] | 5.5-150 (30) |
| | N_UPDIS,bsn | Nitrogen uptake distribution parameter | NA | 1-31 | 28 |
| | RSDCO.bsn | Residue decomposition coefficient | NA | 0.02-1 | 0.02 |
| | SDNCO.bsn | Denitrification threshold water content | NA | 0-1 | 1 |
| Phosphorous | ERORGP.hru | Organic phosphorous enrichment ratio | NA | 0-5 | 0-0.25 (0.1) |
| | PSETLR1.lwq= PSETLR2.lwq[1] | Phosphorous settling rate | m/year | 1-150[2] | 9.5-150 (57) |

1) The nitrogen and phosphorous settling rate didn't change during the year.
2) The range of settling rate of nutrients in reservoirs was set larger that the default accordingly with Paniska and Robertson (1999).

### 4.2.5 The calibration of crop yields

Simulating crop-yield is in general a difficult task because of the limitations in the input data, especially the management data such as planting and harvesting time, fertilizer and irrigation water inputs (Abbaspour et al., 2015). In the Danube River Basin 23 crops were simulated, and the AGRR (generic agricultural crop, mainly corn) and SWHT (wheat) are the dominant crops that cover approximately 24% and 16% respectively of total crop land areas (~408000 $km^2$). The observed crop yields were obtained from EUROSTAT (2013).

The following figures show a visual appraisal of comparison between annual simulated and observed crop yields (period 1995-2009) for each country in the Danube for AGRR and SWHT crops.

It is noticeable that the SWAT model is able to reproduce the annual variability of the crop yields in all countries, except in Slovenia (code SI), Moldova (MD) and Ukraine (UA). For these countries however, no data are available and the mean annual crops yields in the entire Danube was used as references.

In Austria (AT) the yields of AGRR is slightly underestimated, likely for the particular variety of corn here cultivated.

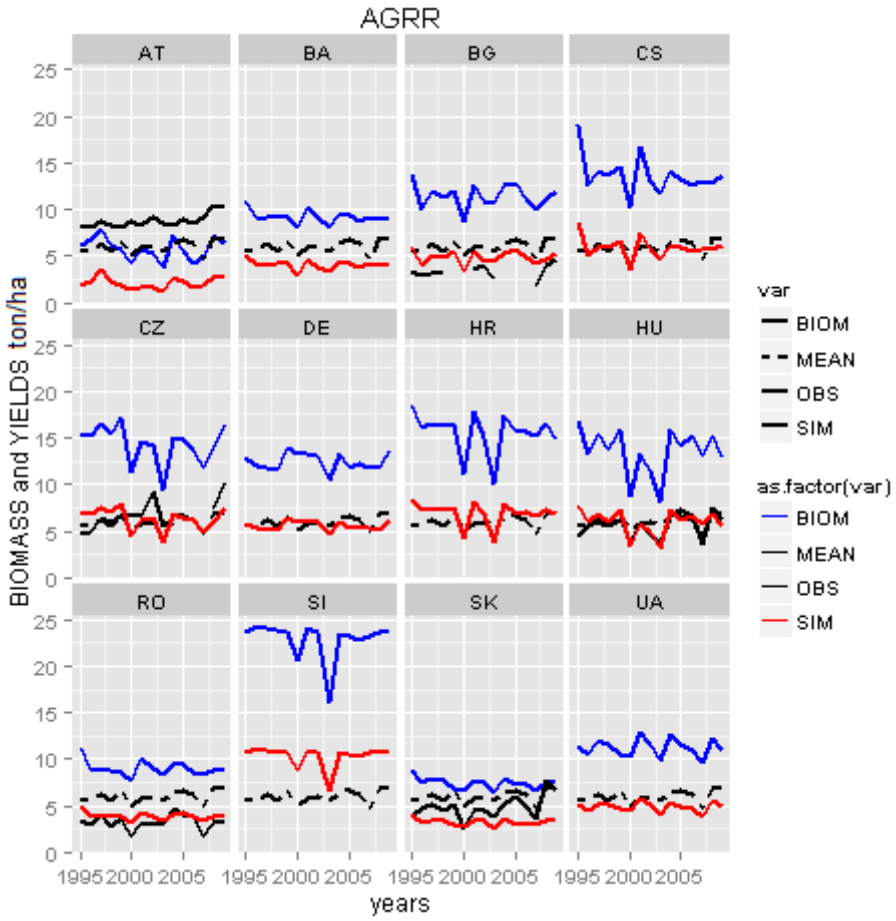


Figure 71. Comparison of annual observed (OBS, continuous black line) and simulated (SIM, continuous red line) crop yields (ton/ha) for the SWAT crop AGRR. The black dotted lines indicate the mean of annual observed values in the entire Danube, while the continuous blue lines indicate the biomass (ton/ha). AT: Austria; BA: Bosnia and Herzegovina; BG: Bulgaria; CS: Serbia and Montenegro; CZ: Czech Republic; DE: Germany; HR: Croatia; HU: Hungary; RO: Romania; SI: Slovenia; SK: Slovakia; UA: Ukraine.

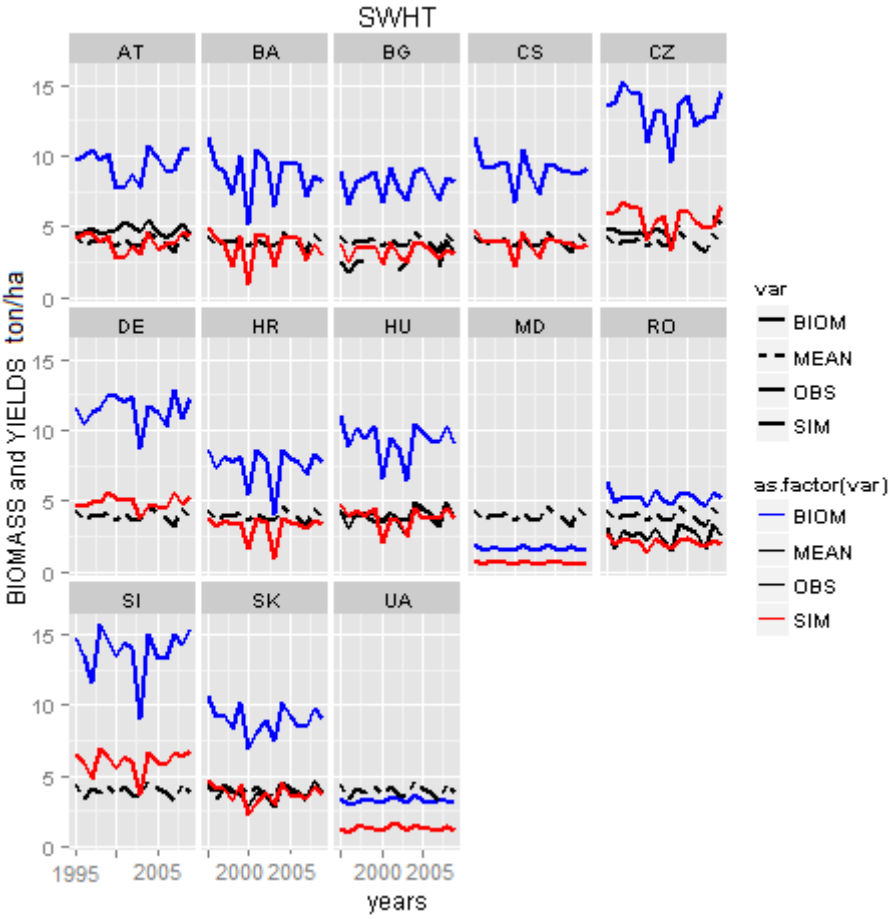


Figure 72. Comparison of annual observed (OBS, continuous black line) and simulated (SIM, continuous red line) crop yields (ton/ha) for the SWAT crop SWHT. The black dotted lines indicate the mean of annual observed values in the entire Danube, while the continuous blue lines indicate the biomass (ton/ha). AT: Austria; BA: Bosnia and Herzegovina; BG: Bulgaria; CS: Serbia and Montenegro; CZ: Czech Republic; DE: Germany; HR: Croatia; HU: Hungary; RO: Romania; SI: Slovenia; SK: Slovakia; UA: Ukraine; MD: Moldova.

### 4.2.6 The calibration of denitrification process

Section 2 describes the denitrification process in SWAT as affected by soil temperature, soil saturation level and the presence of NO3 and carbon. The annual denitrification is controlled in SWAT by parameters CDN (denitrification exponential coefficient) and SDNCO (denitrification threshold water content, or the fraction of field capacity water content above which denitrification is assumed to be occur) (see [eq.8] and [eq.9] in section 2). In this study the annual denitrification was constrained using literature data obtained from the integrated assessment tool MITERRA-EUROPE (Velthof et al., 2009) as detailed in Oenema et al. (2009).

The value of SDNCO equal to 1.1 (default SWAT value) inhibits the denitrification since the water soil content, considered as a fraction of field capacity (from 0 to 1), is less than 1.1 (see [eq.9] in section 2). Thus to activate the denitrification, the SDNCO has to be set below

1.1, albeit low values should be avoided (Sui and Frankenberger, 2008; Yen et al., 2014). Using low values of SDCO leads to unrealistic high denitrification since the denitrification should in reality reflect a value of near saturation when anaerobic conditions are present, or rather when the fraction of field capacity that represents the water soil content approximate the value 1.

The CDN coefficient ranges between 0 and 3, and in literature generally is greater than 0.5. Arnold et al. (2012a) showed that there exists a linear relationship between the nitrogen lost to denitrification and the CDN values. This correlation was also confirmed in our study.

Figure 73 shows the long-term mean annual denitrification values (kg/ha), in the period 1995-2009, for the Danube River Basin changing CDN from 0.6 to 3 and SDNCO from 0.8 to 1, resulting in 9 different configurations as following;

- a1) CDN=0.6 and SDNCO=1
- a2) CDN=0.6 and SDNCO=0.9
- a3) CDN=0.6 and SDNCO=0.8
- b1) CDN=1.4 and SDNCO=1
- b2) CDN=1.4 and SDNCO=0.9
- b3) CDN=1.4 and SDNCO=0.8
- c1) CDN=3 and SDNCO=1
- c2) CDN=3 and SDNCO=0.9
- c3) CDN=3 and SDNCO=0.8

The long term annual denitrification increased with decreasing the SDNCO from 1 to 0.8, and with increasing the CDN. The highest value of denitrification (31.5 kg/ha) was obtained with CDN and SDNCO respectively equal to 3 and 0.8, while the lowest value (13.5 kg/ha) was simulated when CDN was 0.6 and the SDNCO equal to 1.

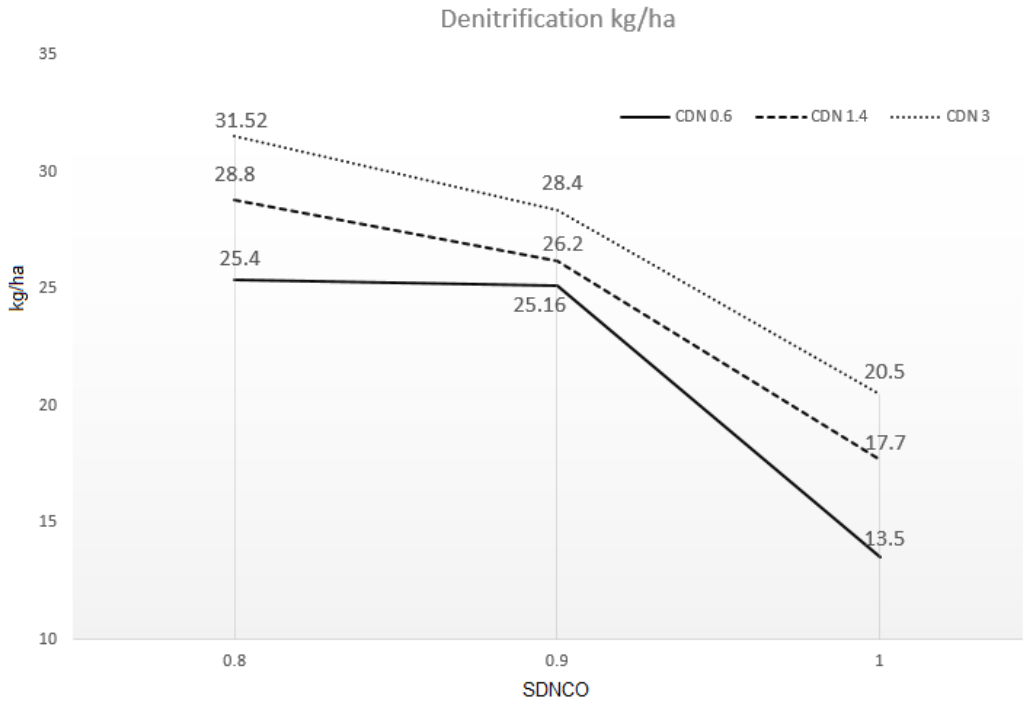


Figure 73. Long-term mean annual denitrification values (kg/ha, period 1995-2009) in the Danube River Basin with 9 combinations of CDN and SDNCO.

Figure 74 shows the spatial distribution of the log-term mean annual denitrification across the entire Danube considering the aforementioned 9 configurations. It is noteworthy that denitrification occurred in the crop land areas, reaching the highest values in the Upper Danube, especially in the Danube Source and Morava River Basin, as well as in the Middle Danube mainly in the Pannonian Danube, where the highest transport of nitrates in the soil profile occurred from agricultural activity. The correlation between the highest values of denitrification and the large amount of fertilizer applied can be observed in Figure 57 and Figure 58.

Among the 9 configurations, a1, b1 and c1 were considered able to simulate realistic denitrification process in the Danube River Basin since saturation of soils was guaranteed imposing SCDNO to 1. The others were instead unrealistic.

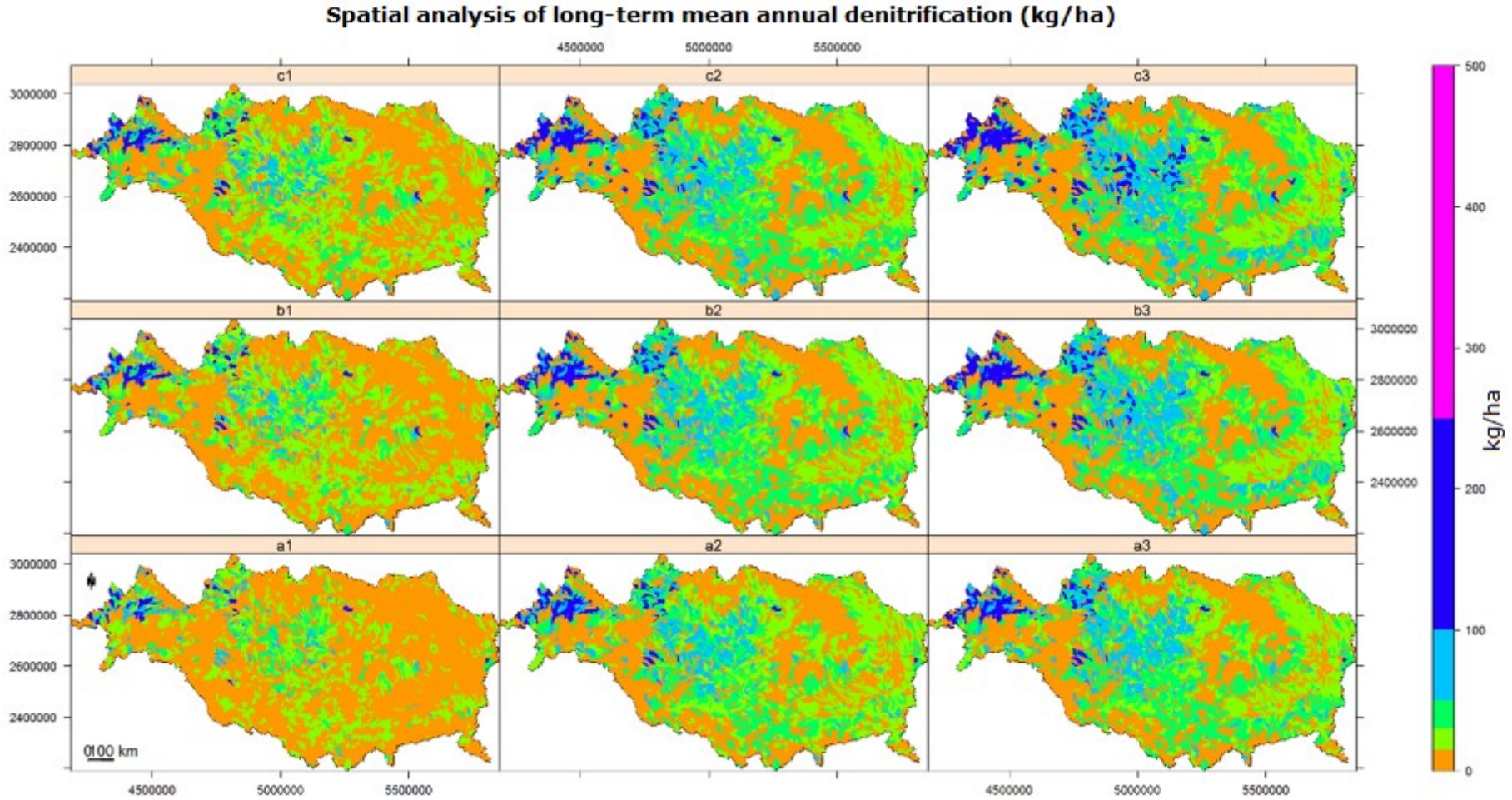


Figure 74. Spatial variation of long-term mean annual denitrification (kg/ha) in the Danube River Basin (period 1995-2009) with 9 combinations of CDN and SDNCO. Combinations: a1: CDN=0.6; SDNCO=1, a2: CDN=0.6; SDNCO=0.9, a3: CDN=0.6; SDNCO=0.8, b1: CDN=1.4; SDNCO=1, b2: CDN=1.4; SDNCO=0.9, b3: CDN=1.4; SDNCO=0.8, c1: CDN=3; SDNCO=1, c2: CDN=3; SDNCO=0.9, c3: CDN=3; SDNCO=0.8.

Setting SDNCO equal to 1, the parametrization of CDN was constrained using the annual denitrification values calculated by Oenema et al. (2009) for each country in Europe. From that source, only the denitrification values that concern the largest Countries in the Danube River Basin were considered, and it was estimated that the interquartile ranges between 6 and 33 kg/ha with 21 kg/ha of median value.

Consequently, CDN was reasonable set to 2.5 obtaining a long-term mean annual denitrification of about 19 kg/ha, matching well with the soft data available. Thus configuration a3 was considered the most reliable parametrization for the denitrification process, albeit CDN was set to a lower value in order to keep the monthly seasonal variations of nitrates concentrations. As matter of fact, it was observed that increasing the CDN, the seasonal concentration behavior, characterized generally by higher values in winter and lower values in summer (i.e. in the Upper Danube), had a tendency to be lost. These findings highlighted the need to improve the denitrification spatially in large river basins where the reliability of the process is limited by setting the parameters at watershed level.

Figure 75 shows the spatial variation of long-term annual denitrification using SDCNO equal to 1 and CDN sets to 2.5, while Figure 76 shows the box and whisker plots of calibrated denitrification for each water management region compared to the long-term mean annual simulated value for the entire Danube and the interquartile range calculated using the aforementioned soft data.

It is noteworthy that the highest median value of long-term mean annual denitrification was found in the Upper Danube (22.6 kg/ha), in the Morava River Basin (19.4 kg/ha) and in Pannonian region (20.8 kg/ha).

Furthermore, it was observed a gradient of decreasing values of denitrification from Upper to Lower Danube that follows the gradient of decreasing precipitation. The lower precipitation in the Lower Danube leads to lower soils saturation and thus less denitrification.

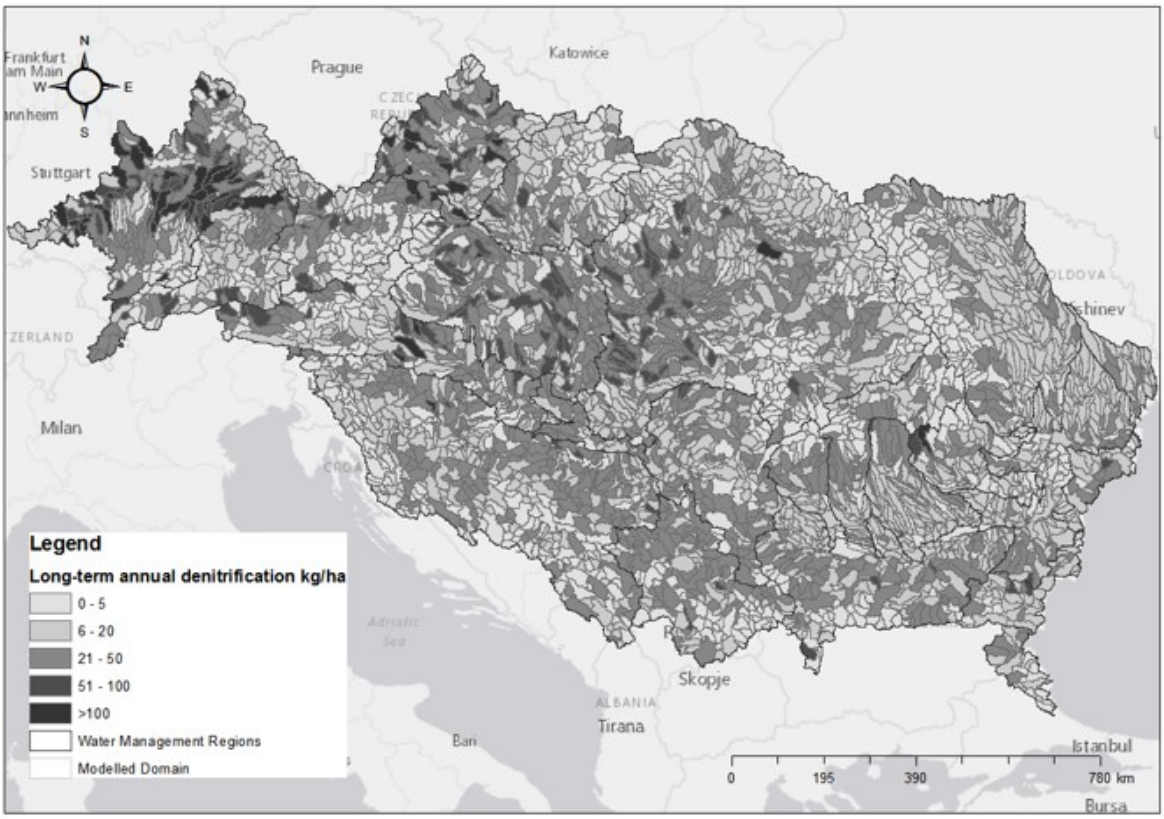


Figure 75. Spatial long-term mean annual denitrification (kg/ha) in the Danube River Basin with CDN and SDNCO respectively to 2.5 and 1.

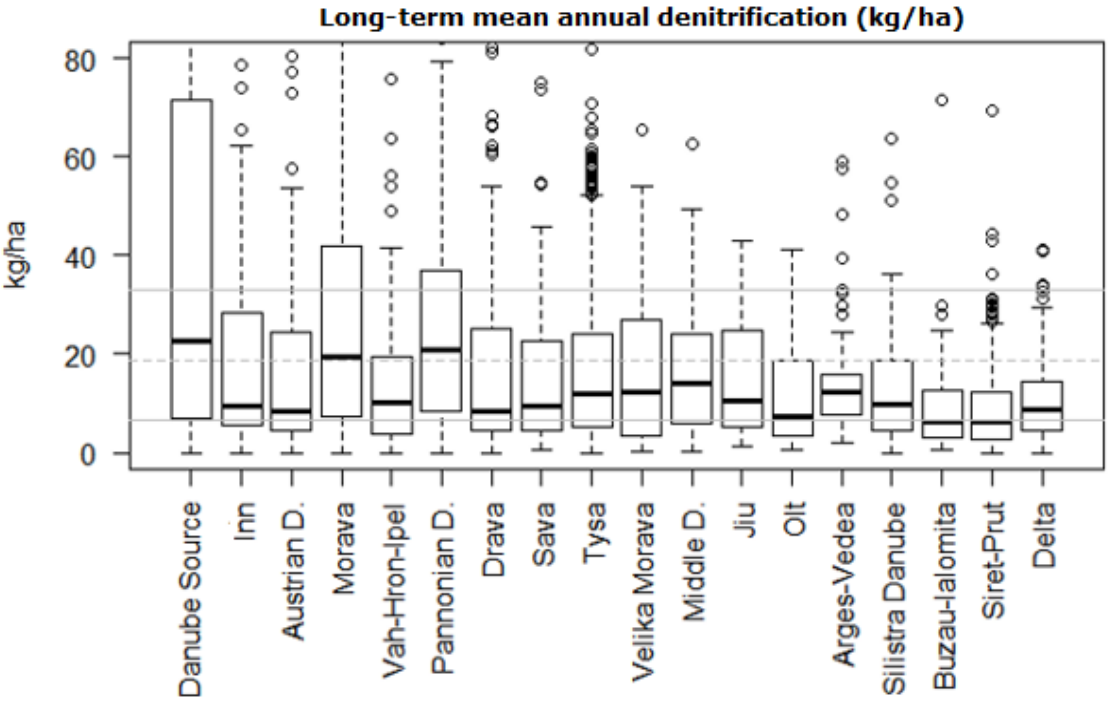


Figure 76. Box and whisker plots of long-term mean annual denitrification (kg/ha) simulated in the period 1995-2009 in each water management region (CDN=2.5; SDNCO = 1). The grey dotted line indicates the long-term mean annual denitrification simulated in the whole Danube; the grey continuous lines indicate the 25$^{th}$ and 75$^{th}$ of denitrification values from soft data (Oenema et al., 2009).

Finally, Figure 77 shows the long-term mean monthly denitrification in the Danube River Basin. It was observed that the denitrification reached the lowest values in summer (from May to July) where the water content in soil is lower than in winter and spring seasons, and fertilization is not applied.

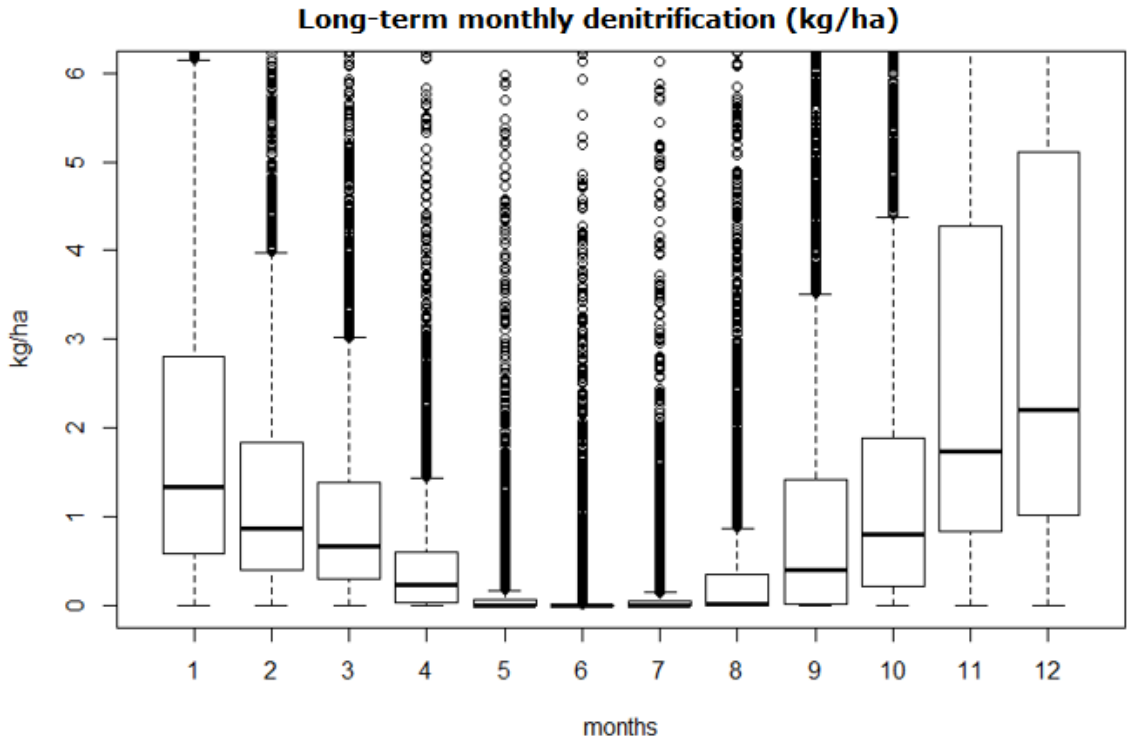


Figure 77. Long-term mean monthly denitrification (kg/ha, period 1995-2009) with CDN and SDNCO respectively to 2.5 and 1.

### 4.2.7 Results of calibration and evaluation of nutrients

Based on the general performance rating reported in Table 4 (section 2.4.6), calibration and evaluation results were summarized in Table 18.

PBIAS% and residuals (simulation-observation) were used to carry out the performance analysis. For the assessment of model calibration PBIAS% was calculated between monthly simulated and observed concentration, while for model evaluation it was evaluating using monthly simulated and calculated loads. The calculated loads estimated from observed concentration and streamflow will be referred to as “Observed loads”.

The model was able to simulate correctly nitrate-nitrogen concentration for 66% and 74% of gauging stations respectively in the calibration and evaluation dataset reached performance values from satisfactory to very good. Similarly, the total nitrogen was well simulated for 70% of gauging stations both in the calibration and validation dataset. Instead, for total phosphorous the model performed better in the evaluation dataset than in the

calibration (60% of gauging stations had generally good performance in the evaluation, while 50% in the calibration).

However, the spatial variation of PBIAS% (from Figure 78 to Figure 83) highlighted that local errors are important, such us in headwaters subbasins. In particular, it was observed that errors in predicted concentrations decrease with increasing the subbasin area and streamflow. Conversely, errors in monthly loads estimations increase with decreasing subbasin area and streamflow.

Table 18. Overview of calibration and evaluation results in terms of performance rating as explained in Table 4. For each class of performance, the percentage (%) of gauging stations that reached each of them is reported. The symbol # represents the number of gaging stations.

| Dataset | Data Type | # gauging stations | Very Good (%) | Good (%) | Satisfactory (%) | Unsatisfactory (%) |
|---|---|---|---|---|---|---|
| calibration | N-NO3 (mg/l) | 340 | 23 | 17 | 26 | 34 |
| evaluation | N-NO3 (ton/month) | 202 | 26 | 15 | 33 | 27 |
| calibration | TN (mg/l) | 191 | 38 | 12 | 24 | 27 |
| evaluation | TN (ton/month) | 121 | 35 | 11 | 26 | 28 |
| calibration | TP (mg/l) | 333 | 25 | 11 | 12 | 52 |
| evaluation | TP (ton/month) | 202 | 22 | 16 | 22 | 41 |

An in-depth analysis about model residuals (simulation-observation) was conducted per water management region investigating in detail those local errors.

Observed monthly N-NO3 concentrations did not vary considerably between management region (Figure 84a). However, in Morava and Pannonian Danube the interquartile was the highest, with medium values typically observed for intensively agricultural watersheds, while in the Danube Source and Inn River Basin the concentrations were the lowest. SWAT model N-NO3 (mg/l) simulations were able to capture the regional values, albeit underestimations were observed in Morava, Pannonian, Middle Danube, Siret Prut and Delta (Figure 84b). Visual appraisal of the times series of monthly N-NO3 concentration in Figure 85 shows the difficult of SWAT to reproduce accurately the seasonality of the concentration in the Inn River Basin, in the Danube Source, and in the area extended from the Middle Danube to Delta. These results confirm the preliminary results on model denitrification that highlighted the difficulties to reproduce the spatial variation of the soil denitrification explained by the fact that the parameters that regulate the process reefer to the whole modelled area. Thus, in the Upper Danube the denitrification (in soil) resulted

excessive and it was demonstrated that the simulations of N-NO3 concentration improved with decreasing the parameter CDN to 0.6; conversely in the Middle and lower Danube the soil denitrification should be higher, thus increasing the CDN values until 3.

Furthermore, the in-stream denitrification process is not simulated by SWAT, limiting the accuracy of prediction. For instance, SWAT was not able to reproduce accurately the nitrate concentration in the Morava River probably linked to the uncertainty in the estimated timing of fertilizers application or the absence of denitrification in-stream process.

N-NO3 concentration were however well captured in Drava, Prut and Siret.

Observed monthly loads of N-NO3 vary considerably between all management regions, since they are directly dependent on streamflow. Higher loads were observed in the Danube Source and in Morava, reaching the highest value in Sava River Basin, in Middle and Silistra Danube, as well as in the Delta (Figure 86a). SWAT however was able to reproduce the monthly loads in almost all the regions, excepted in the Middle, Silista and Delta (overestimation), as well as in the Danube Source (underestimation), confirming the aforementioned inaccurate concentration results in these areas (Figure 86b). Visual appraisals of monthly loads comparison for N-NO3 are shown in Figure 87.

Observed monthly concentration of TN did not vary considerably between management regions located in the Lower Danube (from Velika Morava to Delta the concentration was around 2.2 mg/l), while in the Upper Danube some differences were noticeable (in the Inn River Basin the median of concentration reached the lowest value of around 0.75 mg/l) (Figure 88a). SWAT model simulations captured well these differences (Figure 88b), albeit larger errors were observed in regions with limited data availability (i.e. Morava River Basin). However, visual appraisals of monthly TN concentration in some outlets of the water management regions show satisfactory match between simulations and observations (Figure 89).

A markedly variability of monthly TN loads was observed between the water management regions in the Danube basin as showed in Figure 90a. These variabilities were well captured by SWAT since the median of monthly residuals was around 0 in all water management regions (Figure 90b). Comparisons between observed and simulated time series in the period 1995-2009 (Figure 91) confirmed these satisfactory findings.

Observed total phosphorous concentrations were different between management regions, with highest values in dominant agricultural regions where artificial drainage systems were markedly present, i.e. in Morava, Vah-Hron-Ipel and Tysa (Figure 92a). However, the median value of TP concentration in the Danube was around 0.11 mg/l (Figure 92a). The median residual values were close to zero in all water management regions (Figure 92b),

except in the Arges-Vedea probably due to the lack of simulation of certain peak flow at the gauging station Oltenita near the outlet of Arges River Basin (Figure 93).

The distribution of the observed monthly TP loads was less variable than TN loads in the Upper Danube albeit larger values were observed in Morava, Sava, Middle Daube, Silistra Danube and Delta regions (Figure 94a). The SWAT model simulations matched well the observed monthly loads, resulting in a median of residuals close to zero for all water management regions, although in Sava, Silistra Danube and Delta regions the maximum interquartile of residuals ranged between +/-500 ton/month (Figure 94b). However, visual appraisal of monthly TP loads in Figure 95 shows that the monthly variation was well captured in most of the water management regions' outlets.

Finally, in light of the high variability of input nutrients sources (section 4.2.2) and observation datasets (section 4.2.3) across the entire Basins, both calibration and evaluation were thus considered satisfactory.

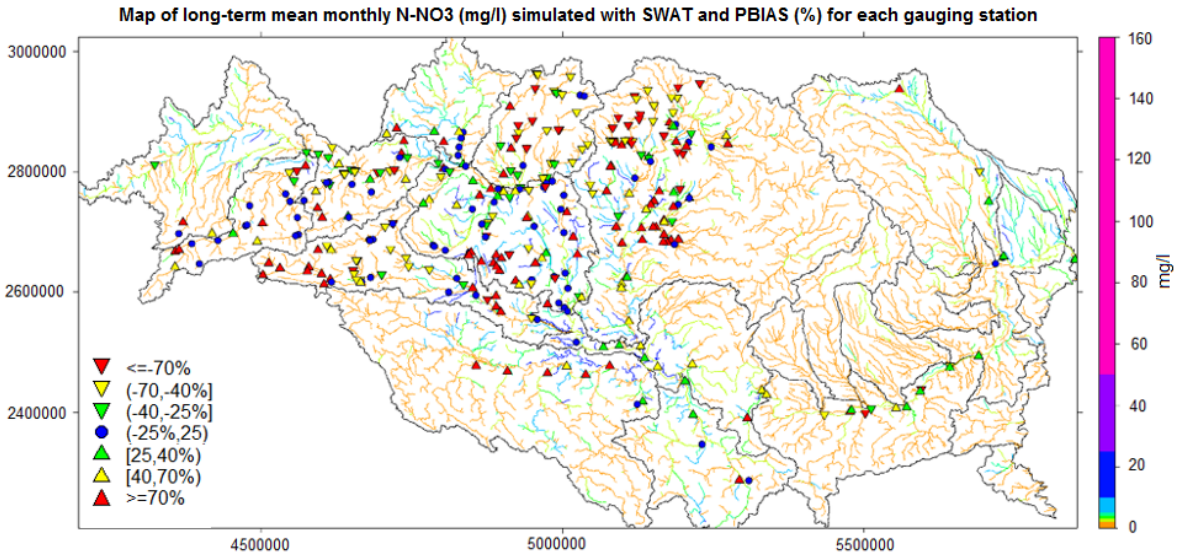


Figure 78. Percent bias (PBIAS %) calculated between monthly simulated and observed nitrate-nitrogen concentration (mg/l) in the calibration dataset (period 1995-2009); positive PBIAS% indicates overestimation, while negative PBIAS% indicates underestimation. In the reaches the long-term mean monthly nitrate-nitrogen concentrations are showed.

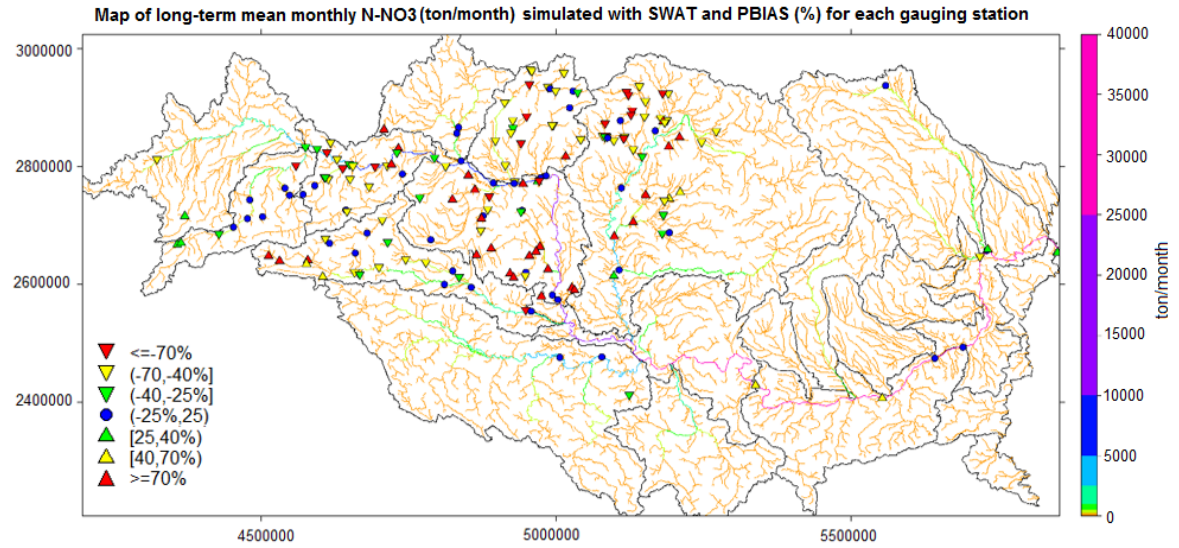


Figure 79. Percent bias (PBIAS %) calculated between monthly simulated and observed nitrate-nitrogen loads (ton/month) in the evaluation dataset (period 1995-2009); positive PBIAS% indicates overestimation, while negative PBIAS% indicates underestimation. In the reaches the long-term mean monthly loads are showed.

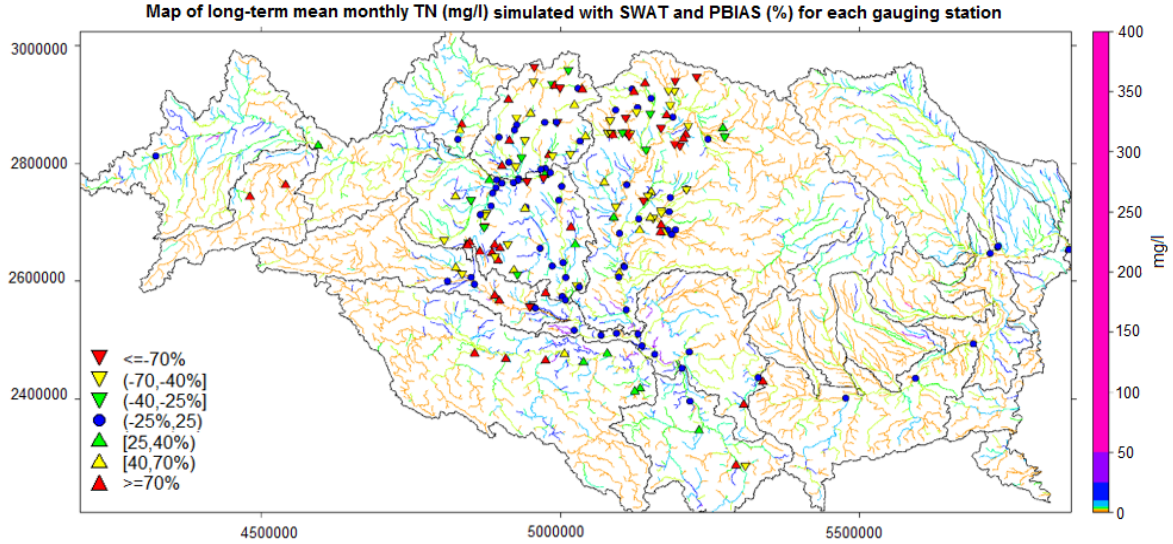


Figure 80. Percent bias (PBIAS %) calculated between monthly simulated and observed total nitrogen concentrations (mg/l) in the calibration dataset (period 1995-2009); positive PBIAS% indicates overestimation, while negative PBIAS% indicates underestimation. In the reaches the long-term mean monthly total nitrogen concentrations are showed.

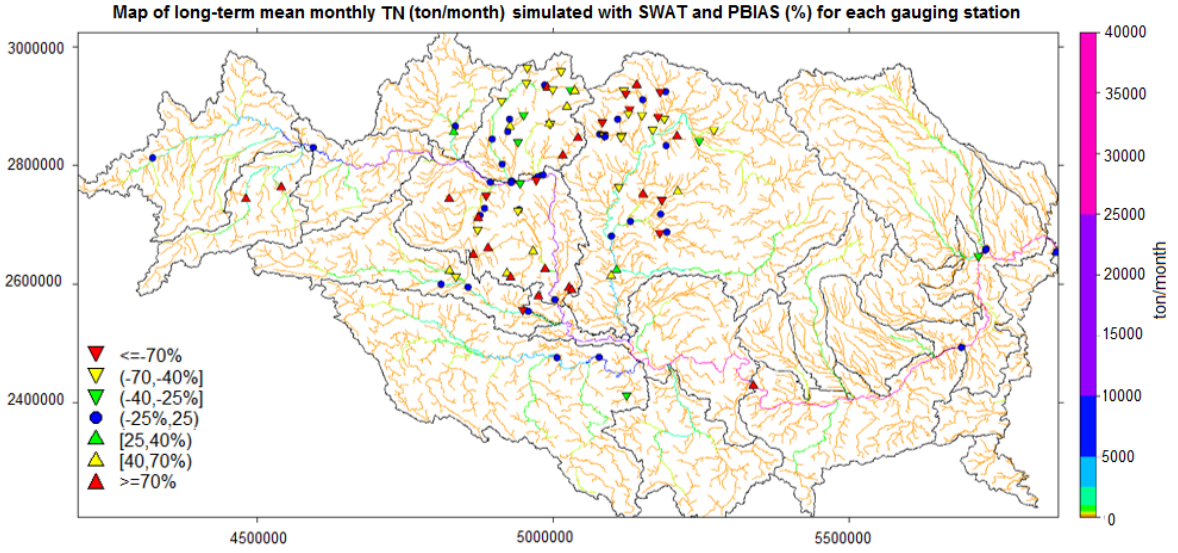


Figure 81. Percent bias (PBIAS %) calculated between monthly simulated and observed total nitrogen loads (ton/month) in the evaluation dataset (period 1995-2009); positive PBIAS% indicates overestimation, while negative PBIAS% indicates underestimation. In the reaches the long-term mean monthly loads are showed.

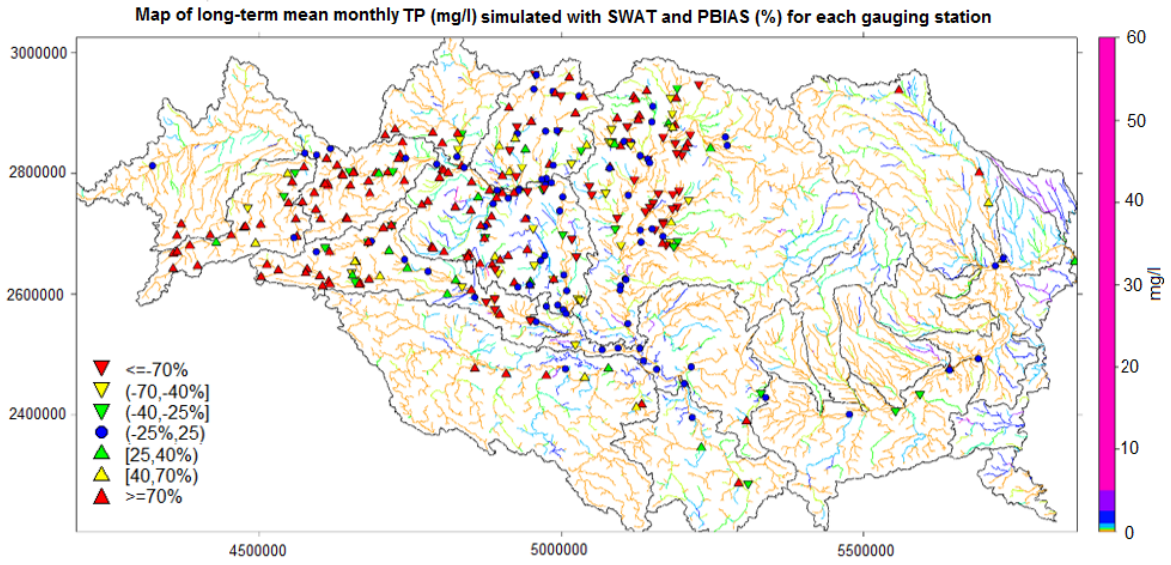


Figure 82. Percent bias (PBIAS %) calculated between monthly simulated and total phosphorous concentration (mg/l) in the calibration dataset (period 1995-2009); positive PBIAS% indicates overestimation, while negative PBIAS% indicates underestimation. In the reaches the long-term mean monthly total phosphorous concentrations are showed.

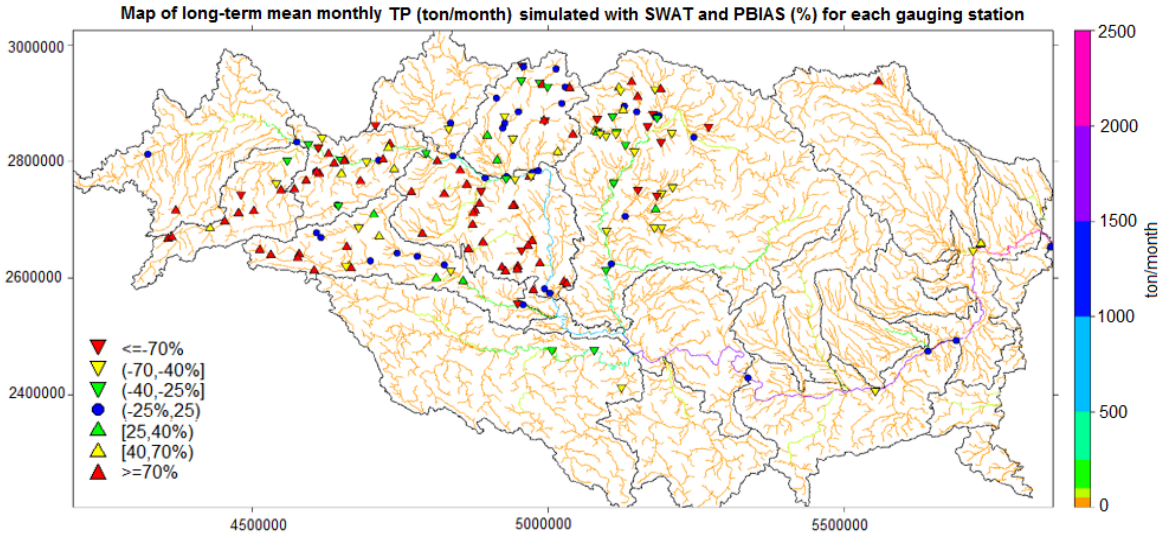


Figure 83. Percent bias (PBIAS %) calculated between monthly simulated and observed total phosphorous loads (ton/month) in the evaluation dataset (period 1995-2009); positive PBIAS% indicates overestimation, while negative PBIAS% indicates underestimation. In the reaches the long-term mean monthly loads are showed.

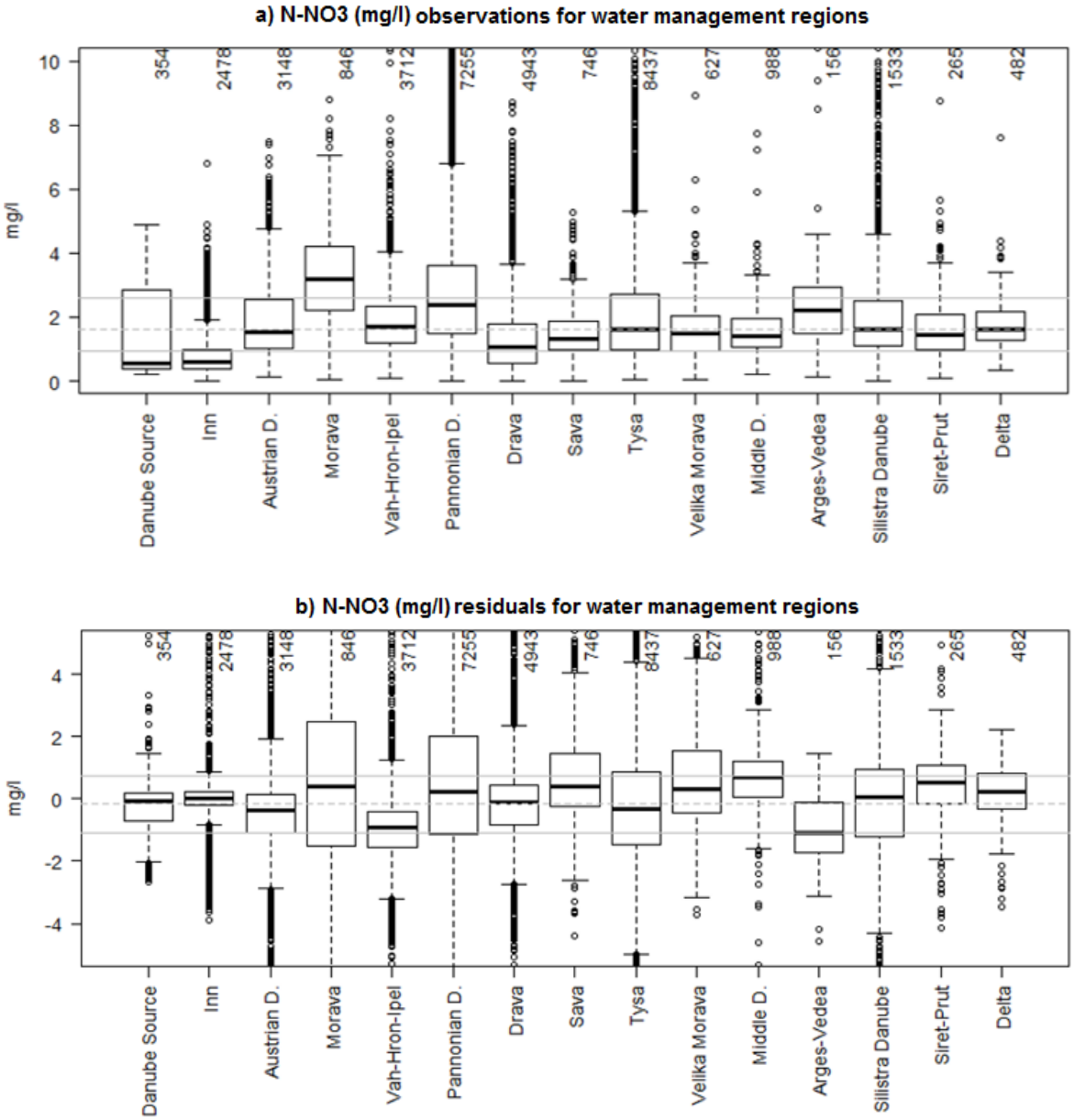


Figure 84. a) Distribution of monthly concentration of N-NO3 (mg/l) observed in the water management regions of the Danube Basin (1995-2009); b) SWAT simulations residuals (simulation –observation) for the same data entries as reported for each box and whisker plot. The grey dotted line indicates the median value of the whole dataset, while the continuous grey lines indicate the interquartile range.

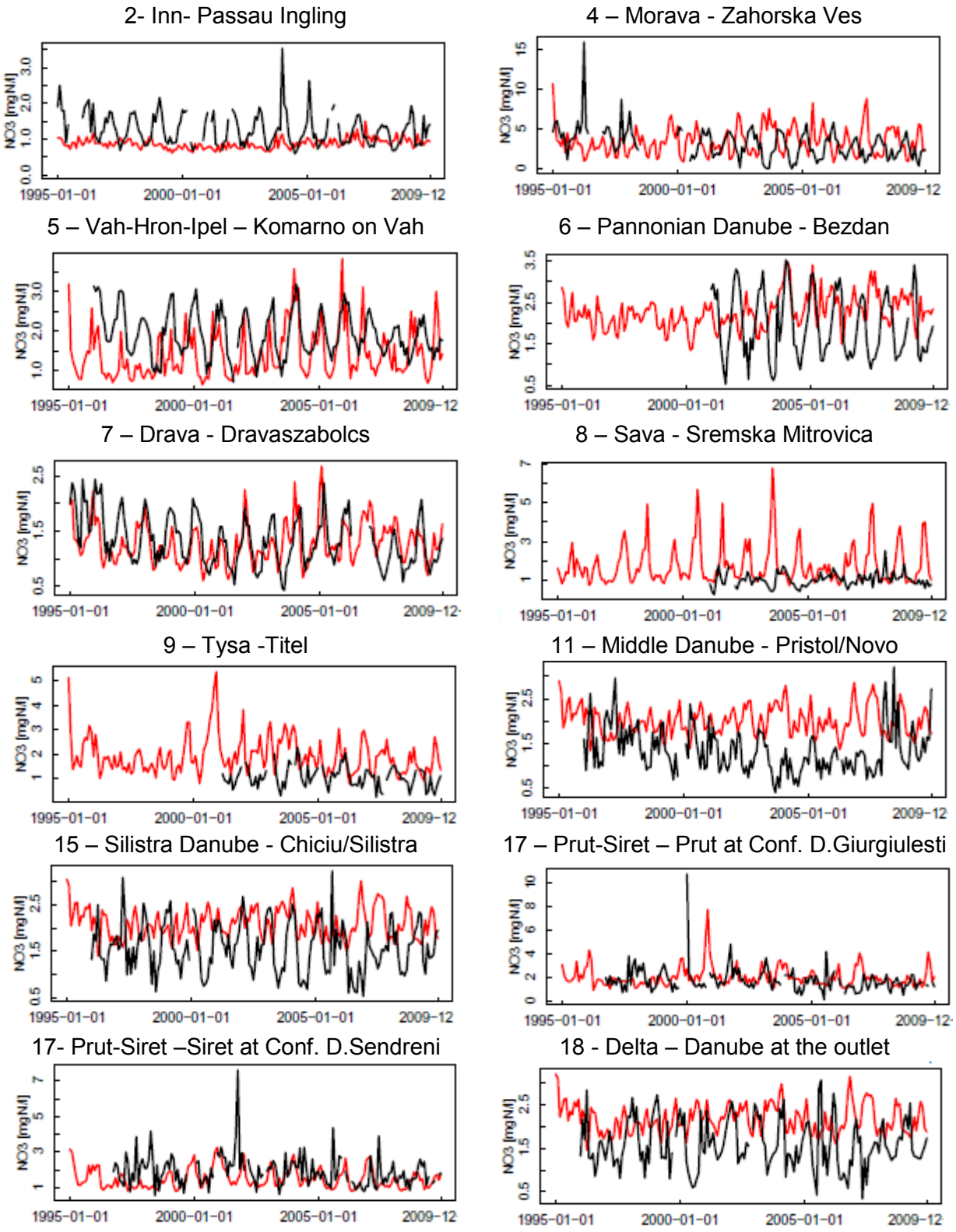


Figure 85. Monthly time series of N-NO3 concentration (mg/l) as observed at the outlet of some water management regions (black line) and as simulated by SWAT model (red line) for the period 1995-2009. Note the differences in y axis.

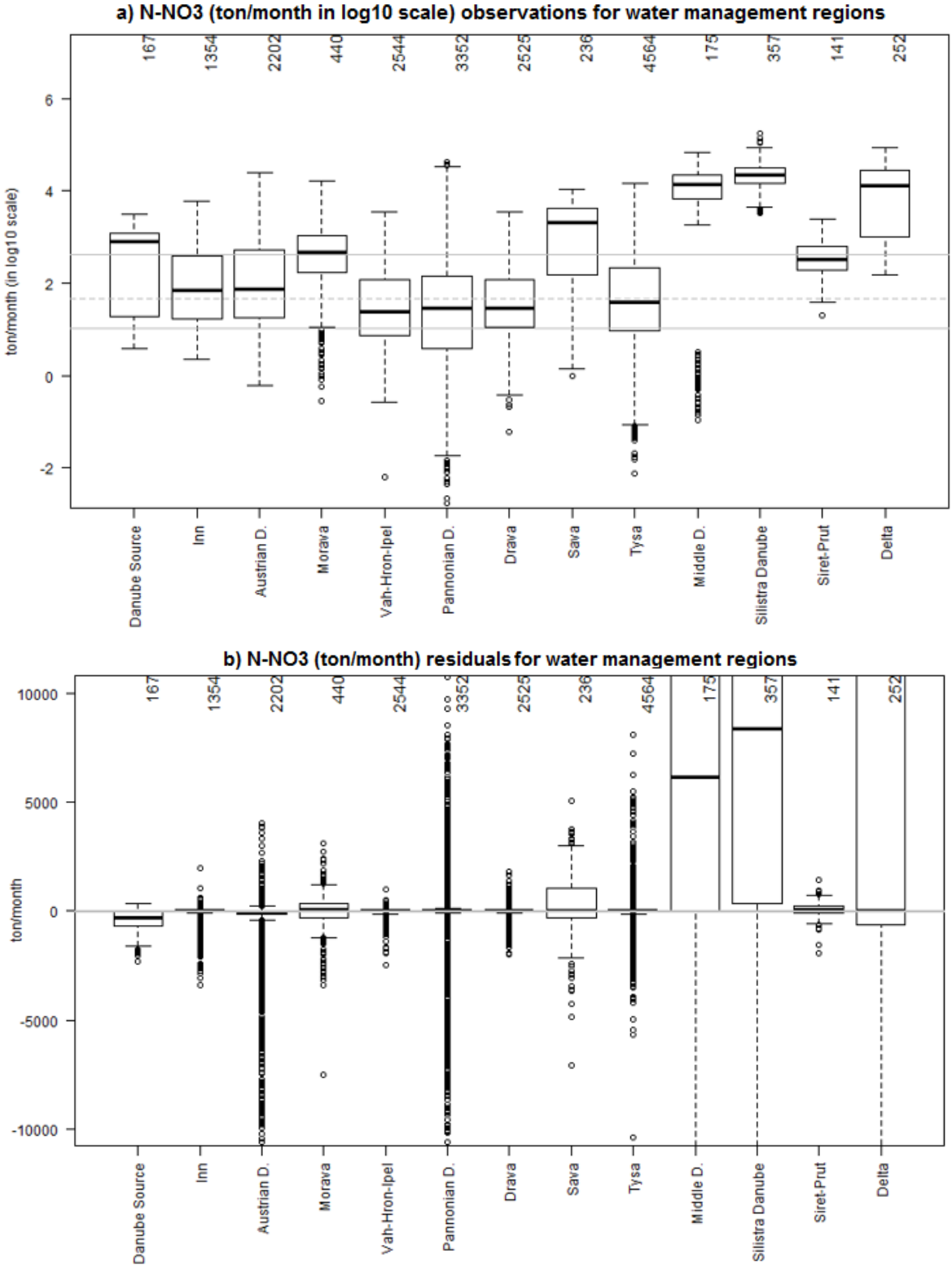


Figure 86. a) Distribution of monthly loads of N-NO3 (ton/month in log10 scale) "observed" in the water management regions of the Danube Basin (1995-2009); b) SWAT simulations residuals (simulation –observation) for the same data entries as reported for each box and whisker plot. The grey dotted line indicates the median value of the whole dataset, while the continuous grey lines indicate the interquartile range

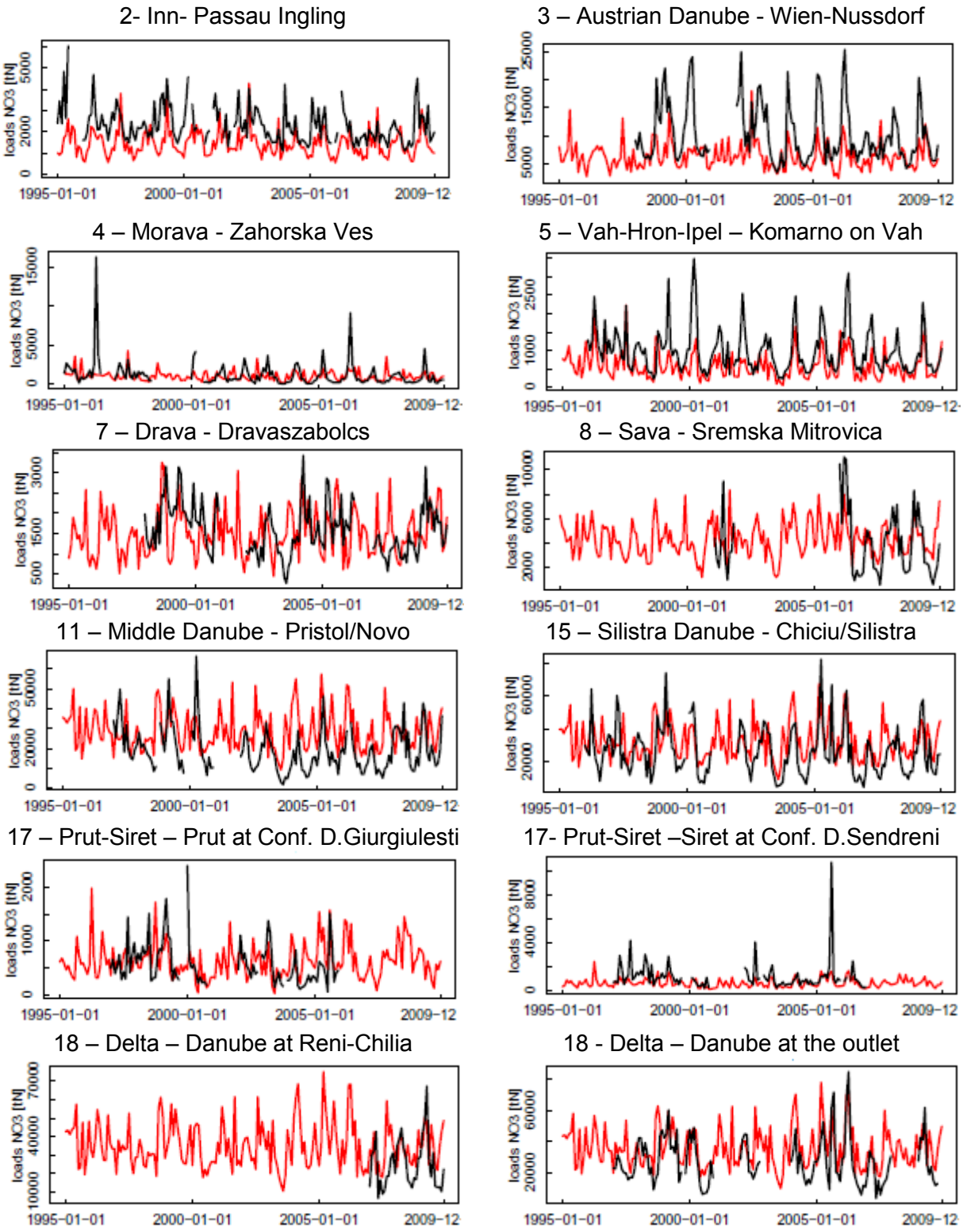


Figure 87. Monthly time series of N-NO3 loads (ton/month indicate with tN in the plots) as “observed” at the outlet of some water management regions (black line) and as simulated by SWAT model (red line) for the period 1995-2009. Note the differences in y axis.

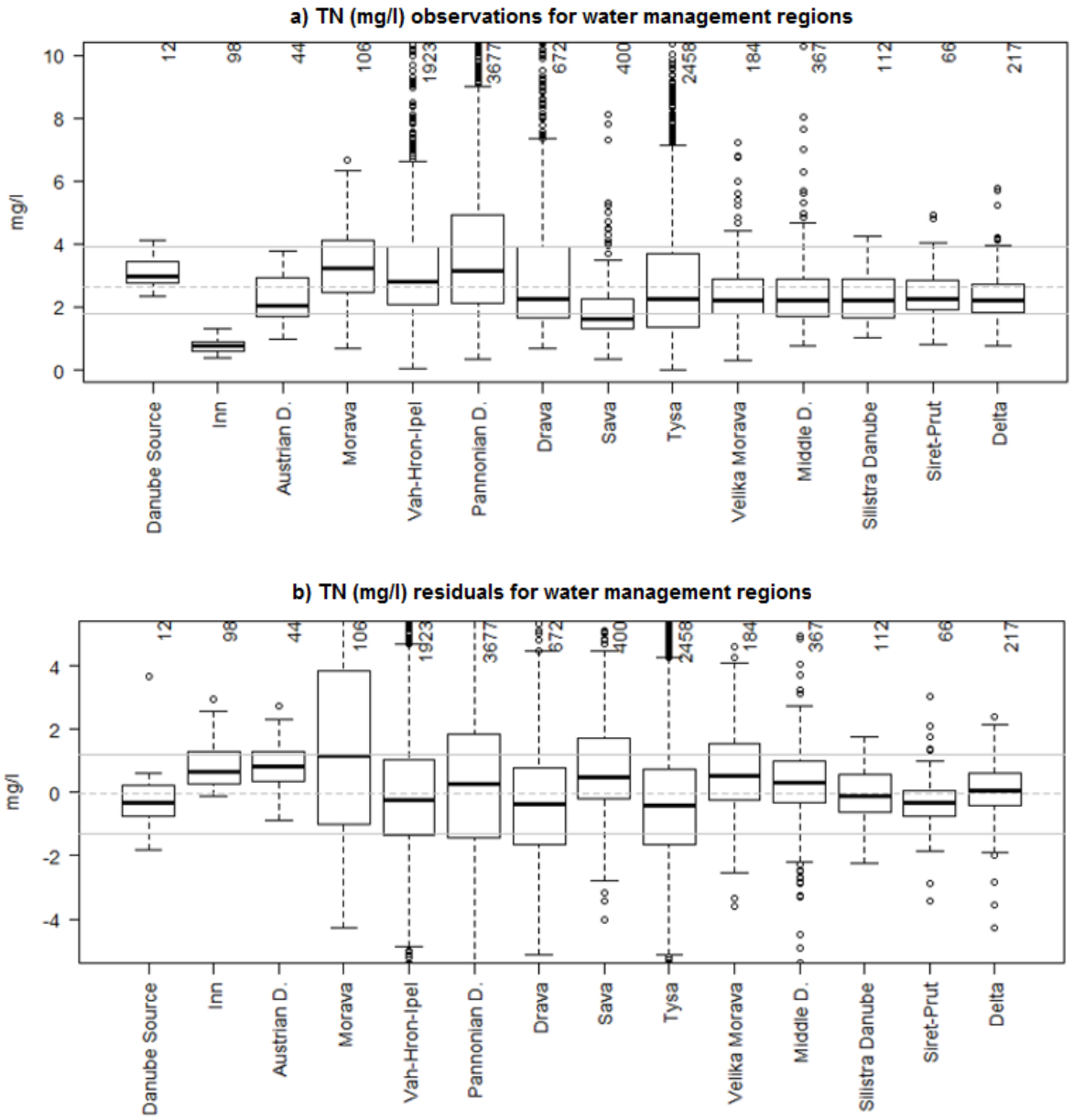


Figure 88. a) Distribution of monthly concentration of TN (mg/l) observed in the water management regions of the Danube Basin (1995-2009); b) SWAT simulations residuals (simulation –observation) for the same data entries as reported for each box and whisker plot. The grey dotted line indicates the median value of the whole dataset, while the continuous grey lines indicate the interquartile range.

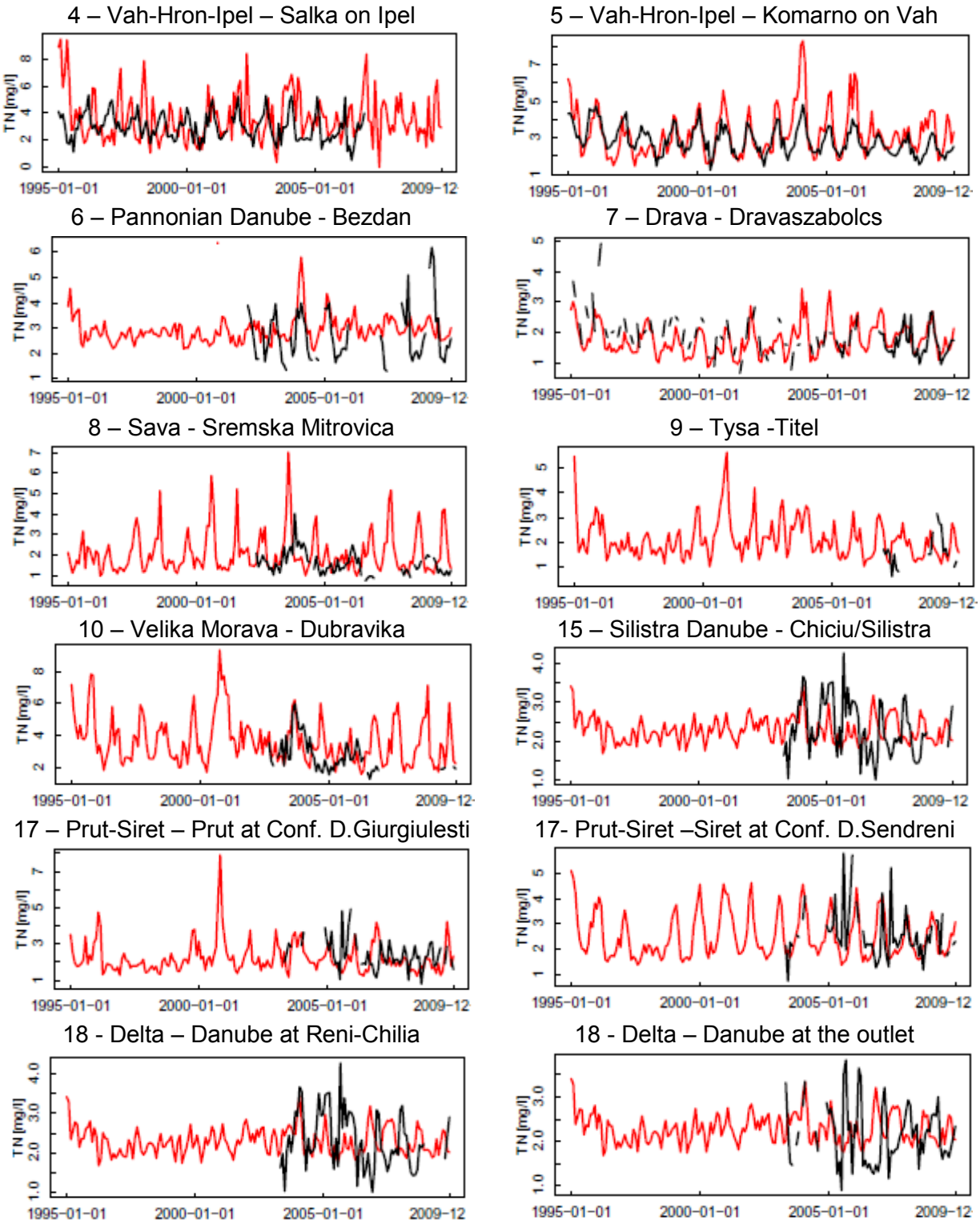


Figure 89. Monthly time series of TN concentration (mg/l) as observed at the outlet of some water management regions (black line) and as simulated by SWAT model (red line) for the period 1995-2009. Note the differences in y axis.

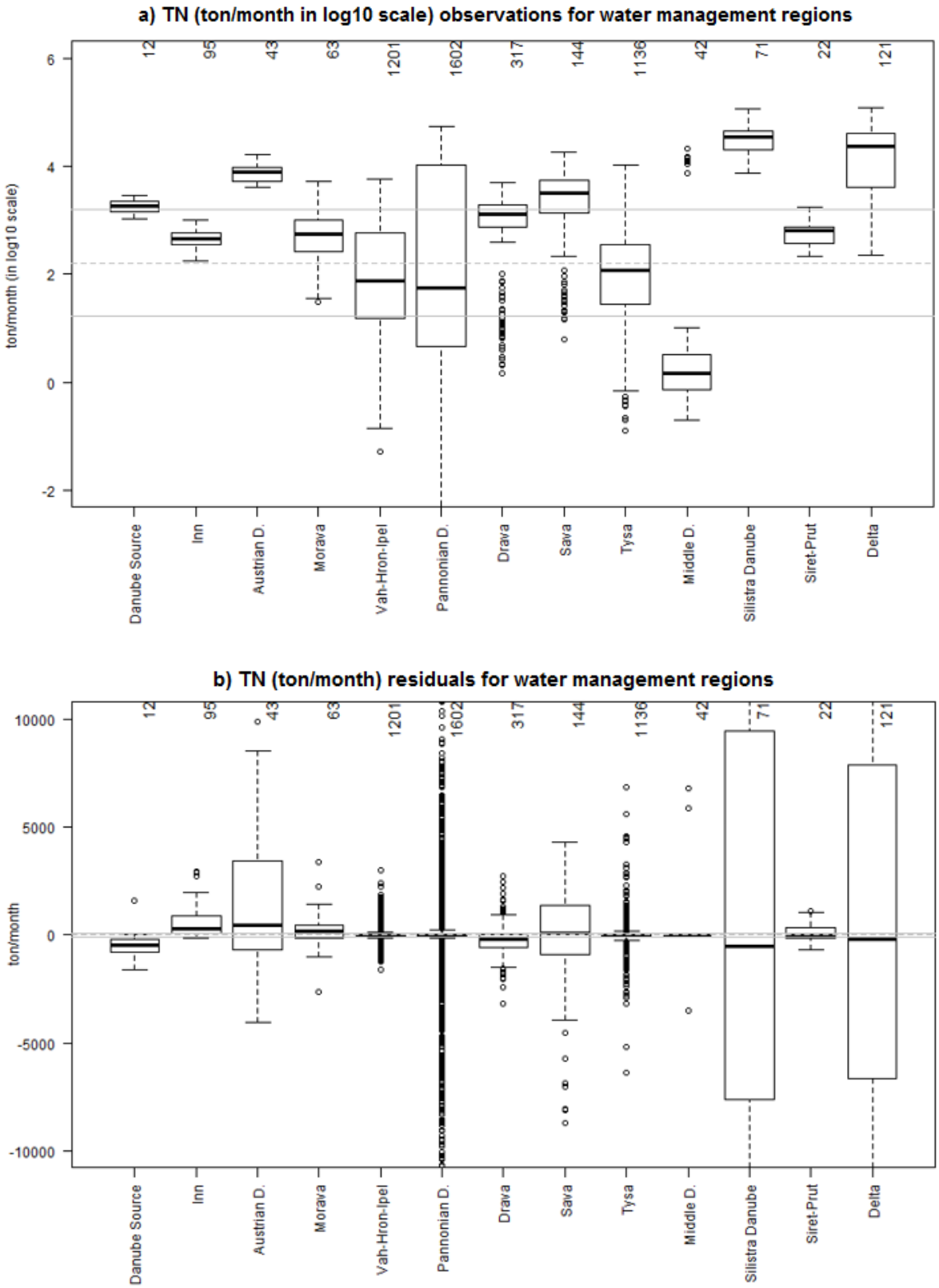


Figure 90. a) Distribution of monthly loads of TN (ton/month in log10 scale) "observed" in the water management regions of the Danube Basin (1995-2009); b) SWAT simulations residuals (simulation –observation) for the same data entries as reported for each box and whisker plot. The grey dotted line indicates the median value of the whole dataset, while the continuous grey lines indicate the interquartile range

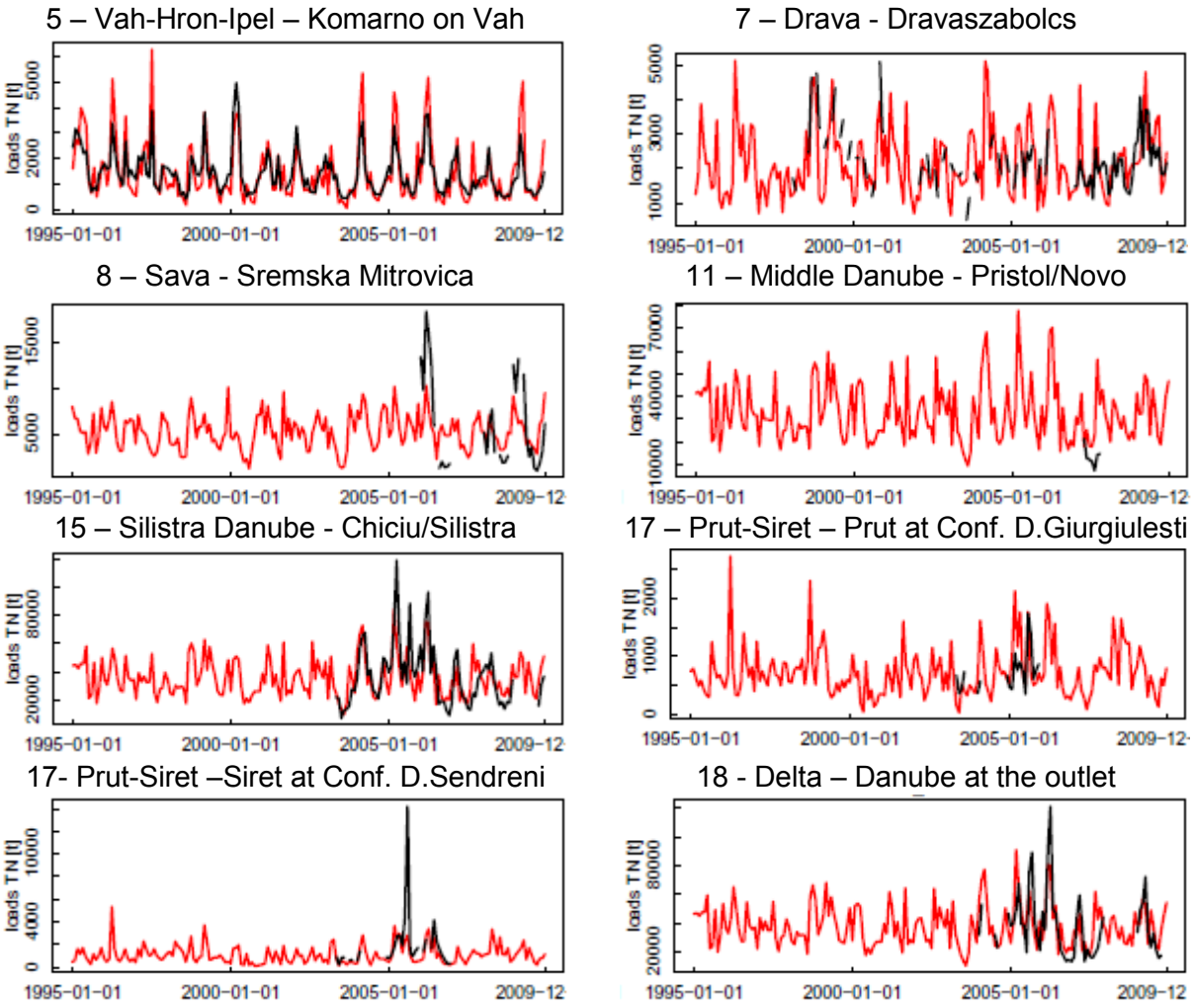


Figure 91. Monthly time series of TN loads (mg/l) as “observed” at the outlet of some water management regions (black line) and as simulated by SWAT model (red line) for the period 1995-2009. Note the differences in y axis.

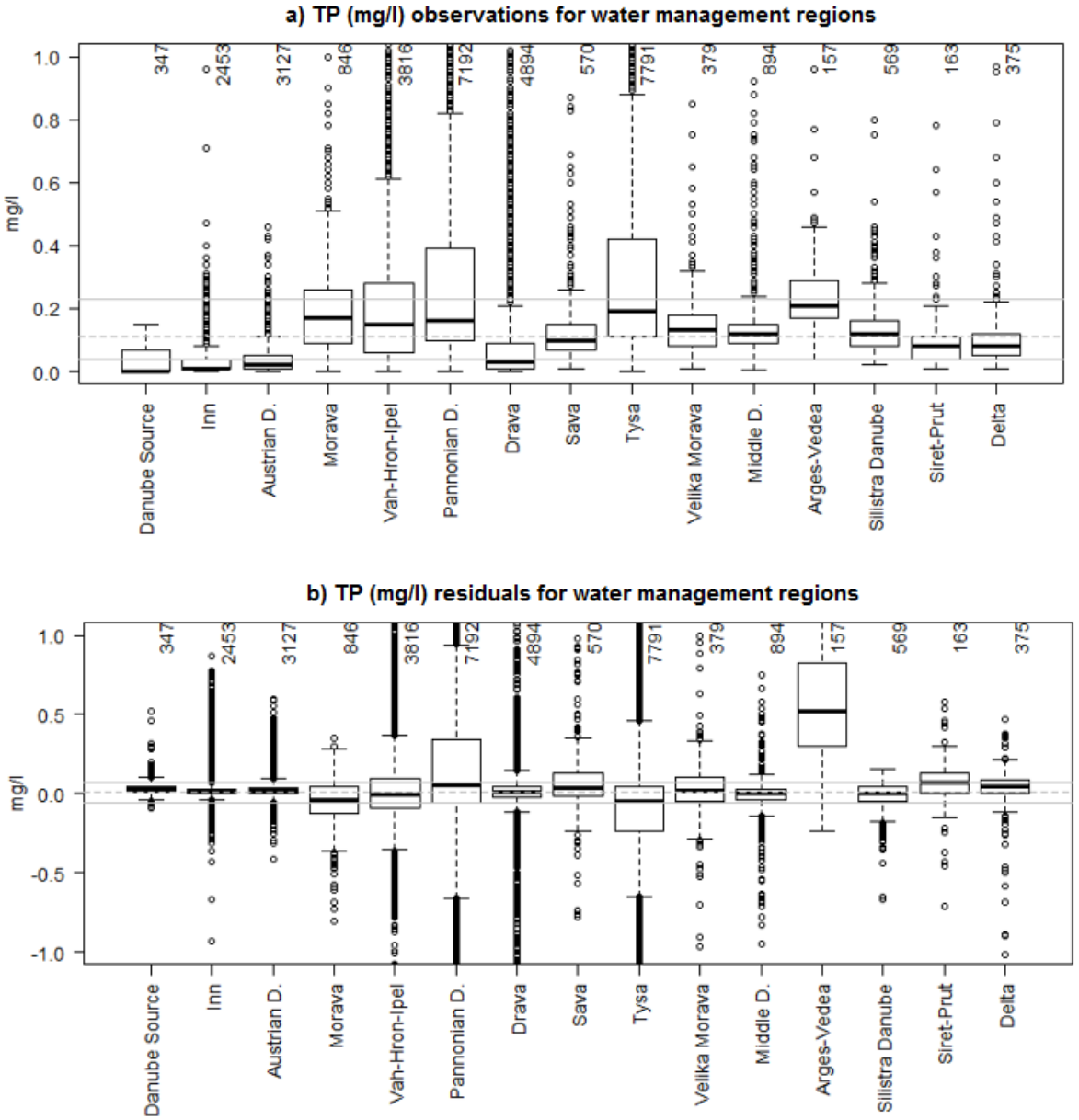


Figure 92. a) Distribution of monthly concentration of TP (mg/l) observed in the water management regions of the Danube Basin (1995-2009); b) SWAT simulations residuals (simulation –observation) for the same data entries as reported for each box and whisker plot. The grey dotted line indicates the median value of the whole dataset, while the continuous grey lines indicate the interquartile range.

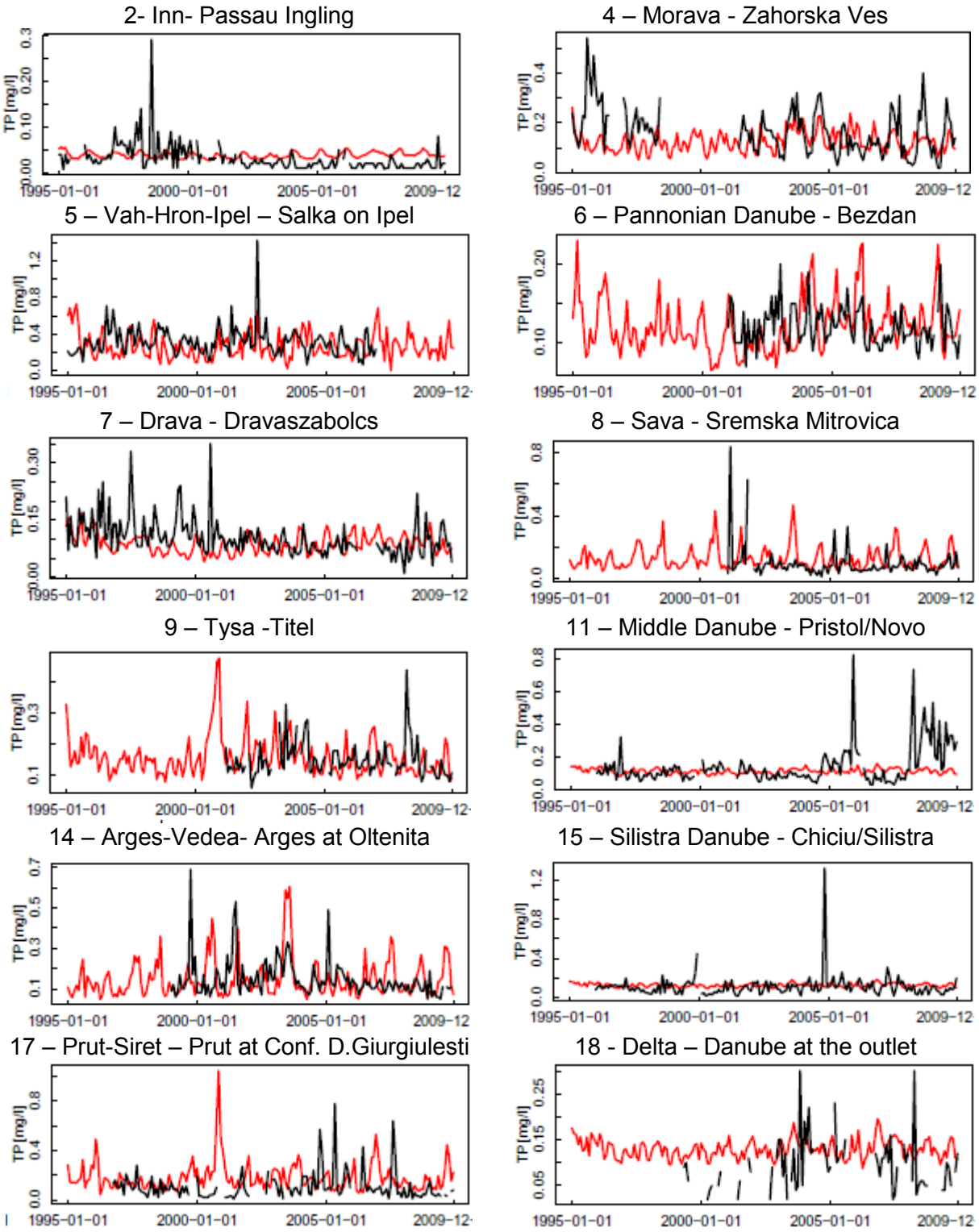


Figure 93. Monthly time series of TP concentration (mg/l) as observed at the outlet of some water management regions (black line) and as simulated by SWAT model (red line) for the period 1995-2009. Note the differences in y axis.

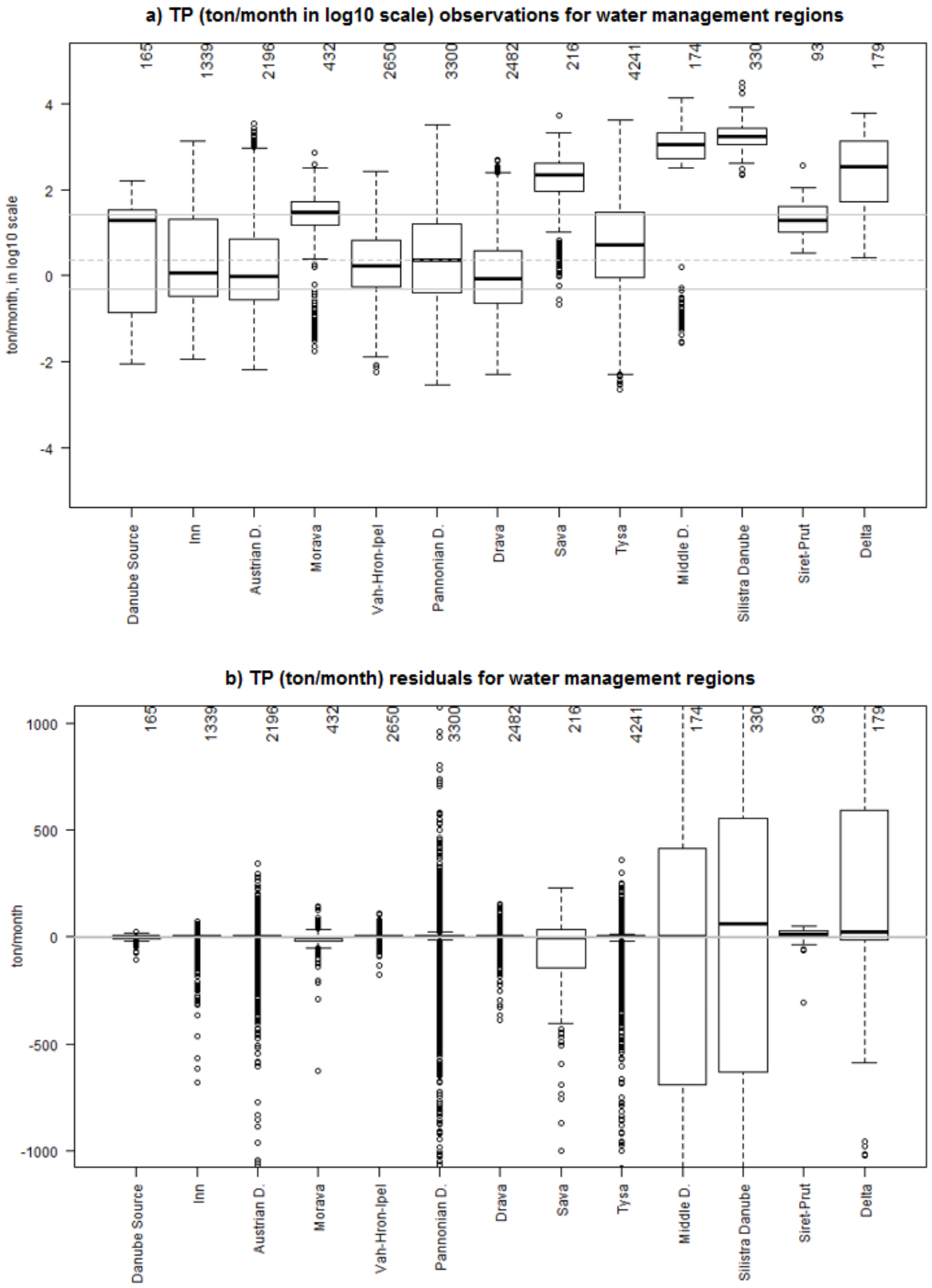


Figure 94. a) Distribution of monthly loads of TP (ton/month in log10 scale) "observed" in the water management regions of the Danube Basin (1995-2009); b) SWAT simulations residuals (simulation –observation) for the same data entries as reported for each box and whisker plot. The grey dotted line indicates the median value of the whole dataset, while the continuous grey lines indicate the interquartile range.

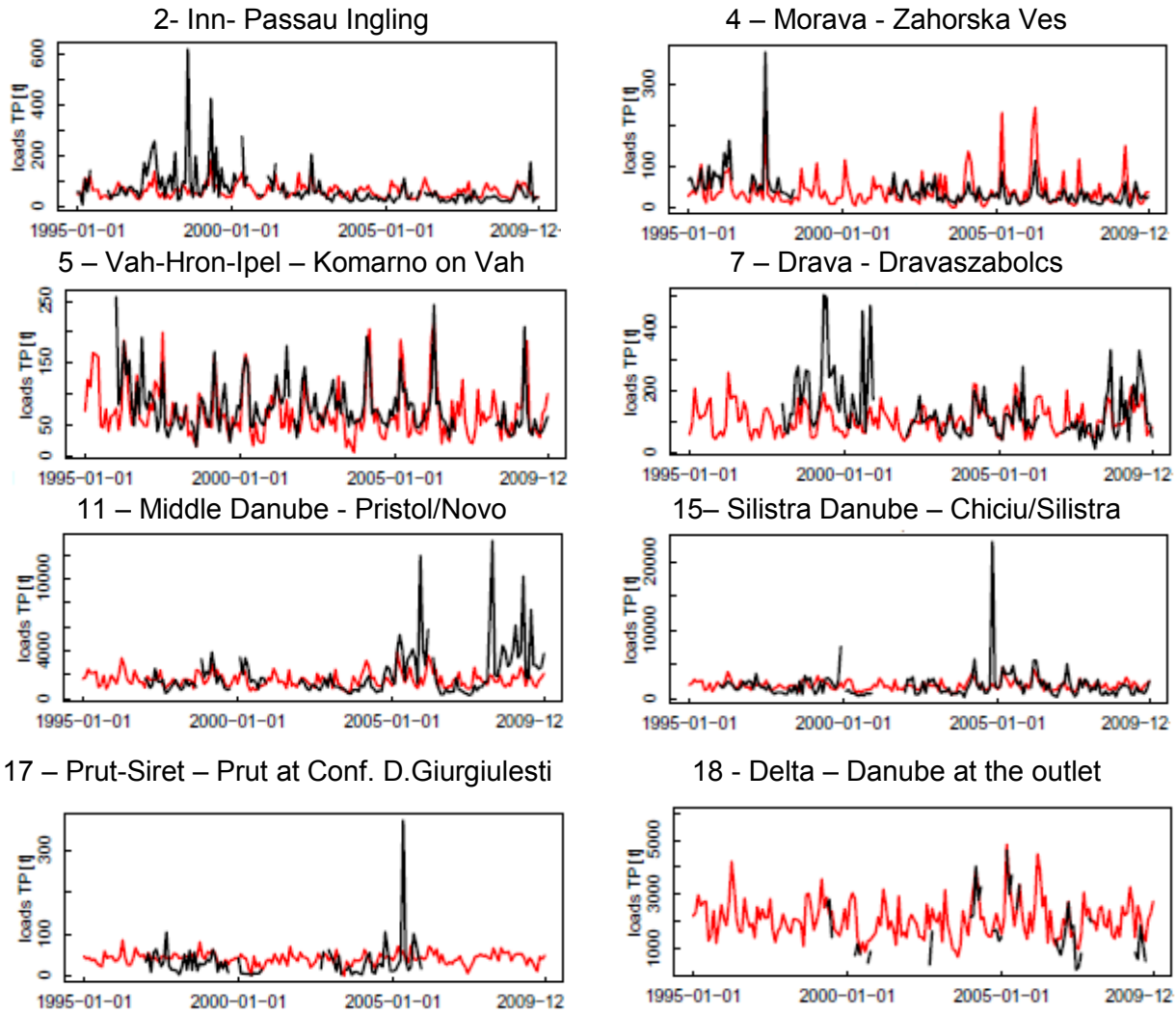


Figure 95. Monthly time series of TP loads (ton/month) as observed at the outlet of some water management regions (black line) and as simulated by SWAT model (red line) for the period 1995-2009. Note the differences in y axis.

### 4.2.8 The long-term annual nutrients balance of the Danube River Basin

Figure 96 and Figure 97 show respectively the nitrogen and phosphorous fluxes and retentions in the Danube river according to the SWAT model results. The long-term mean annual specific loads (kg/ha) of total nitrogen (TN) and total phosphorous (TP) in the period 1995-2009 were calculated for the entire Danube River Basin and used to perform the nutrient balances.

Regarding TN, the diffuse sources were estimated at 86 kg/ha, in which fertilizers application contributed for 41.2 kg/ha, nitrogen from atmospheric deposition for 13 kg/ha and the nitrogen fixed by plat for 31.8 kg/ha. Point sources instead amounted to 2.6 kg/ha.

The nitrogen removed by crop yield and soil had the most significant impact on diffuse sources reduction, applying a reduction of 60% (48,2 kg/ha) and 37% (30 kg/ha). Part of the soil retention was lost through denitrification for about 19 kg/ha (24% of diffuse sources). The nitrogen lost in the aquifer was estimated equal to 2.3 kg/ha, i.e. about 3% of diffuse sources reached the aquifers.

The resulting total emission was estimated to be around 6.14 kg/ha, in which organic nitrogen and nitrogen transported via surface runoff contributed 2.7 and 2.6 kg/ha rispectively. Nitrogen transported via tile drain, lateral flow and base flow had less impact, contributing in total with 0.64 kg/ha.

The riparian filter strips reduced the diffuse emissions up to 4.8 kg/ha, thus cutting about 20% of emissions from land. Furthermore, albeit the point sources increase the loads in the river to 7.4 kg/ha, the in-stream processes applied a retention of about 30%, resulting in a final loads of 5.5 kg/ha.

In terms of TP, the diffuse sources (fertilizers application) were estimated to be around 6 kg/ha. The soil had a dominant role in their reduction (90% of retention). Thus the diffuse emissions were estimated only at 0.38 kg/ha, further reduced by riparian filter strips to 0.33 kg/ha (about 13% of retention). The main components of diffuse emissions were the organic phosphorous and the mineral phosphorous adsorbed to sediment and transported to river, while unexpectedly the phosphate transported via tile drains contributed only with 0.06 kg/ha.

The TP emissions in the river were estimated of about 0.59 kg/ha, in which the half was the contribution of the point sources (0.26 kg/ha). However, the in-stream processes yielded a retention of about 50%, resulting in 0.29 kg/ha of TP loads in the river.

However, it is noteworthy that in these simplified balances the reduction of nutrients by trapping process in reservoirs was considered together with the river retention, thus this should be accounted in the interpretation of TP and TN retention in rivers.

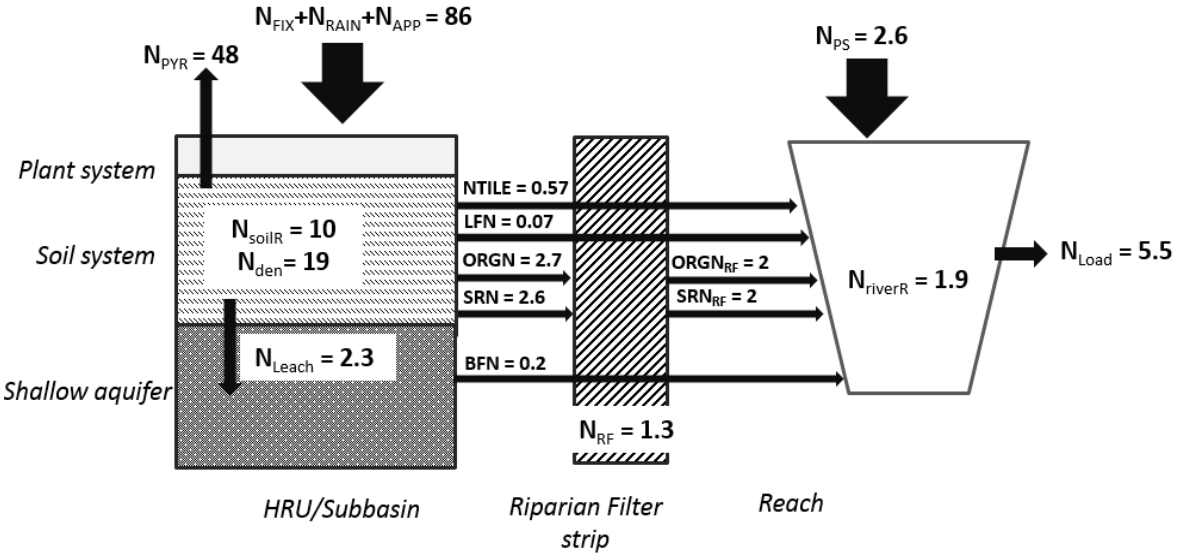


Figure 96. Nitrogen fluxes and retention (kg/ha) in the Danube River Basin according to SWAT model results in the period 1995-2009. See Figure 3 for the symbols/abbreviations.

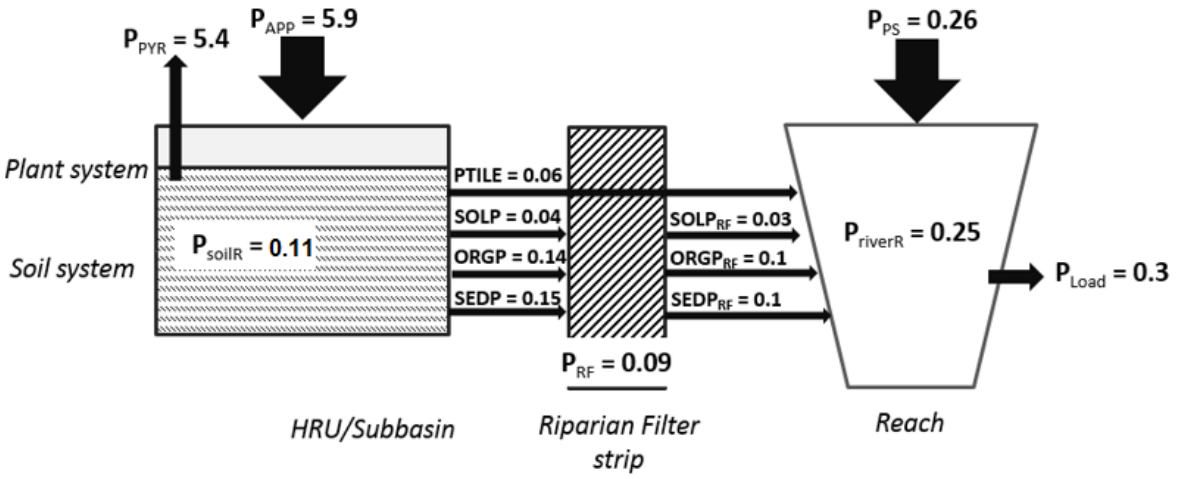


Figure 97. Phosphorous fluxes and retention (kg/ha) in the Danube River Basin according to SWAT model results in the period 1995-2009. See Figure 4 for the symbols/abbreviations.

### 4.2.9 Conclusions of the section

The application of the SWAT model to predict reliable nutrient fluxes in the Danube River Basin has involved the use of soft (i.e. literature information of denitrification, crop yields from statistics) and hard data (i.e. long time series of concentrations).

Huge efforts were necessary to collect hard data and their correction/validation before the calibration has been a crucial step.

The calibration/validation was applied using directly concentrations, thus avoiding uncertainty issues related to loads estimation. The directly use of concentration is an innovation in the SWAT applications at large scale. It has allowed to capture the seasonality, that generally is strongly influenced by hydrological conditions, and also can be used directly to assess the requirements of the European Directives.

The results showed that the use of soft data is necessary for an accurate modelling of nutrients transformation and transport, and to perform robust scenarios analysis of BMPs implementation. However, it was observed that the SWAT model should be improved in representing soil denitrification especially its spatial variation, as well as the simulation of in–stream denitrification should be included.

Notwithstanding these limits, calibration and evaluation of SWAT nutrient outputs showed that concentrations and loads were well captured in the Danube Basin.

Furthermore, the analysis of nutrients balances has allowed to identify the most important factor of pollutant reduction in the Basin, adding valuable scientific information for planning conservation actions.

## 4.3 Sediment yields representation: a case study applied to the Upper Danube river

### 4.3.1 Synopsis

Suspended sediments and sediment pollutants deteriorate the ecological status of many European freshwater bodies and cause considerable economic losses (Rickson, 2014). Maintaining and restoring the ecological status of European waterbodies as demanded by the European Water Framework Directive (WFD; EC, 2000) requires good planning strategies, which strongly rely on integrated basin models that correctly identify the main sources and sinks within the basin (Collins and McGonigle, 2008; de Vente et al., 2013; Rickson, 2014).

The semi-distributed process-based Soil and Water Assessment Tool (SWAT; Neitsch et al., 2011; Arnold et al., 2012a) is increasingly used to develop such strategies as its cascading structure of erosion and sediment transport processes allows to in principle simulate dominant sediment sources and sinks (de Vente et al., 2013; Gassman et al., 2014).

However, SWAT has some limitations in predicting sediment yields that should be carefully taken into account in the application in large river basins. These limitations are related to the MUSLE equation implemented in SWAT ([eq.10] in section 2) and to the LS factor algorithm ([eq.11] in section 2), as well as the hillslope length calculation as discussed in section 3.3.

To overcome these issues, a modified version of MUSLE equation was proposed, as well as three alternative of LS and hillslope length (L) based on DEM resolutions were investigated. The new MUSLE equation and alternative algorithm for LS and L are explained in section 2.3.

In this Chapter, thirteen SWAT models were investigated in the Upper Danube to define which area threshold in the new MUSLE equation, which LS and L algorithms allow predicting reliable sediment yields and concentrations.

Table 19 summaries the SWAT configurations evaluated in this section.

Furthermore, the study shows the application and results of C/V procedure for sediments as explained in section 2.4.4., that involves the calibration of gross erosion, GE, the calibration of sediment concentrations, SSC, as well as an evaluation of specific sediment yields, RSSY. In addition, a sensitivity analysis was initially performed for selecting the most sensitive parameters, their ranges and values.

Table 19. Default and modified SWAT configurations evaluated in this study. For the number of equation see section 2.

| Name of configuration | MUSLE equation | DEM pixel size (m) | Hillslope length | LS equation |
|---|---|---|---|---|
| L0LS1 | 10 | 100 | L1 | 11 |
| L1LS1 | 13 | 100 | L1 | 11 |
| L1LS2 | 13 | 100 | L1 | 15 |
| L1LS3 | 13 | 100 | L1 | 16 |
| L2LS1 | 13 | 100 | L2 | 11 |
| L2LS2 | 13 | 100 | L2 | 15 |
| L2LS3 | 13 | 100 | L2 | 16 |
| L3LS1 | 13 | 100 | L3 | 11 |
| L3LS2 | 13 | 100 | L3 | 15 |
| L3LS3 | 13 | 100 | L3 | 16 |
| L25LS1 | 13 | 25 | L2 | 11 |
| L25LS2 | 13 | 25 | L2 | 15 |
| L25LS3 | 13 | 25 | L2 | 16 |

### 4.3.2 Sensitivity analysis and parametrization

SUFI-2 semi-automated calibration software (Abbaspour, 2008) was initially employed to explore parameter sensitivity of ten sediment parameters. Global sensitivity was measured by the value of the t-test (and associated probability level p) of the regression coefficient of each parameter against the objective function. The larger in absolute term is the t-test value (and the lower the probability level p) of the parameter coefficient, the more sensitive is the parameter (Abbaspour, 2008). Parameters were sampled in a Latin hypercube sampling scheme of 1500 model runs. The objective function was the root mean square error of the simulations divided by the standard deviation of the observations (RSR; Moriasi et al., 2007b).

Table 20 summarizes the results of the global sensitivity analysis for configuration L2LS3 since the findings were consistent across configurations described in Table 19.

The global sensitivity analysis revealed that the most sensitive parameters were quite different between concentration and specific sediment yields. For concentration, the parameter $c_{sp}$ ([eq. 12]) was the most sensitive parameter regulating stream power, whereas vegetation cover (CH_COV) was the most sensitive among those regulating the critical shear stress threshold of the reaches $\tau_c$. SSC was also sensitive to MUSLE parameters ($A_t$, USLE K) and to the equilibrium sediment concentration in reservoirs (RES_NSED), regulating sediment trapping in reservoirs and upstream dams or locks.

Similarly, RSSY (specific sediment yields, t/km$^2$/y) were sensitive to the $c_{sp}$ and $e_{sp}$ coefficients, while vegetation cover (CH_COV) and peak rate adjustment factor for sediment

routing in the main channel (*Prf*) resulted more sensitive for RSSY than for SSC. The MUSLE parameters resulted instead less sensitive than for SSC.

The peak rate adjustment factor for sediment routing in the tributaries (ADJ_PKR) resulted not sensitive for both SCC and RSSY, as well as CH_BNK/BED_D50 (median particle size diameter of sediment in reach bank and bed) and CH_BNK/BED_BD (bulk density of reach bank/bed sediment).

Table 20. Results of a global sensitivity analysis of the mean annual suspended sediment concentrations (SSC; mg/L) and annual reach specific sediment yields (RSSY, t/km$^2$/y) for the modified SWAT (configuration L2LS3) evaluated in this study. Sensitivity was conducted on 1500 runs changing all parameters in the specified range. t = t test value of the regression coefficient of each parameter against the objective function; in brackets the probability p value. Rank = from highest to lowest sensitivity.

| Parameter | range | SSC | | RSSY | |
|---|---|---|---|---|---|
| | | t(p value) | Rank | t(p value) | Rank |
| $A_t$ [1] | 0.01-1 | 13.04(<0.001) | 2 | 11.12 (<0.001) | 6 |
| USLE K [1] | -20%; +20% | 16.33(<0.001) | 1 | 12.82(<0.001) | 5 |
| $c_{sp}$ [2] | 0.0001-0.01 | 10.18(<0.001) | 3 | 74.01(<0.001) | 1 |
| $e_{sp}$ [2] | 1-2 | -4.48(<0.001) | 6 | 17.77(<0.001) | 4 |
| *Prf* [2] | 0.5-2 | 9.86(<0.001) | 4 | 52.67(<0.001) | 2 |
| ADJ_PKR[3] | 0.5-2 | 0.37 (0.71) | 10 | 0.00(0.99) | 10 |
| CH_COV[3] | 10-20 | -3.15(0.002) | 7 | -26.41(<0.001) | 3 |
| CH_BKD/BED_D50[3] | 5000-10000 | 0.80(0.427) | 8 | -0.30(0.767) | 9 |
| CH_BNK/BED_BD[3] | 1.1-1.9 | 0.38(0.707) | 9 | 5.054(<0.001) | 7 |
| RES_NSED[c] | 10-20 | 4.66(<0.001) | 5 | 1.88(0.060) | 8 |

[1] = Area threshold and soil erodibility as specified in [eq. 13]; [2] = as specified in [eq]. 12; [3] = as specified in SWAT manual (Neitsch et al.,2011): ADJ_PKR= adjusted peak of runoff for sediment routing in tributary channels; CH_COV: reach vegetation cover; CH_BNK/BED_D50: median particle size diameter of sediment in reach bank and bed (μm); CH_BNK/BED_BD: bulk density of reach bank/bed sediment (g/cm$^3$); RES_NSED: equilibrium sediment concentration in reservoirs (mg/l).

Based on the results of sensitive analysis and considering that the objective of the work is to calibrate the concentrations and capturing the intra-watershed behavior, the parameterization was performed as following.

The threshold area $A_t$ in [eq. 13] was set at 0.01 km$^2$ (1 ha) in all configurations. This value was set based on the ratio between HRU long-term (1995–2009) mean annual specific sediment yields (HSSY) and the gross erosion, GE, (t/ha/year). It was observed that the ratio increases with A*t* (Vigiak et al., 2015a) and the calibrated values was selected considering that HSSY should be in principle less than GE due to hillslope deposition. In this study, A*t* equal to 0.01 km$^2$ corresponded to the median ratio HSSY/GE of 0.74.

Topsoil USLE erodibility *K,* or support practice factor*,* (USLE K) was estimated with the freeware Kuery 1.4 (Borselli et al., 2009; 2012), which provides a distribution of erodibility values extracted from a worldwide database based on climate and soil properties. Climate zones were identified according to the Köppen-Geiger climate map of Peel et al. (2007),

albeit areas at high altitude (>1500 m a.s.l.) were kept as temperate/cold. Topsoil properties considered for the estimation of *K* were texture (clay, silt, and sand content), stoniness cover, and organic carbon content. The 1 km resolution European Soil Database (ESDB v2; Panagos et al., 2012) was used to derive soil units and topsoil characteristics. The median estimated K-factor was attributed to soil units where the topsoil Exchangeable Sodium Percentage (ESP) was less or equal to 4%. For units where topsoil ESP exceeded 4%, a low aggregate stability was assumed, and the 90th percentile of the erodibility distribution was attributed to the soil-climate unit.

The USLE P, support practice factor, and also USLE C, the cover management factor (not involved in the sensitivity analysis) were further adjusted during the calibration of gross erosion GE accordingly with the soft data available of water erosion rates reported in the literature (Maetens et al., 2012; Panagos et al., 2014; Cerdan et al., 2010).

The $c_{sp}$ was calibrated independently for each configuration, and the final values ranged from 0.003 to 0.006 and changes between the configuration. Instead, $e_{sp}$ was set = 1.4 accordingly with Prosser and Rustomji (2000).

CH_COV was set to 15, corresponding to a relatively dense tree cover of the banks, for all configurations in Table 19. Sediment equilibrium concentration in reservoirs (RES_NSED) was set at 15 mg/L to match mean concentrations in gauging stations placed immediately downstream of some reservoirs.

Instead channel bank and bed bulk densities (CH_BNK/BED_BD) were set at default values, while bank and bed median particle diameter (CH_BNK/BED_D50) was set at 7500 μm after Rákóczi (2010).

Finally, the parameters PRF and ADJ_PKR were set at default values.

### 4.3.3 Topography settings

The subbasin combinations of hillslope length, slope, and LS algorithm yielded the distributions of LS factors shown in Figure 98. Differences were negligible at slopes < 10%, however on steep slopes large differences were apparent. The LS1 algorithm always yielded the highest LS values; however, this was much less dramatic in L1 than for the other hillslope lengths. This is because in L1, steep slopes are always associated to short hillslope lengths (Neitsch et al., 2011; Malagó et al., 2015b). This is not the case for L2 and L3 settings, so very high LS1 values may occur in combination with L2 and L3, exceeding a factor of 20, with a high risk of overestimating soil erosion on steep slopes. LS2 and LS3 had very similar ranges and distributions, with LS2 always slightly lower than LS3.

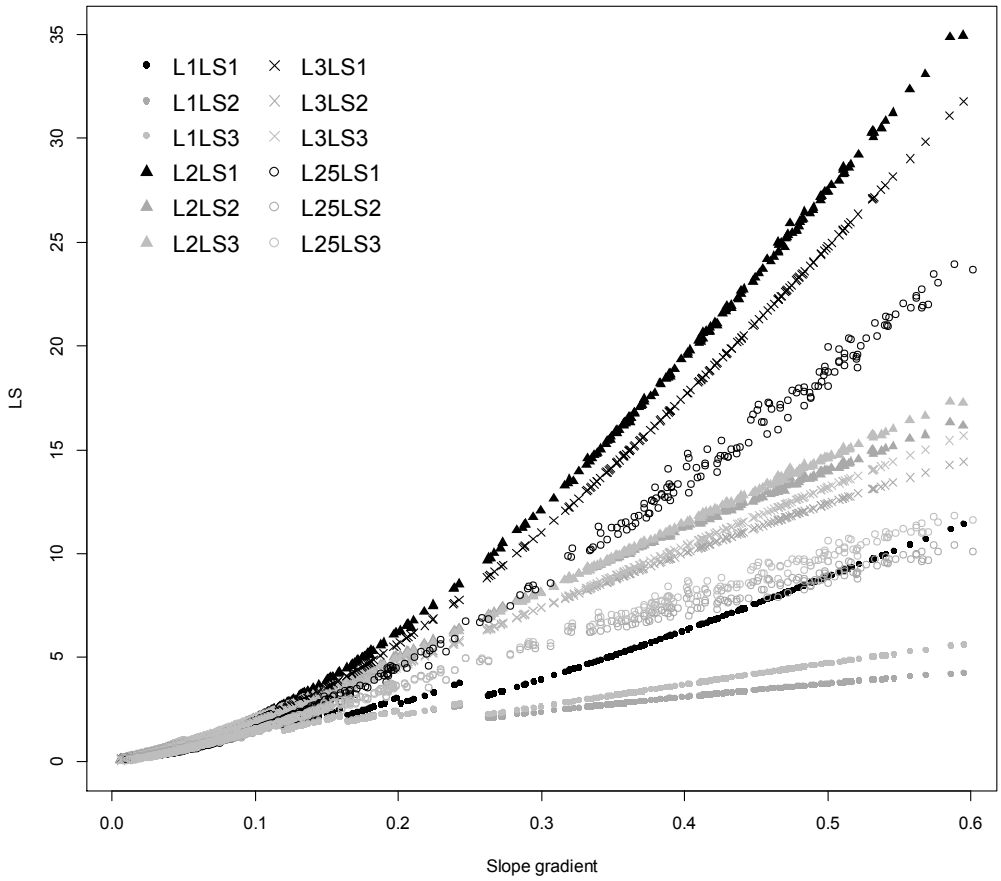


Figure 98. Subbasin slope length (LS) factors against slope gradient for all the possible combinations between 4 L factors and 3 LS algorithms

### 4.3.4 The calibration of Gross Erosion (GE)

Mean annual gross erosion, GE, calculated with the classic USLE equation (Nietsch et al., 2011) for the whole simulation period (1995–2009) of the default SWAT configuration (L0LS1), was compared to water erosion rates reported in the literature (Maetens et al., 2012; Panagos et al., 2014; Cerdan et al., 2010) for major land use types. Based on this evaluation, the USLE C value was increased from 0.001 to 0.005 in forest land. GE in pastures in the uncalibrated model was too high, but was insensitive to USLE C. A further analysis showed that pasture biomass was generally under-predicted in the SWAT application to the study area. This explained the insensitivity of sediment to USLE C, whose use in SWAT is regulated by the amount of residues on the soil surface (Neitsch et al., 2011).

To correct for erosion overestimations, the USLE P factor for pasture land was set to 0.1. This was a practical solution for reducing the excessive GE from pasture; the USLE P factor

was used as a surrogate of the C factor and should not be interpreted as a soil management factor.

After calibration, GE broadly matched erosion rates reported in literature (Figure 99), although GE in forest land and pastures seemed high in comparison with plot observations or estimates from maps.

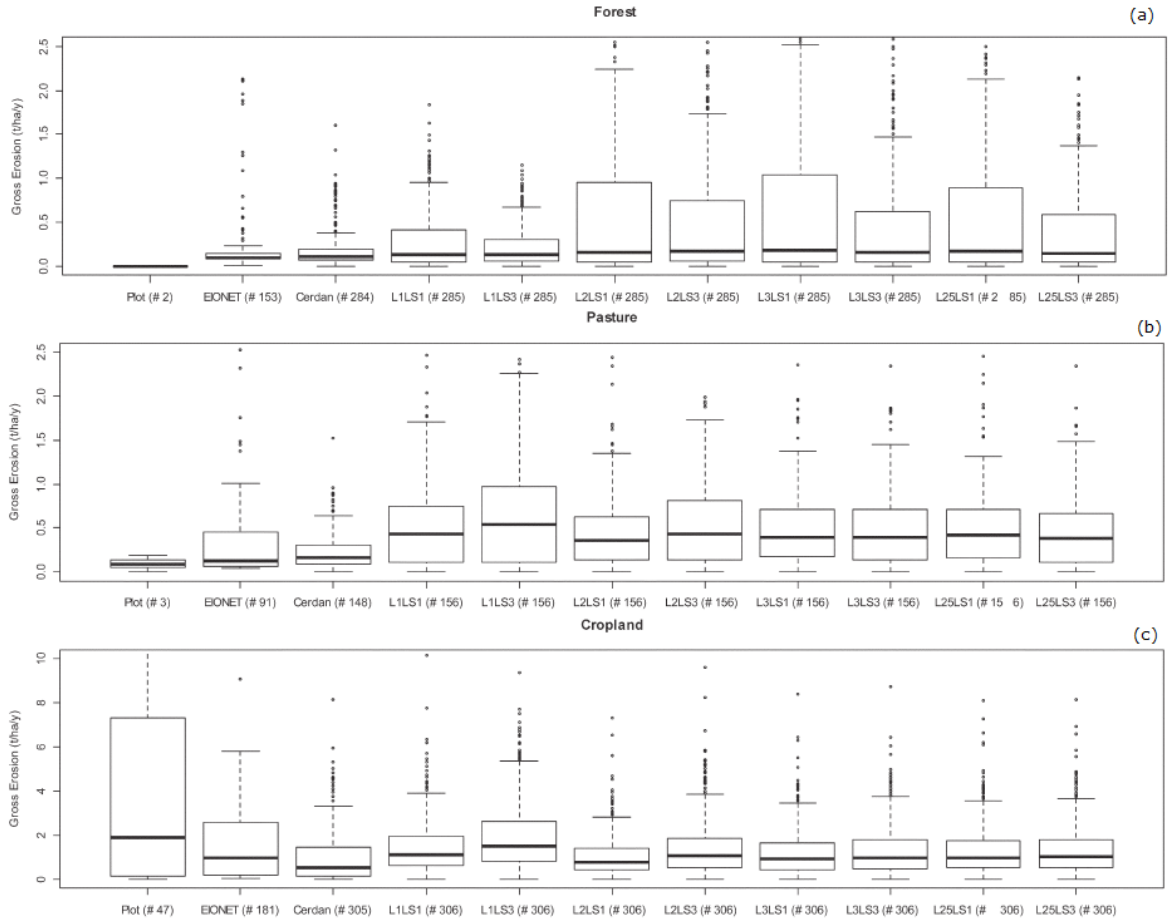


Figure 99. Gross erosion rates (GE, t/ha/year) for three major land use types as measured on runoff plots in or near the Upper Danube basin, as derived from previously published erosion maps, or as predicted with USLE for the period 1995–2009 in the Upper Danube basin under the indicated L–LS configurations. Plot=soil loss data from the region extracted from a plot database compiled by Maetens et al. (2012); EIONET=median erosion rates for SWAT HRUs as estimated in EIONET national assessment (Panagos et al., 2014); Cerdan=median erosion rates for SWAT HRUs as estimated by Cerdan et al. (2010). LS2 configurations (Table 19) are not shown, but were close to LS3. # indicates the number of units for each boxplot.

However, considering that runoff plot data for forest and pastures were few, and the simplifications in the use of map data, the calibration was considered adequate. GE differences between L–LS configurations were more noticeable in forest land, which extends mainly on the steeper slopes. Hillslope length L1 GE were the lowest and better corresponded to the distribution of GE from observations and maps, thanks to the calibration of forest USLE C which was done on L1LS1 and applied to all configurations.

GE in L2, L3, and L25 was generally higher than in L1, because of the association of steep slopes with longer hillslopes than in L1 case. Differences in LS values at steep slopes (Figure 98) also explain why LS1 yielded higher GE than LS3 (and LS2, data not shown because it was close to LS3). The reverse could be observed in cropland, which extends mainly on flat areas, where L1 yielded higher GE than in other cases, due to its longer values, close to 122 m.

### 4.3.5 Calibration and validation of suspended sediment concentration (SSC)

Based on the parametrization described in section 4.3.2, the interquartile of SSC residuals (simulation–observation) was within the interval−15 to+15 mg/l for all configurations, while the median residual values were close to zero both in the calibration and in the validation period (Figure 100). L1 showed a longer tail of negative residuals (underestimations) compared to other configurations. Some large positive residuals observed in L3LS2 and L3LS3 configuration in the calibration period did not occur during the validation period. Considering both the calibration period and the validation period, the default L0LS1 and all L2 configurations showed a distribution of residuals that was broadly symmetric around zero; L2LS2 and L2LS3 also attained the smallest residual ranges.

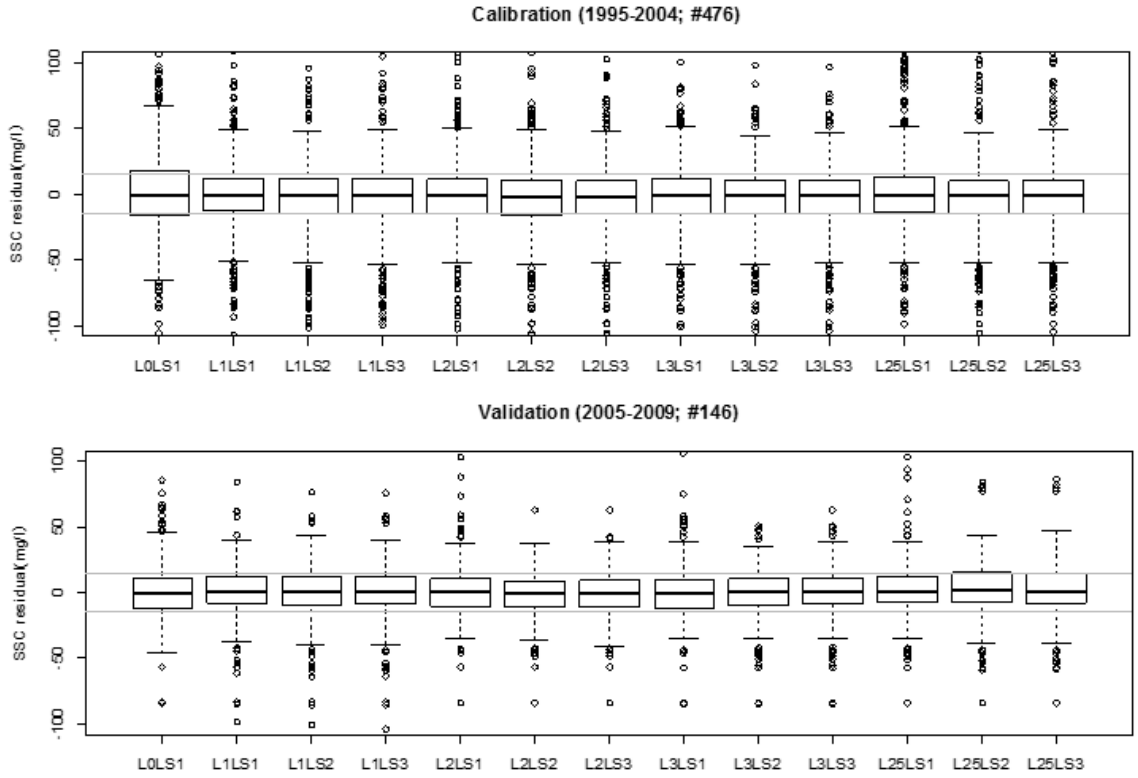


Figure 100. Box-and-whisker plot of suspended sediment concentrations (SSC) residuals (=simulation – observation) of the mean annual values for the observations of the 13 SWAT configurations analyzed in this study (Table 19). # is the number of station-year entries in the calibration and validation periods. The grey horizontal lines indicate an error of + / – 15 mg/l. Note that y axis is cut at +/- 100 mg/l.

It was observed also that the low correlation between L0LS1 and L1LS1 indicates that the introduction of a threshold area had a profound impact on SSC outputs at the basin scale too (Vigiak et al., 2015a). LS2 and LS3 configurations that shared the same hillslope length were always highly correlated, reflecting the similarities in LS distributions (Figure 98). Conversely, configurations L2LS2/LS3 were not strongly correlated to L3LS2/LS3, despite these four LS factor distributions were similar (Figure 98). Quite surprisingly, SSC outputs of L2 (all configurations), L3LS1, and to a lower extent L25LS1, were well correlated to the default (L0LS1) setting.

### 4.3.6 Evaluation of specific sediment yields (RSSY)

The distribution of reach specific sediment yield (RSSY, t/km$^2$/year) residuals highlighted more differences among SWAT configurations (Figure 101). In this case, most configurations, particularly L0LS1 and L1, showed a tendency to overestimate RSSY (positive residuals). Only in configurations L2LS2 and L2LS3 the interquartile range of residuals was within the interval +/−10 t/km$^2$/year in the simulation period (1995–2009). It was observed also that RSSY were more correlated among SWAT configurations than SSC (Vigiak et al., 2015a). Configurations L1 were the least correlated to the others, whereas configurations L2, L3 and L25 were well correlated among them and to L0LS1. An explanation in the difference in correlations can be found in the impact of streamflow simulation on SSC. SSC are the ratio of sediment yields divided by the streamflow, thus differences in streamflow simulations among SWAT hillslope length configurations (Malagó et al., 2015b) are partly reflected in the lower correlations found for SSC than for RSSY results.

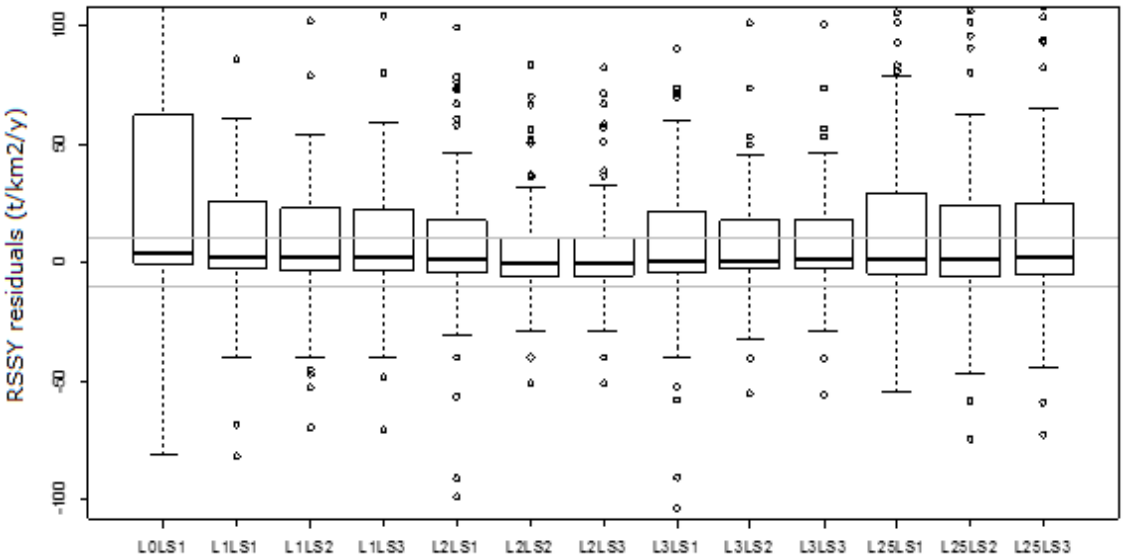


Figure 101. Box-and-whisker plot of Reach Specific Sediment Yields (RSSY) residuals (= simulation – observation; t/km$^2$/y) of the 13 SWAT configurations analyzed in this study (Table 19). Residuals are for the full simulation period 1995-2009 (86 station-year entries). The grey horizontal lines indicate an error of +/ – 10 t/km$^2$/y. Note that y axis are limited at +/- 100 t/km$^2$/y.

### 4.3.7 Best configuration

The analysis of SSC and RSSY residuals indicated that albeit all configurations could provide good simulations of sediment concentrations and yields, the configurations L2LS2 and L2LS3 were the best performing overall. Among these two, L2LS3 was considered the best configuration from a conceptual viewpoint, as it combined the use of a 3D algorithm for hillslope length with a 3D slope-length factor (Moore and Wilson, 1992), so the combination is intrinsically consistent and appropriate for basin modeling.

The L2LS3 model results for the full simulation period (1995–2009) in terms of SSC and RSSY are reported in Figure 102 and Figure 103.

The mean percent bias (PBIAS, Moriasi et al., 2007) of SSC simulations was 11% for the full dataset (622 data entries) and 24% as mean PBIAS per station.

It was observed that the distribution of SSC residuals with the drainage area (km$^2$) shows that model errors could be large in small drainage areas, where the influence of local conditions could not be fully accounted for by the model (Vigiak et al., 2015a). The attribution of a subbasin to a single land use class (a dominant HRU) is certainly an important source of this error. The only exception was at the mouth of the Inn at Passau (with about 26,000 km$^2$ of drainage area), where sediment concentrations were underestimated.

The spatial distribution of mean annual SSC in the Upper Danube (Figure 102a) results from the combination of hillslope erosion, stream processes (aggradation and degradation),

as well as siltation in reservoirs. The highest sediment concentrations were simulated for the Alpine foot slopes. However, along the main tributaries and on the Danube itself, the many locks reduced sediments considerably. The Austrian Alpine region appeared an important sediment source also in terms of RSSY (Figure 102b). The spatial distribution of RSSY errors as measured with the PBIAS showed no evident spatial pattern (Figure 102b).

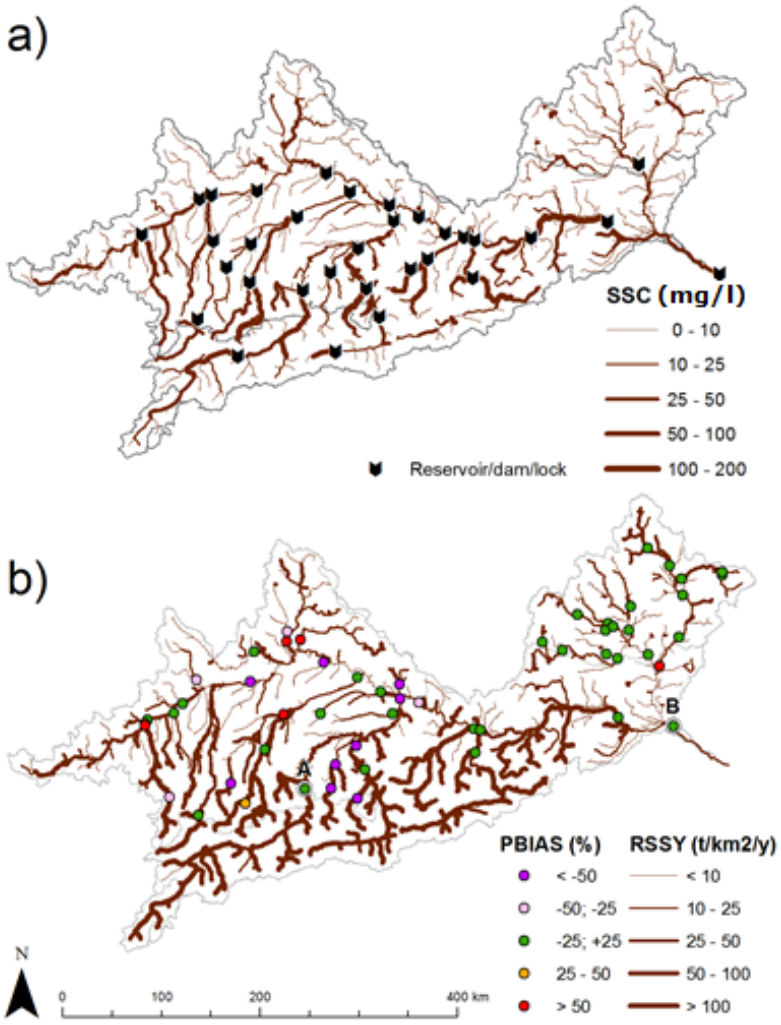


Figure 102. Mean annual reach sediment outputs in the Upper Danube for the simulation period 1995-2009: a) simulated Suspended Sediment Concentration (SSC, mg/L) in relation to reservoirs/dam/locks; b) specific sediment yields (RSSY, t/km$^2$/y) with percent bias (PBIAS, %) at the available gauging stations. The letters A-B indicate the location of two stations for which time-series simulations are provided in Figure 103. The results refer to configuration L2LS3.

Figure 103 shows the annual time-series of SWAT SSC and RSSY simulations for two stations that differs for environmental conditions (an upstream and a downstream station, Figure 102b), versus SSC and RSSY observed mean values. Visual appraisal of the time-series indicates good correlation between simulations and observations. Some discrepancies between SSC and RSSY outputs in comparison with observations could be detected. At Kirchdorf (Germany) SSC simulations matched only broadly the mean SSC of

the time-series, but RSSY followed the annual observations well. At Bratislava (Slovakia), at the Upper Danube Basin outlet, annual SSC and RSSY appear to be satisfactorily simulated (SSC PBIAS at this station was 51% and RSSY PBIAS was−3.8%).

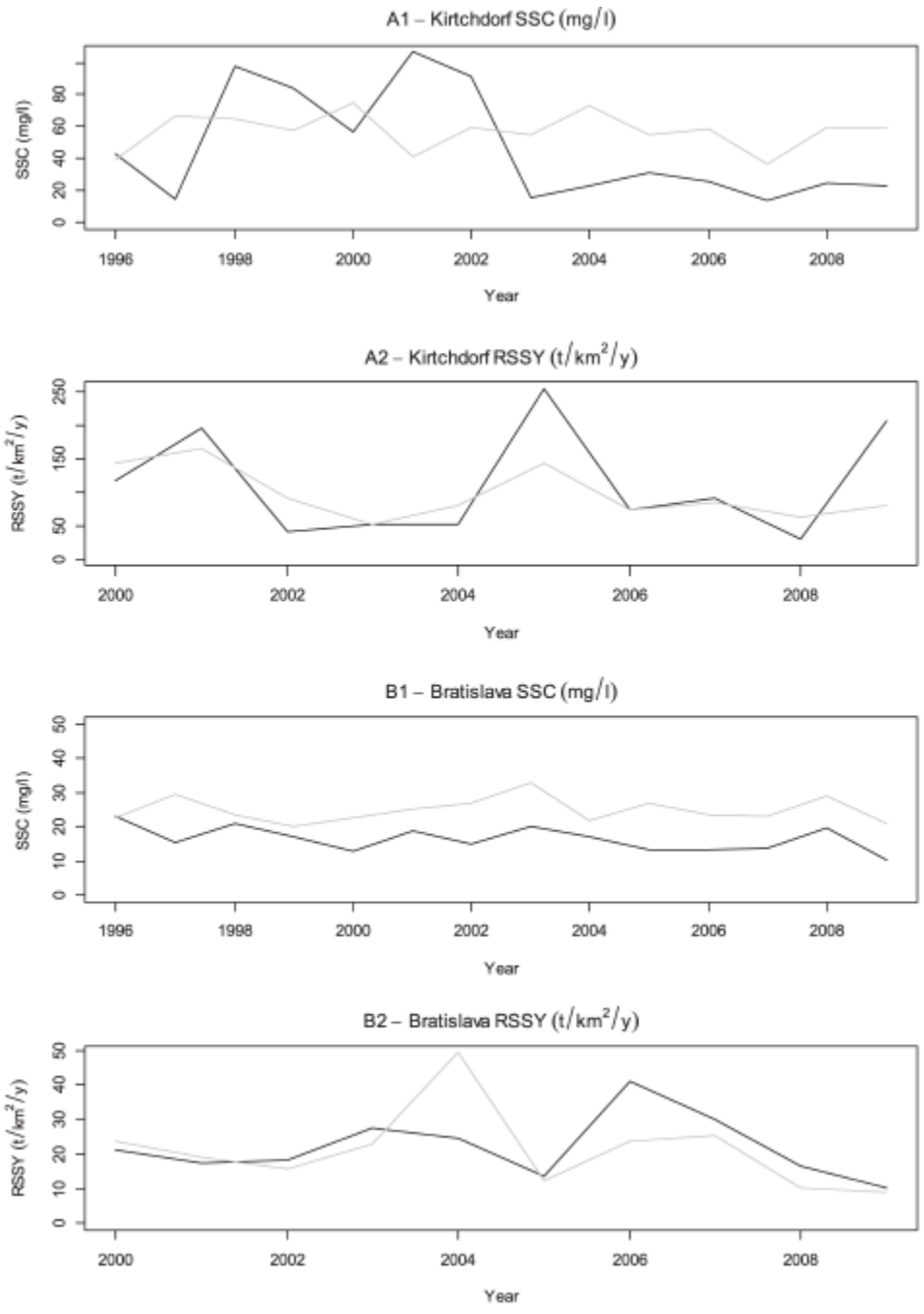


Figure 103.Comparison of SWAT outputs (grey lines) with observations (black lines) at three selected monitoring gauging stations (locations shown in Figure 103b). A: Kirchdorf station (Germany) on the Inn river: (A1: mean annual suspended sediment concentration SSC, mg/l; A2: reach specific sediment yield RSSY, t/km$^2$/y). B) Bratislava (Slovakia), at the outlet of the Upper Danube Basin (B1: SSC; B2: RSSY). Note the varying ranges of the y axis. The results refer to configuration L2LS3.

### 4.3.8 Sediment balance in the Upper Danube

The sediment budget at the Basin outlet (Figure 104) highlights the main sources and sinks of sediments in the Basin (Walling and Collins, 2008). Because the MUSLE provides directly sediment yields, hillslope erosion, i.e. the HRUs sediment yields to the reach network system, could not be further partitioned between gross erosion and hillslope deposition. Hillslope erosion accounted for 54% of sediment production, whereas stream degradation processes produced 46% of sediments in the system. In terms of stream processes, however, aggradation, thus sediment deposition in the reaches, was the dominant process of the region. Degrading reaches were mostly confined to the Alpine area and on some short Danube reaches. Siltation in reservoirs/locks accounted for 30% of sediment deposition in the region. The net export of sediments from the Basin was estimated at about 8% of total sediment yield generated in the catchment (corresponding to 21.2 t/km$^2$/year).

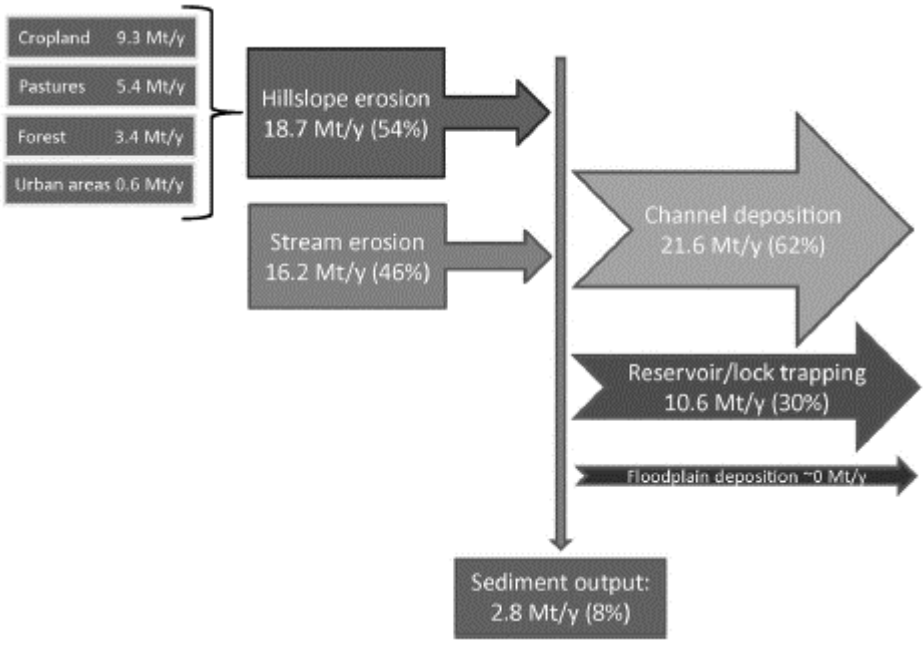


Figure 104. The modeled sediment budget of the Upper Danube Basin for the simulation period (1995–2009)

### 4.3.9 Conclusions of the section

In this study, several modifications for SWAT hillslope sediment yield estimations were tested for applications to large basins, i.e. where the spatial data are most often of coarse resolution and with large spatial units (HRU > 100 km$^2$). The introduction of a threshold area above which specific sediment yields were linearized in relation to HRU area ([eq.13]) overcame the risk of overestimating sediment yields in large HRUs. This modification had large impact on sediment yields both at the hillslope and at the basin scale. The threshold area was set at 0.01 km$^2$, thus interpreting a functional HRU as a hillslope, for which sheet

and rill erosion would be dominant sources of sediments while hillslope deposition would be the dominant sediment sink.

The analysis of topography settings highlighted the importance of combining hillslope length with LS factor algorithms. The use of hillslope length (L2) and topography factor (LS3) estimated with DEM-derived flow accumulation analysis not only performed the best, but was intrinsically consistent and well suited for a basin model. Given that GIS tools to apply flow accumulation analysis even to large areas are readily available (e.g. Zhang et al., 2013), the L2LS3 combination should become part of the default SWAT GIS pre-analysis.

The multi-type and multi-site data calibration methodology pursued in this study allowed achieving robust constraining of sediment modelling. In the Upper Danube basin, the SWAT configuration that combined a threshold area and 3D topography settings resulted in good simulation of sediment concentrations and specific sediment yields for the period 1990-2009. No evident bias was detected with drainage area, slope, or spatial distribution. Yet, large errors were occasionally observed, particularly in small drainage areas. Hence, model outputs are more reliable at the aggregated scale (e.g. tributaries) than at the local scale of a single HRU or subbasin.

Finally, the modelled sediment budget for the Upper Danube Basin for the period 1995-2009 indicates that hillslope and streambank erosion produce respectively 54 and 46 % of all sediments. Siltation in reservoir or upstream locks account for 30 % of the sediment trapping and only 8 % of sediments (about 21 t/km$^2$/y) leaves the basin. To the best of our knowledge this is the first sediment budget of the region, providing valuable information to natural resources managers.

## 4.4 Balancing environmental advantages with investment costs: a multi-objective approach

### 4.4.1 Synopsis

Nutrient losses of Nitrogen (N) and Phosphorus (P) from Point (PS) and Diffuse sources (DS) are recognized as the main causes of water body impairment throughout Europe. Implementation of conservation programs (Best Management Practices, BMPs) is crucial for restoring and protecting the good ecological status of freshwater bodies. However, their application should be pursued considering both environmental and economic objectives. For this purpose, a multi-objective R-SWAT framework was developed, combining the use of the Soil and Water Assessment Tool (SWAT) model, the spatial representation of BMPs, an economic component, and multi objective optimization libraries (Udias et al., 2015). The main characteristics of R-SWAT model are provided in Appendix A5.

The framework was applied to the case study of the Upper Danube Basin, previously described in section 3.4, with the main objective the identification of BMP allocation minimizing both nutrient losses and management costs running a multi-objective optimization process in the R-SWAT-DM.

Two groups of nutrient reduction management practices were considered in the application. The first is related to point sources reduction in terms of upgrading of Waste Water Treatment Plants (WWTPs), while the second is related to diffuse source reduction in terms of decreasing mineral fertilizers.

### 4.4.2 The multi-objective optimization tool

In the Upper Danube case study, two objectives were simultaneously considered: an environmental and economic objective.

The environmental objective focused on nitrate-nitrogen N-NO3 contamination reduction, since it is the most important issue in the region. Among the available environmental objective function in R-SWAT-DM (see Appendix A5), the cumulative contaminant was selected as *sum of N-NO3 concentration exceeding the limit of 50* mg/l as prescribed by the Water Framework Directive. This limit identified the *Th* threshold in equation [eq. A5.2].

The economic objective was identified as the *global income*, defined as the difference between the total net income for a scenario (sum of WWTP cost, crop income and crop management cost) less total net income in the base line scenario (BLS).

To achieve these two objectives in the Upper Danube case study, scenarios, or rather strategies, of mineral fertilizers application in 291 fertilized HRU were considered, as well as the WWTP upgrading for each of the 533 point sources in the watershed.

Figure 105 shows a comparison between different strategies of fertilizers application and upgrading WWTP respect to the aforementioned objective functions. The Baseline Scenario (*BLS*) represents the current state of the basin according to SWAT model. Changing the rate of fertilizers in the same way in all HRUs (BLS fertilizer Iteration in all HRU), the *SmartFert* solution (corresponding to the maximum global income) was identified as the best.

WWTP upgrading can be included starting from the *BSL* or *SmartFert* solution. Thus the number of optimal solutions increase, the more considering the WWTP upgrade for type of treatment levels (identified in Figure 105 as *WWTP->1* and *WWTP->2*). SmartWWTP, SmartG, OptiWWTP strategies in Figure 105 represents some of the optimal solutions form these combination of strategies.

However, to identify the optimal combined solution, a multi-objective optimization based on Pareto front algorithm (Pareto,1971) was applied using the R-SWAT-DM.

Figure 106 compares the previous strategies showed in Figure 105 with the Pareto Strategies, in which about 3000 simulations were investigated for each of them.

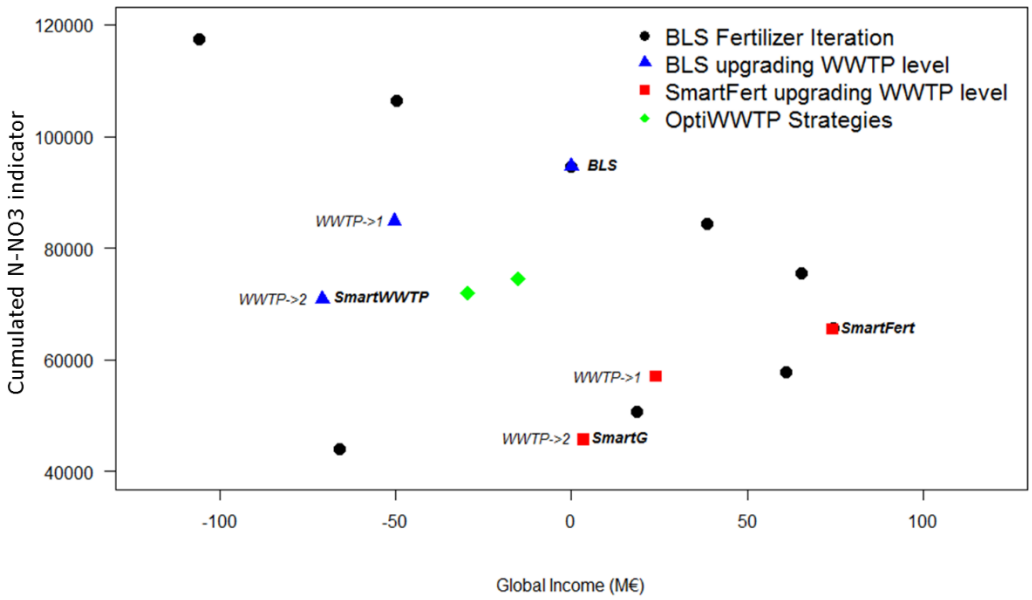


Figure 105. Comparison between economic and environmental objective for iterative simulations. The BLS Fertilizer Iteration (black point) refers to the variation of the rate of fertilization equally in all HRUs. Strategies of upgrading all WWTPs are shown as blue triangle for the *BLS* and red square for the *SmartFert* strategy (both *BLS* and *SmartFert* points are the actual WWTP status; WWTP->1: all the plants are upgraded to CND level; WWTP->2: all plants are upgraded to CNDP level as described in Appendix A5).

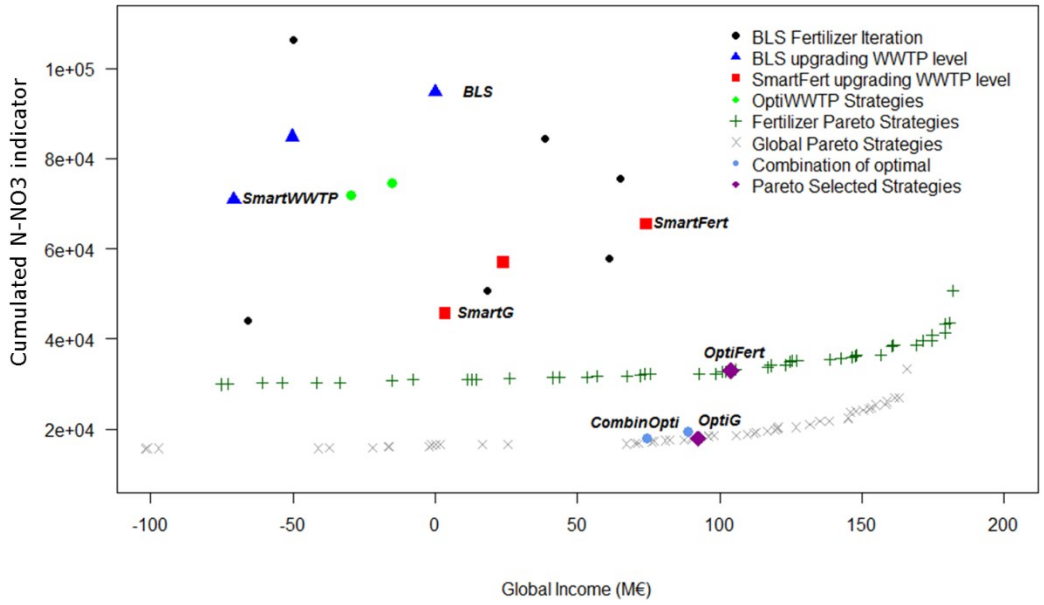


Figure 106. The Pareto front strategies for the multi-objective scenarios compared to strategies of Figure 105.

It is noticeable that the multi-objective optimization is able to find the optimal solution (i.e. OptiG in Figure 106) that allows achieving the combined objective of N-NO3 pollutant reduction and increase of global income.

Figure 107 shows the results obtaining applying the OptiG scenario (Figure 105c) in terms of long-term monthly N-NO3 concentration in each reach in the study area. It is noticeable, that the OptiG scenario decrease the number of reaches that exceeded 50 mg/l (red color) in the BLS (Figure 105a) and OptiFert (Figure 105b) scenarios, confirming the advantage of applying the Pareto front strategy.

### 4.4.3 Conclusions of the section

Using R-SWAT-DM is possible to obtain a comprehensive picture of a complex scenarios of BMPs in a watershed helping decision makers in finding the optimal management solution that combines environmental and economic objectives.

The strength of this tool concerns the use of the Pareto optimal strategies, especially useful in the definition of the limits of improvements, as well as the automatic visualization of results in maps (see for instance Figure 107) that helps to identify areas polluted (or at risk of pollution) and the spatial distribution of the conservation strategy improvements to be implemented.

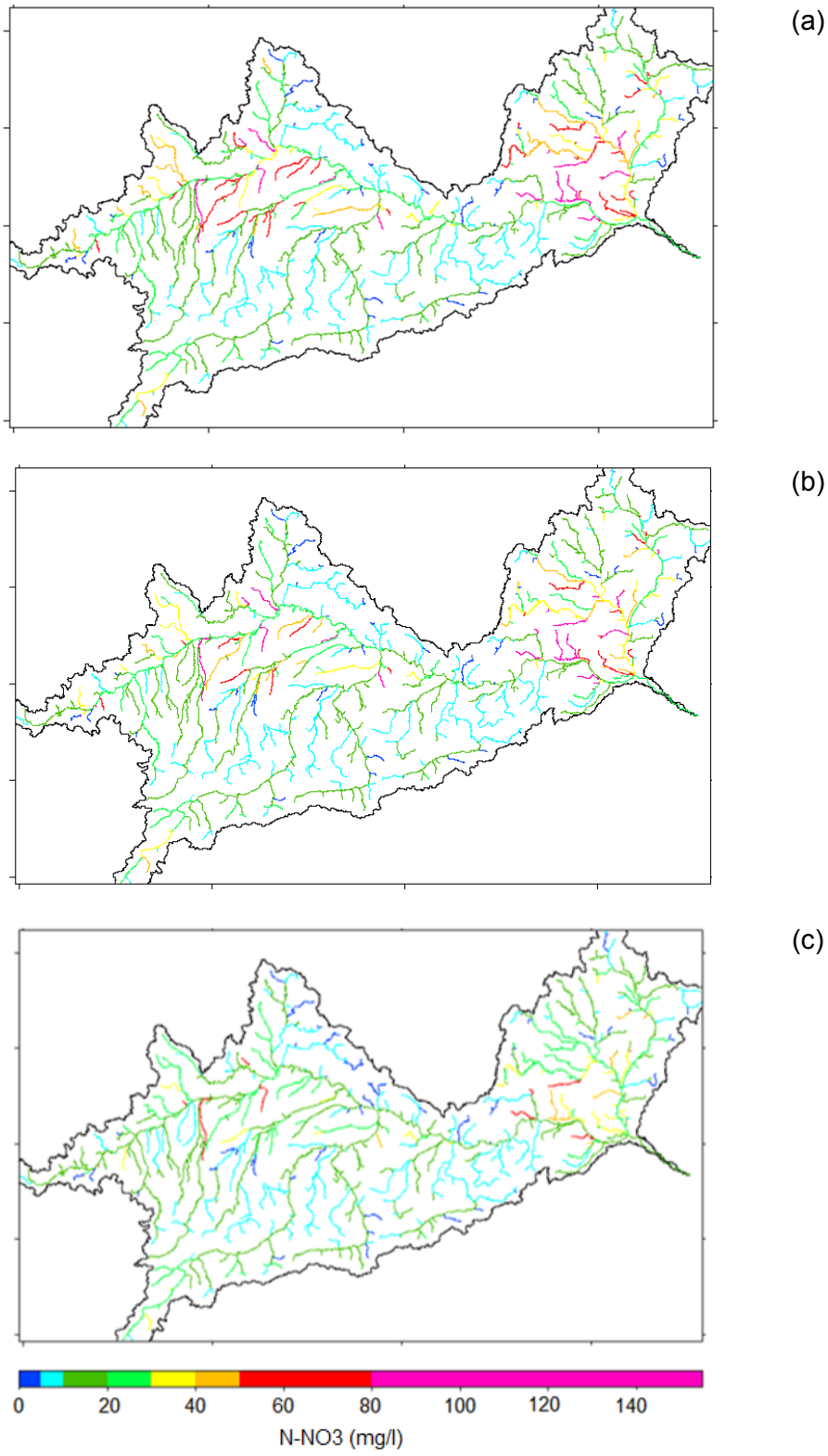


Figure 107. Long-term mean monthly N-NO3 concentration (mg/l) in each reach in the Upper Danube applying three different management strategies. In (a): BLS; (b) SmartFert; (c) OptiG. The results refer to the period of simulation 1995-2009.

# CHAPTER 5

# 5 Benchmarking

## 5.1 Chapter Introduction

Most European rivers suffer significant nutrient pollution. The Water Framework Directive (WFD; EC, 2000) requires regional authorities to develop and implement river basin management plans to improve current conditions. River basin management plans are developed with the involvement of stakeholders to design appropriate remediation actions, based on the analysis of the socio-economic and biophysical river basin characteristics. The scientific community supports the process by providing information on nutrient fluxes and pathways within the river basin and in developing decision support tools such as Integrated Basin Models to help identifying cost-effective strategies to reduce water pollution.

Integrated Basin Models provide a transparent framework to address the dominant processes that affect nutrient sources and pathways, as well as their multiple interactions. They capture the current understanding of biophysical processes that govern the transport of nutrients from land to rivers and to the sea. At the same time, they allow assessing the potential impacts of envisaged management plans. Given the complexities of real world systems, Integrated Basin Models can only provide a partial representation of the biophysical processes, capturing the dominant trends as inferred from observation data. Observed nutrient data usually consist of concentration measured at monitoring stations in rivers. By definition they provide local information, representing at the same time an integral of the entire upstream catchment, and are assumed to be representative for the considered period (month, year). Additionally, data of the main environmental factors upon which models simulate the biophysical processes, such as land use/coverage, climate, geology, soil, and topography are of limited spatio-temporal resolution, extent and accuracy. Any Integrated Basin Model is thus suffering a structural uncertainty, i.e. the representation of the main processes and interactions, and a data uncertainty, i.e. implicit in the environmental data used to feed them or to calibrate/evaluate their outputs. Beyond that, as a result of differences in the process representations, included in the models and in the data used to create them, different Integrated Basin Models applied to the same basin may differ in the type and resolution of their outputs, and in the partition of nutrient sources and pathways.

Since both data and models are affected by uncertainty, decision makers have to plan management actions on the basis of incomplete knowledge of the systems. Comparison of

results from different Integrated Basin Models however, may provide further insights to help decision-making, for example in pointing out knowledge gaps or consolidated assessments and increase acceptability by end-users (Grizzetti et al., 2015).

Within the context of fostering scientific collaboration in the Danube region, an inter-comparison of independent assessments is here envisaged to identify opportunities and knowledge gaps in the region. The overall objective of the inter-comparison was to reach a shared and robust assessment of nutrient pressures and the drivers in the Danube River Basin to strengthen water management planning.

The assessments of water nutrient pollution in the Danube River Basin as estimated by three independent models are compared. Accepting that the three models differed in structural complexity and data requirements, the comparison focuses on model outputs of water balance, nitrogen and phosphorus fluxes. The analysis aims at identifying regions where models agreement indicated congruent baseline assessments, and regions where models disagreement indicated uncertainty in the assessments, where more investigation would be warranted.

## 5.2 Comparing SWAT performances with other models of different structure with reference to a real case: the Danube River Basin.

### 5.2.1 Scope and approach of the inter-comparison

Model comparison exercises are not new in the scientific literature. For example, several Integrated Basin Models using the same data, whenever possible, have been compared in the project EUROHARP (Silgram et al., 2009). Unlike previous works, in this study the objective of the inter-comparison was not on the models, but on model outputs to gain insights useful from a management perspective. The comparison thus focused on the quality of the model results, including indications on expected model performances and pointing out the strengths and weaknesses in the region (Grizzetti et al., 2015; Thunis et al., 2011).

The spatial units selected for conducting the comparison were the 18 ICPDR main regions (or water management regions) as showed in Figure 22 in section 3.3.2, excluding the littoral regions for which no gauging station was available. The period for the comparison was the decade 2000-2009, which was considered long enough to allow for being relevant to management planning, representative of current conditions, and was covered in total or at least in part by all three models (Figure 108). Model outputs considered in the comparison were annual streamflow ($m^3/s$), total nitrogen (TN, ton/y), and total phosphorus (TP, ton/y) loads at the outlet of each water management regions.

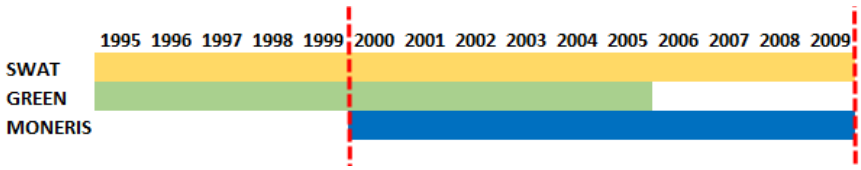


Figure 108. Temporal scale of model simulations. The red lines define the period of interest for this study (2000-2009).

The evaluation was conducted using two different types of graphics: bar plots with 95% confidence intervals (CI) and Taylor diagrams (Taylor, 2001). More details about these plots and their interpretation are reported in Appendix A6. However, in this thesis only a limited part of the created plots is reported, and for a complete visualization the reader can refer to Malagò et al. (2015a). Observations of streamflow and nutrient loads were not available at all region outlets. Table 21 summarizes the monitoring stations for which observed data of at least 5 out of 10 years (2000-2009) were available. Figure 109 shows the location of the gauging stations. Mean annual streamflow was computed from daily streamflow data. Nutrient loads used as observations were estimated from nutrient concentration and daily flow, and calculated based on different methods: flow weighted concentrations method proposed by Moatar and Meybeck (2005) as well as the ICPDR method described in the ICPDR yearbooks (ICPDR, 2000-2009a) and literature estimations (van Gils, 2004).

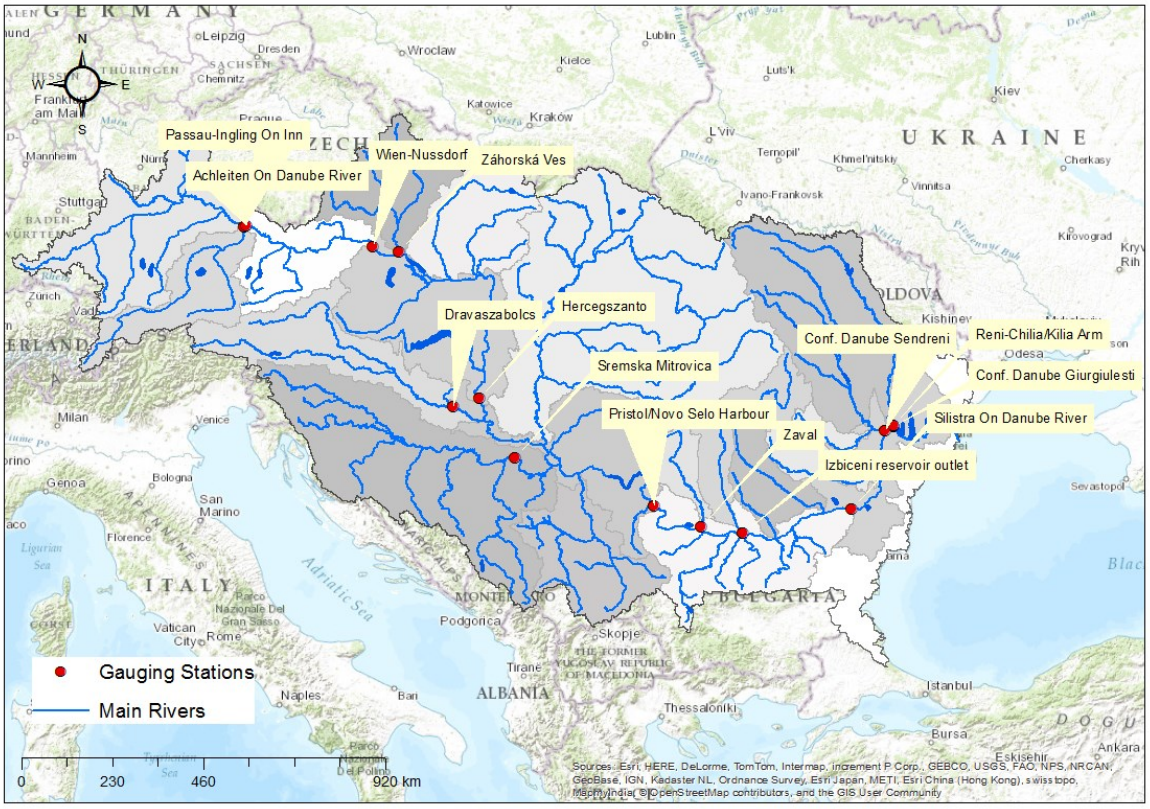


Figure 109. Gauging stations used in performing the benchmarking approach

Table 21. Water management regions code, names, drain area (km$^2$), and gauging stations of reference used in the inter-comparison. The term “available” indicates that observed data for the variable were available for at least five years in the decade 2000-2009.

| ID-Regions | Drain Area (km$^2$) | Name of Regions | Station Name | STREAMFLOW | TN LOADS | TP LOADS |
|---|---|---|---|---|---|---|
| 1 | 49769 | Danube Source | Upstream Achleiten station (excluding the Passau Ingling) | available | | |
| 2 | 25999 | Inn | Passau Ingling | available | | available |
| 3 | 101803 | Austrian Danube | Wien-Nussdorf | available | | available |
| 4 | 26628 | Morava | Zahorska Ves | available | | available |
| 5 | 30589 | Vah-Hron-Ipel | | | | |
| 6 | 211103 | Pannonian Danube | Hercegszanto | available | available | available |
| 7 | 39679 | Drava | Dravaszabolcs | available | available | available |
| 8 | 100102 | Sava | Sremska Mitrovica | available | | |
| 9 | 149567 | Tisa | | | | |
| 10 | 37702 | Velika Morava | | | | |
| 11 | 582414 | Middle Danube | Pristol/Novo Selo harbour | available | | available |
| 12 | 10333 | Jiu | Zaval | available | | |
| 13 | 23841 | Olt | Izbiceni reservoir | available | | |
| 14 | 18118 | Arges-Vedea | | | | |
| 15 | 685320 | Silistra Sanube | Chiciu/Silistra | available | available | available |
| 16 | 16358 | Buzau-Ialomita | | | | |
| 17 | 71490 | Siret-Prut-Buzau | Sendreni and Giurgiulesti | available | | available |
| 18 | 802032 | DELTA | Reni Chilia | available | available | available |

Streamflow data near the outlet were available for most regions, except for Region 5 (Vah-Hron-Ipel), Region 8 (Sava), Region 9 (Tisa), Region 10 (Velika Morava), Region 14 (Arges-Vedea), and Region 16 (Buzau-Ialomita). Estimates of TN loads from gauging stations were available only for Region 18 (Delta), Region 6 (Pannonian Danube), Region 7 (Drava) and Region 15 (Middle Danube). In contrast, estimates of TP loads were available in most regions. In order to include more observations in the analysis the stations Dravaszabolcs in region 7 (Drava Basin) was considered as the outlet of region because the drainage area of station Dravaszabolcs (about 37500 km$^2$) is very close to the drainage area of the whole Drava river (about 39700 km$^2$). Similarly, for Region 6 (Pannonian) and Region 8 (Sava) the station Hercegszanto and Sremska Mitrovica respectively were used as references for the correspondent outlet. For Region 17 (rivers Siret and Prut), the Buzau basin (5240 km$^2$), a tributary of river Siret, was included.

Where no observed data was available, the arithmetic means of estimates of the three models were used as reference solely for understanding similarities and differences between the models. Henceforth, the abbreviation AVG is used for the arithmetic means of the models.

### 5.2.2 Streamflow comparison

The comparison between observed and simulated long-term mean annual streamflow ($m^3/s$) in the Danube River Basin is shown in Figure 110 and Figure 111. The map in Figure 110 highlights the strong correlation between the models and the good agreement with the observations. However, some important differences and similarities between the models, as more noticeable in Figure 111 can be captured. The results and statistics detected by bar plots and Taylor Diagrams, and summarised in Table 22, are used for this purpose.

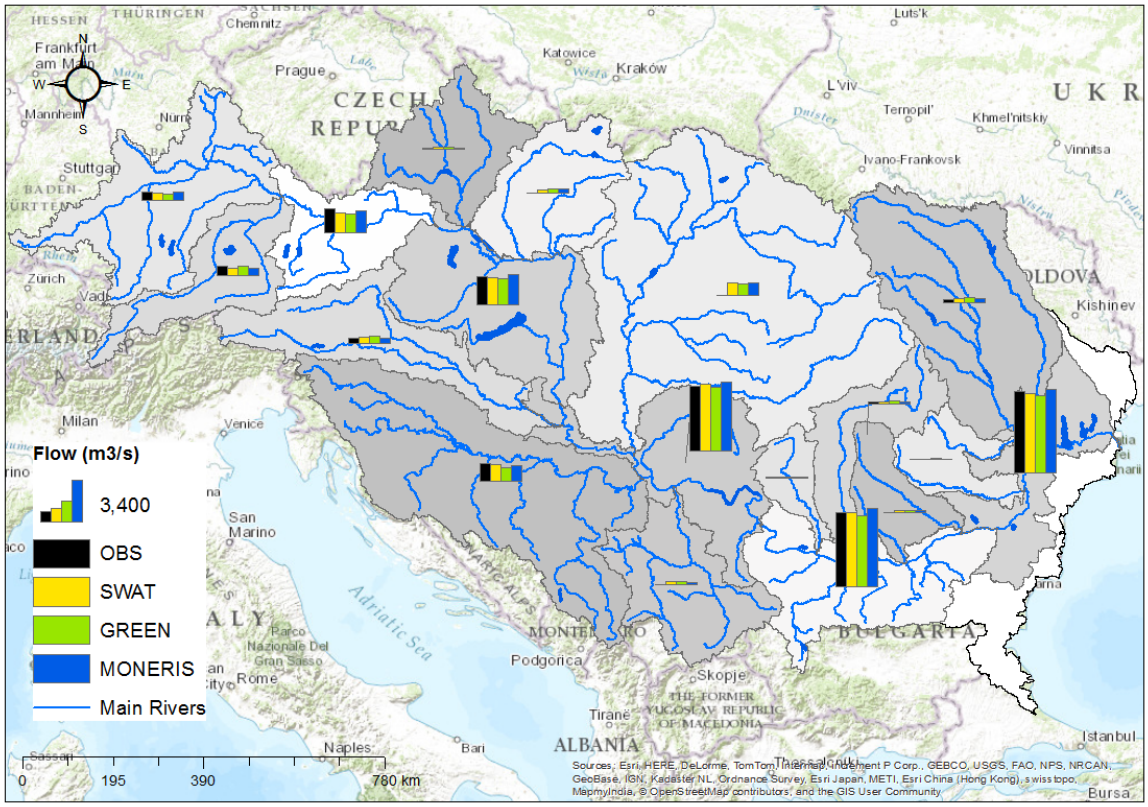


Figure 110. Map of the mean annual streamflow (period 2000-2009) in the Danube Basin. The three model outputs are compared to available observations.

In Region 1 (Danube sources) GREEN and SWAT slightly underestimated the long mean annual streamflow, whereas MONERIS agreed best with the observations. The Taylor diagram and bar plot in Figure 112 (see also Table 22) shows that GREEN and MONERIS had the correct standard deviation of 151 and 136 $m^3/s$ respectively and very high correlation with the observations (0.78 and 0.92). GREEN, however, had a slightly higher RMS error (97 $m^3/s$) than MONERIS (56 $m^3/s$). SWAT RSM error was close to that of

MONERIS (around 64 $m^3/s$), but SWAT overestimated the standard deviation. As a consequence, the amplitude of variations of annual streamflow was simulated better by MONERIS and GREEN than SWAT.

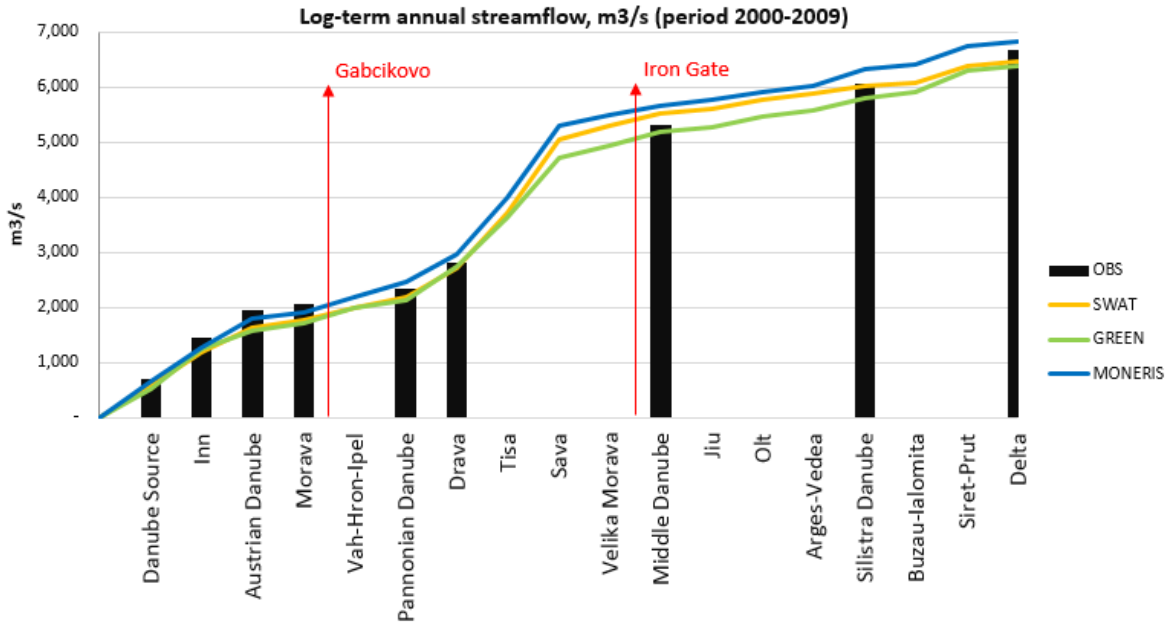


Figure 111. Cumulative annual streamflow estimated along the Danube River with SWAT, GREEN and MONERIS models for the period 2000-2009. The black bars represent the observation at the outlets of the water management regions. The red arrows indicate the position of the two main reservoirs, the Gabcikovo and the Iron Gate, along the Danube River.

A strong correspondence between MONERIS and the observations was observed in Region 2 (Inn Basin), 3 (Austrian Danube) and 4 (Morava), followed by SWAT and then GREEN (Table 22). In particular, in Region 2 MONERIS and SWAT generally agreed well with observations, each with about the same RMS error (50 and 58 respectively). GREEN scored a higher RMS error (84 $m^3/s$) and lower correlation (around 0.68), but the standard deviation was similar to that of MONERIS (around 111 $m^3/s$) and observations (standard deviation of observations was around 93 $m^3/s$). In Region 3, the three models had very high correlation with the observations. MONERIS simulated best the annual variations of streamflow (standard deviation of 271 $m^3/s$, very close to the standard deviation of observations that was a 288 $m^3/s$) with the lowest RMR error. In Region 4 MONERIS performed better than SWAT and GREEN, because it laid relatively close to the reference point of observations. Similarly to MONERIS, SWAT had high correlation with observation (0.88), but the standard deviation was larger (around 37 $m^3/s$) than that of the observations (21 $m^3/s$). As well, GREEN standard deviation was larger than that of observations, but the correlation was the lowest among the models (around 0.56).

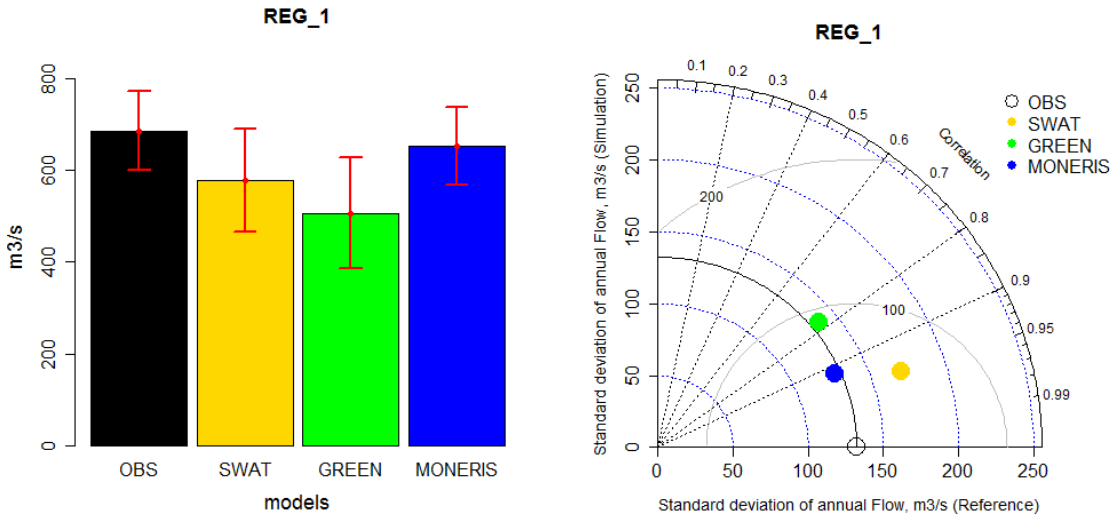


(a) (b)

Figure 112. Bar plot (a) and Taylor Diagram for streamflow of Region 1 (period 200-2009). In (a) the error bars in red indicate the 95% confidence intervals.

In Region 5 (Vah-Hron-Ipel, see Table 22) the three models had about the same correlation and RMS errors, but SWAT and MONERIS simulated the annual variability better than GREEN with respectively a standard deviation of 50 and 41 $m^3/s$ compared to the reference value of 46 $m^3/s$. In Region 6 (Pannonia Danube, Figure 113 and Table 22) SWAT simulated streamflow agreed best with observations, in terms of both error and annual variability (with a standard deviation 373 $m^3/s$ compared to observed value of 382 $m^3/s$) and a relatively small RMS error. MONERIS had about the same RMS error of SWAT, but higher standard deviation. In addition, the correlation coefficients of predictions with observations of SWAT and MONERIS were higher than GREEN.

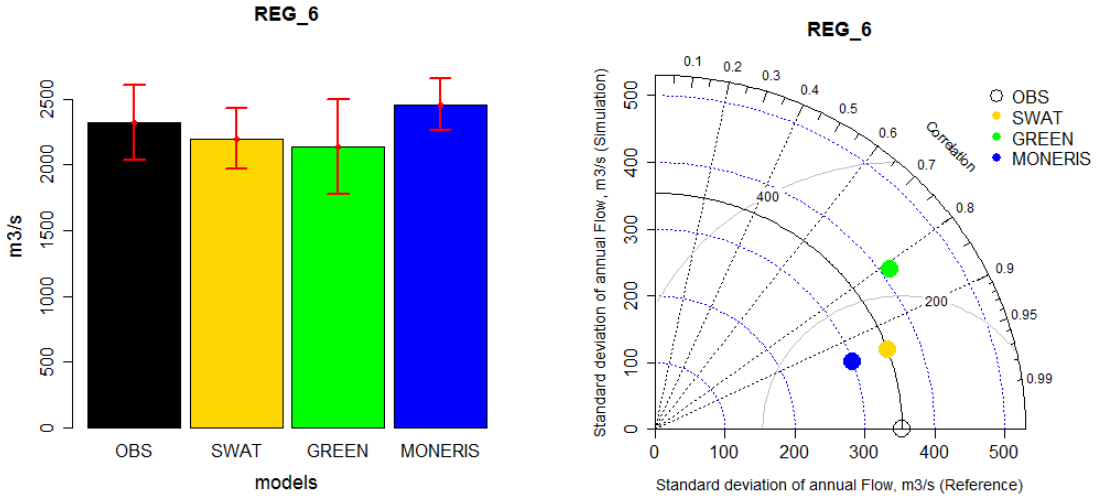


(a) (b)

Figure 113. Bar plot (a) and Taylor Diagram for streamflow in Region 6 (period 2000-2009). In (a) the error bars in red indicate the 95% confidence intervals.

In Region 7 (Drava) GREEN overestimated the long mean annual streamflow, whereas SWAT and MONERIS were close to observations. The Taylor diagram (Figure 114a) confirms that GREEN had the lowest correlation with observations and the highest RMS error (about 67 $m^3/s$) among the three models.

In Region 8 (Sava, Figure 114b) SWAT and MONERIS had the same annual variability of the observations (the standard deviation was around 256 and 229 $m^3/s$ compared to 204 $m^3/s$ of observed value). GREEN had about the same RMS error of MONERIS but higher standard deviation, highlighting an overestimation of the amplitude of annual streamflow variations.

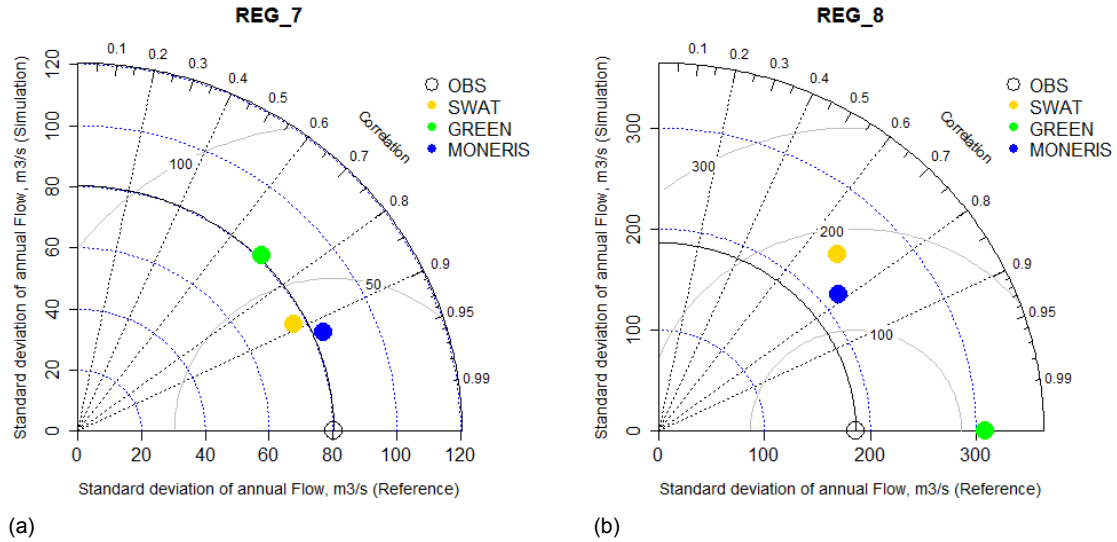


Figure 114. Taylor Diagrams of annual streamflow ($m^3/s$) in the period 2000-2009 for Region 7 and 8.

Similar results were found in Region 9 (Tysa, Table 22). SWAT and MONERIS agreed well with reference values: they had high correlation coefficients and same standard deviation (291 and 280 $m^3/s$ respectively), very close to the observed value (273 $m^3/s$). GREEN had the highest correlation with the observations; however, the standard deviation was overestimated, highlighting the largest amplitude of annual streamflow variations.

For Region 10 (Velika Morava) SWAT and MONERIS described better the reference values (Table 22), but while SWAT slightly overestimated the amplitude of the annual streamflow variations (standard deviation 72 $m^3/s$), MONERIS slightly underestimated it (54 $m^3/s$). GREEN had the highest standard deviation (102 $m^3/s$).

In Region 11 (Middle Danube, Figure 115) MONERIS and SWAT agreed well with observations, but SWAT had a slightly higher RMS error than MONERIS (494 $m^3/s$ of RMS error for SWAT compared to 208 $m^3/s$ of MONERIS). GREEN overestimated the annual

variations of streamflow, with higher RMS error around 878 $m^3/s$ and a smaller correlation coefficient.

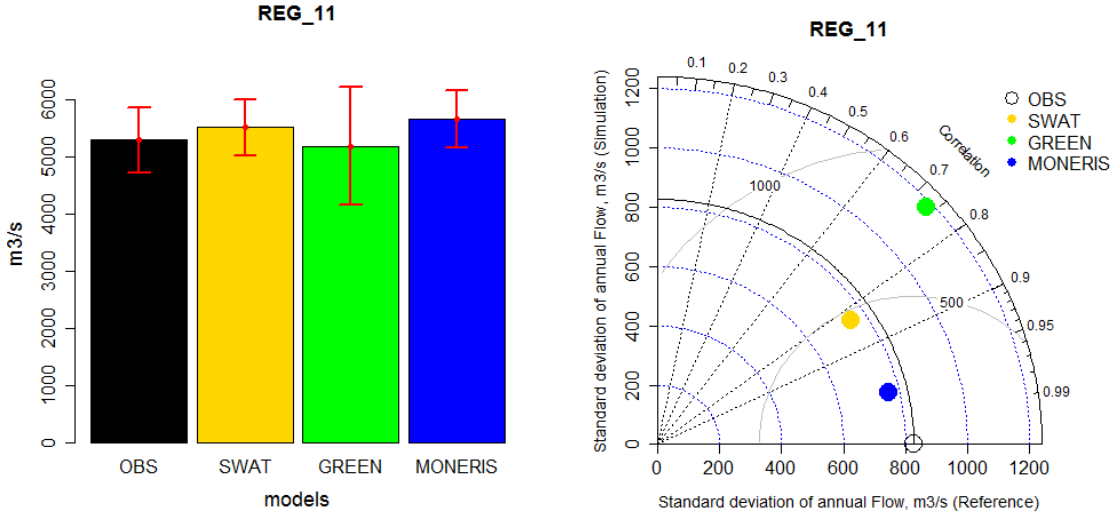


(a) (b)

Figure 115. Bar plot (a) and Taylor Diagram (b) for streamflow Region 11. In (a) the error bars in red indicate the 95% confidence intervals.

In Region 12 (Jiu, Table 22) MONERIS simulated better the long mean annual streamflowthan SWAT and GREEN, which slightly underestimated the observations. MONERIS and SWAT simulated correctly the variability of observations as measured by the standard deviation, even though SWAT had a higher RMS error. GREEN overestimated the standard deviation of observations with the highest RMS error.

In Region 13 (Olt, Table 22) MONERIS and SWAT simulated better than GREEN the long mean annual streamflow. In particular, GREEN overestimated the water streamflow and its annual variability, with a standard deviation (106 $m^3/s$) that was about twice the observed one (59 $m^3/s$).

In Region 14 (Arges-Vedea) SWAT agreed best with the reference values showing a high correlation coefficient (0.97), low RMS error (13 $m^3/s$), and standard deviation very close to the reference value (57 $m^3/s$ compared to the observed standard deviation of 55 $m^3/s$). MONERIS had about the same performances of SWAT, but had a slightly larger RMS error (20 $m^3/s$). GREEN's RMS error was about 30 $m^3/s$, and the standard deviation was higher (82 $m^3/s$) than that of observations. All three models had high correlation coefficients (see Table 22)

In Region 15 (Silistra Danube) the long mean annual values of the models were very close to observations (Table 22). MONERIS resulted in the lowest RMS error (around 150 $m^3/s$) and the annual variability was close to observations. SWAT simulated correctly the amplitude of annual variations (the standard deviation was estimated around 934 $m^3/s$

compared to the observed value of 985 $m^3/s$) but had a larger error than MONERIS (538 $m^3/s$). GREEN overestimated the observed annual variation, and its RMS error was the highest.

In Region 16 (Buzau-Ialomita) GREEN largely overestimated the long mean annual streamflow (Figure 116a). The Taylor diagram (Figure 116b) confirms the overestimation; the GREEN point falls outside the diagram due to the large standard deviation (75 $m^3/s$). SWAT and MONERIS results were similar, with low RMS error (around 14 and 19 $m^3/s$ respectively) and similar standard deviation (28 and 31 $m^3/s$ respectively).

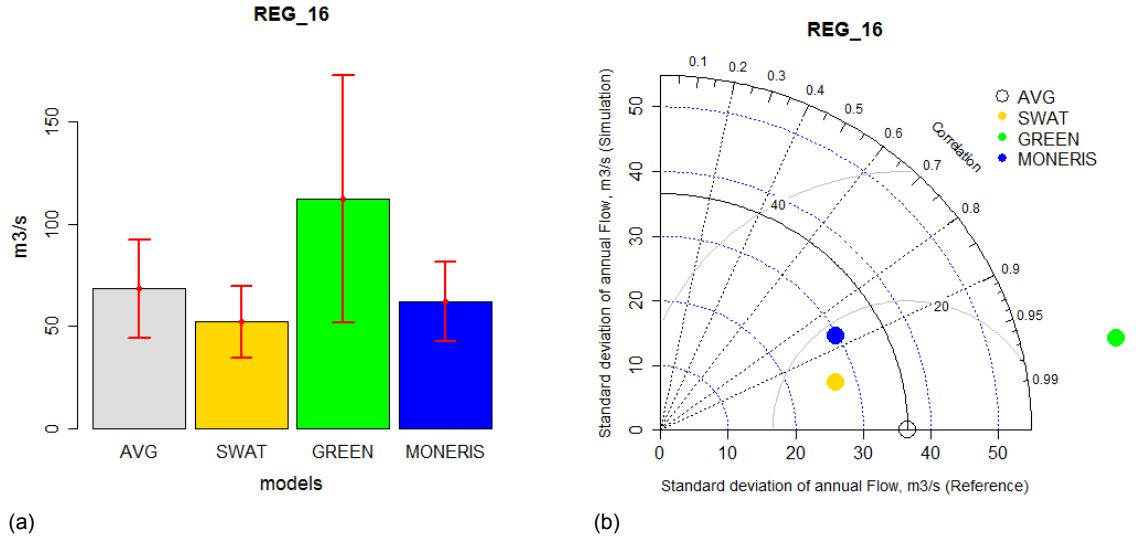


Figure 116. Bar plot (a) and Taylor Diagram (b) for streamflow in Region 16. In (a) the grey bar represents the average of annual streamflow for the three model predictions as observations were not available (period 2000-2009). The error bars in red indicate the 95% confidence intervals.

In Region 17 (Siret-Prut-Buzau), SWAT and MONERIS agreed well with the observations in terms of long mean annual streamflow and performance statistics (Table 22), with both models scoring small RMS error (in the range of 65-85 $m^3/s$) and simulating well the amplitude of mean annual variability, with high correlation coefficients. GREEN was not able to reproduce correctly the annual variability, resulting in the highest RMS error and the lowest correlation coefficient (0.63).

In Region 18 (mouth of Danube at Reni Chilia (Figure 117) MONERIS generally agreed best with the observations with the smallest RMS error (around 144 $m^3/s$), the highest correlation estimated equal 1, and a standard deviation of 1103 $m^3/s$, very close to the standard deviation of observations (1211 $m^3/s$) indicating similar annual variations in observed and modelled streamflow. SWAT had the same standard deviation of MONERIS (1061 $m^3/s$), high correlation with observations (0.84), but higher RMS error (656 $m^3/s$).

GREEN resulted in a slightly lower coefficient of correlation (around 0.81), a large RMS error of 1102 $m^3/s$ and the highest standard deviation. These results highlight the different methodologies used in the calibration process. While for MONERIS monitoring stations evenly distributed in the entire Danube River Basin were considered for the streamflow calibration, SWAT calibrated only the headwaters (10% for the whole) and used extrapolation techniques to extend the calibrated parameter to the whole river basin.

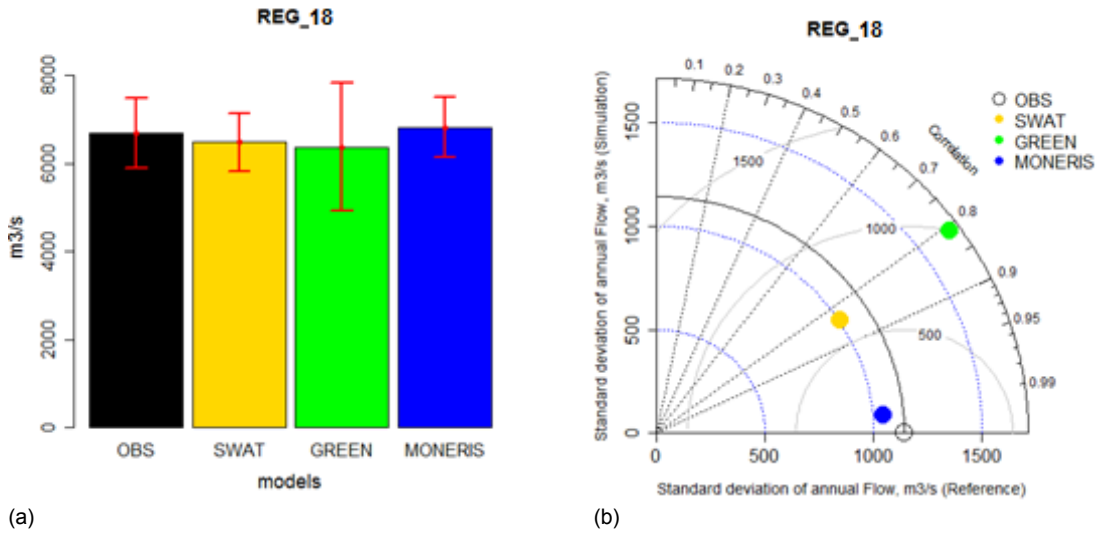


Figure 117.Bar plot (a) and Taylor Diagram (b) for streamflow in Region 18 (period 2000-2009). In (a) the error bars in red indicate the 95% confidence intervals.

### 5.2.3 Total Nitrogen comparison

The map in Figure 118 and the profile in Figure 119 shows the long mean annual TN load in the 18 selected main regions of the Danube basin as estimated by the three models and from measured concentrations. The three models had comparable mean values in the upper Danube macro-region (Regions 1-3), along the Danube river (the Pannonian, Middle and Lower Danube; Regions 6, 11 and 15), in the tributaries Vah-Hron-Ipel, Sava, and Velika Morava (Region 5, 8, and 10). In the other regions the differences between the models were more marked. Table 23 summarizes the statistics of model simulations in each region.

In Regions 1 (Danube Source) and 3 (Austrian Danube) all models were similar, while in Region 2 (Inn) the standard deviation for SWAT (around 7200 ton/y) was higher than for MONERIS and GREEN (5306 and 5057 ton/y respectively compared to the reference value of 5275 ton/y) (Table 23).

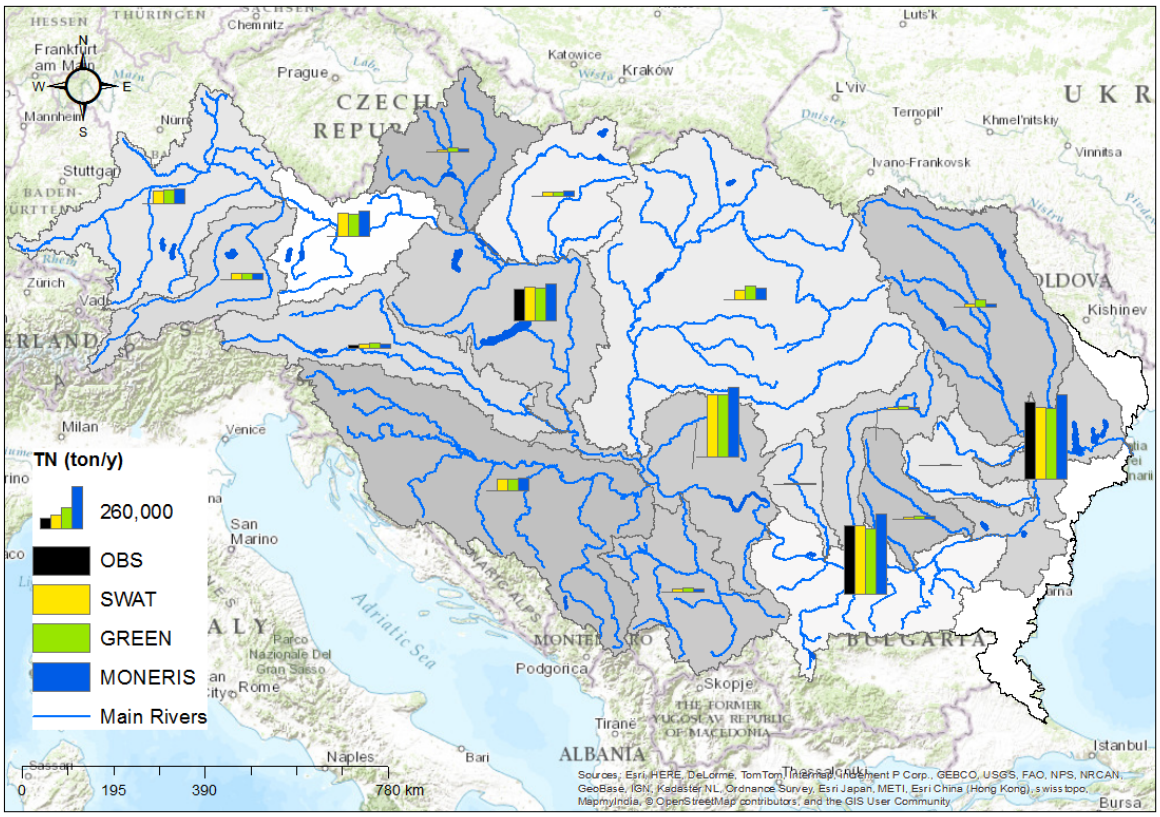


Figure 118. Map of long mean annual total nitrogen (TN, ton/y) for the decade 2000-2009 in the Danube River Basin. The three model outputs are compared to available observations.

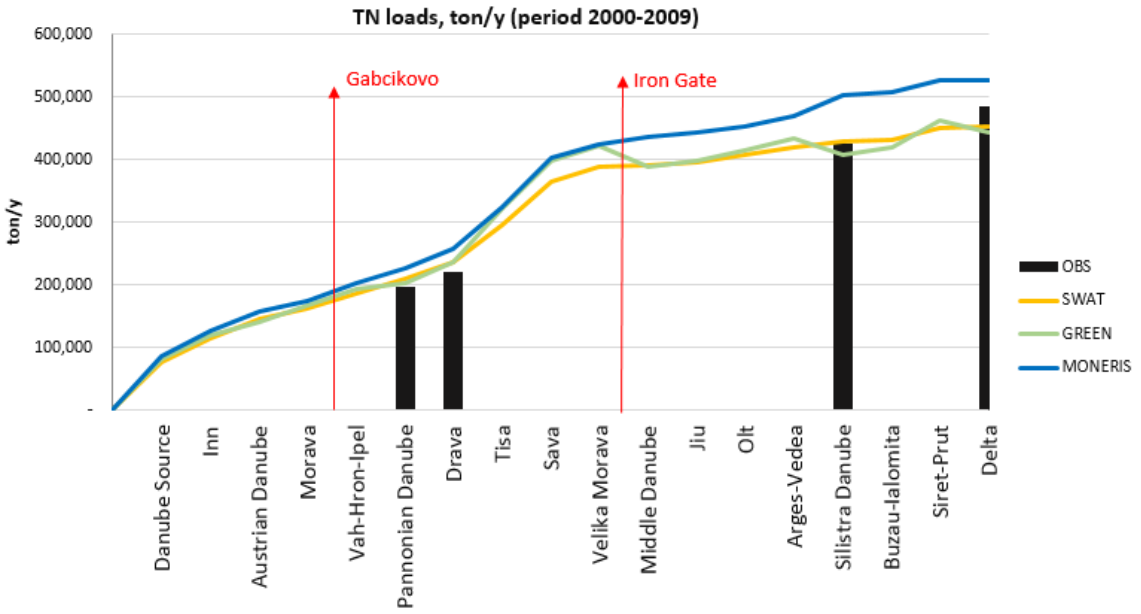


Figure 119. Cumulative annual total nitrogen loads estimated along the Danube River with SWAT, GREEN and MONERIS models for the period 2000-2009. The black bars represent the “observed” loads at the outlets of the water management regions. The red arrows indicate the position of the two main reservoirs, the Gabcikovo and the Iron Gate, along the Danube River.

In Region 4 (Morava), GREEN simulated the highest TN annual load (26325 ton/y), whereas SWAT and MONERIS simulated about 15000 and 17000 ton/y respectively (Figure 120). GREEN and MONERIS standard deviations (4042 and 4016 ton/y) were very close to the reference value (3794 ton/y), but they had different RMS error. SWAT slightly differed from MONERIS and GREEN, with the lowest correlation coefficient (0.78) and standard deviation (2791 ton/y). The RMS error of SWAT and MONERIS were similar (2362 and 2282 ton/y).

In Region 5 (Vah-Hron-Ipel), MONERIS predicted the largest mean TN load (28340 ton/y) followed by GREEN (24965 ton/y) and SWAT (23908 ton/y). Although all models were highly correlated with the observations (Table 23), MONERIS better represented the standard deviation (4302 ton/y compared to the reference value of 4071 ton/y). Despite similar RMS errors, SWAT slightly overestimated the standard deviation compared to MONERIS (5221 ton/y). GREEN had the smallest RMS error (1285 ton/y) and standard deviation (3141 ton/y), the latter being slightly lower than the observed value.

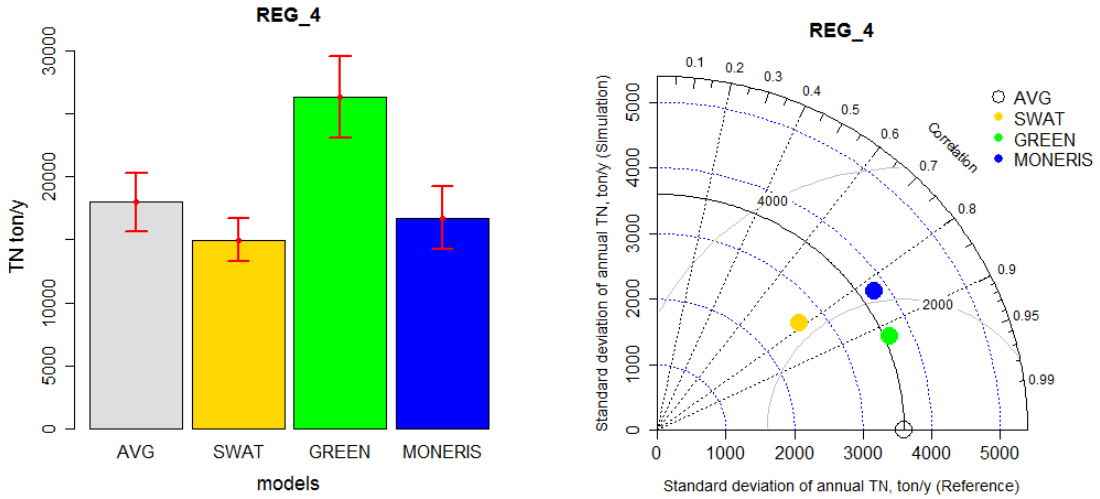


Figure 120. Bar plot (a) and Taylor Diagram (b) for total nitrogen (TN) in Region 4. In (a) the grey bar represents the average of annual loads for the three model predictions as observations were not available (period 2000-2009). The error bars in red indicate the 95% confidence intervals.

In Region 6 (Pannonian Danube), all models agreed well with the observations with similar mean annual loads (Table 23). GREEN, however, agreed best with the observations, with the lowest RMS error, the highest correlation coefficient, and similar standard deviation. Instead, MONERIS had the largest long mean annual load and the lowest correlation coefficient (0.27) with the observations.

In Region 7 (Drava), SWAT and MONERIS agreed best with the observed value of 25271 ton/y, but SWAT had a higher correlation (0.83) coefficient with the observation and a lower RMS error (Figure 121a). GREEN overestimated the long mean annual loads (34521 ton/y) respect to the observations.

In Region 8 (Sava), the three models had similar long-term annual TN load (Table 23), but different standard deviations. GREEN had the highest standard deviation (12445 ton/y), followed by MONERIS (11450 ton/y) and SWAT (9157 ton/y).

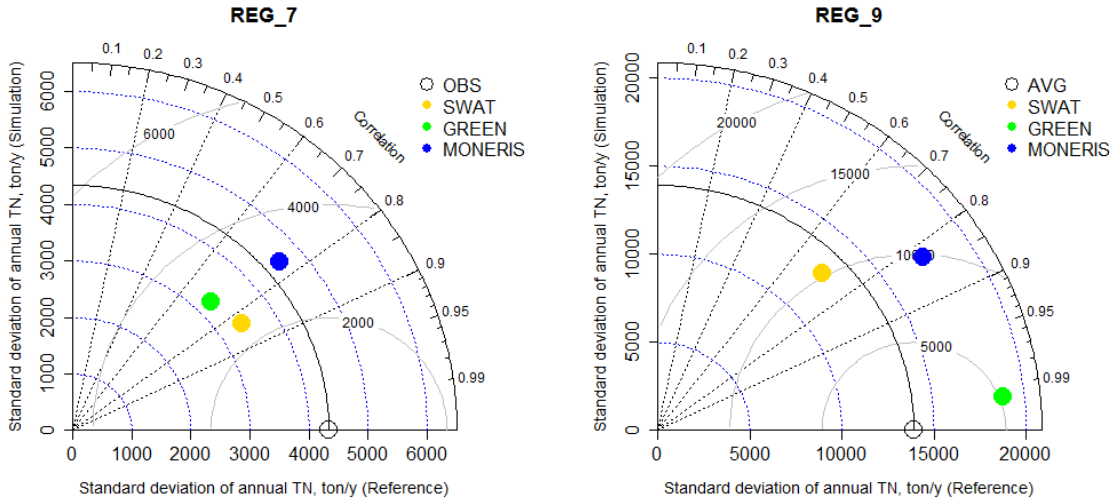


(a) (b)

Figure 121.Taylor Diagrams of annual total nitrogen for Region 7 (a) and 9 (b) (period 2000-2009).

In Region 9 (Tisa) GREEN simulated the highest annual TN load (85802 ton/y). Its standard deviation (20620 ton/y) also exceeded the SWAT and MONERIS values (Figure 121b). SWAT and MONERIS had similar RMS error but opposite estimation of annual variability. The standard deviation for SWAT (13310 ton/y) was lower than the reference standard deviation and those of other models.

In Region 10 (Velika Morava) GREEN long mean annual TN load (25125 ton/y) was slightly larger than that of the other models (Table 23). GREEN standard deviation (6417 ton/y) was about twice those of SWAT and MONERIS. SWAT and MONERIS had very close standard deviations and high correlation with the reference value. However, SWAT simulated better TN reference loads, with the smallest RMS error.

In Region 11 (Middle Danube), SWAT and GREEN had similar TN loads, whereas MONERIS slightly exceeded the others and the reference value (Table 23). This was confirmed also by the Taylor diagram (Figure 122a), in which the blue point (MONERIS model) is laid near the dashed arc of standard deviation correspondent to 60000 ton/y, slightly far from the reference value (51481 ton/y).

In Regions 12, 13 and 14 (Jiu, Olt, and Arges-Vedea), GREEN simulated the highest mean annual TN loads, followed by MONERIS and SWAT. All models had high correlation coefficients but different standard deviations, with MONERIS being closest to the reference value (Table 23).

In Region 15 (Silistra Danube), all three models agreed well with the observations (Table 23). GREEN had perfect correlation with the observed values, followed by MONERIS (0.87), and SWAT (0.71). However, all models clearly underestimated the annual variability as measured by the standard deviation of 56210 ton/y for SWAT, 68301 ton/y for GREEN and 79105 ton/y for MONERIS, compared to the observed 138315 ton/y (Figure 122b).

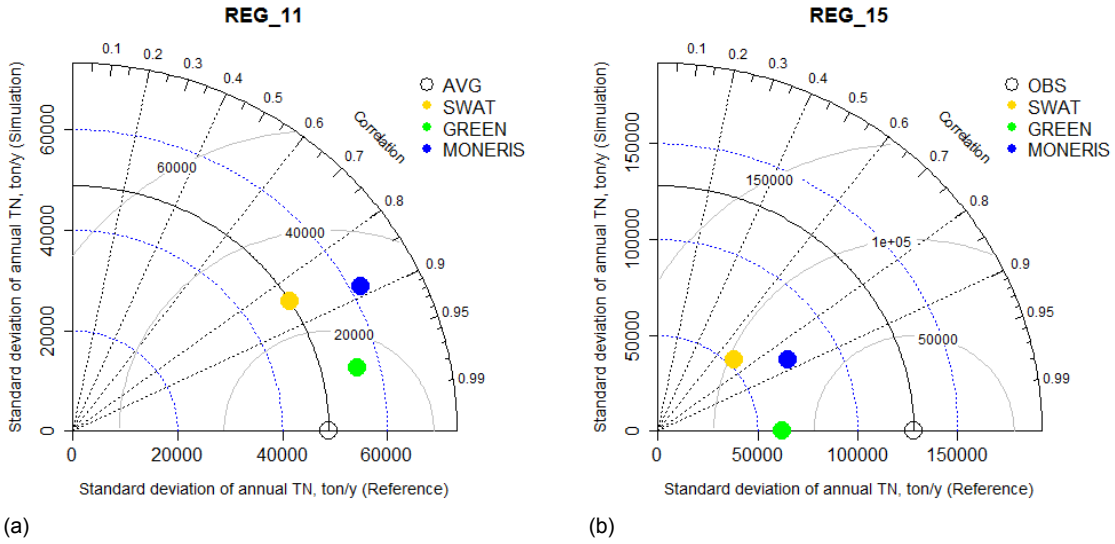


(a) (b)

Figure 122. Taylor Diagrams of annual total nitrogen for Region 11 (a) and 15 (b) (period 2000-2009).

In Region 16 (Buzau-Ialomita) and 17 (Siret-Prut-Buzau), SWAT and MONERIS agreed well with each other, whereas GREEN resulted in the highest mean annual TN load (12862 ton/y in Region 16 and 44745 ton/y in Region 17), standard deviation and coefficient of correlation (Table 23). SWAT and MONERIS produced comparable results. In Region 16, the average TN load was 3065 ton/y according to SWAT and 4825 ton/y according to MONERIS and their standard deviations were in the range of 1100-1350 ton/y. In Region 17, the average TN load was 21021 ton/y according to SWAT and 20054 ton/y according to MONERIS and their standard deviations were in the range of 5900-6000 ton/y.

In Region 18 (Delta), SWAT and GREEN slightly underestimated the long mean annual TN (453210 ton/y for SWAT, 442614 ton/y for GREEN and 484290 ton/y for the observations), whereas MONERIS slightly exceeded (527157 ton/y) the reference value (Figure 123a). All three models, however, had high correlation coefficients, simulating correctly the annual phase in observed loads, but none of the models simulated correctly the amplitude of the annual variations (Figure 123b).

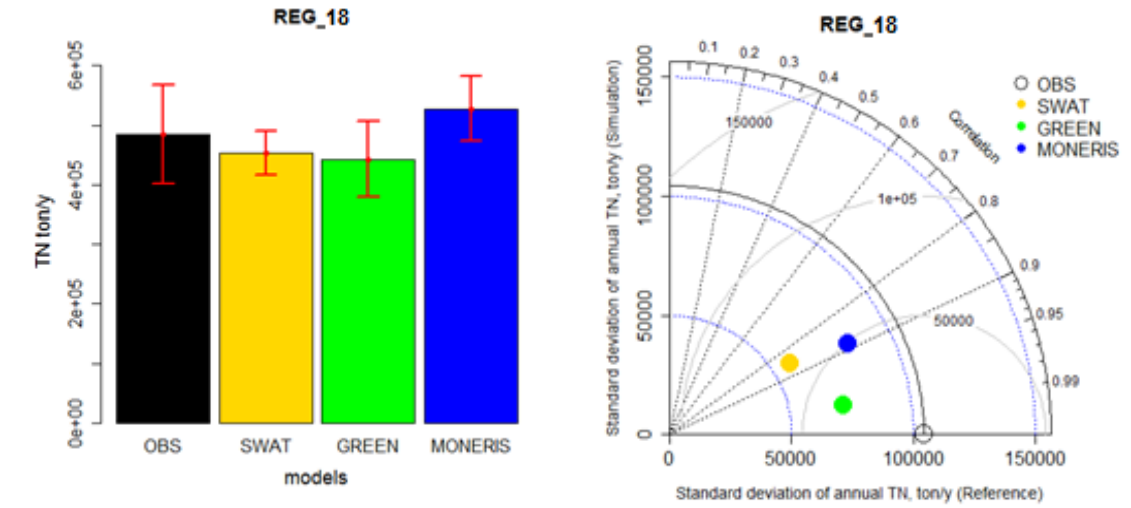


(a) (b)

Figure 123. Bar plot (a) and Taylor Diagram (b) of annual total nitrogen for Region 18 (period 2000-2009). In (a) the error bars in red indicate the 95% confidence intervals.

### 5.2.4 Total Phosphorous comparison

The map in Figure 124 shows the spatial distribution of long mean annual loads of total phosphorous (TP, ton/y) estimated in the Danube River Basin with the three models and from measured concentrations. It highlights the overall agreement between the models and the observations, especially in the Lower Danube and Delta Regions. Conversely, the comparison between the cumulative annual TP along the Danube in Figure 125 shows more noticeable differences. The bar plots and the Taylor diagrams help analysing differences and similarities in detail. Table 24 summarizes the detected statistics of model simulations in each region.

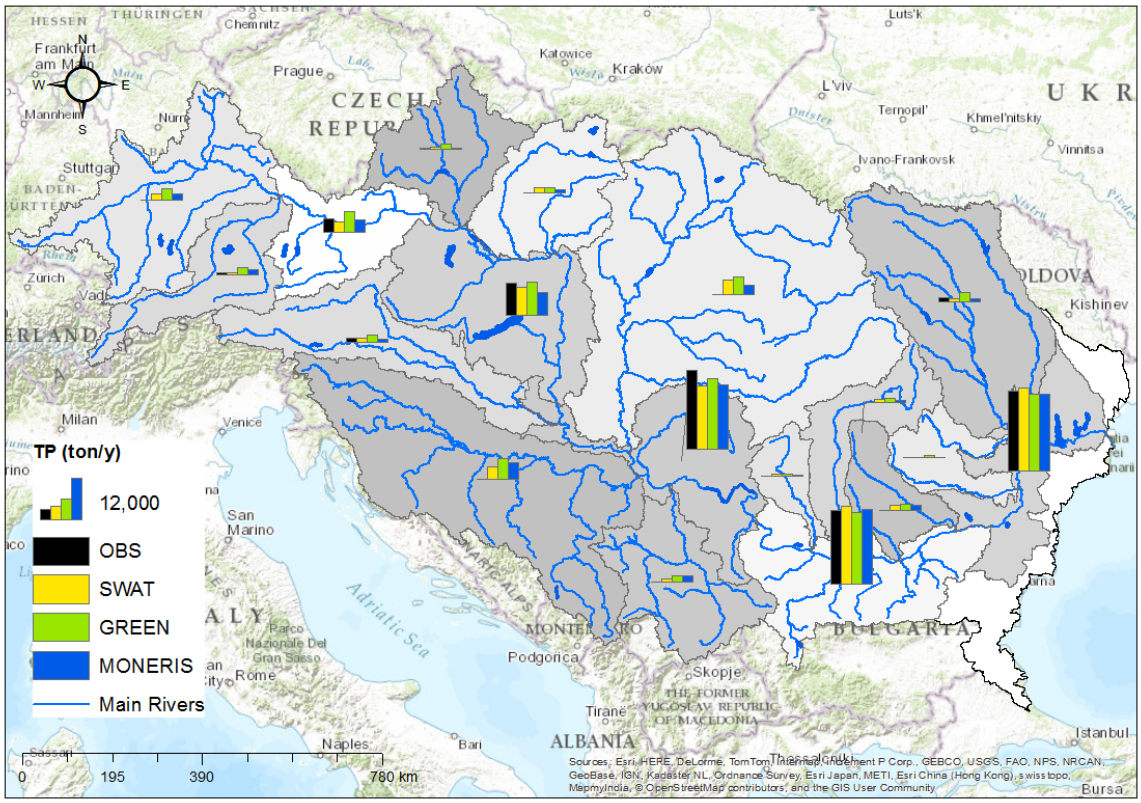


Figure 124. Maps of the long mean annual total phosphorous comparisons (period 2000-2009) in each region. The three model outputs are compared to available observations.

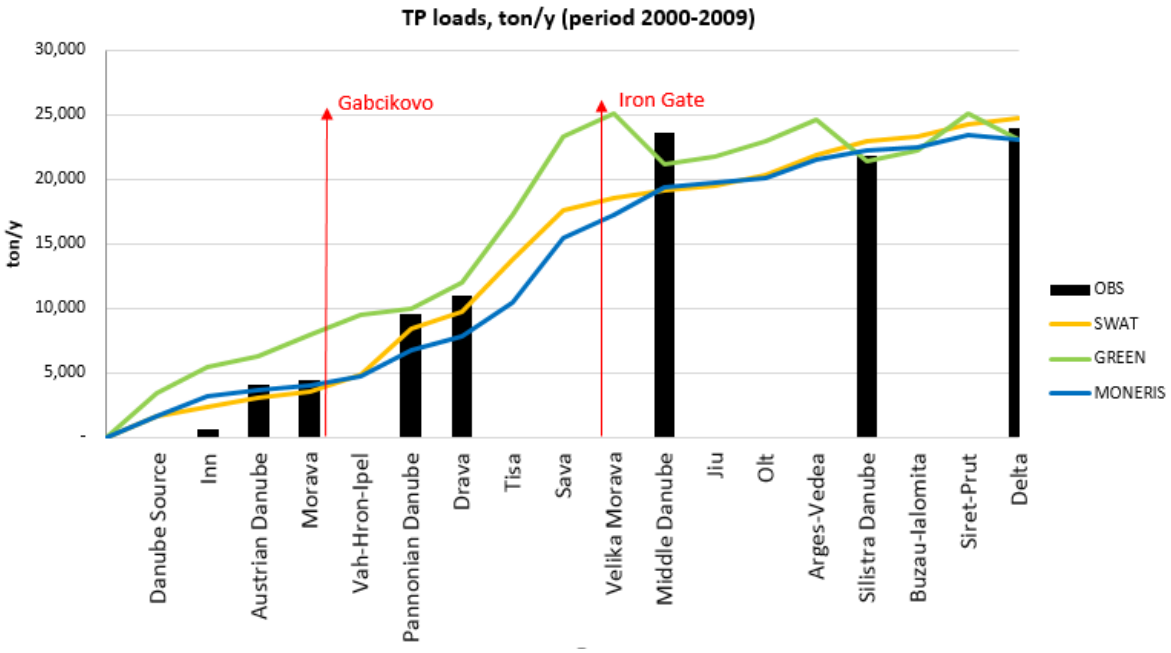


Figure 125. Cumulative annual total phosphorous loads estimated along the Danube River with SWAT, GREEN and MONERIS models for the period 2000-2009. The black bars represent the "observed" loads at the outlets of the water management regions. The red arrows indicate the position of the two main reservoirs, the Gabcikovo and the Iron Gate, along the Danube River.

In Region 1 (Danube Source), GREEN estimated the highest annual TP load. SWAT and MONERIS estimations were similar in mean value and standard deviations (226 and 255 ton/y respectively; Table 24).

In Region 2 (Inn), SWAT agreed best with the observed annual TP load (738 ton/y compared to observed 655 ton/y; Figure 126a), but SWAT standard deviation (106 ton/y) was lower than the observed value (307 ton/y). MONERIS and GREEN overestimated the TP loads, with standard deviations of 132 and 391 ton/y respectively. GREEN was the least correlated to observations (coefficient of 0.30) and had the highest RMS error (Figure 126b).

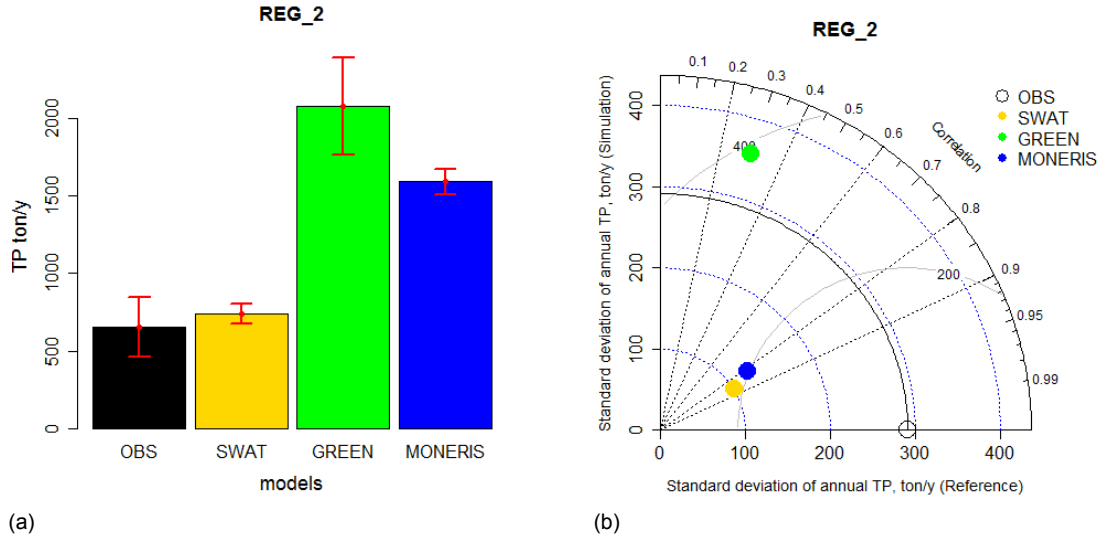


Figure 126. Bar plot (a) and Taylor Diagram (b) of annual phosphorous for Region 2 (period 2000-2009). In (a) the error bars in red indicate the 95% confidence intervals.

In Region 3 (Austrian Danube), MONERIS and SWAT gave similar annual TP loads (3020 and 3638 ton/y), standard deviation (around 400 ton/y), RMS error (around 2,500 ton/y) and coefficient of correlation (0.41 and 0.55 respectively). GREEN resulted in higher mean load (6296 ton/y) and lower correlation (coefficient of 0.13) with observations (Table 24).

In Region 4 (Morava), SWAT and MONERIS predicted loads comparable with the observations (509 and 412 ton/y respectively), unlike GREEN (1662 ton/y, Figure 127a). According to Figure 127b, MONERIS agreed best with the observations with its small RMS error (76 ton/y), its standard deviation of 92 ton/y being close to the observed value (108 ton/y), and a high correlation coefficient (0.72). Albeit SWAT mean TP load agreed better than GREEN to observations, its coefficient of correlation was lower (0.23) and the RMS error (167 ton/y) was higher than for GREEN (coefficient of correlation of 0.6; RMS error of 130 ton/y).

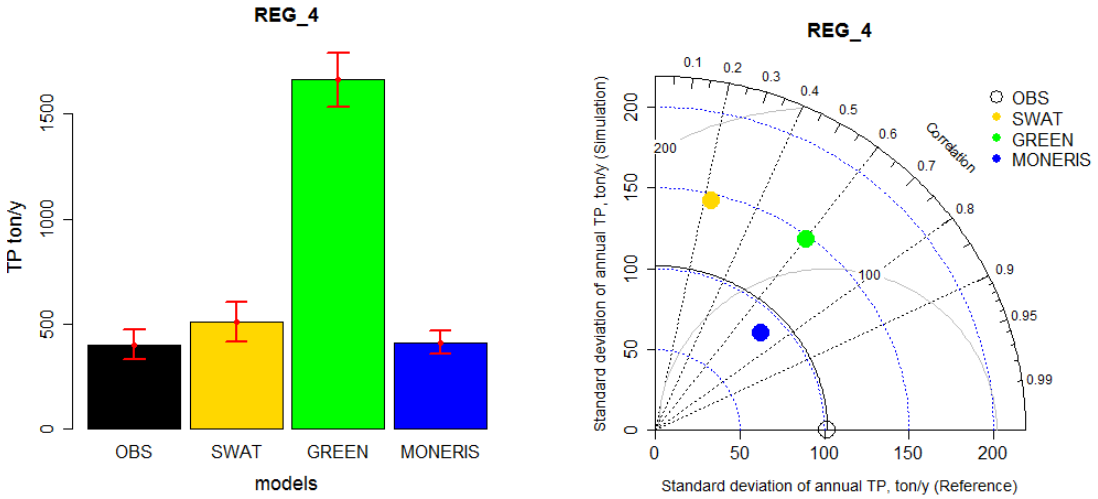


(a) (b)

Figure 127. Bar plot (a) and Taylor Diagram (b) of annual total phosphorous for Region 4 (period 2000-2009). In (a) the error bars in red indicate the 95% confidence intervals.

In Region 5 (Vah-Hron-Ipel), MONERIS simulated the lowest annual TP load (632 ton/y) (Table 24). MONERIS and GREEN had similar standard deviations (119 ton/y and 115 ton/y respectively), whereas SWAT standard deviation was higher (225 ton/y), with a higher RMS error too. However, all three models had high correlation with the observations (coefficients of correlation greater than 0.7).

In Region 6 (Pannonian Danube), the GREEN mean load (about 9900 ton/y) agreed best with the observed value of 9539 ton/y (Table 24). MONERIS underestimated long mean annual TP load (6680 ton/y) and the amplitude of annual variations was lower than for observations, with standard deviation of 864 ton/y compared to the observed value of 2515 ton/y (Figure 128a). SWAT long mean annual TP load (8388 ton/y) was closer to the observations than MONERIS, and SWAT simulated better than MONERIS the amplitude of annual variations (standard deviation of 1311 ton/y) (Figure 128b). However, a significant decrease in observed loads could be detected after the year 2002, indicating that conditions at this station might have changed during the decade 2000-2009.

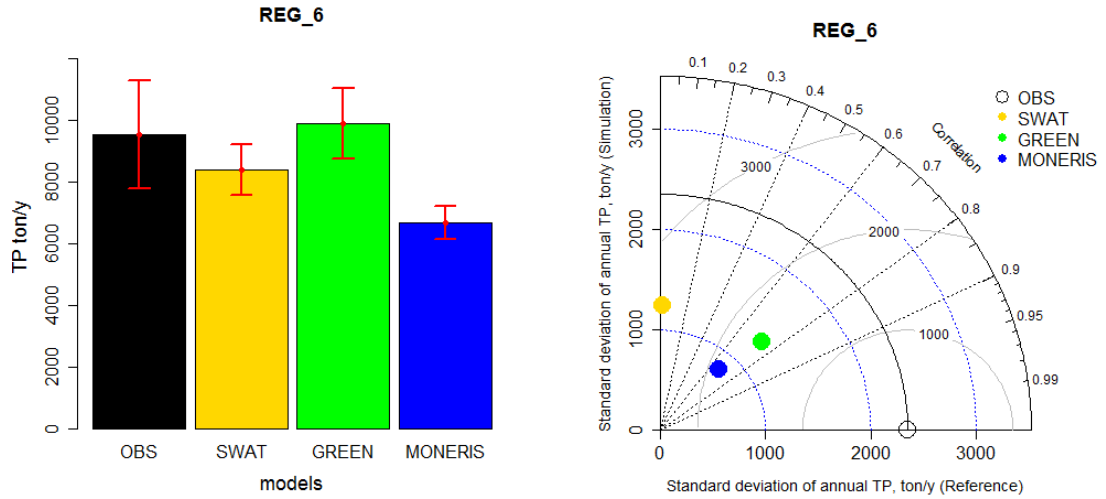


(a) (b)

Figure 128. Bar plot (a) and Taylor Diagram (b) of annual total phosphorous for Region 6 (period 2000-2009). In (a) the error bars in red indicate the 95% confidence intervals.

In Region 7 (Drava) SWAT long mean annual TP of 1289 ton/y was in very good agreement with the observations (1474 ton/y), whereas GREEN (2134 ton/y) and MONERIS (1106 ton/y) overestimated and underestimated it respectively (Table 24). However, none of the model could simulate correctly the amplitude of annual variations and the annual phase.

In Region 8 (Sava) the three model markedly differed from each other (Figure 129a). GREEN estimated a long mean annual TP load of 6052 ton/y (standard deviation of 489 ton/y); MONERIS estimated 5051 ton/y (standard deviation of 766 ton/y), whereas SWAT estimated 3732 ton/y (standard deviation of 334 ton/y) (Figure 129b). It is difficult to quantify model performances because there were no sufficient observations available at the Sava outlet. Thus, there is high uncertainty for TP load estimation that warrants more research effort in the future.

In Region 9 (Tisa) long mean annual TP loads of the three models were very different (Table 24). All models had comparable standard deviations and high correlation with the reference value, although GREEN agreed best with the reference.

In Region 10 (Velika Morava) MONERIS and GREEN predicted similar mean long annual TP loads (1739 and 1797 ton/y respectively ) and standard deviation (210 and 195 ton/y respectively), whereas SWAT estimated lower loads (955 ton/y) and standard deviation (131 ton/y; Table 24).

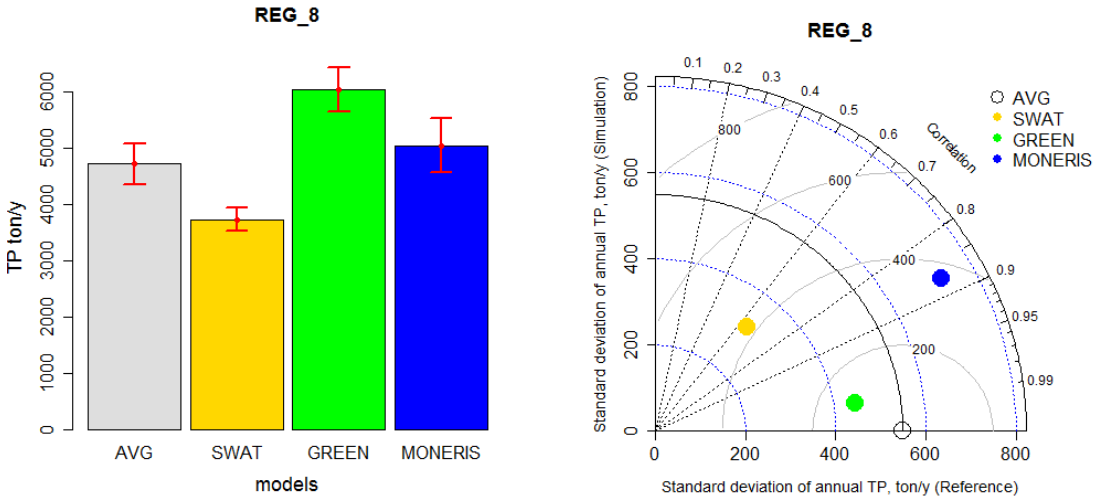


(a) (b)

Figure 129. Bar plot (a) and Taylor Diagram (b) of annual total phosphorous for Region 8 (period 2000-2009). In (a) the grey bar represents the average of the three model predictions as observations were not available. The error bars in red indicate the 95% confidence intervals.

In Region 11 (Middle Danube) all models slightly underestimated the observed long mean annual TP load (Figure 130a and Table 24). Models had similar RMS errors (around 11000 ton/y) and standard deviations (ranging in 2000-3000 ton/y) However, MONERIS scored the lowest correlation coefficient (0.17). Observations had a standard deviation markedly higher (around 12380 ton/y) than those predicted by the models (Figure 130b).

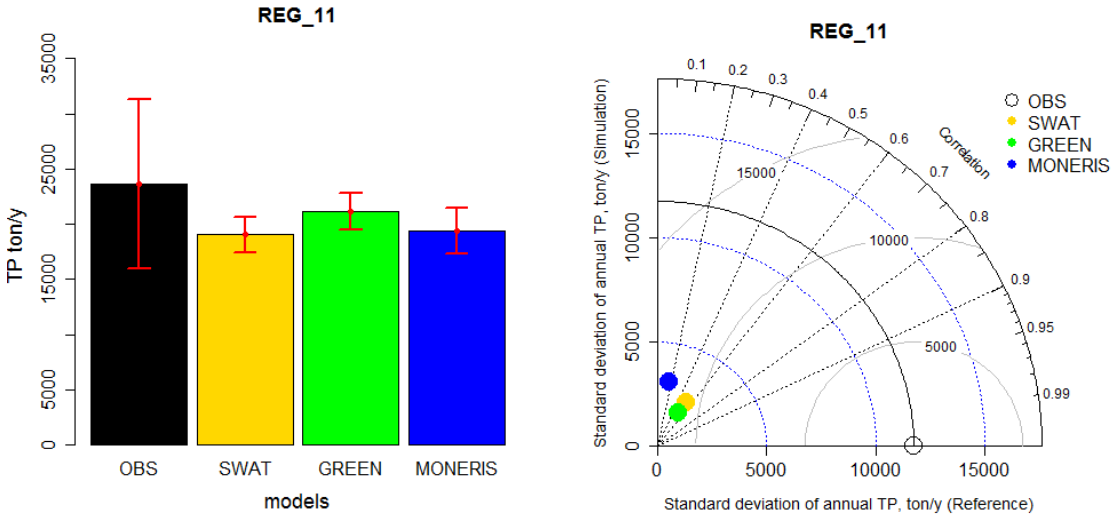


(a) (b)

Figure 130. Bar plot (a) and Taylor Diagram (b) of annual total phosphorous for Region 114 (period 2000-2009). In (a) the error bars in red indicate the 95% confidence intervals.

In Regions 12, 13, 14 (Jiu, Olt, Arges-Vedea) and 16 (Buzau-Ialomita) GREEN had the highest long mean annual TP load, followed by SWAT and MONERIS. Also, GREEN

standard deviations were the highest (Table 24). In Region 12 MONERIS agreed better with the reference value, whereas in Regions 13, 14 and 16 models diverged from the reference in different ways (i.e. higher or lower coefficient of correlations) and no observation was available.

In Region 15 (Silistra Danube) all models had similar long mean predicted TP loads and in agreement with the observed value (Table 24). As in Region 11, models underestimated the standard deviation of the observations.

In Region 17 (Siret-Prut-Buzau) long mean annual TP loads of SWAT (1129 ton/y) and MONERIS (1027 ton/y) agreed well with the observation (1351, ton/y, Table 24), albeit they slightly underestimated it. Conversely, GREEN overestimated TP load at about 3000 ton/y. As in Regions 11 and 15 all models markedly underestimated the observed standard deviation.

In Region 18 (Delta) the long mean annual loads of the models were very close to observations (Figure 131a) with similar coefficients of correlation and RMS errors (Figure 131b). However, the observations had a standard deviation markedly higher (around 20489 ton/y) than those predicted by the models.

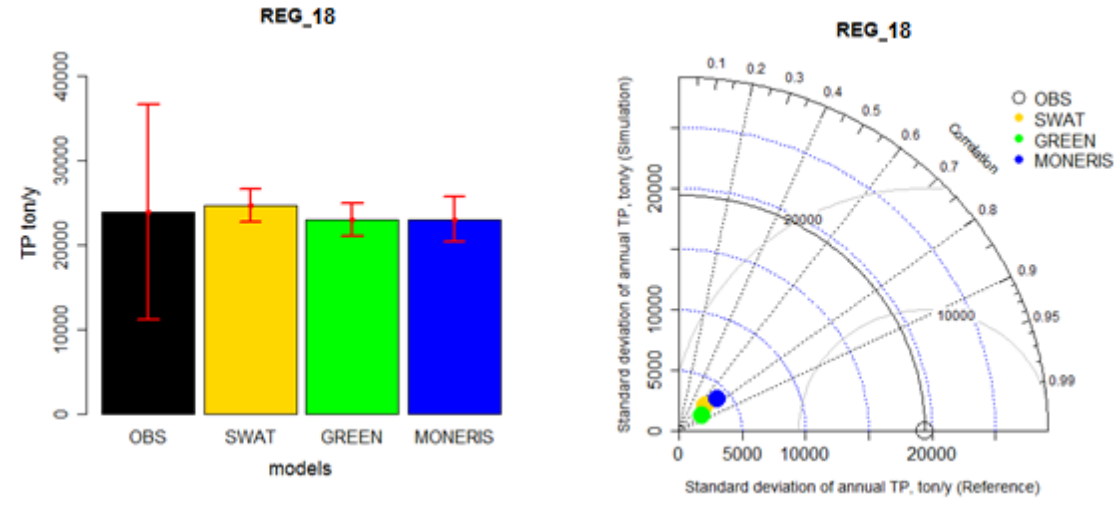


(a) (b)

Figure 131. Bar plot (a) and Taylor Diagram (b) of annual total phosphorous for Region 18 (period 2000-2009). In (a) the error bars in red indicate the 95% confidence intervals.

### 5.2.5 Conclusions of the section

The comparison of model outputs showed that the models SWAT, MONERIS and GREEN performed well in simulating water flow and nutrient loads at the outlets of the main Danube regions. The model results in general agreed well with each other and with the observed

streamflow data. Similarly, the models showed good agreement in estimating total nitrogen loads. Differences among models estimates were more noticeable in Morava, Sava, Tisa, Jiu, Olt, Arges-Vedea, Buzau-Ialomita, Siret-Prut-Buzau (Regions 4, 8, 9, 12, 13, 14, 16, 17, respectively). Observations of total nitrogen concentration at the outlet of these regions would improve the understanding of the nitrogen fluxes in the Danube basin. Concerning phosphorus loads, SWAT and MONERIS resulted in similar long-term mean annual total phosphorus loads at the region outlets, but differed in the amplitude and variability of annual values. Estimations of GREEN were generally higher than of the other models, especially in the upstream part of the Danube basin.

The estimations of water and nutrient flows of SWAT and MONERIS are in good agreement with the available observations, which supports the use of these tools as Integrated Basin Models to describe the dominant processes affecting nutrient transfer from land to rivers and to the sea. Also the results of the model GREEN were in good agreement with the other models and the available observations, despite the model was calibrated at a coarser spatial scale (the whole Europe) and for a different temporal period (GREEN simulation covered only the period 2000-2005 that might not be representative of the period 2000-2009 considered in the comparison).

In conclusion, these results show that, despite the differences in model approaches and input data, assessments from the three models are coherent; hence all three models may be confidently used as tools in river basin management. In particular, SWAT and MONERIS models might support the analysis of the impact of management measures in the Danube River Basin, as they were specifically set-up and calibrated for the region. Sharing the same baseline can help capturing the uncertainty when predicting the impact of measures in the river basins. Further analysis should focus on comparing sources and pathways of the nutrient fluxes, as this would improve support to the assessment of measures.

The inter-comparison allowed to identify areas where good agreement between models reinforced the independent assessments, for example in terms of streamflow across the basin, and areas where disagreements pointed to the need to collect more environmental data, such as nitrogen concentrations at some regions outlets and phosphorus concentrations in the Middle and Lower Danube regions.

Finally, the exercise provided the opportunity to promote dialogue and cooperation within the scientific community working in the region, enhancing the transparency of the modelling approaches and results, and improving the scientific support to the Danube River Basin management.

Table 22. Mean annual water streamflow ($m^3/s$) in the period (2000-2009) ("average" column) and the statistics derived from Taylor diagram. The table includes where available the observations (and correlated statistics) in black, otherwise the average of the three model simulations (and correlated statistics) in grey.

| | Streamflow average ($m^3/s$) | | | | standard deviation ($m^3/s$) | | | | Coeff. Of Correlation | | | RMS error ($m^3/s$) [3] | | |
|---|---|---|---|---|---|---|---|---|---|---|---|---|---|---|
| **Region** | **Reference** | **SWAT** | **GREEN** | **MONERIS** | **Reference** | **SWAT** | **GREEN** | **MONERIS** | **SWAT** | **GREEN** | **MONERIS** | **SWAT** | **GREEN** | **MONERIS** |
| REG_0 | 6,681 | 6,477 | 6,371 | 6,814 | 1,211 | 1,061 | 1,824 | 1,103 | 0.84 | 0.81 | 1.00 | 656 | 1,102 | 144 |
| REG_1 | 685 | 578 | 506 | 652 | 140 | 180 | 151 | 136 | 0.95 | 0.78 | 0.92 | 64 | 97 | 56 |
| REG_2 | 751 | 612 | 734 | 606 | 93 | 122 | 111 | 86 | 0.89 | 0.68 | 0.85 | 58 | 84 | 50 |
| REG_3 | 1,959 | 1,628 | 1,570 | 1,806 | 288 | 337 | 336 | 271 | 0.90 | 0.87 | 0.95 | 147 | 166 | 90 |
| REG_4 | 102 | 136 | 140 | 112 | 21 | 37 | 34 | 23 | 0.88 | 0.56 | 0.98 | 21 | 28 | 4 |
| REG_5 | 257 | 232 | 268 | 277 | 46 | 50 | 68 | 41 | 0.93 | 0.97 | 0.89 | 19 | 26 | 21 |
| REG_6 | 2,322 | 2,196 | 2,138 | 2,458 | 382 | 373 | 452 | 316 | 0.94 | 0.81 | 0.94 | 130 | 263 | 137 |
| REG_7 | 490 | 507 | 592 | 496 | 85 | 80 | 89 | 88 | 0.89 | 0.71 | 0.92 | 39 | 67 | 34 |
| REG_8 | 1,403 | 1,337 | 1,091 | 1,292 | 204 | 256 | 338 | 229 | 0.69 | 1.00 | 0.78 | 186 | 133 | 144 |
| REG_9 | 1,004 | 1,000 | 890 | 1,038 | 273 | 291 | 393 | 280 | 0.90 | 0.96 | 0.81 | 126 | 148 | 171 |
| REG_10 | 242 | 270 | 231 | 214 | 64 | 72 | 102 | 54 | 0.95 | 0.89 | 0.84 | 23 | 54 | 35 |
| REG_11 | 5,301 | 5,522 | 5,192 | 5,667 | 877 | 790 | 1,293 | 807 | 0.83 | 0.74 | 0.97 | 494 | 878 | 208 |
| REG_12 | 97 | 79 | 81 | 100 | 32 | 28 | 49 | 30 | 0.83 | 0.91 | 0.95 | 18 | 23 | 10 |
| REG_13 | 139 | 156 | 179 | 148 | 59 | 52 | 106 | 61 | 0.72 | 0.79 | 0.65 | 42 | 69 | 50 |
| REG_14 | 108 | 110 | 113 | 104 | 55 | 57 | 82 | 52 | 0.97 | 0.98 | 0.93 | 13 | 30 | 20 |
| REG_15 | 6,059 | 6,013 | 5,807 | 6,338 | 985 | 934 | 1,569 | 970 | 0.84 | 0.79 | 0.99 | 538 | 1,001 | 150 |
| REG_16 | 68 | 52 | 112 | 62 | 39 | 28 | 75 | 31 | 0.96 | 0.98 | 0.87 | 14 | 39 | 19 |
| REG_17 | 299 | 331 | 416 | 343 | 115 | 119 | 184 | 114 | 0.85 | 0.63 | 0.74 | 65 | 142 | 83 |

[3] The RMS error was derived from the geometric relationship between standard deviation of reference and simulation ($\sigma_r$ and $\sigma_s$ respectively) and the coefficient of correlation (R): $RMS^2 = \sigma_s^2 + \sigma_r^2 - 2\,\sigma_s \cdot \sigma_r \cdot R$

Table 23. Mean annual total nitrogen (TN, ton/y) in the period (2000-2009) ("average" column) and the statistics derived from Taylor diagram. The table includes where available the observations (and correlated statistics) in black, otherwise the average of the three model simulations (and correlated statistics) in grey.

| | TN average (ton/y) | | | | standard deviation (ton/y) | | | | Coeff. Of Correlation | | | RMS error (ton/y)[4] | | |
|---|---|---|---|---|---|---|---|---|---|---|---|---|---|---|
| **Region** | **Reference** | **SWAT** | **GREEN** | **MONERIS** | **Reference** | **SWAT** | **GREEN** | **MONERIS** | **SWAT** | **GREEN** | **MONERIS** | **SWAT** | **GREEN** | **MONERIS** |
| REG_0 | 484,290 | 453,210 | 442,614 | 527,157 | 112,737 | 60,677 | 79,472 | 87,068 | 0.85 | 0.98 | 0.89 | 68,609 | 37,138 | 53,681 |
| REG_1 | 79,565 | 75,129 | 80,173 | 86,129 | 15,196 | 15,803 | 17,908 | 17,411 | 0.96 | 0.98 | 0.94 | 4,311 | 4,484 | 5,992 |
| REG_2 | 39,125 | 38,643 | 40,144 | 40,265 | 5,275 | 7,180 | 5,057 | 5,306 | 0.94 | 0.88 | 0.93 | 2,893 | 2,499 | 1,972 |
| REG_3 | 148,433 | 146,140 | 140,898 | 157,650 | 22,867 | 26,428 | 26,709 | 25,943 | 0.95 | 0.98 | 0.92 | 8,894 | 6,619 | 10,055 |
| REG_4 | 17,965 | 14,988 | 26,325 | 16,714 | 3,794 | 2,791 | 4,042 | 4,016 | 0.78 | 0.92 | 0.83 | 2,362 | 1,582 | 2,282 |
| REG_5 | 25,889 | 23,908 | 24,966 | 28,340 | 4,071 | 5,221 | 3,141 | 4,302 | 0.88 | 0.97 | 0.86 | 2,558 | 1,285 | 2,255 |
| REG_6 | 195,714 | 209,282 | 201,953 | 227,330 | 43,078 | 30,845 | 30,989 | 33,507 | 0.63 | 0.81 | 0.27 | 33,750 | 25,797 | 46,911 |
| REG_7 | 25,271 | 26,986 | 34,521 | 28,875 | 4,638 | 3,613 | 3,582 | 4,843 | 0.83 | 0.72 | 0.76 | 2,578 | 3,252 | 3,286 |
| REG_8 | 73,195 | 69,486 | 74,514 | 77,031 | 9,812 | 9,157 | 12,445 | 11,450 | 0.94 | 0.97 | 0.94 | 3,388 | 3,774 | 3,969 |
| REG_9 | 68,241 | 59,184 | 85,802 | 68,497 | 14,666 | 13,310 | 20,620 | 18,378 | 0.71 | 0.99 | 0.83 | 10,734 | 6,212 | 10,395 |
| REG_10 | 23,627 | 23,040 | 25,125 | 23,373 | 3,899 | 4,053 | 6,417 | 3,576 | 0.93 | 0.95 | 0.81 | 1,446 | 2,954 | 2,309 |
| REG_11 | 407,723 | 391,863 | 389,326 | 436,705 | 51,481 | 51,412 | 61,039 | 65,457 | 0.85 | 0.97 | 0.89 | 28,370 | 15,909 | 31,106 |
| REG_12 | 5,849 | 4,317 | 8,081 | 6,254 | 1,206 | 893 | 2,336 | 1,120 | 0.69 | 0.97 | 0.79 | 869 | 1,194 | 767 |
| REG_13 | 11,475 | 10,157 | 16,532 | 10,291 | 3,041 | 2,137 | 5,417 | 2,901 | 0.71 | 0.99 | 0.91 | 2,154 | 2,458 | 1,239 |
| REG_14 | 15,140 | 12,448 | 19,000 | 16,092 | 2,999 | 1,918 | 4,952 | 3,226 | 0.83 | 0.98 | 0.90 | 1,768 | 2,091 | 1,400 |
| REG_15 | 424,168 | 428,121 | 406,922 | 502,216 | 138,315 | 56,210 | 68,301 | 79,105 | 0.71 | 1.00 | 0.87 | 105,755 | 70,018 | 79,884 |
| REG_16 | 5,725 | 3,065 | 12,862 | 4,825 | 2,352 | 1,105 | 4,132 | 1,340 | 0.71 | 0.99 | 0.69 | 1,746 | 1,831 | 1,735 |
| REG_17 | 25,482 | 21,021 | 44,745 | 20,054 | 7,147 | 5,975 | 9,887 | 5,992 | 0.63 | 0.96 | 0.80 | 5,760 | 3,586 | 4,260 |

[4] The RMS error was derived from the geometric relationship between standard deviation of reference and simulation ($\sigma_r$ and $\sigma_s$ respectively) and the coefficient of correlation (R): $RMS^2 = \sigma_s^2 + \sigma_r^2 - 2\,\sigma_s \cdot \sigma_r \cdot R$

Table 24. Mean annual total phosphorous (TP, ton/y) in the period (2000-2009) ("average" column) and the statistics derived from Taylor diagram. The table includes where available the observations (and correlated statistics) in black, otherwise the average of the three model simulations (and correlated statistics) in grey.

| | TP average (ton/y) | | | | standard deviation (ton/y) | | | | Coeff. Of Correlation | | | RMS error (ton/y) [5] | | |
|---|---|---|---|---|---|---|---|---|---|---|---|---|---|---|
| Region | Reference | SWAT | GREEN | MONERIS | Reference | SWAT | GREEN | MONERIS | SWAT | GREEN | MONERIS | SWAT | GREEN | MONERIS |
| REG_0 | 23,930 | 24,697 | 23,030 | 23,063 | 20,489 | 3,165 | 2,476 | 4,250 | 0.70 | 0.82 | 0.75 | 18,396 | 18,523 | 17,532 |
| REG_1 | 1,954 | 1,580 | 3,373 | 1,629 | 508 | 226 | 990 | 255 | 0.91 | 0.99 | 0.63 | 316 | 495 | 399 |
| REG_2 | 655 | 738 | 2,079 | 1,590 | 307 | 106 | 391 | 132 | 0.87 | 0.30 | 0.81 | 221 | 419 | 214 |
| REG_3 | 4,046 | 3,020 | 6,296 | 3,638 | 2,770 | 400 | 1,620 | 446 | 0.55 | 0.13 | 0.41 | 2,573 | 3,020 | 2,618 |
| REG_4 | 402 | 509 | 1,662 | 412 | 108 | 154 | 162 | 92 | 0.23 | 0.60 | 0.72 | 167 | 130 | 76 |
| REG_5 | 1,060 | 1,268 | 1,497 | 632 | 171 | 225 | 115 | 119 | 0.73 | 0.94 | 0.77 | 153 | 74 | 110 |
| REG_6 | 9,539 | 8,388 | 9,899 | 6,680 | 2,515 | 1,311 | 1,428 | 864 | 0.01 | 0.74 | 0.68 | 2,820 | 1,752 | 2,033 |
| REG_7 | 1,474 | 1,289 | 2,134 | 1,106 | 406 | 161 | 219 | 160 | 0.26 | 0.33 | 0.38 | 396 | 393 | 375 |
| REG_8 | 4,721 | 3,732 | 6,052 | 5,051 | 578 | 334 | 489 | 766 | 0.64 | 0.99 | 0.87 | 444 | 118 | 384 |
| REG_9 | 3,754 | 4,121 | 5,161 | 2,630 | 738 | 826 | 708 | 849 | 0.79 | 0.98 | 0.82 | 515 | 151 | 486 |
| REG_10 | 1,438 | 955 | 1,797 | 1,739 | 164 | 131 | 195 | 210 | 0.71 | 0.82 | 0.80 | 116 | 112 | 127 |
| REG_11 | 23,637 | 19,065 | 21,131 | 19,391 | 12,377 | 2,597 | 2,043 | 3,314 | 0.53 | 0.51 | 0.17 | 11,209 | 11,461 | 12,267 |
| REG_12 | 435 | 424 | 614 | 355 | 75 | 50 | 116 | 75 | 0.69 | 0.99 | 0.80 | 54 | 44 | 47 |
| REG_13 | 718 | 862 | 1,143 | 356 | 149 | 131 | 247 | 101 | 0.53 | 0.99 | 0.77 | 137 | 103 | 95 |
| REG_14 | 1,465 | 1,477 | 1,679 | 1,362 | 172 | 105 | 205 | 246 | 0.75 | 0.95 | 0.92 | 117 | 66 | 112 |
| REG_15 | 21,862 | 22,956 | 21,345 | 22,194 | 12,352 | 2,959 | 2,079 | 3,748 | 0.71 | 0.64 | 0.49 | 10,454 | 11,145 | 11,024 |
| REG_16 | 397 | 290 | 908 | 254 | 171 | 67 | 209 | 160 | 0.62 | 0.99 | 0.76 | 140 | 45 | 115 |
| REG_17 | 1,351 | 1,129 | 2,989 | 1,027 | 1,045 | 163 | 402 | 352 | 0.99 | 0.99 | 0.72 | 885 | 649 | 827 |

[5] The RMS error was derived from the geometric relationship between standard deviation of reference and simulation ($\sigma_r$ and $\sigma_s$ respectively) and the coefficient of correlation (R): $RMS^2 = \sigma_s^2 + \sigma_r^2 - 2\,\sigma_s \cdot \sigma_r \cdot R$

# CHAPTER 6

# 6 Conclusion

The research topic of the thesis was motivated by the need to provide realistic hydrological and water quality (sediment and nutrients) simulations for a valuable policy support and decision making in large Basins in Europe, as well as for the acceptance of environmental policies and their successful implementation.

For such purposes, the main objectives of this thesis were to use the Soil and Water Assessment Tool model (SWAT), one of the most worldwide used hydrological and water quality model, in several large basins providing a diagnostic modelling approach.

The proposed approach involved in sequence: the setup of the model, the calibration of crop yields, the calibration/validation of streamflow and its components, followed by sediments and then nutrients calibration. The sequential approach is essential due to the fact that each step is influenced by the previous one.

Several innovations were introduced in the modeling approach as explained in section 2.3 and 2.4, aimed both to improve model structure and calibration procedure. First of all, modifications of SWAT model were applied to produce new useful outputs for calibration and interpretation of specific processes. New algorithms for the calculation of hillslope length parameter and LS factor were also proposed and tested, as well as a new MUSLE equation. Furthermore, karst processes were represented using the KSWAT model, a combination of SWAT with a karst-flow model. Concerning the calibration/validation, a process-based approach was developed involving both hard (i.e. long time series in multiple gauging stations) and soft data (i.e. literature information of a specific process within a water, sediment, or nutrient balance that may not be directly measured within the study area, e.g. average annual estimate) for a threefold objective: to match well the observations, to understand the processes within a basin and to provide accurate cost-benefit scenarios analysis for achieving the goals of the main European Directives.

To that regard, the two main innovative aspects concern (i) for streamflow, the application of a step-wise calibration coupled with a parameter regionalization and (ii) for sediment and nutrients, the calibration of concentrations instead of the loads.

In particular, the main work carried out in this thesis and the findings can be summarized as follows:

1. Calibration and Validation (C/V) of streamflow and it components

A step-wise calibration coupled with a regionalization of calibrated parameters (Near Optimal Parameter set, NOP) was proposed for streamflow calibration as described in section 3.2. The step-wise approach consists in calibrating step by step each component of the hydrograph in selected independent subbasins (headwaters). The procedure was applied in two regions with very different climate conditions, the Scandinavia and Iberian Peninsulas, to study the spatial variation of calibrated parameter sets and to identify the most relevant hydrological processes in these regions. It was demonstrated that the step-wise approach allowed obtaining good performance of the models both in gauged and ungauged subbasins, as well as gaining a good knowledge of each hydrological process and their mechanism of generation. Furthermore, this modelling procedure has shown that the use of homogenous continental input data to setup the model allowed yielding robust results.

In conclusion, using the step-wise calibration approach a threefold advantage was pursued: first, generally only 10% of total number of subbasins were calibrated, thus reducing substantially the computational burden of SWAT application in large basins; second, the regionalization technique allowed increasing the scientific knowledge of the study area, identifying hydrological similarities and thus similar mechanisms of generation of streamflow; third; in each step of the calibration the hydrological processes were controlled and constrained in reliable ranges, allowing to capture the spatial variation of calibrated parameter sets and identifying the most relevant hydrological processes in regions with very different climate conditions.

For that reasons, the step wise calibration approach was applied in each modelled area in this thesis.

2. The validation of water balance

   Section 3.3 demonstrated that the satisfactory match between observations and simulations does not guarantee that all the water balance components are well represented. For that reason, a diagnostic approach was proposed to control the evapotranspiration, one of the most important component of the water balance, and the baseflow, albeit it was calibrated in the step-wise calibration.

   The Budyko-framework approach was adopted to perform the diagnosis. In particular, two mono-parametric Budyko-type equations were used: the Turc-Pike equation (Turc, 1954 and Pike, 1964) for defining the relationship between the aridity index (PET/P) and evaporative index (ET/P), and a complementary Turc-Pike formulation proposed by Wang and Wu (2012) for controlling the baseflow index (BFI/P) respect to the aridity index.

The procedure was tested in the Danube River Basin.

It was demonstrated that the evapotranspiration was well simulated by SWAT in the whole Danube, as well in each water management region, highlighting that crop yields were well simulated. Instead, the baseflow was underestimated in the Upper part (e.g. Inn River Basin) due to anthropogenic impacts, such as deviation and abstraction, that influenced the parametrization in the step-wise approach.

In conclusion, the Budyko approach has the advantage to identify immediately, and with limited user's efforts, model inconsistencies through the analysis of the relationship between the evaporative index and the aridity index. Furthermore, using a complementary relationship between baseflow index and aridity index, problems in baseflow estimations can be detected and thus fixed.

3. Modification of the hillslope length calculation

Section 3.4 demonstrated that the hillslope length parameter (L) has a strong impact on water yields components affecting the estimation of lateral flow. Currently, the default method to set hillslope length in SWAT, based on a look-up table that relates hillslope length to the subbasin slope gradient, leads to overestimates the lateral flow in steep subbasins. As a consequence, two additional algorithms for hillslope length calculation (L2, Zhang et al., 2013; L3, Neitsch et al., 2011) were investigated. Six different configurations of L methods and DEM resolutions, were tested in the Upper Danube to find which of them was able to represent correctly the streamflow components. It was shown that each method had no impact on total streamflow and surface runoff, but had an important impact on the partition between lateral flow and baseflow. This bears important consequences in the simulation of pollutant movements, like nitrates, in the landscape. The current default SWAT method was shown to produce larger errors in the simulation of streamflow components in steep areas, while L2 method, and in particular configuration 100L2 (combination of method L2 with 100 m DEM pixel size), resulted in the most adequate estimations of lateral flow and baseflow in steep regions. L3 method (constant value of 50 m) however was a good second alternative to be considered when DEM resolution is of 25 m or coarser, especially if the DEM accuracy is low.

In conclusion, the L2 method was considered appropriate for application in spatially distributed models than the current SWAT method, since it provides a more reliable description of the landscape morphologies throughout a 3D analysis, and thus was applied in the Danube and Crete models.

4. Karst processes representation

Section 3.5 demonstrated the importance of representing the karst processes in SWAT model. This new SWAT model (KSWAT) structure represents the concept of the karst model and its hydrological pathways and combines an adapted SWAT model and a karst-flow model. Valuable water balances can be predicted in different hydrological conditions increasing the knowledge of water resources available as shown for the case study of the island of Crete.

5. The nutrients simulations and balances

Unlike other studies, in this thesis the calibration of nutrients (i.e. nitrate-nitrogen, total nitrogen and phosphorous) focused on the prediction of the seasonal nutrient concentration, avoiding uncertainty issues related to loads estimation and thus a more valuable parametrization of the processes. This is a key aspect of the procedure that allows to assess easily the requirements of several Directives, as shown later in section 4.4. The loads were only used in the evaluation of the model.

The procedure was applied in the Danube River Basin as described in section 4.2, and involved the use of soft and hard data, as well as a sensitivity analysis. The soft data were used to setup the model parameters related to nutrients processes (i.e. concentration of nitrogen in the precipitation) and during the calibration of the terrestrial denitrification. The hard data (times series of concentration at multi gauging stations) were used in the calibration performed at monthly time step.

It was demonstrated that SWAT was not able to represent accurately the spatial variation of terrestrial denitrification due to the model structure that allows to calibrate denitrification parameters only at watershed level, and the in–stream denitrification should be included.

However, notwithstanding these limits, calibration and evaluation of SWAT nutrient outputs showed that concentrations and loads were well captured in the Danube Basin. Finally, nutrients balances were performed and analyzed, identifying the most important factor of pollutant reduction in the Basin and thus adding valuable scientific information for planning conservation actions.

6. The sediment yield simulations and balance

   In section 4.3 several modifications were applied in the Upper Danube to increase the reliability of sediment predictions, as described in section 2.3.3. In particular, a

modified MUSLE equation was applied for accounting that the HRU specific sediment yields are non-linearly related to the HRU area, as well as different L and LS algorithms were proposed, respectively for the calculation of hillslope length and LS factor. Thirteen SWAT models were investigated in the Upper Danube to define which area threshold in the new MUSLE equation, which LS and L algorithms allow predicting reliable sediment yields and concentrations. Furthermore, the C/V procedure explained in section 2.4.4, that involves the calibration of gross erosion, the calibration of sediment concentrations, as well as an evaluation of specific sediment yields, was performed.

The study confirmed the impact of the area threshold on sediment yields estimations, highlighting the need to calibrate this parameter for each case study. Similarly to the study of L on streamflow in section 3.4, also for sediments the algorithm L2 for hillslope length calculation resulted the most appropriate and was intrinsically consistent and well suited in large basins.

Accordingly, LS3 resulted the best algorithm for representing the topography factor LS.

The multi-type and multi-site data calibration methodology pursued in this study allowed achieving robust constraining of sediment modelling. Finally, the modelled sediment balance for the Upper Danube Basin has allowed to identify the most sources and sinks of sediments, providing valuable information to natural resources managers.

7. A multi-objective approach for balancing environmental advantages with investment costs

The R-SWAT-DM framework tool, a model linkage between SWAT–R software and economic models, was developed for scenarios analysis of Best Management Practices (BMPs) implementations and related economic values in terms of global income. This tool was applied in the case study of Upper Danube and its main components were described in Appendix A5.

The tool was recognized as useful instrument for policy makers in evaluating long-term benefit with a long-term perspective based on simulations of water quality indicators (i.e. concentrations of nitrates in surface water) when complex scenarios of BMPs are implemented, i.e. reducing fertilizer application and upgrading WWTPs. Furthermore, the visual appraisal of maps of the results can easily allow to assess the requirements of several Directives. For instance, the Drinking Water Directive (98/ 83/EC) requires a maximum allowable concentration for nitrate of 50 mg/l, the Surface Water for Drinking Directive (75/440/EEC) provides a guideline

concentration for nitrate of 25 mg/l, the Nitrates Directive (91/676/EEC) requires the identification of groundwater sites/bodies where annual average nitrate concentrations exceed or could exceed 50 mg/l of NO3, and also the Urban Waste Water Treatment Directive (91/71/EEC) aims to decrease organic pollution.

8. The benchmarking approach

   An inter-comparison of independent model results was performed for the Danube River Basin in Chapter 5. Annual streamflow, total nitrogen and phosphorous for the period 2000-2009 were compared for SWAT, GREEN and MONERIS models. The comparison has allowed identifying areas with good agreement between models, or conversely areas where disagreements, highlighting the need to collect more environmental data. In addition, the inter-comparison of models promoted the dialogue and cooperation within the scientific community working in large basins (i.e. JRC, Joint Research Centre of the European Commission, and ICPDR, International Commission for the Protection of the Danube River), enhancing the transparency of the modelling approaches and results.

These findings can be also summarised as several useful recommendations for SWAT modellers. First off all, the collection of multi-site gauging stations with long time-series of more than 10 years is necessary to capture the heterogeneous spatial and temporal characteristics of large basins and to allow for a robust model calibration. As required in the proposed procedure, long daily time series should be collected for streamflow and the hydrograph should be split into its components (surface runoff, lateral flow and baseflow) using a digital filter (i.e. Lyne and Hollink, 1979). Similarly, for sediment and nutrients long time-series of concentration with at least one sample each month are recommended. Generally, an analysis of the reliability of the measurements should be performed albeit the collection of method and associated uncertainty are generally not available. For instance, in this thesis several unrealistic values were observed in the collected nutrients time series due to typing errors, different units, or sometimes when the concentration referred to molecules instead of each element (i.e. nitrate, NO3 mg/l, instead of nitrate-nitrogen, N-NO3 mg /l). In this case, corrections have to be applied.

These available time series should be temporally and spatially split, as it is well known that data-splitting is an essential step to assess the CV procedure under different conditions. In this thesis streamflow database was spatially subdivided in a calibration dataset, that comprises only headwater subbasins, and in a validation dataset with all the remaining stations. For sediments and nutrients, the calibration and validation dataset include multi-site long time series of concentration, while an additional database, namely evaluation database, consists of multi-site loads (ton/year or ton/month) or specific loads (ton/km$^2$/year

or month). Generally, the calibration dataset has a shorter period (i.e. 1996-2006) than the validation and evaluation dataset that instead cover the entire period (i.e. 1995-2009). However, the calibrated dataset should include a long period in order to contain a wide range of hydrological conditions, such as wet and dry extremes over multiple years.

Also the use of soft data (generally identified using literature information) are strongly recommended. For instance, the soft data used in this thesis are the annual crop yields, soil denitrification values, gross erosion estimates and the extension of karst areas. Each of them was involved in the calibration procedure to capture the dominant processes in large basins, and thus determine which parameters need further adjustment during the calibration.

Concerning the whole procedure of calibration and validation, the calibration should be performed in sequence starting from the calibration of crop yields, then the calibration/validation of streamflow and its components, followed by sediments and in the end by nutrients calibration/evaluation. Accordingly with other several studies (e.g., Santhi et al., 2001; Engel et al., 2007), this sequential approach is necessary because of interdependencies between constituents due to shared transport processes. For instance, the calibration of crop yields is necessary to obtain realistic evapotranspiration, as well as a correct nutrient plant uptake. Instead, the calibration of streamflow components is crucial for predicting reliable pollutant losses through the various pathways. Nutrients calibration follows sediment calibration since contaminants transported with sediment is are important components of the nutrient balance.

In particular, for calibrating streamflow the step-wise calibration approach coupled with the regionalization of calibrated parameters is recommended in large basins, in order to well capture the hydrological processes with decreasing the computational burden of simulations. However, after the calibration the simple Budyko framework approach is recommended for controlling the evapotranspiration and the baseflow components since the first is strongly influenced by the parametrization of crops and calibration of crop yields and the second by the anthropogenic activities in headwaters, such as deviation, that have impacts on parametrization of donors subbasins involved in the regionalization.

The change of the SWAT algorithm for hillslope length calculation with the L2 method (L2; Zhang et al., 2013) is strongly recommended to simulate correctly the lateral flow and baseflow components, as well as the use of the LS3 algorithm for topographic factor calculation and the modified MUSLE equation for a reliable estimation of sediments yields in large basins.

Furthermore, in large river basins where soluble carbonate rocks are dominant and karst processes are significant components of the physical geography of the basins, the use of

KSWAT model is recommended to well represent the hydrological balance and thus provide valuable information of water resources in these complex areas.

Both sediment and nutrient calibration have to be carried out in three phases using both soft and hard data: first, a sensitivity analysis should be performed to select the most representative parameters; second; the land-phase processes have to be calibrated (i.e. gross erosion for sediment and denitrification for nutrients); third, a multi-site calibration and validation of concentrations, at monthly time step, should be carried out. Then, the model should be evaluated at multi gauging stations using the loads. Finally, annual sediment and nutrients balances should be performed and each component compared with other studies.

To that regard, the inter-comparison of independent model results is recommended in large river basins for identifying areas with good agreement between models, or conversely areas where disagreements, thus given explanation of uncertain results of the models.

Finally, the R-SWAT-DM tool should be applied and used both by scientists and policy makers to develop scenarios analysis that balance environmental advantages with investment costs, testing efficiently several complex BMPs allocation with the requirements of the European Directives.

In conclusion, the proposed systematic approach for C/V procedure with SWAT has shown to be pedagogic and a powerful tool both for scientists, policy makers and also stakeholders, and could be extended to other hydrological and water quality models with similar structure as SWAT.

# Appendix

## A1. Summary of the main input data used in the different SWAT applications

Table A1.1. Data description and sources used in the SWAT applications

| INPUT DATA | Scandinavia Peninsula ed Iberian Peninsula | Danube | Upper Danube | Crete Island |
|---|---|---|---|---|
| ***DEM Digital Elevation Model)*** | CCM2 DEM Vogt et al. (2007) 100 m pixel size | CCM2 DEM Vogt et al. (2007) 100 m pixel size | CCM2 DEM Vogt et al. (2007) 100 m pixel size; EU-DEM Metadata, (2013) 25 m pixel size. | EU-DEM Metadata, (2013) 25 m pixel size. |
| ***Subbasin and Reach*** | Catchment Characterization Modelling version 2 database CCM2, Vogt et al. (2007) | | | |
| ***Reservoirs*** | Reservoirs and lakes exceeding 20 $km^2$ Lehner and Döll (2004); Vogt et al. (2007) | Reservoirs and lakes exceeding 20 $km^2$ (Lehner and Döll, 2004; Vogt et al., 2007) and hydropower plants of large generation capacity >10MW (ICPDR, 2013) | | NA |
| ***Soil*** | Map of 1 × 1 km was from the Harmonized World Soil Database (HWSD; FAO, 2008), using top soil layer data | | | |
| ***Landuse*** | Landcover map of 1 × 1 km for year 2000, built from the combination of CAPRI (Britz, 2004), SAGE (Monfreda et al., 2008), HYDE 3 (Goldewijk and Van Drecht, 2006) and GLC (Bartholome and Belward, 2005) databases. Optimized distribution of crops-area of EUROSTAT | | | Landcover map (CAPRI-SAGE -HYDE 3 1kmx1km);Land use was obtained from the Agriculture statistics of Greece (2005) |
| ***Climate Data*** | daily precipitation, temperature, solar radiation, wind speed and relative humidity were obtained from EFAS-METEO at spatial resolution of 5 km x 5 km Ntegeka et al. (2013) | | | Daily precipitation and temperature from regional institutions and public sector organization; overall monthly statistics of all climate data using EFAS-METEO |
| ***Elevation Bands*** | Implementation of four elevation bands | | | |
| ***Irrigation*** | irrigated areas from the land-use map and the FAO Global map of irrigation areas Siebert et al. (2007), national statistics retrieved from EUROSTAT | Volume and irrigated areas from MIRCA database (Portmann et al., 2008) | | |
| ***Fertilization*** | manure and mineral fertilization applied from the CAPRI model (Britz, 2004) | | | |

## A2. Summary of model discretization and hard data

Table A2.1 Subbasin and HRUs for each model and numbers of calibration (C), validation (V) and evaluation (E) gauging stations used in the C/V procedure. #=number; C/V= Calibration / Validation; MP: monitoring point.

| # subbasin/# HRUs/ # MP | # C/V | Scandinavia Peninsula [Area=$10^6$ km$^2$] | Iberian Peninsula Area=$556 \cdot 10^3$ km$^2$) | Danube 800,000 km$^2$) | Upper Danube 132,000 km$^2$) | Crete Island 8,336 km$^2$) |
|---|---|---|---|---|---|---|
| **# subbasin** | | 5447 [~184 km$^2$] | 3019 [~184 km$^2$] | 4663 [~178 km$^2$] | 753 [~174 km$^2$] | 352 [~19 km$^2$] |
| **# HRUs** | | | | 5181 [~160 km$^2$] [0.01-1232 km$^2$ ] | 822 [~160 km$^2$] [0.01-1010 km$^2$ ] | 502 [~13 km$^2$] [0.01-65 km$^2$ ] |
| **# streamflow gauged stations** | # C | 61 (1995-2004) | 81 (1995-2004) | 264 (1995-2006)[2] | 98 (1995-2006)[2] | 15 (1983-2009) 47* (1980-2009) |
| | # V | 346 (1995-2004) | 215 (1995-2004) | 708 (1995-2009)[3] | 150 (1995-2009) | 7 (1983-2009) |
| **# sediment gauged stations** | # C | NA | NA | NA[1] | 476 (1995-2004) | NA |
| | # V | NA | NA | NA[1] | 146 (2005-2009) | NA |
| **#N-NO3 gauging stations** | # C | NA | NA | 340 (1995-2009) | NA | NA |
| | # E | NA | NA | 202 (1995-2009) | NA | NA |
| **# TN gauging stations** | # C | NA | NA | 191 (1995-2009) | NA | NA |
| | # E | NA | NA | 121 (1995-2009) | NA | NA |
| **# TP gauging stations** | # C | NA | NA | 333 (1995-2009) | NA | NA |
| | # E | NA | NA | 202 (1995-2009) | NA | NA |

1. The sediment gauging stations, as well as the analysis of sediments, in the whole Danube will be published in summer 2016.
2. In the Danube and Upper Danube models the calibration dataset was included in the validation dataset extended the period up to year 2009.
3. For 16 gauging stations in the validation dataset only measures of streamflow at monthly time step were available.

Table A2. 2. Streamflow and nutrients data sources used in the compilation of water disgorge and nutrients databases of the modelled regions. #=number; Data type: Q=streamflow $m^3/s$), N_NO3= nitrates mg/l); TN=total nitrogen mg/l), TP=total phosphorous mg/l); MP=monitoring points.

| Model | Acronym | Data Type | Time step | #MP | #data entries | Period extension | | Data provider and Owner |
|---|---|---|---|---|---|---|---|---|
| Danube | AU | Q | daily | 151 | 824723 | 1995 | 2009 | http://ehyd.gv.at/ |
| | AU | N_NO3 | daily | 106 | 10913 | 1995 | 2009 | Umweltbundesamt GmbH (http://www.umweltbundesamt.at) - Contact: Dr. Olivier Gabriel |
| | AU | TP | daily | 106 | 10817 | 1995 | 2009 | Umweltbundesamt GmbH (http://www.umweltbundesamt.at) - Contact: Dr. Olivier Gabriel |
| | BAFU | Q | daily | 1 | 5479 | 1995 | 2009 | Swiss Federal Office for the Environment (http://www.bafu.admin.ch/hydrologie/index.html?lang=en) |
| | BG | N_NO3 | daily | 6 | 882 | 1995 | 2009 | JRC (European Commission, Joint Research Centre) |
| | CZR | Q | monthly | 16 | 983 | 2004 | 2009 | Czech Hydrometeorological Institute (http://hydro.chmi.cz/ismnozstvi/) |
| | EWA | Q | daily | 25 | 135297 | 1995 | 2009 | http://www.ewa-online.eu/ |
| | HU | N_NO3 | daily | 183 | 43173 | 1995 | 2009 | BME (http://www.vkkt.bme.hu/munkatars/?mid=10) - Contact: Dr. Adrienne Clement |
| | HU | TN | daily | 149 | 17415 | 1995 | 2009 | BME (http://www.vkkt.bme.hu/munkatars/?mid=10) - Contact: Dr. Adrienne Clement |
| | HU | TP | daily | 182 | 41317 | 1995 | 2009 | BME (http://www.vkkt.bme.hu/munkatars/?mid=10) - Contact: Dr. Adrienne Clement |
| | HU | Q | daily | 118 | 587525 | 1995 | 2009 | General Directorate of Water Management of Hungary (http://www.ovf.hu/en/) |
| | ICPDR | Q | daily | 5 | 11689 | 1995 | 2009 | International Commission for the Protection of the Danube River (http://www.icpdr.org/wq-db/) |
| | ICPDR | N_NO3 | daily | 2 | 498 | 1996 | 2009 | International Commission for the Protection of the Danube River (http://www.icpdr.org/wq-db/) |
| | ICPDR | TN | daily | 2 | 272 | 2000 | 2009 | International Commission for the Protection of the Danube River (http://www.icpdr.org/wq-db/) |
| | ICPDR | TP | daily | 2 | 370 | 1996 | 2009 | International Commission for the Protection of the Danube River (http://www.icpdr.org/wq-db/) |
| | JRC | Q | daily | 112 | 531012 | 1995 | 2009 | JRC (European Commission, Joint Research Centre) database |
| | JRC | N_NO3 | daily | 51 | 8988 | 1996 | 2009 | JRC (European Commission, Joint Research Centre) database |
| | JRC | TN | daily | 43 | 3434 | 1995 | 2009 | JRC (European Commission, Joint Research Centre) database |

| | | | | | | | | |
|---|---|---|---|---|---|---|---|---|
| | JRC | TP | daily | 51 | 7916 | 1996 | 2009 | JRC (European Commission, Joint Research Centre) database |
| | LFU | Q | daily | 103 | 556640 | 1995 | 2009 | Bavarian State Office for the Environment (http://www.lfu.bayern.de/index.htm) |
| | SAVA | Q | daily | 45 | 94791 | 1995 | 2009 | International Sava River Basin Commission (http://www.savacommission.org/) |
| | SERBIA | N_NO3 | daily | 13 | 1897 | 1996 | 2009 | Serbian Environmental Protection Agency (http://www.sepa.gov.rs/index.php) |
| | SERBIA | TN | daily | 13 | 484 | 2002 | 2009 | Serbian Environmental Protection Agency (http://www.sepa.gov.rs/index.php) |
| | SERBIA | TP | daily | 13 | 1136 | 1996 | 2009 | Serbian Environmental Protection Agency (http://www.sepa.gov.rs/index.php) |
| | SIRET | Q | daily | 32 | 173493 | 1995 | 2009 | University of Suceava, Romania (Dr Obreja Florin; Radoane et al., 2013) |
| | SK | N_NO3 | daily | 55 | 6753 | 1995 | 2009 | Slovak University of Technology in Bratislava – Contact: Lea Mrafková |
| | SK | TN | daily | 53 | 2711 | 1995 | 2009 | Slovak University of Technology in Bratislava – Contact: Lea Mrafková |
| | SK | TP | daily | 55 | 6589 | 1995 | 2009 | Slovak University of Technology in Bratislava – Contact: Lea Mrafková |
| | SK | Q | daily | 62 | 318696 | 1995 | 2009 | Slovak University of Technology in Bratislava – Contact: Lea Mrafková |
| | SLV | Q | daily | 38 | 192329 | 1995 | 2009 | Agency of the Republic of Slovenia for the Environment (http://vode.arso.gov.si/) |
| **Upper Danube** | BAFU | Q | daily | 1 | 5479 | 1995 | 2009 | Swiss Federal Office for the Environment (http://www.bafu.admin.ch/hydrologie/index.html?lang=en) |
| | EWA | Q | daily | 18 | 97798 | 1995 | 2009 | http://www.ewa-online.eu/ |
| | JRC | Q | daily | 54 | 276282 | 1995 | 2009 | JRC (European Commission, Joint Research Centre) database |
| | LFU | Q | daily | 75 | 406007 | 1995 | 2009 | Bavarian State Office for the Environment (http://www.lfu.bayern.de/index.htm) |
| | TNMN | Q | daily | 2 | 6575 | 1995 | 2009 | The Transnational Monitoring Network (http://www.icpdr.org/wq-db/) |
| **Crete** | DARC | Qk | daily | 47 | 9974 | 1983 | 2009 | Water Resources at the Decentralized Administration of the Region of Crete - Contact: Dr. Marinos Kritsotakis |
| | DARC | Q | monthly | 22 | 4892 | 1980 | 2009 | Water Resources at the Decentralized Administration of the Region of Crete - Contact: Dr. Marinos Kritsotakis |
| **Scandinavia** | SCAN | Q | monthly | 407 | 47478 | 1995 | 2004 | Swedish Meteorological and Hydrological Institute –Contact:Dr: Håkan Olsson; Wingqvist Else-Marie.<br>Section Manager Norwegian Water Resources and Energy Directorate – Contact: Dr. Svein Taksdal. |

| | | | | | | | | |
|---|---|---|---|---|---|---|---|---|
| | | | | | | | | Freshwater Centre/ Monitoring and Assessment Unit – Contact:Dr. Johanna Korhonen.<br>Finnish Environment Institute – Contact: Jari Hakal. |
| **Iberian Peninsula** | IBER | Q | monthly | 296 | 35520 | 1995 | 2004 | JRC (European Commission, Joint Research Centre) database |

## A3. Table of BMPs applied in the Danube SWAT model

Table A3. 1 Best Management Practices (BMPs) included in SWAT setup of the Danube Basin, with reference to available data and SWAT literature.

| Class of BMP | BMP type | Area ($km^2$) | Spatial European data | Reference of SWAT implementation |
|---|---|---|---|---|
| Agriculture management | Cover crops | 15013 | Eurostat (2010) | Arabi et al. (2008) |
| | Conservation tillage | 77469 | Eurostat (2010) | Ullrich and Volk (2009); Lam et al. (2011) |
| | Residue management | 18400 | Eurostat (2010) | Neitsch et al. (2011) |
| | Terraces | 2565 | Eurostat (2010) | Neitsch et al. (2011) |
| Water management | Irrigation | 9200 | MIRCA database (Portmann et al., 2008) | Neitsch et al. (2011) |
| | Artificial drainage systems | 65000 | Global Drainage Map (http://www.uni-frankfurt.de/45218077/Global_Drainage_Map) | Moriasi et al. (2007a, 2013a, 2013b) |
| | Water uses | 830000 | Vandecasteele et al. (2013) | Neitsch et al. (2011) |
| | Riparian filter strips | 12580 | Clerici et al. (2011, 2013); EEA (2000); Vigiak et al. (2015b) | White and Arnold (2009); Neitsch et al. (2011) |
| Measures in surface water | Reservoirs | 2172 | Lehner and Döll (2004); Vogt et al. (2007) | Neitsch et al. (2011) |
| | Streambank protection | NA | Vigiak et al. (2015b) | Neitsch et al. (2011) |

## A4. Budyko framework

Based on observed datasets from a large number of watersheds, Budyko (1974) proposed a relationship between mean annual evaporation index (EI=E/P) and mean annual climate aridity index (AI=PET/P):

[eq. A4. 1] $$\frac{E}{P} = \sqrt{\frac{PET}{P}\left[1 - exp\left(-\frac{PET}{P}\right)\right] tanh\left(\frac{1}{\frac{PET}{P}}\right)}$$

where E is the mean actual evapotranspiration at annual level, PET is the mean annual potential evapotranspiration and P is the mean annual precipitation.

As showed in Figure A4.1, evaporation index EI, which is captured by the Budyko curve, increases from humid (when AI<1) to arid (when AI>1) regions. The slope of the Budyko curve is steep in energy-limited regions (when AI<1) and becomes flat in water-limited regions (when AI>1) (Wang and Wu, 2013).

Other functional forms of Budyko-type have been developed for assessing long-term balance (i.e Turc, 1954; Pike, 1964; Fu, 1981; Zhang et al., 2001; Yang et al., 2008).

One parametric Budyko-type function is the Turc-Pike equation:

[eq. A4. 2] $$\frac{E}{P} = \left[1 + \left(\frac{PET}{P}\right)^{-n}\right]^{-\frac{1}{n}}$$

where *n* is the parameter representing the effects of watershed descriptive factors such as vegetation, soil and topography on precipitation partitioning.

The scatter of data points each point is related to a site representing a subbasin (or a watershed) in Figure A4.1 is caused by data uncertainty and other controlling factors such as climate seasonality, vegetation, soil and topography (Milli, 1994; Zhang et al., 2001; Donohue et al., 2007; Yang et al., 2007; Yokoo et al., 2008; Zhang et al, 2008).

However, at mean annual scale soil storage can be assumed as negligible. As a consequence, the Budyko curve is expected to represent the position of the observed mean annual data of EI-AI; thus in presence of an excessive dispersion the reasons of such a dispersion or distance should be taken into account. In other words, using the Budyko plot it is possible to understand how much the annual water balance in a site can be considered as realistic.

For instance, if a site is plotted above the energy limit (red point in Figure A4.1), the contribution of some components were probably missed, i.e groundwater storage and baseflow contributions to the river. Conversely, if a site overcomes the water limit blue (point in Figure A4.1) perhaps it will be necessary to consider an additional contribution to precipitation (i.e external input of discharge) (Jones et al, 2012).

The Budyko-type curve in [eq. A4.2] is obtained fitting the point site through the adjustment of the parameter n for the. This curve help understanding the differences between the components of water balance estimations and their generation. In additions, a natural change in climate condition (increment or decrement of AI index) can be easily recognized as a movement up and down with the Budyko.

Wang and Wu (2013) defined a complementary Budyko curve for the baseflow index (BFI=BF/P) assuming that at the mean annual scale in steady–state condition the baseflow is mainly controlled by aridity index, and the surface runoff components is hypothesized as negligible. A complementary Turc-Pike curve can be formulated as following:

[eq. A4. 3] $$\frac{BF}{P} = 1 - \left[1 + \left(\frac{PET}{P}\right)^{-m}\right]^{-\frac{1}{m}}$$

as showed in Figure A4.2 the baseflow index, which is captured by the complementary Budyko curve [[eq. A4. 3], decreases from humid (AI<1) to arid (AI>1) regions. The slope of the complementary Budyko curve is steep in energy-limited regions (i.e. AI<1), and becomes flat in water limited regions (AI>1) (Wang and Wu, 2013). In addition, Figure A4.2 shows that when the AI is lower than 1 humid regions) a high baseflow index is expected and the site-point should be close to the energy limit. For instance, the red point in Figure A4.2 suggests that the baseflow index for this site is probably underestimated or some factors (i.e. geology, land cover and urbanization) have influenced its estimation (Price et al., 2011).

This approach requires the separation of baseflow from streamflow as described in section 2.4.3.

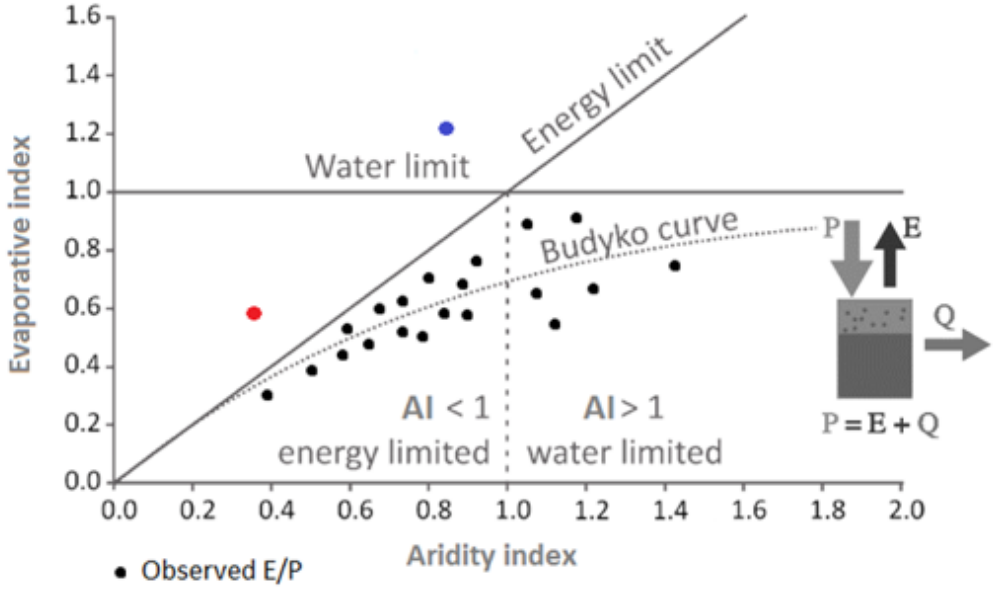


Figure A4.1. Estimates of evaporative indexes and Budyko curve. The red point represents a situation where the energy limit is forced, the blue point represents where the water limit is forced.

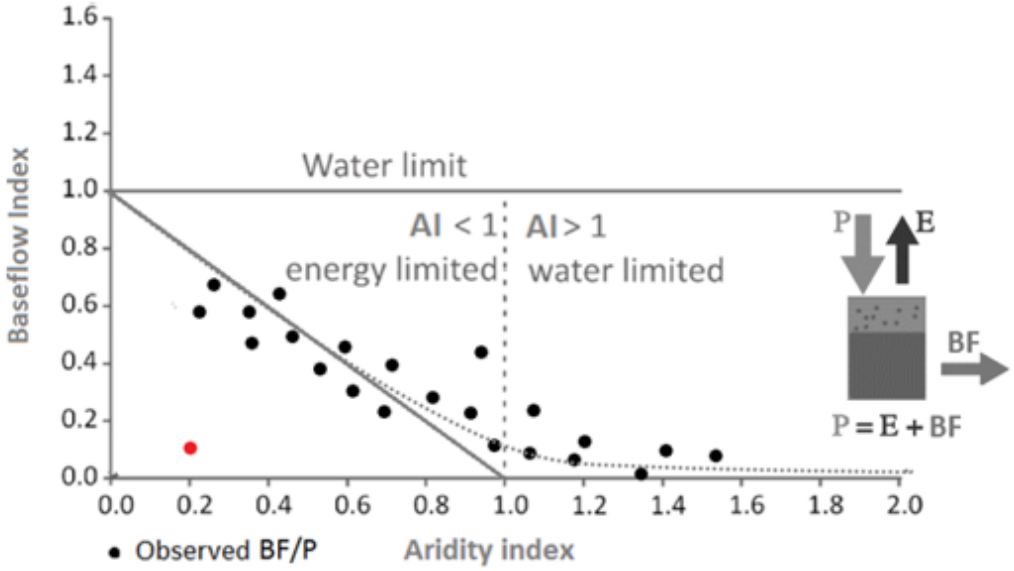


Figure A4.2. Example of comparison between baseflow indexes with estimates represented by the Budyko curve. The red point represents a situation of overcoming of complementary energy limit for BFI.

## A5. R-SWAT-DM model

The R-SWAT-DM framework was developed by Udias et al. (2015) as an integrated decision making tool to assesses the economic and water quality impacts of different types/levels of management practices. The framework was developed in R software. R is an open-source programming language and a free software environment for statistical computing and graphics (R Development Core Team, 2009; Ihaka & Gentleman, 1996).

Figure A5.1 shows the interaction of the proposed R-SWAT-DM between SWAT and the economic model.

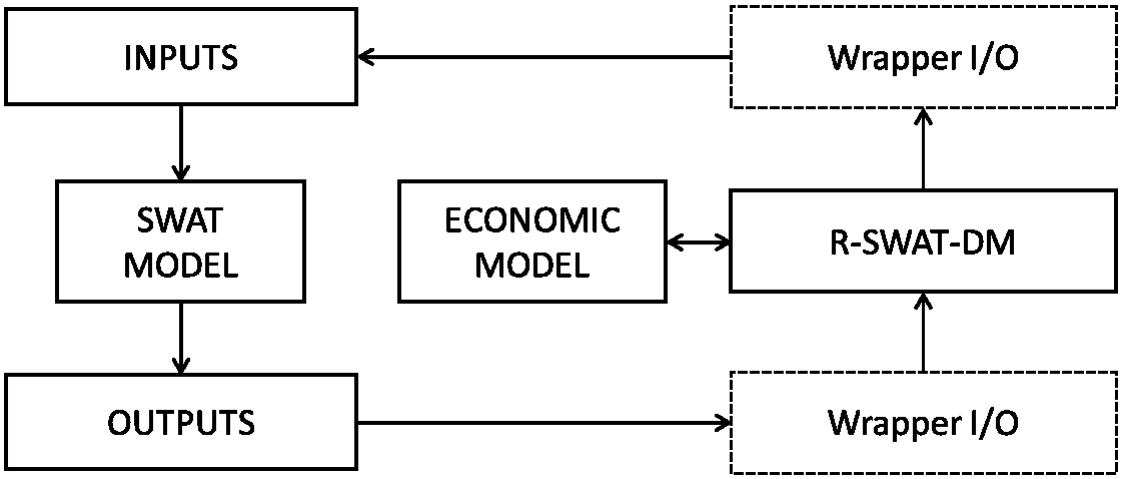


Figure A5.1: Flowchart of the interactions between R-SWAT-DM, SWAT and the Economic Models. Dashed-line boxes represent basic I/O wrapper functions to read/write model files.

The R-SWAT-DM communicates with the SWAT model through simple ASCII files and/or R wrapper functions (Figure A5.1), modifying model input files and reading outputs files. Users can run single or combined simulations of management practices, or more complex iterative simulations, as well as multi-objective optimization process (i.e. upgrading Waste Water Treatment Plants, WWTPs, decreasing mineral fertilizers and increasing the global income/benefits)

After the simulation and/or optimization, the user can analyse and compare the management scenario outputs graphically and statistically. The R-SWAT-DM can also generate maps with detailed spatial information about a selected scenario.

### The environmental objective function

The R-SWAT-DM comprise three different alternatives as objective functions: the average pollutant in all rivers, the cumulated contaminant and the total loads at the outlet of the watershed.

The average pollutant concentration in all stretches and for the whole simulation period:

[eq. A5. 1] $$\frac{1}{ns}\frac{1}{nt}\sum_{i=1}^{ns}\sum_{j=1}^{nt}Q_{ij}$$

Where:

nt: number of time-steps in the simulation period.

ns: number of modeled reaches

Qij: concentration (mg/l) of pollutant in reach "i" and simulation time-step "j".

The cumulated contaminant: sum of contaminant concentrations in reaches that exceeded an environmentally acceptable threshold:

[eq. A5. 2] $$\sum_{i=1}^{ns}\sum_{j=1}^{nt}\left(Q_{ij}\right) \quad \forall\, i,j \mid Q_{ij} > Th$$

Where:

*Th*: threshold that is considered as environmentally acceptable.

The total load at the watershed outlet:

[eq. A5. 3] $$\frac{1}{nt}\sum_{j=1}^{nt}TL_j$$

Where:

$TL_j$: is the load of the pollutant exported at the watershed outlet in the simulation period *"j"*.

**The economic objective function**

The economic objective function combine both:

[eq. A5. 4] $$TNI = g_1(x,y|\theta,I\,,wc,cr,T) - g_2(z|\theta,I\,,wc,cr,T) - g_1(BL)$$

Where:

- TNI: total net income (considering together gross margin of the farmers and cost of the WWTP);
- x: decision variables that describes the amount and distribution of fertilizers in each Hydrological Response Units in SWAT;
- y: decision variables that describes the amount and distribution of irrigation in each Hydrological Response Units in SWAT;
- z: decision variables that describes the type and allocation of the WWTPs in each subbasin in SWAT;
- g1: total gross margin related with the agricultural production.

- g2: cost related to upgrading the WWTP (additional cost in relation with baseline situation);
- T: simulation period;
- $\theta$: vector of calibrated watershed model parameters;
- $I$: driving forces (i.e., precipitation, temperature, and other environmental factors).
- wc: unit cost for implementing the conservation practice.
- cr: unit price of beneficial products of the conservation practice.
- g1(BL): base line situation gross margin related with the agricultural production.

In particular, the g1 (total gross margin for agricultural production) component was defined as follows:

[eq. A5. 5] $g_1^{mp} = \sum_{i=1}^{HRU} \sum_{j=1}^{crop} \left( Y_{ij}^{mp} * A_{ij} * Up_j - Fc_{ij}^{mp} * Qf_{ij}^{mp} - Qw_{ij}^{mp} * Wc - Oc_j \right)$

Where:

- $g_1^{mp}$: agricultural total gross margin for the BMP;
- $Y_{ij}^{mp}$: yield of crop j in HRU i under a BMP;
- Aij : area (ha) of crop j in HRU i;
- Upj : unit price (income €/ton) of crop j;
- $Qf_{ij}^{mp}$: quantity of fertilizer applied (kg/ha) to crop j in HRU i under a BMP;
- $Fc_{ij}^{mp}$: unit cost of fertilizer (€/kg) of crop j in HRU i under a BMP;
- $Wc$ : the water irrigation unit cost (€/mm), constant across HRUs;
- $Qw_{ij}^{mp}$: irrigation quantity (mm/ha) for crop j in HRU i under a BMP;
- $Oc_j$: operational management cost for the crop j;

Currently, the R-SWAT-DM has included the prizes related to fertilizers from MARM (2010) for each crop modelled by SWAT.

The total wastewater treatment cost for upgrading g2 in a basin was estimated as the sum of the treatment cost for each plant, based on the treatment type and the volume of water, using the following equation:

[eq. A5. 6 ] $g_2^{mp} = \sum_{k=1}^{WWTP} \left( 365 * Q_k * Coef_1[Y_k] * Q_k^{Coef_2[Y_k]} \right)$

- $g_2^{mp}$ : WWTP upgrading annual cost for the mp water restoration management practices;
- Qk : flow average ($m^3$/day) for each WWTP k;

- Yk: type of upgrade of the WWTP k. 0: no upgrade; 1: upgrade from C to CND; upgrade from C to CNDP. Table A5.1 explains in detail C, CDD and CNDP configuration;
- Coef1 [Yk]: coefficient 1 for the WWTP type of upgrade (Yk). It is related to the type of upgrade treatment as showed in Table A5.1;
- Coef2 [Yk]: coefficient 2 for the Yk WWTP type of upgrade (Yk). It is related to the type of upgrade treatment as showed in Table A5.1;

Table A5.1. Cost and nutrients reduction efficiency for each type of WWTP upgrading and the flow used in [[eq. A5. 6].

| **Upgrade Treatment** | **coef1** | **coef2** | **Cost (€/m$^3$)** | **Nutrient Effic. Remov. (%)** | | |
|---|---|---|---|---|---|---|
| | | | | **NH4** | **NO3** | **PO3** |
| No Upgrade | 0 | 0 | 0 | 0 | 0 | 0 |
| C to CND | 0.1115 | -0.126 | 0. 1115Q-0.126 | 20 | 20 | 0 |
| C to CNDP | 0.1464 | -0.119 | 0.1464Q-0.119 | 55 | 55 | 5 |

Source: Dvorak et al. (2008). Q: capacity of WWTP in m$^3$/day

## A6. Benchmarking modelling approach: some details

### *The graphical comparison*

Bar plots with confidence intervals were used to compare observed and simulated mean annual values of streamflow, TN and TP for the period 2000-2009. The 95% confidence interval was computed by multiplying the standard error of the mean (i.e. the ratio of standard deviation to the square root of the sample size) by 1.96. The value of 1.96 is based on the fact that 95% of the area of a normal distribution is within 1.96 standard deviations of the mean.

Taylor diagrams (Figure A6.1) allow a combined presentation of different statistical indicators, such as the Pearson's correlation coefficient R, the centred root-mean-square error RMS[6] between observations and models, and the standard deviation of observed and models samples. Figure A6.1 is an example showing how to interpret it. The standard deviation and RMS error are on the correspondent arcs, whereas the correlation coefficient is on the circumference. The reference point (red dot) is always collocated on the x-axis, whereas the model point moves on the arcs of the quadrant. The position of a model (black dot) on the plot quantifies how closely the model outputs match the reference: the closer the black dot is to the red dot, the better the model performance.

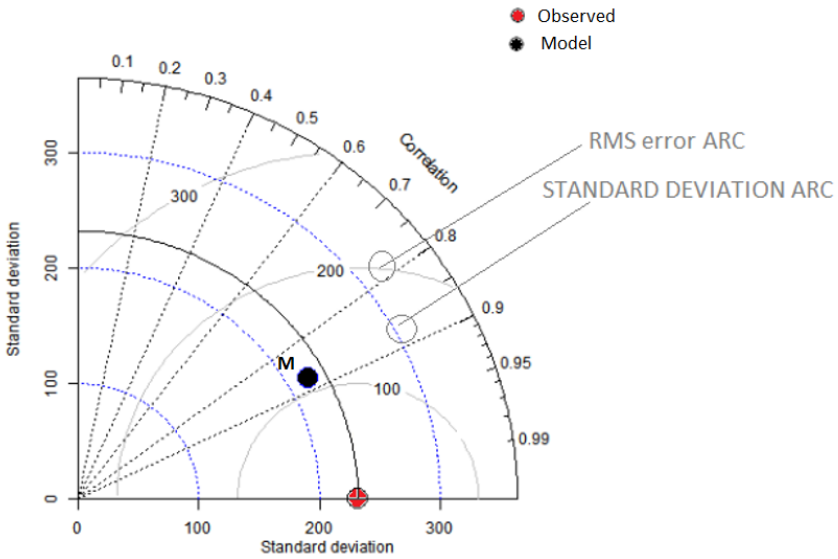


Figure A6.1. Example of a Taylor diagram

[6] The RMS is the Centered Root Mean Square error calculated as described in Taylor (2001). It was calculated based on the assumption that the Centered Root Mean Square Error is a function of standard deviation of reference, standard deviation of test, and the correlation coefficient between the test and reference fields.

***MONERIS and GREEN models***

There is a large number of models used to assess nutrients loads in river basins. They vary in process descriptions, spatial and temporal scale and data requirements. In this study two conceptual models, GREEN (Grizzetti et al., 2008) and MONERIS (Venohr et al., 2011) were compared with the process-based model SWAT (Arnold et al., 1998). They are among the most commonly used models to assess diffuse and point source nutrient pollution. A comparison of the models for assessing remediation measures for nitrogen water pollution have been explored in Bouraoui and Grizzetti (2014). Here a shorth description of MONERIS and GREEN models is provided focusing on (i) processes representation; (ii) the spatial and temporal scale; and (iii) the main characteristics in the application to the Danube River Basin.

*MONERIS*

The model Modeling Nutrient Emissions into River Systems (MONERIS, Behrendt et al., 2000; Venohr et al., 2011) is a semi-empirical, semi-distributed, steady-state model for monthly, annual and long-term average nutrient emissions in river basins (Behrendt et al., 2000; Venohr et al., 2011). The model considers point emissions and several pathways and sources of nutrients, and takes into account the retention and transformation of nutrients in soils, groundwater, rivers and lakes for calculating nutrient loads. MONERIS aims at a moderate demand of input data, a short computing time, and offers an easy application to large river basins.

While the empirical approaches for the pathways included in MONERIS have been developed and calibrated independently, the in-stream retention and remobilisation is calibrated against observation data (i.e. nutrient loads) and the output of other models. Runoff is derived via a simplified runoff distribution procedure, considering precipitation, evaporation, water withdrawal/addition and it is validated against obsereved data. For each pathway, the flow components and nutrient concentrations are modelled. In MONERIS, groundwater discharge comprises the natural interflow and base flow (Venohr et al., 2011) and it is calculated as the residual of total flow and all other flow components.

MONERIS uses “analytical units” as smallest modelling unit based on topography, hydrological catchments and administrative units. In this study, the Danube River Basin was subdivided into 1578 units with an average area of 510 km². It was also the first monthly application of MONERIS for the Danube River Basin (Venohr et al., 2015).

*GREEN*

GREEN is a conceptual statistical model that consists of a regression equation based on spatially referenced data (Grizzetti et al., 2008; 2012). The model estimates annual nitrogen

and phosphorus loads in surface waters. It uses a routing structure to establish the emitting-receiving sub-basins relationship. It considers two different pathways of nutrient transfer from sources to the basin outlet: diffuse and point sources. GREEN does not simulate nutrient cycles but calculates the diffuse emissions (from land to the streamflow) as sum of all diffuse sources reduced by a basin reduction factor that takes into account the retention in the soil, aquifers and the nitrogen removed by plants. Finally, it estimates the loads in the river considering a river reduction factor (river retention). The model requires the calibration of only two parameters of retention. The streamflow in the rivers was calculated outside GREEN using the Budyko framework approach (Grizzetti et al., 2012). The basis of spatial resolution is the sub-basin, the same used in SWAT (4663 sub-basins), with an average area of about 180 $km^2$.

# Bibliography


Abbaspour, K.C. (2008) SWAT-CUP2: SWAT Calibration & Uncertainty Programs – A User Manual. Department of Systems Analysis, Integrated Assessment & Modelling (SIAM), Eawag, Swiss Federal Institute of Aquatic Science & Technology, Duebendorf, Switzerland.

Abbaspour, K. C., Rouholahnejad, E., Vaghefa, S., Srinivasan, R., Yang, H., & Kløve, B. (2015). A continental-scale hydrology & water quality model for Europe: Calibration & uncertainty of a high-resolution large-scale SWAT model. Journal of Hydrology, 524(1), 733–752.

Afinowicz, J. D., Munster, C. L., & Wilcox, B. P. (2005). Modelling effects of brush management on the rangeland water budget. (E. P. Texas, Ed.). Journal American Water Resources Association, 41(1), 181-193.

Agriculture statistics of Greece (2005). ΠΕΙΡΑΙΑΤΜ -2009-PIREAS.

Alcamo, J., Döll, P., Henrichs, T., Kaspar, F., Lehner, B., Rösch, T., & Siebert, S. (2003). Development & testing of the WaterGAP 2 global model of water use & availability. Hydrolog. Sci. J., 48, 317–337. doi:10.1623/hysj.48.3.317.45290.

Andreassian, V., Hall, A., Chahinian, N., & Schaake, J. (2006). Large Sample Basin Experiment for Hydrological Model Parameterization:Results of the Model Parameter Experiment – MOPEX,IAHS Publication, Wallingford, 307.

Aouissi, J., Benabdallah, S., Chabaane, Z.L., & Cudennec, C. (2014). Modelling water quality to improve agricultural practices & land management in a Tunisian catchment using the Soil & Water Assessment Tool. J. Environ.Qual., 43:18‐25. doi:10.2134/jeq2011.0375.

Arabi, M., Frankenberger, J.R., Engel, B.A., Arnold, & J.G. (2008). Representation of agricultural conservation practices with SWAT. Hydrological Processes, 22, 3042-3055. doi: 10.1002/hyp.6890.

Arfib, B., de Marsily, G., & Ganoulis, J. (2000). Pollution by seawater intrusion into a karst system: new research in the case of the Almyros source (Heraklion, Crete, Greece). Acta Carsologica 29 (1), 15-31.

Arheimer, B. & Brandt, M. (1998). Modelling nitrogen transport & retention in the catchments of southern Sweden. Ambio, 27, 471–480.

Arnold, J.G., Srinivasan, R., Muttiah, R.S., & Allen, P.M. (1999). Continental scale simulation of the hydrologic balance. J. Am. Water Resour. Assoc., 35 (5), 1037–1051.

Arnold, J. G., R. Srinivasan, R. S. Muttiah, & Williams, J. R. (1998). Large area hydrologic modeling & assessment: Part I. Model development. J. American Water Resour. Assoc., 34(1), 73-89.

Arnold, J. G., & Fohrer, N. (2005). SWAT2000: Current capabilities & research opportunities in applied watershed modeling. Hydrol. Process., 19(3), 563‐572.

Arnold, J.G., Kiniry, J.R., Srinivasan, R., Williams, J.R., Haney, E.B., & Neitsch, S.L. (2012a). Soil & Water Assessment Tool Input/Output documentation Version 2012. Texas Water Resources Institute Technical report 436. Texas A&M University System College Station, Texas, U.S. http://swat.tamu.edu/documentation/2012-io/ (accessed Dec 1, 2014).

Arnold, J. G., Moriasi, D. N., Gassman, P. W., Abbaspour, K. C., White, M. J., Srinivasan, R., Santhi, C., Harmel, R. D., van Griensven, A., Van Liew, M. W., Kannan, N., Van Liew, M. W., & Jha, M. K. (2012b). SWAT: Model use, calibration, & validation. Trans. ASABE, 55(4), 1491-1508. http://dx.doi.org/10.13031/2013.42256.

Arnold, J. G., Youssef, M. A., Yen, H., White, M. J., Sheshukov, A. Y., Sadeghi, A. M., Moriasi, D. N., Steiner, J. L., Amatya, D. M., Skaggs, R. W., Haney, E. B., Jeong, J., Arabi, M., & Gowda, P. H. (2015). Hydrological processes & model representation: Impact of soft data on calibration. Trans. ASABE, 58(6), 1637-1660. http://dx.doi.org/10.13031/trans.58.10726.

Baffaut, C. & Benson, V. W. (2009). Modeling flow & pollutant transport in a karst watershed with SWAT. T. ASABE, 52, 469–479.

Baffaut, C., Dabney, S. M., Smolen, M. D., Youssef, M. A., Bonta, J. V., Chu, M. L., Guzman, J. A., Shedekar, V., Jha, M. K., & Arnold, J. G. (2015). Hydrologic & water quality modeling: Spatial & temporal considerations. Trans. ASABE, 58(6), 1661-1680. http://dx.doi.org/10.13031/trans.58.10714.

Bagnold, R.A. (1977). Bed load transport by natural rivers.Water Resources Research 13, 303-312.

Bakalowicz (2015). Karst & karst groundwater resources in the Mediterranean. Environ Earth Sci., 74, 5-14.

Baltas, E. & Tzoraki, O. (2013). Water resources management on the island of Crete: Lessons learnt, in: United Nations International Year of Water Cooperation (Eds.), Free Flow - Reaching Water Security through Cooperation, Tudor Rose, 285-289.

Barfield, B.J., Blevins, R.L., Fogle, A.W., Madison, C.E., Inamdar, S., Carey, D.I., & Evangelou, V.P. (1998). Water quality impacts of natural filter strips in karst areas. Transactions of the ASAE, 41(2), 371‐381.

Bartholome, E., & A.S. Belward (2005). GLC2000: A new approach to global land cover mapping from earth observation data. Int. J. Remote Sens., 26(9), 1959–1977. doi:10.1080/01431160412331291297.

Bazilian, M., Rogner, H., Howells, M., Hermann, S., Arent, D., Gielen, D., Steduto, P., Mueller, A., Komor, P., Tol, R. S. J. & Yumkella, K. K. (2011). Considering the energy, water

& food nexus: Towards an integrated modelling approach. Energy Policy, 39(12), 7896-7906.

Behrendt, H. & Opitz, D. (2000) Retention of nutrients in river systems: Dependence on specific runoff & hydraulic load. Hydrobiologia, 410, 111–122.

Benham, B. L., Baffaut, C., Zeckoski, R. W., Mankin, K. R., Pachepsky, Y. A., Sadeghi, A. M., Brannan, K. M., Soupir, M. L., & Habersack, M. J. (2006). Modeling bacteria fate & transport in watershed to support TMDLs. Trans. ASABE, 49(4), 987-1002.

Bieger, K., Hörmann, G., & Fohrer, N. (2012). Using residual analysis, auto-and cross-correlations to identify processes for the calibration of the SWAT model in a data scarce region. Adv. Geosci., 31, 23-30.

Bonacci, O., (1995). Brackish karst spring Pantan. Acta Carsologica, 24, 97-107.

Bonacci, O. & Fistanic, I. (2006). Contribution to hydrological analysis of the coastal karst spring Almyros (Creete, Greece). Conference on Water Observation & information system for decision support, Balwois (Ohrid, Republic of Macedonia). Radic (Eds.). UNDP-Agency of Skopje,.191-192.

Bonacci, O. & Ljubenkov, I. (2005) Nova saznanja o hidrologiji rijeke Krke. Hrvatske Vode, 13 (52), 265-281.

Borah, D. K., & Bera, M. (2003). Watershed‐scale hydrologic & nonpoint‐source pollution models: Review of mathematical bases. Trans. ASAE, 46(6), 1553‐1566.

Borselli, L., Cassi P., & Salvador Sanchis P. (2009). Soil erodibility assessment for applications at watershed scale. In Costantini, E.A.C. (ed.), Manual of methods for soil and land evaluation, Science Publishers, Enfield, USA. ISBN 978-1-57808-571-2, 98-117.

Borselli L., Torri D., Poesen, J., Iaquinta, P. (2012). A robust algorithm for estimating soil erodibility in different climates. Catena, 97, 85-94.

Bouraoui, F., & Grizzetti, B. (2014). Modelling mitigation options to reduce diffuse nitrogen water pollution from agriculture. Sci. Total Environ., 468–469, 1267 –77.

Britz, W. (2004). CAPRI Modelling System Documentation, Final report of the FP5 shared cost project CAP-STRAT "Common Agricultural Policy Strategy for Regions, Agriculture and Trade", QLTR 2000-00394, Universität Bonn, Germany.

Brown, L. C. & Barnwell, T. O. Jr. (1987). The enhanced stream water quality models QUAL2E & QUAL2E-UNCAS: Documentation & User Manual. Tufts University & US EPA, Athens, Georgia.

Buchanan, T. J. & Somers, W. P. (1976). Discharge measurements at gaging stations. Techniques of Water-Resources Investigations of the United States Geological Survey. Washington, D.C.: USGS. Book 3, Chapter A8.

Budyko, M. I. (1974). Climate & Life, 508, Academic Press, New York.

Cerdan, O., Govers, G., Le Bissonais, Y., Van Oost, K., Poesen, J., saby, N., Gobin, A., Vacca, A., Quinton, J., Auerswald, K., Klik, A., Kwaad, F.J.P.M., Raclot, D., Ionita, I., Rejman, J., Rousseva, S., Muxart, T., Roxo, M.J., & Dostal, T. (2010). Rates & spatial variations of soil erosion in Europe: a study based on erosion plot data. Geomorphology, 122, 167-177.

Cerro,I., Antigüedad,I., Srinavasan, R., Sauvage,S., Volk, M., & Sanchez-Perez, J.M. (2012). Simulating land management options to reduce nitrate pollution in an agricultural watershed dominated by an alluvial aquifer. Jounral of Environmental Quality. doi:10.2134/jeq2011.0393.

Cerro, I., Antiguedad, I., Srinavasan, R., Sauvage,S., & Volk, M., & Sanchez-Perez, J.M. (2014). Simulating land management options to reduce nitrate pollution in an agricultural watershed dominated by an alluvial aquifer. J.Environ. Qual, 43, 67‐74. doi:10.2134/jeq2011.0393.

Chaplot, V. (2005). Impact of DEM mesh size & soil map scale on SWAT runoff, sediment, & NO3CN loads predictions. J. Hydrology, 312, 207-222.

Chaplot, V. (2014). Impact of spatial input data resolution on hydrological & erosion modeling: recommendations from a global assessment. Physics & Chemistry of the Earth, 67-69, 23-35.

Chartzoulakis, K.S., Paranychianakis, N.V., & Angelakis, A.N. (2001). Water resources management in the island of Crete, Greece, with emphasis on the agricultural use. Water Policy, 3 (3), 193-205.

Chaubey, I., Cotter, A.S., Costello, T.A., & Soerens, T.S. (2005). Effect of DEM data resolution on SWAT output uncertainty. Hydrol.Process., 19, 621-628.

Chen, E. & Mackay, D.S. (2004). Effects of distribution-based parameter aggregation on a spatially distributed agricultural nonpoint source pollution model. Journal of Hydrology, 295, 211-224.

Chow, V.T., Maidment, D., & Mays, L. W. (1988). Applied Hydrology. McGraw Hill.

Chu, T. W., Shirmohammadi, A., Montas, H., Sadeghi, A. (2004). Evaluation of the swat model's sediment

and nutrient components in the piedmont physiographic region of Maryland. Transaction of the American Society of Agricultural Engineering (ASAE), 47 (5), 1523−1538.

Clark, M. P., Slater, A. G., Rupp, D. E., Woods, R. A., Vrugt, J. A., Gupta, H. V., Wagener, T., & Hay, L. E. (2008). Framework for Understanding Structural Errors (FUSE): A modular framework to diagnose differences between hydrological models. Water Resour. Res., 44, W00B02. doi:10.1029/2007WR006735.

Clerici N., Weissteiner C.J., Paracchini M.L., & Strobl P. (2011). Riparian zones: where the green and blue networks meet. Pan-European zonation modelling based on remote sensing and GIS. JRC Scientific and technical report EUR 24774EN.

Clerici, N., Weissteiner, C. J., Paracchini, M.L., Boschetti, L., Baraldi, A., & Storbl, P. (2013). Pan-European distribution modelling of stream riparian zones based on multi-source Earth Observation data. Ecological Indicators, 24, 211-223.

Clive G. Page (1988). The professional programmers guide to Fortran 77. FORTRAN (Computer program language), Computer systems Programming languages Fortran 77 language. London, Pitman, 1988.

Coffey, M. E., Workman, S. R., Taraba, J. L. & Fogle, W. A. (2004). Statistical procedures for evaluations daily & monthly hydrologic model predictions. Trans. ASAE, 47(1), 59-68.

Collins, A.L., & McGonigle, D.F. (2008). Monitoring and modelling diffuse pollution from agriculture for policy support: UK and European experience. Environmental Science and Policy, 11, 97-101.

Coron, L., Andréassian, V., Perrin, C., Lerat, J., Vaze, J., Bourqui, M., & Hendrickx, F., (2012) Crash testing hydrological models in contrasted climate conditions: an experiment on 216 Australian catchments, Water Resour. Res., 48, W05552. doi:10.1029/2011WR011721.

Cotter, A.S., Chaubey, I., Costello, T.A., Soerens, T.S., &Nelson, M.A. (2003). Water quality model output uncertainty as affected by spatial resolution of input data. J. Am. Water Resour. Assoc., 39, 977-986.

Daly, D., Dassargues, A., Drew, D., Dunne, S., Goldscheider, N., Neale, S., Popescu, C., & Zwhalen, F. (2002). Main concepts of the “European Approach” for (karst) groundwater vulnerability assessment & mapping. Hydrogeol. J., 10(2), 340–345.

de Vente, J. Poesen, J., Verstraeten, G., Govers, G., Vanmaercke, M., Van Rompaey, A., Arabkhedri, M., & Boix-Fayos, C. (2013). Predicting soil erosion & sediment yield at regional scales: where do we stand? Earth-Science Reviews, 127, 16-29.

Dettling, M. & Maechler, M. (2012). Supclust, Supervised clustering of predictor variables such as genes. R package version 1, 0-7.

Di Luzio, M., R. Srinivasan, & J.G. Arnold. (2004). A GIS-coupled hydrological model system for the watershed assessment of agricultural nonpoint & point sources of pollution. Trans. GIS, 8(1), 113–136.

Di Luzio, M., Arnold, J.G., & Srinivasan, R. (2005). Effect of GIS data quality on small watershed streamflow & sediment simulations. Hydrol. Process., 19, 629-650.

Dietz, T., Dolsak, N., Ostrom, E. & Stern, P. C. (2002). The Drama of the Commons. In Ostrom, E., Dietz, T., Dolsak, N., Stern, P. C., Stonich, S. & Weber, E. U. (Eds.) The Drama of the Commons. Washington, D. C., USA, National Academy Press.

Dietz, T., Ostrom, E. & Stern, P. C. (2003). The Struggle to Govern the Commons. Science, 302 (5652): 1907-1912.

Dingman S. L. (1994). Physical Hydrology; Prentice Hall, New Jersey, 575

Dixon, B. & Earls, J. (2009). Resample or not?! Effects of resolution of DEMs in watershed modeling. Hydrol. Process. 23, 1714-1724.

Döll, P. & Fiedler, K. 2008. Global-scale modeling of groundwater recharge. Hydrol. Earth Syst. Sci., 12, 863-885.

Döll, P., Fiedler K., & Zhang, J. (2009). Global-scale analysis of river flow alterations due to water withdrawals & reservoirs. Hydrol Earth Syst Sci, 13(12), 2413-2432. doi:10.5194/hess-13-2413-2009.

Donnelly, C., Andersson, J. C. M., & Arheimer, B. (2015). Using flow signatures & catchment similarities to evaluate the E-HYPE multi-basin model across Europe, Hydrolog. Sci. J., doi:10.1080/02626667.2015.1027710.

Doorenbos J. & Pruitt, W.O., (1977). Guidelines for predicting crop water requirements, FAO-ONU, Rome, Irrigation & Drainage Paper no. 24 (rev.), 144.

Donohue, R. J., Roderick, M. L., and & McVicar, T. R. (2007). On the importance of including vegetation dynamics in Budyko's hydrological model. Hydrol. Earth Syst. Sci., 11, 983–995. doi:10.5194/hess-11-983-2007.

Douglas-Mankin, K. R., Srinivasan, R., & Arnold, J. G. (2010). Soil & Water Assessment Tool (SWAT) model: Current development & applications. Trans. ASABE 53(5), 1423-1431.

DPRP Danube Pollution Reduction Programme (1999) Strategic action plan for the Danube River Basin 1995-2005. Revision 1999. Programme Coordination Unit UNDP/GEF Assistance.180pp. https://www.icpdr.org/main/activities-projects/danube-pollution-reduction-programme [accessed 16/12/2015].

Du, B., J. G. Arnold, A. Saleh, & D. B. Jaynes (2005). Development & application of SWAT to landscapes with tiles & potholes. Trans. ASAE 48(3), 1121‐1133.

Duda, P. B., Hummel, P. R., Donigian Jr., A. S., & Imhoff, J. C. (2012). BASINS/HSPF: Model use, calibration, & validation. Trans. ASABE, 55(4), 1523-1547. http://dx.doi.org/10.13031/2013.42261.

Duru, U. (2015). Modeling sediment yield & deposition using the swat model: a case study of Cubuk I & Cubuk II reservoirs, Turkey. PhD Thesis. Colorado State University.

Dworak, T, Berglund M., Schilling C., Zessner. M. & Lampert, M. (2008). Case study on calculating cost-effective measures to tackle nutrient pollution from the agricultural, municipal and industrial sectors in the Black Sea. Final Report of the UNDP-GEF Black Sea Ecosystem Recovery Project (PIMS 3065).

EC (2000). Establishing a framework for community action in the field of water policy. Directive 2000/60/EC of the European Parliament & of the Council of 23 October 2000, Official Journal of the European Communities, Brussels, http://ec.europa.eu/environment/ water/water-framework/index en.html, 2000.

EC (2003). Vulnerability & risk mapping for the protection of carbonate (Karst) aquifers 2003. In: Zwahlen, F., (Eds.), COST-620 Action Final Report, European Commission, DG-Research; 320.

EC (2004). The main coastal karstic aquifers of southern Europe 2004, in: Calaforra, J.M., (Eds.), COST-621 Action, Groundwater management of coastal karstic aquifers, European Commission, DG-Research, 126.

European Environmental Agency (EEA) (2000). Corine Land Use Map 2000. Available at http://land.copernicus.eu/pan-european/corine-land-cover/clc-2000/view1-73. [accessed 5.01.2016].

EMEP (The Co-operative Programme for the Monitoring and Evaluation of the Long-Range Transmission of Air Pollutants in Europe) (2001). EMEP measurement database. Available at: http://www.emep.int/ (accessed 28 October 2011).

Engel, B., D. Storm, M. White, J. Arnold, & Arabi, M. (2007). A hydrologic/water quality model application protocol. J. American Water Resour. Assoc., 43(5), 1223-1236.

ENVIROGRIDS (2015). enviroGRIDS - Core datasets [Online]. Available: http://129.194.231.164 [Accessed 07/09/2015.

EU-DEM Metadata (2013). http://www.eea.europa.eu/data-and-maps/data/eu-dem#tab-metadata/ (accessed Dec 1, 2013).

European Soil Portal (2014). http://eusoils.jrc.ec.europa.eu/ESDB Archive/ESDB/. [accessed April 2014].

EUROSTAT (2010). Agri-environmental indicators. Available at http://ec.europa.eu/eurostat/statistics-explained/index.php/Agri-environmental_indicators [accessed 4.01.2016].

EUROSTAT (2013). Agriculture–Agricultural products–Crops products–Crops products: Areas & productions. Crop products. accessed 10 September 2013 (Available at http://ec.europa.eu/eurostat/data/database performed search for “apro_cpp_crop”).

FAO/IIASA/ISRIC/ISS-CAS/JRC (2008). Harmonized world soil database (version 1.0). FAO, Rome. Italy and IIASA, Laxenburg, Austria.

Faramarzi, M., Abbaspour, K.C., Schulin, R., & Yang, H. (2009). Modeling blue & greenwater availability in Iran. Hydrol. Proc., 23 (3), 486–501.

Faramarzi, M., Abbaspour, K.C., Vaghefi, S.A., Farzaneh, M.R., Zehnder, A.J.B., & Yang, H. (2013). Modelling impacts of climate change on freshwater availability in Africa. J. Hydrol., 250, 1–14.

Feeny, D., Berkes, F., McCay, B. J. & Acheson, J. M (1990). The Tragedy of the Commons: Twenty-two years later. Human Ecology, 18 (1), 1-19.

Fehér, J., Muerth, M. & Pistocchi, A. (2015). Water models & scenarios inventory for the Danube region. European Commission Joint Research Centre Institute for Environment & Sustainability. Report EUR 27357EN. doi: 10.2788/412928.

Fu, B. P. (1981). On the calculation of the evaporation from land surface (in Chinese), Scientia Atmospherica Sinica, 5, 23–31.

Gassman, P.W., Reyes, M.R., Green, C.H., & Arnold, J.G. (2007). The Soil & Water Assessment Tool: historical development, applications, & future research directions. Trans. ASABE, 50 (4), 1211–1250.

Gassman, P.W., Sadeghi, A.M.,& Srinivasan, R. (2014). Applications of the SWAT Model Special Section: overview & insights. J. Environ. Qual. 43 (1), 1–8. http:// dx.doi.org/10.2134/jeq2013.11.0466.

Geladi, P. & Kowlaski, B., 1986. Partial least squares regression: a tutorial. Anal. Chim. Acta, 35, 1-17.

GLOWA (2011). GLOWA-Danube Projekt. Global Change Atlas Einzugsgebiet Obere Donau, 6th ed.; LMU Munich, Department of Geography: Munich, Germany, 2010. Available online: http://www.glowa-danube.de [accessed on 9 September 2013].

Goldewijk, K., & G. van Drecht (2006). HYDE 3: Current and historical population and land cover. In: Integrated modeling of global environmental change. An overview of IMAGE 2.4.93–111. Netherlands Environmental Assessment Agency (MNP), Bilthoven, The Netherlands.

Goldscheider, N. (2005). Fold structure & underground drainage pattern in the alpine karst system Hochifen-Gottesacker, Eclogae Geol. Helv., 98(1), 1–17, doi:10.1007/s00015-005-1143-z.

Gosain, A.K., Rao, S., Basuray, D. (2006). Climate change impact assessment on hydrology of Indian river basins. Curr. Sci. 90 (3), 346–353.

Green, C. H., M. D. Tomer, M. Di Luzio, & Arnold, J. G. (2006). Hydrologic evaluation of the Soil & Water Assessment Tool for a large tile‐drained watershed in Iowa. Trans. ASABE, 49(2), 413‐422.

Grizzetti, B., Bouraoui, F., & De Marsily, G (2008). Assessing nitrogen pressures on European surface water Glob. Biogeochem. Cycles, 22, GB4023.

Grizzetti, B., Bouraoui, F., Aloe A. (2012). Changes of nitrogen and phosphorus loads to European seas. Global Change Biology, 18, 769–782.

Grizzetti B., Passy P., Billen G., Bouraoui F., Garnier J., & Lassaletta L. (2015). The role of water nitrogen retention in integrated nutrient management: assessment in a large

basin by different modelling approaches. Environmental Research Letters, 10, 065008.

Gudmundsson, L., Wagener, T., Tallaksen, L. M., & Engeland, K. (2012). Evaluation of nine largescale hydrological models with respect to the seasonal runoff climatology in Europe, Water Resour. Res., 48, W11504. doi:10.1029/2011WR010911.

Gupta, H. V., S. Sorooshian, & P. O. Yapo (1999). Status of automatic calibration for hydrologic models: Comparison with multilevel expert calibration. J. Hydrologic Eng., 4(2), 135-143.

Gupta, H. V., Perrin, C., Blöschl, G., Montanari, A., Kumar, R.,Clark, M., & Andréassian, V. (2014). Large-sample hydrology: a need to balance depth with breadth, Hydrol. Earth Syst. Sci., 18, 463–477. doi:10.5194/hess-18-463-2014.

Habersack, H., Jäger, E., & Hauer, C. (2013). The status of the Danube River sediment regime & morphology as a basis for future basin management. International Journal of River Basin Management 11, 153-166.

Hargreaves, G.H. (1975). Moisture availability and crop production. Trans. ASAE, 18,980-984.

Harmel, R.D., P.K. Smith, K.W. Migliaccio, I. Chaubey, K.R. Douglas-Mankin, B. Benham, S. Shukla, R. Muñoz-Carpena, & Robson, B.J. (2014). Evaluating, interpreting, & communicating performance of hydrologic/water quality models considering intended use: A review & recommendations. Environmental Modelling & Software, 57, 40-51.

Hartmann, A., Mudarra, M., Andreo, B., Marín, A., Wagener, T. & Lange, J. (2014). Modeling spatiotemporal impacts of hydroclimatic extremes on groundwater recharge at a Mediterranean karst aquifer. Water Resour. Res., 50(8), 6507–6521. doi:10.1002/2014WR015685.

Hartmann, A., Gleeson, T., Rosolem, R., Pianosi, F., Wada, Y., & Wagener, T. (2015). A simulation model to assess groundwater recharge over Europe's karst regions. Geosci. Model Dev. 8, 1729-1746. doi:10.5194/gmd-8-1729-2015.

Haas, M., Guse, B., Pfannerstill, M., & Fohrer, N. (2015) Detection of dominant nitrate processes in ecohydrological modelling with temporal parameter sensitivity analysis. Ecol. Model., 314, 62–71. doi:10.1016/j.ecolmodel.2015.07.009, 2015.

Henning, C. (2010). fpc: Flexible procedures for clustering. R package version 2.0-3.

Herr, J. W., & Chen, C. W. (2012). WARMF: Model use, calibration, and validation. Trans. ASABE, 55(4), 1385-1394. http://dx.doi.org/10.13031/2013.42249.

Heuvelmans, G., Muys, B. & Feyen, J. (2004). Analysis of the spatial variations in the parameters of the SWAT model with application in Flanders, Northern Belgium. Hydrol. Earth Syst. Sci., 8 (5), 931–939.

Heuvelmans, G., Muys, B., & Feyen, J. (2006). Regionalization of the parameters of a hydrological model: Comparison of linear regression models with artificial neural nets. J. Hydrol., 319, 245–265. doi:10.1016/j.jhydrol.2005.07.030.

Hickey, R. (2000). Slope Angle & Slope Length Solutions for GIS.Cartography, 29 (1), 1–8. doi:10.1080/00690805.2000.9714334.

Holling, C. S. (1978). Adaptive Environmental Assessment & Management. Chichester, U.K.: John Wiley & Sons (reprinted by Blackburn Press in 2005).

Hooghoudt, S.B. (1940). Bijdragen tot de kenins van enige natuurkundige grootheden van de ground. No. 7. Versl. Landbouwk. Onderz (Contributions to the knowledge of some physical constants of the soil. No.7). Report Agric. Resour., 46, 515–707.

Huber, W.C., & Dickinson, R.E. (1988). Storm water management model, version 4: user's manual. U.S. Environmental Protection Agency, Athens, GA.

Hubert, L. & Arabie, P. (1995). Comparing partitions. Journal of Classification,193-2108.

Hunger, M. & Döll, P. (2008). Value of river discharge data for global-scale hydrological modeling. Hydrology & Earth System Sciences, 12, 841–861. doi: 10.5194/hess-12-841-2008.

Hussey, K. & Pittock, J. (2012). The Energy-Water Nexus: Managing the Links between Energy & Water for a Sustainable Future. Ecology & Society, 17(1), 31.

Huyck, A.A.O., Pauwels, V.R.N., & Verhoest, N.E.C. (2005). A base flow separation algorithm based on the linearized Boussinesq equation for complex hillslopes. Water Resources Research, 41. doi: 10.1029/2004WR003789.

ICM, European Topic Centre on Islands, Coastal and Marine waters (ICM) (2011). Waterbase – Urban Waste Water treatment directive. Version 2. Date of delivery: 07/02/2011. Available at: http://www.eea.europa.eu/data-and-maps/data/waterbase-uwwtd-urban-waste-water-treatment-directive-1 [accessed 23/04/2015].

ICPDR (2000). Water quality in the Danube river Basin, 2000 (TNMN-Yearbook), International Commission for the protection of the Danube River, Vienna, Austria, 2000.

ICPDR (2002). Water quality in the Danube river Basin, 2002(TNMN-Yearbook), International Commission for the protection of the Danube River, Vienna, Austria, 2002.

ICPDR (2003). Water quality in the Danube river Basin, 2003(TNMN-Yearbook), International Commission for the protection of the Danube River, Vienna, Austria, 2003.

ICPDR (2004). Water quality in the Danube river Basin, 2004 (TNMN-Yearbook), International Commission for the protection of the Danube River, Vienna, Austria, 2004.

ICPDR (2005). Water quality in the Danube river Basin, 2005 (TNMN-Yearbook), International Commission for the protection of the Danube River, Vienna, Austria, 2005.

ICPDR (2006). Water quality in the Danube river Basin, 2006 (TNMN-Yearbook), International Commission for the protection of the Danube River, Vienna, Austria, 2006.

ICPDR (2007). Water quality in the Danube river Basin, 2007 (TNMN-Yearbook), International Commission for the protection of the Danube River, Vienna, Austria, 2007.

ICPDR (2008). Water quality in the Danube river Basin, 2008 (TNMN-Yearbook), International Commission for the protection of the Danube River, Vienna, Austria, 2008.

ICPDR (2009a). Water quality in the Danube river Basin, 2009 (TNMN-Yearbook), International Commission for the protection of the Danube River, Vienna, Austria, 2009.

ICPDR (2009b). The Danube River Basin District Management Plan. Part A: Basin-wide overview. ICPDR Document IC/151.International Commission for the Protection of the Danube River, Vienna, Austria.

ICPDR (2013). Assessment report on hydropower generation in the Danube basin. http://www.icpdr.org/main/sites/default/files/nodes/documents/hydropower_assessment_report_danube_basin_-_final.pdf (Vienna, 140 pp., accessed 23rd Dec 2014).

Ihaka, R. & Gentleman, R. (1996) A language for data analysis and graphics. Journal of Computational and Graphical Statistics, 5(3), 299-314.

Jaber, F. H., & Shukla, S. (2012). MIKE SHE: Model use, calibration, & validation. Trans. ASABE, 55(4), 1479-1489. http://dx.doi.org/10.13031/2013.42255.

Jayakrishnan, R., Srinivasan, R, Santhi, C. & Arnold, J.G. (2005). Advances in the application of the SWAT model for water resources management. Hydrological Processes,19(3),749-762.

Jiang, J., Shiyu, L., Jiatang, H., & Huang, J. (2014). A modeling approach to evaluating the impacts of policy-induced land management practices on non-point source pollution: A case study of the Liuxi River watershed, China. Agricultural Water Management, 131(C),1-16.

Johnston, R. & Smakhtin, V. (2014). Hydrological modeling of large river basins: how much is enough?. Water Resour. Manag., 28, 2695–2730. doi:10.1007/s11269-014-0637-8.

Jones, J.A., Creed, I.F., Hatcher, K.L., Warren, R.J., Adams, M.B., Benson, M.H., Boose,E., Brown, W.A., Campbell, J.L., Covich,A., Clow, D.W., Dahm, C.N., Elder, K., Ford, C.R., Grimm, N.B., Henshaw, D.L., Larson, K.L., Miles, E.S., Miles, K.M., Sebestyen, S.D., Spargo, A.T., Stone, A.B., Vose, J.M., & Williams, M.W. (2012). Ecosystem Processes and Human Influences Regulate Streamflow Response to Climate Change at Long-Term Ecological Research Sites. BioScience, 62, 390-404.

Kalma, J., McVicar, T., & McCabe, M. (2008). Estimating Land Surface Evaporation: A Review of Methods Using Remotely Sensed Surface Temperature Data. Surveys in Geophysics, 29(4), 421-469, 2008.

Kirchner, J. W. (2006). Getting the right answers for the right reasons: Linking measurements, analyses, & models to advance the science of hydrology. Water Resources Res., 42(3), W03S04. http://dx.doi.org/10.1029/2005WR004362.

Kirkham, D. (1957). Theory of land drainage. In: Drainage of Agricultural Lands Agronomy Monograph No. 7. American Soc. Agron, Madison, WI.

Knapen, A., Poesen, J., Govers, G., Gyssels, G., & Nachtergaele, J. (2007). Resistance of soils to concentrated flow erosion: a review. Earth-Science Reviews, 80, 75-109.

Knithakis, M. (1995). Hydrogeological investigation of Rethymnon region (prefecture of Rethymnon). Institute of Geological & Mineralogical Investigations (IGME), Rethymnon.

Kourgialas, N.N., Karatzas, G.P., & Nikolaidis, N.P. (2010). An integrated framework for the hydrologic simulation of a complex geomorphological river basin. J. Hydrol., 381, 308–321.

Koutroulis, A.G., Tsanis, I.K., & Jacob, D. (2013). Impact of climate change on water resources status: a case study for Crete Island, Greece. Journal of Hydrology, 479, 146-158. http://dx.doi.org/10.1016/j.jhydrol.2012.11.055

Krause, P., Boyle, D.P., & Base, F. (2005). Comparison of different efficiency criteria for hydrological model assessment. Adv. Geosci. 5, 89-97.

Kritsotakis, M. & Tsanis, I.K. (2009). An integrated approach for sustainable water resources management of Messara Basin, Crete, Greece. EWRA, 27/28, 15-30.

Krysanova, V & J.G. Arnold (2008). Advances in ecohydrological modeling with SWAT – a review. Hydrological Sciences Journal, 53 (5), 939-947.

Krysanova, V., & White, M. (2015). Advances in water resources assessment with SWAT - an overview. Hydrological Sciences Journal, 60(5), 771-783. doi: 10.1080/02626667.2015.1029482.

Krysanova, V., & Srinivasan, R. (2015). Assessment of climate & land use change impacts with SWAT. Reg. Environ. Change, 15, 431-434. doi:10.1007/s10113-014-0742-5.

Kumar, R., Livneh, B., & Samaniego, L. (2013). Toward computationally efficient large-scale hydrologic predictions with a multiscale regionalization scheme. Water Resour. Res., 49, 5700–5714. doi:10.1002/wrcr.20431.

Lam, Q.D., Schmalz, B., Fohrer, & N. (2011). The impact of agricultural Best Management Practices on water quality in a North German lowland catchment. Environmental Monitoring Assessment, 183, 351-379. doi: 10.1007/s10661-011-1926-9.

Lambrakis, N., Andreou, A.S., Polydoropoulos, P., & Georgopoulos, E. (2000). Nonlinear analysis and forecasting of a brackish karstic spring. Water Resources Research., 36 (4), 875-884.

Lehner, R. & Döll, P. (2004). Development and validation of a global database of lakes, reservoirs and wetlands. Journal of Hydrology, 296(1-4), 1-22.

Liepolt, R. (1967). Limnologie der Donau. Schweizerbart'sche Verl, Stuttgart, 591.

Lin, S.P., Jing, C.W., Coles, N.A., Chaplot, V., Moore, N.J., & Wu, J.P. (2013). Evaluating DEM source and resolution uncertainties in the soil & water assessment tool. Stoch. Environ. Res. Risk Assess., 27, 209-221.

Lin, S., Jing, C., Chaplot, V., Yu, X., Zhang, Z., Moore, N., & Wu, J. (2010). Effect of DEM resolution on SWAToutputs of runoff, sediment & nutrients. Hydrol.EarthSyst.Sci., 7,4411-4435

Lindenschmidt, K.-E., F. Hattermann, V. Mohaupt, B. Merz, Z. W. Kundzewicz & Bronstert, A. (2007).Large-scale hydrological modelling & the Water Framework Directive & Floods Directive of the European Union. Proceedings of the 10th Workshop on Large-Scale Hydrological Modelling. Advances in Geosciences, 11, -6.

Liu, Y. & Gupta, H.V. (2007). Uncertainty in hydrological modeling: towards an integrated data assimilation framework. Water Resources Research, 43, W07401. doi:10D1029/2006WR005756.

Lloyd, C.E.M., Freer, J.E., Johnes, P.J., Coxon, G., & Collins, A.L. (2015). Discharge and nutrient uncertainty: implications for nutrient flux estimation in small streams. Hydrological Processes http://dx.doi.org/10.1002/hyp.10574.

Lyne, V. & Hollink, M. (1979). Stochastic time-variable rainfall-runoff modelling. I.E. Aust. Natl. Conf. Publ., of Eng. 79, 89-93.

Maetens, W., Vanmaercke, M., Poesen, J., Jankauskas, B., Jankauskiene, G., & Ionita, I. (2012). Effects of land use on annual runoff & soil loss in Europe & the Mediterranean: a meta-analysis of plot data. Progress in Physical Geography, 36, 599-653.

Malagó, A., Pagliero, L., Bouraoui, F., & Franchini, M. (2015a). Comparing calibrated parameter sets of the SWAT model for the Scandinavian and Iberian peninsulas. Hydrological Sciences Journal. Special issue: Evaluation of Water Resources with SWAT. doi: 10.1080/02626667.2014.978332.

Malagó, A., Vigiak, O., Bouraoui, F., & Franchini, M. (2015b). The hillslope Length impact on SWAT streamflow prediction in large Basins. Submitted to Journal of Environmental Informatics in May 2015.

Malagó, A., Efstathiou, D., Bouraoui, F., Nikolaidis, N.P., Franchini, M., Bidoglio, G., & Kritsotakis, M. (2015c). Regional scale hydrologic modeling of a karst-dominant geomorphology: the case study of the island of Crete. Submitted to Journal of Hydrology in April 2015.

Malagó, A., Venohr, M., Gericke, A., Vigiak, O., Bouraoui, F., Grizzetti, B., & Kovacs, A. (2015d). Modelling nutrient pollution in the Danube River Basin: a comparative study

of SWAT, MONERIS & GREEN models. JRC TECHNICAL REPORT. EUR 27676 EN. Scientific & Technical Research series – ISBN 978-92-79-54239-8.

McElroy, A.D., S.Y. Chiu, J.W. Nebgen, A. Aleti, & Bennett, F.W. (1976). Loading Functions for Assessment of Water Pollution from Nonpoint Sources. Environ. Prot. Tech. Serv., EPA 600/2-76-151, Environmental Protection Agency, Washington, D.C.

Me, W., Abell, J. M. & Hamilton, D.P. (2015). Effects of hydrologic conditions on SWAT model performance and parameter sensitivity for a small, mixed land use catchment in New Zealand. Hydrol. Earth Syst. Sci., 19, 4127-4147.

MEDIWAT (2013). State of the art of water resources in Mediterranean islands. Available at: http://www.mediwat.eu/sites/default/files/D.3.1.1.pdf

Meilă, M. (2007). Comparing clusterings- an information based distance. J. Multivariate Anal., 98,873–895. doi:10.1016/j.jmva.2006.11.013.

Mevic, B., & Wehrens, R. (2007). The pls package: principal component analysis & partial least squares regression in R. J. Stat. Software, 18(2), 1-23.

Milly, P. C. D. (1994). Climate, interseasonal storage of soil water, and the annual water balance. Adv. Water Resour., 17, 19–24, doi: 10.1016/0309-1708(94)90020-5.

Moatar, F., & Meybeck, M. (2005). Compared performances of different algorithms for estimating annual nutrients loads discharged by the eutrophic Loire. Hydrol. Process, 19, 429-444.

Monfreda, C., N. Ramankutty, and J. Foley (2008). Farming the planet: 2. Geographic distribution of crop areas, yields, physiological types, and net primary production in the year 2000. Global Biogeochem. Cycles 22:GB1022. doi:10.1029/2007GB002947.

Monteith, J.L. (1965) Evaporation & the Environment. 19th Symposia of the Society for Experimental Biology, 19, 205-234.

Moraetis, D., Efstathiou, D., Stamati, F., Tzoraki, O., Nikolaidis, N.P., Schnoor, J.L., & Vozinakis, K. (2010). High frequency monitoring for the identification of hydrological & biochemical processes in a Mediterranean river basin. J. Hydrol. 389, 127–136.

Moriasi, D. N., Arnold, J. G., & Green, C. H. (2007a). Incorporation of Hooghoudt & Kirkham tile drain equations into SWAT2005. Proc. 4th Intl. SWAT Conf. (139-147). Delft, The Netherlands: UNESCO-IHE.

Moriasi, D. N., Arnold, J. G., Van Liew, M. W., Bingner, R. L., Harmel, R. D., & Veith, T. L. (2007b). Model evaluation guidelines for systematic quantification of accuracy in watershed simulations. Trans. ASABE, 50(3), 885-900. http://dx.doi.org/10.13031/2013.23153.

Moriasi, D., Rossi, C., Arnold, J., & Tomer, M. (2012). Evaluating hydrology of the Soil and Water Assessment Tool (SWAT) with new tile drain equations. J. Soil Water Cons., 67(6), 513-524. http://dx.doi.org/10.2489/jswc.67.6.513.

Moriasi, D. N., Gowda, P. H., Arnold, J. G., Mulla, D. J., Ale, S., & Steiner, J. L. (2013a). Modeling the impact of nitrogen fertilizer application & tile drain configuration on nitrate leaching using SWAT. Agric. Water Mgmt., 130, 36-43. http://dx.doi.org/10.1016/j.agwat.2013.08.003.

Moriasi, D. N., Gowda, P. H., Arnold, J. G., Mulla, D. J., Ale, S., Steiner, J. L., & Tomer, M. D. (2013b). Evaluation of the Hooghoudt & Kirkham tile drain equations in the Soil & Water Assessment Tool to simulate tile flow & nitrate-nitrogen. J. Environ. Qual., 42(6), 1699-1710. http://dx.doi.org/10.2134/jeq2013.01.0018.

Moriasi, D. N., Gitau, M. W., Pai, N., & Daggupati, P. (2015). Hydrologic & water quality models: Performance measures & evaluation criteria. Trans. ASABE, 58(6), 1763-1785. http://dx.doi.org/10.13031/trans.58.10715.

Munoz-Carpena, R., Parsons, J.E., & Wendell, G.J. (1999). Modeling hydrology and sediment transport in vegetative filter strips. Journal of Hydrology ,214, 111‐129.

Neitsch, S.L., Arnold J.G., Kiniry, J.R., & Williams, J.R. (2011). Soil & water assessment Tool Theoretical documentation. Version 2009. Temple, Tex.: USDA-ARS Grassland, Soil & Water Research Laboratory. Availbale at: http://swat.tamu.edu/documentation/. [Accessed 16 Febraury 2013].

Nemes, A., Rawls, W.J. & Pachepsky, Y.A. (2005). Influence of organic matter on the estimation of saturated hydraulic conductivity. SSSA J., 69(4), 1330-1337.

Nester, T., Kirnbauer, R., Gutknecht, D., & Blöschl, G. (2011). Climate & catchment controls on the performance of regional flood simulations. Journal of Hydrology, 402(3–4),340–356. doi:10.1016/j.jhydrol.2011.03.028.

Ntegeka, V., Salamon, P., Gomes, G., Sint, H., Lorini, V. and & Thielen, J. (2013). EFAS-Meteo: A European daily high-resolution gridded meteorological data set for 1990 – 2011.

Nikolaidis, N.P, Bouraoui, F., & Bidoglio, G. (2013). Hydrologic & geochemical modeling of a karstic Mediterranean watershed. Journal of Hydrology 477, 129-138..

Oenema, O., H.P. Witzke, Z. Klimont, J.P. Lesschen, & Velthof, G.L. (2009). Integrated assessment of promising measures to decrease nitrogen losses from agriculture in EU-27. Agric. Ecosyst. Environ., 133:280–288. doi:10.1016/j.agee.2009.04.025.

Ol'dekop, E. M. (1911), On evaporation from the surface of river basins, Trans. Meteorol. Obs., 4, 200.

Olivera, F., M. Valenzuela, R. Srinivasan, J. Choi, H. Cho, S. Koka ,& Agrawal, A. (2006). ArcGIS SWAT: A geodata model and GIS interface for SWAT. J. Am. Water Resour. Assoc., 42(2), 295–309.

Omani, N., Srinivasan, R., & Lee, T. (2012). Estimating Sediment and Nutrient loads of Texas Coastal Watersheds with SWAT. Conference: 2012 Dallas, Texas, July 29 - August 1, 2012. doi: 10.13031/2013.42175.

Ostrom, E., Burger, J., Field, C. B., Norgaard, R. B. & Policansky, D. (1999). Revisiting the Commons: Local Lessons, Global Challenges. Science, 284 (5412), 278-282.

Overgaard, J., Rosbjerg, D., & Butts, M.B. (2006). Land-surface modelling in hydrological perspective –a review. Biogeosciences, 3, 229-241.

Paavola, J. (2008). Governing Atmospheric Sinks: the architecture of entitlements in the global commons. International Journal of the Commons, 2 (2), 313-336.

Pagliero, L., Bouraoui, F., Willems, P., & Diels, J. (2014). Large-Scale Hydrological Simulations Using the Soil Water Assessment Tool, Protocol Development, & Application in the Danube Basin. Journal of Environmental Quality, 43,145–154.

Panagos, P., Van Liedekerke, M., Jones, A., & Montanarella, L. (2012). European soil Data Centre: responses to European policy support and public data requirements. Land Use Policy, 29, 329-338

Panagos, P., Meusburger, K., Van Liedekerke, M., Alewell, C., Hiederer, R., & Montanarella, L. (2014). Assessing soil erosion in Europe based on data collected through a European Network. Soil Science & Plant Nutrition. 60 (1), 15-29.

Panuska, J.C., & Robertson, D.M. (1999). Estimating Phosphorus Concentrations Following Alum Treatment Using Apparent Settling Velocity. Lake and Reservoir Management, 15(1), 28-38. doi: 10.1080/07438149909353949.

Parajka, J., Merz, R., & Blöschl, G. (2007). Uncertainty & multiple objective calibration in regional water balance modeling Case study in 320 Austrian catchments. Hydrol. Process., 21, 435–446.

Pareto, V. (1971). Manual of Political Economy, Translated Ann S. Schwier, edited by A. S. Schwier and A. N. Page, Augustus M. Kelley Publ., New York, NY.

Pechlivanidis, I. G. & Arheimer, B. (2015). Large-scale hydrological modelling by using modified PUB recommendations: the India-HYPE case, Hydrol. Earth Syst. Sci., 19, 4559-4579. doi:10.5194/hess-19-4559-2015.

Peel, M.C., Finlayson, B.L., McMahon, T.A. (2007). Updated world map of the Köppen-Geiger climate classification. Hydrological Earth Systems Sciences, 11, 1633-1644.

Pekárová, P., Onderka, M., Pekár, J., Miklánek, P., Halmová, D., Škoda, P.,& Bačová Mitková, V. (2008). Hydrologic Scenarios for the Danube River at Bratislava. Ostrava, KEY Publishing, http://pavla.pekarova.sk/monografie, 159.

Petrovič, P., Brilly, M. & Šraj, M. (2006). Basin-wide water balance in the Danube river basin, Water Research Institute.

Petrovic, P., Mravcová, K., Holko, L., Kostka, Z., Miklánek, P. (2010). Basin-wide water balance inthe Danube river basin. Hydrological Processes of the Danube River Basin: Perspectives from the Danubian Countries 227.

Pike, J. G. (1964), The estimation of annual runoff from meteorological data in a tropical climate. Journal of Hydrology, 2 (2), 116–123.

Portmann, F., Siebert, S., Bauer, C. & Döll, P. (2008). Global data set of monthly growing areas of 26 irrigated crops. Frankfurt Hydrology Paper 06, Institute of Physical Geography, University of Frankfurt, Frankfurt am Main, Germany.

Priestley, C.H.B., & Taylor, R.J. (1972). On the assessment of surface heat flux and evaporation using large –scale parameters. Mon. Weather Rev. 100, 81-83.

Prosser, I.P., & Rustomji, P. (2000). Sediment transport capacity relations for overland flow. Progress in Physical Geography, 24, 179-193

R Development Core Team (2008). R: A language & environment for statistical computing. R Foundation for Statistical Computing, Vienna, Austria. ISBN 3-900051-07-0, URL http://www.R-project.org.

Rahman, K., Maringanti, C., Beniston, M., Widmer, F., Abbaspour, K.C. & Lehmann, A. (2013). Stream flow Modelling in a Highly Managed Mountainous Glacier Watershed Using SWAT: The Upper Rhone River Watershed Case in Switzerland. Water Resources Management, 27(2), 323-339.

Raje, D., Priya, P., & Krishnan, R. (2013). Macroscale hydrological modelling approach for study of large scale hydrologic impacts under climate change in Indian river basins. Hydrol. Process., 28, 1874–1889. doi:10.1002/hyp.9731.

Rank,D., Papesch, W., Tesch, R. (2005). Runoff characteristics of the upper Danube basin: conclusions from long-term environmental isotope records. Geophysical Research Abstracts 7, 03315.

Rantz, S. E., & others. (1982). Measurement and Computation of Streamflow: Volume 1. Measurement of Stage & Discharge. U.S. Geological Survey Water-Supply Paper 2175.

Ravbar, N., Engelhardt, I. & Goldscheider, N. (2011). Anomalous behaviour of specific electrical conductivity at a karst spring induced by variable catchment boundaries: the case of the Podstenjšek spring, Slovenia. Hydrol. Process., 25(13), 2130–2140. doi:10.1002/hyp.7966.

Rákóczi, L. (2010). Chapter 9: Sediment Regime of the River Danube (1956–1985). In: Brilly, M. (Ed.), Hydrological Processes of the Danube River Basin. Perspectives from the Danubian Countries. Springer. ISBN: 978-90-481-3422-9, pp. 293–304.

RGC (2002). Integrated water resources management on Crete. Study made under the Department of Water Resources Management (in Greek).

Rickson, R.J. (2014). Can control of soil erosion mitigate water pollution by sediments? Science of the Total Environment ,468-469, 1187-1197.

Rossi (2014). Il progetto Sigev.Sistema Idroelettrico Gallo-Engadina-Venosta. Padova, 29/10/2014.

Rouholahnejad, E., Abbaspour, K. C., Srinivasan, R., Bacu, V. & Lehmann, A. (2014). Water resources of the Black Sea Basin at high spatial & temporal resolution. Water Resources Research, 50, 5866-5885.

Rouholahnejad, E., K. C. Abbaspour, R. Srinivasan, V. Bacu, & A. Lehmann (2014), Water resources of the Black Sea Basin at high spatial & temporal resolution. Water Resour. Res., 50, 5866–5885, doi:10.1002/ 2013WR014132.

Rusco, E., Jones, R.J.A., & Bidoglio, G. (2001). Organic matter in the soils of Europe: Present status & future trends, EUR 20556 EN, 14. Office for Official Publications of the European Communities, Luxembourg.

Russev, B. (1979). Saprobiologische Ubersicht der Donau. Special Issue: XIX. Jubilaumstagung Donauforschung, Bulg. Akademie d. Wiss. Sofia, 1979. pp. 32–45.

Santhi, C., J. G. Arnold, J. R. Williams, W. A. Dugas, R. Srinivasan, & Hauck, L. M. (2001). Validation of the SWAT model on a large river basin with point and nonpoint sources. J. American Water Resour. Assoc., 37(5), 1169-1188.

Sawicz, K., Wagener, T., Sivapalan, M., Troch, P. A., & Carrillo, G. (2011). Catchment classification: empirical analysis of hydrologic similarity based on catchment function in the eastern USA. Hydrol. Earth Syst. Sci., 15, 2895–2911. doi:10.5194/hess-15-2895-2011, 2011.

Schneider-Jacoby, M. 2005. The Sava and Drava flood plains: Threatened ecosystems of international importance. Archiv f€ur Hydrobiologie, Supplement 158/1–2: 249–288, Large Rivers.

Scherer,L., Venkatesh, A., Karuppiah, R., & Pfister, S. (2015). Large-Scale Hydrological Modeling for Calculating Water Stress Indices: Implications of Improved Spatiotemporal Resolution, Surface-Groundwater Differentiation, and Uncertainty Characterization. Environ. Sci. Technol., 49 (8), 4971–4979. doi: 10.1021/acs.est.5b00429.

Schiller, H., Miklos, D., & Sass, J. (2010). The Danube River & its Basin physical characteristics, water regime & water balance. In: Brilly, M. (Ed.), Hydrological Processes of the Danube River Basin. Perspectives from the Danubian Countries. Springer. ISBN: 978-90-481-3422-9, 25–78.

Schneider, E. (2002). The ecological functions of the Danubian floodplains & their restoration with special regard to the Lower Danube. Archivfur Hydrobiologie, Supplement 141/1–2, Large Rivers 13/1–2, 129–149.

Schreiber, P. (1904), Uber die Beziehungen zwischen dem Niederschlagund der Wasserfuhrung der Flusse in Mitteleuropa. Z. Meteorol., 21(10), 441– 452.

Schuol, J., Abbaspour, K.C., Srinivasan, R., & Yang, H. (2008). Modelling blue and green water availability in Africa at monthly intervals & subbasin level. Water Resour. Res., 44, W07406. http://dx.doi.org/10.1029/2007WR006609.

Seibert, J., & McDonnell, J. J. (2002), On the dialog between experimentalist & modeler in catchment hydrology: Use of soft data for multicriteria model calibration. Water Resources Research, 38:11, 1241. ISSN: 0043-1397. doi: http://dx.doi.org/10.1029/2001WR000978

Seo, M., H. Yen, M.-K. Kim & Jeong, J. (2014). Transferability of SWAT Models between SWAT2009 & SWAT2012. Journal of Environmental Quality, 43(3), 869–880. doi:10.2134/jeq2013.11.0450.

Shepherd, B., D. Harper, & Millington, A. (1999). Modelling catchment‐scale nutrient transport to watercourses in the U.K. Hydrobiologia 395‐396, 227‐237.

Silgram, M., Anthony,S.G., Collins, A.L., Strőmqvist , J., Bouraoui, F., Schoumans, O., Lo Porto, A., Groenendijk, P., Arheim, B., Mimikouf, M. & Johnssong, H. (2009). Evaluation of diffuse pollution model applications in EUROHARP catchments with limited data. J. Environ. Monit.,11, 554-571.

Sloan, P.G. & Moore, I.D. (1984). Modelling subsurface stormflow on steeply sloping forested watersheds. Water Resources Research, 20(12), 1815-1822.

Sloan, P.G., Moore, I.D., Coltharp, G.B., & Eigel, J.D., 1983. Modelling surface and subsurface stormflow on steeply-sloping forested watersheds. Water Resources Inst., Report 142.Univ. Kentucky, Lexington.

Smart, C.C., & Worthington, S.R.H. (2004). Springs, in: J.Gunn (Eds.), Encyclopedia of caves & Karst Science. Fitzroy Dearbon, London, 699-703.

Smedema, L.K. & Rycroft, D.W. (1983). Land drainage: planning & design of Agricultural Drainage Systems. Batsford, London, 376.

Schmidt, W.F. (2001). Ecology – a true-blue vision for the Danube. Science, 294(5546), 1444–1447.

Sommerwerk, N., Hein, T., Schneider-Jakoby, M., Baumgartner, C., Ostojic´Momir Paunovic,, A., Bloesch, J., Siber, R., & Tockner, K. (2009). The Danube River Basin. CAP3. BOOK. River of Europe.

Sood, A.,& Ritter, W.F. (2010). Evaluation of Best Management Practices in Millsboro Pond Watershed Using Soil & Water Assessment Tool (SWAT) Model. Journal of Water Resource & Protection, 2 (5), 403.

Spruill, C. A., Workman, S. R., & Taraba, J. L. (2000). Simulation of daily & monthly stream discharge from small watersheds using the SWAT model. Trans. ASAE, 43(6), 1431-1439.

Stringer, L. C., Quinn, C. H., Berman, R. J., Le, H. T. V., Msuya, F. E., Orchard, S. E. & Pezzuti, J. C. B. (2014). Combining nexus & resilience thinking in a novel framework to enablemore equitable and just outcomes. Sustainability Research Institute Paper No. 73, Centre for Climate Change Economics & Policy Working Paper No.193.

Sui, Y., and J.R. Frankenberger. 2008. Nitrate loss from subsurface drains in an agricultural watershed using SWAT2005. Trans. ASABE, 51, 1263-1272.doi:10.13031/2013.25243.

Sun, Q., Wennersten, R. & Brandt, N. (2010). Governance of large-scale environmental problems – the case of cilmate change, International Journal of Global Warming, 2 (2), 162-178.

Tasker, G. D., & Driver, N.E. (1988). Nationwide regression models for predicting urban runoff water quality at unmonitored sites. Water Resources Bulletin, 24(5), 1091–1101.

Taylor, R. (1990). Interpretation of the Correlation Coefficient: A Basic Review, Journal of Diagnostic Medical Sonography, January/February, 35-39.

Taylor, K.E. (2001). Summarizing multiple aspects of model performance in a single diagram. Journal of Geophysical Research, 106, 7183–7192.

Thunis, P., Georgieva, E., Galmarini, S. (2011). A procedure for air quality models benchmarking, Version 2. JRC Technical Report.

Tockner, K.,Uehlinger, U., Robinson, C.T. (2009). "Rivers of Europe" Academic Press: London, UK.

Tuppad, P., K. R. Douglas-Mankin, T. Lee, R. Srinivasan, & Arnold, J.G. (2011). Soil & Water Assessment Tool (SWAT) hydrologic/water quality model: Extended capability & wider adoption. Trans. ASABE, 54(5), 1677-1684.

Turc, L. (1954), Water balance in soils, relationship between precipitation, evapotranspiration & runoff (in French), Annales Agronomique, 5, 491–595.

Tzoraki, O., & Nikolaidis, N.P. (2007). A generalized framework for modeling the hydrologic & biogeochemical response of a Mediterranean temporary river basin. J. Hydrol., 346, 112–121.

Ullrich, A., & Volk, M. (2009). Application of the Soil and Water Assessment Tool (SWAT) to predict the impact of alternative management practices on water quality and quantity. Agricultural Water Management 96, 1207-1217.

Ullrich, A. & M. Volk (2010). Influence of different nitrate–N monitoring strategies on load estimation as a base for model calibration and evaluation. Environmental Monitoring and Assessment, 171, 513-527.

Udias, A., Malagó, A., Reynaud, A., Pastori, M., Vigiak, O., & Bouraoui, F. (2015). A new R-SWAT Decision Making Framework for the Spatial Identification of BMP Related to Freshwater Management. In Cau et al. (eds) SWAT 2015 Conference, 24th-26th June 2015, Pula (Italy), Book of Abstracts, pp 35. http://swat.tamu.edu/media/114734/b3-3-vigiak.pdf

USDA Soil Conservation Service (1972). SCS National Engineering Handbook. Section 4, Hydrology. Washington, DC: USDA.

Van Gils (2004). Revised Danube WQ Model: Analysis of available data (deliverable D5.9a). Report prepared in the framework of the daNUbs project (EU 5th Framework Programme), by Delft Hydraulics, Delft. The Netherlands, version 2, January 2004.

van Laerhoven, F. & Ostrom, E. (2007). Traditions & Trends in the Study of the Commons. International Journal of the Commons, 1 (1), 3-28.

Vandecasteele, I., Bianchi, A.,Batistae Silva, F.,Lavalle, C., & Batelaan, O. (2013). Mapping current and future European public water withdrawals and consumptions.

Vardavas, I., Chartzoulakis, K., Papamastorakis, D., Xepapadeas, A., Spanoudaki, K., Zacharioudakis, G., Kritsotakis, M., & Bertaki, M. (2004). Report of Water Resources of Crete, 2004. Technical report.

Venohr, M., Hirt, U., Hofmann, J., Opitz, D., Gericke, A., Wetzig, A., Natho, S., Neumann, F., Hürdler, J., Matranga, M., Mahnkopf, J., Gadegast, M., & Behrendt, H. (2011). Modelling of Nutrient Emissions in River Systems - MONERIS - Methods & Background. International Review of Hydrobiology, 96(5), 435-483.

Venohr, M., Mahnkopf, J., Bremerich, V., Birk, S., Duell, H. and Tockner, K. (2015). Spatial distribution and source apportionment of nutrient emission in Europe, Journal of Environmental Management (Forthcoming).

Verstraeten, W., Veroustraete, F., & Feyen, J. (2008). Assessment of Evapotranspiration & Soil Moisture Content Across Different Scales of Observation. Sensors, 8(1), 70-117.

Vigiak O., Malagó A., Bouraoui F., Vanmaercke M., & Poesen J., 2015a. Adapting SWAT hillslope erosion model to predict sediment concentrations and yields in large Basins. Science of the Total Environment, 538, 855–875.

Vigiak, O., Malagó, A., Bouraoui, F., Pastori, M., Borrelli, P., & Pistocchi, A. (2015b). Impact of current conservation practices on sediment load reduction in the Danube River Basin. In Cau et al. (eds) SWAT 2015 Conference, 24th-26th June 2015, Pula (Italy), Book of Abstracts, pp 66. http://swat.tamu.edu/media/114758/d3-2-vigiak.pdf.

Vogel, B., & Pall, K. (2002). Chapter 3: Nine Geomorphological Danube reaches. In Literáthy, P. Koller-Kreimel, V. Liška, I. Final report of the Joint Danube Survey. International Commission of River Danube Protection, Wien, pp. 22-31.

Vogt, J. et al. (2007). A pan-European River and catchment Database. JRC Reference Reports, EUR 229220 EN.

Wachs, B. (1997). Zustand und Qualitat der Donau. Verantwortung fur eineneuropaischen Strom. Schriftenreihe des Bundesamtes fur Wasserwirtschaft4, 28–51.

Wagener, T., & Gupta, H. V. (2005). Model identification for hydrological forecasting under uncertainty. Stochastic Environmental Research & Risk Assessment 19 (6), 378–387. doi: 10D1007/s00477-005-0006-5.

Walling, D.E., & Collins, A.L. (2008). The catchment sediment budget as a management tool. Environmental Science & Policy, 11, 136-143.

Wang, D., & Wu, L. (2013). Similarity of climate control on base flow & perennial stream density in the Budyko framework. Hydrol. Earth Syst. Sci., 17, 315–324..

Wang, K., Li, Z., & Cribb, M. (2006) Estimation of evaporative fraction from a combination of day and night land surface temperatures and NDVI: A new method to determine the Priestley–Taylor parameter. Remote Sensing of Environment,102(3-4),293-305.

Ward, J.H. (1963). Hierarchical grouping to optimize an objective function. J. Am.Stat. Assoc., 48, 236–244.

Wechsler, S. P. (2007). Uncertainties associated with digital elevation models for hydrologic applications: a review. Hydrol. Earth Syst. Sci., 11, 1481-1500. doi:10.5194/hess-11-1481-2007.

White, M.J., & Arnold, J.G. (2009). Development of a simplistic vegetative filter strip model for sediment & nutrient retention at the field scale. Hydrological Processes, 23(11), 1099-1085. doi:10.1002/hyp.7291.

White, M.J., Santhi, C., Kannan, N., Arnold, J.G., Harmel, D., Norfleet, L., Allen, P., Di Luzio, M,. Wang, X., Atwood, J., Haney, E., & Vaughn Johnson, M. (2014). Nutrient delivery from the Mississippi River to the Gulf of Mexico and effects of cropland conservation. Journal of Soil and Water Conservation, 69 (1), 26-40.

Widén-Nilsson, E., Halldin, S., & Xu, C. (2007). Global water balance modelling with WASMOD-M: Parameter estimation and regionalization. J. Hydrol., 340, 105–118. doi:10.1016/j.jhydrol.2007.04.002.

Wilkinson, S.N., Olley, J.M., Prosser, I.P., & Read, A.M. (2005). Targeting erosion control in large river systems using spatially distributed sediment budgets. In: Geomorphological Processes and Human Impacts in River Basins. International Association of Hydrological Sciences Publication No. 299, IAHS Press, Wallingford, UK, pp. 56–64.

Williams, J.R. (1969). Flood routing with variable travel time or variable storage coefficients. Trans. ASAE, 12(1), 100-103.

Williams, J. R. (1975). Sediment – yield prediction with universal equation using runoff energy factor. Proceedings of the sediment- Yield Workshop, USDA Sedimentation Laboratory, Oxford, Mississippi.

Williams, J. R., Jones, C. A., & Dyke, P. T. (1984). A modeling approach to determining the relationship between erosion & soil productivity. Trans. ASAE, 27(1),129‐144.

Williams, J.R., & Hann, R.W. (1978). Optimal operation of large agricultural watersheds with water quality constraints. Texas Water Resources Institute, Texas A&M University System, Texas, U.S. Technical Report TR96.

Williams, P.W. (2004). Karst Evaluation, in J. Gunn (Eds.), Encyclopedia of caves & Karst Science. Fitzroy Dearbon, London, 475, pp.8.

Winchell, M., Srinivasan, R., Di Luzio, M., & Arnold, J. G. (2013). ArcSWAT Interface For SWAT 2012: User's Guide, Texas Agricultural Experiment Station (Texas) & USDA Agricultural Research Service (Texas), Temple (Texas), March 2013.

Wishmeier, W.H., & Smith, D.D. (1978). Predicting rainfall erosion losses. USDA Agricultural Research Service (USDA-ARS) Handbook 537.

Wold, H. (1966). Nonlinear estimation by iterative least squares procedures. In Research Papers in Statistics, (Edited by F. David), Wiley, New York.

Wooldridge, S.A., & Kalma, J.D. (2001). Regional-scale hydrological modelling using multiple-parameter landscape zones and a quasi-distributed water balance model. Hydrology and Earth System Sciences Discussions, 5 (1), 59-74.

Wu, S., Li, J., & Huang, G.H. (2008). A study on DEM-derived primary topographic attributes for hydrologic applications: Sensitivity to elevation data resolution. Applied Geography, 28, 210-223.

Yang, D., Sun, F., Liu, Z., Cong, Z., Ni, G., and & Lei, Z. (2007). Analyzing spatial and temporal variability of annual water-energy balance in non humid regions of China using the Budyko hypothesis. Water Resour. Res., 43, W04426. doi:10.1029/2006WR005224.

Yang, H., D. Yang, Z. Lei, & F. Sun (2008), New analytical derivation of the mean annual water-energy balance equation. Water Resources Research, 44, W03410, doi:10.1029/2007WR006135.

Yao, C., McCool, D.K., & Elliot, W.J. (2010). DEM Resolution Effects on Hillslope Length andSteepness Estimates for Erosion Modeling Conference Paper. doi: 10.13031/2013.32045. Conference: 2010 Pittsburgh, Pennsylvania, June 20 - June 23, 2010.

Yen, H., Bailey, R. T., Arabi, M., Ahmadi, M., White, M. J., & Arnold, J. G. (2014). The role of interior watershed processes in improving parameter estimation and performance of

watershed models. J. Environ. Qual., 43(5), 1601-1613. http://dx.doi.org/10.2134/jeq2013.03.0110.

Yokoo, Y., Sivapalan, M., & Oki, T. (2008). Investigating the roles of climate seasonality and landscape characteristics on mean annual and monthly water balances, J. Hydrol., 357, 255–269.

Zambrano-Bigiarini, M. (2013). hydroGOF: Goodness-of-fit functions for comparison of simulated and observed hydrological time series, R package version 0.3-7,http://CRAN.R-project.org/package=hydroGOF, last access: 1 October 2013.

Zhang, L., W. R. Dawes, & G. R. Walker (2001), Response of mean annual evapotranspiration to vegetation changes at catchment scale. Water Resources Research, 37(3), 701–708, doi:10.1029/2000WR900325.

Zhang, L., Potter, N., Hickel, K., Zhang, Y., & Shao, Q. (2008). Water balance modeling over variable time scales based on the Budyko framework – Model development and testing. J. Hydrol., 360, 117–131

Zhang, H., Yang, Q., Li, R., Liu, Q., Moore, D., He, P., Ritsema, C.J., & Geissen, V. (2013). Extension of a GIS procedure for calculating the RUSLE equation LS factor. Computers & Geosciences, 52, 177-188.

Zhang, P., Liu, R. Bao, Y., Wang, J., Yu, W., & Shen., Z. (2014). Uncertainty of SWAT model at different DEM resolutions in a large mountainous watershed. Water Research, 53, 132-144.

# Acknowledgements

I would like to express my sincere gratitude to the people who have supported me during my PhD study. My deepest gratitude goes to my supervisor Faycal Bouraoui for his excellent supervision, contribution and support throughout the research. I thank also my Professor Marco Franchini for his valuable support and scientific advice.

Many thanks to the JRC (Joint Research Centre) of the European Commission for providing the financial support which made my PhD work possible, as well as for the possibility to work in enriching multi-cultural and multi-lingual work environment.